

# Charge Separation in Ligand Design

## A Dianionic $C_3$ -Symmetric Scorpionate That Supports $Fe^{IV}$ and $Si^{II}$ Centers

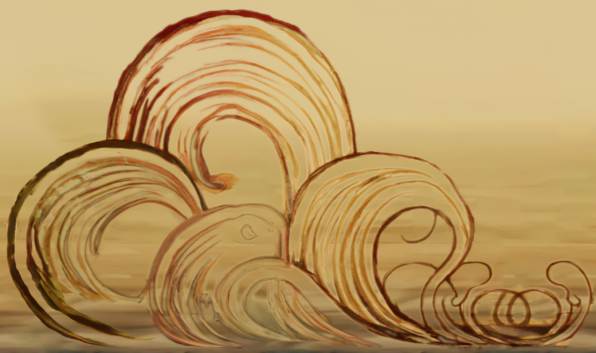
Charge Separation in Ligand Design

Serhii Tretiakov

2023



Serhii Tretiakov



# **Charge Separation in Ligand Design**

A Dianionic  $C_3$ -Symmetric Scorpionate  
That Supports  $Fe^{IV}$  and  $Si^{II}$  Centers

# **Ladingscheiding in Ligandontwerp**

$Fe^{IV}$  en  $Si^{II}$  Verbindingen Afgeleid van  
een Dianionisch  $C_3$ -Symmetrisch Scorpionaat Ligand

(met een samenvatting in het Nederlands)

## **Proefschrift**

ter verkrijging van de graad van doctor aan de Universiteit Utrecht op gezag van de rector magnificus, prof. dr. H. R. B. M. Kummeling, ingevolge het besluit van het college voor promoties in het openbaar te verdedigen op 04 december 2023 des middags te 4.15 uur

door

**Serhii Volodymyrovych Tretiakov**

geboren op 8 juni 1990 te Dnjepropetrovsk, Oekraïne

**Promotor:**

prof. dr. Robertus J. M. Klein Gebbink

**Copromotor:**

dr. Marc-Etienne Moret

The work described in this thesis was financially supported by the European Union Horizon 2020 funding program under the “NoNoMeCat” Marie Skłodowska-Curie ITN Network grant agreement (675020-MSCA-ITN-2015-ETN).

# Charge Separation in Ligand Design

A Dianionic  $C_3$ -Symmetric Scorpionate  
That Supports  $Fe^{IV}$  and  $Si^{II}$  Centers

*Dedicated to my mother  
and grandfather*

Tretiakov, Serhii Volodymyrovych

Charge Separation in Ligand Design: A Dianionic C<sub>3</sub>-Symmetric Scorpionate That Supports Fe<sup>IV</sup> and Si<sup>II</sup> Centers

ISBN: 978-90-39375-98-3

DOI: 10.33540/1917

Elements of cover design were generated by Midjourney to the prompt “charge separation in chemistry” and were further refined and connected by Serhii Tretiakov using DALL·E 2 and Adobe Photoshop

Print: Ridderprint | [www.ridderprint.nl](http://www.ridderprint.nl)

The work described in this doctoral thesis was carried out in the Organic Chemistry and Catalysis (OCC) group, Institute for Sustainable & Circular Chemistry (ISCC), Faculty of Science, Utrecht University, The Netherlands.

*Locked out of the trusted orbits' path,  
Unmatched in prayer books of perfect order –  
Deprived of earth we'll be at earthly border  
By earthly servants of the earthly math.*

*Insane's our incense, and our ship's a lath,  
Like bees gone stray, we seek our swarm by odor.  
We passed between our warder and rewarder,  
And city fire fills our sail with laugh.*

*For breath of storms' mysterious appeal,  
By scrolls of trails, by tangled road turns  
We hasten, and our way is hard and stern.*

*So let the thunders ring the clouds' peal,  
Let doubts swirl embittering and tough!  
The truth of dreams escapes the earthly wrath.*

Alex Romanovsky, translator  
"Corona Astralis", Sonnet II  
By Maximilian Voloshin, 1909



# Contents

<b>Preface: Aim and Scope of the Thesis</b>	<b>11</b>
<b>1. Charge Separation in Chemistry</b>	<b>15</b>
1.1 Introduction	16
1.2 Electrostatic reactivity control	17
1.2.1 Electric fields in enzymes	17
1.2.2 Charges in coordination chemistry and catalysis	19
1.2.2.1 Control of electronic structure	22
1.2.2.2 Homogeneous catalysis and bond activation	24
1.2.2.3 Electrochemical applications	26
1.3 Charge frustration	27
1.3.1 Elementenes: 1,1-zwitterions	28
1.3.2 Ylides: 1,2-zwitterions	29
1.3.3 Between 1,2- and 1,3-zwitterions: 1,3-dipoles	33
1.3.4 Geminal charge separation: 1,3-zwitterions	37
1.3.5 Remote zwitterions	40
1.3.5.1 Organic zwitterions	41
1.3.5.2 Coordination compounds	42
1.3.5.3 Naked tetrel anions	44
1.4 Concluding remarks	47
1.5 References	48
<b>2. A Dianionic C<sub>3</sub>-Symmetric Scorpionate: Synthesis and Coordination Chemistry</b>	<b>69</b>
2.1 Introduction	71
2.2 Results and discussion	73
2.2.1 Ligand synthesis	73
2.2.2 Coordination chemistry of TSMP <sup>2-</sup>	76
2.2.3 Redox behavior of the metal complexes	82
2.3 Conclusions and outlook	83
2.4 Author contributions and acknowledgements	84
2.5 Experimental methods	85
2.5.1 General remarks	85
2.5.2 Synthesis and characterization	86



---

2.5.2.1 Synthesis of TSMPK <sub>2</sub> (1)	86
2.5.2.2 Metal complexes	89
2.5.3 Additional experiments	94
2.5.4 X-ray crystal structure determinations	95
2.6 References	103
<b>3. Homoleptic Fe<sup>III</sup> and Fe<sup>IV</sup> complexes of a Dianionic C<sub>3</sub>-Symmetric Scorpionate</b>	<b>109</b>
3.1 Introduction	111
3.2 Synthesis and characterization	112
3.3 Electrochemical behavior	116
3.4 Spin crossover in the [(TSMP) <sub>2</sub> Fe <sup>III</sup> ] <sup>-</sup> complex (3)	118
3.5 Electronic structure of [(TSMP) <sub>2</sub> Fe <sup>IV</sup> ] (4)	122
3.5.1 Cyclic voltammetry	122
3.5.2 <sup>57</sup> Fe Mössbauer spectroscopy	124
3.5.3 XAS spectroscopy	124
3.5.4 SQUID magnetometry	125
3.5.5 THz-EPR spectroscopy	126
3.5.6 DFT calculations	128
3.5.7 CASSCF calculations	130
3.5.8 Paramagnetic <sup>1</sup> H NMR spectroscopy	131
3.5.9 Optical spectroscopy and TDDFT	133
3.6 Conclusions	134
3.7 Author contributions and acknowledgements	135
3.8 Experimental and computational methods	137
3.8.1 General remarks	137
3.8.2 Synthesis and basic characterization	139
3.8.2.1 Metal complexes	139
3.8.2.2 Deuterium-labeled ligand	145
3.8.2.3 Deuterium-labeled complexes	147
3.8.2.4 Additional experiments	149
3.8.3 X-ray crystal structure determinations	149
3.8.4 Computational details	155
3.9 References	157
<b>4. Strain-Modulated Reactivity: an Acidic Silane</b>	<b>163</b>
4.1 Introduction	165

---

4.2 Synthesis and characterization of the acid-base pair	166
4.3 Experimental solution $pK_a$ determination	169
4.4 Computational analysis of acidity of [TSMPSiH] <sup>+</sup> ( <b>2</b> )	171
4.4.1 Factors contributing to the acidity	171
4.4.2 On the role of strain	174
4.5 Reactivity of the zwitterionic silanide TSMPSi ( <b>1</b> )	176
4.6 Reactivity of the cationic silane [TSMPSiH] <sup>+</sup> ( <b>2</b> )	178
4.7 Fluxionality of the THF ring-opening product <b>11a/b</b>	182
4.7.1 Cage opening	182
4.7.2 Positional exchange	186
4.8 Conclusions and outlook	193
4.9 Author contributions and acknowledgements	194
4.10 Experimental and computational methods	195
4.10.1 General remarks	195
4.10.2 Synthesis and characterization	196
4.10.2.1 Silicon and germanium compounds	196
4.10.2.2 Fluorenes	202
4.10.2.3 Additional experiments	206
4.10.3 X-ray crystal structure determinations	207
4.10.4 Computational studies	215
4.11 References	217
<b>5. Outlook</b>	<b>223</b>
5.1 Concluding remarks and perspective	224
5.2 References	229
<b>Summary</b>	<b>231</b>
<b>Samenvatting</b>	<b>239</b>
<b>Acknowledgements</b>	<b>249</b>
<b>About the author</b>	<b>253</b>
<b>Appendices</b>	<b>255</b>
<b>A:</b> Supporting information to Chapter 2	257
<b>B:</b> Supporting information to Chapter 3	263
<b>C:</b> Supporting information to Chapter 4	309



# *Preface*

---

## **Aim and Scope of the Thesis**

---

As chemists, we are bound by the laws of the universe in which we exist. We do not invent new reactions, we discover them. We cannot force atoms into molecules unless they are capable of binding to one another in the first place. Rather, we find the starting points and conditions that allow things to naturally fall into a desired state – these are the only two degrees of freedom a synthetic chemist can actually use. Despite how claustrophobia-inducing it may sound, varying just these two parameters gives rise to a wealth of fields, spanning from organic, organometallic and main-group chemistry/catalysis to electro-, mechano- and photochemistry among others. All of them are concerned with harnessing chemical reactivity by means of understanding and using this knowledge to achieve a desired outcome. Ultimate reactivity control is the holy grail of synthetic chemistry, especially in the face of the ongoing environmental crisis and the quest for inexpensive and sustainable transformations.

Aside from varying conditions, chemists have come up with a number of clever ways to steer reactivity in a preferred direction. Among these are the use of elements with an incomplete electron shell, such as transition metals or main-group compounds (often in unusual oxidation states), introducing strain or charge separation (CS). The latter approach remains largely underutilised and, therefore, was chosen as the central point of this thesis. CS occurs when the nuclear electrostatic potential is out of balance with that of the surrounding electrons. The latter can be a consequence of an electron gain or loss, i.e. ionization, or breaking of the spherical symmetry of electronic states, e.g. covalent bond formation, where the bonding electrons localize in the interatomic space.

As such, some extent of CS is present in every molecule. However, large CS can be implemented by design in molecules that bear unquenched charges of opposite sign, i.e. zwitterions.

The aim of the current work is to develop a ligand with built-in CS that allows the study of its effects in the contexts of both transition metal and main-group chemistry. We introduce a novel 1,3-zwitterionic scaffold, tris-skatylmethylphosphonium (TSMP<sup>2-</sup>), isolated as a potassium salt TSMPK<sub>2</sub> (*Figure 0.1*), which is also the first known C<sub>3</sub>-symmetric dianionic homoscorpionate capable of metal exchange.

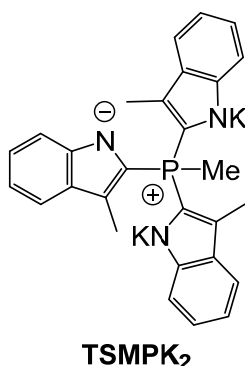


*Figure 0.1.* 1,3-Zwitterionic TSMPK<sub>2</sub> salt.

**Chapter 1** of this thesis discusses the mechanisms through which CS may affect reactivity. Charges give rise to oriented electric fields, which may polarize the neighbouring electrons, providing a degree of control that is complementary to the electronic and ligand field effects. Additionally, CS in zwitterions stores energy, which can be used for chemical transformations or to achieve designer-made HOMO-LUMO gaps. Finally, having opposite charges in the second coordination sphere of otherwise ionic catalytically-active coordination compounds obviates the need for counter-ions, greatly simplifying the association behavior in solution and allowing for more systematic and straightforward catalyst design.

**Chapter 2** describes the synthesis of the TSMPK<sub>2</sub> salt (*Figure 0.1*) followed by its structural characterization. Its complexation with Fe(II), Ni(II) and Cu(I) centers leads to coordination compounds of various topology depending on the metal, stoichiometry and the presence of co-ligands. In particular, we show that the bis-ligated Fe(II) complex, [(TSMP)<sub>2</sub>Fe<sup>II</sup>]<sub>2</sub>K<sub>2</sub>, features a tetrahedral geometry instead of the expected octahedral one, whereas replacement of one or both TSMP<sup>2-</sup> ligands for the equivalent number of pyridines yields an octahedral metal center. This highlights the likely influence of charge repulsion in the first ligand sphere on coordination geometry.

**Chapter 3** continues with the [(TSMP)<sub>2</sub>Fe<sup>II</sup>]<sub>2</sub>K<sub>2</sub> complex, exploring its one- and two-electron oxidations to the corresponding anionic Fe(III) and neutral Fe(IV) species,

which demonstrates the ability of the TSMP<sup>2-</sup> scaffold to support catalytically-relevant high oxidation states. We then extensively study the electronic structure of the [(TSMP)<sub>2</sub>Fe<sup>IV</sup>]<sup>0</sup> complex using a combination of experimental and computational techniques, briefly touching upon the ligand field stabilization by the positive phosphonium atoms.

**Chapter 4** explores applications of the TSMP<sup>2-</sup> scaffold to main-group chemistry. There, we exchange the potassium cations of TSMPPK<sub>2</sub> for a silicon from an NHC-stabilized Si(II) precursor. This reaction yields a stable and isolable, C<sub>3</sub>-symmetric, zwitterionic, naked silanide, TSMPSi. Its nucleophilicity, basicity and ability to coordinate to metal centers are greatly reduced, in particular due to electrostatic stabilization by the positive phosphonium charge. Specifically, it is so weakly basic that the conjugate silane, [TSMPSiH]<sup>+</sup>, has a solution acidity higher than those of phenol and benzoic acid. We study the electronic origins of this unusual acidity and connect it to strain as well as the presence of a linker-separated positive charge. At last, TSMPSi undergoes reactions connecting the Si(II) and Si(IV) oxidation states under mild conditions, which presents intriguing similarities with transition-metal-mediated processes.

Finally, **Chapter 5** – the outlook – reflects on the work done in the previous experimental chapters, while also providing suggestions on possible improvements and future developments.



# Chapter 1

---

## Charge Separation in Chemistry

---

### Abstract

Faced with new global challenges, mankind experiences an unprecedented pressure for developing more sustainable and waste-effective chemical processes, which requires a high degree of reactivity control. In this respect, control *via* charge separation is often overlooked. Charges generate static electric fields that polarize the neighboring electrons and, if placed strategically, control reactivity in a manner that is complementary to electronic and ligand field effects. Furthermore, charge separation in zwitterions stores energy, which can be harnessed for chemical transformations and to endow the molecules with designer-made HOMO-LUMO gaps relevant for photovoltaics, molecular switching and sensing. Finally, the presence of opposite charges in the second coordination sphere of otherwise ionic coordination compounds obviates the need for counterions, greatly simplifying association behavior in solution and allowing for more systematic and straightforward catalyst design.



## **1.1 Introduction**

In the face of climate change and growing world population, mankind is confronted with unprecedented pressure to build a more sustainable and less wasteful society, which involves overcoming a number of humanitarian and environmental challenges. The ever-increasing demand for circular and energy-efficient chemical processes is now higher than ever. To be feasible on a large scale, processes must either rely on low-toxicity and abundant elements such as base metals and main-group elements, or make extremely efficient use of scarce elements such as noble metals. For developing either of these options, one needs a high extent of reactivity control. One underexplored strategy for achieving this goal is charge separation, which is the focus of this introductory chapter.

Charge separation is ubiquitous in chemistry: it emerges whenever the nuclear electrostatic potential is out of balance with that of the surrounding electrons. The latter can be a consequence of an electron gain or loss, i.e. ionization, or breaking of the spherical symmetry of electronic states, e.g. covalent bond formation, where the bonding electrons localize in the interatomic space. These two situations are not mutually exclusive with their combination giving rise to zwitterions. In either case, charge separation generates an electric field that may affect the neighboring electrons through polarization, altering global molecular properties and reactivity. In the context of coordination compounds this provides a means to control electronic structure that is complementary to ligand field effects. Charge separation also imposes a significant potential energy penalty, which is often compensated by the gain from electron pairing. In the event when this is insufficient or even impossible, like in charge-frustrated zwitterions, the energy surplus can be harnessed for chemical transformations or other applications such as photovoltaics, switching and sensing.

This introductory chapter is divided into two parts, the first of which is dedicated to the influence of electric fields on electronic structure and reactivity in both natural and synthetic systems. We specifically dwell on enzymatic catalysis as it illustrates in full an almost untapped potential of electrostatic reactivity control. The second part of this chapter deals with charge-frustrated zwitterions, where the charges cannot quench one another by simple functional group migration. We further show how the energy of this separation can be converted into chemical reactivity and unusual physical properties. Aside from this, we discuss how strategic placement of charges affects ion pairing and aggregation behavior in solution, thus opening new avenues for fine reactivity control.

## 1.2 Electrostatic reactivity control

Electric fields (EFs) underlie all chemical reactions and interact with dipoles and permanent charges in reactants, transition states, and products. The relevance of electrostatic reactivity control for enzymatic catalysis had been highlighted over forty years ago,<sup>1,2</sup> however since then the field was remaining virtually dormant with the EFs attracting attention for rational reaction design only recently.<sup>3-7</sup>

According to valence-bond calculations, directional EFs can modify the ionicity of a reactant up to the point of reversing bond polarity or heterolytic dissociation. If the system is already (partly) ionic, one can stabilize it by applying an EF whose polarity complements the ionic dipole.<sup>2,5</sup> Therefore, most electrostatic effects can be comprehended as field-induced stabilization of ionic structures. Additionally, directional EFs are capable of (de)stabilizing specific molecular orbitals<sup>8,9</sup> or the entire valence manifolds in general,<sup>10</sup> which may alter redox potentials and reactivity patterns.

Moderate EFs applied with specific polarity along the axis wherein the electronic reorganization occurs (the so-called “reaction axis”) can perturb the electronic wave function towards or away from the desired transition state, thus catalyzing or inhibiting the transformation.<sup>5,11</sup> This catalysis can even be accompanied by the change of a reaction pathway in order to accommodate more ionic transition states – this phenomenon was dubbed “mechanistic crossover”.<sup>4,5,12,13</sup> Aside from this, applying off-reaction-axis EFs can alter selectivity by deforming transition states and allowing otherwise forbidden orbital mixing. It is expected that two-directional fields may control both reactivity and selectivity.<sup>4</sup>

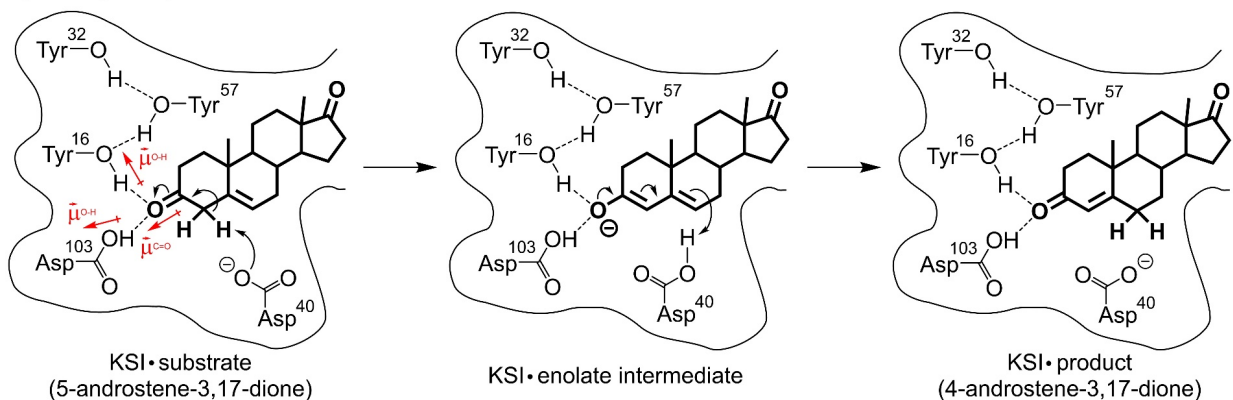
In this section, which is not meant to be exhaustive, we review some of the existing evidence of electrostatic control in enzymes as well as how this knowledge was transferred to and applied in the domains of coordination chemistry and catalysis.

### 1.2.1 Electric fields in enzymes

Along with strain and population of near-transition-state conformations,<sup>14</sup> oriented EFs are proposed to significantly contribute to the phenomenal efficiency of enzymes: while only a handful of amino acids at an active site actually participate in a chemical reaction, the rest of the peptide macromolecule is thought to generate a highly-specific EF that complements the charge distribution of the transition state.<sup>15</sup> This phenomenon was dubbed electrostatic preorganization<sup>2,16</sup> and can be regarded as “specific solvation” of the transition state within the structured enzyme cavity, lowering the activation free energy more efficiently than less organized polar solvents like water.<sup>1</sup> Empirical valence

bond calculations show that the rate enhancement for enzymatic reactions with significantly ionic transition states is proportional to the degree of electrostatic stabilization of an ionic resonance within the binding pocket; covalent transition states exhibit little to no EF dependence.<sup>2,17</sup>

**A) Catalysis by KSI:**



**B) Inhibited KSI:**

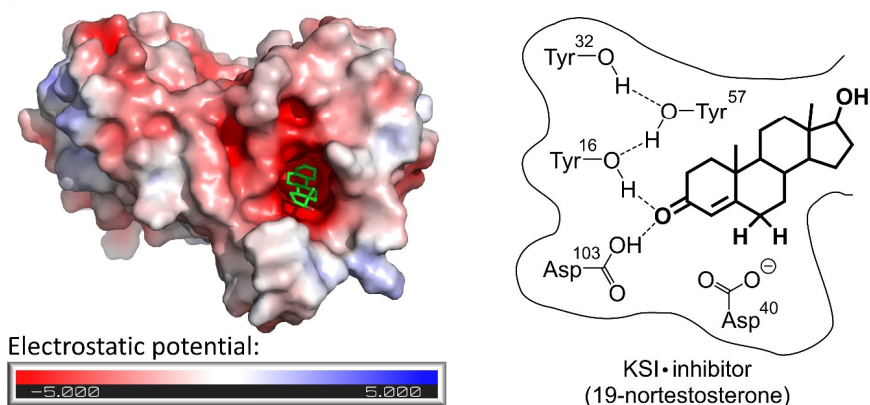


*Figure 1.1. A:* Catalysis by KSI.<sup>18</sup> Note that the dipole moment of the substrate increases upon enolate formation, which is facilitated by the dipoles in the KSI-substrate complex; *B:*  $\pm 5$  kT/e electrostatic potential surface in the crystal structure of wild-type KSI inhibited by 19-nortestosterone (PDB accession code: 5KP4).<sup>18</sup> The surface was generated using PyMOL<sup>19</sup> and APBS software.<sup>20</sup>

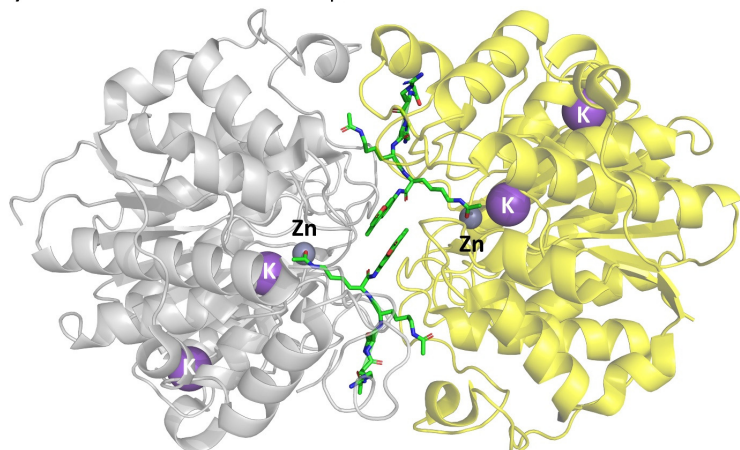
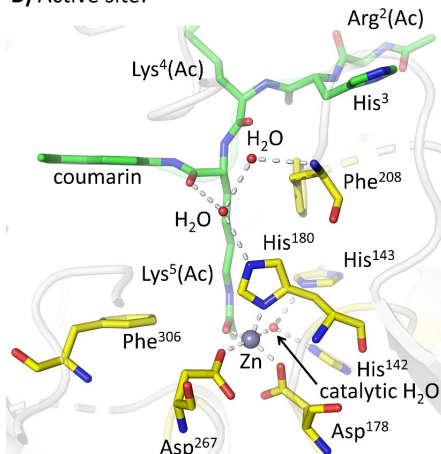
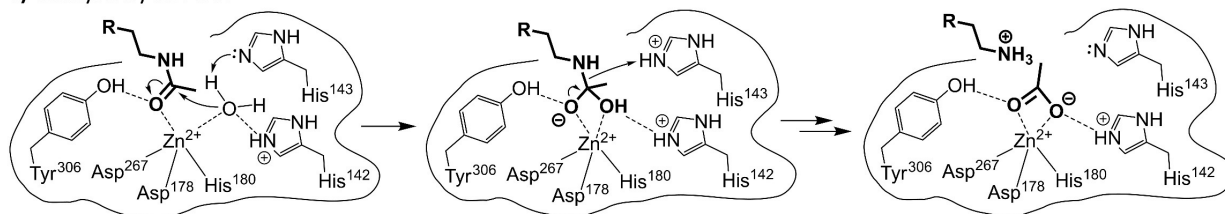
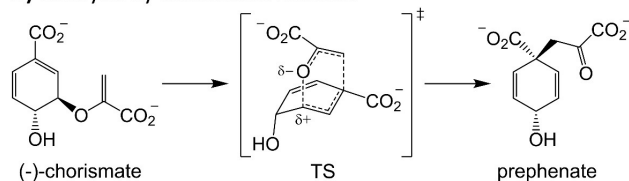
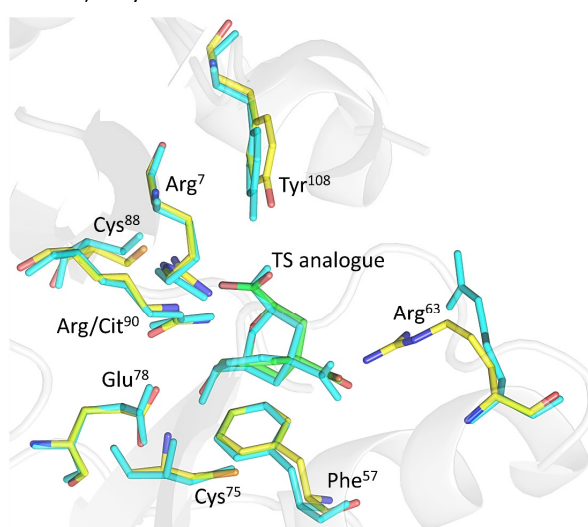
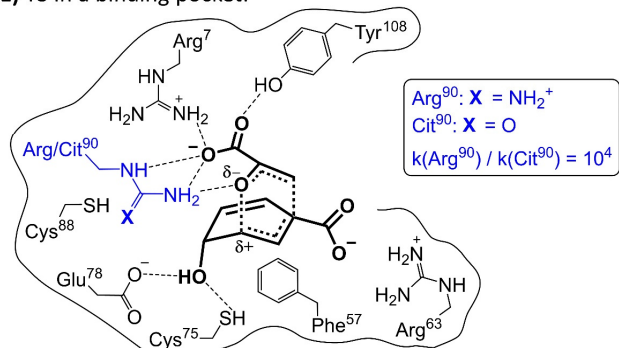
The presence of oriented EFs at enzymatic binding sites was experimentally confirmed by vibrational Stark spectroscopy. This technique gauges EFs by using a field-dependent equilibrium interatomic distance in a polar functional group (a probe), which is then characterized by IR absorption.<sup>21</sup> By using carbonyl- and nitrile-containing unnatural amino acids as probes in ribonuclease S<sup>22,23</sup> and dihydrofolate reductase,<sup>24</sup> respectively, it was possible to detect the presence of moderate electric fields in and around enzymatic binding pockets. Furthermore, the use of a carbonyl-containing inhibitor (19-nortestosterone) as a probe for ketosteroid isomerase (KSI; *Figure 1.1A*) and its mutants<sup>18,25</sup> showed an extremely strong EF within the binding

pocket (*Figure 1.1B*), whose strength linearly correlates with the activation free energy for the enolate formation step, directly proving electrostatic rate enhancement. One striking detail is that in all cases the IR absorption bands of an enzyme-bound probe were considerably narrower than those measured in water.<sup>21</sup> This suggests that a substrate is locked firmly inside the binding pocket and experiences a significantly smaller range of electric fields when introduced into the protein, highlighting the significance of the EF directionality.

Similarly, deliberate interference with enzymatic EFs is detrimental to the catalytic function up to the point of complete deactivation. To exemplify, histone deacetylase 8 (HDAC8) is a zinc-dependent enzyme that catalyzes deacetylation of lysine residues of the core histones and plays an important role in cell cycle progression and developmental processes (*Figure 1.2A-C*).<sup>32</sup> The crystal structure of the active site of HDAC8 reveals a K<sup>+</sup> cation buried into the interior of the protein approximately 7 Å away from the Zn center involved in the actual deacetylation.<sup>26,33</sup> While the role of the cation is not completely understood, computational studies demonstrate that its removal deactivates the enzyme with general retention of a hydrogen bond network within the active site,<sup>34</sup> therefore suggesting that the K<sup>+</sup> cation plays a part in electrostatic preorganization.<sup>15</sup> Another example is chorismate mutase responsible for Claisen rearrangement of chorismate to prephenate in the shikimate pathway of phenylalanine and tyrosine biosynthesis (*Figure 1.2D-F*). Replacement of a cationic arginine residue in the active site for an isostructural but neutral citrulline retains the substrate orientation and general geometry of the original enzyme while incurring a significant penalty in the catalytic activity.<sup>28,29</sup>

### 1.2.2 Charges in coordination chemistry and catalysis

Despite much relevance for enzymatic catalysis, EFs are often overlooked as a tool for rational reactivity control. This is somewhat surprising in view of the fact that biological systems have been a major source of inspiration for synthetic design within the past decades.<sup>14</sup> It is more than likely that, not by design but by chance, there already exists a plethora of synthetic reactions taking advantage of electrostatic effects in one way or another. However, given the difficulty of separating through-space Coulombic and through-bond covalent interactions (which also have an electrostatic component), identifying EF effects and keeping a balanced discussion about their magnitude is often very challenging.<sup>35,36</sup> Such analysis is also complicated by the fact that formal atomic charges are not physical, representing only one resonance structure, while the real molecules “store” charges in fractions distributed among several atoms or the entire functional groups. In other words, there is no fundamental difference between formal

**A) Dimeric HDAC8-substrate complex:****B) Active site:****C) Catalysis by HDAC8:****D) Catalysis by chorismate mutase:****F) Inhibited wild-type (Arg<sup>90</sup>, cyan) vs. mutated (Cit<sup>90</sup>, multi-colored) enzyme:****E) TS in a binding pocket:**

**Figure 1.2.** **A:** The crystal structure of a dimeric HDAC8-substrate complex (PDB accession code: 2V5W).<sup>26</sup> The substrate corresponds to the acetylated peptide Arg(Ac)-His-Lys(Ac)-Lys(Ac) with a coumarin group at the carbonyl terminus. The enzyme was mutated (Tyr<sup>306</sup> to Phe<sup>306</sup>) to inhibit the transformation; **B:** The corresponding active site;<sup>26</sup> **C:** Catalysis by the wild-type HDAC8;<sup>27</sup> **D:** Catalysis by chorismate mutase;<sup>28</sup> **E:** The corresponding transition state in a binding pocket;<sup>29</sup> **F:** Superimposed crystal structures of an active site in the wild-type (Arg<sup>90</sup>) and mutated (Arg<sup>90</sup>Cit) enzymes inhibited by a transition state analogue (PDB accession codes: 2CHT and 3ZP4, respectively).<sup>30,31</sup> The crystallographic images were generated using PyMOL software.<sup>19</sup>

charges in molecular ions and partial charges in neutral molecules, and either can exert electrostatic control. More so, unlike electrostatic potential, the atomic charges are not quantum observables, meaning that they must be quantified through theoretical means. The problem lies in the fact that there are multiple schemes for doing so, which can give different results,<sup>37</sup> hindering quantitatively relating atomic charges to the experimental observations. In the end, a researcher is often left with molecular electrostatic potential maps which, in the best case, provide qualitative conclusions for the systems where the charges are so high that they dominate the reactivity pattern. It goes without saying that identifying subtle electrostatic effects in this way is nearly impossible. Still, there exist computational methods aimed at modelling chemical reactions in the presence of oriented electric fields,<sup>1,2,4,5,7,38</sup> allowing to determine possible electrostatic effects and correlate them to the experiment.

In view of the above and for the sake of simplicity, we choose to limit the discussion of synthetic applications of EFs to the systems where electrostatic control is implemented by design or the EF influence is identified and discussed in detail. Aside from the biochemical field (*vide supra*), the relevant literature examples are mostly confined to the following: (i) the use of bulk homogenous fields from charged surfaces and STM tips;<sup>3,39-41</sup> (ii) guest-charged host complexes to mimic EFs in enzymatic bonding pockets: mainly encapsulation with supramolecular cages<sup>42-51</sup> and zeolites;<sup>51,52</sup> (iii) electrostatic stabilization of *in situ*-generated radicals;<sup>41,53-56</sup> (iv) charge-assisted pre-organization of reaction intermediates/transition states for selectivity control;<sup>57-61</sup> (v) counterion effects on reaction selectivity/discrimination between alternative transition states;<sup>62-69</sup> and (vi) the influence of charges on electronic structure, reaction rates and catalytic activity.

The last group of applications forms the scope of the present thesis and is, therefore, discussed in more detail below. In it, one can differentiate the systems where a charged group is the only EF source, and the systems where the spectator charge is complemented by an associated ion in the vicinity. In such cases, it is the ion-counterion dipole that exerts electrostatic control. Nevertheless, this division is rather vague since in many studies the influence of ion association is not explored specifically. It is worth separately mentioning the systems that do not include a charged group *per se* but instead contain a crown ether fragment that can complex a metal cation thus creating a local EF source. This approach allows to take advantage of ionic charges by attenuating their solvation which would otherwise weaken Coulombic interactions.

### 1.2.2.1 Control of electronic structure

When applied to coordination compounds, charges can provide a degree of control over the electronic structure that is complementary to ligand field effects. This is well-exemplified by a family of salen-based complexes of the Yang group (*Figure 1.3A*), where the authors varied the  $M^{n+}$  cation within the crown cavity thereby adjusting the Co(II)/Co(I) redox potential by up to 0.3 V.<sup>70</sup> Conveniently, the ligand contains two imine ( $-C=N-$ ) functionalities, allowing to gauge the EF around the Co(II) center using vibrational Stark spectroscopy (see *Section 1.2.1*). Measured frequencies indicate the expected: smaller ions with higher charge result in more intense electric fields, which correlates with the observed redox potentials. At the same time, UV/Vis spectra show little to no change in the Co(II) ligand field regardless of  $M^{n+}$ , leading one to conclude that the difference in redox potentials is mostly due to non-specific electrostatic stabilization of the Co(II)-based orbitals rather than Lewis acidity of  $M^{n+}$ . Later on, the same group discussed electrostatic effects in similar complexes of the Fe(II) and Ni(II) ions.<sup>10</sup> In a related study on Fe(III) complexes with a diamine pyridine pincer ligand decorated with a crown-ether pocket, the authors showed that the ions with a higher charge density stabilize both the occupied and unoccupied metal-centered  $d$ -orbitals. However, the extent of stabilization for the lowest unoccupied orbitals is somewhat higher, facilitating Fe(III) to Fe(II) reduction.<sup>71</sup> Impressively, providing other redox-innocent ligands with a similar crown-ether pocket proved to have a beneficial effect on aerobic Fe(III)-catalyzed oxidation<sup>72</sup> and stabilized Mn(VI) nitrides by disfavoring  $N_2$  formation.<sup>73</sup> On a related note, crown ether-encapsulated  $Na^+$  cations were also used for redox fine-tuning of ferrocenes.<sup>74</sup>

A sophisticated study of Tomson and co-workers<sup>8</sup> demonstrated that not only can charges shift the energies of the entire valence manifold but they can do so specifically. The authors investigated a series of tetracoordinate Cu(I) complexes with tris(phosphinimine) substituents of increasing polarity (*Figure 1.3B*). It was found that strongly  $\sigma$ -donating phosphinimine moieties destabilize the  $2e$  ( $d_{xy}/d_{x^2-y^2}$ ) orbital set in the  $xy$ -plane and stabilize the  $a_1$  ( $d_{z^2}$ ) orbitals, the latter being a result of Coulombic interactions with the partly positively charged phosphorus atoms. This study highlights the fact that even partial charges are sufficient to exert electrostatic control.

Another prominent example is the combined experimental/computational study by Holland and co-workers,<sup>9</sup> where the authors reported an Fe complex involving an SCS-pincer ligand (*Figure 1.3C*). Its Mössbauer parameters can only be satisfactorily modelled if a  $K^+$  counterion is included either directly coordinated to the complex (not shown in *Figure 1.3*) or separated from it in the form of an 18-crown-6-THF associate. Both models feature very similar isomer shifts and quadrupole splittings despite

significant distortion of the pincer plane in the former case. The authors also found that removal of the THF molecules in the crown ether associate without changing the rest of the geometry gives Mössbauer parameters close to those in the potassium-free model. This can be explained by THF taking part in delocalization of the positive charge on potassium, placing it close enough to the Fe center to affect the electronic structure. Detailed analysis reveals that the charge stabilizes the  $d_{z^2}$  orbital thereby causing an inversion in the valence manifold.

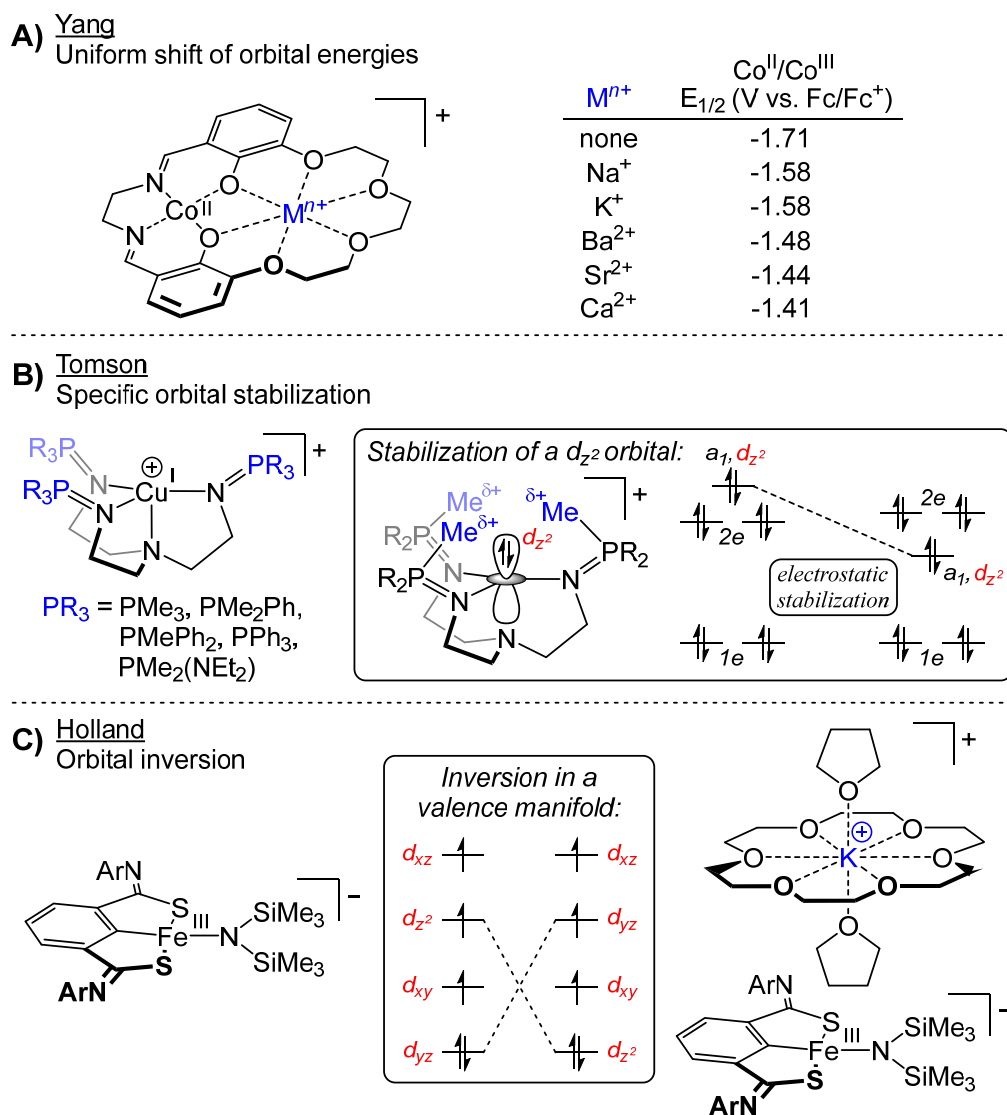


Figure 1.3. Examples of electrostatic control of electronic structure in metal complexes.<sup>8,9,70</sup>

Such changes of electronic structure along with subtle charge stabilization and transition state preorganization effects translate into numerous applications of spectator charges in both homogeneous catalysis and electrochemistry, some of which are discussed below.



### 1.2.2.2 Homogeneous catalysis and bond activation

There is a number of homogenous catalytic systems as well as those for small molecule activation that take advantage of spectator charges. Some of the prominent examples are based on porphyrins or related scaffolds, which is not surprising given the ubiquity of these ligands in metalloenzymes and the prevalence of electrostatic control in nature (*vide supra*). More specifically, the Groves group published a cytochrome P450 model Fe(IV) compound (*Figure 1.4A*) featuring a porphyrin ligand decorated with four pyridinium cations that shows extraordinarily high rates of C–H oxidation in aqueous solution.<sup>75</sup> In a similar vein, the authors also reported a related porphyrazine Fe(III) compound (*Figure 1.4A*)<sup>76</sup> capable of C–H oxidation 5-6 orders of magnitude faster than other known Fe(III)–OH complexes and that is more active than many ferryl complexes. Later on, Shaik and co-workers were able to computationally reproduce the experimentally observed activation barriers for both complexes by replacing charged groups with oriented electric fields, thereby showing that the observed catalytic rate enhancement is almost entirely electrostatic in nature.<sup>77</sup> On a related note, in another computational study, Shaik and co-workers showed that the unparalleled reactivity of the cytochrome P450 enzymes themselves is at least partially owed to the oriented electric fields within the binding pocket, which increase the spectroscopic oxidation state of the iron center.<sup>5</sup>

Next, Wiedner and co-workers synthesized a Ru(I) complex bearing a remote cationic charge (*Figure 1.4B*),<sup>78</sup> which they show to be a superior catalyst for CO<sub>2</sub> hydrogenation in terms of rate, yield and selectivity compared to the neutral isostructural analogues. The authors, however, point out that the role of the positive charge is not entirely clear: it could modulate electron donicity of the ligand *via* inductive effects; alternatively, or perhaps concurrently, it could also stabilize one of the Ru-based *d*-orbitals, thus lowering the barrier for the key steps of the catalytic cycle.

Another example was published by Gilbertson and co-workers and concerned a cationic Fe(II) complex with a redox-non-innocent ligand and a (benzo-15-crown)sodium motif in the secondary coordination sphere (*Figure 1.4C*).<sup>79</sup> This complex is capable of accelerated reduction of nitrite to nitric oxide. According to the authors, while the presence of the encapsulated Na<sup>+</sup> cation does not significantly influence the redox potential of the Fe complex, it entices the reduction of NO<sub>2</sub><sup>-</sup> to NO, likely assisting with preorganization of the transition state.

Further, the group of Lavallo described a zwitterionic Au(I) complex with a phosphine bearing an anionic non-coordinating carborane substituent, CB<sub>11</sub>Cl<sub>11</sub><sup>-</sup> (*Figure 1.4D*).<sup>80</sup> This system proves to be a potent alkyne hydroamination catalyst, which, as the

authors speculate, could be due to the presence of a negative charge: it either stabilizes positively-charged intermediates or, perhaps concomitantly, acts as an electrostatic tether preventing phosphine dissociation throughout the catalytic cycle.

Finally, the same group synthesized a dianionic Pd(0) complex supported by two monoanionic carboranyl phosphines (*Figure 1.4E*), which rapidly undergoes oxidative addition to chloroarenes at room temperature, thus acting as a competent catalyst for Kumada cross-coupling.<sup>81</sup> Importantly, the isosteric complex supported by neutral *o*-carboranyl (R = CH) phosphines does not display the same reactivity, supporting the involvement of electrostatic control.

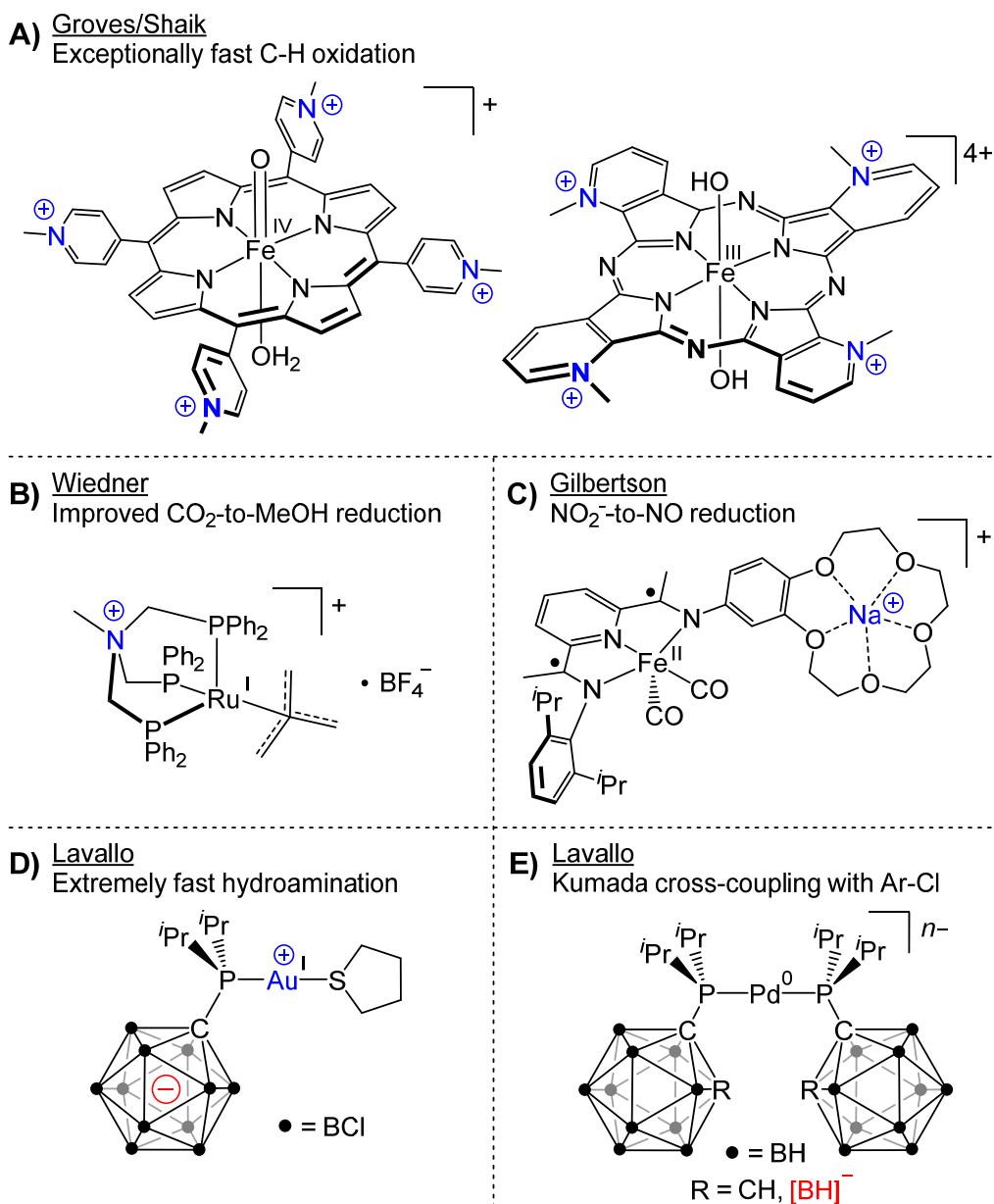


*Figure 1.4.* Examples of electrostatic control in homogeneous catalysis.<sup>76,78–81</sup>

### 1.2.2.3 Electrochemical applications

Aside from the examples discussed above in *Section 1.2.2.1*,<sup>10,70,74</sup> charges have been used for tuning redox potentials and optimizing electrocatalysts. For instance, in the elegant study of Savéant and co-workers,<sup>82</sup> a series of Fe(0)/porphyrin-based CO<sub>2</sub> electroreduction catalysts was designed wherein charged groups were placed at a different distance from a reactive metal center (*Figure 1.5A*). High turnover frequency and a dramatic decrease in overpotential were observed with the cationic NMe<sub>3</sub><sup>+</sup> groups located in the closest proximity to the metal (R<sub>1</sub> = H, R<sub>2</sub> = NMe<sub>3</sub><sup>+</sup>). Earlier on, Mayer and co-workers reported the same complex to be an excellent electrocatalyst for oxygen reduction.<sup>83,84</sup>

Next, Zhang and Warren described a modified Co(II)(5,10,15,20-tetraphenylporphyrin) where one of the phenyl groups bears a cationic NMe<sub>3</sub><sup>+</sup> moiety (*Figure 1.5B*).<sup>85</sup> This modification results in electrostatic stabilization of anionic intermediates in the electrocatalytic O<sub>2</sub> reduction cycle, thus providing superior selectivity over a wider pH range compared to other cobalt porphyrins. Other electrostatically-controlled Co-based systems were employed for the CO<sub>2</sub> electroreduction and contain porphyrine<sup>86</sup> and phthalocyanine motifs.<sup>87</sup>

In a similar vein, the group of McCrory demonstrated that introduction of an *N*-methylpyridinium group into a cobalt pyridyldiimine complex (*Figure 1.5C*) allows to increase its reactivity towards CO<sub>2</sub> electroreduction while dramatically decreasing the overpotential.<sup>88</sup> According to the authors, this effect is due to Coulombic stabilization of anionic intermediates in the catalytic cycle by a remote positive charge. As a matter of fact, this system is comparable to or more active than other CO<sub>2</sub> electroreduction catalysts employing imidazolium groups<sup>89,90</sup> or charged macromolecular ligands.<sup>91</sup>

Further, the group of Agapie investigated a series of heterometallic cubane clusters with three Mn(II) centers and a redox-inactive metal M<sup>n+</sup> (*Figure 1.5D*).<sup>92,93</sup> The redox potential of the clusters varies depending on both the Lewis acidity and charge of M<sup>n+</sup>, indicating a certain extent of electrostatic control.

Finally, Tolman and co-workers reported a family of [CuOH]<sup>+</sup> complexes bearing NNN pincer-type bis(carboxamide)pyridine ligands with distal charged groups (*Figure 1.5E*).<sup>94</sup> While all these compounds are structurally and spectroscopically similar, the Cu(II)/Cu(III) redox potential shifts by ca. 0.3 V upon switching between SO<sub>3</sub><sup>-</sup> and NMe<sub>3</sub><sup>+</sup> groups, implying significant through-space electrostatic influence.

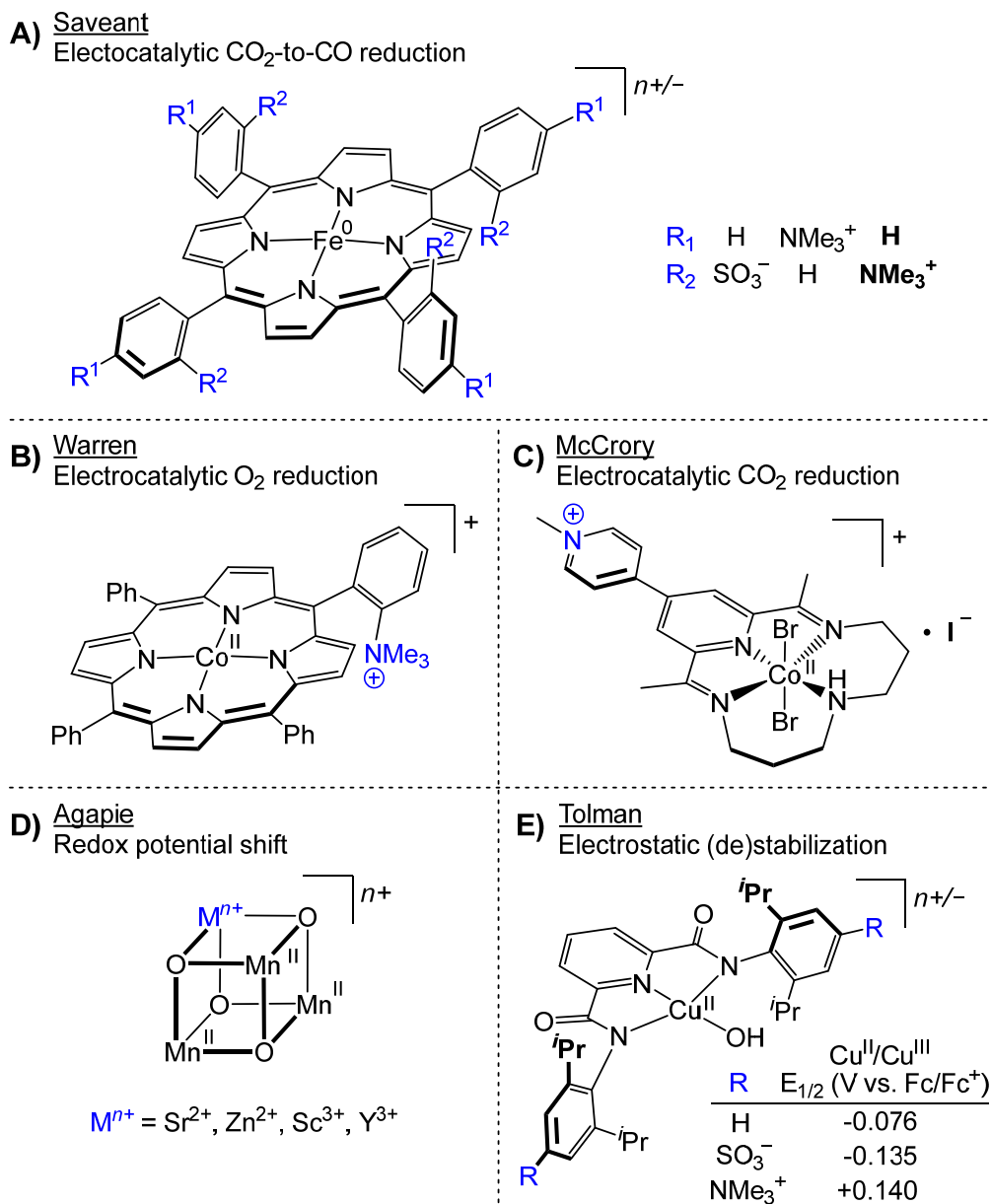


Figure 1.5. Examples of electrostatic control in electrochemically active systems.<sup>88,92–94</sup>

### 1.3 Charge frustration

Molecules with separated charges that cannot quench one another have been at the forefront of chemistry for decades<sup>95</sup> with many prominent applications in synthetic (in)organic chemistry, catalysis, click chemistry, photochemistry, switching and sensing. In addition to amphiphilic properties provided by such an unusual electronic structure, this charge frustration stores a significant amount of energy that can be harnessed for chemical transformations. Furthermore, and this pertains to coordination

compounds in particular, the presence of charged groups in the second coordination sphere affects the net molecular charge, influencing association behavior in solution and solubility in general with far-reaching effects on reactivity.

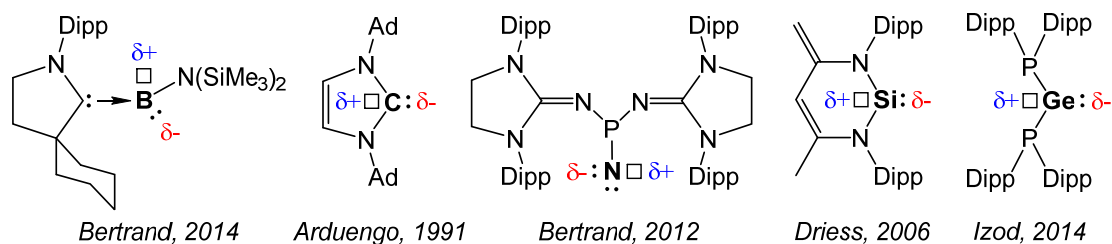
According to the IUPAC Gold Book, zwitterions are “neutral compounds having formal unit electrical charges of opposite sign”.<sup>96</sup> For the purpose of the present thesis, this definition appears incomplete as it omits a plethora of charge-separated systems with non-zero net charge as well as those where atoms bear multiple charge. Instead, we choose to define a zwitterion as any neutral or otherwise species that has separated electrical charges in one of the major canonical descriptions. Here, a number of cases may be distinguished depending on the kind of charge separation. If no non-zwitterionic connected Lewis structure can be drawn by  $\pi$ -electron resonance, the system is classified as truly zwitterionic. Otherwise, one can only speak of varying extents of zwitterionic character.

In this section, which is not meant to be exhaustive, we outline a number of frustrated zwitterionic literature compounds sorted by the distance between separated charges. Of course, this division is somewhat artificial since formal atomic charges are not experimental observables<sup>37</sup> and do not represent true electron density distribution within a molecule. A strict discussion about the extent of charge separation can only be held on theoretical grounds.<sup>37,97–99</sup> Nevertheless, even rough grouping by the distance helps to rationalize reactivity and make useful predictions.

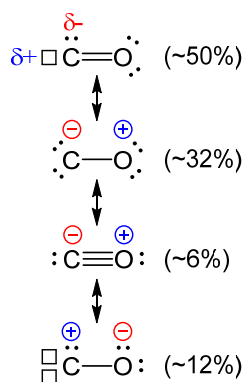
### 1.3.1 Elementenes: 1,1-zwitterions

The simplest of the charge-frustrated systems are represented by singlet elementenes: carbenes, nitrenes, borylenes and their heavier congeners, like silylenes and germylenes (*Figure 1.6A*),<sup>100–105</sup> featuring a negative electron lone pair and a positive vacant orbital on the same atom. This defines elementenes as single-site zwitterions, where the simultaneous presence of the features associated with both nucleophilicity and electrophilicity enables them, among other spectacular transformations, to add to strong bonds,<sup>101,106,115,116,107–114</sup> stabilize unusual oxidation states<sup>107,117–121</sup> and serve as stirring ligands in transition metal catalysis.<sup>120,122–127</sup> The archetypical member of this group is carbon monoxide, which, despite some ylidic character, can be considered a strongly-stabilized carbene as indicated by the dominant resonance structure (*Figure 1.6B*).<sup>128–131</sup> One should also mention mesoionic (or non-classical)<sup>132</sup> carbenes, which, alongside the single-site charge separation, do not have canonical resonance structures without additional charges elsewhere in the molecule (*Figure 1.6C*).<sup>133–135</sup>

### A) Examples of isolable element-enes



### B) Carbon monoxide



### C) Representative mesoionic carbene

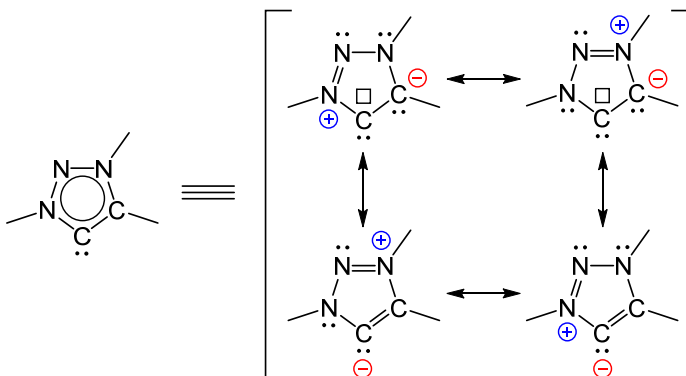
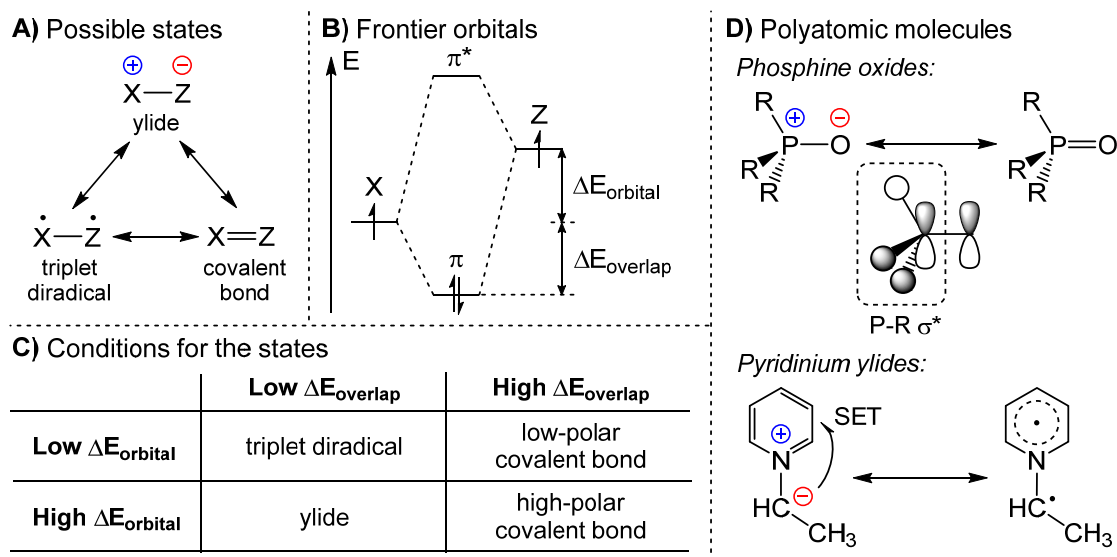


Figure 1.6. **A**: examples of isolable elementenes;<sup>101–105</sup> **B**: carbon monoxide and its four main resonance structures as identified by ELF analysis<sup>130,131</sup> and valence bond method<sup>136</sup> (unlike the classical textbook description where  $\text{C}\equiv\text{O}^+$  is the main zwitterionic Lewis structure<sup>137</sup>); **C**: Mesoionic 1,3,4-triazol-(1H-1,2,3)-5-ylidene and its resonance structures.<sup>135</sup>

## 1.3.2 Ylides: 1,2-zwitterions

The second prominent class of charge-frustrated systems are ylides – molecules with adjacent atoms of opposite charge (1,2-zwitterions) in one of their major canonical descriptions.<sup>138</sup> For a diatomic molecule, the difference between ylidic charge separation, a triplet diradical and a polar  $\sigma,\pi$ -multiple bond (Figure 1.7A) can be understood in terms of the simplified frontier orbital diagram that features the  $\pi$ -bond orbitals (Figure 1.7B). In it,  $\Delta E_{\text{orbital}}$  is the energy difference between the overlapping atomic orbitals, roughly corresponding to the electronegativity difference, and  $\Delta E_{\text{overlap}}$  is the extent of the overlap. Both ylidic and diradical character only emerge at poor orbital overlap, i.e. in case of a weak  $\pi$ -bond caused by orbital misalignment or size/energy mismatch; although  $\pi$ -bonds between heavier elements are inherently weaker. An additional condition for an ylide is a considerable electronegativity difference between the bound elements. All other situations, regardless of the electronegativity difference, and provided the  $\sigma$ -bond is preserved, lead to the formation of covalent  $\pi$ -bonds of varied polarity (Figure 1.7C). That being said, in polyatomic molecules, the situation may be complicated by the availability of the low-

lying antibonding orbitals, whereto the electrons of the ylidic lone pair may be promoted. This, for instance, characterizes the bonding situation in phosphine oxides, in which the negative charge on oxygen is donated into a low-lying P–R  $\sigma^*$ -orbital (*Figure 1.7D*), leading to a partial double bond character.<sup>139</sup> It may also happen that only one electron of the ylidic pair gets donated, as it is the case in pyridinium ylides (*Figure 1.7D*) that exhibit diradicaloid character.<sup>140</sup> All this variety of bonding situations highlights the fact that the ground-state wavefunction of the actual ylides is often described as a linear combination of several states with the weights regulating the reactivity pattern.



*Figure 1.7.* **A:** possible resonances of a diatomic doubly-bound molecule; **B:** its truncated MO diagram; **C:** conditions for the dominant resonance; **D:** ylidic polyatomic molecules.<sup>139,140</sup>

Organoelement ylides can be based on many non-metals,<sup>141–148</sup> but the most common ones are phosphorus,<sup>149,150</sup> sulphur<sup>141,151–153</sup> and nitrogen<sup>141</sup> (*Figure 1.8A*). Among other types of reactivity,<sup>154</sup> these compounds are key to such pivotal transformations as various cycloadditions,<sup>155–158</sup> Wittig<sup>159–161</sup> and Corey-Chaykovsky<sup>162–164</sup> reactions as well as diazo chemistry,<sup>a,165</sup> in which they serve as synthetic equivalents of carbenes. It is important to note that, out of these ylides, the nitrogen ones are the purest type since frequently there are no sufficiently low-lying antibonding orbitals available for  $\pi$ -bonding, securing a high extent of charge separation and rendering many of these compounds elusive.<sup>141</sup> The compounds of the elements from the third period onwards often do have such orbitals, and it is up to theoretical models such as Valence Bond Theory<sup>97</sup> or Natural Resonance Theory<sup>98,99</sup> to strictly define the extent of ylidic character.

<sup>a</sup> Even though diazo alkenes can be considered 1,3-dipoles (see *Section 1.3.3*), diazomethane, for instance, as well as some other asymmetric 1,3-dipoles have a strong ylidic character.<sup>205</sup>

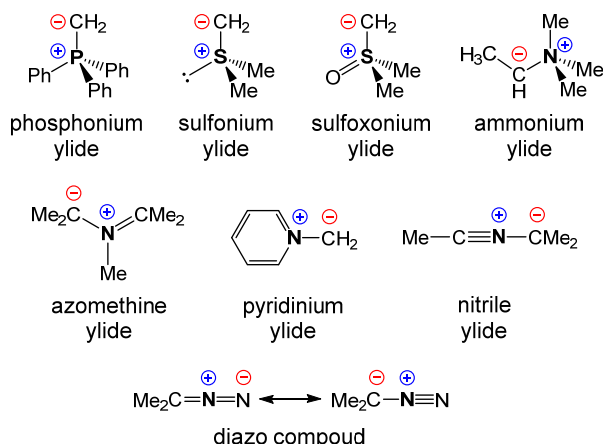
Indirectly, this can often be deduced from the molecular orbital occupancies or X-ray crystallographic data. Nevertheless, such analysis is not always done in the literature with the preference given to the phenomenological assignment of the ylide character based on the reactivity patterns and as long as the bond between the elements from different periods is concerned, causing poor  $p$ - $p$  or  $d$ - $p$  orbital overlap. In order to maintain consistency with the current literature, we shall not differentiate between these approaches in the further discussion.

When it comes to inorganic ylides, some of the best known examples include  $N$ -oxides and nitro compounds (*Figure 1.8B*), both of which feature multiple applications as oxidizing agents. Less known are heavier congeners of carbonyl compounds:  $R_2E=O$ , where  $E = Si, Ge, Sn$  and  $Pb$  (*Figure 1.8B*). While in normal carbonyls the energies of  $\sigma$ - and  $\pi$ -bonds are almost equal, for heavier tetrels, due to poor  $p$ - $p$  orbital overlap,  $\pi$ -bonding is significantly weaker.<sup>176</sup> The same applies to the  $E=N$  and  $E=S$  bonds, where the energy of the  $\sigma$ - and  $\pi$ -components are roughly equal only when  $E$  is a carbon atom.<sup>177</sup> Given the high electronegativity difference between the bound elements, this leads to charge separation<sup>178</sup> as indicated by very high dipole moments<sup>179</sup> and extremely high reactivity.<sup>179–181</sup> Similar charge separation also holds for hypervalent iodine compounds with formal  $I=O$  and  $I=N$  bonds (*Figure 1.8B*), among which are common oxidizing agents such as iodozobenzene, 2-iodoxybenzoic acid (IBX) and  $N$ -sulfonylimidoiodinanes. Computational studies<sup>182</sup> indicate that these molecules are better described in terms of  $\sigma$ -dative  $I^+ \rightarrow O^-$  and  $I^+ \rightarrow N^-$  interactions. Of other reactive inorganic ylides, a prominent example is a dipolar  $Sn(IV)$  imide that readily inserts into a pyridine  $C_\alpha-H$  bond (*Figure 1.8C*).<sup>166</sup>

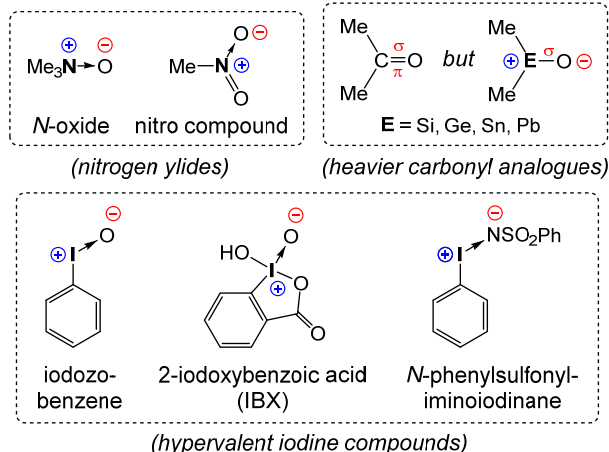
Similarly, organometallic ylides are known for small-molecule activation under mild conditions, not unlike frustrated Lewis pairs, where bond polarization is also a guiding design principle.<sup>183</sup> One of the most well-known examples of a metalla-ylide is titanocene methylenide (*Figure 1.8D*), a Schrock carbene that can be generated from either Tebbe's<sup>167,168</sup> or Petasis<sup>169</sup> reagents –  $[(Cp)_2Ti(\mu-CH_2)(\mu-Cl)Al(CH_3)_2]$  and  $[(Cp)_2Ti(CH_3)_2]$ , respectively. Because of the mismatch in orbital energy and poor overlap due to the size difference, the titanium-carbon bond has a strong ylidic character. Just like phosphorus ylides, titanocene methylenide is competent in olefination of carbonyl compounds,<sup>170</sup> giving an analogous titanaoxacyclobutane intermediate, which, upon immediate decomposition, leads to the target alkene. As a matter of fact, due to high oxophilicity of the  $Ti(IV)$  atom, this compound performs better than the analogous Wittig reagent, especially for sterically encumbered carbonyl groups. More recent developments in this direction led to alkylidyne analogues  $L_nTi \equiv CR$ , capable of activating strong  $C-H$  bonds.<sup>184,185</sup>



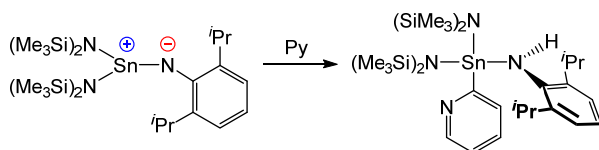
## A) Representative organoylides of P, S and N



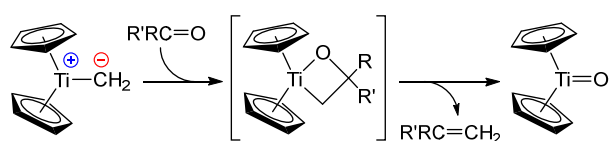
## B) Examples of inorganic ylides



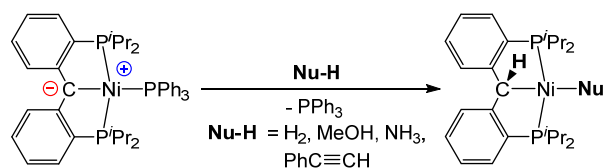
## C) Pyridine activation by an inorganic ylide



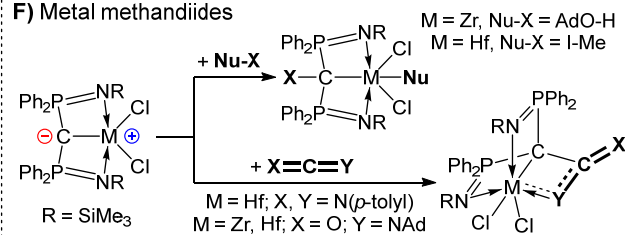
## D) Wittig-like reaction of titanocene methylenide



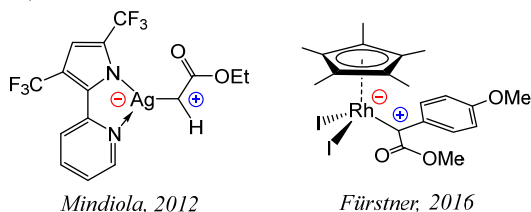
## E) Ylidic nucleophilic metallocarbene



## F) Metal methandiides



## G) Representative metal-stabilized carbenium ions



## H) Ylidic electrophilic metallocarbene

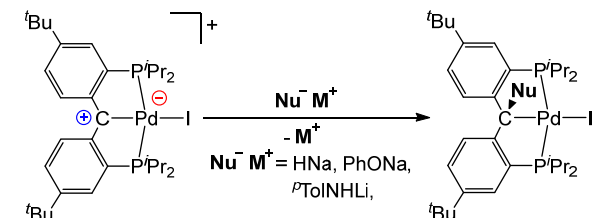


Figure 1.8. Examples of organic, inorganic and metalorganic ylides. The preference was given to showing ylide resonance structures as opposed to the covalently-bound ones. **A**: representative organoylides of phosphorus, sulfur and nitrogen; **B**: inorganic ylides of nitrogen, heavier tetrrels and iodine; **C**:  $\alpha$ -C-H activation of pyridine by an ylidic Sn(IV) imide;<sup>166</sup> **D**: olefination of carbonyl compounds with titanocene methylenide;<sup>167–170</sup> **E**: reactivity of a nucleophilic Ni(II) metallocarbene;<sup>171</sup> **F**: reactivity of Zr(IV) and Hf(IV) methandiides;<sup>172</sup> **G**: examples of metal-stabilized carbenium ions;<sup>173,174</sup> **H**: reactivity of an electrophilic Pd(II) metallocarbene.<sup>175</sup>

When it comes to nucleophilic metallocarbenes in general, a common strategy to enforce ylidic character lies in the use of carbene pincer ligands combined with middle-late transition metals (Figure 1.8E): this way, filled metallic *d*-orbitals prevent the efficient  $\pi$ -bond formation, securing the separation of charges. Such an approach was

first applied in the 1970s with complexes of Ir(III)<sup>186</sup> and was later expanded to Rh(V),<sup>187</sup> Ru(IV) and Os(IV)<sup>188</sup> coordination compounds, the latter of which can reversibly activate dihydrogen. The complexes of Ni(II)<sup>171</sup> and Pd(II),<sup>175,189</sup> more *d*-electron-rich and, thus, presumably, more ylidic, showed greater reactivity, being capable of activating amines, alcohols and some other substrates with an acidic proton. Of other ylidic nucleophilic metallocarbenes it is worth to mention Zr(IV) and Hf(IV) complexes supported by phosphorus imide methandiides: these compounds are capable of activating O–H, N–H and H–H bonds (*Figure 1.8F*) as well as take part in [2+2] cycloadditions.<sup>172,190–193</sup>

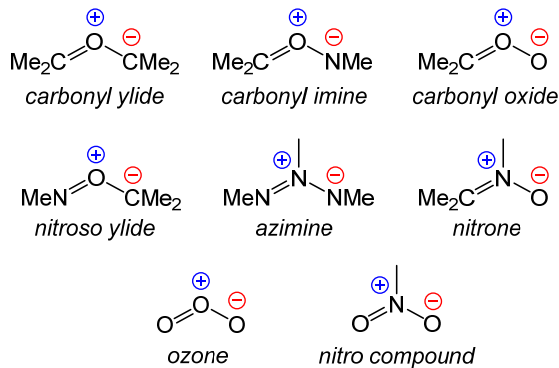
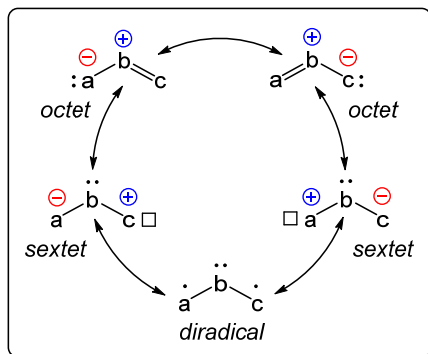
Electrophilic metallocarbenes with separated charges are far less common, supposedly due to the difficulty of accumulating a negative charge on an electropositive metal center. There exists a number of extremely electrophilic late transition metal carbene complexes with high ylidic character (*Figure 1.8G*),<sup>194</sup> which are well-established in C–H functionalization chemistry.<sup>195,196</sup> Nonetheless, the role of a metal atom in these likely comes down to stabilization of a positive charge on a carbon, while the metal does not directly participate in the carbene C–H insertion step, allowing to consider these compounds as metal-stabilized carbenium ions. That being said, the regioselectivity of the insertion does not always obey the rules stemming from the acidity of the substrate, suggesting radical involvement or steric influence.<sup>174,197,198</sup> Revisiting the pincer carbene complexes, the polarity of the carbon-metal bond can be reversed upon one-electron oxidation.<sup>175,199,200</sup> At least one of such systems<sup>95,175</sup> shows a rather low metal-carbon Wiberg Bond Index<sup>201</sup> of 0.98, which, combined with the electrophilic behavior of the carbene carbon atom (*Figure 1.8H*), allows to infer at least some extent of ylidic character.

### 1.3.3 Between 1,2- and 1,3-zwitterions: 1,3-dipoles

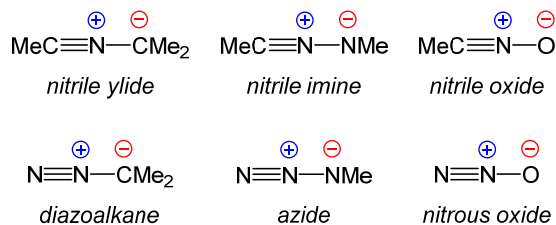
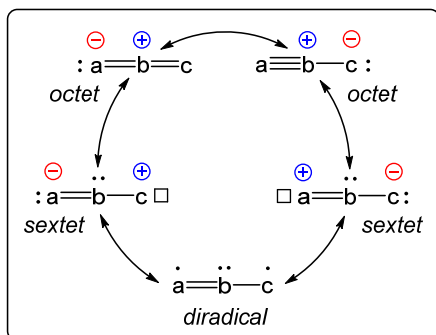
Somewhat further in terms of frustrated charge separation are 1,3-dipoles, including, among others, such molecules as ozone, nitrous oxide, nitro and diazo compounds, azides and nitrones. In these, three atoms share delocalized  $\pi$ -electrons with at least one significant resonance structure containing separated charges in a 1,3-relationship to one another,<sup>202</sup> although 1,2-resonances are non-negligible either. Two major types of 1,3-dipoles are bent allylic (*Figure 1.9A*) and linear propargyl-allenyl (*Figure 1.9B*) ones, both of which can be represented as a linear combination of two ylidic octet resonance structures, two 1,3-zwitterionic sextet structures and an open-shell singlet diradical, where the electrons of the peripheral atoms are coupled through a non-bonding interaction.<sup>203</sup> A more precise way to describe the electronics of a 1,3-dipole is to assign a major resonance contributor based on experimental (e.g. dipole moment

measurements<sup>204</sup>) or computational data.<sup>203,205–208</sup> For instance, ozone is better represented as a 1,3-diradical, which explains its extreme reactivity, while valence-isoelectronic sulfur dioxide is dominated by ylidic resonances, rendering it more timid reactivity-wise.<sup>206</sup> Likewise, even though diazo compounds, azomethine and nitrile ylides are indeed better described as ylides, the structural weight of a diradical resonance in them can reach one-third,<sup>207</sup> thereby imparting a significant diradicaloid character.

### A) Allyl type dipoles



### B) Propargyl-allenyl type dipoles



### C) 1,3-Dipolar cycloaddition with a double bond

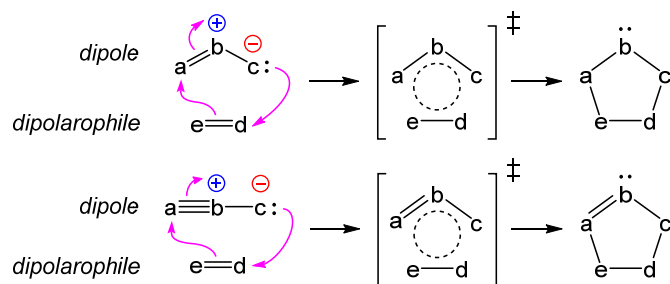


Figure 1.9. **A, B**: representative 1,3-dipoles. Systems with heavier elements are also known,<sup>209–212</sup> although used less routinely; **C**: 1,3-dipolar cycloadditions with an -ene dipolarophile.

Due to their ambivalence, 1,3-dipoles can simultaneously act as nucleophiles and electrophiles. The extent of such behavior at each end of the molecule can be evaluated using frontier molecular orbitals accessible computationally. Normally, the atom with the highest coefficient in the HOMO functions as a nucleophile, whereas that in the LUMO shows electrophilic behavior. Combined, these two properties allow 1,3-dipoles to engage into the cycloaddition with dipolarophiles (mostly alkenes or alkynes, though other  $\pi$ -systems are also possible), leading to formation of 5-membered rings (*Figure 1.9C*).<sup>213</sup> This [3+2] pericyclic reaction found multiple applications in chemical synthesis<sup>155–157</sup> and bioconjugation<sup>214</sup> as an extremely powerful tool for the construction of various heterocyclic systems.

Another peculiar mode of reactivity of some 1,3-dipoles is a single-atom transfer accompanied by the release of a thermodynamically more stable species, such as dinitrogen ( $N_2$ ) or a less polarized organic molecule. An archetypical example of this behavior is carbene transfer from diazo compounds, in particular diazomethane.<sup>215</sup> In the context of transition metal chemistry, such reactivity was first demonstrated for a  $[Mn^{III}(\text{tetramesitylporphyrinato})N_3]$  complex<sup>216</sup> which, upon irradiation, releases  $N_2$  and produces a corresponding  $Mn^V$  nitride compound (*Figure 1.10A*). This transformation proceeds *via* metal-to-ligand charge transfer (MLCT) into the  $\pi^*$  orbital of the azide, leading to  $N_\alpha-N_\beta$  bond cleavage and two-electron oxidation of the metal center.<sup>217,218</sup> In general, azide complexes of low-valent metals with favorable *d*-orbital symmetry often eliminate  $N_2$  spontaneously at room temperature or under heating (*Figure 1.10B*).<sup>219,220</sup> Furthermore, the electrophilic  $N_\beta$  atom of the azido ligand may undergo substitution with other small molecules as exemplified by a  $Ni^{II}$  complex reacting with CO to cleanly generate the corresponding isocyanate (*Figure 1.10C*).<sup>221</sup> Interestingly, the parent azido complex is stable up to 200 °C as a solid and can withstand five days of reflux in toluene. At the same time, the reaction with 5 bar of CO occurs at room temperature regardless of the presence of light, implying direct attack of CO onto the azide with the expulsion of isoelectronic  $N_2$ . Considering that CO has a higher bond dissociation energy than  $N_2$  ( $1076.38 \pm 0.67$  vs.  $944.84 \pm 0.10$  kJ/mol, respectively),<sup>222</sup> the fact that this reaction still occurs highlights how much energy is stored within the azide group charge separation. A number of similar reactions, with or without irradiation, are reviewed elsewhere.<sup>223</sup>

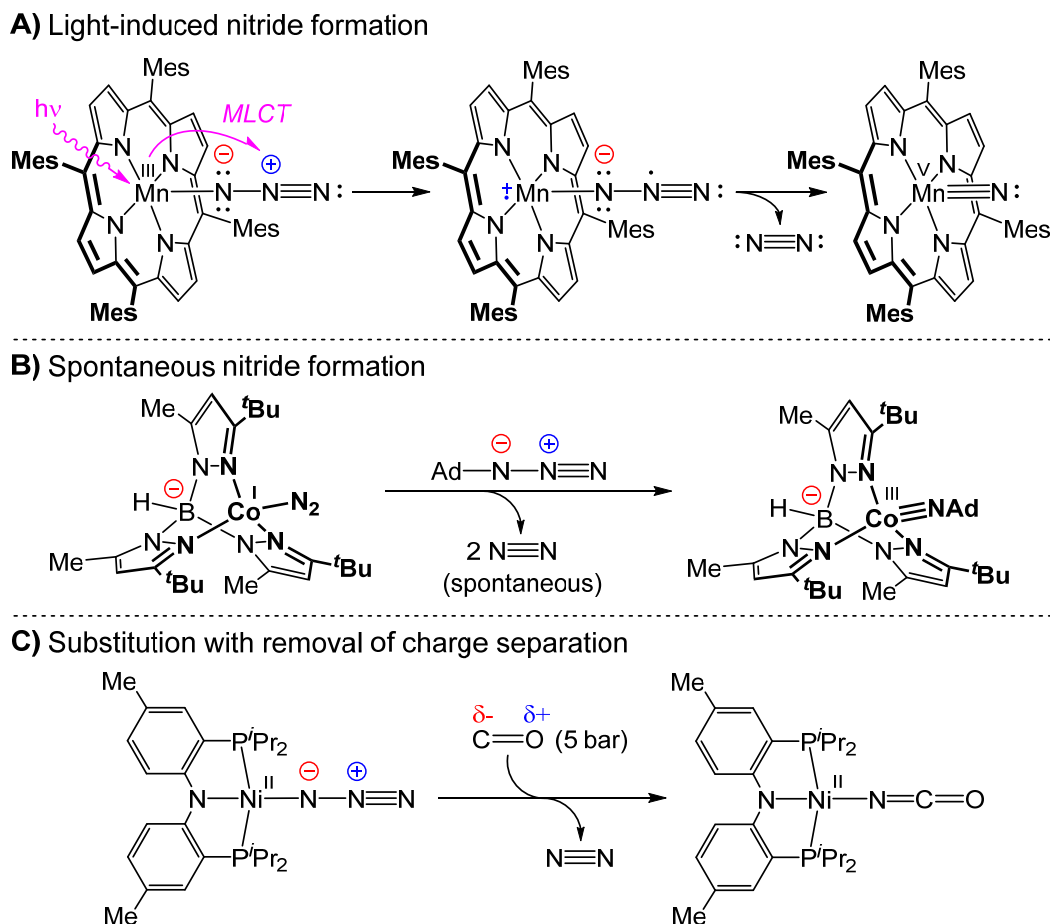
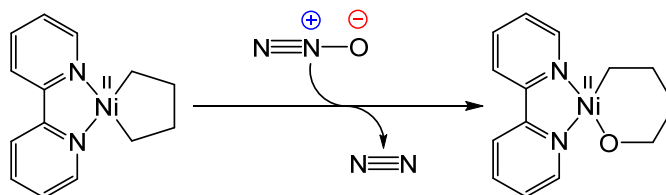


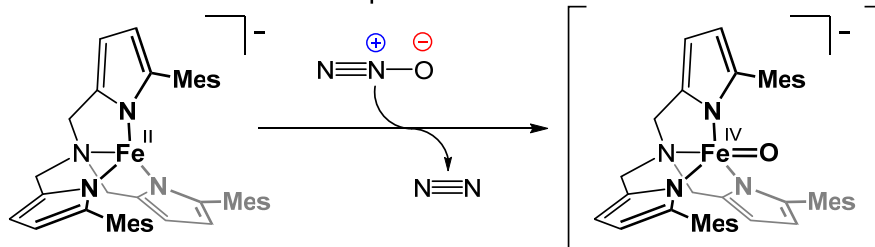
Figure 1.10. Single-atom transfer from azides.<sup>216,219–221</sup>

One more 1,3-dipole commonly capable of single-atom transfer is nitrous oxide ( $\text{N}_2\text{O}$ ),<sup>224</sup> which can be formally thought of as dinitrogen *N*-oxide. Aside from the use as an oxygen source in the automotive industry, it has shown to stoichiometrically transfer an oxygen atom to a number of complexes of oxophilic metals, such as Ti,<sup>225</sup> Zr,<sup>226–228</sup> Mo,<sup>229</sup> V,<sup>225</sup> U<sup>230</sup> and others.<sup>231–233</sup> Reactions with first-row late transition metals are known as well, leading to either oxygen atom insertion (*Figure 1.11A*)<sup>234–236</sup> or formation of terminal oxo-species (*Figure 1.11B*).<sup>237</sup> Finally, nitrogen atom transfer from  $\text{N}_2\text{O}$  has also been observed for tricoordinate Mo complexes with formation of a stoichiometric mixture of nitride and nitrosyl species (*Figure 1.11C*),<sup>238,239</sup> although the reports of this kind are scarce. Even more scant are the accounts of single-atom transfer from other 1,3-dipoles: a notable example is a nitrogen atom transfer from an azomethine imine in a tungsten pentacarbonyl complex (*Figure 1.11D*).<sup>240</sup>

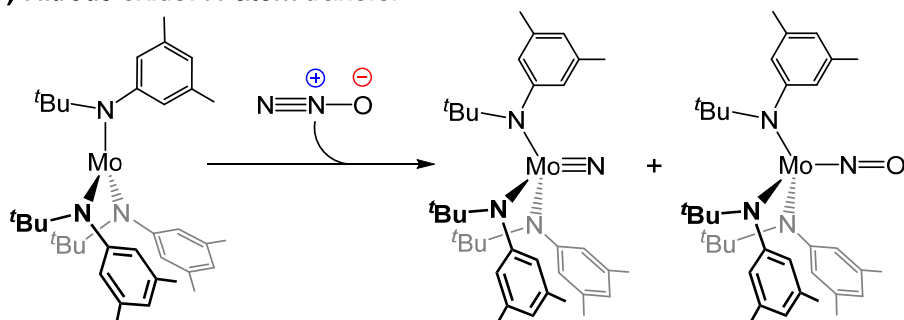
## A) Nitrous oxide: O-atom insertion



## B) Nitrous oxide: terminal oxo-species



## C) Nitrous oxide: N-atom transfer



## D) Azomethine imine: N-atom transfer

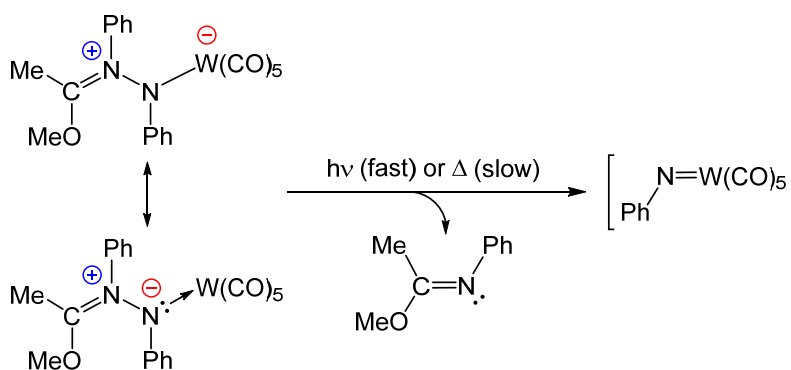


Figure 1.11. Single-atom transfer from nitrous oxide and azomethine imine.<sup>234,237,238,240</sup>

### 1.3.4 Geminal charge separation: 1,3-zwitterions

In contrast to 1,3-dipoles, main-group compounds with strong geminal zwitterionic character that lack  $\pi$ -resonance stabilization between the charges (i.e., true zwitterions) are relatively rare. One prominent example results from the addition of  $B(C_6F_5)_3$  to acetylenes.<sup>241</sup> Some of these compounds are isolable and act as intermediates in alkyne

hydroboration (*Figure 1.12A*).<sup>242</sup> Another type of reactive 1,3-zwitterionic systems are phosphirenium borates<sup>243</sup> that, upon heating, rearrange into charge-neutral phospholes<sup>244</sup> or vicinal B/P frustrated Lewis pairs (FLP; *Figure 1.12B*).<sup>245,246</sup> On a related note, geminal B/P FLPs may yield 1,3-zwitterions upon small molecule activation,<sup>247–252</sup> although other elemental combinations, such as Al/P,<sup>253–255</sup> Ga/P,<sup>256</sup> Si/P,<sup>257</sup> Ge/P<sup>258</sup> and Sn/P,<sup>259,260</sup> are also known (*Figure 1.12C*). Some of these compounds are capable of undergoing charge neutralization by transferring activated molecular fragments to a substrate and regenerating the original FLP, thereby closing a catalytic cycle.<sup>247,250,251</sup>

As for the system where  $\pi$ -resonance charge stabilization may take place, allenes that normally have a linear rigid C=C=C skeleton can be destabilized to exhibit zwitterionic electronic structure and behavior.<sup>261,262,271,263–270</sup> This can be achieved either geometrically through twisting and bending of the C=C=C fragment or electronically by polarizing the  $\pi$ -bonds. Often, it is the combination of the two,<sup>262,263,265,269</sup> yet regardless of the mechanism of destabilization, the allene scaffold always bends. Electronic destabilization can be attained *via* push-pull or push-push substitution patterns (*Figure 1.12D*).<sup>261</sup> Push-pull allenes show carbene-like electronic structure, which makes them very reactive and hard to isolate as monomers.<sup>272,273</sup> Push-push allenes, on the other hand, have increased electron density on the central carbon atom, which, in the resonance limit, allows to view them as coordination compounds of zero-valent carbon or, in other terms, carbones.<sup>274,275</sup> Such systems rely on strongly  $\sigma$ -donating and weakly  $\pi$ -accepting ligands, like some phosphines and carbenes (*Figure 1.12E*). If an employed carbene has a donor heteroatom in the  $\alpha$ -position to the carbene center, one speaks of 1,3-zwitterionic carbones.<sup>261,263–265</sup> These compounds are capable of small molecule activation on their own (*Figure 1.12F*)<sup>276</sup> or in the presence of Lewis acids to form FLPs.<sup>274</sup> Moreover, they can ligate two metal centers at a time, one for each lone pair on a central carbon,<sup>262</sup> which highlights the strong electron donor properties of carbones. Owing to this, their coordination compounds exhibit rich redox behavior, allowing to achieve high (formal) oxidation states.<sup>277–279</sup> Moreover, some rhodium-carbene complexes exhibit excellent reactivity and selectivity in hydroamination,<sup>280</sup> hydroarylation<sup>281,282</sup> and hydroallylation<sup>283</sup> of dienes. Of note is the application of carbene ligands for internal photosensitization in Pd-photocatalyzed C–H arylation of arenes and aldehyde-imine coupling in open air.<sup>284</sup> There, the Pd complex features strong ligand-to-ligand charge transfer, in part owing to the zwitterionic nature of the auxiliary ligand. Interestingly, allenes of heavier tetrrels like silicon or germanium exhibit a bent structure regardless of the substitution pattern,<sup>285–288</sup> reflecting the inherent weakness of the  $\pi$ -bonding for larger orbitals. The electronic structures

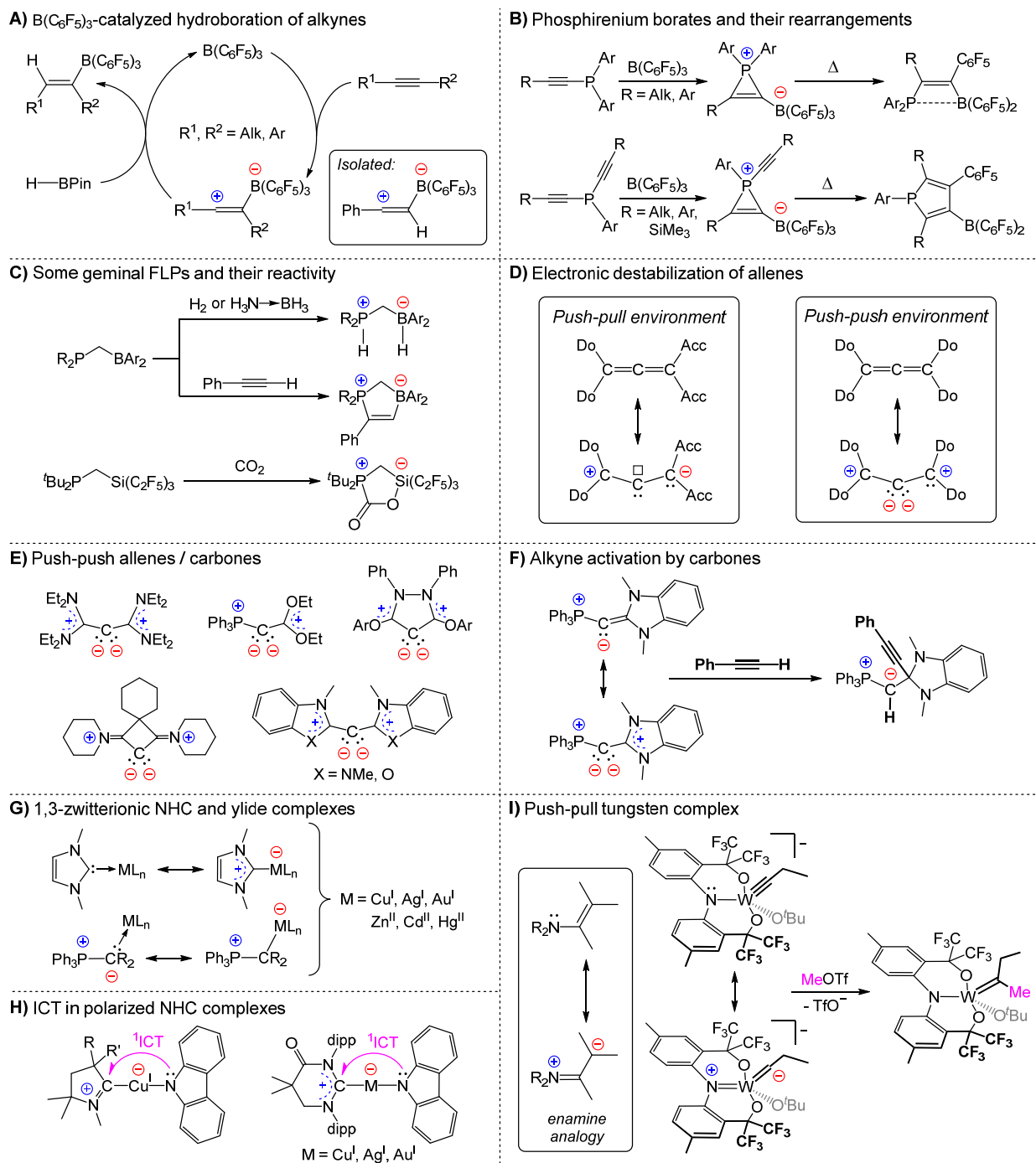


**Figure 1.12.** Reactivity of geminal zwitterions. **A:** zwitterionic intermediates in alkene hydroboration;<sup>241,242</sup> **B:** synthesis and reactivity of phosphirenium borates;<sup>246</sup> **C:** geminal FLPs;<sup>247,248,250,252,257</sup> **D:** strategies for electronic destabilization of alkenes;<sup>261</sup> **E:** allenes in a push-pull environment;<sup>261–265</sup> **F:** alkyne activation of carbones;<sup>276</sup> **G:** zwitterionic NHC and phosphorus ylide complexes;<sup>289,291</sup> **H:** NHC-bound metals in a push-pull environment;<sup>292,294</sup> **I:** push-pull tungsten complex.<sup>297</sup>



of NHC-stabilized silylones and germylones feature two tetrel-based lone pairs, which allows to assign them as 1,3-zwitterions as well.<sup>286</sup>

When it comes to metal coordination compounds, some phosphorus ylide<sup>289,290</sup> and NHC complexes<sup>291</sup> are better described as 1,3-zwitterions. A necessary condition for the NHC ligand is to have a nitrogen atom in the geminal position to the metal (*Figure 1.12G*). Furthermore, the metal ion itself should not be capable of strong  $\pi$ -backdonation so that the NHC acts as almost a pure  $\sigma$ -donor. These criteria are fulfilled in  $d^{10}$  complexes of group 11 ( $\text{Cu}^+ - \text{Ag}^+ - \text{Au}^+$ ) and group 12 ( $\text{Zn}^{2+} - \text{Cd}^{2+} - \text{Hg}^{2+}$ ) metal ions, where ligand-to-metal charge transfer reaches  $\geq 0.6\bar{e}$ . Since the carbene carbon in such complexes is considerably  $\pi$ -acidic, the introduction of additional  $\pi$ -donor ligands may give rise to new chemistry. For example, strongly polarized push-pull environments in  $[\text{M}(\text{NHC})\text{NR}_2]$  complexes (*Figure 1.12H*) can undergo photoinduced interligand charge transfer ( $^1\text{ICT}$ ), thereby affording fluorescence with quantum yields in excess of 99%.<sup>292-295</sup> This behavior was characterized as “thermally enhanced luminescence”<sup>292</sup> and is conceptually similar to thermally activated delayed fluorescence (TADF) in purely organic donor-acceptor systems.<sup>296</sup> A noteworthy difference is that incorporation of a metal atom leads to significantly longer-lived excited states due to the spin-orbit coupling that enables mixing with the  $^3\text{ICT}$  state.

Another example of a metal atom in a push-pull environment is a N,O,O-pincer tungsten alkylidyne complex with a nucleophilic  $\alpha$ -carbon (*Figure 1.12I*).<sup>297</sup> This reactivity is achieved by placing a metal atom into a rigid meridional environment, wherein the angle of  $42.8^\circ$  between the nitrogen lone pair and alkylidyne bond results in a significant orbital overlap. This antibonding combination is analogous to a HOMO in enamines, leading to the build-up of electron density at the  $\text{C}_\alpha$ , thereby rendering it nucleophilic. The latter is illustrated by a reaction with methyl triflate that gives a corresponding methylalkylidene complex. It must be noted that even though the DFT-optimized geometries demonstrate almost complete linearity of the  $\text{W}\equiv\text{C}-\text{CH}_2$  fragment ( $\text{W}^\wedge\text{C}^\wedge\text{C}$  angle of  $176.2^\circ$ ) and, therefore, low weight of the structure with a lone pair on the alkylidynyl carbon, it appears that this structure is not too high in energy so that its reactivity can still be accessed.

### 1.3.5 Remote zwitterions

With higher degrees of charge separation comes a larger variety of ways it can be utilized. Aside from energy storage and enhanced reactivity, which is still the case for FLP chemistry,<sup>298</sup> zwitterionic charge separation can control molecular energy levels and, consequently, physical properties. Furthermore, it can also influence ion pairing

and aggregation behavior in solution, allowing for fine reactivity and solubility control. All these applications are discussed in more detail below.

### 1.3.5.1 Organic zwitterions

Remote organic zwitterions have attracted a lot of attention for the design of molecules with tunable HOMO-LUMO energy gaps, leading to highly-tunable electrochemical and optical properties with absorption/luminescence in red and near-IR regions.<sup>299,300</sup> Such systems proved instrumental for sensing and switching, data storage, photovoltaics, non-linear optics, bioimaging and fluorescent probing among many other applications.<sup>301,302</sup> Perhaps the most well-known remote organic zwitterion is Reichardt's dye (*Figure 1.13A*), notable for its extreme solvatochromism<sup>303</sup> and high tunability by introduction of additional functionalities.<sup>304,305</sup> Its charge-separated form is stabilized by polar solvents, which inspired the use of such compounds as solvent polarity probes.<sup>303</sup> Furthermore, they also excel as thermochromic and piezochromic materials. Similar properties are also shown by Brooker's merocyanine (*Figure 1.13B*).<sup>300</sup> Other popular systems are azolium-derived squaranes (*Figure 1.13C*) and their polymers<sup>306–309</sup> that demonstrate remarkable photostability coupled with intense emission/fluorescence in red and near-IR parts of the spectrum, which led to their applications in photovoltaics and biomedical fields. Open shell remote organic zwitterions such as tetrathiafulvalene-based donor-acceptor dyads (*Figure 1.13D*)<sup>310</sup> show remarkable complex aggregation behavior and change of optical and magnetic properties in solution depending on temperature and solvent polarity. Several other types of zwitterionic systems are also of interest, including carbene-derived diradicaloids and perylenes.<sup>311–316</sup>

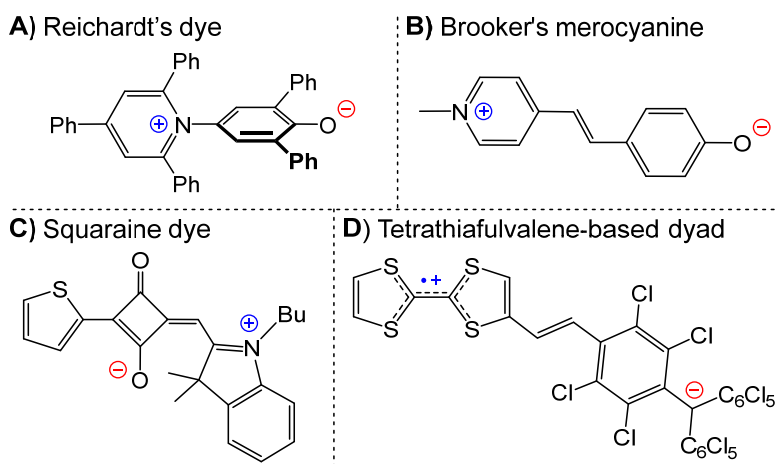


*Figure 1.13.* Representative remote organic zwitterions.<sup>300,303,309,310</sup>

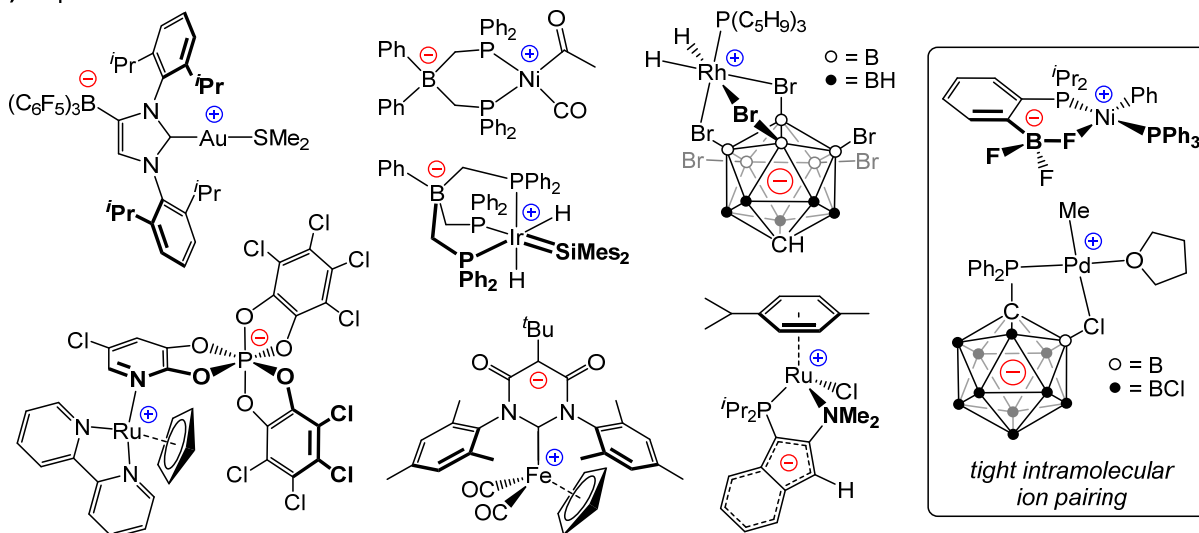
### 1.3.5.2 Coordination compounds

Neutral zwitterionic metal complexes have recently attracted considerable attention in the fields of organometallic chemistry and catalysis with uses in polymerization, hydrogenation, hydrofunctionalization, cross-couplings and other reactions.<sup>317–319</sup> With electroneutrality secured by a remote charge on the ligand, they can emulate the electronic structure of ionic analogues,<sup>320</sup> combining the reactivity of ionic transition metal complexes with the solubility patterns of neutral species, especially in low polarity media. Furthermore, neutral zwitterions are not subject to counterion effects such as ion-pairing, which are hard to predict, assess and control.<sup>69,321,322</sup> This opens an avenue for more straightforward and systematic catalyst design.

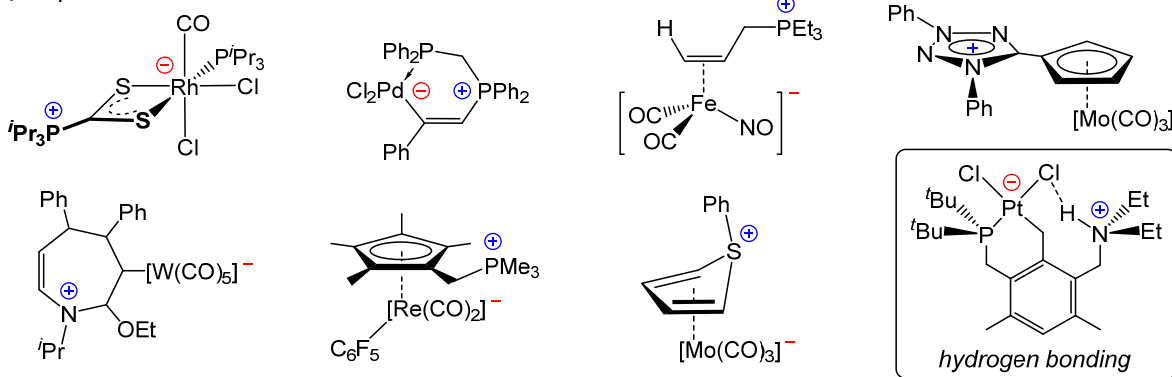
Depending on the polarity, remote zwitterionic metal complexes can be classified into two main types: those with a formal positive charge on the metal center and an anionic ligand (*Figure 1.14A*),<sup>318</sup> and those with a formal negative charge on the metal and a cationic ligand (*Figure 1.14B*).<sup>317</sup> As an intermediate group stand zwitterionic complexes with both cationic and anionic metals that compensate the charge of one another (*Figure 1.14C*).<sup>317</sup> Even though a negatively-charged, electropositive transition metal center might seem paradoxical, in the actual electronic structure the negative charge is often stabilized by delocalization into the ancillary ligands (CO, Ar, Hal etc.). If the ligands are sufficiently rigid, the charges are mutually stabilized electrostatically as well as by means of through-bond electronic effects. Otherwise, geometric shortening of the charge separation may occur *via* hydrogen bonding or tight intramolecular ion pairing by back-folding of the ligand onto the metal center (*Figure 1.14A, B*).

As mentioned above, despite a limited number of comparative studies, the performance of zwitterionic catalysts is similar to that of the ionic analogues.<sup>318,329,354,355,346–353</sup> However, in some cases, increased activity and divergent reactivity were observed,<sup>329,344,345,348,356,357</sup> in particular owing to the charge separation endowing these systems with amphiphilic character. For instance, a carboxylate-functionalized zwitterionic bis-NHC Ir(I)cod complex (*Figure 1.14D*) shows increased CO<sub>2</sub> hydrogenation activity with respect to the cationic carboxylate-free analogue.<sup>344</sup> The authors proposed that the carboxylate moiety stabilizes the active Ir(III) hydride through coordination, resulting into a *fac*- $\kappa^3$ -C,C',O complex. Another notable example is a dimethyldi(2-pyridyl)boratoplatinum complex (*Figure 1.14E*) than can activate alcohols and transfer one of the borate methyls to the metal accompanied by nucleophilic attack of the solvent at boron.<sup>345</sup>

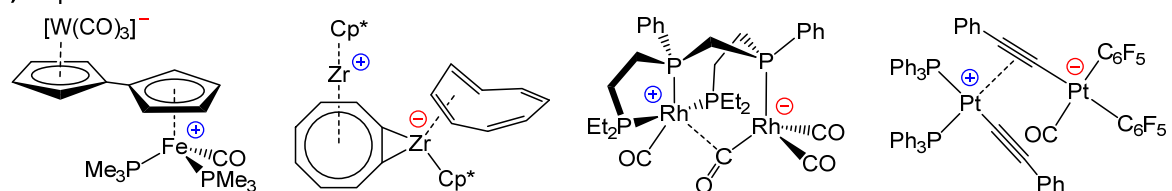
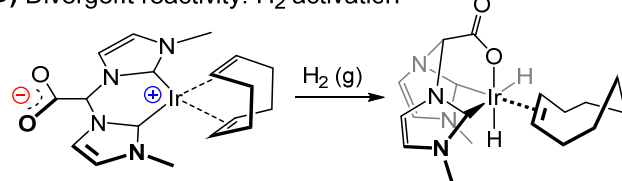
## A) Representative zwitterions with cationic metal



## B) Representative zwitterions with anionic metal



## C) Representative zwitterions with both cationic and anionic metals

D) Divergent reactivity: H<sub>2</sub> activation

## E) Divergent reactivity: methyl group transfer

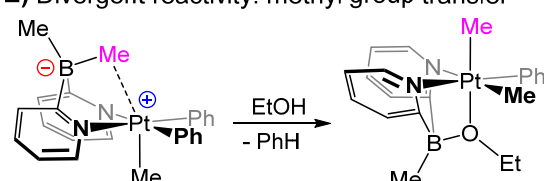


Figure 1.14. A selection of remote zwitterionic metal complexes and some of their divergent reactivity. **A**: complexes with cationic metal;<sup>323–331</sup> **B**: complexes with anionic metal;<sup>332–339</sup> **C**: complexes with both cationic and anionic metals;<sup>340–343</sup> **D**: hydrogen activation;<sup>344</sup> **E**: methyl group migration.<sup>345</sup>

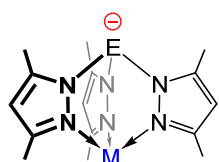
As mentioned above, despite a limited number of comparative studies, the performance of zwitterionic catalysts is similar to that of the ionic analogues.<sup>318,329,354,355,346–353</sup> However, in some cases, increased activity and divergent reactivity were observed,<sup>329,344,345,348,356,357</sup> in particular owing to the charge separation endowing these systems with amphiphilic character. For instance, a carboxylate-functionalized zwitterionic bis-NHC Ir(I)cod complex (*Figure 1.14D*) shows increased CO<sub>2</sub> hydrogenation activity with respect to the cationic carboxylate-free analogue.<sup>344</sup> The authors proposed that the carboxylate moiety stabilizes the active Ir(III) hydride through coordination, resulting into a *fac*- $\kappa^3$ -C,C',O complex. Another notable example is a dimethyldi(2-pyridyl)boratoplatinum complex (*Figure 1.14E*) than can activate alcohols and transfer one of the borate methyls to the metal accompanied by nucleophilic attack of the solvent at boron.<sup>345</sup>

### 1.3.5.3 Naked tetrel anions

Naked anions are another class of compounds that can benefit from remote charge separation. Normally, naked anions are complemented by weakly-coordinating cations and/or emerge due to differential solvation effects in dipolar aprotic solvents that stabilize positive charges better than the negative ones.<sup>358</sup> As follows from the name, zwitterionic naked anions have a positive charge elsewhere in the molecule, electronically insulated from the anionic center *via* the linker groups. While this leads to formal cancellation of the negative charge, stabilization by means of electrostatic and electronic effects is not sufficient to quench the reactivity of the anionic lone pair. This translates into high nucleophilicity and basicity, which found applications in FLP chemistry, along with high electron donor strength that attracted attention of the coordination and organometallic chemists. These applications are discussed in more detail below.

The major bulk of research in the field of zwitterionic naked anions is centered around tetrels, the lightest of which – carboanions – are mostly represented by various C<sub>3</sub>-symmetric trigonal pyramidal topologies. The most common systems of such type are tris(pyrazolyl)methanides<sup>359–368</sup> and hexa(pyrazolyl)dimethanides<sup>363,364,368–371</sup> (*Figure 1.15A*) stabilized by mono- and dicationic metals, respectively. Given that tris(pyrazolyl)methanides are isoelectronic to tris(pyrazolyl)borates (CH $\leftrightarrow$ BH<sup>-</sup>), several studies were done to compare the coordination behavior of these two systems:<sup>362,369</sup> while the hard cations bind methanides similarly to pyrazolylborates in an N<sub>3</sub>-capping manner, the soft ions tend to form covalent metal-carbon bonds. It was also demonstrated that, in case of N<sub>3</sub>-capping, the carbanionic center is capable of ligation

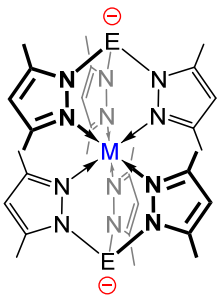
## A) Tris(pyrazolyl)tetrelides



**E = C:**  $M = \text{Li}^+(\text{THF}), \text{Ca}^+\text{HMDS}(\text{THF}),$   
 $\text{Mg}^+\text{Cl}, \text{Zn}^+\text{Me}, \text{Ag}^+(\text{PPh}_3)_3,$   
 ${}^t\text{BuN}=\text{Ti}^+\text{Cl}(\text{THF})$

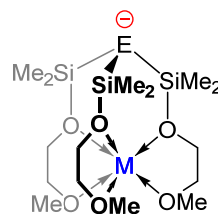
**E = Si:**  $M = \text{Li}^+(\text{THF})$

**E = Ge:**  $M = \text{Na}^+(\text{THF})_3$

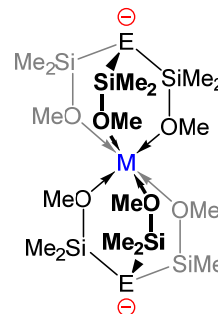


**E = C:**  $M = \text{Mg}^{2+}, \text{Ca}^{2+}, \text{Zn}^{2+},$   
 $\text{Cd}^{2+}, \text{Fe}^{2+}, \text{Co}^{2+}$

## B) Tris(dimethylsilyl)methanide ethers

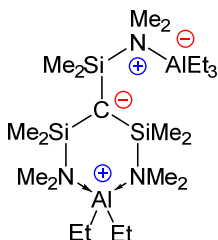
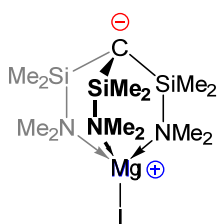
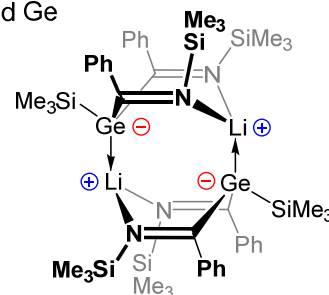
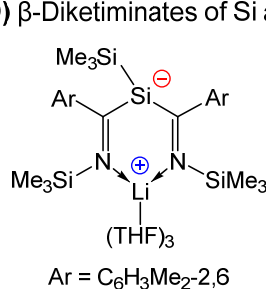


**E = C, Si, Ge:**  $M = \text{Li}^+, \text{Na}^+, \text{K}^+$

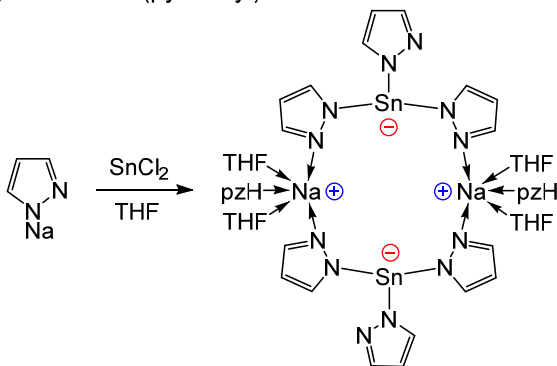


**E = C:**  $M = \text{Mg}^{2+}, \text{Ca}^{2+}, \text{Zn}^{2+},$   
**E = Si:**  $M = \text{Mg}^{2+}, \text{Ca}^{2+}, \text{Ba}^{2+},$   
 $\text{Eu}^{2+}, \text{Yb}^{2+}, \text{Sm}^{2+}$

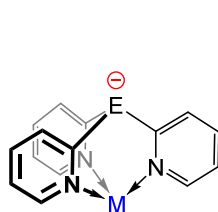
## C) Other naked carbanions

D)  $\beta$ -Diketiminates of Si and Ge

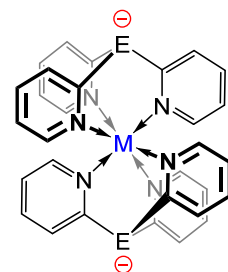
## E) Dimeric tris(pyrazolyl)stannide



## F) Heavy tris(pyridyl)tetrelides



**E = Sn, Pb:**  $M = \text{Li}^+(\text{THF})$



**E = Sn:**  $M = \text{Yb}^{2+}, \text{Eu}^{2+}$

Figure 1.15. Remote zwitterionic naked tetrel anions. **A:** tris(pyrazolyl)tetrelides of carbon, silicon and germanium;<sup>359,360,369–374,361–368</sup> **B:** Tris(dimethylsilyl)methanide ether tetrelides of carbon, silicon and germanium;<sup>375–377</sup> **C:** other naked carbanions;<sup>375,378</sup> **D:**  $\beta$ -diketiminates of silicon and germanium;<sup>379</sup> **E:** non- $\text{C}_3$ -symmetric dimeric tris(pyrazolyl)stannide;<sup>380</sup> **F:** tris(pyridyl)tetrelides of tin and lead.<sup>381–386</sup>

with another metal ion, leading to bimetallic complexes.<sup>368</sup> In addition, if the N<sub>3</sub>-capped metal is redox-active, it may lead ligand to non-innocence with respect to the C-bound metal.<sup>369</sup> Another type of zwitterionic naked carbanions are substituted tris(dimethylsilyl)methanides (*Figure 1.15B*),<sup>375–377</sup> which envelop a metal cation with their (silyl)ether or silylamine linkers. In terms of reactivity and coordination behavior, these systems are similar to tris(pyrazolyl)methanides. Systematic studies with different cations as a source of positive charge have revealed that the basicity of the anionic carbon, its atomic charge and, consequently, donor strength, are a function of the charge-to-size ratio of the employed cation,<sup>376</sup> providing opportunities for ligand tunability. Additionally, it was shown that the carbanionic center can act as a base in the FLP pair with boranes, as illustrated by dihydrogen splitting.<sup>377</sup> A rare example of a planar naked zwitterionic carboanion is stabilized by an Al(III) cation and was characterized by X-ray crystallography (*Figure 1.15C*).<sup>378</sup>

For the heavier tetrrels, silicon<sup>376,387–391</sup> and germanium,<sup>376</sup> tris(dimethylsilyl)-based systems appear to be the most popular (*Figure 1.15B*). A series of comparative studies by Krempner and co-workers<sup>376,389</sup> revealed that, similarly to the analogous methanides, the donor strength of such silanides and germanides can be tuned with the charge density of the trapped cation. Moreover, the silanides are capable of ligating to transition metal and metalloid sites, such as ZnCl<sub>2</sub>, ZnI<sub>2</sub>, ZnMe<sub>2</sub>,<sup>390</sup> W(CO)<sub>5</sub> and BPh<sub>3</sub>,<sup>391</sup> clearly demonstrating the potential of such systems for transition metal and FLP chemistry. Tris(pyrazolyl) zwitterions of silicon<sup>372–374</sup> and germanium<sup>380</sup> are also known (*Figure 1.15A*), but most of the relevant publications are dedicated to their synthesis/structural characterization, and not so much to their properties. A rare example of a non-C<sub>3</sub>-symmetric naked zwitterion, a 3-sila-β-diketimate, was synthesized in a reaction of Li(Si(SiMe<sub>3</sub>)<sub>3</sub>)(THF)<sub>3</sub> with two equivalents of 2,6-dimethylbenzotrile (*Figure 1.15D*). The attempts to produce an analogous germanide led to a dimeric solid-state structure that does not have a naked anionic site (*Figure 1.15D*);<sup>379</sup> its solution behavior, however, was not studied.

Neither tris(dimethylsilyl) nor tris(pyrazolyl) naked zwitterions of tin and lead are known. An attempt to synthesize tris(pyrazolyl)stannide by salt metathesis between SnCl<sub>2</sub> and pyrazolylsodium led to a dimer with only four bridging pyrazoles out of six (*Figure 1.15E*).<sup>380</sup> Instead, by far the most popular type of architecture for heavier tetrrels are tris(pyridyl)-based systems (*Figure 1.15F*).<sup>392</sup> Such naked zwitterions of tin<sup>381–384</sup> and lead<sup>385,386</sup> not only retain their solid-state structure in solution but also have an ability to complex to lanthanides (LaCp<sub>3</sub>, YbCp<sub>3</sub>)<sup>381,382,386</sup> and Lewis-acidic metal sites (AlMe<sub>3</sub>, GaMe<sub>3</sub>, InMe<sub>3</sub>).<sup>383</sup>

## 1.4 Concluding remarks

Charge separation is an important and diverse control tool that is complementary to electronic and ligand field effects. It occurs in nature, wherein oriented electric fields in enzymes impose a bias towards a desired product, in particular by affecting the spectroscopic oxidation state of a metal center. It is also employed by chemists for fine manipulation of electronic structure and energy storage, which affects reactivity and global molecular properties. However, given that charges are not quantum observables, and charge separation occurs, to some extent, in every molecule, scrutinizing these effects is a challenging problem inviting further investigation. Aside from computational models, one approach is to use the systems with large built-in charge separation implemented by design, i.e. zwitterions, which forms the subject of the present thesis.



## 1.5 References

- (1) Warshel, A. Energetics of Enzyme Catalysis. *Proc. Natl. Acad. Sci.* **1978**, *75* (11), pp 5250–5254. DOI: 10.1073/pnas.75.11.5250.
- (2) Warshel, A. Electrostatic Basis of Structure-Function Correlation in Proteins. *Acc. Chem. Res.* **1981**, *14* (9), pp 284–290. DOI: 10.1021/ar00069a004.
- (3) Aragonès, A. C.; Haworth, N. L.; Darwish, N.; Ciampi, S.; Bloomfield, N. J.; Wallace, G. G.; Díez-Pérez, I.; Coote, M. L. Electrostatic Catalysis of a Diels–Alder Reaction. *Nature* **2016**, *531* (7592), pp 88–91. DOI: 10.1038/nature16989.
- (4) Shaik, S.; Ramanan, R.; Danovich, D.; Mandal, D. Structure and Reactivity/Selectivity Control by Oriented-External Electric Fields. *Chem. Soc. Rev.* **2018**, *47* (14), pp 5125–5145. DOI: 10.1039/C8CS00354H.
- (5) Shaik, S.; Mandal, D.; Ramanan, R. Oriented Electric Fields as Future Smart Reagents in Chemistry. *Nat. Chem.* **2016**, *8* (12), pp 1091–1098. DOI: 10.1038/nchem.2651.
- (6) Ciampi, S.; Darwish, N.; Aitken, H. M.; Díez-Pérez, I.; Coote, M. L. Harnessing Electrostatic Catalysis in Single Molecule, Electrochemical and Chemical Systems: A Rapidly Growing Experimental Tool Box. *Chem. Soc. Rev.* **2018**, *47* (14), pp 5146–5164. DOI: 10.1039/C8CS00352A.
- (7) Stuyver, T.; Danovich, D.; Joy, J.; Shaik, S. External Electric Field Effects on Chemical Structure and Reactivity. *WIREs Comput. Mol. Sci.* **2020**, *10* (2), p e1438. DOI: 10.1002/wcms.1438.
- (8) Weberg, A. B.; McCollom, S. P.; Thierer, L. M.; Gau, M. R.; Carroll, P. J.; Tomson, N. C. Using Internal Electrostatic Fields to Manipulate the Valence Manifolds of Copper Complexes. *Chem. Sci.* **2021**, *12* (12), pp 4395–4404. DOI: 10.1039/D0SC06364A.
- (9) Skubi, K. L.; Hooper, R. X.; Mercado, B. Q.; Bollmeyer, M. M.; Macmillan, S. N.; Lancaster, K. M.; Holland, P. L. Iron Complexes of a Proton-Responsive SCS Pincer Ligand with a Sensitive Electronic Structure. *Inorg. Chem.* **2022**, *61* (3), pp 1644–1658. DOI: 10.1021/acs.inorgchem.1c03499.
- (10) Kang, K.; Fuller, J.; Reath, A. H.; Ziller, J. W.; Alexandrova, A. N.; Yang, J. Y. Installation of Internal Electric Fields by Non-Redox Active Cations in Transition Metal Complexes. *Chem. Sci.* **2019**, *10* (43), pp 10135–10142. DOI: 10.1039/C9SC02870F.
- (11) Hoffmann, N. M.; Wang, X.; Berkelbach, T. C. Linear Free Energy Relationships in Electrostatic Catalysis. *ACS Catal.* **2022**, No. 4, pp 8237–8241. DOI: 10.1021/acscatal.2c02234.
- (12) Meir, R.; Chen, H.; Lai, W.; Shaik, S. Oriented Electric Fields Accelerate Diels-Alder Reactions and Control the *Endo/Exo* Selectivity. *ChemPhysChem* **2010**, *11* (1), pp 301–310. DOI: 10.1002/cphc.200900848.
- (13) Joy, J.; Stuyver, T.; Shaik, S. Oriented External Electric Fields and Ionic Additives Elicit Catalysis and Mechanistic Crossover in Oxidative Addition Reactions. *J. Am. Chem. Soc.* **2020**, *142* (8), pp 3836–3850. DOI: 10.1021/jacs.9b11507.
- (14) *Bioinspiration and Biomimicry in Chemistry: Reverse-Engineering Nature*; Swiegers, G. F., Ed.; John Wiley & Sons: Hoboken, N.J., 2012. DOI: 10.1002/9781118310083.
- (15) Morgenstern, A.; Jaszai, M.; Eberhart, M. E.; Alexandrova, A. N. Quantified Electrostatic Preorganization in Enzymes Using the Geometry of the Electron Charge Density. *Chem. Sci.* **2017**, *8* (7), pp 5010–5018. DOI: 10.1039/C7SC01301A.
- (16) Childs, W.; Boxer, S. G. Solvation Response along the Reaction Coordinate in the Active Site of Ketosteroid Isomerase. *J. Am. Chem. Soc.* **2010**, *132* (18), pp 6474–6480. DOI: 10.1021/ja1007849.
- (17) Fuxreiter, M.; Mones, L. The Role of Reorganization Energy in Rational Enzyme Design. *Curr. Opin. Chem. Biol.* **2014**, *21*, pp 34–41. DOI: 10.1016/j.cbpa.2014.03.011.
- (18) Wu, Y.; Boxer, S. G. A Critical Test of the Electrostatic Contribution to Catalysis with Noncanonical Amino Acids in Ketosteroid Isomerase. *J. Am. Chem. Soc.* **2016**, *138* (36), pp 11890–11895. DOI: 10.1021/jacs.6b06843.
- (19) Schrödinger, L.; DeLano, W. PyMOL. 2020.
- (20) Jurrus, E.; Engel, D.; Star, K.; Monson, K.; Brandi, J.; Felberg, L. E.; Brookes, D. H.; Wilson, L.; Chen, J.; Liles, K.; Chun, M.; Li, P.; Gohara, D. W.; Dolinsky, T.; Konecny, R.; Koes, D. R.; Nielsen, J. E.; Head-Gordon, T.; Geng, W.; Krasny, R.; Wei, G.; Holst, M. J.; McCammon, J. A.; Baker, N. A. Improvements to the APBS Biomolecular Solvation Software Suite. *Protein Sci.* **2018**, *27* (1), pp 112–128. DOI: 10.1002/pro.3280.
- (21) Fried, S. D.; Boxer, S. G. Measuring Electric Fields and Noncovalent Interactions Using the Vibrational

- Stark Effect. *Acc. Chem. Res.* **2015**, *48* (4), pp 998–1006. DOI: 10.1021/ar500464j.
- (22) Fafarman, A. T.; Boxer, S. G. Nitrile Bonds as Infrared Probes of Electrostatics in Ribonuclease S. *J. Phys. Chem. B* **2010**, *114* (42), pp 13536–13544. DOI: 10.1021/jp106406p.
- (23) Bagchi, S.; Fried, S. D.; Boxer, S. G. A Solvatochromic Model Calibrates Nitriles' Vibrational Frequencies to Electrostatic Fields. *J. Am. Chem. Soc.* **2012**, *134* (25), pp 10373–10376. DOI: 10.1021/ja303895k.
- (24) Liu, C. T.; Layfield, J. P.; Stewart, R. J.; French, J. B.; Hanoian, P.; Asbury, J. B.; Hammes-Schiffer, S.; Benkovic, S. J. Probing the Electrostatics of Active Site Microenvironments along the Catalytic Cycle for Escherichia Coli Dihydrofolate Reductase. *J. Am. Chem. Soc.* **2014**, *136* (29), pp 10349–10360. DOI: 10.1021/ja5038947.
- (25) Fried, S. D.; Bagchi, S.; Boxer, S. G. Extreme Electric Fields Power Catalysis in the Active Site of Ketosteroid Isomerase. *Science* **2014**, *346* (6216), pp 1510–1514. DOI: 10.1126/science.1259802.
- (26) Vannini, A.; Volpari, C.; Gallinari, P.; Jones, P.; Mattu, M.; Carfi, A.; De Francesco, R.; Steinkühler, C.; Di Marco, S. Substrate Binding to Histone Deacetylases as Shown by the Crystal Structure of the HDAC8–Substrate Complex. *EMBO Rep.* **2007**, *8* (9), pp 879–884. DOI: 10.1038/sj.embor.7401047.
- (27) Porter, N. J.; Christianson, D. W. Structure, Mechanism, and Inhibition of the Zinc-Dependent Histone Deacetylases. *Curr. Opin. Struct. Biol.* **2019**, *59*, pp 9–18. DOI: 10.1016/j.sbi.2019.01.004.
- (28) Štrajbl, M.; Shurki, A.; Kato, M.; Warshel, A. Apparent NAC Effect in Chorismate Mutase Reflects Electrostatic Transition State Stabilization. *J. Am. Chem. Soc.* **2003**, *125* (34), pp 10228–10237. DOI: 10.1021/ja0356481.
- (29) Kienhöfer, A.; Kast, P.; Hilvert, D. Selective Stabilization of the Chorismate Mutase Transition State by a Positively Charged Hydrogen Bond Donor. *J. Am. Chem. Soc.* **2003**, *125* (11), pp 3206–3207. DOI: 10.1021/ja0341992.
- (30) Chook, Y. M.; Ke, H.; Lipscomb, W. N. Crystal Structures of the Monofunctional Chorismate Mutase from Bacillus Subtilis and Its Complex with a Transition State Analog. *Proc. Natl. Acad. Sci.* **1993**, *90* (18), pp 8600–8603. DOI: 10.1073/pnas.90.18.8600.
- (31) Burschowsky, D.; van Eerde, A.; Ökvist, M.; Kienhöfer, A.; Kast, P.; Hilvert, D.; Krenkel, U. Electrostatic Transition State Stabilization Rather than Reactant Destabilization Provides the Chemical Basis for Efficient Chorismate Mutase Catalysis. *Proc. Natl. Acad. Sci.* **2014**, *111* (49), pp 17516–17521. DOI: 10.1073/pnas.1408512111.
- (32) Drazic, A.; Myklebust, L. M.; Ree, R.; Arnesen, T. The World of Protein Acetylation. *Biochim. Biophys. Acta - Proteins Proteomics* **2016**, *1864* (10), pp 1372–1401. DOI: 10.1016/j.bbapap.2016.06.007.
- (33) Somoza, J. R.; Skene, R. J.; Katz, B. A.; Mol, C.; Ho, J. D.; Jennings, A. J.; Luong, C.; Arvai, A.; Buggy, J. J.; Chi, E.; Tang, J.; Sang, B.-C.; Verner, E.; Wynands, R.; Leahy, E. M.; Dougan, D. R.; Snell, G.; Navre, M.; Knuth, M. W.; Swanson, R. V.; McRee, D. E.; Tari, L. W. Structural Snapshots of Human HDAC8 Provide Insights into the Class I Histone Deacetylases. *Structure* **2004**, *12* (7), pp 1325–1334. DOI: 10.1016/j.str.2004.04.012.
- (34) Wu, R.; Wang, S.; Zhou, N.; Cao, Z.; Zhang, Y. A Proton-Shuttle Reaction Mechanism for Histone Deacetylase 8 and the Catalytic Role of Metal Ions. *J. Am. Chem. Soc.* **2010**, *132* (27), pp 9471–9479. DOI: 10.1021/ja103932d.
- (35) Kelty, M. L.; McNeece, A. J.; Kurutz, J. W.; Filatov, A. S.; Anderson, J. S. Electrostatic vs. Inductive Effects in Phosphine Ligand Donor Properties and Reactivity. *Chem. Sci.* **2022**, *13* (15), pp 4377–4387. DOI: 10.1039/D1SC04277G.
- (36) Martin, D. J.; Johnson, S. I.; Mercado, B. Q.; Raugei, S.; Mayer, J. M. Intramolecular Electrostatic Effects on O<sub>2</sub>, CO<sub>2</sub>, and Acetate Binding to a Cationic Iron Porphyrin. *Inorg. Chem.* **2020**, *59* (23), pp 17402–17414. DOI: 10.1021/acs.inorgchem.0c02703.
- (37) Gonthier, J. F.; Steinmann, S. N.; Wodrich, M. D.; Corminboeuf, C. Quantification of “Fuzzy” Chemical Concepts: A Computational Perspective. *Chem. Soc. Rev.* **2012**, *41* (13), p 4671. DOI: 10.1039/c2cs35037h.
- (38) Shaik, S.; Danovich, D.; Joy, J.; Wang, Z.; Stuyver, T. Electric-Field Mediated Chemistry: Uncovering and Exploiting the Potential of (Oriented) Electric Fields to Exert Chemical Catalysis and Reaction Control. *J. Am. Chem. Soc.* **2020**, *142* (29), pp 12551–12562. DOI: 10.1021/jacs.0c05128.
- (39) Gorin, C. F.; Beh, E. S.; Bui, Q. M.; Dick, G. R.; Kanan, M. W. Interfacial Electric Field Effects on a Carbene Reaction Catalyzed by Rh Porphyrins. *J. Am. Chem. Soc.* **2013**, *135* (30), pp 11257–11265. DOI: 10.1021/ja404394z.

- (40) Gorin, C. F.; Beh, E. S.; Kanan, M. W. An Electric Field–Induced Change in the Selectivity of a Metal Oxide–Catalyzed Epoxide Rearrangement. *J. Am. Chem. Soc.* **2012**, *134* (1), pp 186–189. DOI: 10.1021/ja210365j.
- (41) Zhang, L.; Laborda, E.; Darwish, N.; Noble, B. B.; Tyrell, J. H.; Pluczyk, S.; Le Brun, A. P.; Wallace, G. G.; Gonzalez, J.; Coote, M. L.; Ciampi, S. Electrochemical and Electrostatic Cleavage of Alkoxyamines. *J. Am. Chem. Soc.* **2018**, *140* (2), pp 766–774. DOI: 10.1021/jacs.7b11628.
- (42) Hastings, C. J.; Bergman, R. G.; Raymond, K. N. Origins of Large Rate Enhancements in the Nazarov Cyclization Catalyzed by Supramolecular Encapsulation. *Chem. Eur. J.* **2014**, *20* (14), pp 3966–3973. DOI: 10.1002/chem.201303885.
- (43) Frushicheva, M. P.; Mukherjee, S.; Warshel, A. Electrostatic Origin of the Catalytic Effect of a Supramolecular Host Catalyst. *J. Phys. Chem. B* **2012**, *116* (45), pp 13353–13360. DOI: 10.1021/jp3084327.
- (44) Cullen, W.; Misuraca, M. C.; Hunter, C. A.; Williams, N. H.; Ward, M. D. Highly Efficient Catalysis of the Kemp Elimination in the Cavity of a Cubic Coordination Cage. *Nat. Chem.* **2016**, *8* (3), pp 231–236. DOI: 10.1038/nchem.2452.
- (45) Yoshizawa, M.; Tamura, M.; Fujita, M. Diels-Alder in Aqueous Molecular Hosts: Unusual Regioselectivity and Efficient Catalysis. *Science* **2006**, *312* (5771), pp 251–254. DOI: 10.1126/science.1124985.
- (46) Morimoto, M.; Bierschenk, S. M.; Xia, K. T.; Bergman, R. G.; Raymond, K. N.; Toste, F. D. Advances in Supramolecular Host-Mediated Reactivity. *Nat. Catal.* **2020**, *3* (12), pp 969–984. DOI: 10.1038/s41929-020-00528-3.
- (47) Hong, C. M.; Bergman, R. G.; Raymond, K. N.; Toste, F. D. Self-Assembled Tetrahedral Hosts as Supramolecular Catalysts. *Acc. Chem. Res.* **2018**, *51* (10), pp 2447–2455. DOI: 10.1021/acs.accounts.8b00328.
- (48) Welborn, V. V.; Li, W.-L.; Head-Gordon, T. Interplay of Water and a Supramolecular Capsule for Catalysis of Reductive Elimination Reaction from Gold. *Nat. Commun.* **2020**, *11* (1), p 415. DOI: 10.1038/s41467-019-14251-6.
- (49) Vaissier Welborn, V.; Head-Gordon, T. Electrostatics Generated by a Supramolecular Capsule Stabilizes the Transition State for Carbon–Carbon Reductive Elimination from Gold(III) Complex. *J. Phys. Chem. Lett.* **2018**, *9* (14), pp 3814–3818. DOI: 10.1021/acs.jpcclett.8b01710.
- (50) Kaphan, D. M.; Toste, F. D.; Bergman, R. G.; Raymond, K. N. Enabling New Modes of Reactivity via Constrictive Binding in a Supramolecular-Assembly-Catalyzed Aza-Prins Cyclization. *J. Am. Chem. Soc.* **2015**, *137* (29), pp 9202–9205. DOI: 10.1021/jacs.5b01261.
- (51) Welborn, V. V.; Ruiz Pestana, L.; Head-Gordon, T. Computational Optimization of Electric Fields for Better Catalysis Design. *Nat. Catal.* **2018**, *1* (9), pp 649–655. DOI: 10.1038/s41929-018-0109-2.
- (52) Mansoor, E.; Van der Mynsbrugge, J.; Head-Gordon, M.; Bell, A. T. Impact of Long-Range Electrostatic and Dispersive Interactions on Theoretical Predictions of Adsorption and Catalysis in Zeolites. *Catal. Today* **2018**, *312*, pp 51–65. DOI: 10.1016/j.cattod.2018.02.007.
- (53) Klinska, M.; Smith, L. M.; Gryn'ova, G.; Banwell, M. G.; Coote, M. L. Experimental Demonstration of pH-Dependent Electrostatic Catalysis of Radical Reactions. *Chem. Sci.* **2015**, *6* (10), pp 5623–5627. DOI: 10.1039/C5SC01307K.
- (54) Gryn'ova, G.; Coote, M. L. Directionality and the Role of Polarization in Electric Field Effects on Radical Stability. *Aust. J. Chem.* **2017**, *70* (4), p 367. DOI: 10.1071/CH16579.
- (55) Zhang, K.; Noble, B. B.; Mater, A. C.; Monteiro, M. J.; Coote, M. L.; Jia, Z. Effect of Heteroatom and Functionality Substitution on the Oxidation Potential of Cyclic Nitroxide Radicals: Role of Electrostatics in Electrochemistry. *Phys. Chem. Chem. Phys.* **2018**, *20* (4), pp 2606–2614. DOI: 10.1039/C7CP07444A.
- (56) Zhang, L.; Vogel, Y. B.; Noble, B. B.; Gonçalves, V. R.; Darwish, N.; Brun, A. Le; Gooding, J. J.; Wallace, G. G.; Coote, M. L.; Ciampi, S. TEMPO Monolayers on Si(100) Electrodes: Electrostatic Effects by the Electrolyte and Semiconductor Space-Charge on the Electroactivity of a Persistent Radical. *J. Am. Chem. Soc.* **2016**, *138* (30), pp 9611–9619. DOI: 10.1021/jacs.6b04788.
- (57) Davis, H. J.; Mihai, M. T.; Phipps, R. J. Ion Pair-Directed Regiocontrol in Transition-Metal Catalysis: A Meta-Selective C–H Borylation of Aromatic Quaternary Ammonium Salts. *J. Am. Chem. Soc.* **2016**, *138* (39), pp 12759–12762. DOI: 10.1021/jacs.6b08164.
- (58) Chattopadhyay, B.; Dannatt, J. E.; Andujar-De Sanctis, I. L.; Gore, K. A.; Maleczka, R. E.; Singleton, D. A.; Smith, M. R. Ir-Catalyzed Ortho-Borylation of Phenols Directed by Substrate–Ligand

- Electrostatic Interactions: A Combined Experimental/in Silico Strategy for Optimizing Weak Interactions. *J. Am. Chem. Soc.* **2017**, *139* (23), pp 7864–7871. DOI: 10.1021/jacs.7b02232.
- (59) Olivo, G.; Farinelli, G.; Barbieri, A.; Lanzalunga, O.; Di Stefano, S.; Costas, M. Supramolecular Recognition Allows Remote, Site-Selective C–H Oxidation of Methylenic Sites in Linear Amines. *Angew. Chemie Int. Ed.* **2017**, *56* (51), pp 16347–16351. DOI: 10.1002/anie.201709280.
- (60) Olivo, G.; Capocasa, G.; Lanzalunga, O.; Di Stefano, S.; Costas, M. Enzyme-like Substrate-Selectivity in C–H Oxidation Enabled by Recognition. *Chem. Commun.* **2019**, *55* (7), pp 917–920. DOI: 10.1039/C8CC09328H.
- (61) Montero Bastidas, J. R.; Oleskey, T. J.; Miller, S. L.; Smith, M. R.; Maleczka, R. E. Para-Selective, Iridium-Catalyzed C–H Borylations of Sulfated Phenols, Benzyl Alcohols, and Anilines Directed by Ion-Pair Electrostatic Interactions. *J. Am. Chem. Soc.* **2019**, *141* (39), pp 15483–15487. DOI: 10.1021/jacs.9b08464.
- (62) Lau, V. M.; Pfalzgraff, W. C.; Markland, T. E.; Kanan, M. W. Electrostatic Control of Regioselectivity in Au(I)-Catalyzed Hydroarylation. *J. Am. Chem. Soc.* **2017**, *139* (11), pp 4035–4041. DOI: 10.1021/jacs.6b11971.
- (63) Lau, V. M.; Gorin, C. F.; Kanan, M. W. Electrostatic Control of Regioselectivity via Ion Pairing in a Au(I)-Catalyzed Rearrangement. *Chem. Sci.* **2014**, *5* (12), pp 4975–4979. DOI: 10.1039/c4sc02058h.
- (64) Qu, X.; Persson, K. A. Toward Accurate Modeling of the Effect of Ion-Pair Formation on Solute Redox Potential. *J. Chem. Theory Comput.* **2016**, *12* (9), pp 4501–4508. DOI: 10.1021/acs.jctc.6b00289.
- (65) Smith, P. J.; Wilcox, C. S. The Chemistry of Synthetic Receptors and Functional Group Arrays. 13. The Intramolecular Salt Effect. *J. Org. Chem.* **1990**, *55* (22), pp 5675–5678. DOI: 10.1021/jo00309a006.
- (66) Smith, P. J.; Wilcox, C. S. The Chemistry of Functional Group Arrays. Electrostatic Catalysis and the “Intramolecular Salt Effect”. *Tetrahedron* **1991**, *47* (14–15), pp 2617–2628. DOI: 10.1016/S0040-4020(01)81794-4.
- (67) Smith, P. J.; Kim, E.; Wilcox, C. S. Substrate-Specific Catalysis by Ion Pairs. *Angew. Chemie Int. Ed. English* **1993**, *32* (11), pp 1648–1650. DOI: 10.1002/anie.199316481.
- (68) Raposo, C.; Wilcox, C. S. The Intramolecular Salt Effect in Chiral Auxiliaries. Enhanced Diastereoselectivity in a Nitrile Oxide Cycloaddition via Rational Transition State Stabilization. *Tetrahedron Lett.* **1999**, *40* (7), pp 1285–1288. DOI: 10.1016/S0040-4039(98)02692-6.
- (69) Macchioni, A. Ion Pairing in Transition-Metal Organometallic Chemistry. *Chem. Rev.* **2005**, *105* (6), pp 2039–2074. DOI: 10.1021/cr0300439.
- (70) Reath, A. H.; Ziller, J. W.; Tsay, C.; Ryan, A. J.; Yang, J. Y. Redox Potential and Electronic Structure Effects of Proximal Nonredox Active Cations in Cobalt Schiff Base Complexes. *Inorg. Chem.* **2017**, *56* (6), pp 3713–3718. DOI: 10.1021/acs.inorgchem.6b03098.
- (71) Teptarakulkarn, P.; Lorpaiboon, W.; Anusanti, T.; Laowiwatkasem, N.; Chainok, K.; Sangtrirutnugul, P.; Surawatanawong, P.; Chantarojsiri, T. Incorporation of Cation Affects the Redox Reactivity of Fe–NNN Complexes on C–H Oxidation. *Inorg. Chem.* **2022**. DOI: 10.1021/acs.inorgchem.2c00762.
- (72) Chantarojsiri, T.; Ziller, J. W.; Yang, J. Y. Incorporation of Redox-Inactive Cations Promotes Iron Catalyzed Aerobic C–H Oxidation at Mild Potentials. *Chem. Sci.* **2018**, *9* (9), pp 2567–2574. DOI: 10.1039/C7SC04486K.
- (73) Chantarojsiri, T.; Reath, A. H.; Yang, J. Y. Cationic Charges Leading to an Inverse Free-Energy Relationship for N–N Bond Formation by Mn<sup>VI</sup> Nitrides. *Angew. Chemie Int. Ed.* **2018**, *57* (43), pp 14037–14042. DOI: 10.1002/anie.201805832.
- (74) Beer, P. D. Transition Metal and Organic Redox-Active Macrocycles Designed to Electrochemically Recognize Charged and Neutral Guest Species; 1992; pp 79–157. DOI: 10.1016/S0898-8838(08)60259-7.
- (75) Bell, S. R.; Groves, J. T. A Highly Reactive P450 Model Compound I. *J. Am. Chem. Soc.* **2009**, *131* (28), pp 9640–9641. DOI: 10.1021/ja903394s.
- (76) Gao, H.; Groves, J. T. Fast Hydrogen Atom Abstraction by a Hydroxo Iron(III) Porphyrzine. *J. Am. Chem. Soc.* **2017**, *139* (11), pp 3938–3941. DOI: 10.1021/jacs.6b13091.
- (77) Stuyver, T.; Ramanan, R.; Mallick, D.; Shaik, S. Oriented (Local) Electric Fields Drive the Millionfold Enhancement of the H-Abstraction Catalysis Observed for Synthetic Metalloenzyme Analogues. *Angew. Chemie Int. Ed.* **2020**, *59* (20), pp 7915–7920. DOI: 10.1002/anie.201916592.
- (78) Erickson, J. D.; Preston, A. Z.; Linehan, J. C.; Wiedner, E. S. Enhanced Hydrogenation of Carbon Dioxide to Methanol by a Ruthenium Complex with a Charged Outer-Coordination Sphere. *ACS Catal.*

- 2020**, *10* (13), pp 7419–7423. DOI: 10.1021/acscatal.0c02268.
- (79) Burns, K. T.; Marks, W. R.; Cheung, P. M.; Seda, T.; Zakharov, L. N.; Gilbertson, J. D. Uncoupled Redox-Inactive Lewis Acids in the Secondary Coordination Sphere Entice Ligand-Based Nitrite Reduction. *Inorg. Chem.* **2018**, *57* (16), pp 9601–9610. DOI: 10.1021/acs.inorgchem.8b00032.
- (80) Lavallo, V.; Wright, J. H.; Tham, F. S.; Quinlivan, S. Perhalogenated Carba- Closo -Dodecaborate Anions as Ligand Substituents: Applications in Gold Catalysis. *Angew. Chemie Int. Ed.* **2013**, *52* (11), pp 3172–3176. DOI: 10.1002/anie.201209107.
- (81) Chan, A. L.; Estrada, J.; Kefalidis, C. E.; Lavallo, V. Changing the Charge: Electrostatic Effects in Pd-Catalyzed Cross-Coupling. *Organometallics* **2016**, *35* (19), pp 3257–3260. DOI: 10.1021/acs.organomet.6b00622.
- (82) Azcarate, I.; Costentin, C.; Robert, M.; Savéant, J.-M. Through-Space Charge Interaction Substituent Effects in Molecular Catalysis Leading to the Design of the Most Efficient Catalyst of CO<sub>2</sub>-to-CO Electrochemical Conversion. *J. Am. Chem. Soc.* **2016**, *138* (51), pp 16639–16644. DOI: 10.1021/jacs.6b07014.
- (83) Martin, D. J.; Mercado, B. Q.; Mayer, J. M. Combining Scaling Relationships Overcomes Rate versus Overpotential Trade-Offs in O<sub>2</sub> Molecular Electrocatalysis. *Sci. Adv.* **2020**, *6* (11), p eaaz3318. DOI: 10.1126/sciadv.aaz3318.
- (84) Martin, D. J.; Mayer, J. M. Oriented Electrostatic Effects on O<sub>2</sub> and CO<sub>2</sub> Reduction by a Polycationic Iron Porphyrin. *J. Am. Chem. Soc.* **2021**, *143* (30), pp 11423–11434. DOI: 10.1021/jacs.1c03132.
- (85) Zhang, R.; Warren, J. J. Controlling the Oxygen Reduction Selectivity of Asymmetric Cobalt Porphyrins by Using Local Electrostatic Interactions. *J. Am. Chem. Soc.* **2020**, *142* (31), pp 13426–13434. DOI: 10.1021/jacs.0c03861.
- (86) Zhu, M.; Yang, D.-T.; Ye, R.; Zeng, J.; Corbin, N.; Manthiram, K. Inductive and Electrostatic Effects on Cobalt Porphyrins for Heterogeneous Electrocatalytic Carbon Dioxide Reduction. *Catal. Sci. Technol.* **2019**, *9* (4), pp 974–980. DOI: 10.1039/C9CY00102F.
- (87) Wang, M.; Torbensen, K.; Salvatore, D.; Ren, S.; Joulié, D.; Dumoulin, F.; Mendoza, D.; Lassalle-Kaiser, B.; İsci, U.; Berlinguette, C. P.; Robert, M. CO<sub>2</sub> Electrochemical Catalytic Reduction with a Highly Active Cobalt Phthalocyanine. *Nat. Commun.* **2019**, *10* (1), p 3602. DOI: 10.1038/s41467-019-11542-w.
- (88) Nie, W.; Tarnopol, D. E.; McCrory, C. C. L. Enhancing a Molecular Electrocatalyst's Activity for CO<sub>2</sub> Reduction by Simultaneously Modulating Three Substituent Effects. *J. Am. Chem. Soc.* **2021**, *143* (10), pp 3764–3778. DOI: 10.1021/jacs.0c09357.
- (89) Sung, S.; Kumar, D.; Gil-Sepulcre, M.; Nippe, M. Electrocatalytic CO<sub>2</sub> Reduction by Imidazolium-Functionalized Molecular Catalysts. *J. Am. Chem. Soc.* **2017**, *139* (40), pp 13993–13996. DOI: 10.1021/jacs.7b07709.
- (90) Sung, S.; Li, X.; Wolf, L. M.; Meeder, J. R.; Bhuvanesh, N. S.; Grice, K. A.; Panetier, J. A.; Nippe, M. Synergistic Effects of Imidazolium-Functionalization on Fac-Mn(CO)<sub>3</sub> Bipyridine Catalyst Platforms for Electrocatalytic Carbon Dioxide Reduction. *J. Am. Chem. Soc.* **2019**, *141* (16), pp 6569–6582. DOI: 10.1021/jacs.8b13657.
- (91) Sahu, S.; Cheung, P. L.; Machan, C. W.; Chabolla, S. A.; Kubiak, C. P.; Gianneschi, N. C. Charged Macromolecular Rhenium Bipyridine Catalysts with Tunable CO<sub>2</sub> Reduction Potentials. *Chem. – A Eur. J.* **2017**, *23* (36), pp 8619–8622. DOI: 10.1002/chem.201701901.
- (92) Tsui, E. Y.; Tran, R.; Yano, J.; Agapie, T. Redox-Inactive Metals Modulate the Reduction Potential in Heterometallic Manganese–Oxido Clusters. *Nat. Chem.* **2013**, *5* (4), pp 293–299. DOI: 10.1038/nchem.1578.
- (93) Tsui, E. Y.; Agapie, T. Reduction Potentials of Heterometallic Manganese–Oxido Cubane Complexes Modulated by Redox-Inactive Metals. *Proc. Natl. Acad. Sci.* **2013**, *110* (25), pp 10084–10088. DOI: 10.1073/pnas.1302677110.
- (94) Dhar, D.; Yee, G. M.; Tolman, W. B. Effects of Charged Ligand Substituents on the Properties of the Formally Copper(III)-Hydroxide ([CuOH]<sub>2</sub><sup>+</sup>) Unit. *Inorg. Chem.* **2018**, *57* (16), pp 9794–9806. DOI: 10.1021/acs.inorgchem.8b01529.
- (95) Munz, D.; Meyer, K. Charge Frustration in Ligand Design and Functional Group Transfer. *Nat. Rev. Chem.* **2021**, *5* (6), pp 422–439. DOI: 10.1038/s41570-021-00276-3.
- (96) Zwitterionic Compounds/Zwitterions. In *The IUPAC Compendium of Chemical Terminology*; International Union of Pure and Applied Chemistry (IUPAC): Research Triangle Park, NC, 2014. DOI:

- 10.1351/goldbook.Z06752.
- (97) Shaik, S.; Hiberty, P. C. *A Chemist's Guide to Valence Bond Theory*; John Wiley & Sons, Inc.: Hoboken, NJ, USA, 2007. DOI: 10.1002/9780470192597.
- (98) Glendening, E. D.; Weinhold, F. Natural Resonance Theory: I. General Formalism. *J. Comput. Chem.* **1998**, *19* (6), pp 593–609. DOI: 10.1002/(SICI)1096-987X(19980430)19:6<593::AID-JCC3>3.0.CO;2-M.
- (99) Glendening, E. D.; Weinhold, F. Natural Resonance Theory: II. Natural Bond Order and Valency. *J. Comput. Chem.* **1998**, *19* (6), pp 610–627. DOI: 10.1002/(SICI)1096-987X(19980430)19:6<610::AID-JCC4>3.0.CO;2-U.
- (100) Soleilhavoup, M.; Bertrand, G. Stable Carbenes, Nitrenes, Phosphinidenes, and Borylenes: Past and Future. *Chem* **2020**, *6* (6), pp 1275–1282. DOI: 10.1016/j.chempr.2020.04.015.
- (101) Dahcheh, F.; Martin, D.; Stephan, D. W.; Bertrand, G. Synthesis and Reactivity of a CAAC-Aminoborylene Adduct: A Hetero-Allene or an Organoboron Isoelectronic with Singlet Carbenes. *Angew. Chemie Int. Ed.* **2014**, *53* (48), pp 13159–13163. DOI: 10.1002/anie.201408371.
- (102) Arduengo, A. J.; Harlow, R. L.; Kline, M. A Stable Crystalline Carbene. *J. Am. Chem. Soc.* **1991**, *113* (1), pp 361–363. DOI: 10.1021/ja00001a054.
- (103) Dielmann, F.; Back, O.; Henry-Ellinger, M.; Jerabek, P.; Frenking, G.; Bertrand, G. A Crystalline Singlet Phosphinonitrene: A Nitrogen Atom–Transfer Agent. *Science* **2012**, *337* (6101), pp 1526–1528. DOI: 10.1126/science.1226022.
- (104) Driess, M.; Yao, S.; Brym, M.; van Wüllen, C.; Lentz, D. A New Type of *N*-Heterocyclic Silylene with Ambivalent Reactivity. *J. Am. Chem. Soc.* **2006**, *128* (30), pp 9628–9629. DOI: 10.1021/ja062928i.
- (105) Izod, K.; Rayner, D. G.; El-Hamruni, S. M.; Harrington, R. W.; Baisch, U. Stabilization of a Diphosphagermylene through  $\pi\pi$ - $\pi\pi$  Interactions with a Trigonal-Planar Phosphorus Center. *Angew. Chemie Int. Ed.* **2014**, *53* (14), pp 3636–3640. DOI: 10.1002/anie.201308002.
- (106) Song, H.; Kim, Y.; Park, J.; Kim, K.; Lee, E. Activation of Small Molecules at *N*-Heterocyclic Carbene Centers. *Synlett* **2015**, *27* (04), pp 477–485. DOI: 10.1055/s-0035-1560366.
- (107) Martin, D.; Soleilhavoup, M.; Bertrand, G. Stable Singlet Carbenes as Mimics for Transition Metal Centers. *Chem. Sci.* **2011**, *2* (3), pp 389–399. DOI: 10.1039/C0SC00388C.
- (108) Vermeeren, P.; Doppert, M. T.; Bickelhaupt, F. M.; Hamlin, T. A. How Metallylenes Activate Small Molecules. *Chem. Sci.* **2021**, *12* (12), pp 4526–4535. DOI: 10.1039/D0SC05987K.
- (109) Fujimori, S.; Inoue, S. Small Molecule Activation by Two-Coordinate Acyclic Silylenes. *Eur. J. Inorg. Chem.* **2020**, *2020* (33), pp 3131–3142. DOI: 10.1002/ejic.202000479.
- (110) Wang, L.; Li, Y.; Li, Z.; Kira, M. Isolable Silylenes and Their Diverse Reactivity. *Coord. Chem. Rev.* **2022**, *457*, p 214413. DOI: 10.1016/j.ccr.2022.214413.
- (111) Shan, C.; Yao, S.; Driess, M. Where Silylene–Silicon Centres Matter in the Activation of Small Molecules. *Chem. Soc. Rev.* **2020**, *49* (18), pp 6733–6754. DOI: 10.1039/D0CS00815J.
- (112) Peng, Y.; Guo, J.-D.; Ellis, B. D.; Zhu, Z.; Fettinger, J. C.; Nagase, S.; Power, P. P. Reaction of Hydrogen or Ammonia with Unsaturated Germanium or Tin Molecules under Ambient Conditions: Oxidative Addition versus Arene Elimination. *J. Am. Chem. Soc.* **2009**, *131* (44), pp 16272–16282. DOI: 10.1021/ja9068408.
- (113) Usher, M.; Protchenko, A. V.; Rit, A.; Campos, J.; Kolychev, E. L.; Tirfoin, R.; Aldridge, S. A Systematic Study of Structure and E–H Bond Activation Chemistry by Sterically Encumbered Germylene Complexes. *Chem. Eur. J.* **2016**, *22* (33), pp 11685–11698. DOI: 10.1002/chem.201601840.
- (114) Gullett, K. L.; Lai, T. Y.; Chen, C.-Y.; Fettinger, J. C.; Power, P. P. Reversible Binding of Ethylene and Propylene by Germylenes. *Organometallics* **2019**, *38* (7), pp 1425–1428. DOI: 10.1021/acs.organomet.9b00109.
- (115) Mangan, R. J.; Rit, A.; Sindlinger, C. P.; Tirfoin, R.; Campos, J.; Hicks, J.; Christensen, K. E.; Niu, H.; Aldridge, S. Activation of Protic, Hydridic and Apolar E–H Bonds by a Boryl-Substituted Ge II Cation. *Chem. – A Eur. J.* **2020**, *26* (1), pp 306–315. DOI: 10.1002/chem.201904171.
- (116) Dielmann, F.; Bertrand, G. Reactivity of a Stable Phosphinonitrene towards Small Molecules. *Chem. Eur. J.* **2015**, *21* (1), pp 191–198. DOI: 10.1002/chem.201405430.
- (117) Wittwer, B.; Dickmann, N.; Berg, S.; Leitner, D.; Tesi, L.; Hunger, D.; Gratzl, R.; van Slageren, J.; Neuman, N. I.; Munz, D.; Hohloch, S. A Mesoionic Carbene Complex of Manganese in Five Oxidation States. *Chem. Commun.* **2022**, *58* (41), pp 6096–6099. DOI: 10.1039/D2CC00097K.
- (118) Rogers, M. M.; Stahl, S. S. *N*-Heterocyclic Carbenes as Ligands for High-Oxidation-State Metal

- Complexes and Oxidation Catalysis. In *N-Heterocyclic Carbenes in Transition Metal Catalysis*; Springer: Berlin, Heidelberg, 2006; pp 21–46. DOI: 10.1007/978-3-540-36930-1\_2.
- (119) Arrowsmith, M.; Braunschweig, H.; Celik, M. A.; Dellermann, T.; Dewhurst, R. D.; Ewing, W. C.; Hammond, K.; Kramer, T.; Krummenacher, I.; Mies, J.; Radacki, K.; Schuster, J. K. Neutral Zero-Valent s-Block Complexes with Strong Multiple Bonding. *Nat. Chem.* **2016**, *8* (9), pp 890–894. DOI: 10.1038/nchem.2542.
- (120) Blom, B.; Gallego, D.; Driess, M. N-Heterocyclic Silylene Complexes in Catalysis: New Frontiers in an Emerging Field. *Inorg. Chem. Front.* **2014**, *1* (2), p 134. DOI: 10.1039/c3qi00079f.
- (121) Blom, B.; Stoelzel, M.; Driess, M. New Vistas in N-Heterocyclic Silylene (NHSi) Transition-Metal Coordination Chemistry: Syntheses, Structures and Reactivity towards Activation of Small Molecules. *Chem. Eur. J.* **2013**, *19* (1), pp 40–62. DOI: 10.1002/chem.201203072.
- (122) Glorius, F. *N-Heterocyclic Carbenes in Transition Metal Catalysis*; Topics in Organometallic Chemistry; Springer Berlin Heidelberg: Berlin, Heidelberg, 2007; Vol. 21. DOI: 10.1007/978-3-540-36930-1.
- (123) *N-Heterocyclic Carbenes: From Laboratory Curiosities to Efficient Synthetic Tools*; Diez-Gonzalez, S., Ed.; Catalysis Series; Royal Society of Chemistry: Cambridge, 2017. DOI: 10.1039/9781782626817.
- (124) *N-Heterocyclic Carbenes*; Nolan, S. P., Ed.; Wiley-VCH Verlag GmbH & Co. KGaA: Weinheim, Germany, 2014. DOI: 10.1002/9783527671229.
- (125) Benedek, Z.; Szilvási, T. Can Low-Valent Silicon Compounds Be Better Transition Metal Ligands than Phosphines and NHCs? *RSC Adv.* **2015**, *5* (7), pp 5077–5086. DOI: 10.1039/C4RA14417A.
- (126) Benedek, Z.; Szilvási, T. Theoretical Assessment of Low-Valent Germanium Compounds as Transition Metal Ligands: Can They Be Better than Phosphines or NHCs? *Organometallics* **2017**, *36* (8), pp 1591–1600. DOI: 10.1021/acs.organomet.7b00155.
- (127) Ghosh, M.; Sen, N.; Khan, S. Coinage Metal Complexes of Germylene and Stannylene. *ACS Omega* **2022**, *7* (8), pp 6449–6454. DOI: 10.1021/acsomega.1c06771.
- (128) Kirmse, W. Carbene Chemistry; Elsevier Science, 1971; p 5.
- (129) Ulrich, H. 2-Carbon Cumulenes. In *Cumulenes in Click Reactions*; John Wiley & Sons, Ltd: Chichester, UK, 2009; pp 45–241. DOI: 10.1002/9780470747957.ch3.
- (130) Ducéré, J.-M.; Lepetit, C.; Silvi, B.; Chauvin, R. Quantifying the Donor–Acceptor Properties of Carbon Monoxide and Its Carbomer Using ELF Analysis. *Organometallics* **2008**, *27* (20), pp 5263–5272. DOI: 10.1021/om800578c.
- (131) Lepetit, C.; Silvi, B.; Chauvin, R. ELF Analysis of Out-of-Plane Aromaticity and In-Plane Homoaromaticity in Carbo[N]Annulenes and [N]Pericyclines. *J. Phys. Chem. A* **2003**, *107* (4), pp 464–473. DOI: 10.1021/jp0265211.
- (132) Mesoionic Compounds. In *The IUPAC Compendium of Chemical Terminology*; International Union of Pure and Applied Chemistry (IUPAC): Research Triangle Park, NC, 2014. DOI: 10.1351/goldbook.M03842.
- (133) Arnold, P. L.; Pearson, S. Abnormal N-Heterocyclic Carbenes. *Coord. Chem. Rev.* **2007**, *251* (5–6), pp 596–609. DOI: 10.1016/j.ccr.2006.08.006.
- (134) Schuster, O.; Yang, L.; Raubenheimer, H. G.; Albrecht, M. Beyond Conventional N-Heterocyclic Carbenes: Abnormal, Remote, and Other Classes of NHC Ligands with Reduced Heteroatom Stabilization. *Chem. Rev.* **2009**, *109* (8), pp 3445–3478. DOI: 10.1021/cr8005087.
- (135) Aizpurua, J. M.; Sagartzazu-Aizpurua, M.; Monasterio, Z. Mesoionic 1,2,3-Triazoles and 1,2,3-Triazole Carbenes. In *Chemistry of 1,2,3-triazoles*; Springer-Verlag: Berlin Heidelberg, 2014; pp 211–267. DOI: 10.1007/7081\_2014\_120.
- (136) Burritt, A.; Maclagan, R. G. A. R.; Morrison, M. R. A Valence Bond Study of the Dipole Moment of CO. *J. Mol. Struct. THEOCHEM* **1992**, *261*, pp 63–67. DOI: 10.1016/0166-1280(92)87065-8.
- (137) Pauling, L. C. *The Nature of the Chemical Bond*, 3rd ed.; Cornell University Press: Ithaca: NY, 1960.
- (138) Ylides. In *The IUPAC Compendium of Chemical Terminology*; International Union of Pure and Applied Chemistry (IUPAC): Research Triangle Park, NC, 2014. DOI: 10.1351/goldbook.Y06728.
- (139) Albright, T. A.; Burdett, J. K.; Whangbo, M.-H. *Orbital Interactions in Chemistry*, p. 231; John Wiley & Sons, Inc.: Hoboken, NJ, USA, 2013. DOI: 10.1002/9781118558409.
- (140) Liao, F.; Huang, W.; Chen, B.; Ding, Z.; Li, X.; Su, H.; Wang, T.; Wang, Y.; Miao, H.; Zhang, X.; Luo, Y.; Yang, J.; Zhang, G. Are Pyridinium Ylides Radicals? *Chem. Commun.* **2020**, *56* (76), pp 11287–11290. DOI: 10.1039/D0CC04604C.
- (141) *Nitrogen, Oxygen and Sulfur Ylide Chemistry. A Practical Approach in Chemistry*; Clark, J. S., Ed.; Oxford University Press: Oxford, 2002.

- (142) Ochiai, M.; Tada, N.; Miyamoto, K.; Shiro, M. Synthesis and Structure of Aliphatic Phenylchloronium Ylide. *Heteroat. Chem.* **2011**, *22* (3–4), pp 325–330. DOI: 10.1002/hc.20683.
- (143) Ochiai, M.; Tada, N.; Okada, T.; Sota, A.; Miyamoto, K. Thermal and Catalytic Transylidations between Halonium Ylides and Synthesis and Reaction of Stable Aliphatic Chloronium Ylides. *J. Am. Chem. Soc.* **2008**, *130* (7), pp 2118–2119. DOI: 10.1021/ja074624h.
- (144) Drabowicz, J.; Rzewnicka, A.; Żurawiński, R. Selenonium Ylides: Syntheses, Structural Aspects, and Synthetic Applications. *Molecules* **2020**, *25* (10), p 2420. DOI: 10.3390/molecules25102420.
- (145) V. Comasseto, J.; Piovan, L.; P. Wendler, E. Synthesis of Selenium and Tellurium Ylides and Carbanions. Application to Organic Synthesis. In *PATAI'S Chemistry of Functional Groups*; John Wiley & Sons, Ltd: Chichester, UK, 2014; pp 1–78. DOI: 10.1002/9780470682531.pat0705.
- (146) Scherpf, T.; Feichtner, K.-S.; Gessner, V. H. Using Ylide Functionalization to Stabilize Boron Cations. *Angew. Chemie Int. Ed.* **2017**, *56* (12), pp 3275–3279. DOI: 10.1002/anie.201611677.
- (147) Ehlers, F.; Strumberger, J. M.; Mohr, F. Keto-stabilized Arsenic Ylides and Their Coordination to Gold(I). *Zeitschrift für Anorg. und Allg. Chemie* **2020**, *646* (13), pp 889–894. DOI: 10.1002/zaac.202000110.
- (148) Geary, G. C.; Hope, E. G.; Singh, K.; Stuart, A. M. Preparation of Iodonium Ylides: Probing the Fluorination of 1,3-Dicarbonyl Compounds with a Fluoroiodane. *RSC Adv.* **2015**, *5* (21), pp 16501–16506. DOI: 10.1039/C4RA15733H.
- (149) Kolodiazny, O. I. *Phosphorus Ylides*; Wiley-VCH: Weinheim, New York, Chichester, Brisbane, Singapore, Toronto, 1999. DOI: 10.1002/9783527613908.
- (150) Ramazani, A.; Kazemizadeh, A.; Ahmadi, E.; Noshiranzadeh, N.; Souldozi, A. Synthesis and Reactions of Stabilized Phosphorus Ylides. *Curr. Org. Chem.* **2008**, *12* (1), pp 59–82. DOI: 10.2174/138527208783330055.
- (151) Trost, B. M.; Lawrence, S. M. *Sulfur Ylides: Emerging Synthetic Intermediates*; Academic Press: New York, 1975.
- (152) Oost, R.; Neuhaus, J. D.; Merad, J.; Maulide, N. Sulfur Ylides in Organic Synthesis and Transition Metal Catalysis; Gessner, V., Ed.; Springer, Cham, 2017; pp 73–115. DOI: 10.1007/430\_2017\_14.
- (153) Bisag, G. D.; Ruggieri, S.; Fochi, M.; Bernardi, L. Sulfoxonium Ylides: Simple Compounds with Chameleonic Reactivity. *Org. Biomol. Chem.* **2020**, *18* (43), pp 8793–8809. DOI: 10.1039/D0OB01822H.
- (154) Sarbajna, A.; Swamy, V. S. V. S. N.; Gessner, V. H. Phosphorus-Ylides: Powerful Substituents for the Stabilization of Reactive Main Group Compounds. *Chem. Sci.* **2021**, *12* (6), pp 2016–2024. DOI: 10.1039/D0SC03278F.
- (155) Gothelf, K. V.; Jørgensen, K. A. Asymmetric 1,3-Dipolar Cycloaddition Reactions. *Chem. Rev.* **1998**, *98* (2), pp 863–910. DOI: 10.1021/cr970324e.
- (156) Coldham, I.; Hufton, R. Intramolecular Dipolar Cycloaddition Reactions of Azomethine Ylides. *Chem. Rev.* **2005**, *105* (7), pp 2765–2810. DOI: 10.1021/cr040004c.
- (157) Confalone, P. N.; Huie, E. M. The [3+2] Nitrone-Olefin Cycloaddition Reaction. In *Organic Reactions*; John Wiley & Sons, Inc.: Hoboken, NJ, USA, 1988; pp 1–173. DOI: 10.1002/0471264180.or036.01.
- (158) Nunes, C. M.; Reva, I.; Fausto, R. Capture of an Elusive Nitrile Ylide as an Intermediate in Isoxazole–Oxazole Photoisomerization. *J. Org. Chem.* **2013**, *78* (21), pp 10657–10665. DOI: 10.1021/jo4015672.
- (159) Wittig, G.; Geissler, G. Zur Reaktionsweise Des Pentaphenyl-Phosphors Und Einiger Derivate. *Justus Liebigs Ann. Chem.* **1953**, *580* (1), pp 44–57. DOI: 10.1002/jlac.19535800107.
- (160) Byrne, P. A.; Gilheany, D. G. The Modern Interpretation of the Wittig Reaction Mechanism. *Chem. Soc. Rev.* **2013**, *42* (16), p 6670. DOI: 10.1039/c3cs60105f.
- (161) Heravi, M. M.; Ghanbarian, M.; Zadsirjan, V.; Alimadadi Jani, B. Recent Advances in the Applications of Wittig Reaction in the Total Synthesis of Natural Products Containing Lactone, Pyrone, and Lactam as a Scaffold. *Monatshefte für Chemie - Chem. Mon.* **2019**, *150* (8), pp 1365–1407. DOI: 10.1007/s00706-019-02465-9.
- (162) Li, J. J. Corey–Chaykovsky Reaction. In *Name Reactions*; Springer International Publishing: Cham, 2014; pp 171–173. DOI: 10.1007/978-3-319-03979-4\_70.
- (163) Corey, E. J.; Chaykovsky, M. Dimethylloxosulfonium Methylide ((CH<sub>3</sub>)<sub>2</sub>SOCH<sub>2</sub>) and Dimethylsulfonium Methylide ((CH<sub>3</sub>)<sub>2</sub>SCH<sub>2</sub>). Formation and Application to Organic Synthesis. *J. Am. Chem. Soc.* **1965**, *87* (6), pp 1353–1364. DOI: 10.1021/ja01084a034.
- (164) Aggarwal, V. K.; Richardson, J. The Complexity of Catalysis: Origins of Enantio- and Diastereocontrol in Sulfur Ylide Mediated Epoxidation Reactions. *Chem. Commun.* **2003**, No. 21, p 2644. DOI: 10.1039/b304625g.



- (165) Menchikov, L. G.; Shulishov, E. V.; Tomilov, Y. V. Recent Advances in the Catalytic Cyclopropanation of Unsaturated Compounds with Diazomethane. *Russ. Chem. Rev.* **2021**, *90* (2), pp 199–230. DOI: 10.1070/RCR4982.
- (166) Ossig, G.; Meller, A.; Freitag, S.; Herbst-Irmer, R.; Sheldrick, G. M. Reaktionen Eines Freien Stannaimins Und von Basen-stabilisierten Stannylenen. *Chem. Ber.* **1993**, *126* (10), pp 2247–2253. DOI: 10.1002/cber.19931261013.
- (167) Tebbe, F. N.; Parshall, G. W.; Reddy, G. S. Olefin Homologation with Titanium Methylene Compounds. *J. Am. Chem. Soc.* **1978**, *100* (11), pp 3611–3613. DOI: 10.1021/ja00479a061.
- (168) Thompson, R.; Nakamaru-Ogiso, E.; Chen, C.-H.; Pink, M.; Mindiola, D. J. Structural Elucidation of the Illustrious Tebbe Reagent. *Organometallics* **2014**, *33* (1), pp 429–432. DOI: 10.1021/om401108b.
- (169) Petasis, N. A.; Bzowej, E. I. Titanium-Mediated Carbonyl Olefinations. 1. Methyleneations of Carbonyl Compounds with Dimethyltitanocene. *J. Am. Chem. Soc.* **1990**, *112* (17), pp 6392–6394. DOI: 10.1021/ja00173a035.
- (170) Hartley, R. C.; Li, J.; Main, C. A.; McKiernan, G. J. Titanium Carbenoid Reagents for Converting Carbonyl Groups into Alkenes. *Tetrahedron* **2007**, *63* (23), pp 4825–4864. DOI: 10.1016/j.tet.2007.03.015.
- (171) Gutsulyak, D. V.; Piers, W. E.; Borau-Garcia, J.; Parvez, M. Activation of Water, Ammonia, and Other Small Molecules by PC<sub>carbene</sub>P Nickel Pincer Complexes. *J. Am. Chem. Soc.* **2013**, *135* (32), pp 11776–11779. DOI: 10.1021/ja406742n.
- (172) Cavell, R. G.; Kamalesh Babu, R. P.; Aparna, K. Early Transition Metal and Lanthanide Bis(Iminophosphorano)Methandiide Complexes; ‘Pincer’ and Bridging Bis(Phosphorus) Metal Carbenes. *J. Organomet. Chem.* **2001**, *617–618*, pp 158–169. DOI: 10.1016/S0022-328X(00)00735-X.
- (173) Flores, J. A.; Komine, N.; Pal, K.; Pinter, B.; Pink, M.; Chen, C.-H.; Caulton, K. G.; Mindiola, D. J. Silver(I)-Catalyzed Insertion of Carbene into Alkane C–H Bonds and the Origin of the Special Challenge of Methane Activation Using DFT as a Mechanistic Probe. *ACS Catal.* **2012**, *2* (10), pp 2066–2078. DOI: 10.1021/cs300256b.
- (174) Werlé, C.; Goddard, R.; Philipps, P.; Farès, C.; Fürstner, A. Structures of Reactive Donor/Acceptor and Donor/Donor Rhodium Carbenes in the Solid State and Their Implications for Catalysis. *J. Am. Chem. Soc.* **2016**, *138* (11), pp 3797–3805. DOI: 10.1021/jacs.5b13321.
- (175) Cui, P.; Iluc, V. M. Redox-Induced Umpolung of Transition Metal Carbenes. *Chem. Sci.* **2015**, *6* (12), pp 7343–7354. DOI: 10.1039/C5SC02859K.
- (176) Suzuki, H.; Tokitoh, N.; Okazaki, R.; Nagase, S.; Goto, M. Synthesis, Structure, and Reactivity of the First Kinetically Stabilized Silanethione. *J. Am. Chem. Soc.* **1998**, *120* (43), pp 11096–11105. DOI: 10.1021/ja980783c.
- (177) Kapp, J.; Remko, M.; Schleyer, P. von R. H<sub>2</sub>XO and (CH<sub>3</sub>)<sub>2</sub>XO Compounds (X = C, Si, Ge, Sn, Pb): Double Bonds vs Carbene-Like Structures Can the Metal Compounds Exist at All? *J. Am. Chem. Soc.* **1996**, *118* (24), pp 5745–5751. DOI: 10.1021/ja953846p.
- (178) Avakyan, V. G.; Sidorkin, V. F.; Belogolova, E. F.; Guselnikov, S. L.; Gusel’nikov, L. E. AIM and ELF Electronic Structure/G2 and G3  $\pi$ -Bond Energy Relationship for Doubly Bonded Silicon Species, H<sub>2</sub>Si=X (X = E<sup>14</sup>H<sub>2</sub>, E<sup>15</sup>H, E<sup>16</sup>). *Organometallics* **2006**, *25* (26), pp 6007–6013. DOI: 10.1021/om0605478.
- (179) Kudo, T.; Nagase, S. Theoretical Study on the Dimerization of Silanone and the Properties of the Polymeric Products (H<sub>2</sub>SiO)<sub>n</sub> (n = 2, 3, and 4). Comparison with Dimers (H<sub>2</sub>SiS)<sub>2</sub> and (H<sub>2</sub>CO)<sub>2</sub>. *J. Am. Chem. Soc.* **1985**, *107* (9), pp 2589–2595. DOI: 10.1021/ja00295a003.
- (180) Xiong, Y.; Yao, S.; Driess, M. Chemical Tricks To Stabilize Silanones and Their Heavier Homologues with E=O Bonds (E=Si-Pb): From Elusive Species to Isolable Building Blocks. *Angew. Chemie Int. Ed.* **2013**, *52* (16), pp 4302–4311. DOI: 10.1002/anie.201209766.
- (181) Kimura, M.; Nagase, S. The Quest of Stable Silanones: Substituent Effects. *Chem. Lett.* **2001**, *30* (11), pp 1098–1099. DOI: 10.1246/cl.2001.1098.
- (182) Ivanov, A. S.; Popov, I. A.; Boldyrev, A. I.; Zhdankin, V. V. The I=X (X=O,N,C) Double Bond in Hypervalent Iodine Compounds: Is It Real? *Angew. Chemie Int. Ed.* **2014**, *53* (36), pp 9617–9621. DOI: 10.1002/anie.201405142.
- (183) Stephan, D. W. Frustrated Lewis Pairs. *J. Am. Chem. Soc.* **2015**, *137* (32), pp 10018–10032. DOI: 10.1021/jacs.5b06794.
- (184) Bailey, B. C.; Fout, A. R.; Fan, H.; Tomaszewski, J.; Huffman, J. C.; Mindiola, D. J. An Alkylidyne Analogue of Tebbe’s Reagent: Trapping Reactions of a Titanium Neopentylidyne by Incomplete and

- Complete 1,2-Additions. *Angew. Chemie Int. Ed.* **2007**, *46* (43), pp 8246–8249. DOI: 10.1002/anie.200703079.
- (185) Bailey, B. C.; Fan, H.; Baum, E. W.; Huffman, J. C.; Baik, M.-H.; Mindiola, D. J. Intermolecular C–H Bond Activation Promoted by a Titanium Alkylidyne. *J. Am. Chem. Soc.* **2005**, *127* (46), pp 16016–16017. DOI: 10.1021/ja0556934.
- (186) Empsall, H. D.; Hyde, E. M.; Markham, R.; McDonald, W. S.; Norton, M. C.; Shaw, B. L.; Weeks, B. Synthesis and X-Ray Structure of an Unusual Iridium Ylide or Carbene Complex. *J. Chem. Soc. Chem. Commun.* **1977**, No. 17, p 589. DOI: 10.1039/c39770000589.
- (187) Crocker, C.; Errington, R. J.; Markham, R.; Moulton, C. J.; Odell, K. J.; Shaw, B. L. Large-Ring and Cyclometalated Rhodium Complexes from Some Medium-Chain  $\alpha$ ,  $\omega$ -Diphosphines. *J. Am. Chem. Soc.* **1980**, *102* (13), pp 4373–4379. DOI: 10.1021/ja00533a014.
- (188) Gusev, D. G.; Lough, A. J. Double C–H Activation on Osmium and Ruthenium Centers: Carbene vs Olefin Products. *Organometallics* **2002**, *21* (13), pp 2601–2603. DOI: 10.1021/om020355m.
- (189) Comanescu, C. C.; Iluc, V. M. Synthesis and Reactivity of a Nucleophilic Palladium(II) Carbene. *Organometallics* **2014**, *33* (21), pp 6059–6064. DOI: 10.1021/om500682s.
- (190) Cantat, T.; Mézailles, N.; Auffrant, A.; Le Floch, P. Bis-Phosphorus Stabilised Carbene Complexes. *Dalt. Trans.* **2008**, No. 15, p 1957. DOI: 10.1039/b717600g.
- (191) Liddle, S. T.; Mills, D. P.; Wooles, A. J. Early Metal Bis(Phosphorus-Stabilised)Carbene Chemistry. *Chem. Soc. Rev.* **2011**, *40* (5), p 2164. DOI: 10.1039/c0cs00135j.
- (192) Fustier-Boutignon, M.; Nebra, N.; Mézailles, N. Geminal Dianions Stabilized by Main Group Elements. *Chem. Rev.* **2019**, *119* (14), pp 8555–8700. DOI: 10.1021/acs.chemrev.8b00802.
- (193) Gessner, V. H.; Becker, J.; Feichtner, K. Carbene Complexes Based on Dilithium Methandiides. *Eur. J. Inorg. Chem.* **2015**, *2015* (11), pp 1841–1859. DOI: 10.1002/ejic.201500051.
- (194) Peloso, R.; Carmona, E. Non-Heteroatom-Substituted Alkylidene Complexes of Groups 10 and 11. *Coord. Chem. Rev.* **2018**, *355*, pp 116–132. DOI: 10.1016/j.ccr.2017.07.018.
- (195) Doyle, M. P.; Duffy, R.; Ratnikov, M.; Zhou, L. Catalytic Carbene Insertion into C–H Bonds. *Chem. Rev.* **2010**, *110* (2), pp 704–724. DOI: 10.1021/cr900239n.
- (196) Hussong, M. W.; Hoffmeister, W. T.; Rominger, F.; Straub, B. F. Copper and Silver Carbene Complexes without Heteroatom-Stabilization: Structure, Spectroscopy, and Relativistic Effects. *Angew. Chemie Int. Ed.* **2015**, *54* (35), pp 10331–10335. DOI: 10.1002/anie.201504117.
- (197) Olmos, A.; Gava, R.; Noverges, B.; Bellezza, D.; Jacob, K.; Besora, M.; Sameera, W. M. C.; Etienne, M.; Maseras, F.; Asensio, G.; Caballero, A.; Pérez, P. J. Measuring the Relative Reactivity of the Carbon–Hydrogen Bonds of Alkanes as Nucleophiles. *Angew. Chemie Int. Ed.* **2018**, *57* (42), pp 13848–13852. DOI: 10.1002/anie.201807448.
- (198) Kornecki, K. P.; Briones, J. F.; Boyarskikh, V.; Fullilove, F.; Autschbach, J.; Schrote, K. E.; Lancaster, K. M.; Davies, H. M. L.; Berry, J. F. Direct Spectroscopic Characterization of a Transitory Dirhodium Donor-Acceptor Carbene Complex. *Science* **2013**, *342* (6156), pp 351–354. DOI: 10.1126/science.1243200.
- (199) LaPierre, E. A.; Piers, W. E.; Gendy, C. Redox-State Dependent Activation of Silanes and Ammonia with Reverse Polarity (PC<sub>Carbene</sub>P)Ni Complexes: Electrophilic vs. Nucleophilic Carbenes. *Dalt. Trans.* **2018**, *47* (46), pp 16789–16797. DOI: 10.1039/C8DT04409K.
- (200) Sung, S.; Wang, Q.; Krämer, T.; Young, R. D. Synthesis and Reactivity of a PC<sub>Carbene</sub>P Cobalt(i) Complex: The Missing Link in the Cobalt PXP Pincer Series (X = B, C, N). *Chem. Sci.* **2018**, *9* (43), pp 8234–8241. DOI: 10.1039/C8SC02782J.
- (201) Wiberg, K. B. Application of the Pople-Santry-Segal CNDO Method to the Cyclopropylcarbiny and Cyclobutyl Cation and to Bicyclobutane. *Tetrahedron* **1968**, *24* (3), pp 1083–1096. DOI: 10.1016/0040-4020(68)88057-3.
- (202) Dipolar Compounds. In *The IUPAC Compendium of Chemical Terminology*; International Union of Pure and Applied Chemistry (IUPAC): Research Triangle Park, NC, 2014. DOI: 10.1351/goldbook.D01753.
- (203) Fiorot, R. G.; Vilhena, F. de S.; Carneiro, J. W. de M. Diradical-Singlet Character of 1,3-Dipoles Affects Reactivity of 1,3-Dipolar Cycloaddition Reactions and Intramolecular Cyclization. *J. Mol. Model.* **2019**, *25* (10), p 306. DOI: 10.1007/s00894-019-4162-9.
- (204) Cox, A. P.; Thomas, L. F.; Sheridan, J. Microwave Spectra of Diazomethane and Its Deutero Derivatives. *Nature* **1958**, *181* (4614), pp 1000–1001. DOI: 10.1038/1811000a0.
- (205) Hiberty, P. C.; Leforestier, C. Expansion of Molecular Orbital Wave Functions into Valence Bond Wave

- Functions. A Simplified Procedure. *J. Am. Chem. Soc.* **1978**, *100* (7), pp 2012–2017. DOI: 10.1021/ja00475a007.
- (206) Braïda, B.; Galembeck, S. E.; Hiberty, P. C. Ozone and Other 1,3-Dipoles: Toward a Quantitative Measure of Diradical Character. *J. Chem. Theory Comput.* **2017**, *13* (7), pp 3228–3235. DOI: 10.1021/acs.jctc.7b00399.
- (207) Braïda, B.; Walter, C.; Engels, B.; Hiberty, P. C. A Clear Correlation between the Diradical Character of 1,3-Dipoles and Their Reactivity toward Ethylene or Acetylene. *J. Am. Chem. Soc.* **2010**, *132* (22), pp 7631–7637. DOI: 10.1021/ja100512d.
- (208) Parrondo, R. M.; Karafiloglou, P.; Pappalardo, R. R.; Sanchez Marcos, E. Calculation of the Weights of Resonance Structures of Molecules in Solution. *J. Phys. Chem.* **1995**, *99* (17), pp 6461–6467. DOI: 10.1021/j100017a027.
- (209) Morin, M. S. T.; Arndtsen, B. A. Chiral Phosphorus-Based 1,3-Dipoles: A Modular Approach to Enantioselective 1,3-Dipolar Cycloaddition and Polycyclic 2-Pyrroline Synthesis. *Org. Lett.* **2014**, *16* (4), pp 1056–1059. DOI: 10.1021/ol4035512.
- (210) Carty, A. J.; Mott, G. N.; Taylor, N. J.; Ferguson, G.; Khan, M. A.; Roberts, P. J. Phosphorus-Based 1,3-Dipoles as Three-Electron One-Carbon Ligands: X-Ray Structure of  $\mu$ -[Phenyl(Dicyclohexylphosphonio)Ethenidyl]- $\mu$ -(Diphenylphosphido)Hexacarbonyldiiron,  $\text{Fe}_2(\text{CO})_6[\text{CC}(\text{PCy}_2\text{H})\text{Ph}](\text{PPh}_2)$ . *J. Organomet. Chem.* **1978**, *149* (3), pp 345–354. DOI: 10.1016/S0022-328X(00)90400-5.
- (211) Fabian, Jür. Thiocumulenes (S-Centered 1,3-Dipoles)-a Theoretical View. *Phosphorus. Sulfur. Silicon Relat. Elem.* **1999**, *153* (1), pp 357–358. DOI: 10.1080/10426509908546469.
- (212) Varache-Lembege, M.; Nuhrich, A.; Devaux, G.; Duboudin, F. Transient 1,3-Dipoles Containing Sulfur: A Novel Example of Rearrangement from Ethyl-1-Oxo-1-(2,3-Dichloro-4-Phenoxyacetic Acid)-2-[3-Thio-5-(4-Chlorophenyl)-1,2-Dithiolium] Bromide. *Can. J. Chem.* **1992**, *70* (8), pp 2290–2295. DOI: 10.1139/v92-288.
- (213) Huisgen, R. 1,3-Dipolar Cycloadditions. Past and Future. *Angew. Chemie Int. Ed. English* **1963**, *2* (10), pp 565–598. DOI: 10.1002/anie.196305651.
- (214) Kolb, H. C.; Sharpless, K. B. The Growing Impact of Click Chemistry on Drug Discovery. *Drug Discov. Today* **2003**, *8* (24), pp 1128–1137. DOI: 10.1016/S1359-6446(03)02933-7.
- (215) Regitz, M.; Maas, G. *Diazo Compounds: Properties and Synthesis*; Academic Press, Inc., 1986. DOI: 10.1016/B978-0-12-585840-3.X5001-6.
- (216) Groves, J. T.; Takahashi, T. Activation and Transfer of Nitrogen from a Nitridomanganese(V) Porphyrin Complex. Aza Analog of Epoxidation. *J. Am. Chem. Soc.* **1983**, *105* (7), pp 2073–2074. DOI: 10.1021/ja00345a071.
- (217) Meyer, K.; Bill, E.; Mienert, B.; Weyhermüller, T.; Wiegardt, K. Photolysis of Cis- and Trans-[ $\text{Fe}^{\text{III}}(\text{Cyclam})(\text{N}_3)_2$ ] $^+$  Complexes: Spectroscopic Characterization of a Nitridoiron(V) Species. *J. Am. Chem. Soc.* **1999**, *121* (20), pp 4859–4876. DOI: 10.1021/ja983454t.
- (218) Meyer, K.; Bendix, J.; Metzler-Nolte, N.; Weyhermüller, T.; Wiegardt, K. Nitridomanganese(V) and - (VI) Complexes Containing Macrocyclic Amine Ligands. *J. Am. Chem. Soc.* **1998**, *120* (29), pp 7260–7270. DOI: 10.1021/ja980686j.
- (219) Haiges, R. Recent Developments in the Chemistry of Metal Oxopolyazides. *Dalt. Trans.* **2019**, *48* (3), pp 806–813. DOI: 10.1039/C8DT04258F.
- (220) Shay, D. T.; Yap, G. P. A.; Zakharov, L. N.; Rheingold, A. L.; Theopold, K. H. Intramolecular C-H Activation by an Open-Shell Cobalt(III) Imido Complex. *Angew. Chemie Int. Ed.* **2005**, *44* (10), pp 1508–1510. DOI: 10.1002/anie.200462529.
- (221) Vreeken, V.; Siegler, M. A.; de Bruin, B.; Reek, J. N. H.; Lutz, M.; van der Vlugt, J. I. C-H Activation of Benzene by a Photoactivated  $\text{Ni}^{\text{II}}$ (Azide): Formation of a Transient Nickel Nitrido Complex. *Angew. Chemie* **2015**, *127* (24), pp 7161–7165. DOI: 10.1002/ange.201501437.
- (222) Luo, Y.-R. *Comprehensive Handbook of Chemical Bond Energies*; CRC Press, 2007. DOI: 10.1201/9781420007282.
- (223) Beck, W.; Fehlhammer, W. P. Reactions of Metal Carbonyls with the Azide Ion and – Vice Versa – Reactions of Azido Complexes with Carbon Monoxide: Isocyanato Complexes. Analogous Reactions in  $\text{NO}^+/\text{N}_3^-$  Transition Metal Chemistry. *Zeitschrift für Anorg. und Allg. Chemie* **2010**, *636* (1), pp 157–162. DOI: 10.1002/zaac.200900473.
- (224) Holm, R. H.; Donahue, J. P. A Thermodynamic Scale for Oxygen Atom Transfer Reactions. *Polyhedron*

- 1993, 12 (6), pp 571–589. DOI: 10.1016/S0277-5387(00)84972-4.
- (225) Smith, M. R.; Matsunaga, P. T.; Andersen, R. A. Preparation of Monomeric  $(\text{Me}_5\text{C}_5)_2\text{VO}$  and  $(\text{Me}_5\text{C}_5)_2\text{Ti}(\text{O})(\text{L})$  and Their Decomposition to  $(\text{Me}_5\text{C}_5)_4\text{M}_4(\mu\text{-O})_6$ . *J. Am. Chem. Soc.* **1993**, 115 (15), pp 7049–7050. DOI: 10.1021/ja00068a103.
- (226) Howard, W. A.; Trnka, T. M.; Waters, M.; Parkin, G. Terminal Chalcogenido Complexes of Zirconium: Syntheses and Reactivity of  $\text{Cp}_2^*\text{Zr}(\text{E})(\text{NC}_5\text{H}_5)$  (E = O, S, Se, Te). *J. Organomet. Chem.* **1997**, 528 (1–2), pp 95–121. DOI: 10.1016/S0022-328X(96)06584-9.
- (227) Howard, W. A.; Parkin, G. Terminal Oxo, Sulfido, Selenido, and Tellurido Complexes of Zirconium,  $(\eta^5\text{-C}_5\text{Me}_4\text{R})_2\text{Zr}(\text{E})(\text{NC}_5\text{H}_5)$ : Comparison of Terminal Zr-E Single and Zr=E Double-Bond Lengths. *J. Am. Chem. Soc.* **1994**, 116 (2), pp 606–615. DOI: 10.1021/ja00081a022.
- (228) McNeill, K.; Bergman, R. G. Rapid Reduction of Nitric Oxide to Dinitrogen by Zirconium(II): Kinetic Studies on a Reaction Controlled by Gas–Liquid Transport. *J. Am. Chem. Soc.* **1999**, 121 (36), pp 8260–8269. DOI: 10.1021/ja983011p.
- (229) Yonke, B. L.; Reeds, J. P.; Zavalij, P. Y.; Sita, L. R. Catalytic Degenerate and Nondegenerate Oxygen Atom Transfers Employing  $\text{N}_2\text{O}$  and  $\text{CO}_2$  and a  $\text{M}^{\text{II}}/\text{M}^{\text{IV}}$  Cycle Mediated by Group 6  $\text{M}^{\text{IV}}$  Terminal Oxo Complexes†. *Angew. Chemie Int. Ed.* **2011**, 50 (51), pp 12342–12346. DOI: 10.1002/anie.201106074.
- (230) Franke, S. M.; Tran, B. L.; Heinemann, F. W.; Hieringer, W.; Mindiola, D. J.; Meyer, K. Uranium(III) Complexes with Bulky Aryloxo Ligands Featuring Metal–Arene Interactions and Their Reactivity Toward Nitrous Oxide. *Inorg. Chem.* **2013**, 52 (18), pp 10552–10558. DOI: 10.1021/ic401532j.
- (231) Bottomley, F. Cyclopentadienylmetal Oxides. *Polyhedron* **1992**, 11 (14), pp 1707–1731. DOI: 10.1016/S0277-5387(00)83231-3.
- (232) Berg, D. J.; Burns, C. J.; Andersen, R. A.; Zalkin, A. Electron-Transfer Reactions of Divalent Ytterbium Metallocenes. Synthesis of the Series  $[(\text{Me}_5\text{C}_5)_2\text{Yb}]_2[\mu\text{-E}]$  (E = Oxygen, Sulfur, Selenium, or Tellurium) and Crystal Structure of  $[(\text{Me}_5\text{C}_5)_2\text{Yb}]_2[\mu\text{-Se}]$ . *Organometallics* **1989**, 8 (8), pp 1865–1870. DOI: 10.1021/om00110a006.
- (233) Vaughan, G. A.; Rupert, P. B.; Hillhouse, G. L. Selective O-Atom Transfer from Nitrous Oxide to Hydride and Aryl Ligands of Bis(Pentamethylcyclopentadienyl)Hafnium Derivatives. *J. Am. Chem. Soc.* **1987**, 109 (18), pp 5538–5539. DOI: 10.1021/ja00252a047.
- (234) Matsunaga, P. T.; Hillhouse, G. L.; Rheingold, A. L. Oxygen-Atom Transfer from Nitrous Oxide to a Nickel Metallacycle. Synthesis, Structure, and Reactions of [Cyclic] (2,2'-Bipyridine) $\text{Ni}(\text{OCH}_2\text{CH}_2\text{CH}_2\text{CH}_2)$ . *J. Am. Chem. Soc.* **1993**, 115 (5), pp 2075–2077. DOI: 10.1021/ja00058a085.
- (235) Koo, K.; Hillhouse, G. L.; Rheingold, A. L. Oxygen-Atom Transfer from Nitrous Oxide to an Organonickel(II) Phosphine Complex. Syntheses and Reactions of New Nickel(II) Aryloxides and the Crystal Structure of [Cyclic]  $(\text{Me}_2\text{PCH}_2\text{CH}_2\text{PMe}_2)\text{Ni}(\text{O-}o\text{-C}_6\text{H}_4\text{CMe}_2\text{CH}_2)$ . *Organometallics* **1995**, 14 (1), pp 456–460. DOI: 10.1021/om00001a062.
- (236) Matsunaga, P. T.; Mavropoulos, J. C.; Hillhouse, G. L. Oxygen-Atom Transfer from Nitrous Oxide ( $\text{N}=\text{N}=\text{O}$ ) to Nickel Alkyls. Syntheses and Reactions of Nickel(II) Alkoxides. *Polyhedron* **1995**, 14 (1), pp 175–185. DOI: 10.1016/0277-5387(94)00330-H.
- (237) Harman, W. H.; Chang, C. J.  $\text{N}_2\text{O}$  Activation and Oxidation Reactivity from a Non-Heme Iron Pyrrole Platform. *J. Am. Chem. Soc.* **2007**, 129 (49), pp 15128–15129. DOI: 10.1021/ja076842g.
- (238) Laplaza, C. E.; Odom, A. L.; Davis, W. M.; Cummins, C. C.; Protasiewicz, J. D. Cleavage of the Nitrous Oxide NN Bond by a Tris(Amido)Molybdenum(III) Complex. *J. Am. Chem. Soc.* **1995**, 117 (17), pp 4999–5000. DOI: 10.1021/ja00122a033.
- (239) Cherry, J.-P. F.; Johnson, A. R.; Baraldo, L. M.; Tsai, Y.-C.; Cummins, C. C.; Kryatov, S. V.; Rybak-Akimova, E. V.; Capps, K. B.; Hoff, C. D.; Haar, C. M.; Nolan, S. P. On the Origin of Selective Nitrous Oxide N–N Bond Cleavage by Three-Coordinate Molybdenum(III) Complexes. *J. Am. Chem. Soc.* **2001**, 123 (30), pp 7271–7286. DOI: 10.1021/ja0031063.
- (240) Sleiman, H. F.; McElwee-White, L. Photochemical Azo Metathesis by Tungsten Carbene  $(\text{OC})_5\text{W}:\text{C}(\text{OCH}_3)\text{CH}_3$ . Isolation of a Zwitterionic Intermediate. *J. Am. Chem. Soc.* **1988**, 110 (26), pp 8700–8701. DOI: 10.1021/ja00234a023.
- (241) Bismuto, A.; Nichol, G. S.; Duarte, F.; Cowley, M. J.; Thomas, S. P. Characterization of the Zwitterionic Intermediate in 1,1-Carboboration of Alkynes. *Angew. Chemie* **2020**, 132 (31), pp 12831–12835. DOI: 10.1002/ange.202003468.
- (242) Bismuto, A.; Cowley, M. J.; Thomas, S. P. Zwitterion-Initiated Hydroboration of Alkynes and Styrene.

- Adv. Synth. Catal.* **2021**, *363* (9), pp 2382–2385. DOI: 10.1002/adsc.202001323.
- (243) Glueck, D. S. Phosphiranes, Phosphirenes, and Heavier Analogues. In *Comprehensive Heterocyclic Chemistry IV*; Elsevier, 2022; pp 464–505. DOI: 10.1016/B978-0-12-409547-2.14761-4.
- (244) Möbus, J.; Malessa, K.; Frisch, H.; Daniliuc, C. G.; Fröhlich, R.; Kehr, G.; Erker, G. Zwitterionic Phosphirenium Borates Derived from Bis(Alkynyl)Mesityl Phosphanes and Tris(Pentafluorophenyl)Borane. *Heteroat. Chem.* **2014**, *25* (5), pp 396–401. DOI: 10.1002/hc.21184.
- (245) Ekkert, O.; Kehr, G.; Fröhlich, R.; Erker, G. Phosphirenium-Borate Zwitterion: Formation in the 1,1-Carboboration Reaction of Phosphinylalkynes. *Chem. Commun.* **2011**, *47* (37), p 10482. DOI: 10.1039/c1cc13008k.
- (246) Ueno, A.; Möricke, J.; Daniliuc, C. G.; Kehr, G.; Erker, G. Phosphirenium Borate Betaines from Alkynylphosphanes and the Halogeno-B(C<sub>6</sub>F<sub>5</sub>)<sub>2</sub> Reagents. *Chem. Commun.* **2018**, *54* (97), pp 13746–13749. DOI: 10.1039/C8CC07189F.
- (247) Boom, D. H. A.; de Boed, E. J. J.; Nicolas, E.; Nieger, M.; Ehlers, A. W.; Jupp, A. R.; Slootweg, J. C. Catalytic Dehydrogenation of Amine-Boranes Using Geminal Phosphino-Boranes. *Zeitschrift für Anorg. und Allg. Chemie* **2020**, *646* (13), pp 586–592. DOI: 10.1002/zaac.201900313.
- (248) Stute, A.; Kehr, G.; Fröhlich, R.; Erker, G. Chemistry of a Geminal Frustrated Lewis Pair Featuring Electron Withdrawing C<sub>6</sub>F<sub>5</sub> Substituents at Both Phosphorus and Boron. *Chem. Commun.* **2011**, *47* (14), p 4288. DOI: 10.1039/c1cc10241a.
- (249) Wang, Y.; Li, Z. H.; Wang, H. Synthesis of an Oxygen-Linked Geminal Frustrated Lewis Pair and Its Application in Small Molecule Activation. *RSC Adv.* **2018**, *8* (46), pp 26271–26276. DOI: 10.1039/C8RA05108A.
- (250) Samigullin, K.; Georg, I.; Bolte, M.; Lerner, H.-W.; Wagner, M. A Highly Reactive Geminal P/B Frustrated Lewis Pair: Expanding the Scope to C–X (X=Cl, Br) Bond Activation. *Chem. Eur. J.* **2016**, *22* (10), pp 3478–3484. DOI: 10.1002/chem.201504791.
- (251) Yu, J.; Kehr, G.; Daniliuc, C. G.; Bannwarth, C.; Grimme, S.; Erker, G. Direct Synthesis of a Geminal Zwitterionic Phosphonium/Hydridoborate System – Developing an Alternative Tool for Generating Frustrated Lewis Pair Hydrogen Activation Systems. *Org. Biomol. Chem.* **2015**, *13* (20), pp 5783–5792. DOI: 10.1039/C5OB00634A.
- (252) Habraken, E. R. M.; Mens, L. C.; Nieger, M.; Lutz, M.; Ehlers, A. W.; Slootweg, J. C. Reactivity of the Geminal Phosphinoborane *t*Bu<sub>2</sub>PCH<sub>2</sub>BPh<sub>2</sub> towards Alkynes, Nitriles, and Nitrilium Triflates. *Dalt. Trans.* **2017**, *46* (36), pp 12284–12292. DOI: 10.1039/C7DT02570J.
- (253) Appelt, C.; Westenberg, H.; Bertini, F.; Ehlers, A. W.; Slootweg, J. C.; Lammertsma, K.; Uhl, W. Geminal Phosphorus/Aluminum-Based Frustrated Lewis Pairs: C–H versus C≡C Activation and CO<sub>2</sub> Fixation. *Angew. Chemie Int. Ed.* **2011**, *50* (17), pp 3925–3928. DOI: 10.1002/anie.201006901.
- (254) Bertini, F.; Hoffmann, F.; Appelt, C.; Uhl, W.; Ehlers, A. W.; Slootweg, J. C.; Lammertsma, K. Reactivity of Dimeric P/Al-Based Lewis Pairs toward Carbon Dioxide and Tert -Butyl Isocyanate. *Organometallics* **2013**, *32* (22), pp 6764–6769. DOI: 10.1021/om3011382.
- (255) Roters, S.; Appelt, C.; Westenberg, H.; Hepp, A.; Slootweg, J. C.; Lammertsma, K.; Uhl, W. Dimeric Aluminum–Phosphorus Compounds as Masked Frustrated Lewis Pairs for Small Molecule Activation. *Dalt. Trans.* **2012**, *41* (30), p 9033. DOI: 10.1039/c2dt30080j.
- (256) Backs, J.; Lange, M.; Possart, J.; Wollschläger, A.; Mück-Lichtenfeld, C.; Uhl, W. Facile Modulation of FLP Properties: A Phosphinylvinyl Grignard Reagent and Ga/P- and In/P<sub>2</sub>-Based Frustrated Lewis Pairs. *Angew. Chemie Int. Ed.* **2017**, *56* (11), pp 3094–3097. DOI: 10.1002/anie.201612485.
- (257) Waerder, B.; Pieper, M.; Körte, L. A.; Kinder, T. A.; Mix, A.; Neumann, B.; Stammler, H.; Mitzel, N. W. A Neutral Silicon/Phosphorus Frustrated Lewis Pair. *Angew. Chemie Int. Ed.* **2015**, *54* (45), pp 13416–13419. DOI: 10.1002/anie.201504171.
- (258) Kinder, T. A.; Pior, R.; Blomeyer, S.; Neumann, B.; Stammler, H.; Mitzel, N. W. A Neutral Germanium/Phosphorus Frustrated Lewis Pair and Its Contrasting Reactivity Compared to Its Silicon Analogue. *Chem. – A Eur. J.* **2019**, *25* (23), pp 5899–5903. DOI: 10.1002/chem.201901068.
- (259) Holtkamp, P.; Friedrich, F.; Stratmann, E.; Mix, A.; Neumann, B.; Stammler, H.; Mitzel, N. W. A Neutral Geminal Tin/Phosphorus Frustrated Lewis Pair. *Angew. Chemie Int. Ed.* **2019**, *58* (15), pp 5114–5118. DOI: 10.1002/anie.201901037.
- (260) Freitag, S.; Henning, J.; Schubert, H.; Wesemann, L. Phosphastannirane: A Phosphorus/Tin(II) Lewis Pair That Undergoes Alkyne and Alkene Addition. *Angew. Chemie Int. Ed.* **2013**, *52* (21), pp 5640–5643. DOI: 10.1002/anie.201301153.

- (261) Dyker, C. A.; Lavallo, V.; Donnadiu, B.; Bertrand, G. Synthesis of an Extremely Bent Acyclic Allene (A “Carbodicarbene”): A Strong Donor Ligand. *Angew. Chemie Int. Ed.* **2008**, *47* (17), pp 3206–3209. DOI: 10.1002/anie.200705620.
- (262) Alcarazo, M.; Lehmann, C. W.; Anoop, A.; Thiel, W.; Fürstner, A. Coordination Chemistry at Carbon. *Nat. Chem.* **2009**, *1* (4), pp 295–301. DOI: 10.1038/nchem.248.
- (263) Lavallo, V.; Dyker, C. A.; Donnadiu, B.; Bertrand, G. Synthesis and Ligand Properties of Stable Five-Membered-Ring Allenes Containing Only Second-Row Elements. *Angew. Chemie* **2008**, *120* (29), pp 5491–5494. DOI: 10.1002/ange.200801176.
- (264) Ruiz, D. A.; Melaimi, M.; Bertrand, G. Carbodicarbenes, Carbon(0) Derivatives, Can Dimerize. *Chem. - An Asian J.* **2013**, *8* (12), pp 2940–2942. DOI: 10.1002/asia.201300887.
- (265) Melaimi, M.; Parameswaran, P.; Donnadiu, B.; Frenking, G.; Bertrand, G. Synthesis and Ligand Properties of a Persistent, All-Carbon Four-Membered-Ring Allene. *Angew. Chemie* **2009**, *121* (26), pp 4886–4889. DOI: 10.1002/ange.200901117.
- (266) Fürstner, A.; Alcarazo, M.; Goddard, R.; Lehmann, C. W. Coordination Chemistry of Ene-1,1-Diamines and a Prototype “Carbodicarbene.” *Angew. Chemie Int. Ed.* **2008**, *47* (17), pp 3210–3214. DOI: 10.1002/anie.200705798.
- (267) Bestmann, H. J.; Saalfrank, R.; Snyder, J. P. O-Alkylation of Alkoxy-carbonylalkylidetriphenylphosphoranes. *Angew. Chemie Int. Ed. English* **1969**, *8* (3), pp 216–217. DOI: 10.1002/anie.196902161.
- (268) Pyykkö, P.; Runeberg, N. Ab Initio Studies of Bonding Trends. *J. Mol. Struct. THEOCHEM* **1991**, *234*, pp 279–290. DOI: 10.1016/0166-1280(91)89018-V.
- (269) Marrot, S.; Kato, T.; Cossío, F. P.; Gornitzka, H.; Baceiredo, A. Cyclic Carbodiphosphorane–Diphosphinocarbene Thermal Interconversion. *Angew. Chemie* **2006**, *118* (44), pp 7607–7610. DOI: 10.1002/ange.200603151.
- (270) Morosaki, T.; Suzuki, T.; Wang, W.-W.; Nagase, S.; Fujii, T. Syntheses, Structures, and Reactivities of Two Chalcogen-Stabilized Carbenes. *Angew. Chemie Int. Ed.* **2014**, *53* (36), pp 9569–9571. DOI: 10.1002/anie.201404795.
- (271) Fujii, T.; Ikeda, T.; Mikami, T.; Suzuki, T.; Yoshimura, T. Synthesis and Structure of (MeN)Ph<sub>2</sub>S=C=SPh<sub>2</sub>(NMe). *Angew. Chemie Int. Ed.* **2002**, *41* (14), pp 2576–2578. DOI: 10.1002/1521-3773(20020715)41:14<2576::AID-ANIE2576>3.0.CO;2-8.
- (272) Saalfrank, R. W. “Push-Pull” Substituted Allenes. *Isr. J. Chem.* **1985**, *26* (2), pp 181–190. DOI: 10.1002/ijch.198500091.
- (273) Saalfrank, R. W.; Maid, H. Roots: From Carbenes to Allenes and Coordination Polymers : Ever Present Never Twice the Same. *Chem. Commun.* **2005**, No. 48, p 5953. DOI: 10.1039/b510062n.
- (274) Cabrera-Trujillo, J. J.; Fernández, I. Carbenes and Heavier Ylidones (EL<sub>2</sub>) in Frustrated Lewis Pair Chemistry: Influence of the Nature of EL<sub>2</sub> on Dihydrogen Activation. *Inorg. Chem.* **2019**, *58* (12), pp 7828–7836. DOI: 10.1021/acs.inorgchem.9b00501.
- (275) Hänninen, M. M.; Peuronen, A.; Tuononen, H. M. Do Extremely Bent Allenes Exist? *Chem. Eur. J.* **2009**, *15* (30), pp 7287–7291. DOI: 10.1002/chem.200900928.
- (276) Chen, W.-C.; Shih, W.-C.; Jurca, T.; Zhao, L.; Andrada, D. M.; Peng, C.-J.; Chang, C.-C.; Liu, S.; Wang, Y.-P.; Wen, Y.-S.; Yap, G. P. A.; Hsu, C.-P.; Frenking, G.; Ong, T.-G. Carbodicarbenes: Unexpected  $\pi$ -Accepting Ability during Reactivity with Small Molecules. *J. Am. Chem. Soc.* **2017**, *139* (36), pp 12830–12836. DOI: 10.1021/jacs.7b08031.
- (277) Gravogl, L.; Heinemann, F. W.; Munz, D.; Meyer, K. An Iron Pincer Complex in Four Oxidation States. *Inorg. Chem.* **2020**, *59* (8), pp 5632–5645. DOI: 10.1021/acs.inorgchem.0c00355.
- (278) Chan, S.-C.; Ang, Z. Z.; Gupta, P.; Ganguly, R.; Li, Y.; Ye, S.; England, J. Carbodicarbene Ligand Redox Noninnocence in Highly Oxidized Chromium and Cobalt Complexes. *Inorg. Chem.* **2020**, *59* (6), pp 4118–4128. DOI: 10.1021/acs.inorgchem.0c00153.
- (279) Chan, S.-C.; Gupta, P.; Engelmann, X.; Ang, Z. Z.; Ganguly, R.; Bill, E.; Ray, K.; Ye, S.; England, J. Observation of Carbodicarbene Ligand Redox Noninnocence in Highly Oxidized Iron Complexes. *Angew. Chemie Int. Ed.* **2018**, *57* (48), pp 15717–15722. DOI: 10.1002/anie.201809158.
- (280) Goldfogel, M. J.; Roberts, C. C.; Meek, S. J. Intermolecular Hydroamination of 1,3-Dienes Catalyzed by Bis(Phosphine)Carbodicarbene–Rhodium Complexes. *J. Am. Chem. Soc.* **2014**, *136* (17), pp 6227–6230. DOI: 10.1021/ja502275w.
- (281) Marcum, J. S.; Roberts, C. C.; Manan, R. S.; Cervarich, T. N.; Meek, S. J. Chiral Pincer Carbodicarbene

- Ligands for Enantioselective Rhodium-Catalyzed Hydroarylation of Terminal and Internal 1,3-Dienes with Indoles. *J. Am. Chem. Soc.* **2017**, *139* (44), pp 15580–15583. DOI: 10.1021/jacs.7b08575.
- (282) Roberts, C. C.; Matías, D. M.; Goldfogel, M. J.; Meek, S. J. Lewis Acid Activation of Carbodicarbene Catalysts for Rh-Catalyzed Hydroarylation of Dienes. *J. Am. Chem. Soc.* **2015**, *137* (20), pp 6488–6491. DOI: 10.1021/jacs.5b03510.
- (283) Marcum, J. S.; Cervarich, T. N.; Manan, R. S.; Roberts, C. C.; Meek, S. J. (CDC)–Rhodium-Catalyzed Hydroallylation of Vinylarenes and 1,3-Dienes with AllylTrifluoroborates. *ACS Catal.* **2019**, *9* (7), pp 5881–5889. DOI: 10.1021/acscatal.9b01579.
- (284) Hsu, Y.; Wang, V. C. -C.; Au-Yeung, K.; Tsai, C.; Chang, C.; Lin, B.; Chan, Y.; Hsu, C.; Yap, G. P. A.; Jurca, T.; Ong, T. One-Pot Tandem Photoredox and Cross-Coupling Catalysis with a Single Palladium Carbodicarbene Complex. *Angew. Chemie Int. Ed.* **2018**, *57* (17), pp 4622–4626. DOI: 10.1002/anie.201800951.
- (285) Frenking, G.; Tonner, R.; Klein, S.; Takagi, N.; Shimizu, T.; Krapp, A.; Pandey, K. K.; Parameswaran, P. New Bonding Modes of Carbon and Heavier Group 14 Atoms Si–Pb. *Chem. Soc. Rev.* **2014**, *43* (14), pp 5106–5139. DOI: 10.1039/C4CS00073K.
- (286) Yao, S.; Xiong, Y.; Driess, M. A New Area in Main-Group Chemistry: Zerovalent Monoatomic Silicon Compounds and Their Analogues. *Acc. Chem. Res.* **2017**, *50* (8), pp 2026–2037. DOI: 10.1021/acs.accounts.7b00285.
- (287) Takagi, N.; Shimizu, T.; Frenking, G. Divalent Silicon(0) Compounds. *Chem. Eur. J.* **2009**, *15* (14), pp 3448–3456. DOI: 10.1002/chem.200802739.
- (288) Ishida, S.; Iwamoto, T.; Kabuto, C.; Kira, M. A Stable Silicon-Based Allene Analogue with a Formally Sp-Hybridized Silicon Atom. *Nature* **2003**, *421* (6924), pp 725–727. DOI: 10.1038/nature01380.
- (289) Bayat, M.; Sedghi, A.; Ebrahimkhani, L.; Sabounchei, S. J. N-Heterocyclic Carbene or Phosphorus Ylide: Which One Forms a Stronger Bond with Group 11 Metals? A Theoretical Study. *Dalt. Trans.* **2017**, *46* (1), pp 207–220. DOI: 10.1039/C6DT03814J.
- (290) Kaska, W. C. The Coordination Chemistry of Ylides. *Coord. Chem. Rev.* **1983**, *48* (1), pp 1–58. DOI: 10.1016/0010-8545(83)85001-2.
- (291) Nitsch, J.; Wolters, L. P.; Fonseca Guerra, C.; Bickelhaupt, F. M.; Steffen, A. Enhanced  $\pi$ -Back-Donation as a Way to Higher Coordination Numbers in  $d^{10}$  [M(NHC)<sub>n</sub>]<sup>n</sup> Complexes: A DFT Study. *Chem. Eur. J.* **2017**, *23* (3), pp 614–622. DOI: 10.1002/chem.201603861.
- (292) Hamze, R.; Peltier, J. L.; Sylvinson, D.; Jung, M.; Cardenas, J.; Haiges, R.; Soleilhavoup, M.; Jazzar, R.; Djurovich, P. I.; Bertrand, G.; Thompson, M. E. Eliminating Nonradiative Decay in Cu(I) Emitters: >99% Quantum Efficiency and Microsecond Lifetime. *Science* **2019**, *363* (6427), pp 601–606. DOI: 10.1126/science.aav2865.
- (293) Di, D.; Romanov, A. S.; Yang, L.; Richter, J. M.; Rivett, J. P. H.; Jones, S.; Thomas, T. H.; Abdi Jalebi, M.; Friend, R. H.; Linnolahti, M.; Bochmann, M.; Credginton, D. High-Performance Light-Emitting Diodes Based on Carbene-Metal-Amides. *Science* **2017**, *356* (6334), pp 159–163. DOI: 10.1126/science.aah4345.
- (294) Hamze, R.; Shi, S.; Kapper, S. C.; Muthiah Ravinson, D. S.; Estergreen, L.; Jung, M.-C.; Tadler, A. C.; Haiges, R.; Djurovich, P. I.; Peltier, J. L.; Jazzar, R.; Bertrand, G.; Bradforth, S. E.; Thompson, M. E. “Quick-Silver” from a Systematic Study of Highly Luminescent, Two-Coordinate, D10 Coinage Metal Complexes. *J. Am. Chem. Soc.* **2019**, *141* (21), pp 8616–8626. DOI: 10.1021/jacs.9b03657.
- (295) Gernert, M.; Balles-Wolf, L.; Kerner, F.; Müller, U.; Schmiedel, A.; Holzapfel, M.; Marian, C. M.; Pflaum, J.; Lambert, C.; Steffen, A. Cyclic (Amino)(Aryl)Carbenes Enter the Field of Chromophore Ligands: Expanded  $\pi$  System Leads to Unusually Deep Red Emitting Cu I Compounds. *J. Am. Chem. Soc.* **2020**, *142* (19), pp 8897–8909. DOI: 10.1021/jacs.0c02234.
- (296) Yang, Z.; Mao, Z.; Xie, Z.; Zhang, Y.; Liu, S.; Zhao, J.; Xu, J.; Chi, Z.; Aldred, M. P. Recent Advances in Organic Thermally Activated Delayed Fluorescence Materials. *Chem. Soc. Rev.* **2017**, *46* (3), pp 915–1016. DOI: 10.1039/C6CS00368K.
- (297) O’Reilly, M. E.; Ghiviriga, I.; Abboud, K. A.; Veige, A. S. A New ONO<sup>3-</sup> Trianionic Pincer-Type Ligand for Generating Highly Nucleophilic Metal–Carbon Multiple Bonds. *J. Am. Chem. Soc.* **2012**, *134* (27), pp 11185–11195. DOI: 10.1021/ja302222s.
- (298) Kehr, G.; Schwendemann, S.; Erker, G. Intramolecular Frustrated Lewis Pairs: Formation and Chemical Features. In *Topics in Current Chemistry. Frustrated Lewis Pairs I*; 2012; pp 45–83. DOI: 10.1007/128\_2012\_373.

- (299) Beverina, L.; Pagani, G. A. Pi-Conjugated Zwitterions as Paradigm of Donor–Acceptor Building Blocks in Organic-Based Materials. *Acc. Chem. Res.* **2014**, *47* (2), pp 319–329. DOI: 10.1021/ar4000967.
- (300) Mishra, A.; Behera, R. K.; Behera, P. K.; Mishra, B. K.; Behera, G. B. Cyanines during the 1990s: A Review. *Chem. Rev.* **2000**, *100* (6), pp 1973–2012. DOI: 10.1021/cr990402t.
- (301) Fabian, J.; Nakazumi, H.; Matsuoka, M. Near-Infrared Absorbing Dyes. *Chem. Rev.* **1992**, *92* (6), pp 1197–1226. DOI: 10.1021/cr00014a003.
- (302) Qian, G.; Wang, Z. Y. Near-Infrared Organic Compounds and Emerging Applications. *Chem. - An Asian J.* **2010**, *5* (5), pp 1006–1029. DOI: 10.1002/asia.200900596.
- (303) Reichardt, C. Solvatochromic Dyes as Solvent Polarity Indicators. *Chem. Rev.* **1994**, *94* (8), pp 2319–2358. DOI: 10.1021/cr00032a005.
- (304) Shimizu, A.; Ishizaki, Y.; Horiuchi, S.; Hirose, T.; Matsuda, K.; Sato, H.; Yoshida, J. HOMO–LUMO Energy-Gap Tuning of  $\pi$ -Conjugated Zwitterions Composed of Electron-Donating Anion and Electron-Accepting Cation. *J. Org. Chem.* **2021**, *86* (1), pp 770–781. DOI: 10.1021/acs.joc.0c02343.
- (305) Machado, V. G.; Stock, R. I.; Reichardt, C. Pyridinium *N*-Phenolate Betaine Dyes. *Chem. Rev.* **2014**, *114* (20), pp 10429–10475. DOI: 10.1021/cr5001157.
- (306) Ajayaghosh, A.; Chenthamarakshan, C. R.; Das, S.; George, M. V. Zwitterionic Dye-Based Conducting Polymers. Synthesis and Optical Properties of Pyrrole-Derived Polysquaraines. *Chem. Mater.* **1997**, *9* (3), pp 644–646. DOI: 10.1021/cm960475i.
- (307) Ajayaghosh, A. Donor–Acceptor Type Low Band Gap Polymers: Polysquaraines and Related Systems. *Chem. Soc. Rev.* **2003**, *32* (4), pp 181–191. DOI: 10.1039/B204251G.
- (308) He, J.; Jo, Y. J.; Sun, X.; Qiao, W.; Ok, J.; Kim, T.; Li, Z. Squaraine Dyes for Photovoltaic and Biomedical Applications. *Adv. Funct. Mater.* **2021**, *31* (12), p 2008201. DOI: 10.1002/adfm.202008201.
- (309) Maeda, T. Squaraine Dyes. In *Progress in the Science of Functional Dyes*; Springer Singapore: Singapore, 2021; pp 21–47. DOI: 10.1007/978-981-33-4392-4\_2.
- (310) Guasch, J.; Grisanti, L.; Lloveras, V.; Vidal-Gancedo, J.; Souto, M.; Morales, D. C.; Vilaseca, M.; Sissa, C.; Painelli, A.; Ratera, I.; Rovira, C.; Veciana, J. Induced Self-Assembly of a Tetrathiafulvalene-Based Open-Shell Dyad through Intramolecular Electron Transfer. *Angew. Chemie* **2012**, *124* (44), pp 11186–11190. DOI: 10.1002/ange.201203448.
- (311) Ullrich, T.; Pinter, P.; Messelberger, J.; Haines, P.; Kaur, R.; Hansmann, M. M.; Munz, D.; Guldi, D. M. Singlet Fission in Carbene-Derived Diradicaloids. *Angew. Chemie* **2020**, *132* (20), pp 7980–7988. DOI: 10.1002/ange.202001286.
- (312) Messelberger, J.; Grünwald, A.; Pinter, P.; Hansmann, M. M.; Munz, D. Carbene Derived Diradicaloids – Building Blocks for Singlet Fission? *Chem. Sci.* **2018**, *9* (28), pp 6107–6117. DOI: 10.1039/C8SC01999A.
- (313) Pinter, P.; Munz, D. Controlling Möbius-Type Helicity and the Excited-State Properties of Cumulenes with Carbenes. *J. Phys. Chem. A* **2020**, *124* (49), pp 10100–10110. DOI: 10.1021/acs.jpca.0c07940.
- (314) Munz, D.; Chu, J.; Melaimi, M.; Bertrand, G. NHC-CAAC Heterodimers with Three Stable Oxidation States. *Angew. Chemie* **2016**, *128* (41), pp 13078–13082. DOI: 10.1002/ange.201607537.
- (315) Messelberger, J.; Grünwald, A.; Goodner, S. J.; Zeilinger, F.; Pinter, P.; Miehllich, M. E.; Heinemann, F. W.; Hansmann, M. M.; Munz, D. Aromaticity and Sterics Control Whether a Cationic Olefin Radical Is Resistant to Disproportionation. *Chem. Sci.* **2020**, *11* (16), pp 4138–4149. DOI: 10.1039/D0SC00699H.
- (316) Antoni, P. W.; Hansmann, M. M. Pyrylenes: A New Class of Tunable, Redox-Switchable, Photoexcitable Pyrylium–Carbene Hybrids with Three Stable Redox-States. *J. Am. Chem. Soc.* **2018**, *140* (44), pp 14823–14835. DOI: 10.1021/jacs.8b08545.
- (317) Chauvin, R. Zwitterionic Organometallates. *Eur. J. Inorg. Chem.* **2000**, *2000* (4), pp 577–591. DOI: 10.1002/(SICI)1099-0682(200004)2000:4<577::AID-EJIC577>3.0.CO;2-F.
- (318) Stradiotto, M.; Hesp, K. D.; Lundgren, R. J. Zwitterionic Relatives of Cationic Platinum Group Metal Complexes: Applications in Stoichiometric and Catalytic  $\sigma$ -Bond Activation *Angewandte*. **2010**, pp 494–512. DOI: 10.1002/anie.200904093.
- (319) Puerta-Oteo, R.; Ojeda-Amador, A. I.; Jiménez, M. V.; Pérez-Torrente, J. J. Catalytic Applications of Zwitterionic Transition Metal Compounds. *Dalt. Trans.* **2022**, *51* (3), pp 817–830. DOI: 10.1039/D1DT03746C.
- (320) Bendeif, E.-E.; Matta, C. F.; Stradiotto, M.; Fertey, P.; Lecomte, C. Can a Formally Zwitterionic Rhodium(I) Complex Emulate the Charge Density of a Cationic Rhodium(I) Complex? A Combined Synchrotron X-Ray and Theoretical Charge-Density Study. *Inorg. Chem.* **2012**, *51* (6), pp 3754–3769.



- DOI: 10.1021/ic2026347.
- (321) Smidt, S. P.; Zimmermann, N.; Studer, M.; Pfaltz, A. Enantioselective Hydrogenation of Alkenes with Iridium–PHOX Catalysts: A Kinetic Study of Anion Effects. *Chem. Eur. J.* **2004**, *10* (19), pp 4685–4693. DOI: 10.1002/chem.200400284.
- (322) Schirmer, T. E.; König, B. Ion-Pairing Catalysis in Stereoselective, Light-Induced Transformations. *J. Am. Chem. Soc.* **2022**. DOI: 10.1021/jacs.2c04759.
- (323) Weerasiri, K. C.; Chen, D.; Wozniak, D. I.; Dobereiner, G. E. Internal Alkyne Regio- and Chemoselectivity Using a Zwitterionic *N*-Heterocyclic Carbene Gold Catalyst in a Silver-Free Alkyne Hydration Reaction. *Adv. Synth. Catal.* **2016**, *358* (24), pp 4106–4113. DOI: 10.1002/adsc.201601013.
- (324) Schmidt, B. M.; Engle, J. T.; Zhang, M.; Babahan, I.; Ziegler, C. J.; Jia, L. Zwitterionic Nickel(II) Complexes: Synthesis, Characterization, Decomposition, and Stoichiometric and Catalytic Reactivities. *J. Organomet. Chem.* **2016**, *805*, pp 94–99. DOI: 10.1016/j.jorganchem.2016.01.011.
- (325) Peters, J. C.; Feldman, J. D.; Tilley, T. D. Silylene Extrusion from a Silane: Direct Conversion of  $\text{Me}_2\text{SiH}_2$  to an Iridium Silylene Dihydride. *J. Am. Chem. Soc.* **1999**, *121* (42), pp 9871–9872. DOI: 10.1021/ja992367d.
- (326) Douglas, T. M.; Molinos, E.; Brayshaw, S. K.; Weller, A. S. Rhodium Phosphine Olefin Complexes of the Weakly Coordinating Anions  $[\text{BAR}^{\text{F}}_4]^-$  and  $[1\text{-Closo-CB}_{11}\text{H}_6\text{Br}_6]^-$ . Kinetic versus Thermodynamic Factors in Anion Coordination and Comp. *Organometallics* **2007**, *26* (3), pp 463–465. DOI: 10.1021/om060975d.
- (327) Constant, S.; Tortoioli, S.; Müller, J.; Linder, D.; Buron, F.; Lacour, J. Air- and Microwave-Stable ( $\text{C}_5\text{H}_5$ )Ru Catalysts for Improved Regio- and Enantioselective Carroll Rearrangements. *Angew. Chemie Int. Ed.* **2007**, *46* (47), pp 8979–8982. DOI: 10.1002/anie.200704019.
- (328) César, V.; Misal Castro, L. C.; Dombay, T.; Sortais, J.-B.; Darcel, C.; Labat, S.; Miqueu, K.; Sotiropoulos, J.-M.; Brousses, R.; Lugan, N.; Lavigne, G. (Cyclopentadienyl)Iron(II) Complexes of *N*-Heterocyclic Carbenes Bearing a Malonate or Imidate Backbone: Synthesis, Structure, and Catalytic Potential in Hydrosilylation. *Organometallics* **2013**, *32* (16), pp 4643–4655. DOI: 10.1021/om400625q.
- (329) Lundgren, R. J.; Rankin, M. A.; McDonald, R.; Schatte, G.; Stradiotto, M. A Formally Zwitterionic Ruthenium Catalyst Precursor for the Transfer Hydrogenation of Ketones That Does Not Feature an Ancillary Ligand N–H Functionality. *Angew. Chemie Int. Ed.* **2007**, *46* (25), pp 4732–4735. DOI: 10.1002/anie.200700345.
- (330) Gutsulyak, D. V.; Gott, A. L.; Piers, W. E.; Parvez, M. Dimerization of Ethylene by Nickel Phosphino–Borate Complexes. *Organometallics* **2013**, *32* (11), pp 3363–3370. DOI: 10.1021/om400288u.
- (331) Kleinsasser, J. F.; Reinhart, E. D.; Estrada, J.; Jordan, R. F.; Lavallo, V. Ethylene Oligomerization and Polymerization by Palladium(II) Methyl Complexes Supported by Phosphines Bearing a Perchlorinated 10-Vertex Closo -Carborane Anion Substituent. *Organometallics* **2018**, *37* (24), pp 4773–4783. DOI: 10.1021/acs.organomet.8b00772.
- (332) Werner, H.; Tena, M. A.; Mahr, N.; Peters, K.; Schnering, H. Von. Two Alternatives of Heteroallene Insertion in Metal — Ligand Bonds of Five-Coordinate Ruthenium(II) and Osmium(II) Complexes  $[\text{MXY}(\text{CO})(\text{P}i\text{Pr}_3)_2]$ . *Chem. Ber.* **1995**, *128* (1), pp 41–47. DOI: 10.1002/cber.19951280107.
- (333) Allen, A.; Lin, W. Unprecedented Insertion of Alkynes into a Palladium–Phosphine Bond. A Facile Route to Palladium-Bound Alkenyl Phosphorus Ylides. *Organometallics* **1999**, *18* (15), pp 2922–2925. DOI: 10.1021/om990014h.
- (334) Cardaci, G. Zwitterionic Adducts from Trialkylphosphine and ( $\eta$ -Allyl)Dicarbonyl-Nitrosyliron Complexes: Structure and Reactivity. *J. Chem. Soc., Dalt. Trans.* **1984**, No. 5, pp 815–818. DOI: 10.1039/DT9840000815.
- (335) Araki, S.; Butsugan, Y. Syntheses and Structures of Transition-Metal Complexes of Mesoionic Olate, Thiolate, Selenolate, and Cyclopentadienide. *Chem. Ber.* **1993**, *126* (5), pp 1157–1159. DOI: 10.1002/cber.19931260515.
- (336) Aumann, R.; Nienaber, H. (1-Alkynyl)Carbene Complexes (= 1-Metalla-1-Buten-3-Ynes): Tools for Synthesis. In *Advances in Organometallic Chemistry*; 1997; pp 163–242. DOI: 10.1016/S0065-3055(08)60439-6.
- (337) Klahn, A. H.; Oelckers, B.; Godoy, F.; Garland, M. T.; Vega, A.; Perutz, R. N.; Higgitt, C. L. Synthesis and Reactions of the Rhenium Fulvene Complexes  $[\text{Re}(\eta^6\text{-C}_5\text{Me}_4\text{CH}_2)(\text{CO})_2(\text{C}_6\text{F}_4\text{R})]$  (R = F or  $\text{CF}_3$ ): Products Derived from Initial C–F Activation. *J. Chem. Soc. Dalt. Trans.* **1998**, No. 18, pp 3079–3086. DOI: 10.1039/a802899k.

- (338) Dullaghan, C. A.; Carpenter, G. B.; Sweigart, D. A.; Choi, D. S.; Lee, S. S.; Chung, Y. K. Models for the Homogeneous Hydrodesulfurization of Thiophenes: Manganese-Mediated Carbon–Sulfur Bond Cleavage and Hydrogenation Reactions. *Organometallics* **1997**, *16* (26), pp 5688–5695. DOI: 10.1021/om970822d.
- (339) Gandelman, M.; Vigalok, A.; Shimon, L. J. W.; Milstein, D. A PCN Ligand System. Exclusive C–C Activation with Rhodium(I) and C–H Activation with Platinum(II). *Organometallics* **1997**, *16* (18), pp 3981–3986. DOI: 10.1021/om9703200.
- (340) Brown, D. S.; Delville-Desbois, M.-H.; Boese, R.; Vollhardt, K. P. C.; Astruc, D. Electron-Reservoir Complexes[Fe<sup>I</sup>Cp(Arene)] as Selective Initiators for a Novel Electron Transfer Chain Catalyzed Reaction: General Synthesis of Fulvalene-Bridged Homo- and Heterodinuclear Zwitterions. *Angew. Chemie Int. Ed. English* **1994**, *33* (6), pp 661–663. DOI: 10.1002/anie.199406611.
- (341) Sinnema, P. J.; Meetsma, A.; Teuben, J. H. Competitive CH Activation in (Pentamethylcyclopentadienyl)(Cyclooctatetraene)Alkylzirconium Compounds Cp\*Zr(COT)R. Selective Formation of Fulvene or Cyclooctatrienyne Ligands. Molecular Structure of Cp\*Zr(μ-η<sup>8</sup>:η<sup>2</sup>-C<sub>8</sub>H<sub>6</sub>)ZrCp\*(η<sup>4</sup>C<sub>8</sub>H<sub>8</sub>), a dinuclear zwitterionic zirconium complex with a bridging cyclooctatrienyne ligand. *Organometallics* **1993**, *12* (1), pp 184–189. DOI: 10.1021/om00025a032.
- (342) Peng, W.-J.; Train, S. G.; Howell, D. K.; Fronczek, F. R.; Stanley, G. G. Bimetallic Hydroformylation: A Zwitterionic Rh<sup>I</sup>-Rh<sup>I</sup> Tetrphosphine Ligand-Based Bimetallic Complex Exhibiting Facile CO Addition and Phosphine Ligand Rearrangement Equilibrium. *Chem. Commun.* **1996**, No. 22, p 2607. DOI: 10.1039/cc9960002607.
- (343) Berenguer, J. R.; Forniés, J.; Lalinde, E.; Martínez, F.; Urriolabeitia, E.; Welch, A. J. Synthesis of Homo- and Hetero-Dinuclear Complexes Containing Alkynyl Bridges. Molecular Structure of *Cis, Trans*-[(OC)(C<sub>6</sub>F<sub>5</sub>)<sub>2</sub>Pt(μ-η<sup>2</sup>-C≡CPh)Pt(C≡CPh)(PPh<sub>3</sub>)<sub>2</sub>]. *J. Chem. Soc., Dalt. Trans.* **1994**, No. 8, pp 1291–1299. DOI: 10.1039/DT9940001291.
- (344) Puerta-Oteo, R.; Hölscher, M.; Jiménez, M. V.; Leitner, W.; Passarelli, V.; Pérez-Torrente, J. J. Experimental and Theoretical Mechanistic Investigation on the Catalytic CO<sub>2</sub> Hydrogenation to Formate by a Carboxylate-Functionalized Bis(*N*-Heterocyclic Carbene) Zwitterionic Iridium(I) Compound. *Organometallics* **2018**, *37* (5), pp 684–696. DOI: 10.1021/acs.organomet.7b00509.
- (345) Khaskin, E.; Zavalij, P. Y.; Vedernikov, A. N. Oxidatively Induced Methyl Transfer from Boron to Platinum in Dimethyldi(2-Pyridyl)Boratoplatinum Complexes. *Angew. Chemie Int. Ed.* **2007**, *46* (33), pp 6309–6312. DOI: 10.1002/anie.200701257.
- (346) Thomas, J. C.; Peters, J. C. Zwitterionic and Cationic Bis(Phosphine) Platinum(II) Complexes: Structural, Electronic, and Mechanistic Comparisons Relevant to Ligand Exchange and Benzene C–H Activation Processes. *J. Am. Chem. Soc.* **2003**, *125* (29), pp 8870–8888. DOI: 10.1021/ja0296071.
- (347) Lu, C. C.; Peters, J. C. Catalytic Copolymerization of CO and Ethylene with a Charge Neutral Palladium(II) Zwitterion. *J. Am. Chem. Soc.* **2002**, *124* (19), pp 5272–5273. DOI: 10.1021/ja017011s.
- (348) Betley, T. A.; Peters, J. C. Zwitterionic Relatives to the Classic [(P–P)Rh(Solv)<sub>2</sub>] Ions: Neutral Catalysts Active for H–E Bond Additions to Olefins (E=C, Si, B). *Angew. Chemie Int. Ed.* **2003**, *42* (21), pp 2385–2389. DOI: 10.1002/anie.200250378.
- (349) Betley, T. A.; Peters, J. C. Synthesis of the (Dialkylamino)Borate, [Ph<sub>2</sub>B(CH<sub>2</sub>NMe<sub>2</sub>)<sub>2</sub>]<sup>−</sup>, Affords Access to *N*-Chelated Rhodium(I) Zwitterions. *Inorg. Chem.* **2002**, *41* (25), pp 6541–6543. DOI: 10.1021/ic0259336.
- (350) Li, J.; Djurovich, P. I.; Alleyne, B. D.; Yousufuddin, M.; Ho, N. N.; Thomas, J. C.; Peters, J. C.; Bau, R.; Thompson, M. E. Synthetic Control of Excited-State Properties in Cyclometalated Ir(III) Complexes Using Ancillary Ligands. *Inorg. Chem.* **2005**, *44* (6), pp 1713–1727. DOI: 10.1021/ic048599h.
- (351) Stradiotto, M.; Cipot, J.; McDonald, R. A Catalytically Active, Charge-Neutral Rh(I) Zwitterion Featuring a P,*N*-Substituted “Naked” Indenide Ligand. *J. Am. Chem. Soc.* **2003**, *125* (19), pp 5618–5619. DOI: 10.1021/ja034543v.
- (352) Cipot, J.; McDonald, R.; Stradiotto, M. New Bidentate Cationic and Zwitterionic Relatives of Crabtree’s Hydrogenation Catalyst. *Chem. Commun.* **2005**, No. 39, p 4932. DOI: 10.1039/b510253g.
- (353) Cipot, J.; McDonald, R.; Ferguson, M. J.; Schatte, G.; Stradiotto, M. Cationic and Formally Zwitterionic Rhodium(I) and Iridium(I) Derivatives of a P,*N*-Substituted Indene: A Comparative Synthetic, Structural, and Catalytic Investigation. *Organometallics* **2007**, *26* (3), pp 594–608. DOI: 10.1021/om060758c.
- (354) Rankin, M. A.; McDonald, R.; Ferguson, M. J.; Stradiotto, M. Exploring the Influence of Ancillary

- Ligand Charge and Geometry on the Properties of New Coordinatively Unsaturated  $\text{Cp}^*(\kappa^2\text{-}P,M)\text{Ru}^+$  Complexes: Linkage Isomerism, Double C–H Bond Activation, and Reversible  $\alpha$ -Hydride Elimination. *Organometallics* **2005**, *24* (21), pp 4981–4994. DOI: 10.1021/om050534e.
- (355) Rankin, M. A.; McDonald, R.; Ferguson, M. J.; Stradiotto, M. Coordinatively Unsaturated Cationic and Zwitterionic  $[\text{Cp}^*\text{Ru}(\kappa^2\text{-}P,M)]$  Complexes: Ligand-Assisted Double-Geminal C–H Bond Activation and Reversible  $\alpha$ -H Elimination at Ruthenium. *Angew. Chemie Int. Ed.* **2005**, *44* (23), pp 3603–3606. DOI: 10.1002/anie.200500528.
- (356) Lu, C. C.; Peters, J. C. Synthetic, Structural, and Mechanistic Aspects of an Amine Activation Process Mediated at a Zwitterionic Pd(II) Center. *J. Am. Chem. Soc.* **2004**, *126* (48), pp 15818–15832. DOI: 10.1021/ja046415s.
- (357) Hesp, K. D.; McDonald, R.; Ferguson, M. J.; Stradiotto, M. New Cationic and Zwitterionic  $\text{Cp}^*\text{M}(\kappa^2\text{-}P,S)$  Complexes (M = Rh, Ir): Divergent Reactivity Pathways Arising from Alternative Modes of Ancillary Ligand Participation in Substrate Activation. *J. Am. Chem. Soc.* **2008**, *130* (48), pp 16394–16406. DOI: 10.1021/ja8062277.
- (358) Liotta, C. L.; Grisdale, E. E.; Hopkins, H. P. Relative Nucleophilicities of “Naked” Anions. *Tetrahedron Lett.* **1975**, *16* (48), pp 4205–4208. DOI: 10.1016/S0040-4039(00)91149-3.
- (359) Lawrence, S. C.; Skinner, M. E. G.; Green, J. C.; Mountford, P. A Structurally Characterised, Naked  $\text{Sp}^3$ -Hybridised Carbanion in the Zwitterionic Imido Complex  $[\text{Ti}(\text{NBu}^t)\{\text{C}(\text{Me}_2\text{Pz})_3\}\text{Cl}(\text{THF})]$  ( $\text{HMe}_2\text{Pz} = 3,5\text{-Dimethylpyrazole}$ ). *Chem. Commun.* **2001**, No. 8, pp 705–706. DOI: 10.1039/b100315l.
- (360) Breher, F.; Grunenberg, J.; Lawrence, S. C.; Mountford, P.; Rügger, H. A Monomeric Organolithium Compound Containing a Free Pyramidal Carbanion in Solution and in the Solid State. *Angew. Chemie Int. Ed.* **2004**, *43* (19), pp 2521–2524. DOI: 10.1002/anie.200353308.
- (361) Bigmore, H. R.; Dubberley, S. R.; Kranenburg, M.; Lawrence, S. C.; Sealey, A. J.; Selby, J. D.; Zuideveld, M. A.; Cowley, A. R.; Mountford, P. A Remarkable Inversion of Structure–Activity Dependence on Imido N-Substituents with Varying Co-Ligand Topology and the Synthesis of a New Borate-Free Zwitterionic Polymerisation Catalyst. *Chem. Commun.* **2006**, No. 4, pp 436–438. DOI: 10.1039/B514467A.
- (362) Krummenacher, I.; Rügger, H.; Breher, F. Coinage Metal Complexes of Tris(Pyrazolyl)Methanide  $[\text{C}(3,5\text{-Me}_2\text{Pz})_3]^-$ :  $\kappa^3$ -Coordination vs. Backbone Functionalisation. *Dalt. Trans.* **2006**, No. 8, pp 1073–1081. DOI: 10.1039/B512309G.
- (363) Bigmore, H. R.; Meyer, J.; Krummenacher, I.; Rügger, H.; Clot, E.; Mountford, P.; Breher, F. Syntheses, Reactivity and DFT Studies of Group 2 and Group 12 Metal Complexes of Tris(Pyrazolyl)Methanides Featuring “Free” Pyramidal Carbanions. *Chem. Eur. J.* **2008**, *14* (19), pp 5918–5934. DOI: 10.1002/chem.200800181.
- (364) Cushion, M. G.; Meyer, J.; Heath, A.; Schwarz, A. D.; Fernández, I.; Breher, F.; Mountford, P. Syntheses and Structural Diversity of Group 2 and Group 12 Tris(Pyrazolyl)Methanide and Zwitterionic Tris(Pyrazolyl)Methanide Compounds. *Organometallics* **2010**, *29* (5), pp 1174–1190. DOI: 10.1021/om901013b.
- (365) González-Gallardo, S.; Kuzu, I.; Oña-Burgos, P.; Wolfer, T.; Wang, C.; Klinkhammer, K. W.; Klopfer, W.; Bräse, S.; Breher, F. Coinage Metal Complexes of Tris(Pyrazolyl)Methanide-Based Redox-Active Metalloligands. *Organometallics* **2014**, *33* (4), pp 941–951. DOI: 10.1021/om4010498.
- (366) Lalrempuia, R.; Stasch, A.; Jones, C. An Extremely Bulky Tris(Pyrazolyl)Methanide: A Tridentate Ligand for the Synthesis of Heteroleptic Magnesium(II) and Ytterbium(II) Alkyl, Hydride, and Iodide Complexes. *Chem. - An Asian J.* **2015**, *10* (2), pp 447–454. DOI: 10.1002/asia.201403089.
- (367) Li, T.; Zhang, G.; Guo, J.; Wang, S.; Leng, X.; Chen, Y. Tris(Pyrazolyl)Methanide Complexes of Trivalent Rare-Earth Metals. *Organometallics* **2016**, *35* (10), pp 1565–1572. DOI: 10.1021/acs.organomet.6b00166.
- (368) Kriek, S.; Koch, A.; Hinze, K.; Müller, C.; Lange, J.; Görls, H.; Westerhausen, M. S-Block Metal Complexes with Bis- and Tris(Pyrazolyl)Methane and -methanide Ligands. *Eur. J. Inorg. Chem.* **2016**, *2016* (15–16), pp 2332–2348. DOI: 10.1002/ejic.201501263.
- (369) Kuzu, I.; Krummenacher, I.; Hewitt, I. J.; Lan, Y.; Mereacre, V.; Powell, A. K.; Höfer, P.; Harmer, J.; Breher, F. Syntheses, Structures and Electronic Properties of Zwitterionic Iron(II) and Cobalt(II) Complexes Featuring Ambidentate Tris(Pyrazolyl)Methanide Ligands. *Chem. Eur. J.* **2009**, *15* (17), pp 4350–4365. DOI: 10.1002/chem.200802317.
- (370) Kratzert, D.; Leusser, D.; Stern, D.; Meyer, J.; Breher, F.; Stalke, D. Experimental Charge Density

- Distribution of Non-Coordinating  $sp^3$  Carbanions in  $[Mg\{(Pz^*)_3C\}_2]$ . *Chem. Commun.* **2011**, 47 (10), p 2931. DOI: 10.1039/c0cc04688d.
- (371) Meyer, J.; Kuzu, I.; González-Gallardo, S.; Breher, F. Investigations on the Steric Accessibility of the Carbanionic Moiety in Zwitterionic Magnesium Tris(Pyrazolyl)Methanide Complexes. Synthesis and Characterisation of Bi- and Tri-metallic Complexes. *Zeitschrift für Anorg. und Allg. Chemie* **2013**, 639 (2), pp 301–307. DOI: 10.1002/zaac.201200405.
- (372) Styra, S.; González-Gallardo, S.; Armbruster, F.; Oña-Burgos, P.; Moos, E.; Vonderach, M.; Weis, P.; Hampe, O.; Grün, A.; Schmitt, Y.; Gerhards, M.; Menges, F.; Gaffga, M.; Niedner-Schatteburg, G.; Breher, F. Heterobimetallic Cuprates Consisting of a Redox-Switchable, Silicon-Based Metalloligand: Synthesis, Structures, and Electronic Properties. *Chem. Eur. J.* **2013**, 19 (26), pp 8436–8446. DOI: 10.1002/chem.201300586.
- (373) Armbruster, F.; Fernández, I.; Breher, F. Syntheses, Structures, and Reactivity of Poly(Pyrazolyl)Silanes, -Disilanes, and the Ambidentate  $\kappa^1Si/\kappa^3N$ -Coordinating Tris(3,5-Dimethylpyrazolyl)Silanide Ligand  $[Si(3,5-Me_2Pz)_3]^-$ . *Dalt. Trans.* **2009**, No. 29, pp 5612–5626. DOI: 10.1039/b906333a.
- (374) Armbruster, F.; Augenstein, T.; Oña-Burgos, P.; Breher, F. Homoleptic Tetrakis(Silyl) Complexes of Pd(0) and Pt(0) Featuring Metal-Centred Heterocubane Structures: Evidence for the Existence of the Corresponding Mononuclear Pd(I) and Pt(I) Complexes. *Chem. Eur. J.* **2013**, No. 1, pp 1–9. DOI: 10.1002/chem.201303299.
- (375) Eaborn, C.; Farook, A.; Hitchcock, P. B.; Smith, J. D. {Tris[(Dimethylamino)Dimethylsilyl]Methyl}magnesium Iodide. A Grignard Reagent without a Carbon–Magnesium Bond? *Organometallics* **1997**, 16 (4), pp 503–504. DOI: 10.1021/om960891c.
- (376) Li, H.; Aquino, A. J. A.; Cordes, D. B.; Hase, W. L.; Krempner, C. Electronic Nature of Zwitterionic Alkali Metal Methanides, Silanides and Germanides – a Combined Experimental and Computational Approach. *Chem. Sci.* **2017**, 8 (2), pp 1316–1328. DOI: 10.1039/C6SC02390H.
- (377) Li, H.; Aquino, A. J. A.; Cordes, D. B.; Hung-Low, F.; Hase, W. L.; Krempner, C. A Zwitterionic Carbanion Frustrated by Boranes – Dihydrogen Cleavage with Weak Lewis Acids via an “Inverse” Frustrated Lewis Pair Approach. *J. Am. Chem. Soc.* **2013**, 135 (43), pp 16066–16069. DOI: 10.1021/ja409330h.
- (378) Eaborn, C.; Farook, A.; Hitchcock, P. B.; Smith, J. D. A Novel Zwitterionic Species Containing an Aluminum(III) Cation and a Planar Carbanion. Crystal Structure of  $[Et_3AlNMe_2SiMe_2C(SiMe_2NMe_2)_2AlEt_2]^- \cdot C_6H_6$ . *Organometallics* **1998**, 17 (15), pp 3135–3137. DOI: 10.1021/om980347z.
- (379) Hitchcock, P. B.; Lappert, M. F.; Layh, M. Novel Lithium 3-Sila- and 3-Germa- $\beta$ -Diketiminates. *Chem. Commun.* **1998**, No. 20, pp 2179–2180. DOI: 10.1039/a805864d.
- (380) Steiner, A.; Stalke, D. Sodium Tri(Pyrazol-1-Yl)-Germanate and -Stannate: New Tridentate ‘Claw-Ligands’ Containing Group 14 Metals. *J. Chem. Soc., Chem. Commun.* **1993**, No. 22, pp 1702–1704. DOI: 10.1039/C39930001702.
- (381) Reichart, F.; Kischel, M.; Zeckert, K. Lanthanide(II) Complexes of a Dual Functional Tris(2-Pyridyl)Stannate Derivative. *Chem. Eur. J.* **2009**, 15 (39), pp 10018–10020. DOI: 10.1002/chem.200901286.
- (382) Zeckert, K.; Zahn, S.; Kirchner, B. Tin–Lanthanoid Donor–Acceptor Bonds. *Chem. Commun.* **2010**, 46 (15), p 2638. DOI: 10.1039/b924967b.
- (383) Zeckert, K. Syntheses and Structures of Lanthanoid(ii) Complexes Featuring Sn–M (M = Al, Ga, In) Bonds. *Dalt. Trans.* **2012**, 41 (46), p 14101. DOI: 10.1039/c2dt31768k.
- (384) Zeckert, K. Pyridyl Compounds of Heavier Group 13 and 14 Elements as Ligands for Lanthanide Metals. *Organometallics* **2013**, 32 (5), pp 1387–1393. DOI: 10.1021/om301032x.
- (385) Beswick, M. A.; Davies, M. K.; Raithby, P. R.; Steiner, A.; Wright, D. S. Synthesis and Structure of  $[Pb(2-Py)_3Li \cdot THF]$ , Containing a Low-Valent Group 14 Tris(Pyridyl) Ligand (2-Py = 2-Pyridyl). *Organometallics* **1997**, 16 (6), pp 1109–1110. DOI: 10.1021/om9609123.
- (386) Zeckert, K.; Griebel, J.; Kirmse, R.; Weiß, M.; Denecke, R. Versatile Reactivity of a Lithium Tris(Aryl)Plumbate(II) Towards Organolanthanoid Compounds: Stable Lead-Lanthanoid-Metal Bonds or Redox Processes. *Chem. Eur. J.* **2013**, 19 (24), pp 7718–7722. DOI: 10.1002/chem.201300596.
- (387) Krempner, C.; Chisholm, M. H.; Gallucci, J. The Multidentate Ligand  $(MeOMe_2Si)_3Si^-$ : Unusual Coordination Modes in Alkali Metal Silanides. *Angew. Chemie Int. Ed.* **2008**, 47 (2), pp 410–413. DOI: 10.1002/anie.200703575.

- (388) Li, H.; Hope-Weeks, L. J.; Krempner, C. A Supramolecular Approach to Zwitterionic Alkaline Metal Silanides and Formation of Heterobimetallic Silanides. *Chem. Commun.* **2011**, 47 (14), p 4117. DOI: 10.1039/c1cc10148j.
- (389) Carlson, B.; Aquino, A. J. A.; Hope-Weeks, L. J.; Whittlesey, B.; McNerney, B.; Hase, W. L.; Krempner, C. Homoleptic Tris(Methoxydimethylsilyl)Silanides of the Alkaline Earth Metals: First Zwitterionic Silanides with Two Naked Silyl Anions. *Chem. Commun.* **2011**, 47 (39), p 11089. DOI: 10.1039/c1cc13933a.
- (390) Li, H.; Hung-Low, F.; Krempner, C. Synthesis and Structure of Zwitterionic Silylborates and Silylzincates with Pendant Polydonor Arms. *Organometallics* **2012**, 31 (20), pp 7117–7124. DOI: 10.1021/om300652n.
- (391) Thalangamaarachchige, V. D.; Unruh, D. K.; Cordes, D. B.; Krempner, C. Synthesis, Structure, and Reactivity of Zwitterionic Divalent Rare-Earth Metal Silanides. *Inorg. Chem.* **2015**, 54 (9), pp 4189–4191. DOI: 10.1021/acs.inorgchem.5b00542.
- (392) Simmonds, H. R.; Wright, D. S. Main Group Pyridyl-Based Ligands; Strategies to Mixed Metal Complexes. *Chem. Commun.* **2012**, 48 (69), pp 8617–8624. DOI: 10.1039/c2cc33015f.

# Chapter 2

---

## A Dianionic C<sub>3</sub>-Symmetric Scorpionate: Synthesis and Coordination Chemistry<sup>a</sup>

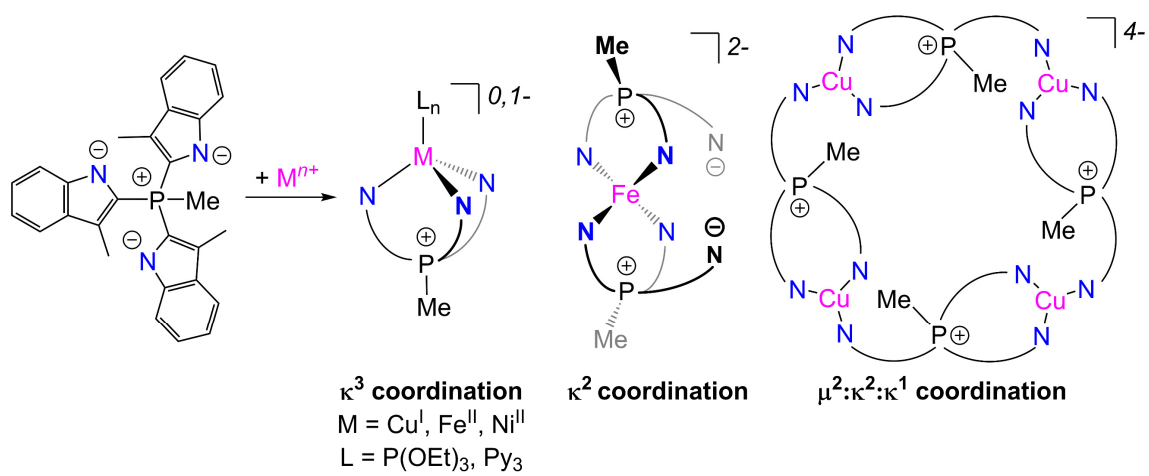
---

### Abstract

Introducing charges into ligand systems fine-tunes their electronic properties and influences coordination behavior and solubility of their metal complexes. Herein, we present a synthesis of a dianionic, C<sub>3</sub>-symmetric ligand combining three anionic N-donors tethered to a positively charged phosphonium center. This tris-skatylmethylphosphonium (TSMP<sup>2-</sup>) ligand, isolated in the form of its dipotassium salt TSMPK<sub>2</sub>, is the first dianionic homoscorpionate capable of metal exchange. The potassium cations in TSMPK<sub>2</sub> are exchangeable for other metals, which results in rich coordination chemistry. More specifically, the ligand displays a bridging  $\mu^2:\kappa^2:\kappa^1$  coordination mode with trigonal planar Cu(I) centers in the tetrameric complex [(TSMP)Cu]<sub>4</sub><sup>4-</sup>. The  $\kappa^3$  mode is accessed upon addition of 1 equiv. of P(OEt)<sub>3</sub> per Cu(I) to yield the tetrahedral monomeric complex [(TSMP)CuP(OEt)<sub>3</sub>]<sup>-</sup>. Both Fe(II) and Ni(II) in pyridine give octahedral high-spin  $\kappa^3$  complexes with composition (TSMP)M(Py)<sub>3</sub> (M=Fe, Ni). Displacement of three pyridine ligands in (TSMP)Fe(Py)<sub>3</sub> for a second equivalent of TSMP<sup>2-</sup> gives a high-spin pseudotetrahedral 2:1 complex [(TSMP)<sub>2</sub>Fe]<sup>2-</sup> with the ligands in  $\kappa^2$  coordination mode. The reduction in coordination number is likely due to electrostatic repulsion of the negatively-charged indolides as well as their weaker  $\pi$ -accepting character compared to pyridine.

---

<sup>a</sup> This chapter is based on: S. Tretiakov, J. A. M. Damen, M. Lutz, M.-E. Moret. A dianionic C<sub>3</sub>-symmetric scorpionate: synthesis and coordination chemistry. *Dalt. Trans.* **2020**, *49*, 13549–13556. DOI: 10.1039/D0DT02601H.



## 2.1 Introduction

The term “scorpionate” was introduced by Trofimenko<sup>1</sup> and refers to tripodal tridentate ligand systems that are able to coordinate to a metal with two identical donor moieties, similarly to pincers of a scorpion. The third donor moiety rotates forward akin to a scorpion stinger to attack the metal in a *fac* manner. If it is identical to the first two, a  $C_3$ -symmetric homoscorpionate complex forms. Otherwise, coordination results into a heteroscorpionate complex. This can be illustrated using the first generation of scorpionates – pyrazolylborates (*Chart 2.1*) also developed by Trofimenko.<sup>1</sup> The present introduction is confined exclusively to homoscorpionates.

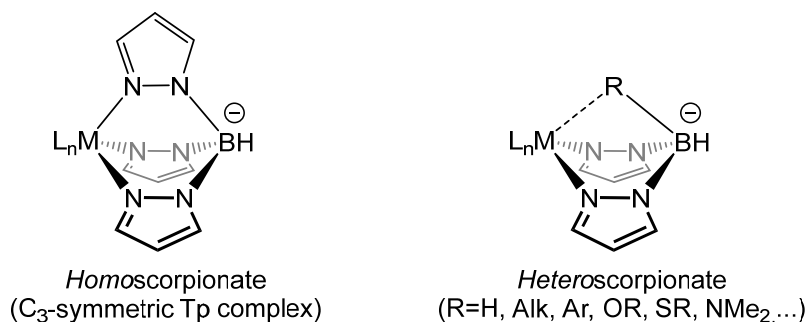


*Chart 2.1.* Examples of scorpionate complexes represented by pyrazolylborates. The homoscorpionate complex is formed by trispyrazolylborate (Tp).<sup>1</sup>

Scorpionates similar to the above are six-electron donors, which makes them isoelectronic to another common ligand, cyclopentadienyl (Cp). A considerable amount of research was done to compare these two systems.<sup>1,2</sup> It is important to point out, however, that while they are isoelectronic, they are not isolobal,<sup>3</sup> therefore the extent of such a comparison is limited. Additionally, in some situations, scorpionates are capable of displaying a  $\kappa^2$  coordination mode freeing the third arm for binding to another metal center,<sup>1</sup> which has no parallels in Cp chemistry.

The first generation of scorpionates proved to be highly-versatile spectator ligands. By modifying the nature, number and position of substituents of the pyrazolyl rings, a wide range of Tp-based ligands was prepared allowing to fine-tune both electronic and steric properties of a coordinated metal. Such systems found applications in biomimetics,<sup>4</sup> catalysis,<sup>5</sup> material science<sup>6</sup> and production of radiopharmaceuticals.<sup>7</sup> Following this success, the definition of scorpionates has been extended to tripodal tridentate systems with other donor groups and bridging atoms. Among the employed donors are imidazole,<sup>8</sup> pyridine,<sup>9</sup> triazole,<sup>10</sup> indole,<sup>11</sup> methimazole,<sup>12</sup> oxazoline,<sup>13</sup> *N*-heterocyclic carbenes<sup>14</sup> and others, and even acyclic donor groups.<sup>15</sup> Variation of the bridging atom allowed to further tune electronics and charge of the scorpionate ligands, thus influencing coordination behavior and solubility of their complexes. Reported systems include



CH/COH,<sup>9</sup> CH<sub>3</sub>/C<sub>6</sub>H<sub>5</sub>-Si,<sup>16</sup> N,<sup>9a</sup> P,<sup>8,9,17</sup> [H-P]<sup>+</sup>,<sup>18</sup> P=O,<sup>9b,19</sup> As,<sup>9a</sup> As=O,<sup>9b</sup> [CH<sub>3</sub>-Al]<sup>-</sup>,<sup>20</sup> [CH<sub>3</sub>-Ga]<sup>-</sup>,<sup>21</sup> C<sup>-</sup>,<sup>22</sup> Si<sup>-</sup>,<sup>23</sup> Ge<sup>-</sup>, Sn<sup>-</sup>,<sup>24</sup> Pb<sup>-</sup>,<sup>20</sup> and other bridges. Systems similar to the above show a potential for stabilization of high oxidation states of the first-row transition metals,<sup>25</sup> which is of relevance for green catalytic applications.

A more general way to classify the existing C<sub>3</sub>-symmetric scorpionates is by formal charge, which is a combined property of the donor moieties and the bridging atom. Thus, one can differentiate neutral, mono-, di- and trianionic scorpionates (*Chart 2.2*).

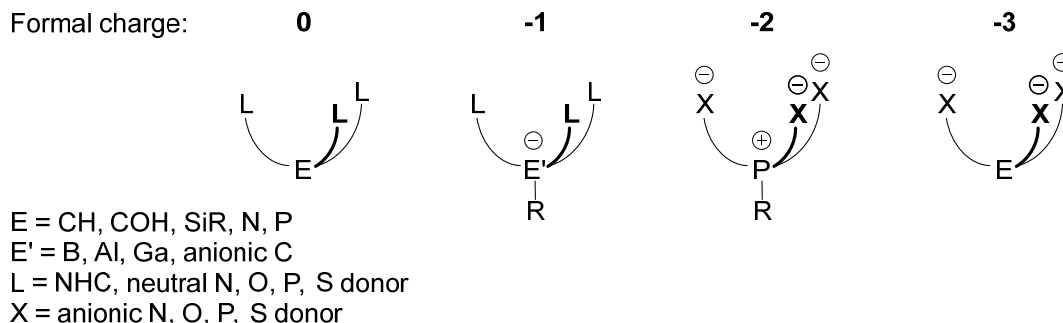


*Chart 2.2.* C<sub>3</sub>-symmetric scorpionates with distinct formal charges.

Whereas there is a plethora of known neutral,<sup>8,9,14,16,17</sup> mono-,<sup>1,10,12,13,20,21,22,24</sup> and trianionic<sup>11</sup> scorpionates, dianionic ones are rare with only one reported precedent<sup>18</sup> (**A** in *Chart 2.3*). However, the published ligand motif was isolated as a LAI<sub>3</sub> complex, which precludes the possibility of a subsequent metal exchange and exploration of its coordination chemistry.

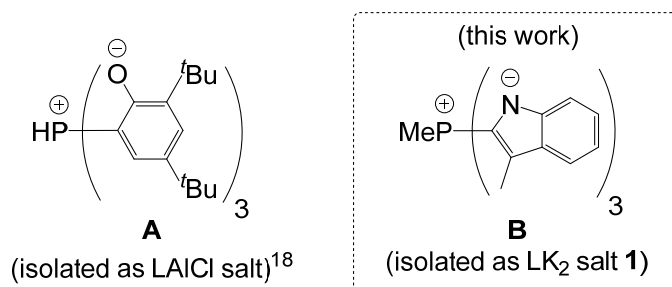


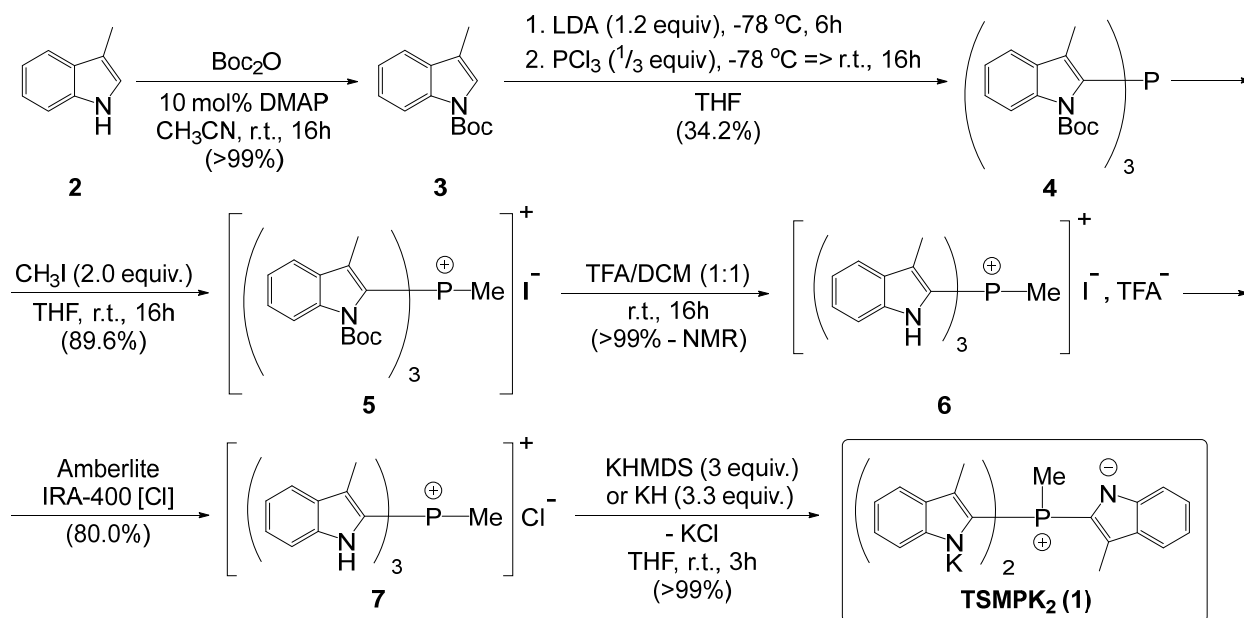
*Chart 2.3.* Dianionic C<sub>3</sub>-symmetric scorpionates.

The focal point of this chapter is filling a gap in the assortment of charged scorpionates available for complexation with a C<sub>3</sub>-symmetric dianionic system **B** (*Chart 2.3*). Herein, we present the synthesis of its dipotassium salt **1**. Taking advantage of the fact that potassium cations are easily exchangeable for other metal ions, we further delve into its coordination chemistry with Cu(I), Fe(II) and Ni(II) salts. Finally, we study the redox properties of the resulting complexes, both electrochemically and chemically.

## 2.2 Results and discussion

### 2.2.1 Ligand synthesis

The dipotassium salt of tris-(2-skatyl)methylphosphonium (**1**), further abbreviated as TSM<sub>2</sub>PK<sub>2</sub>, was synthesized following the synthetic route depicted in *Scheme 2.1*. In the first step, skatole (**2**) was treated with di-*tert*-butyl dicarbonate (Boc<sub>2</sub>O) in the presence of 4-dimethylaminopyridine (DMAP) to yield the corresponding *N*-Boc derivative (**3**). The second position of the indole ring was subsequently lithiated with lithium diisopropylamide (LDA) using *N*-Boc as a directing group. Without isolation, the lithium salt was quenched with a third of an equivalent of PCl<sub>3</sub> to yield tris-2-(*N*-Boc-skatyl)phosphine (**4**). The phosphine was then methylated by treatment with an excess (2.0 equiv.) of methyl iodide to form the corresponding methylphosphonium iodide (**5**). Attempted methylation with an equimolar amount of methyl iodide instead resulted into incomplete methylation and partial deprotection of *N*-Boc-skatole subunits.



*Scheme 2.1.* Synthesis of TSM<sub>2</sub>PK<sub>2</sub> salt **1**. Unless otherwise stated, parentheses underneath reaction arrows indicate isolated yields.

It is worth pointing out that tris-2-(*N*-Boc-skatyl)methylphosphonium iodide (**5**) exists in DCM-*d*<sub>2</sub> solution as a *ca.* 1.00:0.15 mixture of interexchanging tris-*exo* (**5a**) and bis-*exo*-mono-*endo* (**5b**) rotamers (top left corner in *Figure 2.1*).<sup>a</sup> To elaborate, the <sup>31</sup>P NMR

<sup>a</sup> Due to a lot of steric hindrance and, thus, rather high rotational barriers around C<sup>Ar</sup>-P bonds in **5**, there are two possible configurations for each derivatized indole ring: with a Boc group pointing towards and away from a phosphonium methyl. Accordingly, we choose to call the first configuration “*exo*-“, whereas the second one is “*endo*-“.

spectrum of **5** (Figure 2.1, right panel) shows two peaks in a ratio of 1.00 to 0.15: the former being a sharp quartet (**A**), as expected for *J*-coupling with a methyl group, while the latter is a broad singlet (**B**). <sup>1</sup>H-<sup>31</sup>P ASAPHMQC spectra (Appendix A1) show a correlation between these two peaks and two <sup>1</sup>H doublets between 2.7 and 2.9 ppm (CH<sub>3</sub><sup>P</sup><sub>A</sub> and CH<sub>3</sub><sup>P</sup><sub>B</sub> in Figure 2.1, left panel), which have a similar ratio of integral intensities (1.04:0.15). We assign these doublets to methyl phosphonium groups of the individual rotamers, CH<sub>3</sub><sup>P</sup><sub>A</sub> and CH<sub>3</sub><sup>P</sup><sub>B</sub>. Aside from that, <sup>1</sup>H NMR spectrum shows an intense set of four aromatic signals (H<sup>Ar</sup><sub>A</sub>) and two singlets (CH<sub>3</sub><sup>Ar</sup><sub>A</sub> and CH<sub>3</sub><sup>Boc</sup><sub>A</sub>) which are consistent with a C<sub>3</sub>-symmetric topology of **5a**. NOESY spectrum (Figure 2.2, left panel) indicates spatial proximity of CH<sub>3</sub><sup>P</sup><sub>A</sub> and CH<sub>3</sub><sup>Boc</sup><sub>A</sub> protons, therefore signifying a tris-*exo* rotamer **5a**. Another set of <sup>1</sup>H peaks in Figure 2.2 – H<sup>Ar</sup><sub>B</sub>, CH<sub>3</sub><sup>Ar</sup><sub>B</sub> and CH<sub>3</sub><sup>Boc</sup><sub>B</sub> – indicates an asymmetric rotamer **5b**, which is in chemical exchange with **5a** as shown by NOESY spectra (Figure 2.2, right panel). As for its configuration, the NOESY cross-peaks do not have sufficient intensity for us to extract geometric information. However, variable-temperature NMR studies show that population of **5b** decreases with temperature, *viz.*: the ratio of **5a**:**5b** at 25 °C is *ca.* 1.00:0.15 whereas at -40 °C it is 1.00:0.07. This means that rotamer **5b** is more energetic, likely due to steric repulsion. Therefore, from general considerations, we assign **5b** to have a bis-*exo*-mono-*endo* configuration since this is the next least strained one. The presence of two interconverting rotamers for phosphonium salts is not unprecedented and was previously observed by NMR.<sup>26</sup>

Complete deprotection of the isolated methylphosphonium iodide **5** can be achieved in dichloromethane/trifluoroacetic acid (TFA) 1:1 mixture. The product, **6**, was isolated as an amorphous yellow solid with significant traces of TFA, according to <sup>13</sup>C and <sup>19</sup>F NMR. In order to purify the product, numerous recrystallization attempts were made. Unfortunately, none yielded a well-defined crystalline phase, possibly due to the presence of a mixture of counterions with different symmetry (iodide and trifluoroacetate). Hence, we undertook ion exchange using the chloride form of the anion exchange resin Amberlite® IRA-400, affording a white crystalline solid of tris-(2-skatyl)methylphosphonium chloride (**7**). Attempts of cleaner deprotection of **5** using EtOAc/1M HCl mixture at room temperature gave no conversion. Oppositely, refluxing in acetonitrile (b.p. 82 °C) or butyronitrile (b.p. 117 °C) led to complete deprotection within under 4 h accompanied by formation of unidentified by-products.

Deprotonation of tris-indole **7** with either KHMDS or KH gives the TSMPC<sub>2</sub> salt (**1**). A highly pure material (>99% according to NMR) was isolated in a crystalline form from acetonitrile/diethyl ether. X-ray diffraction of the crystals confirmed the expected molecular structure with a K:P ratio of 2:1 (Figure 2.3). The K<sup>+</sup> cations are involved in an extensive network of cation-N and cation-π interactions (η<sup>1</sup> to η<sup>6</sup>). The K–N distances

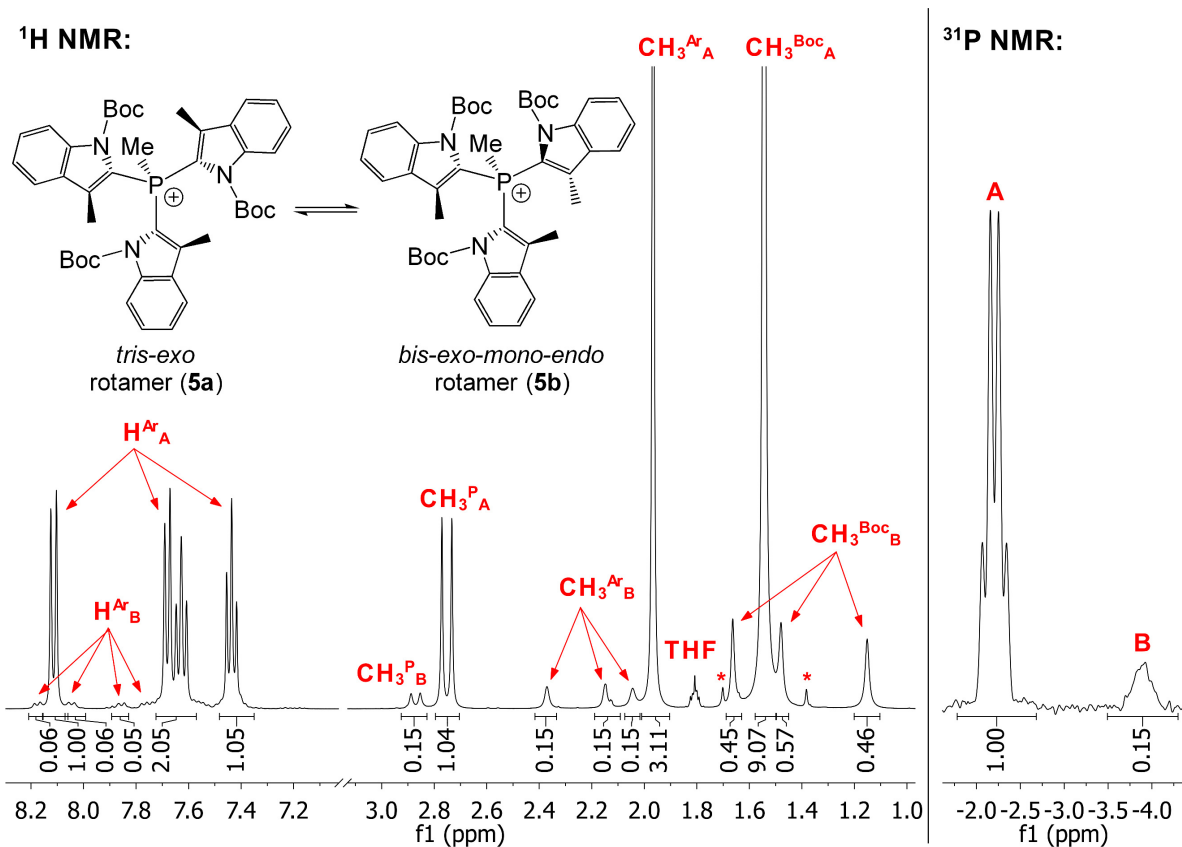


Figure 2.1.  $^1\text{H}$  (400 MHz) and  $^{31}\text{P}$  NMR (162 MHz) spectra of **5** measured in  $\text{DCM-d}_2$ . Integral intensities are extracted using MestReNova<sup>27</sup> peak deconvolution tools. Asterisks indicate  $\text{CH}_3^{\text{Boc}_A}$  peak satellites.

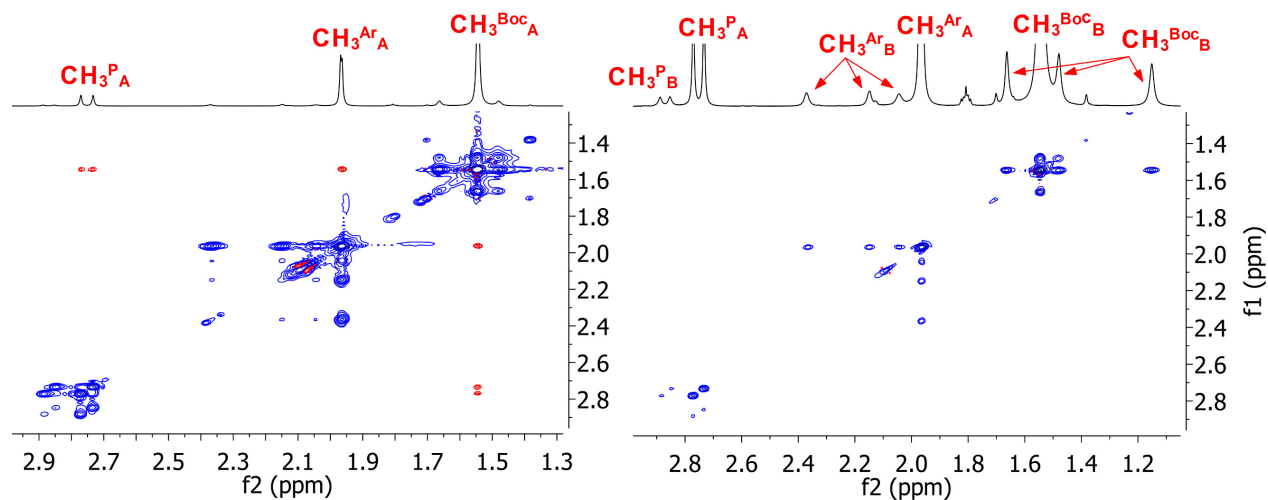


Figure 2.2. NOESY spectrum of **5** in  $\text{DCM-d}_2$  shown at two different levels of intensity. Blue cross-peaks indicate chemical exchange, red cross-peaks show NOE.

vary between 2.723(4) and 3.425(4) Å, and the K–C distances between 2.995(4) and 3.510(4) Å. With such a large variation of distances it is not possible to derive a clearly defined coordination number. Overall, the K coordination leads to the formation of one-dimensional chains in the [110] direction, which are stacked upon each other in  $c$ -direction. This stacking is interrupted by the inclusion of acetonitrile solvent molecules between every second layer (see Section 2.5.4 for more detail).

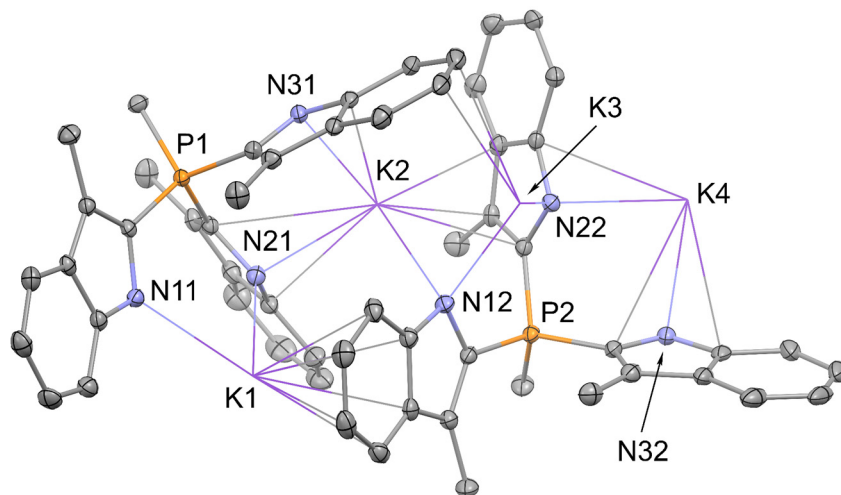
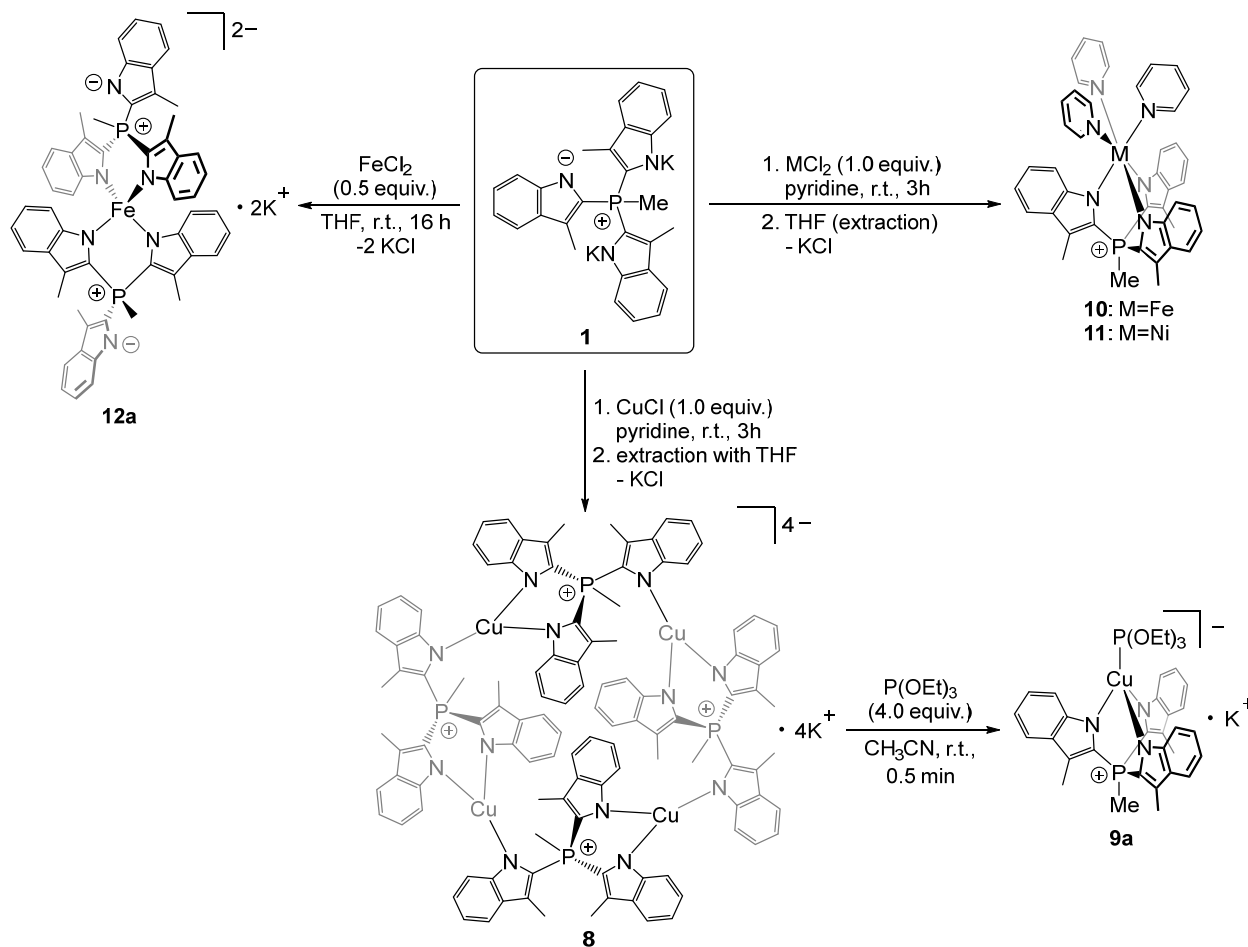


Figure 2.3. Asymmetric unit of the TSMPK<sub>2</sub> (**1**) crystal. Thermal ellipsoids are drawn at the 30% probability level. Potassium atoms are shown in a wireframe style. Hydrogen atoms and acetonitrile solvent molecules are omitted for clarity. Potassium atoms are shown in a wireframe style.

The existence of a free alkaline trianionic-monocationic phosphonium salt is, to our knowledge, unprecedented. It is known from the literature that quaternary phosphonium salts are generally incompatible with basic counterions and convert either into ylides,<sup>28</sup> phosphoranes<sup>29,30</sup> or form charge-transfer complexes followed by complex decomposition manifolds.<sup>31</sup> The exceptions, however, feature electronically stabilized bulky anions (e.g. diphenylamide<sup>32</sup> and 2,4,6-trimethylphenolate<sup>33</sup>). We speculate that the stability of **1** is due to the above reasons as well: anionic indolide nitrogens lose a lot of their nucleophilicity due to being involved into an aromatic  $\pi$ -system, and the phosphonium center is too encumbered to accommodate the fourth indolide in its vicinity. Additionally, the latter will be experiencing electrostatic repulsion from other anionic indolides already present in a molecule.

### 2.2.2 Coordination chemistry of TSMP<sup>2-</sup>

In order to study ligation behavior of a novel TSMP<sup>2-</sup> platform, we undertook a series of metal exchange reactions with salt **1**. It shows rich coordination chemistry with a number of first-row transition metal salts (Scheme 2.2).



Scheme 2.2. Coordination behavior of TSMP<sup>2-</sup> ligand platform.

Thus, equimolar amounts of TSMPK<sub>2</sub> salt **1** and cuprous chloride in pyridine led to an orange-red solution. Upon freeing from solvent *in vacuo* and extraction with THF, NMR spectroscopy in acetonitrile-*d*<sub>3</sub> reveals one predominant species, albeit an oligomer. To elaborate, the <sup>31</sup>P spectrum (Figure 2.4) shows a single quartet consistent with <sup>2</sup>J<sub>P,H</sub> coupling with a methyl group. In <sup>1</sup>H spectrum (Figure 2.4), there are two singlets in a 2:1 ratio corresponding to aromatic methyl groups CH<sub>3</sub><sup>Ar<sub>A</sub></sup> and CH<sub>3</sub><sup>Ar<sub>B</sub></sup>. Moreover, multiplets in the aromatic area are present in the same ratio and, according to magnitude gCOSY (Figure 2.5), constitute two distinct spin systems. This implies 2:1 inequivalence of indolide units in the complex. A NOESY spectrum (Figure 2.5) shows a correlation<sup>a</sup> between the phosphonium methyl group CH<sub>3</sub><sup>P</sup> and two aromatic CH<sub>3</sub><sup>Ar<sub>A</sub></sup> but not CH<sub>3</sub><sup>Ar<sub>B</sub></sup>, from which it follows that CH<sub>3</sub><sup>Ar<sub>B</sub></sup> is pointing away from the phosphonium methyl group. Lastly, H<sup>4</sup><sub>A</sub> and H<sup>7</sup><sub>A</sub> have comparable correlation intensities with CH<sub>3</sub><sup>Ar<sub>A</sub></sup>. Since NOE rapidly decays with distance, and H<sup>7</sup><sub>A</sub> is clearly further away from CH<sub>3</sub><sup>Ar<sub>A</sub></sup> than H<sup>4</sup><sub>A</sub>, it can only be the case if there is an equivalent methyl

<sup>a</sup> This and further NOESY correlations are mapped out in a structural formula in Figure 2.4.

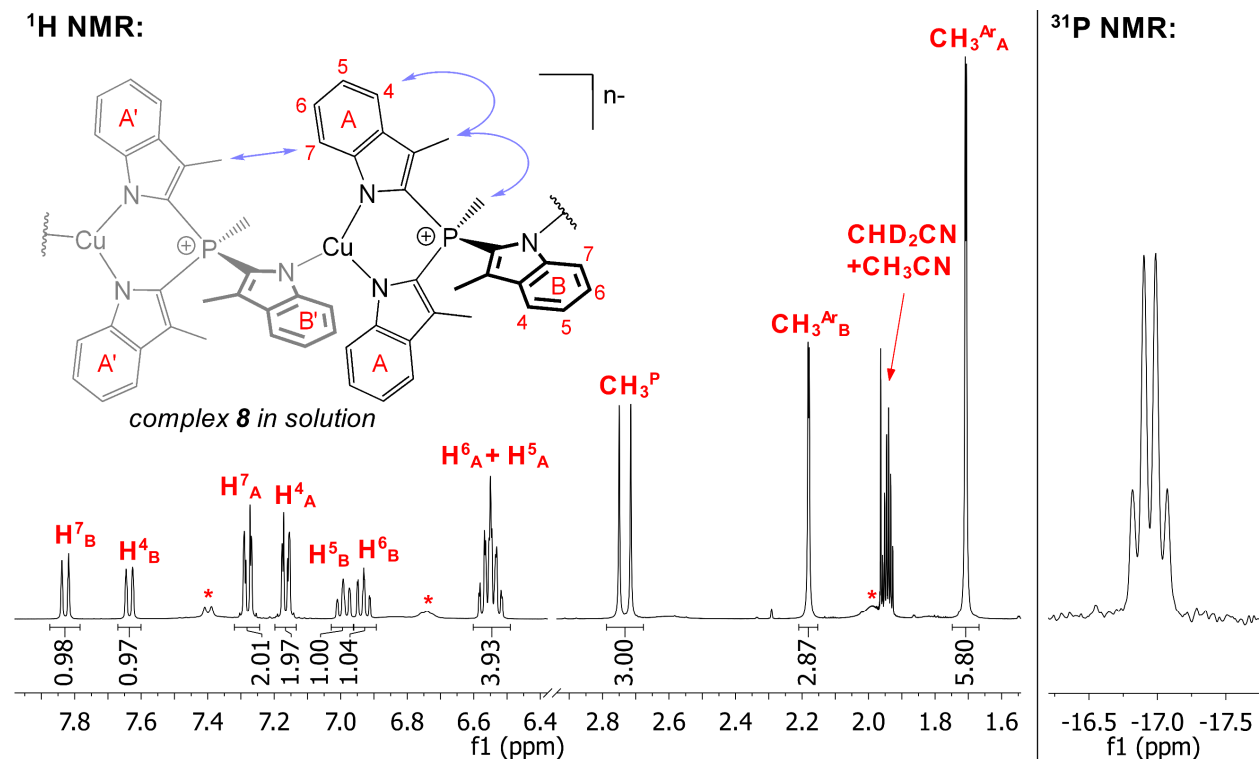


Figure 2.4. <sup>1</sup>H (400 MHz) and <sup>31</sup>P NMR (162 MHz) spectra of **8** in acetonitrile-*d*<sub>3</sub>. Lilac arrows in a structural formula indicate diagnostic NOESY correlations discussed in the text. Only one of two equivalent CH<sub>3</sub><sup>P</sup>–CH<sub>3</sub><sup>Ar</sup><sub>A</sub> correlations is shown.

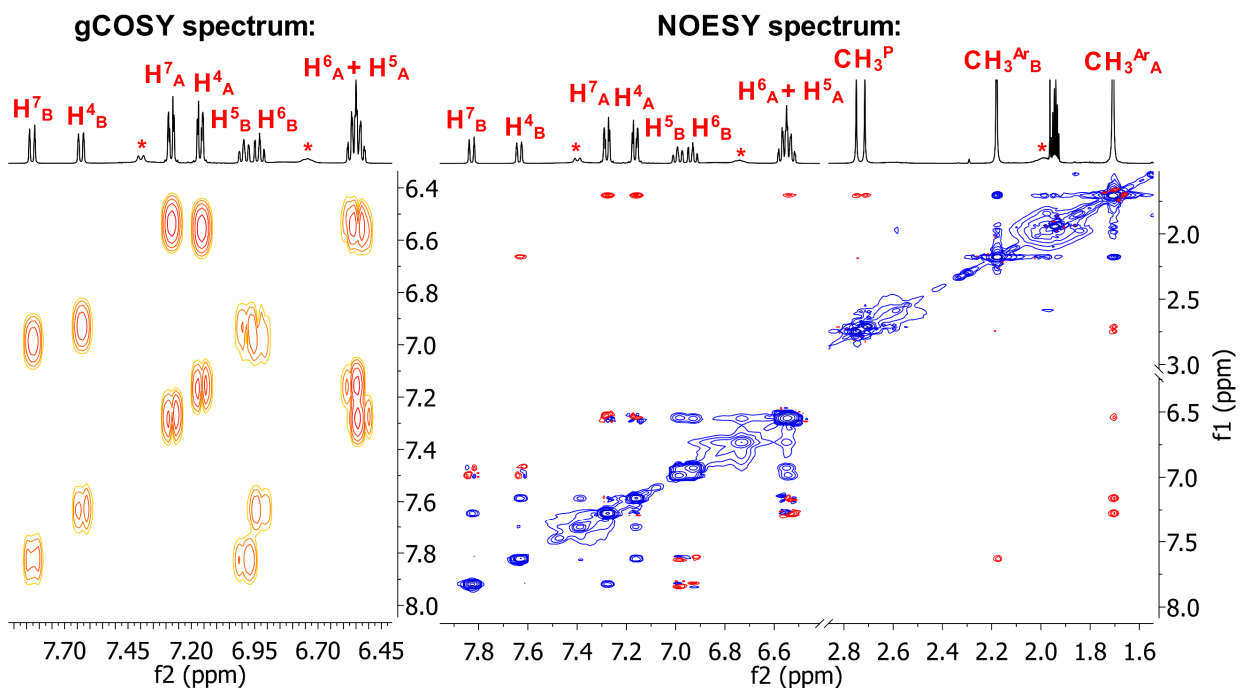


Figure 2.5. Magnitude gCOSY and NOESY NMR spectra of **8** in acetonitrile-*d*<sub>3</sub>. Blue-phase cross-peaks indicate chemical exchange, red-phase cross-peaks show NOE, mixed-phase cross-peaks are due to unsuppressed COSY correlations.

group in the vicinity of  $H^7_A$ , i.e. if the complex is oligomerized. Based on this reasoning, in *Figure 2.4* we suggest an oligomeric structure of the complex **8** in solution.

It is worth mentioning that the NOESY spectrum in *Figure 2.5* also features multiple exchange peaks between indolide groups **A** and **B**, which means that these positions exchange on the mixing timescale. This could either be due to reversible dissociation of the oligomer to smaller units or to an intramolecular exchange process. Furthermore, the asterisk-labeled aromatic peaks in the spectrum show exchange with some of the assigned signals, which suggests that they may belong to a minor unassigned form of **8** in solution. However, the number and intensity of the peaks do not allow to deduce molecular connectivity.

While the degree of oligomerization in solution is unclear, our NMR assignment is consistent with the X-ray diffraction of a crystal grown from pyridine/hexane. Complex **8** crystallizes as a cyclic  $\{[(\text{TSMP})\text{Cu}]\text{K}\}_4$  tetramer (*Figure 2.6*) with distorted trigonal planar  $\text{CuN}_3$  centers and  $\text{Cu-N}$  distances ranging within 1.926(3)-2.007(3)Å.  $\text{TSMP}^{2-}$  ligand adopts a  $\mu^2:\kappa^2:\kappa^1$  coordination mode, which has been previously observed for other  $\text{Cu(I)}$  complexes with scorpionate ligands.<sup>34</sup> A unit cell contains two independent tetrameric molecules, both being located on an exact, crystallographic inversion centers.  $\text{K}^+$  ions in the proximity of indolide moieties show clear cation- $\pi$  interactions. Their environment is saturated by coordinated pyridine molecules. The two independent  $\{[(\text{TSMP})\text{Cu}]\text{K}\}_4$  molecules differ in the number of  $\text{K}^+$ -coordinated pyridines: 14 pyridine molecules for the first tetramer, and 12 for the second. There are also significant differences between the two independent molecules in the coordination mode of  $\text{K}^+$  to the indolide moieties (see X-ray crystallographic section for more detail). The content of the crystallographic unit cell is completed by six non-coordinated pyridine molecules.

In an attempt to modulate the coordination environment of the  $\text{Cu(I)}$  center and get a well-defined mononuclear complex, we introduced triphenylphosphite,  $\text{P}(\text{OEt})_3$ , which is a monodentate, moderately  $\sigma$ -donating and neutral ligand. The latter two in order to reduce charge repulsion with the metal and the rest of negatively charged coordination sphere. Upon addition of one equivalent per equivalent of copper, the NMR spectrum immediately simplifies to a single aromatic methyl peak, four aromatic multiplets, a methylphosphonium doublet and an ethyl group of triethylphosphite (*Appendix A2*), signifying the formation of the  $\text{C}_3$ -symmetric structure  $[(\text{TSMP})\text{CuP}(\text{OEt})_3]\text{K}$  (**9a**). Furthermore, NOE spectra (*Appendix A3*) do not show a correlation analogous to  $H^4_A-H^7_A$  in **8** (*Figures 2.4* and *2.5*), which points at monomeric structure of **9a** in solution. This assignment is, again, consistent with X-ray diffractometry of the 18-crown-6 adduct **9b** crystallized from acetonitrile/benzene/ether (*Figure 2.6*). With the exception of peaks from



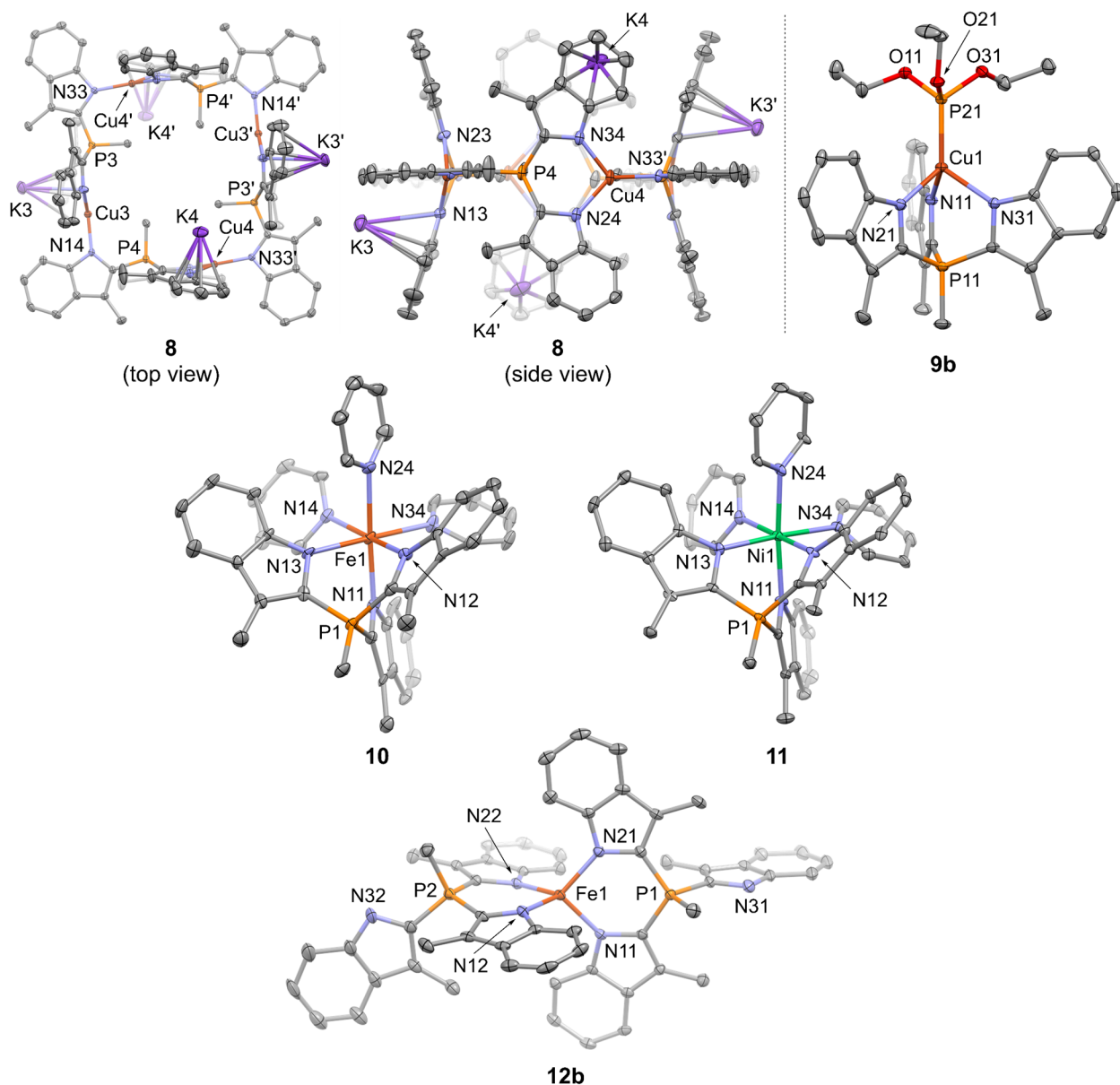


*Figure 2.6.* Molecular structure of **8**, **9b**, **10**, **11** and **12b** according to X-Ray diffraction. Thermal ellipsoids are drawn at 30% probability level. Hydrogen atoms, some counterions and non-coordinated solvent molecules are omitted for clarity. The asymmetric unit of **8** contains two independent molecular fragments that make up two independent molecules; only one full molecule is shown. Symmetry code: *ii*: 1-x, 1-y, 1-z. The asymmetric units of **10** and **11** contains two independent molecules, only one of which is shown. Selected bond distances and angles are provided in the X-ray crystallographic section.

18-crown-6, solution NMR spectra of **9a** and **9b** are identical. The complex features a distorted tetrahedral CuN<sub>3</sub>P center (angle variance<sup>35</sup> of 244.58 deg<sup>2</sup>) with N<sup>^</sup>Cu<sup>^</sup>N angles varying from 92.38(8) to 95.06(7)°. The Cu-P bond length is 2.1201(2) Å, as expected for Cu(I),<sup>36</sup> and Cu-N distances lie within 2.0622(19)-2.0759(19) Å, similarly

to those in tetranuclear **8**. The [(TSMP)CuP(OEt)<sub>3</sub>]<sup>-</sup> anion has approximate C<sub>3</sub> symmetry with the P(OEt)<sub>3</sub> ligand in approximately staggered conformation with respect to the scorpionate [O<sup>^</sup>P<sup>^</sup>Cu<sup>^</sup>N 41.79(11)°]. The geometry of **9b** closely resembles that of the neutral tris(pyrazolyl)methanide analogue {[C(3,5-Me<sub>2</sub>pz)<sub>3</sub>]CuP(OMe)<sub>3</sub>}, which features Cu–N bonds in the range 2.047(2)–2.102(2) Å and a Cu–P bond length of 2.122(2) Å.<sup>36b</sup>

Reactions of equimolar amounts of TSMPK<sub>2</sub> (**1**) with either FeCl<sub>2</sub> or NiCl<sub>2</sub>·dme adduct in pyridine give, correspondingly, bright-yellow or olive-brown solutions. Subsequent evaporation of solvent and extraction with THF yield yellow (TSMP)Fe(Py)<sub>3</sub> (**10**) and green (TSMP)Ni(Py)<sub>3</sub> (**11**) complexes. All attempts to form related complexes with CoCl<sub>2</sub> under the same conditions led to intractable mixtures of products.

According to <sup>1</sup>H NMR of **10** and **11** in pyridine-*d*<sub>5</sub>, these compounds are paramagnetic, and the number of lines with their integral intensity correspond to three-fold symmetric metallabicyclo[2.2.2]octane topology. Remarkably, in both spectra, the spacing between the pyridine peaks deviates from the normal values by up to 0.3 ppm with α-pyridine protons being most affected. This difference is likely due to a hyperfine shift induced in pyridine protons upon labile coordination to the metal centers. Indeed, X-ray diffraction of crystals grown from pyridine/hexane reveals isostructural octahedral complexes that feature one TSMP<sup>2-</sup> and three pyridine ligands (**10** and **11**, respectively, in *Figure 2.6*). Importantly, the FeN<sub>6</sub> core in **10** has much shorter bonds with TSMP<sup>2-</sup> nitrogens than pyridines, *viz.* 2.158(6)–2.201(6) Å *vs.* 2.261(7)–2.351(6) Å. In fact, the latter are even longer in average than Fe–N distances in [FePy<sub>6</sub>]<sup>2-</sup> solvate: 2.22(3)–2.29(3) Å.<sup>37</sup> This is consistent with rather weak bonding and the observed lability of pyridine ligands in solution. The NiN<sub>6</sub> core in **11** shows a similar situation: the Ni–N distances for the TSMP<sup>2-</sup> nitrogen atoms are within 2.115(7)–2.148(7) Å, whereas the corresponding values for pyridines are 2.163(8)–2.241(8) Å. The long metal-ligand distances in **10** and **11** indicate high-spin electronic states.<sup>38</sup> This assignment is also supported by the effective solution magnetic moments measured by Evans method in pyridine-*d*<sub>5</sub>. Thus, it is 5.19 μ<sub>B</sub> for Fe(II) complex **10** and 2.82 μ<sub>B</sub> for Ni(II) complex **11**, whereas the spin-only expectation values for, respectively, *S* = 2 and *S* = 1 metal centers are 4.90 and 2.82 μ<sub>B</sub>.

Interestingly, replacement of three pyridine ligands in **10** with another equivalent of TSMP<sup>2-</sup> gives a highly air-sensitive bright-yellow tetracoordinate complex [(TSMP)<sub>2</sub>Fe]K<sub>2</sub>, **12a** (*Scheme 2.2*). The complex can be crystallized from acetonitrile/toluene/ether as a tetrakis(benzo-15-crown-5) adduct **12b** (*Figure 2.6*). The NMR spectra of **12a** and **12b** in solution are identical with the exception of benzo-15-crown-5 peaks. Compound **12b** features a pseudo-tetrahedral FeN<sub>4</sub> core where each TSMP<sup>2-</sup>

ligand coordinates with two arms while the third one remains uncoordinated ( $\kappa^2$  mode). The N<sup>^</sup>Fe<sup>^</sup>N angles vary from 96.35(13) to 119.68(13)°. The angle variance<sup>35</sup> of 111.29 deg<sup>2</sup> is, consequently, rather large. The distortion is mainly caused by the chelate effect: the dihedral angle between the N11-Fe1-N21 and the N12-Fe1-N22 planes is 85.2(2)° and deviates only slightly from perfect 90°. The Fe–N distances of 2.017(3)-2.028(3) Å indicate a high-spin electronic state of the Fe(II) center. A comparison with structurally related high-spin complexes<sup>39a-h</sup> show similar bonding distances of >2.0Å. Solution effective magnetic moment measurement by Evans method in pyridine-*d*<sub>5</sub> gives 5.17  $\mu_B$ , which is close to the expectation spin-only value of 4.90  $\mu_B$  for an *S* = 2 metal center. The tetrahedral geometry of **12a** contrasts with the common octahedral geometry of neutral and dicationic pyrazolate-based bis(scorpionate) Fe(II) complexes<sup>39i-1</sup> and of the tris-pyridine complex **11**. We speculate that the reduction in coordination number is due to electrostatic repulsion of the negatively-charged indolides as well as their weaker  $\pi$ -accepting properties as compared to pyridine or pyrazolate ligands.

### 2.2.3 Redox behavior of the metal complexes

In order to assess the redox properties of the synthesized complexes, we turned to cyclic voltammetry in 0.1 M <sup>n</sup>Bu<sub>4</sub>NPF<sub>6</sub> acetonitrile electrolyte. Compounds **8**, **9b** and **11** show a set of irreversible features accompanied by precipitation on the working electrode, regardless of the scan window and direction (*Appendix A4*). Chemical oxidation with 1 equiv. of ferrocenium tetrafluoroborate in both acetonitrile and pyridine gives either insoluble or intractable products or mixtures thereof, likewise iodosobenzene with or without scandium triflate as an oxo-species stabilizer. The cyclic voltammogram of the Fe(II) complex **10**, however, shows a quasi-reversible event at -119 mV with respect to the Fc<sup>+</sup>/Fc redox couple (*Figure 2.7*). The quasi-reversibility is indicated by a linear dependence of peak current *vs.* a square root of the scan rate as well as peak-to-peak separation of >57 mV that increases at higher scan rates. Therefore, we tentatively assign events **A** and **C** to a formal Fe(II)/Fe(III) redox couple. Nevertheless, attempts toward chemical oxidation with 1 equiv. of ferrocenium tetrafluoroborate gave, again, an intractable mixture of products according to NMR studies. The same result was obtained upon oxidation tests with iodosobenzene with or without scandium triflate.

Cyclic voltammetry of [(TSMF)<sub>2</sub>Fe][K(benzo-15-crown-5)<sub>2</sub>]<sub>2</sub> (**12b**) shows a rather complex pattern, giving stable one- and two-electron oxidation products. The electrochemical behavior of **12b** as well as chemical oxidation thereof are the subject of the next chapter of this thesis.

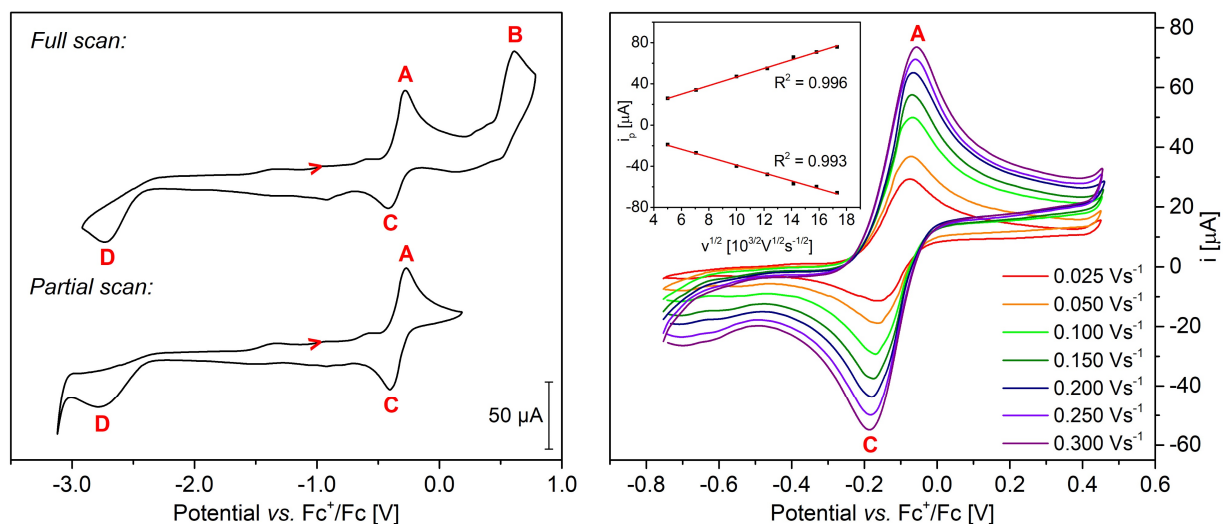


Figure 2.7. Cyclic voltammogram of compound **10** (ca. 8 mM solution) in 0.1 M  $n\text{-Bu}_4\text{NPF}_6$  acetonitrile electrolyte. Potentials are referenced with respect to  $\text{Fc}^+/\text{Fc}$  redox couple. *Left panel*: overview scans at the rate of 100 mV/s (open-circuit potential: -970 mV). *Right panel*: a quasi-reversible redox pair **A-C** centered at  $E_{1/2} = -119$  mV; the insert shows the linear dependence of the peak current *vs.* square root of the scan rate.

## 2.3 Conclusions and outlook

A dianionic  $C_3$ -symmetric tris-skatylmethylphosphonium ( $\text{TSMP}^{2-}$ ) ligand platform can be synthesized in the form of dipotassium salt  $\text{TSMPK}_2$  (**1**). This system is the first dianionic homoscorpionate capable of metal exchange and fills a gap in the assortment of charged scorpionates. Despite a possibility of recombination between negatively charged indolides and a positively charged phosphonium atom, salt **1** is stable both in the solid state and solution, which is likely due to a combination of electronic and steric factors.

The potassium cations in  $\text{TSMPK}_2$  (**1**) are exchangeable for other metals, demonstrating the versatility of  $\text{TSMP}^{2-}$  as a ligand for transition metals. The expected scorpionate  $\kappa^3$  binding mode is observed in octahedral, high spin complexes  $(\text{TSMP})\text{M}(\text{Py})_3$  (**10**:  $\text{M}=\text{Fe}$ ; **11**:  $\text{M}=\text{Ni}$ ) as well as in the tetrahedral complex  $[(\text{TSMP})\text{CuP}(\text{OEt})_3]^-$  (**9**). In addition, the bridging  $\mu^2:\kappa^2:\kappa^1$  mode is preferred with Cu(I) in the absence of a co-ligand, affording the tetrameric complex  $\{[(\text{TSMP})\text{Cu}]\text{K}\}_4$  (**8**). Finally, the bidentate  $\kappa^2$  mode is observed in the tetracoordinate 2:1 Fe(II) complex  $[(\text{TSMP})_2\text{Fe}]^{2-}$  (**12**), which displays a high-spin ground state.

The redox properties of the above metal complexes were probed both electrochemically (cyclic voltammetry, CV) and chemically (oxidation with 1 equiv. of  $\text{Fc}^+\text{BF}_4^-$ ). Cu(I)

complexes **8** and **9** and Ni(II) complex **11** show no electrochemically (quasi-)reversible behaviour. Chemical oxidation leads to insoluble or ill-defined products. The CV of mono-TSMP Fe(II) complex **10** shows several redox events, two of which are a quasi-reversible pair. Nevertheless, chemical oxidation leads, again, to an intractable mixture of products. Similarly, the CV of bis-TSMP Fe(II) complex **12** shows several events with a quasi-reversible pair. Gratifyingly, in this case chemical oxidation affords a well-defined Fe(III) complex that is further discussed in the next chapter.

The rich coordination chemistry of the dianionic homoscorpionate ligand invites further investigations. Amongst other, it has a potential to electronically stabilize high-valent metal states due to its electron-rich character, but additional derivatization might be required for kinetic stabilization. Studies in these directions are currently ongoing in our laboratories.

#### **2.4 Author contributions and acknowledgements**

Serhii Tretiakov and Dr. Marc-Etienne Moret conceived the project. Serhii Tretiakov performed the major part of the synthetic work, while Yuri Damen prepared compounds **8** and **9**. Serhii Tretiakov carried out all spectral measurements followed by interpretation thereof, except for ESI-TOF-MS spectrometry performed by Dr. Thomas Ran, for which he is greatly acknowledged. Dr. Martin Lutz conducted single crystal X-ray diffraction experiments along with solving the structures. Serhii Tretiakov wrote the chapter based on the corresponding publication<sup>55</sup> and with input from Dr. Marc-Etienne Moret. The chapter was read and approved in the final version by all the authors.

## 2.5 Experimental methods

### 2.5.1 General remarks

All reactions involving air-sensitive compounds were conducted under a nitrogen atmosphere by using standard glovebox or Schlenk techniques.

Acetonitrile, diethyl ether and *n*-hexane were dried with an MBRAUN MB SPS-79 system. Acetonitrile was additionally dried by passing through a column of activated alumina after being kept over ca. 5 vol.% of 3Å molecular sieves over 48 h. THF and dioxane were distilled from benzophenone/Na. Pyridine and DCM were distilled from CaH<sub>2</sub>. Other solvents were used as supplied. Dried solvents were degassed by sparging with dry nitrogen for 30 min and stored in a glovebox under nitrogen atmosphere and over molecular sieves, except for acetonitrile which was stored without the sieves. THF-*d*<sub>8</sub> was purchased from ABCR, other deuterated solvents were acquired from Cambridge Isotope Laboratories, Inc. Chloroform-*d* and methylene chloride-*d*<sub>2</sub> were used as supplied, all other deuterated solvents were dried as indicated above for their proteo-analogues. Dried deuterated solvents were degassed by four freeze-pump-thaw cycles and stored in a glovebox over molecular sieves, except for acetonitrile-*d*<sub>3</sub> which was stored without the sieves. Phosphorus trichloride, trifluoroacetic acid and methyl iodide were purchased from Acros. All other chemicals were purchased from Sigma-Aldrich. Potassium hydride was supplied as a 30 wt.% suspension in mineral oil and was washed with dry and degassed *n*-hexane prior to use. FeCl<sub>2</sub> and CuCl were purchased in an anhydrous form. All commercially obtained chemicals were used as received, except for 18-crown-6, which was dried according to the literature procedure.<sup>40</sup>

Unless stated otherwise, all NMR measurements were performed at 298 K on a Varian VNMRs400 or Varian MRF400 spectrometer, chemical shifts are reported relative to TMS with the residual solvent signal as internal standard.<sup>41</sup> In case of paramagnetic Fe- and Ni-complexes **10** and **11**, TMS was used as an internal standard. All NMR experiments involving air-sensitive compounds were conducted in J. Young NMR tubes under a nitrogen atmosphere. Peak multiplicity was quoted as s (singlet), d (doublet), t (triplet) and so on. In cases of unresolved couplings that strongly affect the line shape of individual components of an otherwise well-defined multiplet, the apparent multiplicity was quoted as 's' ('singlet'), 'd' ('doublet'), 't' ('triplet') and so on.

Effective magnetic moments in were obtained by the Evans method<sup>42</sup> using J. Young NMR tubes with a coaxial capillary insert as a reference. The latter was filled with a deuterated solvent with ~1% of TMS. The outer space contained the solution of the paramagnetic complex (5-10 mg/ml) in a deuterated solvent with the same concentration of TMS. Molar magnetic susceptibility was calculated from the difference between the chemical shifts of TMS (or proteo-solvent) signals in the capillary and the outer solution ( $\Delta\delta$  in Hz) using the following equation:

$$\chi_M = \frac{\Delta\delta M}{\nu_0 S_f c} - \chi_M^{dia}, \quad \text{Eq. 2.1}$$

where *M* – molecular weight of the studied compound (g/mol);  $\nu_0$  – frequency of the spectrometer (Hz); *S<sub>f</sub>* – shape factor of the magnet ( $4\pi/3$ ); *c* – concentration of the paramagnetic complex (mg/ml);  $\chi_M^{dia}$  – molar diamagnetic contribution to the paramagnetic susceptibility calculated using Pascal's constants.<sup>43</sup> For variable-temperature measurements, the concentration *c* was adjusted so to take into account volumetric solvent expansion/contraction.

The effective magnetic moment was calculated as follows:

$$\mu_{eff} = \sqrt{8\chi_M T}, \quad \text{Eq. 2.2}$$

where T is temperature.

IR spectra were recorded on a Perkin-Elmer Spectrum Two FT-IR spectrometer. The bands were classified by an absorption intensity as: very weak (VW; 0-10% of the most intense absorption in the spectrum), weak (W; 10-30%), medium (M; 30-60%), strong (S; 60-90%), very strong (VS; 90-100%).

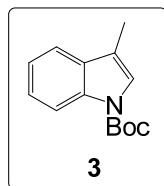
UV-Vis spectra were measured on a PerkinElmer Lambda 35 spectrometer. Cyclic voltammetry (CV) was performed using IVIUM Technologies Vertex Potentiostat/Galvanostat. ESI-MS measurements were performed on a Waters LCT Premier XE KE317 spectrometer. Elemental analysis was conducted by Medac Ltd.

For the sake of brevity, the NMR, IR and UV-Vis spectra of isolated compounds are not shown in this chapter. These can be found in the respective publication.<sup>55</sup>

## 2.5.2 Synthesis and characterization

### 2.5.2.1 Synthesis of TSM<sub>2</sub>PK<sub>2</sub> (1)

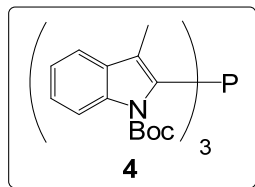
The syntheses of compounds **3**, **5** and **7** were conducted in air. While the synthesis of **4** was done with the exclusion of air and moisture, the work-up was performed at ambient conditions since the product is not air-sensitive. All other procedures, due to both highly reactive starting materials and products, required inert atmosphere and rigorously dried and degassed solvents.



**N-Boc-3-methylindole (3)**. The compound was synthesized using an adapted version of a procedure by Grehn and Ragnarsson.<sup>44</sup>

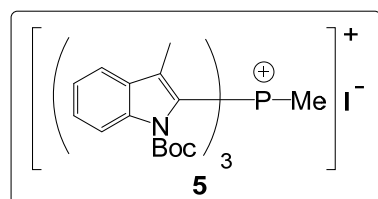
To a stirred solution of 3-methylindole **2** (18.87 g, 143.9 mmol, 1.000 equiv.) in CH<sub>3</sub>CN (170 mL) were added DMAP (1.76 g, 14.4 mmol, 0.100 equiv.) and Boc<sub>2</sub>O (37.68 g, 172.6 mmol, 1.200 equiv.) at room temperature. Evolution of gas commenced, and, after a few minutes, a clear solution formed. The reaction mixture was left to stir for 16 h. After this, all 3-methylindole was consumed (as indicated by TLC), and the reaction was kept at 50 °C for 2 h in order to decompose excess Boc<sub>2</sub>O. Afterwards, the solvent was removed *in vacuo* and replaced with an equal volume of THF. The solution was filtered through a layer of silica, and the solvent was removed *in vacuo* to yield the product as a light-yellow free-flowing oil (98.5%, 32.86 g).

NMR spectra correspond to those published in the literature. <sup>1</sup>H NMR (400 MHz, chloroform-*d*) δ 8.13 (d, *J*<sub>H,H</sub> = 8.0 Hz, 1H, Ar-H), 7.49 (ddd, *J*<sub>H,H</sub> = 7.7, 1.4, 0.7 Hz, 1H, Ar-H), 7.36 (s, 1H, Ar-H), 7.31 (ddd, *J*<sub>H,H</sub> = 8.5, 7.2, 1.4 Hz, 1H, Ar-H), 7.24 (td, *J*<sub>H,H</sub> = 7.6, 1.1 Hz, 1H, Ar-H), 2.26 (s, 3H, Ar-CH<sub>3</sub>), 1.66 (s, 9H, <sup>t</sup>Bu). <sup>13</sup>C NMR (101 MHz, Chloroform-*d*) δ 149.8 (C=O<sup>Boc</sup>), 135.5, 131.5, 124.2, 122.8, 122.3, 118.9, 116.3, 115.1, 83.2 (qC<sup>*t*-Bu</sup>), 28.3 (CH<sub>3</sub><sup>*t*-Bu</sup>), 9.6 (Ar-CH<sub>3</sub>). **ATR-FTIR** (neat)  $\tilde{\nu}$  (cm<sup>-1</sup>): 422 (W), 531 (W), 557(W), 594 (W), 741 (M), 768 (W), 857 (W), 1018 (M), 1084 (S), 1151 (S), 1156 (S), 1224 (M), 1250 (S), 1307 (M), 1347 (S), 1350 (S), 1368 (S), 1388 (S), 1451 (S), 1726 (VS), 2921 (W), 2933 (W), 2978 (W).



**tris-(*N*-Boc-3-methylindol-2-yl)phosphine (4).** A suspension of LDA (18.03 g, 168.3 mmol, 1.100 equiv.) in THF (200 ml) was added to a stirred at  $-78\text{ }^{\circ}\text{C}$  solution of *N*-Boc-3-methylindole **3** (35.39 g, 153.0 mmol, 1.000 equiv.) in THF (300 ml) over 1 h. The reaction was allowed to stir over 4 h at  $-78\text{ }^{\circ}\text{C}$ . Phosphorus trichloride (4.46 ml, 51.0 mmol, 0.330 equiv.) was added to the resulting salmon-pink reaction mixture over 1 h using a syringe pump, resulting in a dark-orange coloration. The reaction mixture was allowed to warm up to room temperature over 16h. Saturated aqueous  $\text{NH}_4\text{Cl}$  (200 ml) was then added in air. The organic layer was separated, dried over  $\text{Na}_2\text{SO}_4$  and passed through a layer of silica. The filtrate was freed from solvent *in vacuo*, and the resulting solid was recrystallized from THF/methanol 1:1 mixture at  $-35\text{ }^{\circ}\text{C}$  overnight. Filtration and drying *in vacuo* yielded colorless cubic crystals (34.2%, 12.58 g).

$^1\text{H NMR}$  (400 MHz, dichloromethane- $d_2$ )  $\delta$  8.14 (d,  $J_{\text{H,H}} = 8.4$  Hz, 1H, Ar-H), 7.45 (d,  $J_{\text{H,H}} = 7.7$  Hz, 1H, Ar-H), 7.31 (ddd,  $J_{\text{H,H}} = 8.4, 7.1, 1.3$  Hz, 1H, Ar-H), 7.22 (ddd,  $J_{\text{H,H}} = 8.0, 7.2, 1.0$  Hz, 1H, Ar-H), 1.87 (d,  $J_{\text{H,P}} = 0.9$  Hz, 3H, Ar- $\text{CH}_3$ ), 1.38 (s, 9H,  $^t\text{Bu}$ ).  $^{13}\text{C NMR}$  (101 MHz, dichloromethane- $d_2$ )  $\delta$  151.0 (d,  $J_{\text{C,P}} = 2.7$  Hz,  $\text{C}=\text{O}^{\text{Boc}}$ ), 137.62, 137.60, 132.2, 131.4, 131.2, 126.11, 126.09, 125.2, 122.8, 118.9, 115.8, 84.8 (q $\text{C}^{\text{t-Bu}}$ ), 28.2 ( $\text{CH}_3^{\text{t-Bu}}$ ), 9.8 (Ar- $\text{CH}_3$ ).  $^{31}\text{P NMR}$  (162 MHz, dichloromethane- $d_2$ )  $\delta$  -48.6. **ATR-FTIR (neat)**  $\tilde{\nu}$  ( $\text{cm}^{-1}$ ): 417 (VW), 461 (VW), 543 (VW), 603 (W), 613 (W), 652 (W), 656 (W), 744 (M), 756 (M), 817 (W), 869 (W), 996 (W), 1099 (S), 1127 (M), 1151 (S), 1158 (M), 1230 (M), 1247 (M), 1293 (M), 1319 (S), 1330 (S), 1354 (S), 1448 (M), 1475 (W), 1721 (VS), 2931 (W), 2971 (W), 2982 (W). **ESI-TOF-MS:** found 722.3336 [ $M+\text{H}$ ] $^+$ , 744.3158 [ $M+\text{Na}$ ] $^+$ , 1465.6705 [ $2M+\text{Na}$ ] $^+$  (calcd. 722.3359 [ $M+\text{H}$ ] $^+$ , 744.3179 [ $M+\text{Na}$ ] $^+$ , 1465.6459 [ $2M+\text{Na}$ ] $^+$ ).



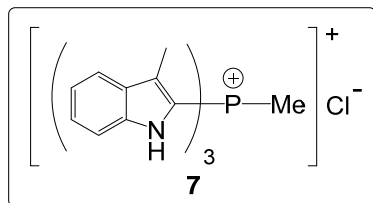
**tris-(*N*-Boc-3-methylindol-2-yl)methylphosphonium iodide (5).** Phosphine **4** (2.00 g, 2.77 mmol, 1.00 equiv.) was dissolved in THF (10.0 ml), and the reaction flask was placed into an ice bath. Methyl iodide (0.35 ml, 5.5 mmol, 2.0 equiv.) was added dropwise over a minute with vigorous stirring. The reaction was allowed to warm up to room temperature, which was accompanied by formation of

a white suspension. After 16h of stirring, the suspension was filtered and the solid was washed with three small portions of cold  $\text{Et}_2\text{O}$ . Upon washing, some additional material that precipitated from the filtrate was collected by filtration and washed with cold  $\text{Et}_2\text{O}$ . The solids were combined and dried *in vacuo* to yield a fine white powder (89.6%, 2.00 g).

In dichloromethane- $d_2$  solution, the compound exists as a  $\sim 1:0.15$  mixture of rotamers.  $^1\text{H NMR}$  signals from the major rotamer are labeled with an asterisk.  $^1\text{H NMR}$  (400 MHz, dichloromethane- $d_2$ )  $\delta$  8.18 (d,  $J_{\text{H,H}} = 8.7$  Hz, 0.05H, Ar-H), 8.11\* (d,  $J_{\text{H,H}} = 8.6$  Hz, 1H, Ar-H), 8.05 (d,  $J_{\text{H,H}} = 8.9$  Hz, 0.05H, Ar-H), 7.86 (d,  $J_{\text{H,H}} = 8.8$  Hz, 0.05H, Ar-H), 7.68\* (d,  $J_{\text{H,H}} = 8.0$  Hz, 1H, Ar-H), 7.63\* (t,  $J_{\text{H,H}} = 7.9$  Hz, 1H, Ar-H), 7.44\* (t,  $J_{\text{H,H}} = 7.6$  Hz, 1H, Ar-H), 2.87 (d,  $J_{\text{H,P}} = 13.9$  Hz, 0.15H, P- $\text{CH}_3$ ), 2.75\* (d,  $J_{\text{H,P}} = 15.1$  Hz, 1H, P $^+$ - $\text{CH}_3$ ), 2.37 (s, 0.15H, Ar- $\text{CH}_3$ ), 2.15 (s, 0.15H, Ar- $\text{CH}_3$ ), 2.04 (s, 0.15H, Ar- $\text{CH}_3$ ), 1.97\* (d,  $J_{\text{H,P}} = 2.1$  Hz, 3H, Ar- $\text{CH}_3$ ), 1.66 (s, 0.45H,  $^t\text{Bu}$ ), 1.54\* (s, 9H,  $^t\text{Bu}$ ), 1.48 (s, 0.45H,  $^t\text{Bu}$ ), 1.15 (s, 0.45H,  $^t\text{Bu}$ ).  $^{13}\text{C NMR}$  (101 MHz, dichloromethane- $d_2$ )  $\delta$  151.1 ( $\text{C}=\text{O}^{\text{Boc}}$ ), 137.2 (d,  $J_{\text{C,P}} = 5.6$  Hz, indole-C9 or C8, or C3), 136.5 (d,  $J_{\text{C,P}} = 12.2$  Hz, indole-C8 or C9, or C3), 131.2 (d,  $J_{\text{C,P}} = 14.5$  Hz, indole-C3 or C8, or C9), 129.7 ( $\text{C}^{\text{Ar-H}}$ ), 124.7 ( $\text{C}^{\text{Ar-H}}$ ), 121.0 ( $\text{C}^{\text{Ar-H}}$ ), 116.6 ( $\text{C}^{\text{Ar-H}}$ ), 116.5 (d,  $J_{\text{C,P}} = 128.8$  Hz, indole-C2), 87.9 (q $\text{C}^{\text{t-Bu}}$ ), 28.0 ( $\text{CH}_3^{\text{t-Bu}}$ ), 24.8 (d,



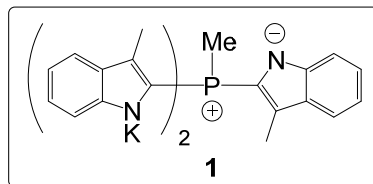
$J_{C,P} = 80.8$  Hz,  $P^+-CH_3$ ), 10.2 (Ar- $CH_3$ ).  $^{31}P$  NMR (162 MHz, dichloromethane- $d_2$ )  $\delta$  -2.2 (q,  $J_{P,H} = 15.2$  Hz, carbon satellites:  $J_{P,C} = 128.9, 80.7$  Hz, 1H), -3.9 (br.s., 0.15H). **ESI-TOF-MS** spectra recorded in positive mode contain signals from the original phosphonium cation and products of partial Boc-deprotection: 736.3525 [ $M$ ]<sup>+</sup>, 636.3006 [ $M$ -Boc+H]<sup>+</sup>, 536.2492 [ $M$ -2Boc+2H]<sup>+</sup> (calcd. 736.3516 [ $M$ ]<sup>+</sup>, 636.2991 [ $M$ -Boc+H]<sup>+</sup>, 536.2467 [ $M$ -2Boc+2H]<sup>+</sup>).



**tris(1H-3-methylindol-2-yl)methylphosphonium chloride (7).**

Phosphonium iodide **5** (10.00 g, 11.57 mmol) was dissolved in DCM (30.0 ml) in a round-bottom flask equipped with a stirring bar. Trifluoroacetic acid (30 ml) was added dropwise over a minute with vigorous stirring. The reaction mixture was left to stir over 16 h. After this, both DCM and trifluoroacetic acid were removed *in vacuo* to yield a sticky brown solid. In order to azeotropically remove trifluoroacetic acid trapped in the solid, the latter was three times redissolved in small portions of DCM (10.0 ml) followed by vacuum drying. This resulted into formation of a dark-yellow amorphous spongy mass that was turned into fine yellow powder by trituration with Et<sub>2</sub>O. The powder was redissolved in 40.0 ml of CH<sub>3</sub>CN/MeOH 1:1 and passed through a column of the chloride form of Amberlite® IRA-400 prewashed with two volumes of the same mixture of solvents. The eluate was concentrated until crystallization commenced. The mixture was left to stand at room temperature overnight. In the morning, white crystalline precipitate was collected, dried *in vacuo* to yield the target phosphonium chloride as white crystalline powder (80.0%, 4.37 g).

$^1H$  NMR (400 MHz, DMSO- $d_6$ )  $\delta$  12.34 (s, 1H, NH), 7.74 (d,  $J_{H,H} = 8.2$  Hz, 1H, Ar-H), 7.59 (d,  $J_{H,H} = 8.4$  Hz, 1H, Ar-H), 7.41 (t,  $J_{H,H} = 7.5$  Hz, 1H, Ar-H), 7.20 (ddd,  $J_{H,H} = 8.0, 6.9, 0.9$  Hz, 1H, Ar-H), 3.27 (d,  $J_{H,P} = 14.7$  Hz, 1H,  $P^+-CH_3$ ), 1.92 (d,  $J_{H,P} = 1.8$  Hz, 3H, Ar- $CH_3$ ).  $^{13}C$  NMR (101 MHz, DMSO- $d_6$ )  $\delta$  139.7 (d,  $J = 11.4$  Hz, indole-C8), 128.0 (d,  $J = 13.0$  Hz, indole C9 or C3), 126.9 (d,  $J = 15.8$  Hz, indole C3 or C9), 126.2 ( $C^{Ar}$ -H), 120.4 ( $C^{Ar}$ -H), 120.3 ( $C^{Ar}$ -H), 112.6 ( $C^{Ar}$ -H), 108.6 (d,  $J = 120.0$  Hz, indole-C2), 12.5 (d,  $J = 59.6$  Hz,  $P^+-CH_3$ ), 8.3 (Ar- $CH_3$ ).  $^{31}P$  NMR (162 MHz, DMSO- $d_6$ )  $\delta$  -14.0 (q,  $J_{P,H} = 14.7$  Hz, carbon satellites:  $J_{P,C} = 120.2, 58.7, 11.9$  Hz). **ATR-FTIR (neat)**  $\tilde{\nu}$  (cm<sup>-1</sup>): 427 (M), 460 (M), 516 (VW), 560 (W), 613 (W), 639 (W), 745 (VS), 805 (M), 908 (S), 1041 (M), 1099 (M), 1130 (M), 1151 (M), 1200 (M), 1238 (M), 1294 (W), 1332 (S), 1431 (W), 1515 (M), 1578 (W), 1617 (W), 2851 (M), 2914 (M), 2975 (S), 3024 (M), 3061 (M), 3437 (W). **ESI-TOF-MS**: found 436.1916 [ $M$ ]<sup>+</sup> (calcd. 436.1943 [ $M$ ]<sup>+</sup>).



**TSMFK<sub>2</sub> (1).** Depending on the base, compound **1** can be prepared according to either of the two following procedures.

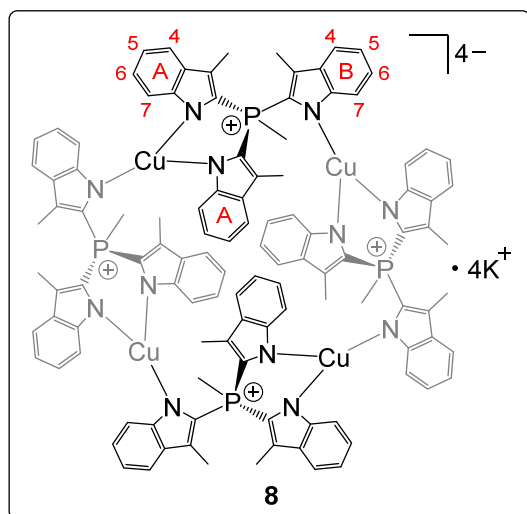
**Procedure A (using KHMDS).** A solution of KHMDS (0.041 g, 0.20 mmol, 3.0 equiv.) in THF (2.0 ml) was added to a stirred solution of chloride **7** (0.030 g, 0.068 mmol, 1.0 equiv.) in THF (2.0 ml).

After stirring for 20 min, the solvent was removed *in vacuo*. After an hour of drying, the amorphous white residue was washed with hexane (3 x 4.0 ml) and dried *in vacuo* for another hour, after which both the solid and hexane washings were analyzed by NMR.  $^{31}P$  spectra of the hexane washings showed no traces of phosphorus, whereas  $^1H$  and  $^{31}P$  spectra of the solid showed quantitative conversion of the starting material into **1**.

*Procedure B (using KH).* To a stirred solution of chloride **7** (0.050 g, 0.11 mmol, 1.0 equiv.) in THF (15.0 ml) was added a suspension of potassium hydride (0.014 g, 0.35 mmol, 3.3 equiv.) in 5.0 ml of THF (5.0 ml). The reaction was stirred for 2 h, filtered, the solvent was removed *in vacuo* to yield an air-sensitive white amorphous solid. The residual THF content of 21.5 wt.% was determined using quantitative  $^1\text{H}$  NMR measurements. With the product mass of 0.072 g this gives a quantitative yield. Crystals suitable for X-ray diffraction analysis were grown by vapor diffusion of diethyl ether into a solution of **1** in acetonitrile at room temperature.

Regardless of the procedure used, the final products show identical NMR spectra.  $^1\text{H}$  NMR (400 MHz, acetonitrile- $d_3$ )  $\delta$  7.44 (d,  $J_{\text{H,H}} = 8.0$  Hz, 1H, Ar-H), 7.31 (d,  $J_{\text{H,H}} = 8.3$  Hz, 1H, Ar-H), 6.86 (‘t’,  $J_{\text{H,H}} = 7.3$  Hz, 1H, Ar-H), 6.76 (‘t’,  $J_{\text{H,H}} = 7.2$  Hz, 1H, Ar-H), 2.62 (d,  $J_{\text{H,P}} = 13.8$  Hz, 1H,  $\text{P}^+\text{-CH}_3$ ), 2.10 (d,  $J_{\text{H,P}} = 1.5$  Hz, 3H, Ar- $\text{CH}_3$ ).  $^{13}\text{C}$  NMR (101 MHz, acetonitrile- $d_3$ )  $\delta$  149.7 (d,  $J_{\text{C,P}} = 24.3$  Hz, indole-C8), 132.3 (d,  $J_{\text{C,P}} = 10.9$  Hz, indole-C9 or C3), 128.7 (d,  $J_{\text{C,P}} = 117.8$  Hz, indole-C2), 119.4 ( $\text{C}^{\text{Ar-H}}$ ), 119.06 ( $\text{C}^{\text{Ar-H}}$ ), 118.7 ( $\text{C}^{\text{Ar-H}}$ ), 117.3 (d,  $J_{\text{C,P}} = 26.4$  Hz, indole-C3 or C9), 116.1 ( $\text{C}^{\text{Ar-H}}$ ), 14.6 (d,  $J_{\text{C,P}} = 63.5$  Hz,  $\text{P}^+\text{-CH}_3$ ), 10.4 (Ar- $\text{CH}_3$ ).  $^{31}\text{P}$  NMR (162 MHz, acetonitrile- $d_3$ )  $\delta$  -7.8 (q,  $J_{\text{P,H}} = 13.7$  Hz, carbon satellites:  $J_{\text{P,C}} = 117.8, 63.6, 25.7, 10.9$  Hz). No satisfactory elemental analysis could be obtained due to the high reactivity of **1** as well as solvation of the potassium cations, which results into the compound retaining an unknown amount of solvent.

### 2.5.2.2 Metal complexes

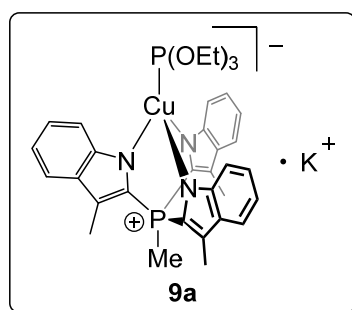


$\{[(\text{TSMPCu})\text{K}]\}_4$  (**8**). A solution of anhydrous  $\text{CuCl}$  (0.076 g, 0.77 mmol, 1.0 equiv.) in pyridine (6.0 ml) was added dropwise to dipotassium salt **1** (contains 21.5 wt% of THF, 0.500 g, 0.768 mmol, 1.00 equiv.) in pyridine (12.0 ml) over a minute. The clear red-orange solution was stirred for 3 h, after which the solvent was evaporated *in vacuo*. The yellow solid was taken up in dry THF (20.0 ml), the resulting suspension was filtered, and the solid was washed with more THF until all color was extracted into the solution. The volume of combined filtrate and washings was reduced by evaporation *in vacuo* until yellow crystals started to form. Immediately after, the mixture was cooled down to  $-35$  °C and kept at this temperature for 48 h until the crystal formation stopped. The crystals were collected by vacuum filtration, washed with  $\sim 2$  ml of cold THF and dried *in vacuo* to yield an air-sensitive fine yellow powder (95.4%, 0.393 g). Crystals suitable for X-ray diffraction analysis were grown by vapor diffusion of hexane into a pyridine solution of **8** at room temperature.

uom filtration, washed with  $\sim 2$  ml of cold THF and dried *in vacuo* to yield an air-sensitive fine yellow powder (95.4%, 0.393 g). Crystals suitable for X-ray diffraction analysis were grown by vapor diffusion of hexane into a pyridine solution of **8** at room temperature.

The  $^1\text{H}$  NMR spectrum in acetonitrile- $d_3$  is dominated by one species, chemical shifts and integral intensities of which are consistent with the solid-state structure of **8** derived from X-ray diffraction. Additionally, gCOSY spectra clearly show the presence of two aromatic spin systems in a ratio of 2:1. Nevertheless, there are some minor signals that, according to NOESY spectra, are connected with the major species *via* chemical exchange. NMR data below are shown only for the major species.  $^1\text{H}$  NMR (400 MHz, acetonitrile- $d_3$ )  $\delta$  7.83 (d,  $J_{\text{H,H}} = 8.2$  Hz, 1H,  $\text{H}^{\text{B}}$ ), 7.64 (d,  $J_{\text{H,H}} = 7.8$  Hz,

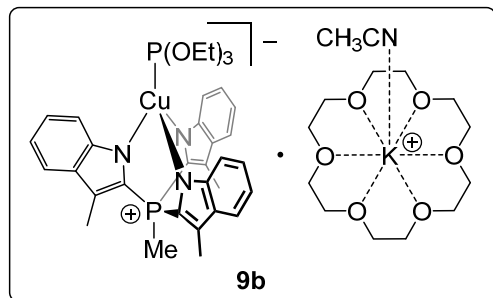
1H, H<sup>4</sup><sub>B</sub>), 7.33 – 7.24 (m, 2H, H<sup>7</sup><sub>A</sub>), 7.20 – 7.13 (m, 2H, H<sup>3</sup><sub>A</sub>), 6.99 (‘t’,  $J_{H,H} = 7.3$  Hz, 1H, H<sup>5</sup><sub>B</sub>), 6.93 (ddd,  $J_{H,H} = 7.8, 6.6, 1.1$  Hz, 1H, H<sup>6</sup><sub>B</sub>), 6.61 – 6.49 (m, 4H, H<sup>6</sup><sub>A</sub>+H<sup>5</sup><sub>A</sub>), 2.73 (d,  $J_{H,P} = 13.9$  Hz, 3H, P<sup>+</sup>-CH<sub>3</sub>), 2.18 (d,  $J_{H,P} = 1.5$  Hz, 3H, CH<sub>3</sub><sup>Ar</sup><sub>B</sub>), 1.71 (d,  $J_{H,P} = 1.5$  Hz, 6H, CH<sub>3</sub><sup>Ar</sup><sub>B</sub>). <sup>13</sup>C NMR (101 MHz, acetonitrile-*d*<sub>3</sub>) δ 150.3 (d,  $J_{C,P} = 19.0$  Hz, indole-C8<sup>A</sup>), 148.8 (d,  $J_{C,P} = 19.9$  Hz, indole-C8<sup>B</sup>), 131.9 (d,  $J_{C,P} = 11.4$  Hz, indole-C9<sup>B</sup> or C3<sup>B</sup>), 130.7 (d,  $J_{C,P} = 12.8$  Hz, indole-C9<sup>A</sup> or C3<sup>A</sup>), 125.4 (d,  $J_{C,P} = 117.9$  Hz, indole-C2<sup>A</sup>), 122.7 (d,  $J_{C,P} = 117.2$  Hz, indole-C2<sup>B</sup>), 120.3, 120.2, 120.2, 120.1, 119.6, 119.4, 119.1, 119.0, 118.8, 118.6, 118.6, 117.0, 116.2, 17.3 (d,  $J_{C,P} = 61.9$  Hz), 10.9 (d,  $J_{C,P} = 2.0$  Hz), 10.1. <sup>31</sup>P NMR (162 MHz, acetonitrile-*d*<sub>3</sub>) δ -16.9 (q,  $J_{P,H} = 13.6$  Hz, carbon satellites:  $J_{P,C} = 117.5, 23.3, 19.0, 12.1$  Hz). UV-Vis (acetonitrile): λ<sub>max</sub> (ε)=307 (8.4·10<sup>4</sup>), 238 nm (2.0·10<sup>5</sup> cm<sup>-1</sup>M<sup>-1</sup>). No satisfactory elemental analysis could be obtained due to high reactivity of **8** as well as solvation of the potassium cations, due to which the compound retains an unknown amount of solvent.



**Generation and characterization of [(TSMP)CuP(OEt)<sub>3</sub>]K (**9a**) *in situ*.** Complex **8** (0.016 g, 0.030 mmol, 1.0 equiv.) was suspended in 0.7 ml of acetonitrile-*d*<sub>3</sub> in a J. Young NMR tube. This was followed by addition of P(OEt)<sub>3</sub> (5 μl, 0.03 mmol, 4 equiv.). The NMR tube was sealed under N<sub>2</sub> atmosphere, and the mixture was stirred until a clear white solution formed. The complex could not be purified by means of crystallization and, hence, was analysed in a crude form using NMR spectroscopy. However, isolation of a crystalline 18-crown-6 adduct **9b** was successful (see the synthesis below), which

allowed for an X-ray diffraction study. Except for 18-crown-6 signals in **9b**, <sup>1</sup>H and <sup>31</sup>P NMR spectra of both **9a** and **9b** in acetonitrile-*d*<sub>3</sub> are virtually identical.

<sup>1</sup>H NMR (400 MHz, acetonitrile-*d*<sub>3</sub>) δ 7.65 (d,  $J_{H,H} = 8.4$  Hz, 1H, Ar-H<sup>7</sup>), 7.43 (‘d’,  $J_{H,H} = 8.0$  Hz, 1H, Ar-H<sup>4</sup>), 6.93 (t,  $J_{H,H} = 7.5$  Hz, 1H, Ar-H<sup>6</sup>), 6.77 (‘t’,  $J_{H,H} = 7.3$  Hz, 1H, Ar-H<sup>5</sup>), 4.25 (p,  $J_{H,H} = J_{H,P} = 7.2$  Hz, 2H, POCH<sub>2</sub>CH<sub>3</sub>), 3.01 (d,  $J_{H,P} = 14.6$  Hz, 1H, P<sup>+</sup>-CH<sub>3</sub>), 2.48 (s, 3H, Ar-CH<sub>3</sub>), 1.34 (t,  $J_{H,H} = 7.0$  Hz, 3H, POCH<sub>2</sub>CH<sub>3</sub>). <sup>13</sup>C NMR (101 MHz, acetonitrile-*d*<sub>3</sub>) δ 149.3 (d,  $J_{C,P} = 18.6$  Hz, indole-C8), 130.8 (d,  $J_{C,P} = 13.3$  Hz, indole-C9 or C3), 127.0 (d,  $J_{C,P} = 118.3$  Hz, indole-C2), 120.1 (indole-C6), 119.2 (indole-C4), 118.0 (indole-C7), 116.5 (indole-C5), 115.6 (d,  $J_{C,P} = 24.6$  Hz, indole-C3 or C9), 60.6 (d,  $J_{C,P} = 6.9$  Hz, POCH<sub>2</sub>CH<sub>3</sub>), 17.0 (d,  $J_{C,P} = 7.1$  Hz, POCH<sub>2</sub>CH<sub>3</sub>), 10.7 (Ar-CH<sub>3</sub>), 8.9 (d,  $J_{C,P} = 57.1$  Hz, P<sup>+</sup>-CH<sub>3</sub>). <sup>31</sup>P NMR (162 MHz, acetonitrile-*d*<sub>3</sub>) δ 130.7 (br. s., 1P), -14.3 (q,  $J_{P,H} = 14.4$  Hz, 1P, carbon satellites:  $J_{P,C} = 117.7, 56.9, 24.2, 18.4, 13.2$  Hz). No satisfactory elemental analysis could be obtained due to a number of impurities in crude **9a** combined with its high reactivity as well as solvation of potassium cations, due to which the compound retains an unknown amount of solvent.



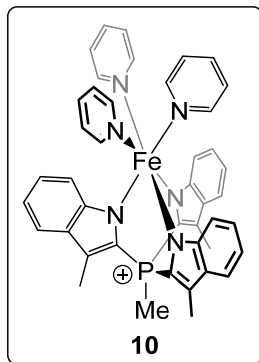
**[(TSMP)CuP(OEt)<sub>3</sub>][K(18-crown-6)·CH<sub>3</sub>CN] (9b)**. Depending on the starting material, compound **9b** can be prepared following either of the two procedures below.

*Procedure A (preparation from 8)*. Complex **8** (0.100 g, 0.187 mmol, 1.00 equiv.) was suspended in 8.0 ml of acetonitrile. This was followed by dropwise addition of a mixture of P(OEt)<sub>3</sub> (32  $\mu$ l, 0.19 mmol, 4.0 equiv.) and 18-crown-6 (0.049 g, 0.19 mmol, 1.0 equiv.) in acetonitrile (12.0 ml)

over 30 sec. During the addition, the yellow suspension became a clear colorless solution. The volume of the latter was reduced *in vacuo* to  $\sim$ 2 ml, which resulted into ample crystal formation. After crystallization stopped at room temperature, the mixture was transferred into a freezer at  $-35$   $^{\circ}$ C for 24h. After that time, the crystals were collected by vacuum filtration, washed with  $\sim$ 1.5 ml of cold acetonitrile in small portions and dried *in vacuo*. The above manipulations yielded air-sensitive white colorless needles in 65.3% (0.123 g) yield.

*Procedure B (preparation from CuCl)*. Dipotassium salt **1** (contains 21.5 wt% of THF, 0.500 g, 0.768 mmol, 1.00 equiv.) in acetonitrile (12.0 ml) was added to a solution of anhydrous CuCl (0.076 g, 0.77 mmol, 1.0 equiv.) and P(OEt)<sub>3</sub> (132  $\mu$ l, 0.768 mmol, 1.00 equiv.) in acetonitrile (6.0 ml). The resulting white suspension was stirred over an hour followed by addition of 18-crown-6 (0.203 g, 0.768 mmol, 1.00 equiv.) in acetonitrile (5.0 ml). Immediately after this, the suspension was filtered and the solid was washed with acetonitrile (2 x 25.0 ml). The volume of combined filtrate and washings was reduced *in vacuo* to  $\sim$ 5 ml, which resulted into ample crystal formation. After crystallization stopped at room temperature, the mixture was transferred into a freezer at  $-35$   $^{\circ}$ C for 24 h. After that time, the crystals were collected by vacuum filtration, washed with  $\sim$ 3 ml of cold acetonitrile in small portions and dried *in vacuo*. The above manipulations yielded air-sensitive white colorless needles in 69.9% (0.541 g) yield. Purity >95% according to NMR spectroscopy. Crystals suitable for X-ray diffraction analysis were grown by vapor diffusion of diethyl ether into an acetonitrile/benzene solution of **9b** at room temperature.

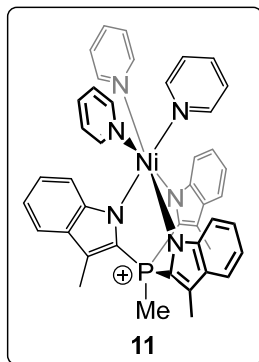
**<sup>1</sup>H NMR** (400 MHz, acetonitrile-*d*<sub>3</sub>)  $\delta$  7.63 (d,  $J_{\text{H,H}} = 8.4$  Hz, 1H, Ar-H<sup>7</sup>), 7.40 (d,  $J_{\text{H,H}} = 8.0$  Hz, 1H, Ar-H<sup>4</sup>), 6.89 ('t',  $J_{\text{H,H}} = 7.3$  Hz, 1H, Ar-H<sup>6</sup>), 6.74 ('t',  $J_{\text{H,H}} = 7.3$  Hz, 1H, Ar-H<sup>5</sup>), 4.23 (p,  $J_{\text{H,H}} = J_{\text{H,P}} = 7.2$  Hz, 2H, POCH<sub>2</sub>CH<sub>3</sub>), 3.53 (s, 8H, CH<sub>2</sub> of 18-crown-6), 2.99 (d,  $J_{\text{H,P}} = 14.6$  Hz, 1H, P<sup>+</sup>-CH<sub>3</sub>), 2.46 (d,  $J_{\text{H,P}} = 1.6$  Hz, 3H, Ar-CH<sub>3</sub>), 1.31 (t,  $J_{\text{H,H}} = 7.1$  Hz, 3H, POCH<sub>2</sub>CH<sub>3</sub>). **<sup>13</sup>C NMR** (101 MHz, acetonitrile-*d*<sub>3</sub>)  $\delta$  148.3 (d,  $J_{\text{C,P}} = 18.6$  Hz, indole-C8), 129.7 (d,  $J_{\text{C,P}} = 13.4$  Hz, indole-C9 or C3), 126.1 (d,  $J_{\text{C,P}} = 117.7$  Hz, indole-C2), 119.0 (indole-C6), 118.2 (indole-C4), 117.1 (indole-C7), 115.5 (indole-C5), 114.3 (d,  $J_{\text{C,P}} = 24.3$  Hz, indole-C3 or C9), 69.9 (CH<sub>2</sub> of 18-crown-6), 59.6 (d,  $J_{\text{C,P}} = 7.4$  Hz, POCH<sub>2</sub>CH<sub>3</sub>), 16.0 (d,  $J_{\text{C,P}} = 7.2$  Hz, POCH<sub>2</sub>CH<sub>3</sub>), 9.7 (Ar-CH<sub>3</sub>), 7.8 (d,  $J_{\text{C,P}} = 57.0$  Hz, P<sup>+</sup>-CH<sub>3</sub>). **<sup>31</sup>P NMR** (162 MHz, acetonitrile-*d*<sub>3</sub>)  $\delta$  131.3 (br. s., 1P), -14.4 (q,  $J_{\text{P,H}} = 14.4$  Hz, 1P, carbon satellites:  $J_{\text{P,C}} = 117.6, 24.2, 18.4, 13.2$  Hz). **UV-Vis** (acetonitrile):  $\lambda_{\text{max}}$  ( $\epsilon$ ) = ca. 349 (shoulder) ( $1.2 \cdot 10^4$ ), 316 ( $2.2 \cdot 10^4$ ), 246 ( $4.2 \cdot 10^4$ ), 214 nm ( $2.8 \cdot 10^4$  cm<sup>-1</sup>M<sup>-1</sup>). **ESI-TOF-MS**: anionic unit: 662.2196 [*M*]<sup>-</sup> (calcd. 662.1763 [*M*]<sup>-</sup>). No satisfactory elemental analysis could be obtained due to high reactivity of **9b**.



**(TSMP)Fe(Py)<sub>3</sub> (10).** Dry pyridine (30.0 ml) was added to a mixture of solid dipotassium salt **1** (contains 21.5 wt% of THF, 0.500 g, 0.768 mmol, 1.00 equiv.) and anhydrous FeCl<sub>2</sub> (0.097 g, 0.77 mmol, 1.00 equiv.). After 12 h of stirring, the reaction mixture turned clear and acquired deep orange coloration. Subsequently, the solvent was removed *in vacuo* to give a bright-yellow solid. The latter was suspended in THF (25.0 ml) with 8 drops of pyridine (in order to improve solubility of the complex). The suspension was filtered, and the solid residue was washed with more THF until all color was extracted into the solution. Combined filtrate and washings were freed of solvent *in vacuo*. After this, the solid was redissolved in a minimal amount of pyridine,

layered with an equal volume of hexane and left at room temperature for a week. Clear orange blocky crystals were collected, washed with a small volume of pyridine/hexane (1:1 (v/v)) solvent mixture and dried on a vacuum line for 30 min (prolonged drying results into a color change from orange to yellow and decreased solubility). Yield: 30.0% (0.167 g) of air-sensitive solid. Crystals suitable for X-ray diffraction analysis were grown by vapor diffusion of hexane into a pyridine solution of **10** at room temperature.

Integral intensities in <sup>1</sup>H NMR spectra were extracted using MestReNova<sup>27</sup> peak deconvolution tool. <sup>1</sup>H NMR (400 MHz, pyridine-*d*<sub>5</sub>) δ 36.7 (br. s., 1H), 27.7 (br. s., 1H), 25.7 (br. s., 3H), 8.9 (br. s., pyridine α-H), 8.1 (br. s., 1H), 7.61 – 7.50 (m, pyridine γ-H), 7.35 – 7.24 (m, pyridine β-H), 5.8 (br. s., 1H), -14.0 (br. s., 1H). <sup>31</sup>P NMR (162 MHz, pyridine-*d*<sub>5</sub>) δ -304.2. **Effective magnetic moment in solution** determined in pyridine-*d*<sub>5</sub> using Evans method: 5.19 μ<sub>B</sub>. **UV-Vis** (acetonitrile): λ<sub>max</sub> (ε)=471 (1.2·10<sup>2</sup>), 442 (2.1·10<sup>2</sup>), 417 (2.5·10<sup>2</sup>), 307 (3.5·10<sup>4</sup>), 231 (6.3·10<sup>4</sup>), 198 nm (5.3·10<sup>4</sup> cm<sup>1</sup>M<sup>-1</sup>). No satisfactory elemental analysis could be obtained due to the high reactivity of **8**.

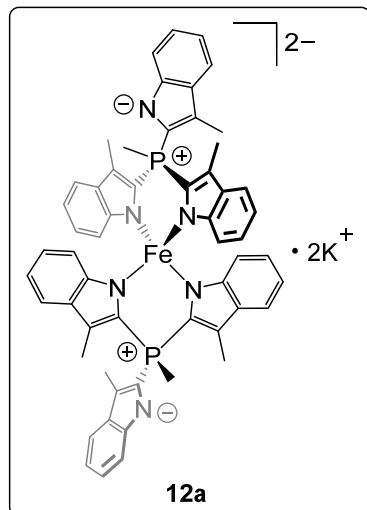


**(TSMP)Ni(Py)<sub>3</sub> (11).** Dry pyridine (30.0 ml) was added to a mixture of solid dipotassium salt **1** (contains 21.5 wt% of THF, 0.500 g, 0.768 mmol, 1.00 equiv.) and anhydrous NiCl<sub>2</sub>·dme (0.169 g, 0.768 mmol, 1.00 equiv.). Deep-brown coloration ensued. After 12 h of stirring, the reaction mixture turned clear and acquired an emerald-green coloration. Subsequently, the solvent was removed *in vacuo* to give an olive-brown solid. The latter was suspended in THF (25.0 ml) with 8 drops of pyridine (improves solubility of the complex). The suspension was filtered, and the solid residue was washed with more THF until all color was extracted into the solution. Combined filtrate and washings were freed of solvent *in vacuo*. After this, the solid was redissolved in a minimal amount of pyridine, layered with an equal volume of hexane and left at room temperature for a week. Clear green blocky crystals were collected, washed with a small volume of pyridine/hexane (1:1 (v/v)) solvent mixture and dried on a vacuum line for 30 min (prolonged drying results into a color change from green to olive-brown and decreased solubility). Yield: 65.8% (0.369 g) of air-sensitive solid. Crystals suitable for X-ray diffraction analysis were grown by vapor diffusion of hexane into a pyridine solution of **11** at room temperature.

Integral intensities in <sup>1</sup>H NMR spectra were extracted using MestReNova<sup>27</sup> peak deconvolution tool. <sup>1</sup>H NMR (400 MHz, pyridine-*d*<sub>5</sub>) δ 29.7 (br. s., 1H), 15.2 (br. s., 1H), 9.1 (br. s., pyridine α-H), 7.67 – 7.52 (m, pyridine γ-H), 7.41 – 7.23 (m, pyridine β-H), 7.0 (br. s., 1H), 6.4 (br. s., 1H), 5.2 (br. s., 1H), 2.1 (br. s., 3H). <sup>31</sup>P NMR (162 MHz, pyridine-*d*<sub>5</sub>) δ -122.7 (br. s.). **Effective magnetic**

moment in solution determined in pyridine-*d*<sub>5</sub> using Evans method: 5.19 μ<sub>B</sub>. **UV-Vis** (acetonitrile): λ<sub>max</sub> (ε)=471 (1.2·10<sup>2</sup>), 442 (2.1·10<sup>2</sup>), 417 (2.5·10<sup>2</sup>), 307 (3.5·10<sup>4</sup>), 231 (6.3·10<sup>4</sup>), 198 nm (5.3·10<sup>4</sup> cm<sup>1</sup>M<sup>-1</sup>). No satisfactory elemental analysis could be obtained due to the high reactivity of **8**.

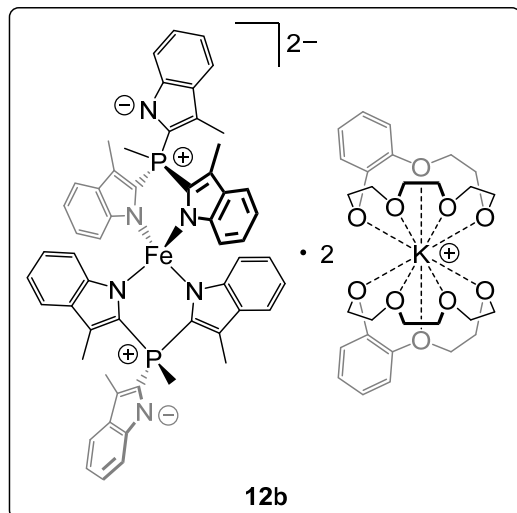
**moment in solution** determined in pyridine- $d_5$  using Evans method:  $2.82 \mu_B$ . **UV-Vis** (acetonitrile):  $\lambda_{\max} (\epsilon) = 198 (5.8 \cdot 10^4)$ ,  $228 (5.7 \cdot 10^4)$ ,  $242 (6.1 \cdot 10^4)$ ,  $316 (3.3 \cdot 10^4)$ ,  $588 \text{ nm} (37 \text{ cm}^{-1} \text{M}^{-1})$ . No satisfactory elemental analysis could be obtained due to the high reactivity of **9**.



**Synthesis and characterization of crude [(TSMPP)<sub>2</sub>Fe]K<sub>2</sub> (**12a**).** Dry THF (15.0 ml) was added to a mixture of solid dipotassium salt **1** (contains 21.5 wt% of THF, 0.150 g, 0.230 mmol, 2.00 equiv.) and anhydrous FeCl<sub>2</sub> (0.015 g, 0.12 mmol, 1.0 equiv.). The colorless mixture was stirred over 16 h until all FeCl<sub>2</sub> dissolved forming a bright-yellow suspension. The latter was filtered, the solvent was removed *in vacuo*, yielding a dark-yellow oil. The complex could not be purified by means of crystallization and, hence, was analysed in a crude form using NMR spectroscopy. However, isolation of a crystalline tetrakis(benzo-15-crown-5) adduct **12b** was successful (see the synthesis below), which allowed to establish atomic connectivity using X-ray diffraction. Except for a number of peaks of impurities as well as benzo-15-crown-5 signals in **12b**, <sup>1</sup>H and <sup>31</sup>P NMR spectra of both **12a** and **12b** in acetonitrile- $d_3$  are identical.

Assuming that the structure of **12a** determined by X-ray diffraction crystallography holds in solution, there should be three non-equivalent indolide units. This means that <sup>1</sup>H NMR spectra should display sixteen peaks: four of triple intensity with the rest of unit intensity. Instead, only six peaks are observed with the ratio of integral intensities that does not match the overall composition of **12a**. This implies two possibilities: either not all peaks are visible due to fast relaxation and subsequent paramagnetic broadening, or the situation in solution is complicated with dynamic equilibria, possibly oligomerization or intermolecular exchange. This point is further addressed below, in the characterization section for tetrakis(benzo-15-crown-5) adduct **12b**.

<sup>1</sup>H NMR (400 MHz, acetonitrile- $d_3$ )  $\delta$  66.3 (br. s.), 21.6 (br. s.), 14.4 (br. s.), 6.0 (br. s.), -0.6 (br. s.), -6.1 (br. s.). <sup>31</sup>P NMR (162 MHz, acetonitrile- $d_3$ )  $\delta$  104.4 (br. s.). **ESI-TOF-MS** spectra recorded in a negative mode show a product of one-electron oxidation of **12a**, which is in line with its high air-sensitivity: 922.3225 [ $M$ ]<sup>-</sup> (calcd. 922.2767 [ $M$ ]<sup>-</sup>). No satisfactory elemental analysis could be obtained due to a number of impurities in crude **12a** combined with its high reactivity as well as solvation of potassium cations, due to which the compound retains an unknown amount of solvent.



**[(TSMF)<sub>2</sub>Fe][K(benzo-15-crown-5)<sub>2</sub>]<sub>2</sub> (12b)**. Dry THF (150.0 ml) was added to a mixture of solid dipotassium salt **1** (contains 21.5 wt% of THF, 1.500 g, 2.302 mmol, 2.000 equiv.) and anhydrous FeCl<sub>2</sub> (0.146 g, 1.15 mmol, 1.00 equiv.). The mixture was stirred over 16h until all FeCl<sub>2</sub> dissolved forming a bright-yellow suspension. The latter was filtered, the volume of the liquor was reduced *in vacuo* to ca. 15 ml, and a solution of benzo-15-crown-5 (0.680 g, 2.53 mmol, 2.20 equiv) in THF (5.0 ml) was added with stirring. After a few minutes, bright-yellow crystalline material started precipitating. The mixture was left standing at room temperature for 16 h, at which point crystal formation stopped. It was then transferred into a freezer at -35 °C for additional 48 h, where more crystalline material formed. The crystals were collected

by vacuum filtration, washed with cold THF (4 x 20.0 ml) in small portions and dried *in vacuo*. This yielded a bright-yellow crystalline material in 40.7% (0.972 g) yield. Crystals suitable for X-ray diffraction analysis were grown by vapor diffusion of diethyl ether into a toluene/THF/acetonitrile (4:1:1 (v/v)) solution of **12b** at room temperature.

Similarly to **12a**, assuming that X-ray crystallographic structure holds for **12b** in solution, there should be three non-equivalent indolide units. This means that <sup>1</sup>H NMR spectra should display sixteen peaks: four of triple intensity with the rest of unit intensity. Instead, only six peaks are observed with the ratio of integral intensities that does not match the overall composition of **12b**. This implies two possibilities: either not all peaks are visible due to fast relaxation and subsequent paramagnetic broadening, or the situation in solution is complicated with dynamic equilibria, possibly oligomerization or intermolecular exchange. Trends observed in variable-temperature NMR studies (Appendix A5) are in favour of the latter. <sup>1</sup>H NMR (400 MHz, acetonitrile-*d*<sub>3</sub>) δ 66.3 (br. s.), 21.6 (br. s.), 14.4 (br. s.), 6.90 (br. s., Ar-H of benzo-15-crown-5), 6.76 (br. s., Ar-H of benzo-15-crown-5), 6.1 (br. s.), 4.20 – 3.17 (m, aliphatic C-H of benzo-15-crown-5), -0.6 (br. s.), -6.1 (br. s.). <sup>31</sup>P NMR (162 MHz, acetonitrile-*d*<sub>3</sub>) δ 104.2 (br. s.). **Effective magnetic moment in solution** determined in acetonitrile-*d*<sub>3</sub> using Evans method: 5.17 μ<sub>B</sub>. **UV-Vis** (acetonitrile): λ<sub>max</sub> (ε) = 308 (3.5·10<sup>4</sup>), 245 nm (7.7·10<sup>4</sup> cm<sup>-1</sup>M<sup>-1</sup>). **ATR-FTIR** (neat)  $\tilde{\nu}$  (cm<sup>-1</sup>): 433 (M), 452 (M), 564 (W), 621 (M), 661 (W), 739 (VS), 808 (M), 853 (M), 884 (S), 937 (M), 1044 (S), 1076 (M), 1098 (S), 1123 (VS), 1217 (S), 1252 (VS), 1297 (M), 1337 (M), 1363 (M), 1455 (M), 1504 (S), 1597 (W), 1651 (VW), 2864 (M), 2904 (M), 3041 (W). **ESI-TOF-MS** spectra recorded in a negative mode show a product of one-electron oxidation of **12b**, which is in line with its high air-sensitivity: 922.2360 [M]<sup>-</sup> (calcd. 922.2767 [M]<sup>-</sup>). No satisfactory elemental analysis could be obtained due to high reactivity of **12b**.

### 2.5.3 Additional experiments

**Attempted preparative oxidation of complexes 8-12a.** Metal complex **8-12a** (0.030 mmol, 1.0 equiv.) was dissolved in acetonitrile or pyridine (5.0 ml), and a solution of ferrocenium tetrafluoroborate (0.008 g, 0.03 mmol, 1 equiv.) in the same solvent (5.0 ml) was added at -78 °C with vigorous stirring within a minute. The reaction was allowed to warm up to room temperature for an hour. Afterwards, the solvent was removed *in vacuo*, the solid crude was washed with *n*-hexane (3 x 3.0

ml) and, after additional drying, NMR analysis was attempted in acetonitrile- $d_3$ , pyridine- $d_5$ , dichloromethane- $d_2$  and THF- $d_8$ . All complexes, except for **12a**, gave intractable or insoluble products or mixtures thereof. Attempted crystallization from various solvents and solvent mixtures yielded amorphous precipitates in all cases except for **12a**, which provided dark-blue crystals suitable for X-ray diffraction. The structure as well as the properties of the product of oxidation of **12a** are discussed in the next chapter.

#### 2.5.4 X-ray crystal structure determinations

**TSMPK<sub>2</sub> (1)**.  $C_{56}H_{48}K_4N_6P_2 \cdot \frac{1}{2}CH_3CN$ , Fw=1043.87, colourless block,  $0.51 \times 0.45 \times 0.16$  mm<sup>3</sup>, monoclinic, Cc (no. 9),  $a=20.0632(12)$ ,  $b=12.0672(10)$ ,  $c=42.305(4)$  Å,  $\beta=95.794(2)^\circ$ ,  $V=10190.0(14)$  Å<sup>3</sup>,  $Z=8$ ,  $D_x=1.361$  g/cm<sup>3</sup>,  $\mu=0.46$  mm<sup>-1</sup>. The diffraction experiment was performed on a Bruker Kappa ApexII diffractometer with sealed tube and Triumph monochromator ( $\lambda=0.71073$  Å) at a temperature of 150(2) K up to a resolution of  $(\sin\theta/\lambda)_{\max}=0.65$  Å<sup>-1</sup>. The crystal appeared to be twinned, with a twofold rotation about  $hkl=(0,0,1)$  as twin operation. Consequently, two orientation matrices were used for the intensity integration with the Eval15 software.<sup>45</sup> A multi-scan absorption correction and scaling was performed with TWINABS<sup>46</sup> (correction range 0.68-0.75). A total of 102232 reflections was measured, 22187 reflections were unique ( $R_{\text{int}}=0.032$ ), 21465 reflections were observed [ $I>2\sigma(I)$ ]. The structure was solved with Patterson superposition methods using SHELXT.<sup>47</sup> Structure refinement was performed with SHELXL-2016<sup>48</sup> on  $F^2$  of all reflections based on an HKLF-5 file.<sup>49</sup> Non-hydrogen atoms were refined freely with anisotropic displacement parameters. All hydrogen atoms were introduced in calculated positions and refined with a riding model. 1270 Parameters were refined with two restraints (floating origin).  $R1/wR2$  [ $I>2\sigma(I)$ ]: 0.0326/0.0827.  $R1/wR2$  [all refl.]: 0.0342/0.0835. The twin fraction BASF refined to 0.1869(5); additional inversion twinning was not included in the refinement.  $S=1.034$ . Residual electron density between -0.29 and 0.49 e/Å<sup>3</sup>. Geometry calculations and checking for higher symmetry was performed with the PLATON program.<sup>50</sup>

**Discussion:** The packing in the non-centrosymmetric space group Cc (no. 9) is characterized by the presence of a local inversion center at approximately (0, 0,  $\frac{1}{4}$ ). This location prevents the transformation to the centrosymmetric space group C2/c (no. 15).

The metrics of the unit cell parameters allow a transformation to a *pseudo*-orthorhombic supercell with 5-fold volume. According to Mallard's law, such a situation can be the driving force for twin formation.<sup>56</sup> Twinning is actually found in the current crystal and can be described by a twofold rotation about  $hkl=(0,0,1)$ , or equivalently about  $uvw=[1,0,0]$ . The a-axis of 20.06 Å indeed becomes a twofold axis in the 5-fold supercell. On a structural level, the twinning can be explained by stacking faults of the one-dimensional coordination polymers (*Figure 2.8*).



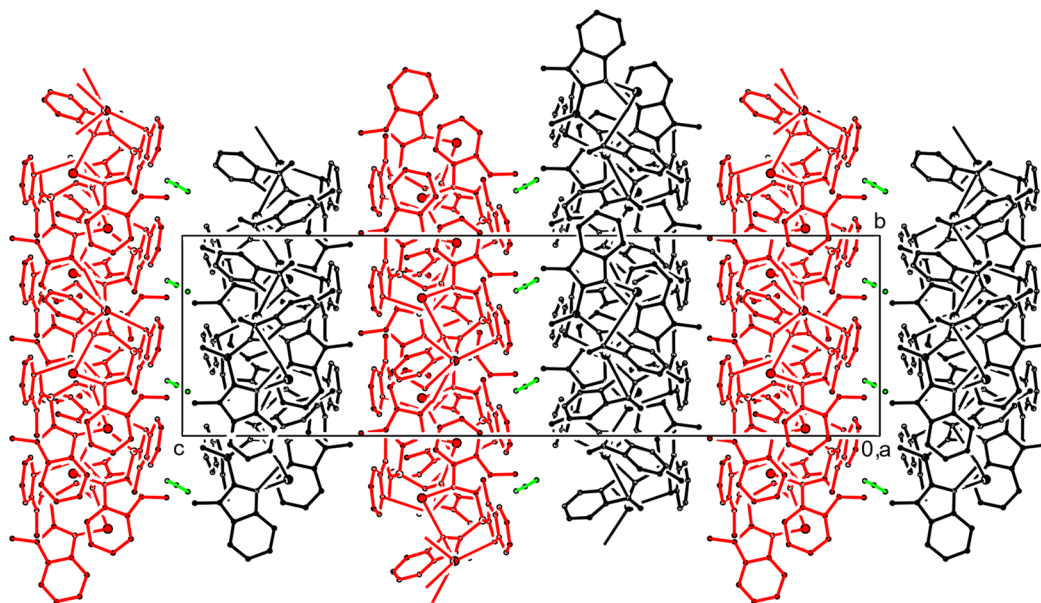


Figure 2.8. Packing of **1** in the crystal, projected along the *a*-axis. The two symmetry independent coordination chains are drawn in black and red, respectively. The acetonitrile solvent molecules are drawn in green. Hydrogen atoms are omitted for clarity. The crystal was twinned, and the twinning was described by a twofold rotation about the reciprocal *c*<sup>\*</sup>-axis. In the monoclinic crystal system, this is equivalent to a rotation about the *a*-axis in direct space. It can be seen that the twinning does not cause much disturbance of the packing.

**{[(TSMP)Cu]K}<sub>4</sub> (8)**. [C<sub>182</sub>H<sub>166</sub>Cu<sub>4</sub>K<sub>4</sub>N<sub>26</sub>P<sub>4</sub>][C<sub>172</sub>H<sub>156</sub>Cu<sub>4</sub>K<sub>4</sub>N<sub>24</sub>P<sub>4</sub>]·6C<sub>5</sub>H<sub>5</sub>N, Fw=6820.07, yellow block, 0.29×0.19×0.17 mm<sup>3</sup>, triclinic, P  $\bar{1}$  (no. 2), *a*=16.4610(6), *b*=20.7224(6), *c*=26.5518(7) Å,  $\alpha$ =78.716(1),  $\beta$ =75.774(1),  $\gamma$ =88.674(1)°, *V*=8606.7(4) Å<sup>3</sup>, *Z*=1, *D<sub>x</sub>*=1.316 g/cm<sup>3</sup>,  $\mu$ =0.68 mm<sup>-1</sup>. The diffraction experiment was performed on a Bruker Kappa ApexII diffractometer with sealed tube and Triumph monochromator ( $\lambda$ =0.71073 Å) at a temperature of 150(2) K up to a resolution of  $(\sin\theta/\lambda)_{\max}$ =0.65 Å<sup>-1</sup>. Intensity integration was performed with the Eval15 software.<sup>45</sup> A multi-scan absorption correction and scaling was performed with SADABS<sup>51</sup> (correction range 0.71-0.75). A total of 219470 reflections was measured, 39483 reflections were unique (*R*<sub>int</sub>=0.045), 26012 reflections were observed [*I*>2σ(*I*)]. The structure was solved with Patterson superposition methods using SHELXT.<sup>47</sup> Structure refinement was performed with SHELXL-2017<sup>48</sup> on *F*<sup>2</sup> of all reflections. Non-hydrogen atoms were refined freely with anisotropic displacement parameters. Six of the coordinated and non-coordinated pyridine molecules were refined with a disorder model. All hydrogen atoms were introduced in calculated positions and refined with a riding model. 2490 Parameters were refined with 4113 restraints (distances, angles, displacement parameters and molecular flatness of the pyridine molecules). *R*<sub>1</sub>/*wR*<sub>2</sub> [*I* > 2σ(*I*)]: 0.0587/0.1538. *R*<sub>1</sub>/*wR*<sub>2</sub> [all refl.]: 0.0964/0.1749. *S*=1.019. Residual electron density between -0.64 and 0.86 e/Å<sup>3</sup>. Geometry calculations and checking for higher symmetry was performed with the PLATON program.<sup>50</sup>

**Discussion:** Selected X-ray crystallographic distances and angles in complexes **8** (Tables 2.1 and 2.2).

Table 2.1. Selected distances (Å) and angles (°) in the X-ray crystal structure of complex **8**. The unit cell of **8** contains two independent  $\{[(\text{TSM})\text{Cu}]\text{K}\}_4$  molecules. Symmetry codes *i*: -x, -y, -z; *ii*: 1-x, 1-y, 1-z.

molecule 1		molecule 2	
Parameter	Value	Parameter	Value
Cu1-N11	2.000(3)	Cu3-N13	1.976(3)
Cu1-N21	1.960(3)	Cu3-N14 <sup>ii</sup>	1.940(2)
Cu1-N32	1.926(3)	Cu3-N23	1.991(3)
Cu2-N12	1.976(3)	Cu4-N24	1.967(3)
Cu2-N22	2.007(3)	Cu4-N33	1.920(2)
Cu2-N31 <sup>i</sup>	1.933(3)	Cu4-N34	2.004(3)
N11 <sup>i</sup> Cu1 <sup>i</sup> N21 (intracyclic)	99.68(10)	N13 <sup>i</sup> Cu3 <sup>i</sup> N23 (intracyclic)	100.62(10)
N11 <sup>i</sup> Cu1 <sup>i</sup> N32	125.74(11)	N13 <sup>i</sup> Cu3 <sup>i</sup> N14 <sup>ii</sup>	132.32(10)
N21 <sup>i</sup> Cu1 <sup>i</sup> N32	134.58(11)	N14 <sup>ii</sup> Cu3 <sup>i</sup> N23	126.60(11)
N12 <sup>i</sup> Cu2 <sup>i</sup> N22 (intracyclic)	99.26(11)	N24 <sup>i</sup> Cu4 <sup>i</sup> N34 (intracyclic)	99.02(11)
N12 <sup>i</sup> Cu2 <sup>i</sup> N31 <sup>i</sup>	136.95(12)	N24 <sup>i</sup> Cu4 <sup>i</sup> N33	133.92(11)
N22 <sup>i</sup> Cu2 <sup>i</sup> N31 <sup>i</sup>	123.61(11)	N33 <sup>i</sup> Cu4 <sup>i</sup> N34	126.85(11)
sum of angles around		sum of angles around	
copper: Cu(1)	360.00(18)	copper: Cu(3)	359.54(18)
Cu(2)	359.8(2)	Cu(4)	359.79(19)

Table 2.2. K...C distances indicating cation- $\pi$  interactions in **8**.

molecule 1		molecule 2	
Parameter	Value	Parameter	Value
K1...C61	3.139(6)	K3...C83	2.906(3)
K1...C51	3.156(5)	K3...C33	3.104(3)
K1...C22	3.225(4)	K3...C13	3.369(3)
K1...C32	3.345(4)	K3...C73	3.370(4)
K2...C152	3.329(4)	K3...C23	3.423(3)
K2...C142	3.358(5)	K4...C214	3.002(4)
		K4...C264	3.018(4)
		K4...C224	3.121(5)
		K4...C254	3.182(4)
		K4...C234	3.242(5)
		K4...C244	3.271(5)

**[(TSM)CuP(OEt)<sub>3</sub>][K(18-crown-6)·CH<sub>3</sub>CN] (9b)**.  $[\text{C}_{14}\text{H}_{27}\text{KNO}_6][\text{C}_{34}\text{H}_{39}\text{CuN}_3\text{O}_3\text{P}_2] \cdot \frac{1}{2}\text{C}_6\text{H}_6 \cdot \text{CH}_3\text{CN}$ , Fw=1087.73, colourless needle, 0.49×0.13×0.06 mm<sup>3</sup>, monoclinic, I2/a (no. 15), a=24.8978(5), b=13.9828(3), c=33.8978(7) Å,  $\beta=110.867(1)^\circ$ , V=11027.2(4) Å<sup>3</sup>, Z=8, D<sub>x</sub>=1.310 g/cm<sup>3</sup>,  $\mu=0.59$  mm<sup>-1</sup>. The diffraction experiment was performed on a Bruker Kappa ApexII diffractometer with sealed tube and Triumph monochromator ( $\lambda=0.71073$  Å) at a temperature of 150(2) K up to a resolution of  $(\sin\theta/\lambda)_{\text{max}}=0.65$  Å<sup>-1</sup>. Intensity integration was performed with the Eval15 software.<sup>45</sup> A multi-scan absorption correction and scaling was performed with SADABS<sup>51</sup> (correction range 0.63-0.75). A total of 108621 reflections was measured, 12649 reflections

were unique ( $R_{\text{int}}=0.049$ ), 9315 reflections were observed [ $I > 2\sigma(I)$ ]. The structure was solved with Patterson superposition methods using SHELXT.<sup>47</sup> Structure refinement was performed with SHELXL-2017<sup>48</sup> on  $F^2$  of all reflections. Non-hydrogen atoms were refined freely with anisotropic displacement parameters. The non-coordinated acetonitrile molecule was refined with a disorder model. All hydrogen atoms were introduced in calculated positions and refined with a riding model. 679 Parameters were refined with 111 restraints (distances, angles, displacement parameters and molecular flatness of the solvent molecules).  $R1/wR2$  [ $I > 2\sigma(I)$ ]: 0.0440/0.1222.  $R1/wR2$  [all refl.]: 0.0658/0.1358.  $S=1.034$ . Residual electron density between -0.65 and 1.05 e/Å<sup>3</sup>. Geometry calculations and checking for higher symmetry was performed with the PLATON program.<sup>50</sup>

**Discussion:** The crystal structure of **9b** is characterized by a [K(18-crown-6)(CH<sub>3</sub>CN)] cation and a [(TSM<sup>-</sup>P)CuP(OEt)<sub>3</sub>] anion. Further, there are non-coordinated benzene and acetonitrile molecules in the unit cell. Selected bond distances and angles are shown in *Table 2.3*.

*Table 2.3.* Selected distances (Å), angles and torsion angles (°) in the X-ray crystal structure of complex **9b**.

Parameter	Value
Cu1-N11	2.0759(19)
Cu1-N21	2.0654(19)
Cu2-N31	2.0622(19)
Cu1-P21	2.1201(6)
N11^Cu1^N21	95.06(7)
N21^Cu1^N31	92.38(8)
N11^Cu1^N31	94.54(7)
P21^Cu1^N11	123.28(6)
P21^Cu1^N21	121.85(6)
P21^Cu1^N31	121.97(5)
O11^P21^Cu1^N11	41.79(11)
angle sum O^P^O	300.37(16)

The packing of the molecules in the crystal leads to a layer structure with the layers stacked in *c*-direction and intercalated with solvent molecules. As a consequence, there are strong *pseudo*-translational effects (*Figure 2.9*) which are also visible in the X-ray diffraction pattern. Within the layers, intermolecular bonding is dominated by C-H... $\pi$  interactions between the crown ether in the cation and the indolide groups of the anion (*Figure 2.10*). The co-crystallized benzene is located on a twofold rotation axis in proximity of the K<sup>+</sup> center.

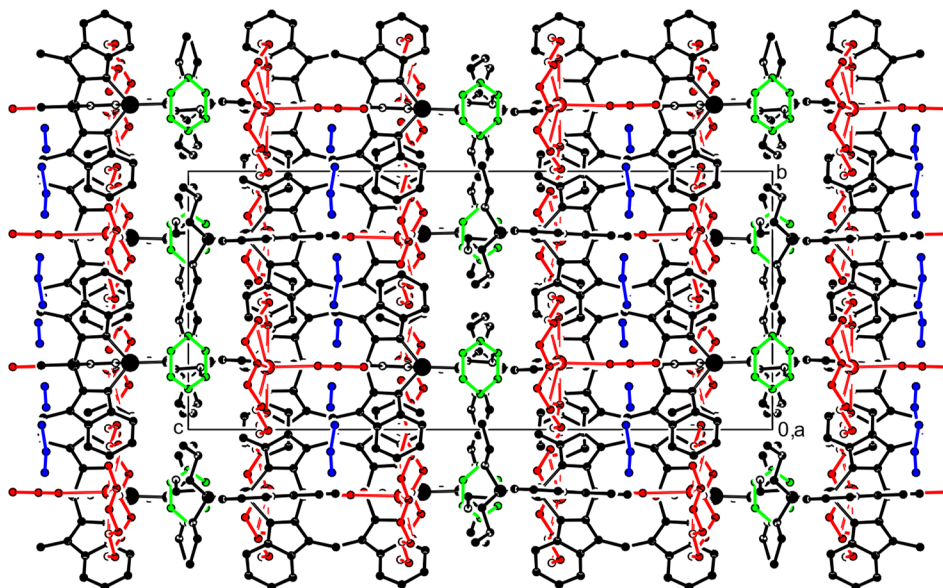


Figure 2.9. Packing of **9b** in the crystal. Projection along the *a*-axis. Cations are drawn in red, anions in black, benzene in green, and acetonitrile in blue. Only the major form of the disordered acetonitrile is shown. Hydrogen atoms are omitted for clarity. The structure has significant *pseudo*-translational symmetry in *c*-direction. Consequently, reflections with  $h=odd$  are weak.

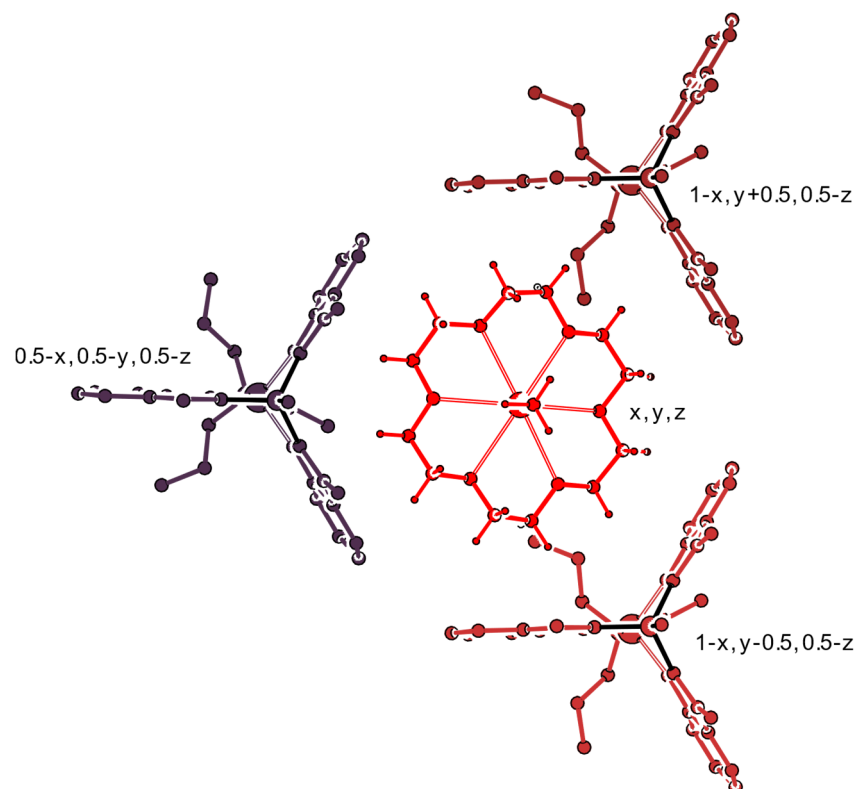


Figure 2.10. Intermolecular C-H... $\pi$  interactions in **9b** viewed along the *c*-axis. The H-atoms of the crown ether act as donors, and the  $\pi$ -systems of the indolide groups as acceptors. C-H... $\pi$  interactions between the methyl group of the coordinated acetonitrile and indolide are omitted for clarity.

**(TSMP)Fe(Py)<sub>3</sub> (10).** C<sub>43</sub>H<sub>39</sub>FeN<sub>6</sub>P + disordered solvent, Fw=726.62<sup>[\*]</sup>, yellow needle, 0.38×0.07×0.03 mm<sup>3</sup>, monoclinic, P2<sub>1</sub>/c (no. 14), a=24.456(3), b=18.0393(16), c=19.450(3) Å, β=113.125(7)°, V=7891.4(17) Å<sup>3</sup>, Z=8, D<sub>x</sub>=1.223 g/cm<sup>3</sup><sup>[\*]</sup>, μ=0.46 mm<sup>-1</sup><sup>[\*]</sup>. The diffraction experiment was performed on a Bruker Kappa ApexII diffractometer with sealed tube and Triumph monochromator (λ=0.71073 Å) at a temperature of 150(2) K up to a resolution of (sinθ/λ)<sub>max</sub>=0.61 Å<sup>-1</sup>. The Eval15 software<sup>45</sup> was used for the intensity integration of this weakly diffracting crystal. A large anisotropic mosaicity<sup>52</sup> of 2.5° about hkl=(0,1,0) was used for the prediction of the reflection profiles. A numerical absorption correction and scaling was performed with SADABS<sup>51</sup> (correction range 0.65-1.00). A total of 55335 reflections was measured, 14669 reflections were unique (R<sub>int</sub>=0.159), 6802 reflections were observed [I>2σ(I)]. The structure was solved with Patterson superposition methods using SHELXT.<sup>47</sup> Structure refinement was performed with SHELXL-2018<sup>48</sup> on F<sup>2</sup> of all reflections. The crystal structure contains large voids (1106 Å<sup>3</sup>/unit cell) filled with disordered solvent molecules. Their contribution to the structure factors was secured by back-Fourier transformation with the SQUEEZE algorithm<sup>53</sup> resulting in 305 electrons/unit cell. Non-hydrogen atoms were refined freely with anisotropic displacement parameters. All hydrogen atoms were introduced in calculated positions and refined with a riding model. 927 Parameters were refined with no restraints. R1/wR2 [I>2σ(I)]: 0.0891/0.1954. R1/wR2 [all refl.]: 0.1942/0.2417. S=1.030. Residual electron density between -0.56 and 0.65 e/Å<sup>3</sup>. Geometry calculations and checking for higher symmetry was performed with the PLATON program.<sup>50</sup>

Discussion: see below in comparison with **11**.

**(TSMP)Ni(Py)<sub>3</sub> (11).** C<sub>43</sub>H<sub>39</sub>N<sub>6</sub>NiP·0.3C<sub>6</sub>H<sub>14</sub>, Fw=755.33, green needle, 0.32×0.08×0.05 mm<sup>3</sup>, monoclinic, P2<sub>1</sub>/c (no. 14), a=24.314(3), b=17.888(2), c=19.297(2) Å, β=113.027(3)°, V=7724.1(15) Å<sup>3</sup>, Z=8, D<sub>x</sub>=1.299 g/cm<sup>3</sup>, μ=0.58 mm<sup>-1</sup>. The diffraction experiment was performed on a Bruker Kappa ApexII diffractometer with sealed tube and Triumph monochromator (λ=0.71073 Å) at a temperature of 150(2) K up to a resolution of (sinθ/λ)<sub>max</sub>=0.56 Å<sup>-1</sup>. The Saint software<sup>54</sup> was used for the intensity integration. A numerical absorption correction and scaling was performed with SADABS<sup>51</sup> (correction range 0.82-1.00). A total of 66286 reflections was measured, 11139 reflections were unique (R<sub>int</sub>=0.221), 5916 reflections were observed [I>2σ(I)]. The structure was solved with Patterson superposition methods using SHELXT.<sup>47</sup> Structure refinement was performed with SHELXL-2018<sup>48</sup> on F<sup>2</sup> of all reflections. Non-hydrogen atoms were refined freely with anisotropic displacement parameters. The *n*-hexane solvent molecule was refined with partial occupancy. All hydrogen atoms were introduced in calculated positions and refined with a riding model. The crystal appeared to be twinned by *pseudo*-merohedry (*pseudo*-orthorhombic C-centered twin cell). The twin operation is a twofold rotation about hkl=(1,0,0) and the corresponding twin matrix (-1,0,-1/0,-1,0/0,0,1) was included in the refinement. 982 Parameters were refined with 1829 restraints (distances, angles and displacement parameters for all atoms except Ni and P). R1/wR2 [I>2σ(I)]: 0.0877/0.1806. R1/wR2 [all refl.]: 0.1954/0.2320. S=1.034. Twin fraction BASF=0.2361(18). Residual electron density between -0.86 and 1.27 e/Å<sup>3</sup>. Geometry calculations and checking for higher symmetry was performed with the PLATON program.<sup>50</sup>

Discussion: X-ray crystal structure determinations of **10** and **11** reveal that the two compounds are isostructural in the solid state. The asymmetric unit contains two independent metal complex

---

[\*] Derived values do not contain the contribution of the disordered solvent molecules.

molecules. They are related by a non-crystallographic twofold rotation approximately about  $uvw=[0,0,1]$ . This operation is not compatible with the monoclinic crystal system but might be the structural basis for twinning. Twinning was indeed found in the crystal of **11** (see Experimental Section) and was described by a twofold rotation about  $hkl=(1,0,0)$ . In the monoclinic case this equivalent to a rotation about  $uvw=[0,0,1]$ .

The large standard uncertainties make a discussion of the geometric parameters difficult (Table 2.4). The longest M-N distances are found for M1-N34 (molecule 1) and M2-N38 (molecule 2). The Ni-N<sup>TSMF</sup> distances are 0.05 Å shorter than Fe-N<sup>TSMF</sup>, and Ni-N<sup>pyridine</sup> are 0.11 Å shorter than Fe-N<sup>pyridine</sup>.

Table 2.4. Selected XRD distances (Å) and angles (°) for complexes **10** and **11**.

molecule 1			molecule 2		
Parameter	Value		Parameter	Value	
	M=Fe (10)	M=Ni (11)		M=Fe (10)	M=Ni (11)
M1-N11 <sup>L</sup>	2.175(6)	2.127(7)	M2-N15 <sup>L</sup>	2.176(6)	2.123(7)
M1-N12 <sup>L</sup>	2.173(6)	2.115(7)	M2-N16 <sup>L</sup>	2.158(6)	2.102(7)
M1-N13 <sup>L</sup>	2.168(6)	2.138(7)	M2-N17 <sup>L</sup>	2.201(6)	2.148(7)
M1-N14 <sup>Py</sup>	2.272(7)	2.168(7)	M2-N18 <sup>Py</sup>	2.261(7)	2.163(8)
M1-N24 <sup>Py</sup>	2.294(6)	2.178(7)	M2-N28 <sup>Py</sup>	2.284(6)	2.164(7)
M1-N34 <sup>Py</sup>	2.351(6)	2.241(8)	M2-N38 <sup>Py</sup>	2.342(6)	2.234(7)
N11 <sup>L</sup> ∧M1∧N12 <sup>L</sup>	89.5(2)	88.7(3)	N15 <sup>L</sup> ∧M2∧N16 <sup>L</sup>	89.7(2)	89.3(3)
N12 <sup>L</sup> ∧M1∧N13 <sup>L</sup>	91.3(2)	90.4(3)	N16 <sup>L</sup> ∧M2∧N17 <sup>L</sup>	91.6(2)	89.9(3)
N11 <sup>L</sup> ∧M1∧N13 <sup>L</sup>	89.9(2)	89.8(3)	N15 <sup>L</sup> ∧M2∧N17 <sup>L</sup>	89.8(2)	89.2(3)
N14 <sup>Py</sup> ∧M1∧N24 <sup>Py</sup>	90.5(3)	91.2(3)	N18 <sup>Py</sup> ∧M2∧N28 <sup>Py</sup>	89.4(2)	90.1(3)
N24 <sup>Py</sup> ∧M1∧N34 <sup>Py</sup>	89.7(2)	91.4(3)	N28 <sup>Py</sup> ∧M2∧N38 <sup>Py</sup>	91.1(2)	92.5(3)
N14 <sup>Py</sup> ∧M1∧N34 <sup>Py</sup>	88.9(2)	89.8(3)	N18 <sup>Py</sup> ∧M2∧N38 <sup>Py</sup>	90.7(2)	91.9(3)
N11 <sup>L</sup> ∧M1∧N24 <sup>Py</sup>			N15 <sup>L</sup> ∧M2∧N28 <sup>Py</sup>		
(trans)	175.1(2)	174.8(3)	(trans)	175.2(2)	176.3(3)
N12 <sup>L</sup> ∧M1∧N14 <sup>Py</sup>			N16 <sup>L</sup> ∧M2∧N18 <sup>Py</sup>		
(trans)	177.7(2)	177.0(4)	(trans)	176.1(2)	176.0(3)
N13 <sup>L</sup> ∧M1∧N34 <sup>Py</sup>			N17 <sup>L</sup> ∧M2∧N38 <sup>Py</sup>		
(trans)	174.4(2)	174.6(3)	(trans)	173.5(2)	174.1(3)

**[(TSMF)<sub>2</sub>Fe][K(benzo-15-crown-5)<sub>2</sub>]** (**12b**). [C<sub>28</sub>H<sub>40</sub>KO<sub>10</sub>]<sub>2</sub>[C<sub>56</sub>H<sub>48</sub>FeN<sub>6</sub>P<sub>2</sub>]·½C<sub>7</sub>H<sub>8</sub>·½C<sub>4</sub>H<sub>10</sub>O·CH<sub>3</sub>CN, Fw=2198.37, yellow block, 0.37×0.10×0.03 mm<sup>3</sup>, triclinic, P  $\bar{1}$  (no. 2), a=17.8742(12), b=18.1808(12), c=19.8655(13) Å, α=109.771(3), β=108.424(2), γ=95.566(1)°, V=5611.4(7) Å<sup>3</sup>, Z=2, D<sub>x</sub>=1.301 g/cm<sup>3</sup>, μ=0.31 mm<sup>-1</sup>. The diffraction experiment was performed on a Bruker Kappa ApexII diffractometer with sealed tube and Triumph monochromator (λ=0.71073 Å) at a temperature of 150(2) K up to a resolution of (sinθ/λ)<sub>max</sub>=0.61 Å<sup>-1</sup>. Intensity integration was performed with the Eval15 software.<sup>45</sup> A multi-scan absorption correction and scaling was performed with SADABS<sup>51</sup> (correction range 0.65-0.75). A total of 83986 reflections was measured, 20904 reflections were unique (R<sub>int</sub>=0.088), 11765 reflections were observed [I>2σ(I)]. The structure was solved with Patterson superposition methods using SHELXT.<sup>47</sup> Structure refinement was performed with SHELXL-2016<sup>48</sup> on F<sup>2</sup> of all reflections. Non-hydrogen atoms were refined freely with anisotropic displacement parameters. The toluene and diethyl ether molecules were disordered on inversion

centers, respectively. All hydrogen atoms were introduced in calculated positions and refined with a riding model. 1426 Parameters were refined with 168 restraints (concerning the disordered solvent molecules). R1/wR2 [ $I > 2\sigma(I)$ ]: 0.0641/0.1423. R1/wR2 [all refl.]: 0.1356/0.1715. S=1.017. Residual electron density between -0.44 and 1.26 e/Å<sup>3</sup>. Geometry calculations and checking for higher symmetry was performed with the PLATON program.<sup>50</sup>

*Discussion:* Selected X-ray crystallographic details for complex **12b** (Table 2.5).

Table 2.5. Selected distances (Å) and angles (°) in the X-ray crystal structure of complex **12b**.

Parameter	Value
Fe1-N11	2.017(3)
Fe1-N12	2.028(3)
Fe1-N21	2.019(3)
Fe1-N22	2.028(3)
N11 <sup>^</sup> Fe1 <sup>^</sup> N21 (endocyclic)	96.78(13)
N12 <sup>^</sup> Fe1 <sup>^</sup> N22 (endocyclic)	96.35(13)
N11 <sup>^</sup> Fe1 <sup>^</sup> N12 (exocyclic)	118.90(13)
N21 <sup>^</sup> Fe1 <sup>^</sup> N22 (exocyclic)	119.68(13)

## 2.6 References

- (1) The following review and references therein: Trofimenko, S. Recent Advances in Poly(Pyrazolyl)Borate (Scorpionate) Chemistry. *Chem. Rev.* **1993**, *93* (3), 943–980. DOI: 10.1021/cr00019a006.
- (2) (a) Trofimenko, S. Introduction. In *Scorpionates*; Imperial College Press: London, 1999; pp 1–25. DOI: 10.1142/9781848160422\_0001. (b) Pettinari, C.; Santini, C. Polypyrazolylborate and Scorpionate Ligands. In *Comprehensive Coordination Chemistry II: From Biology to Nanotechnology. Volume 1: Fundamentals: Ligands, Complexes, Synthesis, Purification, and Structure*; Lever, A. B. P., McCleverty, J. A., Meyer, T. J., Eds.; Elsevier Pergamon: Amsterdam; Boston, 2004; pp 159–210.
- (3) Janiak, C. (Organo)Thallium (I) and (II) Chemistry: Syntheses, Structures, Properties and Applications of Subvalent Thallium Complexes with Alkyl, Cyclopentadienyl, Arene or Hydrotris(Pyrazolyl)Borate Ligands. *Coord. Chem. Rev.* **1997**, *163*, 107–216. DOI: 10.1016/S0010-8545(97)00011-8.
- (4) The following reviews and references therein: (a) Santini, C.; Pellei, M.; Lobbia, G. G.; Papini, G. Synthesis and Properties of Poly(Pyrazolyl)Borate and Related Boron-Centered Scorpionate Ligands. Part A: Pyrazole-Based Systems. *Mini-Rev. Org. Chem* **2010**, *7* (2), 84–124. DOI: 10.2174/157019310791065519. (b) Pellei, M.; Santini, C. *Biomimetic Based Applications*; George, A., Ed.; InTech, 2011. DOI: 10.5772/2237.
- (5) (a) The following review and references therein: Slugovc, C.; Schmid, R.; Kirchner, K. Hydridotris(Pyrazolyl)Borate Ruthenium Complexes—Properties and Applications. *Coord. Chem. Rev.* **1999**, *185–186*, 109–126. DOI: 10.1016/S0010-8545(98)00251-3. (b) Díaz-Requejo, M. M.; Belderrain, T. R.; Trofimenko, S.; Pérez, P. J. Unprecedented Highly Cis -Diastereoselective Olefin Cyclopropanation Using Copper Homoscorpionate Catalysts. *J. Am. Chem. Soc.* **2001**, *123* (13), 3167–3168. DOI: 10.1021/ja0155736. (c) Díaz-Requejo, M. M.; Belderrain, T. R.; Pérez, P. J. Polypyrazolylborate Copper(i) Complexes as Catalysts of the Homogeneous and Heterogeneous Styrene Epoxidation Reaction. *Chem. Commun.* **2000**, No. 19, 1853–1854. DOI: 10.1039/B004806M. (d) Morilla, M. E.; Díaz-Requejo, M. M.; Belderrain, T. R.; Nicasio, M. C.; Trofimenko, S.; Pérez, P. J. Catalytic Insertion of Diazo Compounds into N–H Bonds: The Copper Alternative. *Chem. Commun.* **2002**, No. 24, 2998–2999. DOI: 10.1039/B207389G. (e) Milione, S.; Montefusco, C.; Cuenca, T.; Grassi, A. Cationic Benzyl Zirconium Heteroscorpionates: Synthesis and Characterization of a Novel Ethylene Polymerisation Catalyst Showing an Unusual Temperature Dependent Polymerisation Mechanism. *Chem. Commun.* **2003**, No. 10, 1176–1177. DOI: 10.1039/B301997G. (f) Dias, H. V. R.; Wu, J. Thermally Stable Gold(I) Ethylene Adducts: [(HB{3,5-(CF<sub>3</sub>)<sub>2</sub>Pz}<sub>3</sub>)Au(CH<sub>2</sub>=CH<sub>2</sub>)] and [(HB{3-(CF<sub>3</sub>),5-(Ph)Pz}<sub>3</sub>)Au(CH<sub>2</sub>=CH<sub>2</sub>)]. *Angew. Chem. Int. Ed.* **2007**, *46* (41), 7814–7816. DOI: 10.1002/anie.200703328.
- (6) For example: (a) Silva, R. M.; Gwengo, C.; Lindeman, S. V.; Smith, M. D.; Gardinier, J. R. Janus Scorpionates: Supramolecular Tectons for the Directed Assembly of Hard–Soft Alkali Metallopolymer Chains. *Inorg. Chem.* **2006**, *45* (26), 10998–11007. DOI: 10.1021/ic0615877. (b) Zhai, B.; Shen, W.-Z.; Chen, X.-Y.; Song, H.-B.; Shi, W.; Cheng, P. Terminal Ligand Effect on the Structure Variation of Copper(II) Complexes. *Inorg. Chem. Commun.* **2006**, *9* (12), 1293–1296. DOI: 10.1016/j.inoche.2006.08.002. (c) McCleverty, J. A.; Ward, M. D. The Role of Bridging Ligands in Controlling Electronic and Magnetic Properties in Polynuclear Complexes. *Acc. Chem. Res.* **1998**, *31* (12), 842–851. DOI: 10.1021/ar970315s. (d) Janiak, C.; Scharmann, T. G.; Albrecht, P.; Marlow, F.; Macdonald, R. [Hydrotris(1,2,4-Triazolyl)Borate]Silver(I): Structure and Optical Properties of a Coordination Polymer Constructed from a Modified Poly(Pyrazolyl)Borate Ligand. *J. Am. Chem. Soc.* **1996**, *118* (26), 6307–6308. DOI: 10.1021/ja960530o.
- (7) The following review and references therein: Martini, P.; Pasquali, M.; Boschi, A.; Uccelli, L.; Giganti, M.; Duatti, A. Technetium Complexes and Radiopharmaceuticals with Scorpionate Ligands. *Molecules* **2018**, *23* (8), 2039. DOI: 10.3390/molecules23082039.
- (8) For example: (a) Tazelaar, C. G. J.; Nicolas, E.; van Dijk, T.; Broere, D. L. J.; Cardol, M.; Lutz, M.; Gudat, D.; Slootweg, J. C.; Lammertsma, K. Tris(Pyrazolyl)Phosphines with Copper(I): From Monomers to Polymers. *Dalton Trans.* **2016**, *45* (5), 2237–2249. DOI: 10.1039/C5DT03994K. (b) Bittner, M. M.; Lindeman, S. V.; Popescu, C. V.; Fiedler, A. T. Dioxygen Reactivity of



- Biomimetic Fe(II) Complexes with Noninnocent Catecholate, *o*-Aminophenolate, and *o*-Phenylenediamine Ligands. *Inorg. Chem.* **2014**, *53* (8), 4047–4061. DOI: 10.1021/ic403126p. (c) Fischer, A. A.; Miller, J. R.; Jodts, R. J.; Ekanayake, D. M.; Lindeman, S. V.; Brunold, T. C.; Fiedler, A. T. Spectroscopic and Computational Comparisons of Thiolate-Ligated Ferric Nonheme Complexes to Cysteine Dioxygenase: Second-Sphere Effects on Substrate (Analogue) Positioning. *Inorg. Chem.* **2019**, *58* (24), 16487–16499. DOI: 10.1021/acs.inorgchem.9b02432. (d) Fischer, A. A.; Stracey, N.; Lindeman, S. V.; Brunold, T. C.; Fiedler, A. T. Synthesis, X-Ray Structures, Electronic Properties, and O<sub>2</sub>/NO Reactivities of Thiol Dioxygenase Active-Site Models. *Inorg. Chem.* **2016**, *55* (22), 11839–11853. DOI: 10.1021/acs.inorgchem.6b01931.
- (9) For example: (a) Szczepura, L. F.; Witham, L. M.; Takeuchi, K. J. Tris(2-Pyridyl) Tripod Ligands. *Coord. Chem. Rev.* **1998**, *174* (1), 5–32. DOI: 10.1016/S0010-8545(98)00122-2. (b) Gneuß, T.; Leidl, M. J.; Finger, L. H.; Rau, N.; Yersin, H.; Sundermeyer, J. A New Class of Luminescent Cu(I) Complexes with Tripodal Ligands – TADF Emitters for the Yellow to Red Color Range. *Dalton Trans.* **2015**, *44* (18), 8506–8520. DOI: 10.1039/C4DT02631D.
- (10) The following review and references therein: Papish, E. T.; Dixon, N. A.; Kumar, M. Biomimetic Chemistry with Tris(Triazolyl)Borate Ligands: Unique Structures and Reactivity via Interactions with the Remote Nitrogens. In *Molecular Design in Inorganic Biochemistry. Structure and Bonding, vol 160.*; Rabinovich, D., Ed.; Springer: Berlin, Heidelberg, 2013; pp 115–150. DOI: 10.1007/430\_2012\_86.
- (11) For example: (a) Sazama, G. T.; Betley, T. A. Ligand-Centered Redox Activity: Redox Properties of 3d Transition Metal Ions Ligated by the Weak-Field Tris(Pyrrrolyl)Ethane Trianion. *Inorg. Chem.* **2010**, *49* (5), 2512–2524. DOI: 10.1021/ic100028y. (b) Barnard, T. S.; Mason, M. R. Synthesis, Structure, and Coordination Chemistry of the Bicyclic  $\pi$ -Acid Phosphatri(3-Methylindolyl)Methane. *Organometallics* **2001**, *20* (1), 206–214. DOI: 10.1021/om000793y.
- (12) For example: (a) Garner, M.; Reglinski, J.; Cassidy, I.; Spicer, M. D.; Kennedy, A. R. Hydrotris(Methimazolyl)Borate, a Soft Analogue of Hydrotris(Pyrazolyl)Borate. Preparation and Crystal Structure of a Novel Zinc Complex. *Chem. Commun.* **1996**, *355* (16), 1975–1976. DOI: 10.1039/CC9960001975. (b) Reglinski, J.; Garner, M.; Cassidy, I. D.; Slavin, P. A.; Spicer, M. D.; Armstrong, D. R. Sodium Hydrotris(Methimazolyl)Borate, a Novel Soft, Tridentate Ligand: Preparation, Structure and Comparisons with Sodium Hydrotris(Pyrazolyl)Borate. *J. Chem. Soc. Dalt. Trans.* **1999**, No. 13, 2119–2126. DOI: 10.1039/A901703H.
- (13) For example: Dunne, J. F.; Su, J.; Ellern, A.; Sadow, A. D. A New Scorpionate Ligand: Tris(4,4-Dimethyl-2-Oxazoliny)Borate and Its Zirconium(IV) Complexes. *Organometallics* **2008**, *27* (11), 2399–2401. DOI: 10.1021/om800252p.
- (14) For example: Hu, X.; Tang, Y.; Gantzel, P.; Meyer, K. Silver Complexes of a Novel Tripodal N-Heterocyclic Carbene Ligand: Evidence for Significant Metal–Carbene  $\pi$ -Interaction. *Organometallics* **2003**, *22* (4), 612–614. DOI: 10.1021/om020935j.
- (15) For example: (a) Sargent, A. L.; Titus, E. P.; Riordan, C. G.; Rheingold, A. L.; Ge, P. Poly(2-Thienyl)Borates: An Investigation into the Coordination of Thiophene and Its Derivatives. *Inorg. Chem.* **1996**, *35* (24), 7095–7101. DOI: 10.1021/ic960703a. (b) Shapiro, I. R.; Jenkins, D. M.; Thomas, J. C.; Day, M. W.; Peters, J. C. A Homoleptic Phosphine Adduct of Tl(I). *Chem. Commun.* **2001**, *5652* (20), 2152–2153. DOI: 10.1039/b104447h.
- (16) For example: (a) Pullen, E. E.; Rheingold, A. L.; Rabinovich, D. Methyltris(Pyrazolyl)Silanes: New Tripodal Nitrogen-Donor Ligands. *Inorg. Chem. Commun.* **1999**, *2* (5), 194–196. DOI: 10.1016/S1387-7003(99)00046-5. (b) Blackwell III, W. C.; Bunich, D.; Concolino, T. E.; Rheingold, A. L.; Rabinovich, D. Synthesis and Structure of  $\{\eta^3\text{-MeSi}(\text{CH}_2\text{SPh})_3\}\text{Cr}(\text{CO})_3$ : How Long Can a Cr(0)–S(Thioether) Bond Length Be? *Inorg. Chem. Commun.* **2000**, *3* (6), 325–327. DOI: 10.1016/S1387-7003(00)00079-4. (c) Neumeyer, F.; Lipschutz, M. I.; Tilley, T. D. Group 8 Transition Metal Complexes of the Tripodal Triphosphino Ligands  $\text{PhSi}(\text{CH}_2\text{PR}_2)_3$  (R = Ph, IPr). *Eur. J. Inorg. Chem.* **2013**, *2013* (36), 6075–6078. DOI: 10.1002/ejic.201301074.
- (17) Sorrell, T. N.; Allen, W. E.; White, P. S. Sterically Hindered [Tris(Imidazolyl)Phosphine]Copper Complexes: Formation and Reactivity of a Peroxo-Dicopper(II) Adduct and Structure of a Dinuclear Carbonate-Bridged Complex. *Inorg. Chem.* **1995**, *34* (4), 952–960. DOI: 10.1021/ic00108a030.
- (18) Su, W.-J.; Liang, L.-C. Elusive Scorpionates: C<sub>3</sub>-Symmetric, Formally Dianionic, Facially

- Tridentate Ligands. *Inorg. Chem.* **2018**, *57* (2), 553–556. DOI: 10.1021/acs.inorgchem.7b02884.
- (19) Joshi, V. S.; Kale, V. K.; Sathe, K. M.; Sarkar, A.; Tavale, S. S.; Suresh, C. G. Synthesis and Structure of New Molybdenum  $\pi$ -Allyl Complexes: Unexpected Hydrolysis of Tris(3,5-Dimethyl-1-Pyrazolyl)Phosphine Oxide. *Organometallics* **1991**, *10* (8), 2898–2902. DOI: 10.1021/om00054a067.
- (20) The following review and references therein: Simmonds, H. R.; Wright, D. S. Main Group Pyridyl-Based Ligands; Strategies to Mixed Metal Complexes. *Chem. Commun.* **2012**, *48* (69), 8617–8624. DOI: 10.1039/C2CC33015F.
- (21) Frazer, A.; Piggott, B.; Harman, M.; Mazid, M.; Hursthouse, M. B. Syntheses and X-Ray Crystal Structures of [Bis{(3,5-Dimethylpyrazolyl)3hydridoborato}In]I and [Bis{(Pyrazolyl)3methylgallato}In][InL<sub>4</sub>]. *Polyhedron* **1992**, *11* (23), 3013–3017. DOI: 10.1016/S0277-5387(00)80169-2.
- (22) The following review and references therein: Kuzu, I.; Krummenacher, I.; Meyer, J.; Armbruster, F.; Breher, F. Multidentate Ligand Systems Featuring Dual Functionality. *Dalton Trans.* **2008**, *35* (43), 5836–5865. DOI: 10.1039/B808347A.
- (23) Armbruster, F.; Fernández, I.; Breher, F. Syntheses, Structures, and Reactivity of Poly(Pyrazolyl)Silanes, -Disilanes, and the Ambidentate  $\kappa^1\text{Si}/\kappa^3\text{N}$ -Coordinating Tris(3,5-Dimethylpyrazolyl)Silanide Ligand [Si(3,5-Me<sub>2</sub>pz)<sub>3</sub>]<sup>-</sup> (MeTpsd). *Dalton Trans.* **2009**, No. 29, 5612–5626. DOI: 10.1039/B906333A.
- (24) Steiner, A.; Stalke, D. Poly(Pyrazolyl)Germanium(II) and -Tin(II) Derivatives-Tuneable Monoanionic Ligands and Dinuclear Cationic Cages. *Inorg. Chem.* **1995**, *34* (19), 4846–4853. DOI: 10.1021/ic00123a020.
- (25) (a) Nishiura, T.; Takabatake, A.; Okutsu, M.; Nakazawa, J.; Hikichi, S. Heteroleptic Cobalt(III) Acetylacetonato Complexes with N-Heterocyclic Carbene-Donating Scorpionate Ligands: Synthesis, Structural Characterization and Catalysis. *Dalton Trans.* **2019**, *48* (8), 2564–2568. DOI: 10.1039/C8DT04469D. (b) Scepianiak, J. J.; Vogel, C. S.; Khusniyarov, M. M.; Heinemann, F. W.; Meyer, K.; Smith, J. M. Synthesis, Structure, and Reactivity of an Iron(V) Nitride. *Science* **2011**, *331* (6020), 1049–1052. DOI: 10.1126/science.1198315. (c) Mandimutsira, B. S.; Yamarik, J. L.; Brunold, T. C.; Gu, W.; Cramer, S. P.; Riordan, C. G. Dioxygen Activation by a Nickel Thioether Complex: Characterization of a Ni<sup>III</sup><sub>2</sub>( $\mu$ -O)<sub>2</sub> Core. *J. Am. Chem. Soc.* **2001**, *123* (37), 9194–9195. DOI: 10.1021/ja016209+. (d) Stubbs, A. W.; Dincă, M. Selective Oxidation of C–H Bonds through a Manganese(III) Hydroperoxo in Mn<sup>II</sup>-Exchanged CFA-1. *Inorg. Chem.* **2019**, *58* (19), 13221–13228. DOI: 10.1021/acs.inorgchem.9b02068.
- (26) Martin-Mothes, E.; Puig, E.; Vendier, L.; Bijani, C.; Grellier, M.; Bontemps, S.; Martin-Mothes, E., Puig, E., Vendier, L., Bijani, C., Grellier, M., & Bontemps, S. Ortho-Phenyl Dialkylphosphonium Sulfonate Compounds: Two Rotamers in Equilibrium. *Dalton Trans.* **2018**, *47* (30), 10139–10146. DOI: 10.1039/C8DT02400F.
- (27) MestReNova v.9.0.1-13254. Mestrelab Research S.L. 2014.
- (28) Wittig, G.; Schöllkopf, U. Über Triphenyl-Phosphin-Methylene Als Olefinbildende Reagenzien (I. Mitteil.). *Chem. Ber.* **1954**, *87* (9), 1318–1330. DOI: 10.1002/cber.19540870919.
- (29) Wittig, G.; Rieber, M. Darstellung Und Eigenschaften Des Pentaphenyl-Phosphors. *Justus Liebigs Ann. Chem.* **1949**, *562* (3), 187–192. DOI: 10.1002/jlac.19495620304.
- (30) (a) Schmidbaur, H.; Stühler, H. Tetramethyl(Methoxy)Phosphoranes and Related Compounds. *Angew. Chem. Int. Ed.* **1972**, *11* (2), 145–146. DOI: 10.1002/anie.197201451. (b) Schmidbaur, H.; Buchner, W.; Koehler, F. H. Carbon-13 and Phosphorus-31 Study of Tetramethylmethoxyphosphoranes. *J. Am. Chem. Soc.* **1974**, *96* (19), 6208–6210. DOI: 10.1021/ja00826a056.
- (31) Nesmeyanov, N. A. A.; Rebrova, O. A.; Mikul'shina, V. V.; Petrovsky, P. V.; Robas, V. I.; Reutov, O. A. Interaction of Lithium Alkylamides or Lithium Dialkylamides with Tetraphenylphosphonium Chloride Reaction Course as a Function of Reaction Conditions and Dialkylamide Structures. *J. Organomet. Chem.* **1976**, *110* (1), 49–57. DOI: 10.1016/S0022-328X(00)90157-8.
- (32) Davidson, M. G.; Lamb, S. The First Structural Characterization of a Phosphonium Amide: Synthesis, Isolation and Molecular Structure of (Ph<sub>3</sub>PET)<sup>+</sup>(NPh<sub>2</sub>)<sup>-</sup>. *Polyhedron* **1997**, *16* (24), 4393–4395. DOI: 10.1016/S0277-5387(97)00202-7.

- (33) Davidson, M. G. Protonation of an Ylide Leads to a Unique C–H···O Hydrogen-Bonded Dimer: The First Synthesis, Isolation and X-Ray Structural Characterisation of a Phosphonium Aryloxide. *J. Chem. Soc., Chem. Commun.* **1995**, No. 9, 919–920. DOI: 10.1039/C39950000919.
- (34) (a) Haldón, E.; Delgado-Rebollo, M.; Prieto, A.; Álvarez, E.; Maya, C.; Nicasio, M. C.; Pérez, P. J. Synthesis, Structural Characterization, Reactivity, and Catalytic Properties of Copper(I) Complexes with a Series of Tetradentate Tripodal Tris(Pyrazolylmethyl)Amine Ligands. *Inorg. Chem.* **2014**, *53* (8), 4192–4201. DOI: 10.1021/ic500311y. (b) Carrier, S. M.; Ruggiero, C. E.; Houser, R. P.; Tolman, W. B. Synthesis, Structural Characterization, and Electrochemical Behavior of Copper(I) Complexes of Sterically Hindered Tris(3-Tert-Butyl- and 3,5-Diphenylpyrazolyl)Hydroborate Ligands. *Inorg. Chem.* **1993**, *32* (22), 4889–4899. DOI: 10.1021/ic00074a039.
- (35) Robinson, K.; Gibbs, G. V.; Ribbe, P. H. Quadratic Elongation: A Quantitative Measure of Distortion in Coordination Polyhedra. *Science* **1971**, *172* (3983), 567–570. DOI: 10.1126/science.172.3983.567.
- (36) (a) Mothes, R.; Ruffer, T.; Shen, Y.; Jakob, A.; Walfort, B.; Petzold, H.; Schulz, S. E.; Ecke, R.; Gessner, T.; Lang, H. Phosphite Copper(i) Trifluoroacetates  $[(\text{RO})_3\text{P}]_m\text{CuO}_2\text{CCF}_3$  ( $m = 1, 2, 3$ ): Synthesis, Solid State Structures and Their Potential Use as CVD Precursors. *Dalton Trans.* **2010**, *39* (46), 11235–11247. DOI: 10.1039/C0DT00347F. (b) Krummenacher, I.; Rügger, H.; Breher, F. Coinage Metal Complexes of Tris(Pyrazolyl)Methanide  $[\text{C}(3,5\text{-Me}_2\text{pz})_3]^-$ :  $\kappa^3$ -Coordination vs. Backbone Functionalisation. *Dalt. Trans.* **2006**, No. 8, 1073–1081. DOI: 10.1039/B512309G.
- (37) Doedens, R. J.; Dahl, L. F. Structure of the Hexapyridineiron (II) Salt of the Tetranuclear Iron Carbonyl Anion,  $[\text{Fe}_4(\text{CO})_{13}]^{-2}$ , with Comments Concerning the Nonisolation of the Corresponding Neutral Tetranuclear Iron Carbonyl,  $\text{Fe}_4(\text{CO})_{14}$ . *J. Am. Chem. Soc.* **1966**, *88* (21), 4847–4855. DOI: 10.1021/ja00973a018.
- (38) (a) Oliver, J. D.; Mullica, D. F.; Hutchinson, B. B.; Milligan, W. O. Iron-Nitrogen Bond Lengths in Low-Spin and High-Spin Iron(II) Complexes with Poly(Pyrazolyl)Borate Ligands. *Inorg. Chem.* **1980**, *19* (1), 165–169. DOI: 10.1021/ic50203a034. (b) Michaud, A.; Fontaine, F.-G.; Zargarian, D. Synthesis and Structural Characterization of Bis- and Tris(3,5-Dimethylpyrazolyl)Methane Complexes of  $\text{Ni}(\text{NO}_3)_2$ . *Inorganica Chim. Acta* **2006**, *359* (9), 2592–2598. DOI: 10.1016/j.ica.2005.09.046. (c) Wanke, R.; Guedes Da Silva, M. F. C.; Lancianesi, S.; Silva, T. F. S.; Martins, L. M. D. R. S.; Pettinari, C.; Pombeiro, A. J. L. Synthesis and Coordination Chemistry of a New N<sub>4</sub>-Polydentate Class of Pyridyl-Functionalized Scorpionate Ligands: Complexes of  $\text{Fe}^{\text{II}}$ ,  $\text{Zn}^{\text{II}}$ ,  $\text{Ni}^{\text{II}}$ ,  $\text{V}^{\text{IV}}$ ,  $\text{Pd}^{\text{II}}$  and Use for Heterobimetallic Systems. *Inorg. Chem.* **2010**, *49* (17), 7941–7952. DOI: 10.1021/ic100966u.
- (39) (a) Morris, W. D.; Wolczanski, P. T.; Sutter, J.; Meyer, K.; Cundari, T. R.; Lobkovsky, E. B. Iron and Chromium Complexes Containing Tridentate Chelates Based on Nacnac and Imino- and Methyl-Pyridine Components: Triggering C–X Bond Formation. *Inorg. Chem.* **2014**, *53* (14), 7467–7484. DOI: 10.1021/ic500807y. (b) Panda, A.; Stender, M.; Wright, R. J.; Olmstead, M. M.; Klavins, P.; Power, P. P. Synthesis and Characterization of Three-Coordinate and Related  $\beta$ -Diketiminato Derivatives of Manganese, Iron, and Cobalt. *Inorg. Chem.* **2002**, *41* (15), 3909–3916. DOI: 10.1021/ic025552s. (c) Granum, D. M.; Riedel, P. J.; Crawford, J. A.; Mahle, T. K.; Wyss, C. M.; Begej, A. K.; Arulsamy, N.; Pierce, B. S.; Mehn, M. P. Synthesis and Characterization of Sterically Encumbered  $\beta$ -Ketoiminate Complexes of Iron(II) and Zinc(II). *Dalton Trans.* **2011**, *40* (22), 5881–5890. DOI: 10.1039/C1DT10024F. (d) Hagadorn, J. R.; Arnold, J. Ferrocene-Substituted Amidinate Derivatives: Syntheses and Crystal Structures of Lithium, Iron(II), and Cobalt(II) Complexes. *Inorg. Chem.* **1997**, *36* (2), 132–133. DOI: 10.1021/ic961058a. (e) Vendemiati, B.; Prini, G.; Meetsma, A.; Hessen, B.; Teuben, J. H.; Traverso, O. Paramagnetic Bis(Amidinate) Iron(II) Complexes and Their Diamagnetic Dicarboxyl Derivatives. *Eur. J. Inorg. Chem.* **2001**, *2001* (3), 707–711. DOI: 10.1002/1099-0682(200103)2001:3<707::AID-EJIC707>3.0.CO;2-Z. (f) Nijhuis, C. A.; Jellema, E.; Sciarone, T. J. J.; Meetsma, A.; Budzelaar, P. H. M.; Hessen, B. First-Row Transition Metal Bis(Amidinate) Complexes; Planar Four-Coordination of  $\text{Fe}^{\text{II}}$  Enforced by Sterically Demanding Aryl Substituents. *Eur. J. Inorg. Chem.* **2005**, *2005* (11), 2089–2099. DOI: 10.1002/ejic.200500094. (g) Zhang, L.; Xiang, L.; Yu, Y.; Deng, L. Reactivity of a Bis(Amidinato)Iron(II) Complex  $[\text{Fe}(\text{MesC}(\text{NPr}^i)_2)_2]$  toward Some Oxidizing Reagents. *Inorg. Chem.* **2013**, *52* (10), 5906–5913. DOI: 10.1021/ic400053g. (h) Liu, F.; Qiao, X.; Wang, M.; Zhou,

- M.; Tong, H.; Guo, D.; Liu, D. Syntheses, Crystal Structures and Properties of Four Iron and Cobalt Complexes Bearing 1,3,5-Triazapentadienyl Ligands. *Polyhedron* **2013**, *52*, 639–644. DOI: 10.1016/j.poly.2012.07.093. (i) Jesson, J. P.; Trofimenko, S.; Eaton, D. R. Spectra and Structure of Some Transition Metal Poly(1-Pyrazolyl) Borates. *J. Am. Chem. Soc.* **1967**, *89* (13), 3148–3158. DOI: 10.1021/ja00989a014. (j) Janiak, C.; Temizdemir, S.; Dechert, S.; Deck, W.; Girgsdies, F.; Heinze, J.; Kolm, M. J.; Scharmann, T. G.; Zipffel, O. M. Binary [Hydrotris(Indazol-1-yl)Borato]Metal Complexes,  $M(\text{Tp}^{\text{4Bo}})_2$  with  $M = \text{Fe, Co, Ni, Cu, and Zn}$ : Electronic Properties and Solvent-Dependent Framework Structures through C–H $\cdots\pi$  Interactions. *Eur. J. Inorg. Chem.* **2000**, 2421–2421. DOI: 10.1002/1099-0682(200011)2000:11<2421::AID-EJIC2421>3.0.CO;2-%23. (k) Reger, D. L.; Gardinier, J. R.; Gemmill, W. R.; Smith, M. D.; Shahin, A. M.; Long, G. J.; Rebbouh, L.; Grandjean, F. Formation of Third Generation Poly(Pyrazolyl)Borate Ligands from Alkyne Coupling Reactions of  $\text{Fe}[(p\text{-IC}_6\text{H}_4)\text{B}(3\text{-Rpz})_3]_2$  ( $\text{R} = \text{H, Me; Pz} = \text{Pyrazolyl}$ ): Pathways toward Controlling an Iron(II) Electronic Spin-State Crossover. *J. Am. Chem. Soc.* **2005**, *127* (7), 2303–2316. DOI: 10.1021/ja044900h. (l) Moubaraki, B.; Leita, B. A.; Halder, G. J.; Batten, S. R.; Jensen, P.; Smith, J. P.; Cashion, J. D.; Kepert, C. J.; Létard, J.-F.; Murray, K. S. Structure, Magnetism and Photomagnetism of Mixed-Ligand Tris(Pyrazolyl)Methane Iron(II) Spin Crossover Compounds. *Dalt. Trans.* **2007**, No. 39, 4413–4426. DOI: 10.1039/B708773J.
- (40) Gokel, G. W.; Cram, D. J.; Liotta, C. L.; Harris, H. P.; Cook, F. L. Preparation and Purification of 18-Crown-6. *J. Org. Chem.* **1974**, *39* (16), 2445–2446. DOI: 10.1021/jo00930a037.
- (41) Fulmer, G. R.; Miller, A. J. M.; Sherden, N. H.; Gottlieb, H. E.; Nudelman, A.; Stoltz, B. M.; Bercaw, J. E.; Goldberg, K. I. NMR Chemical Shifts of Trace Impurities: Common Laboratory Solvents, Organics, and Gases in Deuterated Solvents Relevant to the Organometallic Chemist. *Organometallics* **2010**, *29* (9), 2176–2179. DOI: 10.1021/om100106e.
- (42) (a) Evans, D. F. 400. The Determination of the Paramagnetic Susceptibility of Substances in Solution by Nuclear Magnetic Resonance. *J. Chem. Soc.* **1959**, 2003–2005. DOI: 10.1039/JR9590002003. (b) Piguet, C. Paramagnetic Susceptibility by NMR: The “Solvent Correction” Removed for Large Paramagnetic Molecules. *J. Chem. Educ.* **1997**, *74* (7), 815. DOI: 10.1021/ed074p815.
- (43) Bain, G. A.; Berry, J. F. Diamagnetic Corrections and Pascal’s Constants. *J. Chem. Educ.* **2008**, *85* (4), 532. DOI: 10.1021/ed085p532.
- (44) Grehn, L.; Ragnarsson, U. A Convenient Method for the Preparation of 1-(Tert-Butyloxycarbonyl) Pyrroles. *Angew. Chem. Int. Ed.* **1984**, *23* (4), 296–301. DOI: 10.1002/anie.198402961.
- (45) Schreurs, A. M. M.; Xian, X.; Kroon-Batenburg, L. M. J. EVAL15: A Diffraction Data Integration Method Based on Ab Initio Predicted Profiles. *J. Appl. Crystallogr.* **2010**, *43* (1), 70–82. DOI: 10.1107/S0021889809043234.
- (46) Sheldrick, G. M. TWINABS. Universität Göttingen, Germany 2014.
- (47) Sheldrick, G. M. SHELXT – Integrated Space-Group and Crystal-Structure Determination. *Acta Crystallogr. Sect. A Found. Adv.* **2015**, *71* (1), 3–8. DOI: 10.1107/S2053273314026370.
- (48) Sheldrick, G. M. Crystal Structure Refinement with SHELXL. *Acta Crystallogr. Sect. C Struct. Chem.* **2015**, *71* (1), 3–8. DOI: 10.1107/S2053229614024218.
- (49) Herbst-Irmer, R.; Sheldrick, G. M. Refinement of Twinned Structures with SHELXL97. *Acta Crystallogr. Sect. B Struct. Sci.* **1998**, *54* (4), 443–449. DOI: 10.1107/S0108768197018454.
- (50) Spek, A. L. Structure Validation in Chemical Crystallography. *Acta Crystallogr. Sect. D Biol. Crystallogr.* **2009**, *65* (2), 148–155. DOI: 10.1107/S090744490804362X.
- (51) Sheldrick, G. M. SADABS. Universität Göttingen, Germany 2014.
- (52) Duisenberg, A. J. M. Diffractometry and Reflection Profiles of Anisotropic Mosaic and Split Crystals. *Acta Crystallogr. Sect. A Found. Crystallogr.* **1983**, *39* (2), 211–216. DOI: 10.1107/S0108767383000483.
- (53) Spek, A. L. PLATON SQUEEZE: A Tool for the Calculation of the Disordered Solvent Contribution to the Calculated Structure Factors. *Acta Crystallogr. Sect. C Struct. Chem.* **2015**, *71* (1), 9–18. DOI: 10.1107/S2053229614024929.
- (54) Bruker. SAINT-Plus. Bruker AXS Inc., Madison, Wisconsin, USA 2001.
- (55) Tretiakov, S.; Damen, J. A. M.; Lutz, M.; Moret, M.-E. A Dianionic  $\text{C}_3$ -Symmetric Scorpionate: Synthesis and Coordination Chemistry. *Dalt. Trans.* **2020**, *49* (39), 13549–13556. DOI:

10.1039/D0DT02601H.

- (56) Le Page, Y. Mallard's Law Recast as a Diophantine System: Fast and Complete Enumeration of Possible Twin Laws by [Reticular] [Pseudo] Merohedry. *J. Appl. Crystallogr.* **2002**, 35 (2), 175–181. DOI: 10.1107/S0021889801021574.

# Chapter 3

---

## Homoleptic Fe<sup>III</sup> and Fe<sup>IV</sup> Complexes of a Dianionic C<sub>3</sub>-Symmetric Scorpionate<sup>a</sup>

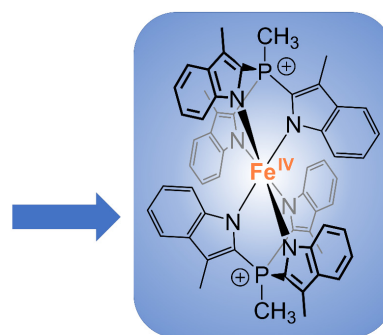
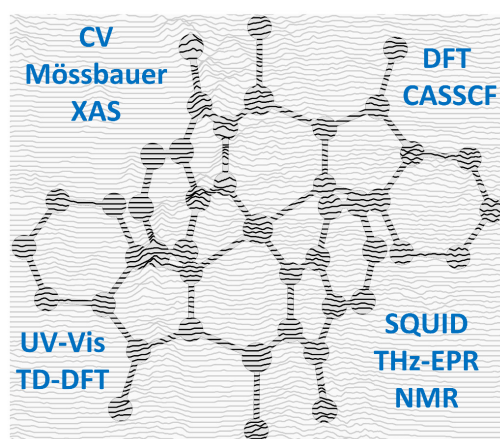
---

### Abstract

High-valent iron species have been implicated as key intermediates in catalytic oxidation reactions, both in biological and synthetic systems. Many heteroleptic Fe(IV) complexes have now been prepared and characterized, especially using strongly  $\pi$ -donating oxo, imido, or nitrido ligands. On the other hand, homoleptic examples are scarce. Herein, we investigate the redox chemistry of iron complexes of the dianionic tris-skatylmethylphosphonium (TSMP<sup>2-</sup>) scorpionate ligand. One-electron oxidation of the tetrahedral, bis-ligated [(TSMP)<sub>2</sub>Fe<sup>II</sup>]<sup>2-</sup> leads to the octahedral [(TSMP)<sub>2</sub>Fe<sup>III</sup>]<sup>-</sup>. The latter undergoes thermal spin-crossover both in the solid state and solution, which we characterize using SQUID, Evans method and paramagnetic NMR spectroscopy. Further, [(TSMP)<sub>2</sub>Fe<sup>III</sup>]<sup>-</sup> can be reversibly oxidized to the stable high-valent [(TSMP)<sub>2</sub>Fe<sup>IV</sup>]<sup>0</sup> complex. We use a variety of electrochemical, spectroscopic and computational techniques as well as SQUID magnetometry to establish a triplet ( $S = 1$ ) ground state with a metal-centered oxidation and little spin delocalization on the ligand. The complex also has a fairly isotropic  $g$ -tensor ( $g_{iso} = 1.97$ ) combined with a positive ZFS parameter  $D$  (+19.1 cm<sup>-1</sup>) and very low rhombicity, in agreement with quantum chemical calculations. This thorough spectroscopic characterization contributes to a general understanding of octahedral Fe(IV) complexes.

---

<sup>a</sup> This chapter is based on: Tretiakov, S.; Lutz, M.; Titus, C. J.; de Groot, F.; Nehr Korn, J.; Lohmiller, T.; Holldack, K.; Schnegg, A.; Tarrago, M. F. X.; Zhang P.; Ye, S.; Aleshin, D.; Pavlov, A.; Novikov, V.; Moret, M.-E. Homoleptic Fe(III) and Fe(IV) Complexes of a Dianionic C<sub>3</sub>-Symmetric Scorpionate. *To be accepted after minor revisions to Inorg. Chem.*, 2023.



- ✓ metal-centered  $S = 1$
- ✓ low  $g$ -anisotropy,  $g_{iso} = 1.97$
- ✓  $D = 19.1 \text{ cm}^{-1}$ ,  $E \leq 0.3 \text{ cm}^{-1}$

### 3.1 Introduction

Fe(IV) compounds, both heme- and non-heme-based,<sup>1–4</sup> are crucial intermediates in many biological transformations. As such, they provide inspiration for the development of small-molecule catalysts for green oxidation processes.<sup>4–6</sup> Due to their generally highly-oxidizing nature, their isolation and spectroscopic characterization have been challenging. Perhaps the most studied members of this family involve heteroleptic Fe(IV) complexes stabilized by strong  $\pi$ -donating ligands<sup>7</sup> (oxo-,<sup>3,5,8,9</sup> imido-,<sup>10–12</sup> nitrido-,<sup>13–16</sup> isocyanide<sup>17</sup> and ketimide<sup>18</sup>). In contrast, homoleptic Fe(IV) complexes are relatively scarce. Among these, a  $[\text{FeF}_4]$  species was cryogenically trapped in neon or argon matrices<sup>19,20</sup> and, according to DFT calculations, is expected to have a quintet ground state ( $S = 2$ ). Due to high ionicity of the Fe–F bond, the existence of  $[\text{FeF}_4]$  as a bulk material under normal conditions is thought unlikely. Next, a family of tetrahedral singlet ( $S = 0$ ) Fe(IV) tetraalkyl complexes is known (**A** in *Chart 3.1*),<sup>21–23</sup> which decompose at room temperature in a matter of days. Similar instability has been reported in a distorted square planar singlet complex **B**,<sup>18,22</sup> an extremely rare example of a non-tetrahedral  $\text{FeX}_4$  compound. The triplet ( $S = 1$ ) dicationic decamethylferrocenium compound **C** was prepared by oxidation of decamethylferrocene in liquid sulfur dioxide<sup>24</sup> and is sufficiently stable for spectroscopic characterization and X-ray crystal structure determination. The latter reveals that the Cp\* rings can tilt with respect to one another depending on the counterion, namely the tilt angle is  $0^\circ$  for the  $[\text{Sb}_2\text{F}_{11}]^-$  anion but  $16.56^\circ$  for  $\text{SbF}_6^-$ , which is caused by coordination of the anion to the Fe(IV) center. Therefore, these complexes can be considered contingently homoleptic. A stable triplet dithiocarbamate complex **D** was synthesized in 1972<sup>25,26</sup> and is one of the first reported homoleptic Fe(IV) complexes. Its electronic structure was revisited in great detail more recently<sup>27</sup> using a combination of spectroscopic and computational techniques, proving its identity as a true Fe(IV) compound. An indefinitely stable triplet hexahydrazide **E** that forms in water upon air oxidation<sup>28</sup> was extensively characterized as having a triplet spin state and trigonal prismatic geometry. Finally, an NHC-based phenylborate complex **F** was synthesized recently,<sup>29</sup> which has a triplet ground state and local  $D_{3d}$  symmetry at the metal center.

Due to the presence of weakly  $\pi$ -donating hard anionic N-donors, pyrrolide-based ligands have a potential for stabilizing high-valent metal centers.<sup>30</sup> As a matter of fact, porphyrin and corrole-based coordination compounds are ubiquitous in nature and often support oxidized reactive intermediates.<sup>31,32</sup> Nonetheless, the majority of these systems feature 4-fold planar coordination geometry around the metal, raising the question of what alternative symmetries could provide in terms of interesting electronic properties and reactivity. Some examples of such geometries include unconju-



gated dipyrrolylmethane<sup>33–37</sup> and tris-pyrrolylethane<sup>38</sup> metal complexes. However, in the case of these molecules, the absence of conjugation on the ligand leads to relatively energetic aromatic  $\pi$ -orbitals which participate in molecular redox events.

We have previously reported a formally dianionic C<sub>3</sub>-symmetric tris-skatylmethylphosphonium (TSMP<sup>2-</sup>) ligand platform that is based on a  $\pi$ -extended pyrrole-based aromatic system, 3-methylindole (skatole).<sup>39–41</sup> It also has a positively charged bridgehead phosphonium atom, which further lowers the energy of its HOMO. Herein, we show that these two aspects are sufficient to access a stable homoleptic, octahedral [(TSMP)<sub>2</sub>Fe<sup>IV</sup>] species (**4**, Chart 3.1) by one electron oxidation of its isostructural Fe(III) analogue. We use a variety of electrochemical (cyclic voltammetry), spectroscopic (XAS, THz-EPR, <sup>57</sup>Fe Mössbauer, paramagnetic NMR and optical spectroscopy) and computational techniques (DFT, TD-DFT, CASSCF/NEVPT2), supported by SQUID magnetometry, to establish a primarily metal-centered oxidation and provide a detailed picture of the electronic structure of **4**.

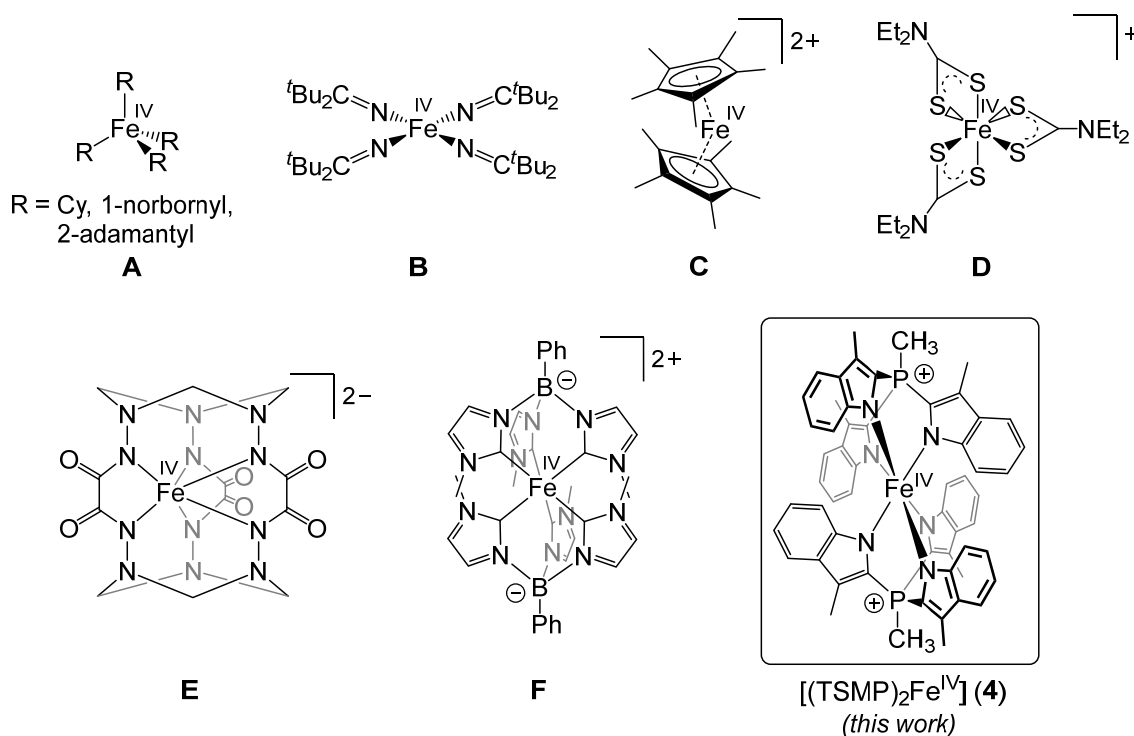
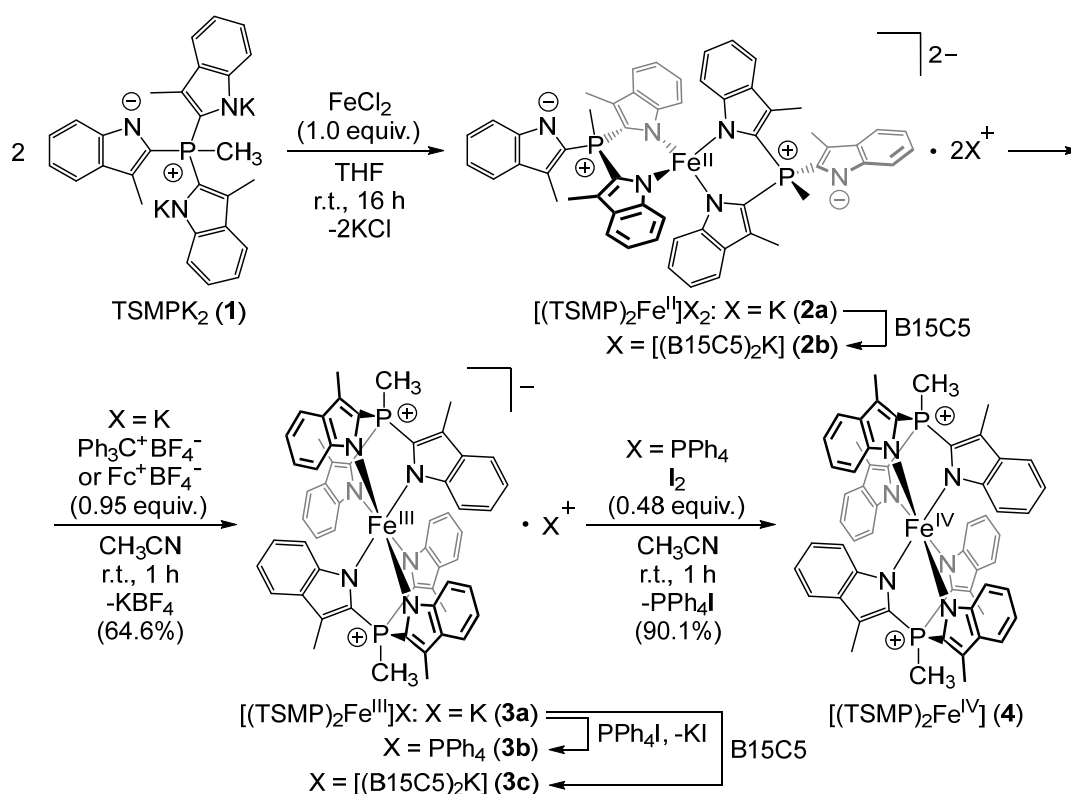


Chart 3.1. Reported homoleptic Fe(IV) complexes.<sup>19,20,29,21–28</sup>

### 3.2 Synthesis and characterization

The high-spin Fe(II) complex [(TSMP)<sub>2</sub>Fe<sup>II</sup>]**K**<sub>2</sub> (**2a**) and its crystallizeable benzo-15-crown-5 (B15C5) adduct [(TSMP)<sub>2</sub>Fe<sup>II</sup>][(B15C5)<sub>2</sub>K]<sub>2</sub> (**2b**) were synthesized as previ-

ously described<sup>40</sup> using iron dichloride and two equivalents of the TSMPK<sub>2</sub> salt (**1**) in THF (*Scheme 3.1*), followed by addition of benzo-15-crown-5 if needed. Complex **2a** is extremely air-sensitive and is immediately converted into the deep-blue Fe(III) compound [(TSMP)<sub>2</sub>Fe<sup>III</sup>]**K** (**3a**) upon exposure to even trace amounts of oxygen. Compound **3a** can also be prepared from **2a** by means of one-electron oxidation with ferrocenium or tritylium tetrafluoroborate in acetonitrile (*Scheme 3.1*). In contrast, repeated attempts to synthesize **3a** directly from dipotassium salt **1** and Fe(III) chloride yielded complex mixtures of paramagnetic products with only small amounts of the target complex as indicated by <sup>1</sup>H NMR spectroscopy, likely due to ligand oxidation and/or polymerization. The potassium cation in **3a** can be easily exchanged for a tetraphenylphosphonium by treatment with PPh<sub>4</sub>I in dichloromethane (DCM), yielding [(TSMP)<sub>2</sub>Fe<sup>III</sup>]**PPh<sub>4</sub>** (**3b**). Furthermore, the potassium cation can also be complexed with two equivalents of B15C5 to form the [(TSMP)<sub>2</sub>Fe<sup>III</sup>][(B15C5)<sub>2</sub>K] adduct (**3c**).



*Scheme 3.1.* Synthesis of metal complexes **2a,b**, **3a-c**, and **4**. Isolated yield is shown in parenthesis.

The solid-state structure of **3a** was established by single-crystal X-ray structure determination of crystals grown from acetonitrile/ether. The compound crystallizes as a one-dimensional coordination polymer with potassium atoms intercalated between aromatic rings of adjacent molecules of **3a** (*Section 3.8.3*). There are two independent

iron centers in the structure, each located on a crystallographic inversion center. The first coordination sphere of the iron atom has approximate octahedral symmetry with N<sup>^</sup>Fe<sup>^</sup>N angles close to 90° and Fe–N bond lengths within 1.9552(12)-2.0020(12) Å (*Figure 3.1*) consistent with a low-spin ( $S = 1/2$ ) state of the metal center.<sup>42,43</sup> The solid-state structure of **3b** and **3c** is similar to that of **3a** (*Section 3.8.3*). Interestingly, the structure of **3c** also has two independent iron centers, each possessing exact inversion symmetry and an approximate octahedral environment, but with distinctly different spin states as can be seen from two sets of the Fe–N bond lengths. More specifically, the low-spin ( $S = 1/2$ ) molecule features bonds within 1.970(2)-2.008(2) Å, while the high-spin ( $S = 5/2$ ) unit has bonds within 2.123(3)-2.155(2) Å, with these ranges being typical for the assigned spin states.<sup>42,43</sup> This discrepancy hints at the possibility of a spin crossover, which is explored in more detail below.

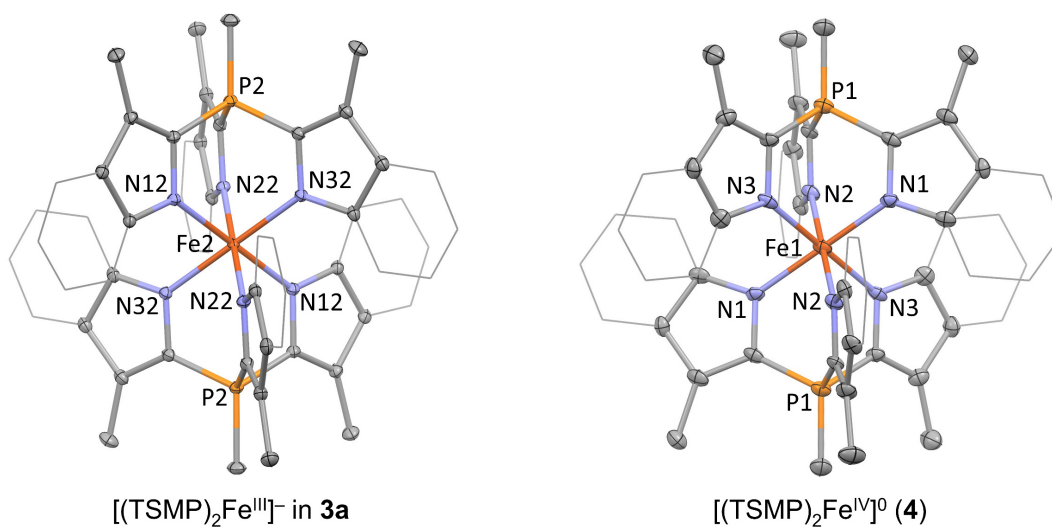


*Figure 3.1.* Molecular structure of complexes **3a** and **4** derived from single crystal X-ray diffraction. Displacement ellipsoids are drawn at 30% probability level. Fused benzene rings are shown in a wireframe style for clarity. Counterions, solvent molecules and hydrogens are omitted for clarity. Selected bond distances (Å) and angles (degrees): **3a**: two molecular fragments in an asymmetric unit, fragment 1: Fe1–N11 1.9885(12), Fe1–N21 2.0019(12), Fe1–N31 1.9805(12), N11<sup>^</sup>Fe1<sup>^</sup>N21 91.11(5), N21<sup>^</sup>Fe1<sup>^</sup>N31 90.70(5), N31<sup>^</sup>Fe1<sup>^</sup>N11 90.73(5); fragment 2: Fe2–N12 1.9889(12), Fe2–N22 1.9885(12), Fe2–N32 1.9552(12), N12<sup>^</sup>Fe2<sup>^</sup>N22 91.56(5), N22<sup>^</sup>Fe2<sup>^</sup>N32 90.44(5), N32<sup>^</sup>Fe2<sup>^</sup>N12 91.16(5); **4**: molecule has C<sub>3</sub> symmetry, Fe1–N1 1.966(5), Fe1–N2 1.975(6), Fe1–N3 1.966(6), N1<sup>^</sup>Fe1<sup>^</sup>N2 91.6(2), N2<sup>^</sup>Fe1<sup>^</sup>N3 91.0(2), N3<sup>^</sup>Fe1<sup>^</sup>N1 90.7(2).

<sup>1</sup>H NMR spectra of **3a** in acetonitrile-*d*<sub>3</sub> solution within 233-348 K show only five paramagnetically shifted and broadened signals (*Figure 3.2*) whereas six signals would be expected based on D<sub>3d</sub> symmetrical solution structure. The effective magnetic moment ( $\mu_{\text{eff}}$ ) in solution measured by Evans method in this temperature range varies from 3.50 to 4.84  $\mu_B$ , indicating thermal spin crossover (SCO) (*Section 3.4*). It suggests

that the signal of the sixth proton, the closest one to the metal center as assigned in *Appendix B15*, is missing due to paramagnetic line broadening, which is often more pronounced at an increased  $\mu_{\text{eff}}$  of the system. This is confirmed by the  $^1\text{H}$  NMR spectrum of  $[(\text{TSMMP})_2\text{Fe}^{\text{III}}]\text{PPh}_4$  (**3b**) in  $\text{DCM-}d_2$  at 173 K, at which temperature most of the complex is in the low-spin  $S = 1/2$  state as indicated by the fitted effective solution magnetic moment of  $1.89 \mu_B$  (*Appendix B2*). There, one can observe the sixth signal spanning over the range of  $>10$  ppm (*Figure B15.2* in *Appendix B15*). The rest of the signals in *Figure 3.2* can be assigned based on the integral intensity, linewidth (*Appendices B13-B15*) and by comparing with the deuterated ( $^2\text{H}_3$ )methylphosphonium analogue, **3a-d**<sub>6</sub>, which was synthesized independently.

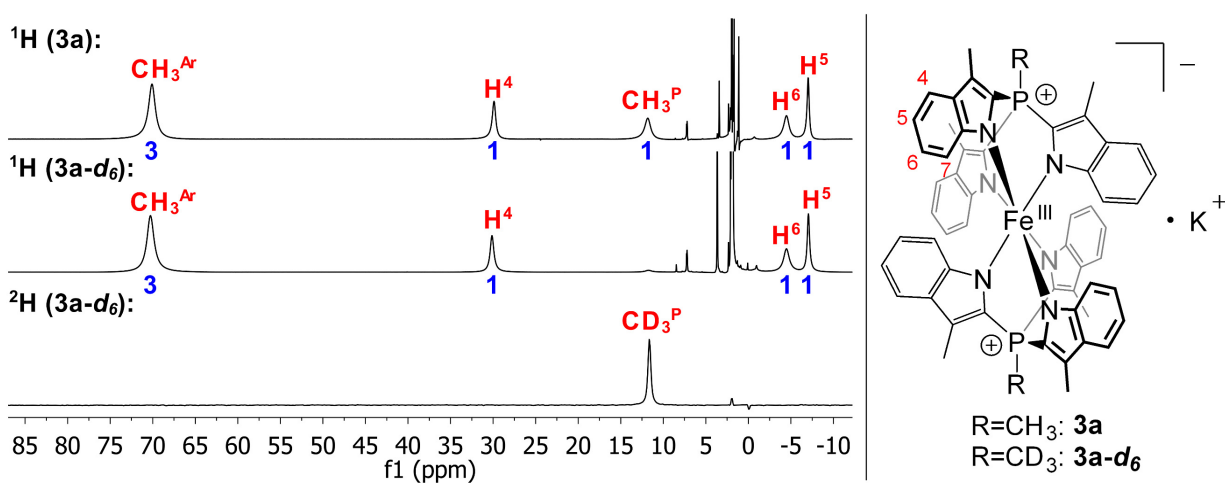


*Figure 3.2.* Stacked  $^1\text{H}$  (400 MHz) and  $^2\text{H}$  (61 MHz) NMR spectra of **3a** and its deuterated analogue **3a-d**<sub>6</sub> in acetonitrile at 298 K. Only paramagnetic signals are assigned. The integrals are given in blue and were rounded to the nearest integer.

Complex  $[(\text{TSMMP})_2\text{Fe}^{\text{IV}}]$  (**4**), for which the Fe(IV) oxidation state is demonstrated below, can be obtained as a bottle-green powder by one-electron oxidation of  $[(\text{TSMMP})_2\text{Fe}^{\text{III}}]\text{PPh}_4$  (**3b**) using elemental iodine in acetonitrile. It is stable both in the solid state and solution for at least six months. Single crystals for X-ray crystal structure determination were grown from pyridine/butyronitrile/ether and contain the electroneutral and roughly octahedral complex with Fe–N distances of 1.966(6)–1.975(5) Å (*Figure 3.1*). This is similar but still somewhat shorter on average than the distances in the isostructural anionic unit of **3a** (1.9552(12)–2.0020(12) Å). Solution  $^1\text{H}$  NMR spectra of  $[(\text{TSMMP})_2\text{Fe}^{\text{IV}}]$  (**4**) in  $\text{DCM-}d_2$  feature six paramagnetically shifted and broadened signals as expected for the  $D_{3d}$  symmetrical solution structure (detailed discussion in *Section 3.5.8*). Very moderate solubility of **4** in all conventional NMR solvents precluded us from determining its effective solution magnetic moment by Evans method. The results of magnetometry in the solid state are discussed below.

### 3.3 Electrochemical behavior

A cyclic voltammogram (CV) of [(TSMP)<sub>2</sub>Fe<sup>II</sup>][(B15C5)<sub>2</sub>K]<sub>2</sub> (**2b**), reveals two couples of redox events: **A/D** and **B/C** (Figure 3.3, top left panel). The full CV scan can be repeated at least a hundred times at rates within 50–250 mV/s with no visible changes, which demonstrates chemical reversibility of the redox cycle it represents. Controlled electrolysis at the points **A** and **B** of the CV using an optically transparent thin-layer electrochemical (OTTLE) cell<sup>44</sup> (Figure 3.3, top right panel) allows the assignment of event **A** as the one-electron oxidation of [(TSMP)<sub>2</sub>Fe<sup>II</sup>]<sup>2-</sup> (**2**) to [(TSMP)<sub>2</sub>Fe<sup>III</sup>]<sup>-</sup> (**3**), whereas event **B** corresponds to the oxidation of [(TSMP)<sub>2</sub>Fe<sup>III</sup>]<sup>-</sup> (**3**) to [(TSMP)<sub>2</sub>Fe<sup>IV</sup>] (**4**). Correspondingly, their reductive counterparts **D** and **C** can be assigned to the same respective processes but in reverse. Importantly, the independently measured CV of [(TSMP)<sub>2</sub>Fe<sup>III</sup>]<sup>-</sup>K (**3a**) is very similar to that of **2b** (Appendix B1), which confirms our assignments.

The pair of redox events **A/D** is characterized by a large peak separation ( $\Delta E_p$  of 1030 mV at 100 mV/s) and a large full width at half maximum (FWHM) of feature **D** (>500 mV). These are clear indications of an irreversible electron transfer, suggesting that a substantial reorganization energy for the [(TSMP)<sub>2</sub>Fe<sup>II</sup>]<sup>2-</sup> (**2**) / [(TSMP)<sub>2</sub>Fe<sup>III</sup>]<sup>-</sup> (**3**) redox couple arises from the different geometries of tetrahedral<sup>39,40</sup> **2** and octahedral **3**.

The pair of events **B/C** can be isolated by means of partial CV scans not involving feature **D** (Figure 3.3, top left panel). During the first cycle, all [(TSMP)<sub>2</sub>Fe<sup>II</sup>]<sup>2-</sup> (**2**) complex in the electrode diffusion layer is consumed to form [(TSMP)<sub>2</sub>Fe<sup>III</sup>]<sup>-</sup> (**3**) (event **A**), followed by oxidation to [(TSMP)<sub>2</sub>Fe<sup>IV</sup>] (**4**; event **B**) with its subsequent reduction back to [(TSMP)<sub>2</sub>Fe<sup>III</sup>]<sup>-</sup> (**3**) (event **C**). Since the potential scan window does not involve feature **D**, corresponding to regeneration of the initial [(TSMP)<sub>2</sub>Fe<sup>II</sup>]<sup>2-</sup> (**2**) ions, by the start of the second cycle the electrode diffusion layer is depleted of the latter, as indicated by the reduced intensity of feature **A** in Figure 3.3, top left panel. The residual intensity is likely due to diffusion of ions of **2** from the outer pool of the [(TSMP)<sub>2</sub>Fe<sup>II</sup>][(B15C5)<sub>2</sub>K]<sub>2</sub> (**2b**) complex. This interpretation is confirmed by varying the potential scanning rate (Figure 3.3, bottom panel): slower scans result in increased intensity of **A**, while the faster ones lead to its complete disappearance.

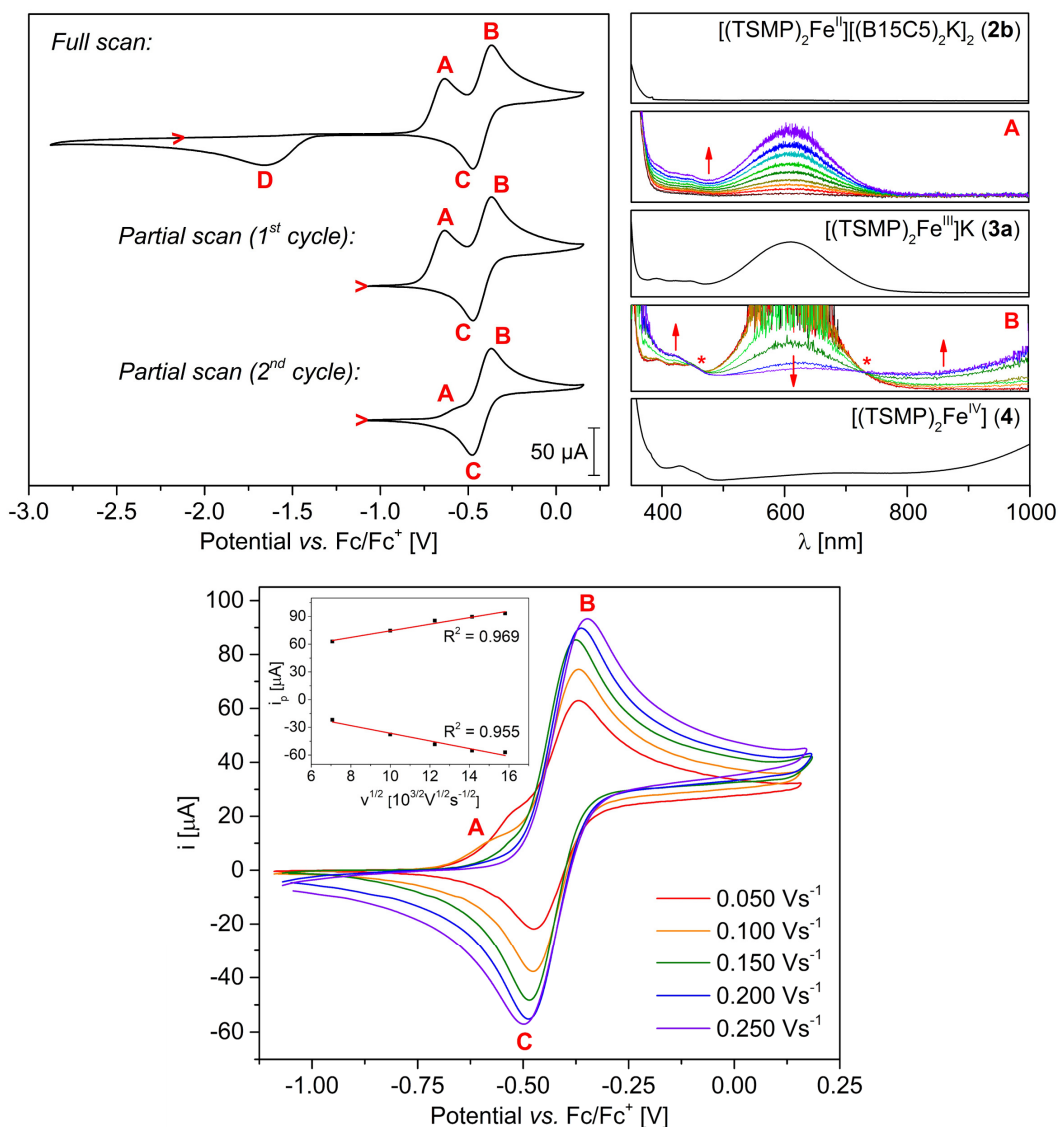


*Figure 3.3.* Cyclic voltammograms of compound **2b** (ca. 8 mM solution) in 0.1 M  $n\text{Bu}_4\text{NPF}_6$  acetonitrile electrolyte. Potentials are referenced with respect to the  $\text{Fc}/\text{Fc}^+$  redox couple. *Top left panel:* overview scans at the rate of 100 mV/s; the full scan starts from an open-circuit potential of  $-2.12$  V. *Top right panel:* UV-Vis of independently synthesized compounds **2b**, **3a** (in MeCN) and **4** (in DCM) and time-dependent UV-Vis spectra of controlled electrolysis at points **A** ( $-0.64$  V) and **B** ( $-0.37$  V) indicated on the CV on the left panel. Absorption in spectrum **B** was truncated due to detector saturation. The asterisks indicate isosbestic points that support a clean conversion between **3a** and **4**. *Bottom panel:* a quasi-reversible redox pair **A-C** centered at  $E_{1/2} = -0.41$  V; the insert shows linear dependence of the peak current vs. square root of the scan rate.

As for the pair of events **B/C** itself, it represents a redox process centered at  $E_{1/2} = -0.41$  V with respect to the  $\text{Fc}/\text{Fc}^+$  couple, which lies within the typical range between  $-1.24$  and  $-0.03$  V for other published  $\text{Fe}(\text{III})/\text{Fe}(\text{IV})$  couples.<sup>11,18,28,45,46</sup> Its  $\Delta E_p$  varies with potential scan rate from 110 mV at 50 mV/s to 152 mV at 250 mV/s,

while the peak current changes linearly with the square root of the scan rate. These are diagnostic criteria for a quasi-reversible electron transfer,<sup>47</sup> implying that the reorganization energy of a transition between [(TSMF)<sub>2</sub>Fe<sup>III</sup>]<sup>-</sup> (**3**) and [(TSMF)<sub>2</sub>Fe<sup>IV</sup>] (**4**) states is rather small, consistently with the similar solid-state geometries of the complexes [(TSMF)<sub>2</sub>Fe<sup>III</sup>]<sup>-</sup>K (**3a**) and [(TSMF)<sub>2</sub>Fe<sup>IV</sup>] (**4**) (*Figure 3.1*).

### 3.4 Spin crossover in the [(TSMF)<sub>2</sub>Fe<sup>III</sup>]<sup>-</sup> complex (**3**)

To probe the electronic structure of [(TSMF)<sub>2</sub>Fe<sup>III</sup>]<sup>-</sup>K (**3a**), we measured the effective magnetic moment ( $\mu_{\text{eff}}$ ) of a powder sample over a temperature range of 2–400 K with a superconducting quantum inference device (SQUID). As shown in *Figure 3.4, left panel*, from 10 to 180 K, the  $\mu_{\text{eff}}$  is nearly constant at  $2.02 \pm 0.01 \mu_{\text{B}}$ . This value is considerably higher than the spin only value of  $1.73 \mu_{\text{B}}$  that is expected for  $S = 1/2$  complexes, which reflects **3** having appreciable unquenched orbital angular momentum, typical of low spin ferric complexes.<sup>48</sup> Starting from 180 K, the  $\mu_{\text{eff}}$  increases with temperature and does not get saturated even at 400 K. These experimental findings show that over the course of the SQUID measurement **3a** undergoes a thermally activated spin crossover (SCO) from the  $S = 1/2$  ground state to an  $S = 5/2$  state. Of note, because the unsaturated  $\mu_{\text{eff}}$  value at 400 K of  $3.98 \mu_{\text{B}}$  exceeds the spin only value of the quartet  $S = 3/2$  state ( $3.87 \mu_{\text{B}}$ ), the spin state the system tends to cannot be  $3/2$  but is rather  $5/2$ , anticipated for the distorted octahedral coordination geometry of **3**. The variation of  $\mu_{\text{eff}}$  was fitted with the domain model of Sorai and Seki,<sup>49</sup> and the satisfactory simulations yielded  $T_{\text{c}} = 450 \pm 5$  K and  $n\Delta H = 15.4 \pm 0.2$  kJ/mol. Here,  $T_{\text{c}}$  represents the critical transition temperature of the SCO,  $\Delta H = H_{\text{HS}} - H_{\text{LS}}$  — the enthalpy difference between the high spin state and low spin state, and  $n$  — the number of molecules per domain. Below 10 K, the precipitous drop of  $\mu_{\text{eff}}$  cannot be simply interpreted as field saturation, but primarily arises from weak intermolecular interactions, for which a mean field model<sup>50</sup> was invoked to fit the SQUID data and gave  $zJ = -6 \pm 1 \text{ cm}^{-1}$ .

The zero-field Mössbauer spectrum (*Figure 3.4, right panel*), of complex **3a** recorded at 77 K displays a well-resolved quadrupole doublet at isotope shift  $\delta = 0.25$  mm/s and quadrupole splitting  $\Delta E_{\text{Q}} = 1.63$  mm/s. Both values are characteristic for low spin ferric centers coordinated by six hard nitrogen donors. DFT calculations performed on both independent anions in the crystal structure of **3a** predict isomer shifts ( $\delta = 0.29$  and  $0.26$  mm/s) and quadrupole splittings ( $|\Delta E_{\text{Q}}| = 2.19$  and  $2.18$  mm/s) in reasonable agreement with experiment (*Appendix B3*). Furthermore, no other iron species was

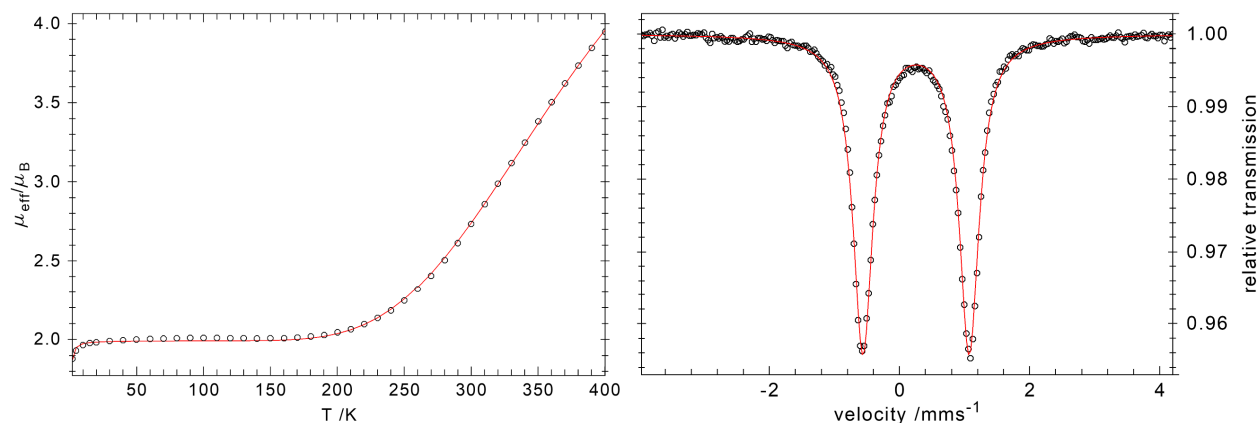


*Figure 3.4. Left panel:* SQUID measurement of **3a** under an applied magnetic field of 1 T. The dots represent experimental data, and the solid red line the fits with the following parameters:  $S = 1/2$ ,  $g_{\text{iso}} = 2.30$ ,  $zJ = -6 \text{ cm}^{-1}$ ;  $S = 5/2$ ,  $D = E = 0$ ,  $g_{\text{iso}} = 2.00$ , and  $\text{TIP} = 0$ . *Right panel:* zero-field Mössbauer spectrum of **3a** measured on a powder sample at 77 K. The fitted parameters are  $\delta = 0.25 \text{ mm/s}$  and  $\Delta E_Q = 1.63 \text{ mm/s}$ .

identified in the spectrum, consistent with the high SCO critical temperature  $T_c$  of  $450 \pm 5 \text{ K}$ .

Interestingly, SQUID magnetometry of the benzo-15-crown-5 adduct  $[(\text{TSMP})_2\text{Fe}^{\text{III}}][(\text{B15C5})_2\text{K}]$  (**3c**) reveals that at low temperatures the system has a magnetic moment  $\mu_{\text{eff}}$  of  $3.61 \mu_{\text{B}}$ , in between the low- and high-spin states, similarly to  $3.88 \mu_{\text{B}}$  for the case of an intermediate-spin ( $S = 3/2$ ). The system crosses over towards the high-spin state at only ca. 140 K (*Appendix B4*). However, an  $S = 3/2$  electronic configuration is unlikely for a  $[(\text{TSMP})_2\text{Fe}^{\text{III}}]^-$  (**3**) ion since it would imply significant distortion of the  $\text{FeN}_6$  environment, leading to strain in the TSMP scaffold, which is expected to be more energetic than the energy gap between the  $S = 3/2$  and other spin states.<sup>43,51,52</sup> 1.970(2)-2.008(2) and 2.123(3)-2.155(2) Å, respectively. Although rare for iron(III) coordination compounds, such behaviour is not unprecedented and was observed for some tris(dithiocarbamate)<sup>51</sup> complexes.

The solution behavior of **3** parallels our observations in the solid-state. The SCO between the  $S = 1/2$  and  $5/2$  states is evident from the strongly temperature-dependent  $\mu_{\text{eff}}$  as measured by Evans method.<sup>53-55</sup> The results of such measurements are shown in *Figure 3.5* for potassium salt **3a** in acetonitrile- $d_3$  and pyridine- $d_5$ , and for tetraphenylphosphonium salt **3b** in DCM- $d_2$  as **3a** is insoluble in this solvent.



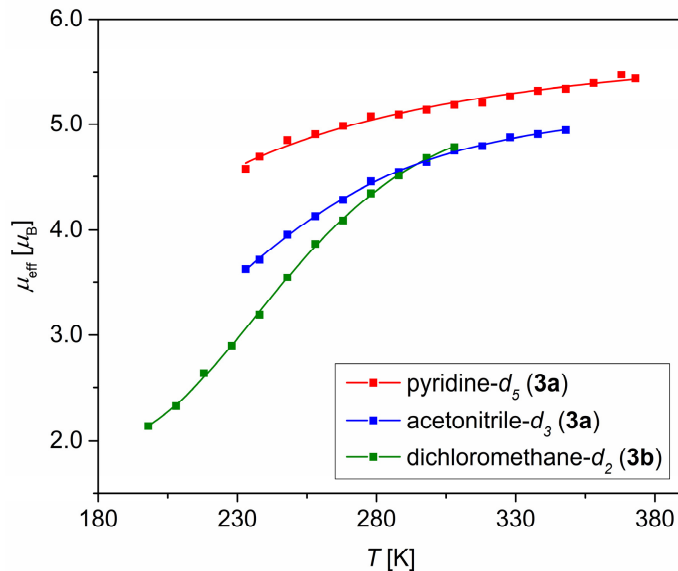


Figure 3.5. SCO curve for the [(TSMMP)<sub>2</sub>Fe<sup>III</sup>]<sup>-</sup> (**3**) complex as obtained by Evans method in different solvents. Data points represent experimental measurements, whereas smooth curves are fits based on the regressive model in Eq. 3.1. Explored temperature ranges are limited by the freezing and boiling points of the respective solvents or precipitation of the compound at low temperature.

The solution SCO behavior can be fitted using Eq. 3.1 (Appendix B2), which allows to extract the enthalpy ( $\Delta H$ ) and entropy ( $\Delta S$ ) of the crossover as well as the limiting magnetic moments for both low- and high-spin states,  $\mu_{LS}$  and  $\mu_{HS}$ , respectively.

$$\mu_{eff} = \mu_{LS} + \frac{\mu_{HS} - \mu_{LS}}{1 + \exp\left(\frac{\Delta H}{RT} - \frac{\Delta S}{R}\right)}, \quad \text{Eq. 3.1}$$

where  $T$  is temperature and  $R$  is the universal gas constant.

The crossover curve for **3b** in DCM- $d_2$  is the most informative since it spans through both low- and high- $\mu_{eff}$  regions. A regressive thermodynamic analysis (Appendix B2) provides the following parameters:  $\Delta H$  and  $\Delta S$  of  $18.1 \pm 1.4$  kJ/mol and  $72.6 \pm 5.8$  J/(mol·K), respectively, with the critical temperature  $\Delta H/\Delta S = T_c$  of  $249 \pm 1$  K. The limiting magnetic moments  $\mu_{LS}$  and  $\mu_{HS}$  are  $1.81 \pm 0.07$  and  $5.35 \pm 0.10$   $\mu_B$ , respectively, which is close to the spin-only expectation values for the low-spin  $S = 1/2$  ( $1.73$   $\mu_B$ ) and high-spin  $S = 5/2$  ( $5.92$   $\mu_B$ ) states. A similar analysis for the SCO of **3a** in acetonitrile- $d_3$  leads to slightly different values with higher standard errors  $\Delta H$  of  $14.4 \pm 2.4$  kJ/mol,  $\Delta S$  of  $59.6 \pm 8.0$  J/(mol·K) and  $T_c$  of  $240 \pm 9$  K. Because the SCO curve does not cover the low- $\mu_{eff}$  range, a significant standard error is also associated with the lower limiting value  $\mu_{LS}$  of  $2.35 \pm 0.45$   $\mu_B$ , while the higher one of  $5.23 \pm 0.08$   $\mu_B$  has smaller uncertainty and is similar to that for **3b**. Lastly, since **3a** in pyridine- $d_5$  has al-

most completely undergone SCO at the lowest accessible temperature (*Figure 3.5*), the corresponding thermodynamic parameters cannot be reliably extracted.

The change of the effective solution magnetic moment with temperature is also apparent from the paramagnetic  $^1\text{H}$  NMR shifts and line broadening (see *Appendix B16* for more detail). In short, the hyperfine part of the observed shifts ( $\delta^{\text{HF}}$ ), obtained by subtracting the diamagnetic contribution ( $\delta^{\text{dia}}$ ) approximated by an isostructural Ga(III) analogue  $[(\text{TSMMP})_2\text{Ga}^{\text{III}}]\text{K}$  (**5a**), shows very strong deviation from the Curie behavior ( $\delta^{\text{HF}}T \neq \text{const}$ , *Figure 3.6*), indicative of the SCO (see the reasons in *Appendix B13*). Note that the temperature-dependent trends parallel those observed in the Evans method measurements for different solvents (*Figure 3.5*).

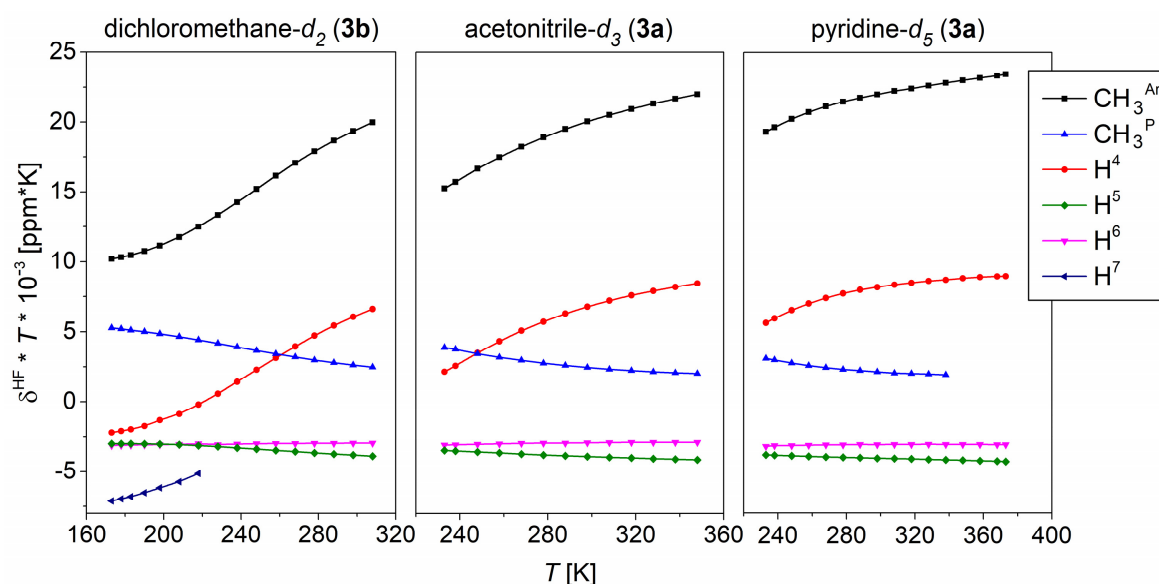


*Figure 3.6.* Variable-temperature  $^1\text{H}$  NMR (400 MHz) hyperfine shift times temperature products of complex  $[(\text{TSMMP})_2\text{Fe}^{\text{III}}]^-$  (**3**) in different solvents. Due to solubility considerations, the  $[(\text{TSMMP})_2\text{Fe}^{\text{III}}]\text{K}$  (**3a**) salt was used for experiments in acetonitrile- $d_3$  and pyridine- $d_5$ , and the  $[(\text{TSMMP})_2\text{Fe}^{\text{III}}]\text{PPh}_4$  (**3b**) salt was measured in dichloromethane- $d_2$ .

Overall, these data indicate that the SCO thermodynamics of **3** is sensitive to solvent and/or counterion, possibly indicating a role of ion pairing in solution. While the difference of  $\sim 200$  K in SCO critical temperatures ( $T_c$ ) in the solid state and in solution is very high, in some cases the crystal packing is known to lock some SCO molecules in a fixed spin state,<sup>56</sup> slow down the spin transition by antiferromagnetic effects<sup>57,58</sup> or even prevent SCO from happening at all.<sup>59</sup>

To the best of our knowledge, **3** is the first synthetic complex with an  $\text{Fe}^{\text{III}}\text{N}_6$  core that undergoes thermal SCO. This behavior is likely due to  $\text{TSMMP}^{2-}$  being a relatively

weak-field ligand with poor  $\pi$ -accepting properties caused by the presence of low-lying  $\pi$ -orbitals in the extended aromatic systems. Gradual transitions as observed for **3** in solid state and in solution are commonly observed for SCO in Fe(III) compounds.<sup>42</sup> A broad range of critical temperatures  $T_c$  (20 K to ca. 400 K) have been observed for Fe(III) compounds with different ligand sets.<sup>43</sup> The pronounced difference between **3a** and **3c** and between solid-state and solution suggests that SCO in anion **3** is strongly sensitive to its environment.

### 3.5 Electronic structure of $[(TSMMP)_2Fe^{IV}]$ (**4**)

The presence of 10-electron conjugated  $\pi$ -systems on the ligand raises the question of the actual electronic structure and metal oxidation state in **4**. In principle, two extremes are possible: a genuine Fe(IV) compound or an Fe(III) compound with a radical on the  $TSMMP^{2-}$  scaffold. In addition, these two states could mix, forming a multi-reference system. Below, we use three key techniques to show that oxidation bears an exclusive metal-centered character: cyclic voltammetry (CV), Mössbauer and X-ray absorption (XAS) spectroscopies. We further delve into the magnetic properties of **4** by means of Superconducting Quantum Interference Device (SQUID) magnetometry, Frequency-Domain Fourier-Transform THz-EPR spectroscopy and paramagnetic  $^1H$  NMR studies. We then verify and refine our conclusions by means of DFT and CASSCF calculations, which seals the assignment of the ground-state electronic structure of **4**. Finally, we briefly touch upon the excited electronic states of **4** by means of assigning its absorption spectra in the optical region with the help of TD-DFT calculations and Natural Transition Orbital (NTO) analysis.

#### 3.5.1 Cyclic voltammetry

A first insight is provided by comparing cyclic voltammograms of  $[(TSMMP)_2Fe^{III}]K$  (**3a**) and its isostructural Ga analogue  $[(TSMMP)_2Ga^{III}]K$  (**5a**) (Figure 3.7) synthesized using  $TSMMPK_2$  salt (**1**) and  $GaCl_3$  in acetonitrile (Section 3.8.2.1; X-ray crystallographic details in Section 3.8.3). If the oxidation event leading from **3a** to **4** was mostly ligand centered, one would expect a small first oxidation potential difference with **5a**. In contrast, the observed significant difference of 450 mV argues in favor of at least partially metal-centered oxidation of the iron in **4**.

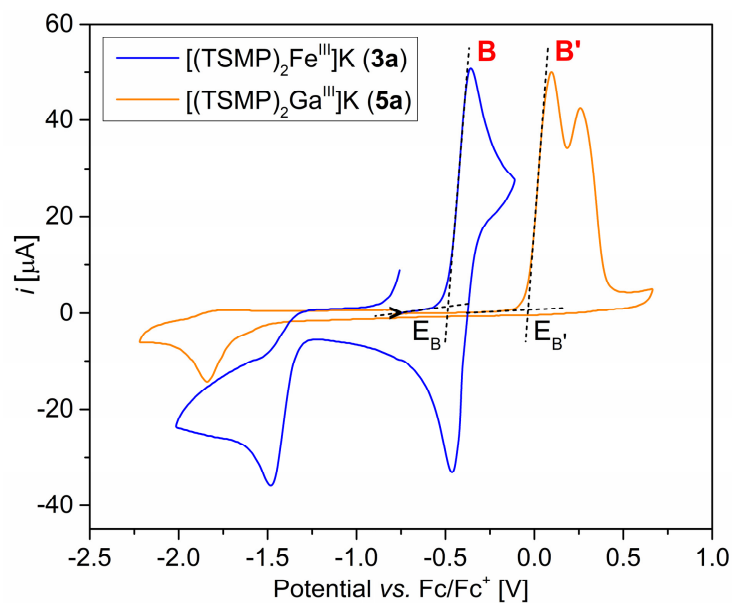


Figure 3.7. Overlay of CVs measured for **3a** and **5a**. The measurements were performed in ca. 8 mM solution in 0.1 M  $n\text{Bu}_4\text{NPF}_6$  acetonitrile electrolyte. Potentials are referenced with respect to the  $\text{Fc}^+/\text{Fc}$  redox couple. The onsets of oxidation of **3a** and **5a** ( $E_B$  and  $E_{B'}$ , respectively) are defined as the points of intersection between extrapolated baseline and a tangent to the oxidation feature **B/B'**.

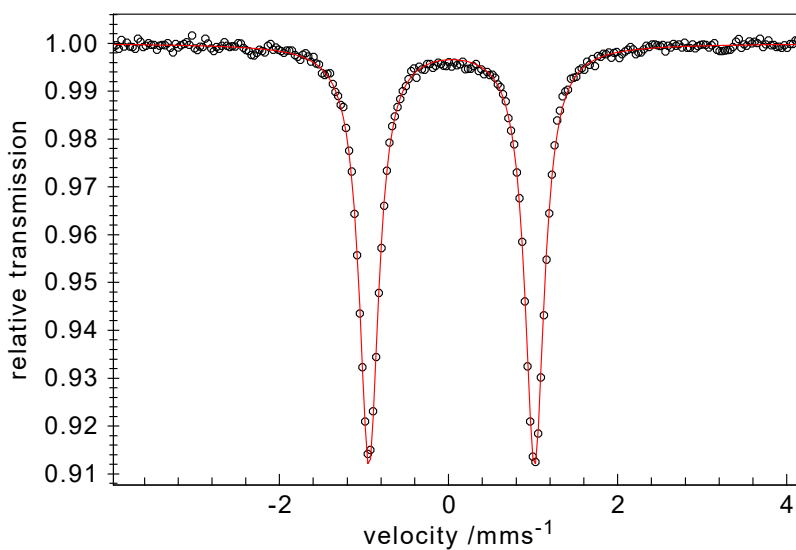


Figure 3.8. Zero-field Mössbauer spectrum of **4** measured on a powder sample at 80 K. The fitted parameters are  $\delta = 0.04$  mm/s and  $|\Delta E_Q| = 1.96$  mm/s.

### 3.5.2 <sup>57</sup>Fe Mössbauer spectroscopy

The electronic structure of the [(TSMP)<sub>2</sub>Fe<sup>IV</sup>] (**4**) complex was further probed by zero-field <sup>57</sup>Fe Mössbauer spectroscopy at 80 K. The spectrum (*Figure 3.8*) shows a very clear quadrupole doublet. The isomer shift ( $\delta$ ) of 0.04 mm/s is substantially lower than 0.25 mm/s measured for the parent Fe(III) compound **3a** and falls within the expected range for a Fe(IV) metal centre,<sup>60</sup> clearly indicating metal-centred oxidation. The quadrupole splitting  $|\Delta E_Q|$  of 1.96 mm/s suggests a significant deviation of the electronic configuration from cubic symmetry. The measured isomer shift is similar to that of E<sup>28</sup> (0.045 mm/s) in *Chart 3.1* but different from that of F<sup>29</sup> (-0.23 mm/s), as expected for their distinct respective donors (N<sup>-</sup> vs. C). At the same time, the measured quadrupole splitting is lower than 2.51 mm/s in E and 3.04 mm/s in F, likely reflecting slightly different local Fe coordination environments.

### 3.5.3 XAS spectroscopy

Our Fe 2p (L<sub>2,3</sub>) X-ray absorption (XAS) measurements generally agree with the conclusions drawn from the cyclic voltammetry above. In XAS, a 2p core electron is excited into an empty 3d state, which for a 3d<sup>5</sup> iron center in [(TSMP)<sub>2</sub>Fe<sup>III</sup>]<sup>-</sup> (**3**) leads to a 2p<sup>5</sup>3d<sup>6</sup> configuration. The experimental XAS spectra of the potassium salt **3a** agree with simulations for anion **3** based on ligand field multiplet theory (*Figure 3.9*).<sup>61</sup> Given the average excitation lifetime of <1 fs, the spectrum of **3a** at 300 K is adequately simulated as a sum of low- and high-spin components in a ratio of 80:20, which is consistent with the solid-state SCO behavior discussed above.

The experimental XAS spectrum of [(TSMP)<sub>2</sub>Fe<sup>IV</sup>] (**4**) is similar but shifted to higher energies by 0.9-1.1 eV compared to **3a** (*Figure 3.9, top panel*), indicating the metal-centered oxidation. This spectrum can be simulated (*Figure 3.9, bottom panel*) considering D<sub>3d</sub> symmetry of **4** with 1a<sub>1</sub>-1e-2e orbital splitting (*Section 3.5.6*), 2-2-0 occupancies and a <sup>3</sup>A<sub>2</sub> ground state.<sup>61</sup> In the simulation, the two biggest peaks can be approximated as transitions into the 1e and 2e orbitals. However, due to strong 2p3d multiplet effects, this assignment is not completely accurate as significant mixing occurs in the final 2p<sup>5</sup>3d<sup>5</sup> state. The shoulder at 710 eV in the experimental spectrum is due to charge transfer, which was not included explicitly in the calculations to limit the number of parameters. These charge transfer excitations were omitted due to the use of the nephelauxetic effect along with reduced electron-electron interactions (factor of 0.85).<sup>62</sup> An overview of the exact parameters used in the calculation is given *Section 3.8.4*.

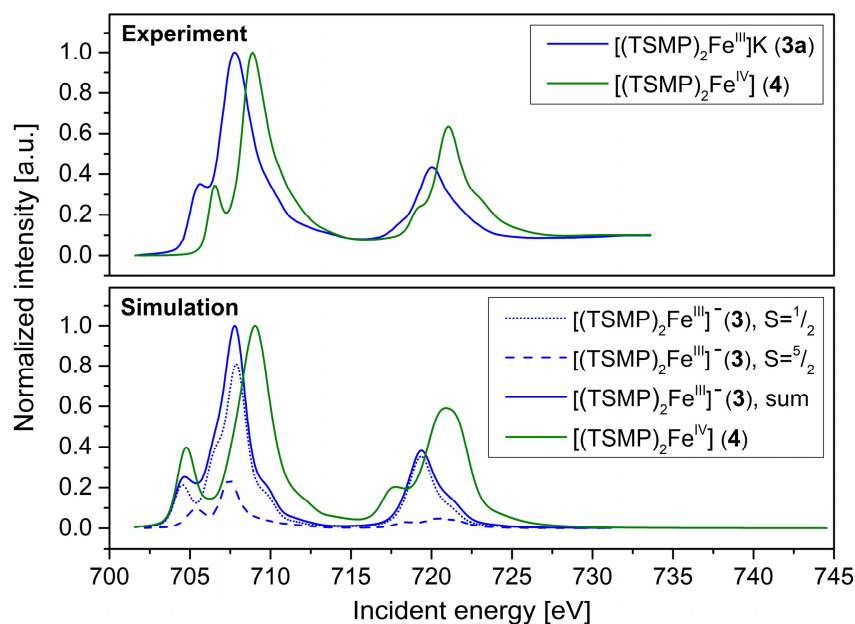


Figure 3.9. Experimental (top panel) and simulated (bottom panel)  $L_{2,3}$  edge XAS spectra of the Fe(III) (**3a/3**) and Fe(IV) (**4**) complexes.

Taken together, the 2p XAS spectra confirm the nature of the  $[(\text{TSMP})_2\text{Fe}^{\text{III}}]^-$  (**3**) and  $[(\text{TSMP})_2\text{Fe}^{\text{IV}}]$  (**4**) systems. At 300 K, **3a** has predominantly a low-spin configuration, while **4** has an  ${}^3\text{A}_2$  triplet ground state with a doubly-occupied  $d_{z^2}$  orbital and a half-filled first  $e(\text{D}_{3d})$  state (*vide infra*, Figure 3.12).

### 3.5.4 SQUID magnetometry

SQUID magnetometry was performed on a microcrystalline sample of **4** in order to determine its spin state and assess its zero-field splitting (ZFS). The fit of the VT measurement (Figure 3.10, right panel) gives a  $\mu_{\text{eff}}$  value of  $2.50 \mu_{\text{B}}$  at room temperature, which is lower but still close to the spin-only expectation value for an intermediate-spin state ( $S = 1$ ) Fe(IV) center ( $2.83 \mu_{\text{B}}$ ). The corresponding  $g_{\text{iso}}$ -value is 1.76. The magnetic susceptibility from the VTVH measurement (Figure 3.10, left panel) could be fitted consistently with an axial ZFS parameter  $D$  of  $+15 \text{ cm}^{-1}$ . The rhombicity  $E/D$  was taken as zero due to the  $\text{C}_3$  axis of symmetry in the molecule. However, these parameters gave a subpar fit for the measurement at 1 T. We attribute this to small anti-ferromagnetic intermolecular interactions which compete with the Zeeman effect under low external field (1 T) and become negligible under higher fields (4 and 7 T). These interactions could be caused by the presence of small amounts of paramagnetic impurities or interactions of the sample molecules with one another.

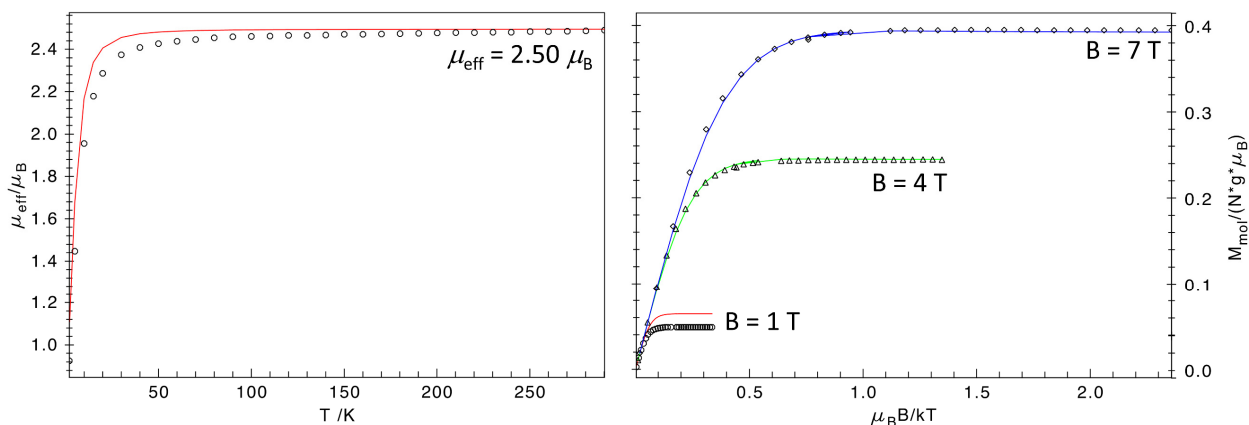


Figure 3.10. VT  $\mu_{\text{eff}}$  at 0.1 T (right panel) and VTVH magnetization at 1, 4 and 7 T (left panel) SQUID measurements of **4**, fitted using the following spin Hamiltonian parameters:  $g_{\text{iso}} = 1.76$ ,  $D = +15 \text{ cm}^{-1}$ ,  $E/D = 0$ .

Overall, the abnormally low effective magnetic moment (corresponding to the unphysically small  $g_{\text{iso}}$ ) and small intermolecular interactions suggest that the measured sample of **4** contains some admixtures, be it paramagnetic impurities or residual solvent. The latter is likely due to the zwitterionic nature of **4**, which makes complete solvent removal very difficult even after prolonged drying *in vacuo*. However, the SQUID measurements still allow to get a qualitative estimate of the zero-field splitting ( $D \approx +15 \text{ cm}^{-1}$ ), as well as a clear determination of the  $S = 1$  spin state ( ${}^3A_2$  ground state).

### 3.5.5 THz-EPR spectroscopy

A more direct way to quantify  $g$ -values and ZFS parameters of **4**, which does not require the mass of the sample to be precisely known, is through EPR spectroscopy. However, as **4** is an integer-spin ( $S = 1$ ) system with low rhombicity and a moderate, positive  $D$ -value, the transitions between its non-Kramers doublets are too energetic to be observed using conventional EPR spectrometers.<sup>63</sup> Indeed, X-band measurements on the microcrystalline samples gave no interpretable signal; featureless spectra were also obtained in parallel mode. Therefore, we resorted to high-energy (THz range) frequency domain EPR spectroscopy.<sup>64</sup>

Variable-field THz-EPR spectra of **4** in Figure 3.11 are shown in a relative absorbance mode as  $\log_{10} \frac{I_{\text{ref}}}{I(B_0)}$ , where  $I_{\text{ref}}$  is a reference transmittance spectrum measured at 31 K and 0 T, and  $I(B_0)$  is a transmittance spectrum measured at 4.8 K and magnetic field  $B_0$  (Appendix B5). For  $B_0 = 0$ , a clear absorption (**I**) can be observed at  $19.1 \text{ cm}^{-1}$ . This

feature broadens and splits with increasing external magnetic field. The field dependence allows for assignment of the peak at  $19.1 \text{ cm}^{-1}$  to the EPR transition from  $m_s = 0$  to the  $m_s = \pm 1$  sublevels of the  $S = 1$  system (*Appendix B6*). Thus, the zero-field spectrum corresponds to an axial ZFS of  $D = 19.1 \text{ cm}^{-1}$  with vanishing rhombicity ( $E \approx 0$ ) due to the lack of a visible splitting in the zero-field spectrum. From the linewidth of the signal,  $E \leq 0.3 \text{ cm}^{-1}$  can be estimated. Simulations using  $D = 19.1 \text{ cm}^{-1}$ ,  $E = 0$  and an isotropic  $g$ -value of 1.97 reproduce the zero-field transition energy as well as the field dependence very well (*Figure 3.11*). We note that the spectra feature a lowering of the relative absorbance around  $18.4 \text{ cm}^{-1}$ , directly below the ZFS energy, which is discussed in *Appendix B7*. Further details of the THz-EPR measurement protocol and simulations, including demonstration of the unfeasibility of alternative EPR parameter sets, are discussed in *Section 3.8.1* and *Appendix B8*.

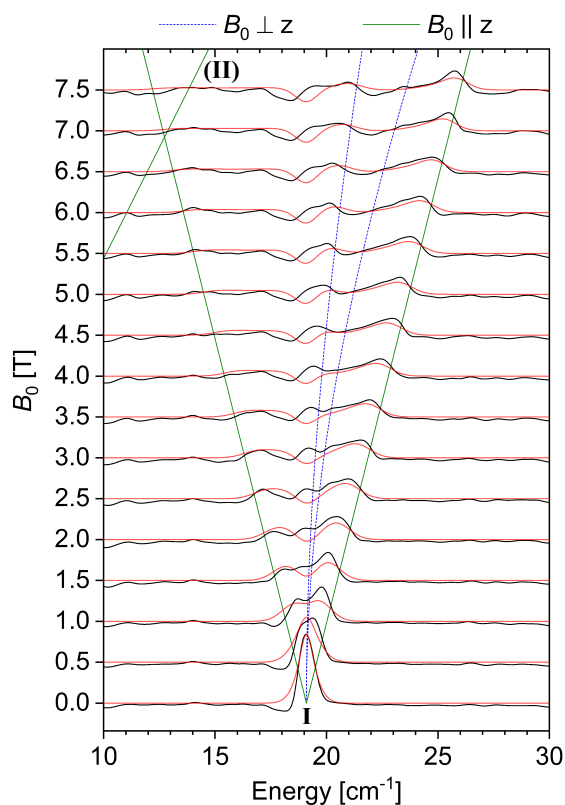


*Figure 3.11.* THz-EPR spectra of **4**. Relative absorbance spectra (black lines) are offset for the magnetic field  $B_0$  at which they were measured. Simulations using  $D = +19.1 \text{ cm}^{-1}$ ,  $E = 0$  and an isotropic  $g$ -value of 1.97 are shown in red. Calculated transition energies for magnetic fields applied parallel and perpendicular to the main anisotropy axis ( $z$ ) are shown as solid green and dashed blue lines, respectively. Branch **II** corresponds to the formally forbidden transitions between the excited  $m_s = \pm 1$  sublevels.



### 3.5.6 DFT calculations

Geometries of the alternative spin states of **4** ( $S = 0, 1, 2$ ) optimized at the BP86-D3BJ/def2-TZVP level of theory show that the  $S = 1$  state is the most energetically favoured, followed by the  $S = 0$  and  $S = 2$  states (*Table 3.1*). Calculated Mössbauer spectral parameters at the B3LYP-D3BJ/def2-TZVP (CP(PPP) basis set for Fe) allow unambiguous assignment of the  $S = 1$  spin state (*Table 3.1*), consistent with the value derived from the SQUID and THz-EPR measurements. The calculated isomer shift ( $\delta$ ) is  $-0.05$  mm/s is within the uncertainty of computations,<sup>65</sup> close to the experimental value of  $+0.04$  mm/s. The calculated quadrupole splitting ( $\Delta E_Q$ ) of  $-2.01$  mm/s is also very close to the absolute experimental absolute value of  $1.96$  mm/s, while the sign of the splitting could not be inferred from the zero-field measurement.

*Table 3.1.* Relative SCF energies and <sup>57</sup>Fe Mössbauer spectral parameters calculated for alternative spin states of **4** ( $S = 0, 1, 2$ ), compared to the experimental parameters. The structures were optimized at the BP86-D3BJ/def2-TZVP level of theory. Energies and Mössbauer spectral parameters were calculated using the B3LYP-D3BJ/def2-TZVP level of theory with the CP(PPP) basis set for Fe.

Spin state	Relative energy, kcal/mol	$\delta$ , mm/s	$\Delta E_Q$ , mm/s
$S = 0$	17.8	0.04	+2.75
$S = 1$	0	-0.05	-2.01
$S = 2$	25.0	0.10	+1.49
Exp.	-	0.04	$\pm 1.96$

Given that the experimental Mössbauer parameters are well reproduced by the calculations for the  $S = 1$  state, the computed electron density can be used for closer examination of the electronic structure of **4**. Despite the optimized geometry featuring a locally octahedral FeN<sub>6</sub> center, the molecule of **4** itself has D<sub>3d</sub> symmetry with a three-fold rotation axis passing through the P–Fe–P atoms. This leads to orbital splitting typical for this kind of symmetry (*Figure 3.12*). The doubly occupied  $1a_1$  orbital has almost entirely  $d_{z^2}$  character, which can be rationalized based on the irreducible representations of  $d$ -orbitals in a D<sub>3d</sub> point group. More specifically, the  $d_{z^2}$  belongs to the representation  $A_1$ , and therefore cannot mix with the four remaining  $d$ -orbitals, ( $d_{xy}, d_{x^2-y^2}$ ) and ( $d_{xz}, d_{yz}$ ), belonging to the double representation  $E$ . At the same time, these four orbitals mix together, forming two degenerate pairs:  $1e$  and  $2e$  (*Figure 3.12*). Both these pairs bear an anti-bonding character:  $1e$  along the  $\pi$ -manifold and  $2e$  along the  $\sigma$ -manifold, leaving  $1a_1$  to be the only non-bonding  $d$ -orbital. The fact that the  $1e$  pair of SOMOs is primarily localized on the metal center implies that this is also where most of the spin density can be found (*Appendix B9*).

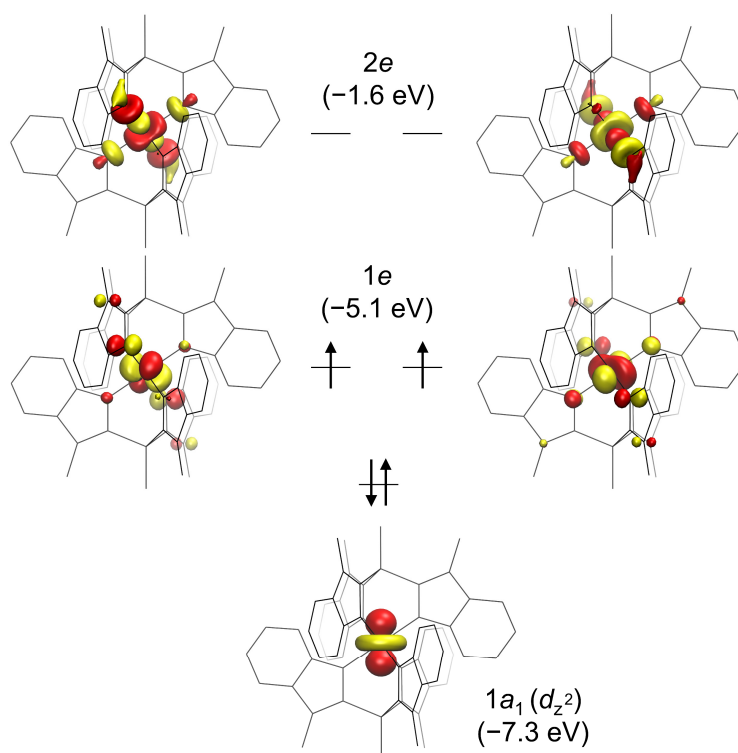


*Figure 3.12.* Quasi-restricted frontier orbitals (isocontour=0.05) of the ground state of **4** calculated at the B3LYP-D3BJ/def2-TZVP (CP(PPP) for Fe) level of theory using a geometry optimized at the BP86-D3BJ/def2-TZVP level. Orbital energies are given in parentheses.

Considering the discussed orbital manifold, the negative sign of the calculated Mössbauer quadrupole splitting ( $\Delta E_Q = -2.01$  mm/s) is dominated by the strongly negative valence contribution of the  $1a_1$  orbital. Note that while the  $1e$  SOMOs influence the quadrupole splitting as well, the positive contribution from  $d_{xy}$  and  $d_{x^2-y^2}$  orbitals is counterbalanced by the negative one from  $d_{xz}$  and  $d_{yz}$ . A detailed analysis of the origin of the quadrupole splitting is given in *Appendix B10*.

It is important to note that the doubly occupied  $1a_1$  orbital in *Figure 3.12* points directly at the positively charged phosphonium atoms, which is expected to lower its energy by providing additional electrostatic stabilization. Indeed, comparison of the quasi-restricted orbital energies of **4** and its isoelectronic Si-tethered analogue (**A** in *Chart 3.2*) calculated at the same level of theory reveals that, while the  $1e$ - $2e$  gap is the same in both molecules, the  $1a_1$  orbital in **4** is stabilized by an additional 0.2 eV. Given the close similarity of the molecular geometries of **4** and **A** (*Appendix B11*), this difference is most likely due to the electrostatic effects. Although, subtle influence of the bridge-head atom on  $\pi$ -donating ability of a ligand cannot be excluded.

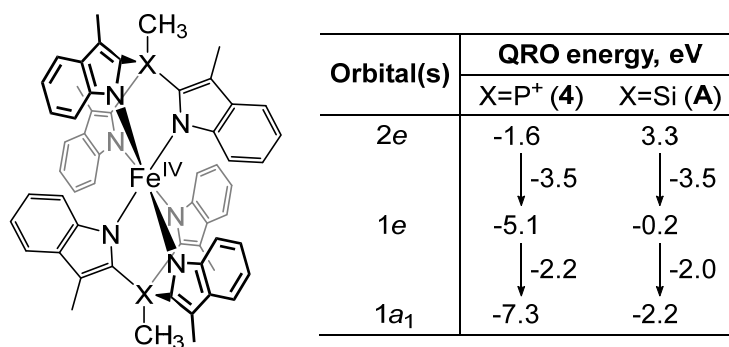


Chart 3.2. Comparison of the quasi-restricted orbital (QRO) energies of **4** and its Si-tethered analogue **A** calculated at the B3LYP-D3BJ/def2-TZVP (CP(PPP) for Fe) level of theory for a geometry optimized at the BP86-D3BJ/def2-TZVP level.

### 3.5.7 CASSCF calculations

To gain more insight into the magnetic properties of **4**, its excited states were calculated using CASSCF. Because only the *d-d* excitations are significantly relevant for the zero-field splitting and *g*-tensor calculations, the active space CAS(4,5) was restricted to only the metal-based *d*-orbitals. The energies were corrected with strongly-contracted NEVPT2 to recover dynamical correlation.

The results are consistent with the orbital picture given by DFT (*Figure 3.12*). They show the large splitting between the doubly- and singly occupied 1a<sub>1</sub> (−11.2 eV) and 1e (−9.5 eV) orbitals and the unoccupied orbital pair 2e (−0.9 eV). The first and second excited states correspond to a single *d-d* excitation from the doubly-occupied non-bonding orbital 1a<sub>1</sub> to the  $\pi$ -antibonding pair 1e, and lie at ca. 10 850 cm<sup>−1</sup> above the ground state. The excitation from the 1a<sub>1</sub> orbital to the highly  $\sigma$ -antibonding orbital pair 2e is 19 000 cm<sup>−1</sup> higher than the ground state (*Appendix B12*).

The zero-field splitting and the *g*-tensor were calculated by the effective Hamiltonian theory (for technical details, see *Appendix B12*). The principal axes of the *g*- and *D*-tensor coincides with the P–Fe–P C<sub>3</sub>-axis of rotation. The calculated *D*-value is +15.3 cm<sup>−1</sup>, while the rhombicity is zero, consistently with the axial symmetry of the system. The calculated *g*-tensor exhibits only small anisotropy ( $g_{\parallel} = 2.00$ ,  $g_{\perp} = 2.04$ ,  $g_{\text{iso}} = 2.03$ ). These parameters are in a good agreement with the data obtained from the SQUID and THz-EPR measurements (*vide supra*):  $D = +19.1$  cm<sup>−1</sup>,  $E \leq 0.3$  cm<sup>−1</sup> and  $g_{\text{iso}}$  of 1.97. The moderate zero-field splitting and fairly isotropic *g*-value are not surprising since the lowest-energy *d-d* excited state, which is also spin-conserving, lies 10 800 cm<sup>−1</sup> above the ground state, which is more than 20 times larger than effective

the spin-orbit coupling constant of the Fe(IV) ion ( $515 \text{ cm}^{-1}$ ).<sup>66</sup> Hence the ground state is fairly isolated and the spin-orbit coupling effect represents a moderate perturbation.

### 3.5.8 Paramagnetic $^1\text{H}$ NMR spectroscopy

Despite the moderate solubility of **4** in conventional solvents, we were able to acquire its  $^1\text{H}$  NMR spectra in  $\text{DCM-}d_2$  (Figure 3.13). The complex shows six paramagnetically shifted and broadened signals, as expected for the  $D_{3d}$  topology in solution. The signals were assigned based on their integral intensity, linewidth and by comparing the spectrum with that of a deuterated ( $^2\text{H}_3$ )methylphosphonium analogue, **4- $d_6$**  (Appendices B13, B14 and B17), which was synthesized independently.

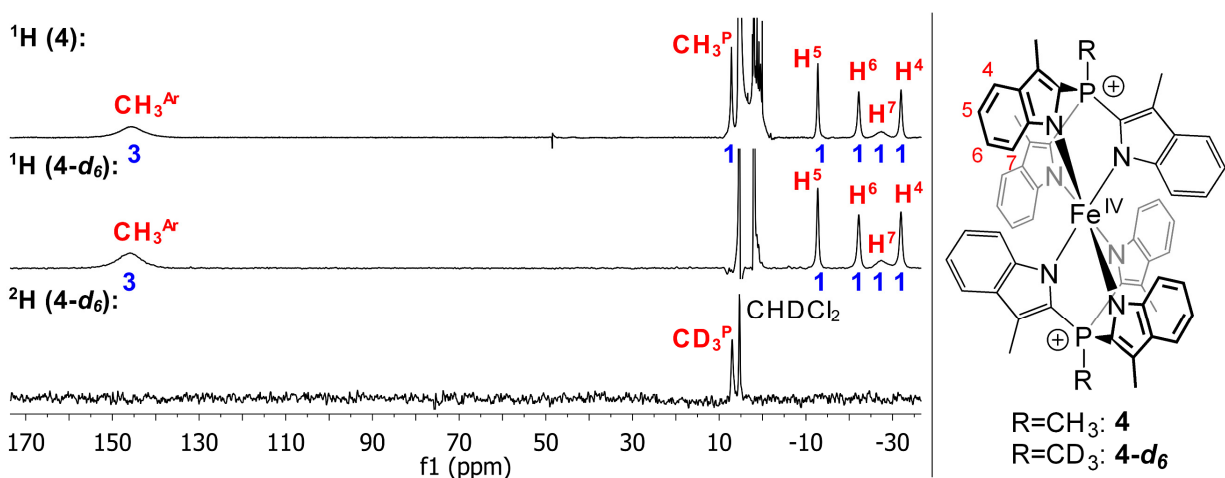


Figure 3.13.  $^1\text{H}$  (400 MHz) and  $^2\text{H}$  (61 MHz) NMR spectra of **4** and its deuterated analogue **4- $d_6$**  in DCM at 298 K. Only paramagnetic signals are assigned. The integrals are given in blue and were rounded to the nearest integer.

The  $^1\text{H}$  NMR spectra of **4** are strongly temperature-dependent (Appendix B18), as expected for a paramagnetic compound. Isolation of the hyperfine shifts ( $\delta^{\text{HF}}$ ) from the observed ones ( $\delta^{\text{obs}}$ ) by subtracting the diamagnetic contribution ( $\delta^{\text{dia}}$ , Appendix B18) approximated by an isostructural Ga(III) analogue,  $[(\text{TSMPP})_2\text{Ga}^{\text{III}}]\text{PPh}_4$  (**5b**), reveals that  $\delta^{\text{HF}}$  does not deviate from the Curie behavior ( $\delta^{\text{HF}}T = \text{const}$ , Figure 3.14, left panel). This implies the dominance of the Fermi contact shifts (see the reasons in Appendix B13), which is in line with a moderate axial ZFS parameter of  $+19.1 \text{ cm}^{-1}$  and low rhombicity, that are not able to induce a significant pseudocontact contribution, as derived from the SQUID and THz-EPR studies as well as DFT and CASSCF calculations (*vide supra*).

The observed <sup>1</sup>H chemical shifts can be computationally modelled using a molecular geometry optimized at the PBE-D3BJ/def2-TZVPP level of theory followed by properties calculation at the PBE0-D3BJ/def2-TZVPP level (*Appendix B19*). By using the calculated isotropic proton hyperfine constants ( $A_{iso}$ ), experimental  $g_{iso}$  of 1.97 obtained from the THz-EPR studies (*vide supra*), diamagnetic shifts ( $\delta^{dia}$ ) approximated using **5b**, and by substituting them into *Eq. 3.2*, which only takes into account the Fermi contact contribution ( $\delta^{FC}$ ), one can arrive to the chemical shifts that are >95% accurate with respect to the experiment (*Figure 3.14, right panel*). This reinforces our prior conclusions as for very strong dominance of the contact shifts, moderate anisotropy and insignificant spin delocalization in the system.

$$\delta^{obs} = \delta^{dia} + \delta^{FC} = \delta^{dia} + \frac{S(S+1)\mu_B}{3kTg_N\mu_N} g_{iso} \cdot A_{iso}, \quad \text{Eq. 3.2}$$

where,  $\delta^{dia}$  – diamagnetic shift;  $\delta^{FC}$  – Fermi contact shift;  $S$  – electronic spin quantum number of the complex;  $\mu_B$  – Bohr magneton;  $g_{iso}$  – nuclear  $g$ -value;  $\mu_N$  – nuclear magneton;  $k$  – Boltzmann constant;  $T$  – temperature;  $g_{iso}$  – isotropic electronic  $g$ -value of the system;  $A_{iso}$  – isotropic hyperfine coupling constant.

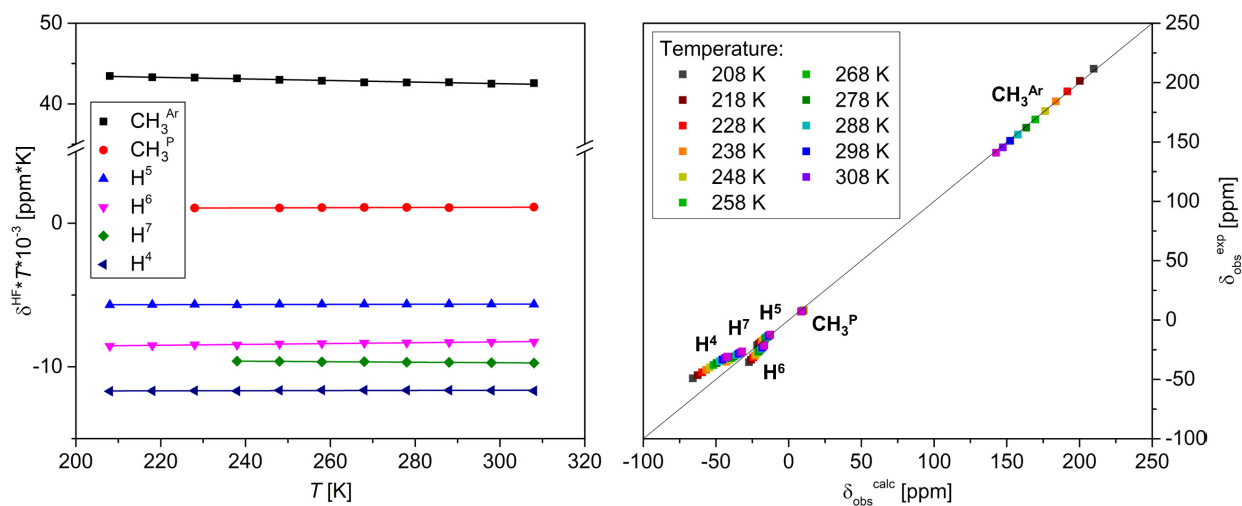


*Figure 3.14. Left panel: variable-temperature <sup>1</sup>H NMR (400 MHz)  $\delta^{HF} T$  products of **4** in dichloromethane-*d*<sub>2</sub>. Dots show experimental values, straight lines show linear fits (*Appendix B18*). Right panel: correlation plots of experimental vs. calculated observed chemical shifts for **4** (*Appendix B19*).*

### 3.5.9 Optical spectroscopy and TDDFT

Optical spectra of  $[(\text{TSMMP})_2\text{Fe}^{\text{II}}][(\text{B15C5})_2\text{K}]_2$  (**2b**),  $[(\text{TSMMP})_2\text{Fe}^{\text{III}}]\text{PPh}_4$  (**3b**) and  $[(\text{TSMMP})_2\text{Fe}^{\text{IV}}]$  (**4**) complexes in solution are shown in *Figure 3.15, right panel*. All three compounds display a set of very intense ( $\epsilon = 3\text{-}13 \cdot 10^4 \text{ cm}^{-1}\text{M}^{-1}$ ) absorptions below 375 nm, which we assign to  $\pi \rightarrow \pi^*$  transitions in aromatic ligands and counterions. Furthermore, both **3b** and **4** display a cluster of fairly weak ( $\epsilon = 2\text{-}4 \cdot 10^3 \text{ cm}^{-1}\text{M}^{-1}$ ) absorptions within 480-375 nm (denoted as **I**), tentatively assigned to higher-lying ligand-to-metal charge transfers (LMCT). Compound **3b** also shows a rather strong ( $\epsilon = 1 \cdot 10^4 \text{ cm}^{-1}\text{M}^{-1}$ ) absorption **II** at 618 nm, likely being another LMCT due to its intensity and position. Considering that in DCM solution, where the spectrum was measured, **3b** exists in a spin-state equilibrium (80.8% of HS component at 298 K, *vide supra*), we undertook variable-temperature UV-Vis studies to ascertain the exact origin of feature **II**. Cooling to 180 K, where the compound almost entirely exists in a LS state (3.4% of the HS component based on Evans method, *vide supra*), results in a feature of roughly the same intensity but shifted to 596 nm (*Appendix B20*). This leads us to conclude that both the LS and HS states of **3b** show LMCT within the same optical region. Interestingly, compound **4** displays an intense ( $\epsilon = 1.8 \cdot 10^4 \text{ cm}^{-1}\text{M}^{-1}$ ) absorption **III** that, rather unusually, peaks in the near-IR region ( $\lambda_{\text{max}} = 1234 \text{ nm}$ ). We interpret it as a higher-oxidation-state counterpart of the LMCT feature **II**, in line with our assignment of **4** as a true Fe(IV) compound.

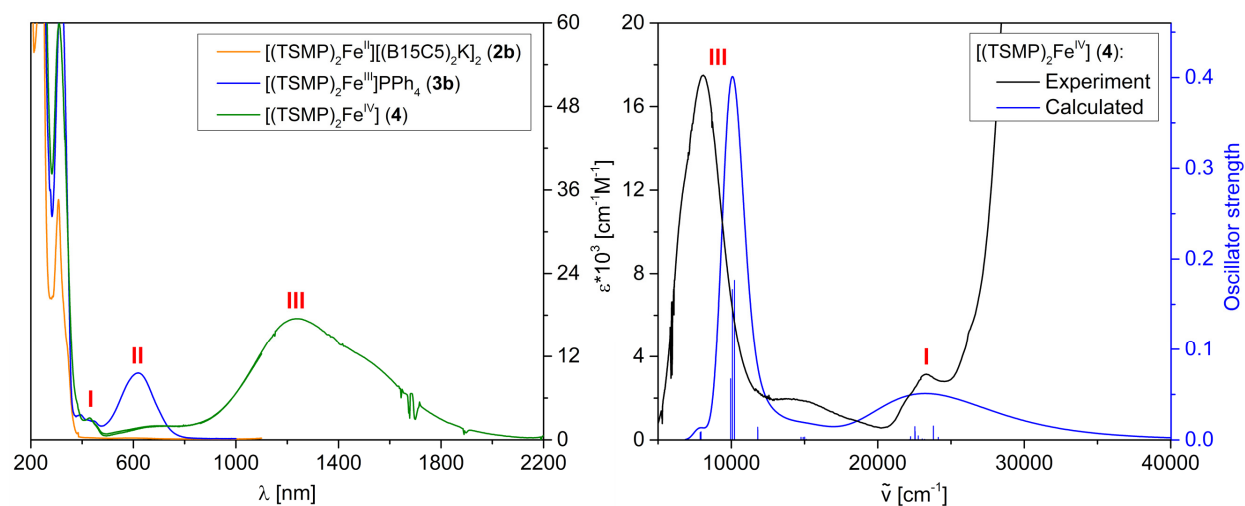


*Figure 3.15. Right panel:* UV-Vis-NIR spectra of complexes **2b**, **3b** and **4** in solution at 298 K. Compound **2b** was measured in acetonitrile,<sup>40</sup> **3b** and **4** were measured in DCM. *Left panel:* experimental and TDDFT-calculated (first 50 excitations) optical spectra of **4**. Calculations were performed at the TPSSh-D3BJ/def2-SVP (with def2-TZVP for Fe) level of theory in DCM. Gaussian broadening with FWHM of 170 nm was applied.

In order to reinforce our assignments of the optical spectra of **4**, we performed time-dependent density functional theory (TDDFT) calculations (for details, see *Appendix B21*). Calculated transitions roughly group in two clusters, which correspond to experimental features **I** and **III** (*Figure 3.15, left panel*). A detailed analysis of these transitions was done using the Natural Transition Orbital (NTO) theory, which performs separate unitary transformations of the occupied and virtual transition molecular orbitals so that only one or very few NTO donor-hole pairs are left, while having the predominant contribution to the transition.<sup>67</sup> According to NTO analysis, transitions in a lower-energy cluster **III** occur into the metal based  $d_{1e}$  orbitals (*Figure 3.12*), while the donor NTOs are combinations of 3-methylindole HOMO or HOMO-1-like orbitals of individual indolide units with different weight for every inversion-related pair (*Appendix B21*). The higher-energy cluster **I** is comprised of similar transitions into the metal-based  $d_{2e}$  orbitals or HOMO-LUMO intra-ligand charge transfer (ICT). In other words, cluster **III** is mostly  $\pi \rightarrow d_{1e}$  LMCT, and cluster **I** is a mixture of  $\pi \rightarrow d_{2e}$  LMCT and  $\pi \rightarrow \pi^*$  ICT. As a matter of fact, similar albeit more energetic transitions were observed for a structurally similar octahedral NHC-derived Fe(IV) phenylborate (**F** in *Chart 3.1*).<sup>29</sup> There, the counterpart of the feature **III** in **F** is 0.74 eV higher in energy, peaking at 715 nm. This observation correlates with the stronger  $\pi$ -accepting properties of the NHC-based borate ligand in **F**, compared to the indolides in TSMP<sup>2-</sup>.

### 3.6 Conclusions

In conclusion, we have shown that the tris-skatylmethylphosphonium (TSMP<sup>2-</sup>) ligand is capable of supporting both Fe(III) and Fe(IV) oxidation states in the respective isostructural complexes: [(TSMP)<sub>2</sub>Fe<sup>III</sup>]<sup>-</sup> (**3**) and [(TSMP)<sub>2</sub>Fe<sup>IV</sup>] (**4**). Both compounds are electrochemically connected and can be reversibly converted into one another as well as into the parent [(TSMP)<sub>2</sub>Fe<sup>II</sup>]<sup>2-</sup> (**2**) by a series of one-electron redox reactions.

Complex **3** undergoes thermal  $S = 1/2 \rightarrow 5/2$  spin-crossover both in solution and in the solid state and, to the best of our knowledge, is the only known synthetic system with an Fe<sup>III</sup>N<sub>6</sub> core capable of doing so. The exact dynamics of this process is highly dependent on the aggregation state, solvent and a counterion. The crossover is likely possible due to TSMP<sup>2-</sup> being a relatively weak-field ligand with poor  $\pi$ -accepting properties caused by the absence of low-lying  $\pi^*$ -orbitals in the extended aromatic systems.

Compound **4** features an Fe(IV) center with metal-centered oxidation and little spin delocalization on the ligand as shown by a series of electrochemical, spectroscopic and computational studies. It possesses a triplet ( $S = 1$ ) ground state, similarly to the

related trigonal antiprismatic Fe(IV) hexahydrazide clathrochelate (**E** in *Chart 3.1*)<sup>28</sup> and octahedral Fe(IV) tris(NHC)phenylborate (**F** in *Chart 3.1*)<sup>29</sup> that were recently reported. All three compounds are  $C_3$ -symmetrical, possessing an axial ZFS parameter  $D$  within the range of 19.1-23.1  $\text{cm}^{-1}$  along with very low rhombicity. Having said that, while **4** features a fairly isotropic  $g$ -tensor ( $g_{\text{iso}} = 1.97$ ), as indicated by THz-EPR, CASSCF calculations and NMR spectroscopy, **F** has significant anisotropy with  $g_{\parallel} = 1.88$  and  $g_{\perp} = 2.40$ .<sup>29</sup> Remarkably, both compounds have a green coloration due to an LCMT transition, which is 0.74 eV less energetic in **4**, peaking in near-IR at 1234 nm. This observation correlates with the lower  $\pi$ -accepting strength of indolides compared to the NHC-based borate ligand in **F**.

Overall, the findings presented in this paper demonstrate the utility of the dianionic TSMP<sup>2-</sup> scorpionate ligand to access the high valent Fe(IV) state in an octahedral  $N_6$  coordination environment. The self-consistent and detailed spectroscopic and computational characterization of the electronic structure of **4** will provide a valuable reference for identification of related systems.

### 3.7 Author contributions and acknowledgements

Serhii Tretiakov and Dr. Marc-Etienne Moret conceived the project. Serhii Tretiakov performed all synthetic work, NMR (including Evans method) measurements, ATR-FTIR, UV-Vis, CV and ESI-MS characterization as well as TD-DFT and some DFT, including hyperfine coupling constant, calculations. Serhii Tretiakov and Dr. Marc-Etienne Moret interpreted the data. Dr. Martin Lutz conducted single crystal X-ray diffraction experiments along with solving the structures. Dr. Charles James Titus carried out synchrotron XAS measurements followed by interpretation by Dr. Frank de Groot. Dr. Thomas Lohmiller and Dr. Karsten Holldack did synchrotron THz-EPR measurements, which were then interpreted by Dr. Joscha Nehr Korn, Dr. Thomas Lohmiller and Dr. Alexander Schnegg. Dr. Maxime François Xavier Tarra go and Dr. Shengfa Ye carried out EPR, Mössbauer and SQUID measurements, interpreted the results and performed some DFT and CASSCF calculations. Serhii Tretiakov, Dr. Valentin Novikov, Dr. Alexander Pavlov and Dmitry Aleshin interpreted paramagnetic NMR spectra. Serhii Tretiakov wrote a tutorial on paramagnetic NMR in *Appendices B13* and *B14*. Serhii Tretiakov wrote this chapter with input from all authors. All authors read and approved the final version.

The authors thank Dr. Serena Busatto and Dr. Celso de Mello Donega for technical support with Near-IR spectroscopy, and Dr. Andrei Gurinov with Dr. Hugo van In-



gen for support with paramagnetic high-field NMR measurements. We thank Dr. Philippe Schollhammer and Dr. Catherine Elleouet for insightful discussion on cyclic voltammetry measurements. We acknowledge the Helmholtz-Zentrum Berlin für Materialien und Energie for the allocation of synchrotron radiation beamtime at BESSY II. We also thank Dirk Ponwitz (Helmholtz-Zentrum Berlin) for technical support with measuring THz-EPR spectra. Andreas Göbels and Bernd Mienert (Max-Planck-Institute for Chemical Energy Conversion) are acknowledged for carrying out SQUID and Mössbauer spectroscopy measurements. We are indebted to late Dr. Eckhard Bill (Max-Planck-Institute for Chemical Energy Conversion) for fruitful discussions on interpretation of EPR, SQUID and Mössbauer results.

## 3.8 Experimental and computational methods

### 3.8.1 General remarks

All reactions involving air-sensitive compounds were conducted under a N<sub>2</sub> atmosphere by using standard glovebox or Schlenk techniques.

Acetonitrile, diethyl ether and *n*-hexane were dried with an MBRAUN MB SPS-79 system. Acetonitrile was additionally dried by passing through a column of activated neutral alumina after being kept over ca. 5 vol.% of 3Å molecular sieves over 48 h. THF was distilled from benzophenone/Na. Pyridine, DCM and butyronitrile were distilled from CaH<sub>2</sub>. Other solvents were used as supplied. Dried solvents were degassed by sparging with dry nitrogen for 30 min. and stored in a glovebox under nitrogen atmosphere and over molecular sieves, except for acetonitrile which was stored without the sieves. Deuterated solvents were acquired from Cambridge Isotope Laboratories, Inc. Chloroform-*d* and methylene chloride-*d*<sub>2</sub> were used as supplied, all other deuterated solvents were dried as indicated above for their proteo-analogues. Dried deuterated solvents were degassed by four freeze-pump-thaw cycles and stored in a glovebox over molecular sieves, except for acetonitrile-*d*<sub>3</sub> which was stored without the sieves. Phosphorus trichloride, trifluoroacetic acid, methyl iodide and methyl iodide-*d*<sub>3</sub> (>99 atom%) were purchased from Acros. All other chemicals were purchased from Sigma-Aldrich. Potassium hydride was supplied as a 30 wt.% suspension in mineral oil and was washed with dry and degassed *n*-hexane prior to use. FeCl<sub>2</sub> and GaCl<sub>3</sub> were purchased in an anhydrous form. Benzo-15-crown-5 was recrystallized from heptane. All other commercially obtained chemicals were used as received.

Unless stated otherwise, all NMR measurements were performed at 298 K on a Varian VNMRS400 or Varian MRF400 spectrometer, chemical shifts are reported relative to TMS with the residual solvent signal as internal standard.<sup>68</sup> All NMR experiments involving air-sensitive compounds were conducted in J. Young NMR tubes under an N<sub>2</sub> atmosphere. Peak multiplicity was quoted as s (singlet), d (doublet), t (triplet) and so on. In cases of unresolved couplings that strongly affect the line shape of individual components of an otherwise well-defined multiplet, the apparent multiplicity was quoted as 's' ('singlet'), 'd' ('doublet'), 't' ('triplet') and so on. In case of an overlap with solvent or impurity signals, where possible, integral intensities were extracted using MNova<sup>69</sup> peak deconvolution tool. ASAPHMQC experiments were conducted using the corresponding pulse sequence<sup>70</sup> as implemented in the VnmrJ 4.2 software.<sup>71</sup>

Effective solution magnetic moments in solution were obtained by the Evans method<sup>53-55</sup> using J. Young NMR tubes with a coaxial capillary insert as a reference. The latter was filled with a deuterated solvent with ~1% of TMS (or, alternatively, the same amount of a proteo-analogue of the deuterated solvent). The outer space contained a solution of the paramagnetic complex (5-10 mg/ml) in a deuterated solvent with the same concentration of TMS (alternatively, proteo-solvent). The absence of precipitation in the low-temperature measurements was controlled by comparing the effective magnetic moments measured at 25 °C before and after the cycle of cooling.

Molar magnetic susceptibility was calculated from the difference between the chemical shifts of TMS (or proteo-solvent) signals in the capillary and the outer solution ( $\Delta\delta$  in Hz) using the following equation:

$$\chi_M = \frac{\Delta\delta M}{\nu_0 S_f c} - \chi_M^{dia}, \quad \text{Eq. 3.3}$$

where  $M$  – molecular weight of the studied compound (g/mol);  $\nu_0$  – frequency of the spectrometer (Hz);  $S_f$  – shape factor of the magnet ( $4\pi/3$ );  $c$  – concentration of the paramagnetic complex (mg/ml);  $\chi_M^{dia}$  – molar diamagnetic contribution to the paramagnetic susceptibility calculated using Pascal's constants.<sup>72</sup> For variable-temperature measurements, the concentration  $c$  was adjusted so to take into account volumetric solvent expansion/contraction.

The effective magnetic moment was calculated as follows:

$$\mu_{eff} = \sqrt{8\chi_M T}, \quad \text{Eq. 3.4}$$

where  $T$  is temperature.

IR spectra were recorded on a Perkin-Elmer Spectrum Two FT-IR spectrometer. The bands were classified by an absorption intensity as: very weak (VW; 0-10% of the most intense absorption in the spectrum), weak (W; 10-30%), medium (M; 30-60%), strong (S; 60-90%), very strong (VS; 90-100%).

UV-Vis spectra were measured on a PerkinElmer Lambda 35 spectrometer. UV-Vis-NIR spectra were recorded using double-beam Perkin Elmer Lambda 950 UV/Vis spectrophotometer. ESI-MS measurements were performed on a Waters LCT Premier XE KE317 spectrometer or, alternatively, Adrion Expression CMS spectrometer. Elemental analysis was conducted by Medac Ltd.

Cyclic voltammetry (CV) was performed using an IVIUM Technologies Vertex Potentiostat/Galvanostat. All measurements were performed in 0.1 M  $nBu_4NPF_6$  acetonitrile electrolyte in a glovebox under dinitrogen atmosphere with strict exclusion of air and moisture.

Solid-state magnetic susceptibility data were measured from powder samples in the temperature range of 2 to 300 K by using a SQUID susceptometer with a field of 0.1 T (MPMS-7, Quantum Design, calibrated with standard palladium reference sample, error <2%). Multiple-field variable-temperature magnetization (VTVH) measurements were done at 1, 4 and 7 T also in the range of 2 to 300 K with the magnetization equidistantly sampled on a  $1/T$  temperature scale. The experimental data were corrected for underlying diamagnetism by use of tabulated Pascal's constants. An additional correction was done for temperature-independent paramagnetism. The susceptibility and magnetization data were simulated with the package julX written by E. Bill (Max-Planck Institute for Chemical Energy Conversion, Mülheim, Germany).

The XAS spectra were measured with electron yield (EY) detection at 300 K on the 10-1 beamline at SSRL, Stanford.<sup>73</sup> Samples were mounted to an aluminum sample holder using conductive carbon tape, placed in the measurement chamber, and pumped to  $1e-8$  Torr vacuum. The iron edge for each sample was scanned using monochromatic X-rays from a 1200 line/mm spherical grating monochromator, with a fixed exit slit of 25 microns, yielding a resolution of 0.2 eV. The total electron yield signal was collected by measuring the drain current from the sample holder, which was held at 37 degrees with respect to the incident beam. To avoid X-ray damage, a large

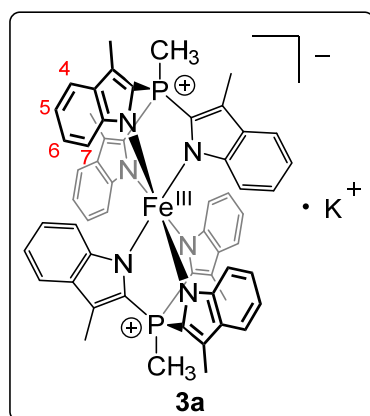
beam of 1 x 1 mm was used, and the sample spot was changed every two scans. No change in the signal was observed from scan to scan.

Mössbauer spectra were recorded on conventional spectrometers with alternating constant acceleration of the g-source. The minimum experimental line width was 0.24 mm/s (full width at half-height). The sample temperature was maintained constant using an Oxford Instruments Variox cryostat. The detector was an Ar/10%CH<sub>4</sub>-filled end-window type proportional counter. Isomer shifts are quoted relative to iron metal at 300 K. The spectra were simulated as Lorentzian doublets with the program *mf.SL* written by E. Bill (Max-Planck Institute for Chemical Energy Conversion, Mülheim, Germany).

Frequency-Domain Fourier-Transform THz-EPR, or THz-EPR in short, was performed at the THz beamline at BESSY II, Helmholtz-Zentrum Berlin. The experiment is described in detail elsewhere.<sup>74–76</sup> Coherent synchrotron radiation provided through the low- $\alpha$  operation mode was used. Experiments were performed in Voigt geometry (radiation propagation direction  $\mathbf{k}$  perpendicular to the external magnetic field  $B_0$ ) and perpendicular mode ( $B_1$  component of radiation perpendicular to the external magnetic field  $B_0$ ). As detector, a liquid He-cooled Si bolometer (Infrared Laboratories) was used. The FTIR settings were: scanner velocity of 20 kHz, resolution of 1 cm<sup>-1</sup>, and phase resolution of 2. Spectra were measured on a pressed pellet, prepared by homogenizing in a mortar 79 mg polycrystalline **4** and 101 mg polyethylene powder. All preparations were done under N<sub>2</sub> atmosphere. The spectra were measured at magnetic fields  $B_0$  varying from 7.5 to 0 T and at a temperature of 4.8 K. A reference spectrum was measured at 31 K and 0 T. All spectra, including the reference, were averaged over 96 scans. Unless stated otherwise, the spectra in the discussion are shown in (relative) absorbance as  $A(B_0) = \log_{10} \frac{I_{ref}}{I(B_0)}$ , with  $I_{ref}$  and  $I(B_0)$  corresponding to the reference transmittance spectrum and a transmittance spectrum measured at magnetic field  $B_0$ , respectively. Raw transmittance spectra are shown in *Appendix B5*. Simulations were performed with EasySpin<sup>77–79</sup> using the spin Hamiltonian in *Eq. B6.1, Appendix B6*.

### 3.8.2 Synthesis and basic characterization

#### 3.8.2.1 Metal complexes



**[(TSMP)<sub>2</sub>Fe<sup>III</sup>]**K** (**3a**). Complex **3a** was prepared by *in situ* oxidation of the precursor [(TSMP)<sub>2</sub>Fe<sup>II</sup>]**K**<sub>2</sub> (**2a**), formed from FeCl<sub>2</sub> and TSMPC<sub>2</sub> salt (**1**) and characterized by us elsewhere.<sup>40</sup> The oxidizing agents, ferrocenium tetrafluoroborate and tritilium tetrafluoroborate, are interchangeable in terms of the procedure below.**

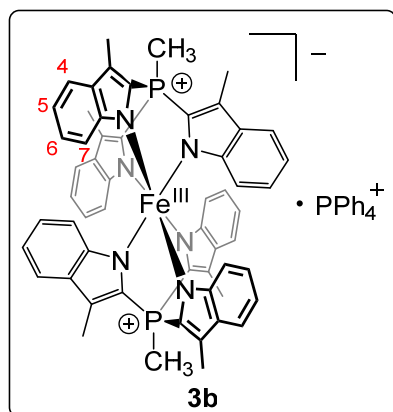
Dry THF (100 ml) was added to a mixture of TSMPC<sub>2</sub> salt (**1**) (contains 28.6 wt% of THF, 2.00 g, 2.79 mmol, 2.00 equiv.) and anhydrous FeCl<sub>2</sub> (0.177 g, 1.40 mmol, 1.00 equiv.) under dinitrogen atmosphere, followed by stirring overnight at room temperature. The stirring was stopped, and the fine bright-yellow suspension was allowed to separate in order to facilitate the subsequent filtration. The reaction was then

filtered through a fine sintered glass funnel. The potassium chloride filter cake was washed with three small portions of THF (3 x 3.0 ml), which were combined with the filtrate. The solvent from the latter was removed *in vacuo* to form a viscous dark-yellow oil, which was then redissolved in anhydrous acetonitrile (50 ml). This was followed by dropwise addition of a solution of an oxidizing agent (ferrocenium or tritylium tetrafluoroborate, 0.95 equiv.) in acetonitrile (30 ml), immediately accompanied by the change of coloration from yellow to green and, finally, navy blue. The mixture was stirred for 30 min. followed by filtration through a fine sintered glass funnel. The potassium tetrafluoroborate filter cake was washed with three small portions of acetonitrile (3 x 3.0 ml), which were combined with the filtrate. The latter was dried *in vacuo* to form a distinctly microcrystalline deep-blue, almost black, solid. The solid was washed with multiple small portions of THF (5 x 15.0 ml) until the washings became pale-blue with no changes in hue between the subsequent washes. The solid was then dried *in vacuo* to afford a black-blue microcrystalline powder of **3a** with 64.6% yield (0.626 g). Crystals suitable for X-ray diffraction analysis were grown by vapor diffusion of diethyl ether into an acetonitrile solution of **3a** at room temperature.

Anion [(TSMP)<sub>2</sub>Fe<sup>III</sup>]<sup>-</sup> (**3**) and, by extension, compound **3a** undergo thermal spin-crossover (SCO) both in the solid state and solution (see *Section 3.4* in the main text as well as *Appendices B2* and *B4*). Moreover, the SCO dynamics in solution depends on the specific solvent, on top of temperature dependence of the hyperfine NMR chemical shifts (*Appendix B15*). Solvent- and temperature dependence are also true for the effective molecular magnetic moment in solution as determined by the Evans method.<sup>53-55</sup> Importantly, the variable-temperature Evans method measurements performed using TMS and a residual underdeuterated NMR solvent signal as a reference are identical within the accuracy of the method (5-10%<sup>80</sup>). This implies that the solvent chemical shifts have no observable hyperfine component which, otherwise, would be a result of a specific interaction such as coordination. Furthermore, the hyperfine <sup>1</sup>H NMR shifts of **3** show the same shape of the trend regardless of solvent (with correction for the SCO critical temperature; *Figure 3.6*). These two observations indicate that dissociation of the ligand arms in **3** followed by the solvent coordination is very unlikely. As will be shown below, this is in contrast with the solution behavior of the [(TSMP)<sub>2</sub>Ga<sup>III</sup>]<sup>-</sup> (**5**) analogue.

All measurements described below were performed at 298 K. The assignments of <sup>1</sup>H NMR signals are discussed in detail in *Appendix B15*. In case of overlap with solvent or impurity signals, where possible, integral intensities were extracted using the MNova<sup>69</sup> peak deconvolution tool. <sup>1</sup>H NMR (400 MHz, acetonitrile-*d*<sub>3</sub>) δ 70.1 (br. s., 3H, Ar-CH<sub>3</sub>), 29.9 (br. s., 1H, H<sup>4</sup>), 11.8 (s, 1H, P<sup>+</sup>-CH<sub>3</sub>), -4.5 (s, 1H, H<sup>6</sup>), -7.0 (br. s., 1H, H<sup>5</sup>). <sup>1</sup>H NMR (400 MHz, pyridine-*d*<sub>5</sub>) δ 76.6 (br. s., 3H, CH<sub>3</sub><sup>A</sup>), 34.8 (br. s., 1H, H<sup>4</sup>), 10.8 (br. s., 1H, P<sup>+</sup>-CH<sub>3</sub>), -4.2 (br. s., 1H, H<sup>6</sup>), -7.4 (br. s., 1H, H<sup>5</sup>). <sup>31</sup>P NMR (162 MHz, acetonitrile-*d*<sub>3</sub>) δ -236.2 (br. s.). <sup>31</sup>P NMR (162 MHz, pyridine-*d*<sub>5</sub>) δ -295.7 (br. s.). **Effective magnetic moment in solution** determined in acetonitrile-*d*<sub>3</sub> is 4.64 μ<sub>B</sub>, which indicates a mid-spin-crossover situation ( $S = 1/2 \rightarrow 5/2$ ; see detailed discussion in *Appendix B2*). Effective magnetic moment of 5.14 μ<sub>B</sub> determined in pyridine-*d*<sub>5</sub> supports this conclusion. **UV-Vis** (acetonitrile): λ<sub>max</sub> (ε) = 211 (8.91·10<sup>4</sup>), 238 (8.87·10<sup>4</sup>), 318 (5.46·10<sup>4</sup>), 392 (2.17·10<sup>3</sup>), 422 (1.84·10<sup>3</sup>), 447 (1.80·10<sup>3</sup>), 609 nm (7.71·10<sup>3</sup> cm<sup>-1</sup>M<sup>-1</sup>). **ATR-FTIR** (neat)  $\tilde{\nu}$  (cm<sup>-1</sup>): 440 (M), 465 (M), 530 (W), 540 (W), 567 (W), 623 (M), 661 (S), 738 (S), 813 (M), 838 (M), 889 (S), 912 (W), 1004 (W), 1042 (M), 1100 (M), 1130 (M), 1198 (S), 1209 (S), 1248 (VS), 1291 (M), 1339 (M), 1362 (M), 1421 (M), 1450 (W), 1499 (M), 1597 (W), 2245 (W), 2249 (VW), 2865 (M), 2928 (M), 2989 (M), 2998 (M), 3040 (M). **ESI-TOF-MS** in CH<sub>3</sub>CN: 922.2214 [M]<sup>-</sup> (calcd. 922.2767 [M]<sup>-</sup>). No satisfactory ele-

mental analysis could be obtained due to the high reactivity of **3a** and its ability to retain variable amounts of solvent.

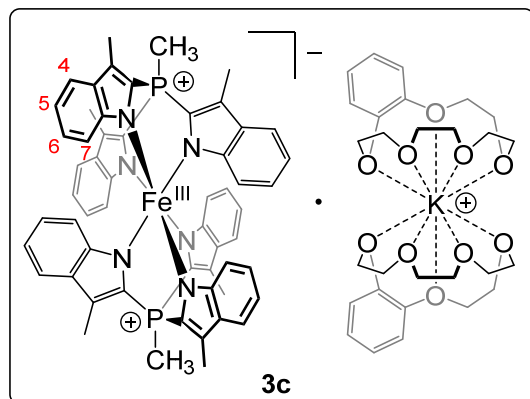


**[(TSMP)<sub>2</sub>Fe<sup>III</sup>]PPh<sub>4</sub> (**3b**).** Complex **3b** was prepared by ion exchange of [(TSMP)<sub>2</sub>Fe<sup>III</sup>]K (**3a**) and tetraphenylphosphonium iodide (PPh<sub>4</sub>I) in DCM. The procedure is as follows.

Dry DCM (25 ml) was added to a mixture of PPh<sub>4</sub>I (0.230 g, 0.494 mmol, 0.950 equiv.) and **3a** (0.500 g, 0.520 mmol, 1.00 equiv.), which is otherwise insoluble in DCM. Immediately, formation of a navy blue solution ensued, and the reaction was stirred for 30 min. followed by solvent removal *in vacuo* (to completely precipitate KI), resuspension in DCM, filtration and another vacuum solvent removal. The above manipulations yielded 0.623 g of a dark-blue, almost black, solid in quantitative

yield with respect to PPh<sub>4</sub>I. In principle, this material is sufficiently pure for further spectroscopic characterization and synthetic use. An additional purification step can be undertaken by recrystallization from DCM solution layered with *n*-hexane (crystallization yield: 88.5%), which is how the crystals for X-ray diffraction analysis were grown.

As discussed in the synthesis of [(TSMP)<sub>2</sub>Fe<sup>III</sup>]K (**3a**) (*vide supra*), anion [(TSMP)<sub>2</sub>Fe<sup>III</sup>]<sup>-</sup> (**3**) undergoes thermal spin-crossover, which also, by extension, applies to **3b**. Therefore, it is important to note that all characterization described below was performed at 298 K. The measurements were performed on the recrystallized material. The assignments of the <sup>1</sup>H NMR signals are discussed in detail in *Appendix B15*. While the <sup>1</sup>H NMR spectra show an increased intensity of the [PPh<sub>4</sub>]<sup>+</sup> signals with respect to what is needed to match the stoichiometry of **3b**, the <sup>31</sup>P spectra display the expected 1:2 intensity ratio. We connect the mismatch with problematic base line correction in <sup>1</sup>H spectra due to the presence of an intense dichloromethane signal. <sup>1</sup>H NMR (400 MHz, dichloromethane-*d*<sub>2</sub>) δ 67.7 (br. s., 3H, Ar-CH<sub>3</sub>), 27.5 (br. s., 1H, H<sup>4</sup>), 12.2 (br. s., 1H, P<sup>+</sup>-CH<sub>3</sub>), 8.14 – 6.89 (m, intensity unreliable/see above, [PPh<sub>4</sub>]<sup>+</sup>), -4.5 (br. s., 1H, H<sup>6</sup>), -6.7 (br. s., 1H, H<sup>5</sup>). <sup>31</sup>P NMR (162 MHz, dichloromethane-*d*<sub>2</sub>) δ 23.1 (s, carbon satellites: *J*<sub>P,C</sub> = 89.5 Hz, 1P, [PPh<sub>4</sub>]<sup>+</sup>), -213.5 (br. s., 2P, P<sup>+</sup>-CH<sub>3</sub>). **Effective magnetic moment in solution** determined in dichloromethane-*d*<sub>2</sub> at 298K is 4.68 μ<sub>B</sub>, which indicates a mid-spin-crossover situation (*S* = 1/2 → 5/2; see detailed discussion in *Appendix B2*). **UV-Vis** (dichloromethane): λ<sub>max</sub> (ε) = 236 (1.31·10<sup>5</sup>), 276 (3.61·10<sup>4</sup>), 320 (6.65·10<sup>4</sup>), 394 (3.62·10<sup>3</sup>), 423 (2.86·10<sup>3</sup>), 444 (2.71·10<sup>3</sup>), 618 nm (9.58·10<sup>3</sup> cm<sup>-1</sup>M<sup>-1</sup>). No satisfactory elemental analysis could be obtained due to high reactivity of **3b** and its ability to retain variable amounts of solvent.

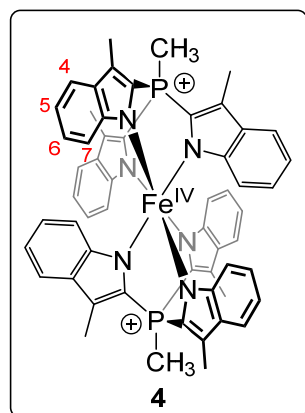


**[(TSMP)<sub>2</sub>Fe<sup>III</sup>][(B15C5)<sub>2</sub>K] (3c).** Complex **3c** was prepared by chelating the potassium cation in [(TSMP)<sub>2</sub>Fe<sup>III</sup>]K (**3a**) with an excess of benzo-15-crown-5. The procedure is as follows.

Dry acetonitrile (40 ml) was added to a mixture of **3a** (0.500 g, 0.520 mmol, 1.00 equiv.) and benzo-15-crown-5 (0.286 g, 1.07 mmol, 2.05 equiv.), and the mixture was stirred for 1 h, upon which the solvent was removed *in vacuo*. The resulting blue solid was thoroughly washed with small portions of *n*-hexane (5 x 10.0 ml) and dried *in vacuo* to yield 0.779 g of fine blue

powder in a quantitative yield. In principle, this material is sufficiently pure for further spectroscopic characterization. An additional purification step can be undertaken by recrystallization from pyridine solution layered with *n*-pentane (crystallisation yield: 93.7%), which is how the crystals for X-ray diffraction analysis were grown.

As discussed in the synthesis of [(TSMP)<sub>2</sub>Fe<sup>III</sup>]K (**3a**) (*vide supra*), anion [(TSMP)<sub>2</sub>Fe<sup>III</sup>]<sup>-</sup> (**3**) undergoes thermal spin-crossover, which also, by extension, applies to **3c**. Therefore, it is important to note that all characterization described below was performed at 298 K. The measurements were performed on the recrystallized material. The assignments of the <sup>1</sup>H NMR signals are discussed in detail in *Appendix B15*. The <sup>1</sup>H NMR spectra show an increased intensity of the bis(benzo-15-crown-5)potassium signals with respect to what is needed to match the stoichiometry of **3c**. A similar situation was observed for [(TSMP)<sub>2</sub>Fe<sup>III</sup>]PPh<sub>4</sub> (**3b**) salt (*vide supra*), which we connect with problematic base line correction due to the presence of intense solvent signals. <sup>1</sup>H NMR (400 MHz, acetonitrile-*d*<sub>3</sub>) δ 70.2 (br. s., 3H, Ar-CH<sub>3</sub>), 30.0 (br. s., 1H, H<sup>4</sup>), 11.8 (br. s., 1H, P<sup>+</sup>-CH<sub>3</sub>), 7.01 – 6.76 (m, intensity unreliable/see above, Ar of benzo-15-crown-5), 4.12 – 3.41 (m, intensity unreliable/see above, CH<sub>2</sub> of benzo-15-crown-5), -4.5 (br. s., 1H, H<sup>6</sup>), -7.1 (br. s., 1H, H<sup>5</sup>). <sup>31</sup>P NMR (162 MHz, acetonitrile-*d*<sub>3</sub>) δ -236.9 (br. s.). No satisfactory elemental analysis could be obtained due to the high reactivity of **3c** and its ability to retain variable amounts of solvent.

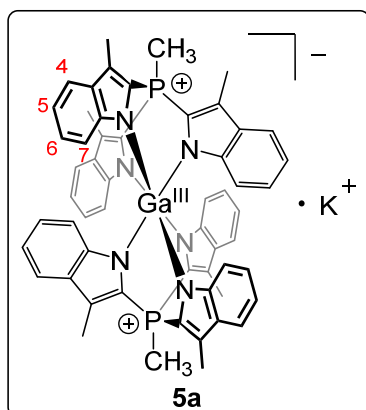


**[(TSMP)<sub>2</sub>Fe<sup>IV</sup>] (4).** Complex **4** was prepared by oxidation of [(TSMP)<sub>2</sub>Fe<sup>III</sup>]PPh<sub>4</sub> (**3b**) with elemental iodine. The advantage of using a PPh<sub>4</sub><sup>+</sup> salt **3b** is that the reaction product PPh<sub>4</sub>I is more soluble in dichloromethane than the target complex **4**, which allows to isolate the latter by washing with the solvent.

A solution of elemental iodine (0.046 g, 0.180 mmol, 0.475 equiv.) in dichloromethane (4.0 ml) was added dropwise over a minute to a stirred dichloromethane solution of **3b** (0.480 g, 0.380 mmol, 1.00 equiv. in 10.0 ml). The dark suspension was stirred over 40 min, after which it was filtered, and the dark-green filter cake was washed with DCM (3 x 2.0 ml) followed by drying *in vacuo*. The above manipulations yielded a

fine bottle green powder with 90.1% yield (0.318 g). Crystals suitable for X-ray diffraction analysis were grown by vapor diffusion of diethyl ether into a solution of **4** in pyridine-butyronitrile 2:1 (v/v) mixture at  $-40\text{ }^{\circ}\text{C}$ .

All measurements described below were performed at 298 K. The assignments of  $^1\text{H}$  NMR signals are discussed in detail in *Appendix B17*.  $^{31}\text{P}$  signals could not be detected within the probed range ( $\pm 400$  ppm).  $^1\text{H}$  NMR (400 MHz, dichloromethane- $d_2$ )  $\delta$  145.4 (br. s., 3H, Ar- $\text{CH}_3$ ), 7.2 (br. s., 1H,  $\text{P}^+-\text{CH}_3$ ), -12.8 (s, 1H,  $\text{H}^5$ ), -22.2 (s, 1H,  $\text{H}^6$ ), -27.4 (br. s., 1H,  $\text{H}^7$ ), -32.0 (br. s., 1H,  $\text{H}^4$ ). **UV-Vis-NIR** (dichloromethane):  $\lambda_{\text{max}}$  ( $\epsilon$ )= 239 ( $9.77 \cdot 10^4$ ), 309 ( $5.99 \cdot 10^4$ ), 429 ( $3.15 \cdot 10^3$ ), 702 ( $2.00 \cdot 10^3$ ), 1234 nm ( $1.75 \cdot 10^4\text{ cm}^{-1}\text{M}^{-1}$ ). **ATR-FTIR** (neat)  $\tilde{\nu}$  ( $\text{cm}^{-1}$ ): 441 (W), 539 (W), 574 (VW), 591 (W), 627 (W), 651 (W), 736 (M), 771 (W), 814 (W), 842 (M), 913 (M), 1061 (M), 1141 (S), 1194 (M), 1238 (VS), 1271 (M), 1323 (M), 1330 (M), 1380 (M), 1413 (M), 1425 (M), 1500 (M), 1559 (VW), 1595 (VW), 2251 (VW), 2901 (S), 2972 (VS), 2988 (VS), 3662 (W), 3675 (M), 3685 (W). **ESI-TOF-MS** spectra in  $\text{CH}_3\text{CN}$  recorded in a negative mode show a product of one-electron reduction of **4**: 922.2103 [ $M$ ] $^-$  (calcd. 922.2767 [ $M$ ] $^-$ ). No satisfactory elemental analysis could be obtained because of **4** retaining an unknown amount of solvent due to the presence of cationic charges.



**[(TSMP) $_2$ Ga $^{III}$ ] $\text{K}$  (**5a**). Complex [(TSMP) $_2$ Ga] $^-$  (**5**) was used to approximate the orbital component of the chemical shifts of [(TSMP) $_2$ Fe $^{III}$ ] $^-$  (**3**) and [(TSMP) $_2$ Fe $^{IV}$ ] (**4**). The potassium salt **5a** was prepared by reaction of  $\text{GaCl}_3$  with two equivalents of the  $\text{TSMPK}_2$  (**1**). The procedure is as follows.**

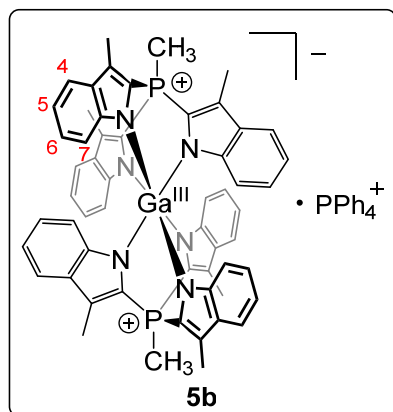
A solution of  $\text{GaCl}_3$  (0.068 g, 0.38 mmol, 1.0 equiv.) in acetonitrile (3.0 ml) was added dropwise over a minute to a solution of  $\text{TSMPK}_2$  salt (**1**) (contains 21.5 wt% of THF, 0.500 g, 0.768 mmol, 2.00 equiv.) in acetonitrile (7.0 ml). The reaction mixture was allowed to stir for 16 h, after which it was filtered and the filter cake was washed with acetonitrile (3 x 2.0 ml). The filtrate was concentrated *in vacuo* to ca. 2 ml, and the precipitated solid was collected and combined with the filter cake while the yellow liquor was discarded. Combined solids were extracted with acetonitrile (100 ml in total), which was then evaporated *in vacuo* to afford a white powder (102 mg, yield: 27.5%). Crystals suitable for X-ray diffraction analysis were grown by vapor diffusion of diethyl ether into an acetonitrile solution of **5a** at room temperature.

The procedure yields a highly pure material as evidenced by the NMR spectra in acetonitrile- $d_3$ . The fact that **5a** retains the assigned geometry on the  $^1\text{H}$  measurement time scale in acetonitrile- $d_3$  solution is evident from only six signals present in the spectrum, which can only correspond to the  $\text{C}_3$ -symmetric heterobicyclo[2.2.2]octane topology of the TSMP scaffold. Furthermore, some of the aromatic signals appear at unusually low chemical shifts with the lowest one corresponding to the  $\text{H}^7$  proton at 5.16 ppm followed by  $\text{H}^6$  at 5.46 ppm,  $\text{H}^5$  at 6.15 ppm and  $\text{H}^4$  at 7.12 ppm, the latter being a normal value for an aromatic proton. Such a progression can only be the case if two TSMP ligands “interlock” around a  $\text{Ga}^{III}$  center forming an  $\text{D}_{3d}$ -symmetric system, within which the protons with a higher assigned index are shielded due to magnetic anisotropy of the aromatic



rings. Interestingly, in pyridine-*d*<sub>5</sub> solution, one can still observe the D<sub>3d</sub>-symmetric configuration of **5a** but accompanied by half the molar amount of a highly-fluxional species with 2:1 symmetry as evidenced by the aromatic methyl group signals. This is in contrast with the analogous [(TSMF)<sub>2</sub>Fe<sup>III</sup>]<sup>-</sup>K<sup>+</sup> (**3a**) complex, which retains its D<sub>3d</sub>-geometry in pyridine-*d*<sub>5</sub> solution as indicated by variable-temperature measurements of the effective molecular magnetic moment by Evans method and variable-temperature hyperfine <sup>1</sup>H NMR chemical shifts (see the synthesis of [(TSMF)<sub>2</sub>Fe<sup>III</sup>]<sup>-</sup>K<sup>+</sup> (**3a**) above for more detail).

<sup>1</sup>H NMR spectral assignments of **5a** in pyridine-*d*<sub>5</sub> below only feature the signals that correspond to the S<sub>6</sub>-symmetric configuration. In case of an overlap with solvent or impurity signals, where possible, integral intensities were extracted using MNova<sup>69</sup> peak deconvolution tool. <sup>1</sup>H NMR (400 MHz, acetonitrile-*d*<sub>3</sub>) δ 7.12 (d, *J*<sub>H,H</sub> = 7.9 Hz, 1H, H<sup>4</sup>), 6.15 (t, *J*<sub>H,H</sub> = 7.3 Hz, 1H, H<sup>5</sup>), 5.46 (t, *J*<sub>H,H</sub> = 7.5 Hz, 1H, H<sup>6</sup>), 5.16 (d, *J*<sub>H,H</sub> = 8.6 Hz, 1H, H<sup>7</sup>), 3.57 (d, *J*<sub>H,P</sub> = 15.2 Hz, 1H, P<sup>+</sup>-CH<sub>3</sub>), 2.79 (d, *J*<sub>H,P</sub> = 1.1 Hz, 3H, Ar-CH<sub>3</sub>). <sup>1</sup>H NMR (400 MHz, pyridine-*d*<sub>5</sub>) δ 7.40 (d, *J*<sub>H,H</sub> = 7.8 Hz, 1H, H<sup>4</sup>), 6.34 (t, *J*<sub>H,H</sub> = 7.3 Hz, 1H, H<sup>5</sup>), 6.25 (d, *J*<sub>H,H</sub> = 8.6 Hz, 1H, H<sup>6</sup>), 5.90 (t, *J*<sub>H,H</sub> = 7.6 Hz, 1H, H<sup>7</sup>), 3.74 (d, *J*<sub>H,P</sub> = 15.1 Hz, 1H, P<sup>+</sup>-CH<sub>3</sub>), 2.85 (s, 3H, Ar-CH<sub>3</sub>). <sup>13</sup>C NMR (101 MHz, acetonitrile-*d*<sub>3</sub>) δ 148.1 (d, *J*<sub>C,P</sub> = 15.2 Hz, indole-C8), 129.4 (d, *J*<sub>C,P</sub> = 14.4 Hz, indole-C9 or C3), 125.7 (d, *J*<sub>C,P</sub> = 112.1 Hz, indole-C2), 119.8 (s, indole-C6), 118.0 (d, *J*<sub>C,P</sub> = 1.6 Hz, indole-C4), 117.4 (d, *J*<sub>C,P</sub> = 1.8 Hz, indole-C7), 116.5 (d, *J*<sub>C,P</sub> = 1.3 Hz, indole-C5), 115.4 (d, *J*<sub>C,P</sub> = 20.0 Hz, indole-C3 or C9), 10.7 (s, Ar-CH<sub>3</sub>), 5.6 (d, *J*<sub>C,P</sub> = 57.8 Hz, P<sup>+</sup>-CH<sub>3</sub>). <sup>31</sup>P NMR (162 MHz, acetonitrile-*d*<sub>3</sub>) δ -14.9 (br. s.). <sup>31</sup>P NMR (162 MHz, pyridine-*d*<sub>5</sub>) δ -12.8 (br. s.). UV-Vis (acetonitrile): λ<sub>max</sub> (ε) = 227 (1.21·10<sup>5</sup>), 238 (1.17·10<sup>5</sup>), 318 nm (8.13·10<sup>4</sup> cm<sup>-1</sup>M<sup>-1</sup>). ESI-TOF-MS in CH<sub>3</sub>CN: 935.2298 [*M*]<sup>-</sup> (calcd. 935.2672 [*M*]<sup>-</sup>). No satisfactory elemental analysis could be obtained due to high reactivity of **5a** and its ability to retain variable amounts of solvent.

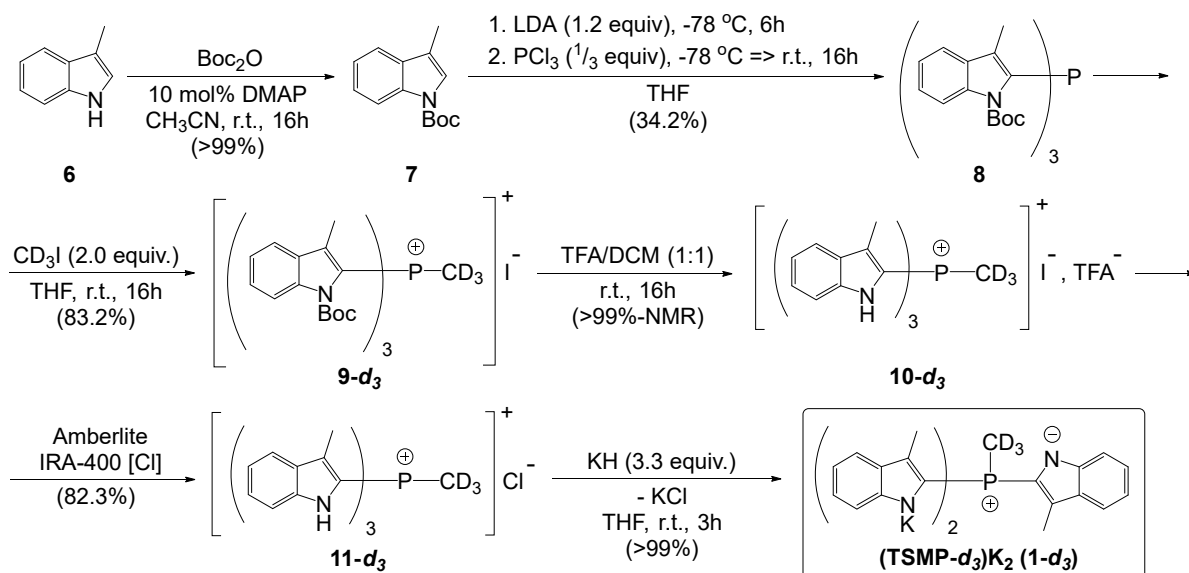


**Generation of [(TSMF)<sub>2</sub>Ga<sup>III</sup>]<sup>-</sup>PPh<sub>4</sub><sup>+</sup> (**5b**).** Complex [(TSMF)<sub>2</sub>Ga]<sup>-</sup> (**5**) was used to approximate the orbital component of the chemical shifts of [(TSMF)<sub>2</sub>Fe<sup>III</sup>]<sup>-</sup> (**3**) and [(TSMF)<sub>2</sub>Fe<sup>IV</sup>]<sup>-</sup> (**4**). An attempt to solubilize the synthesized above [(TSMF)<sub>2</sub>Ga<sup>III</sup>]<sup>-</sup>K<sup>+</sup> (**5a**) (10 mg, 0.010 mmol, 1.0 equiv.) in dichloromethane-*d*<sub>2</sub> (0.6 ml) in the presence of PPh<sub>4</sub>I (3.5 mg, 0.0076 mmol, 0.75 equiv.), led to a homogenous solution. The <sup>1</sup>H NMR spectrum indicates the presence of two species in a ratio of 1.6 to 1, the minor of which can be identified by the unusually low aromatic chemical shifts (*vide supra*) as an D<sub>3d</sub>-symmetric configuration of [(TSMF)<sub>2</sub>Ga<sup>III</sup>]<sup>-</sup> (**5**). The major species is highly fluxional (broad aromatic signals) and shows 1:2 symmetry breaking as indicated by the aromatic methyl group signals. Since the ion exchange clearly happens as evidenced by solubilization of [(TSMF)<sub>2</sub>Ga<sup>III</sup>]<sup>-</sup>K<sup>+</sup> (**5a**), yet no KI precipitation occurs, we speculate that the major species forms due to coordination of an iodide anion to the Ga<sup>III</sup> center in **5**. <sup>1</sup>H NOE spectra indicate that the major and the minor species are in dynamic exchange with one another. Similar spectra are observed if ion exchange is undertaken with an equal amount of PPh<sub>4</sub>Cl instead of PPh<sub>4</sub>I.

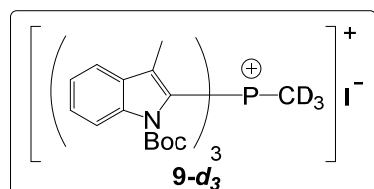
Since the speciation in solution is complicated and a subequivalent amount of  $\text{PPh}_4\text{I}$  was used, the NMR integral intensities of the  $[\text{PPh}_4]^+$  cation are devoid of the straightforward chemical meaning and, therefore, are not provided in the assignment below.  $^1\text{H}$  NMR (400 MHz, dichloromethane- $d_2$ )  $\delta$  7.83 (t,  $J = 7.4$  Hz, intensity uninformative/see above,  $[\text{PPh}_4]^+$ :  $\text{H}^4$ ), 7.65 (td,  $J = 7.8, 3.6$  Hz, intensity uninformative/see above,  $[\text{PPh}_4]^+$ :  $\text{H}^3$ ), 7.51 (dd,  $J = 13.0, 7.8$  Hz, intensity uninformative/see above,  $[\text{PPh}_4]^+$ :  $\text{H}^2$ ), 7.11 (d,  $J_{\text{H,H}} = 7.9$  Hz, 1H,  $\text{H}^4$ ), 6.15 (t,  $J_{\text{H,H}} = 7.2$  Hz, 1H,  $\text{H}^5$ ), 5.55 (t,  $J_{\text{H,H}} = 7.5$  Hz, 1H,  $\text{H}^6$ ), 5.21 (d,  $J_{\text{H,H}} = 8.6$  Hz, 1H,  $\text{H}^7$ ), 3.47 (d,  $J_{\text{H,P}} = 15.2$  Hz, 1H,  $\text{P}^+-\text{CH}_3$ ), 2.78 (s, 3H, Ar- $\text{CH}_3$ ).  $^{31}\text{P}$  NMR (162 MHz, dichloromethane- $d_2$ )  $\delta$  23.2 (s, carbon satellites:  $J_{\text{P,C}} = 89.5, 12.9, 10.2$  Hz, intensity uninformative/see above), -14.7 (br.s.).

### 3.8.2.2 Deuterium-labeled ligand

Deuterium-labeled  $(\text{TSMP-}d_3)\text{K}_2$  (**1- $d_3$** ) salt was prepared following the synthetic pathway for the corresponding proteo-analogue published by us elsewhere,<sup>40</sup> with the exception that we used  $\text{CD}_3\text{I}$  as a methylating agent at the stage of the synthesis of **9- $d_3$**  (Scheme 3.2).



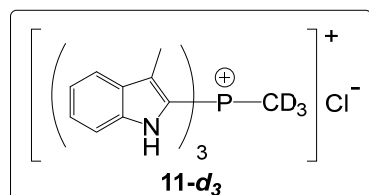
Scheme 3.2. Synthesis of a deuterium labeled dipotassium salt,  $(\text{TSMP-}d_3)\text{K}_2$  (**1- $d_3$** ).



**tris-(N-Boc-3-methylindol-2-yl)( $^2\text{H}_3$ )methylphosphonium iodide (**9- $d_3$** ).** Salt **9- $d_3$**  was synthesized following a synthetic procedure for the analogous proteo-compound published by us elsewhere.<sup>40</sup> Yield: 1.54 g (83.2%).

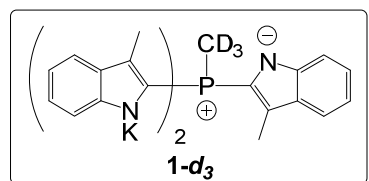
NMR spectroscopic assignments are based on those for the proteo-analogue. In dichloromethane- $d_2$  solution, the compound exists as a  $\sim 1:0.15$  mixture of rotamers.  $^1\text{H}$  NMR signals from the major rotamer are labeled with an asterisk. NMR signal intensities of the minor rotamer were rounded up to be divisible by 0.15 with no remainder for the sake of simplicity.  $^1\text{H}$  NMR (400 MHz, dichloromethane- $d_2$ )  $\delta$  8.18 (d,  $J_{\text{H,H}} = 8.6$  Hz, 0.05H, Ar-H), 8.12\* (d,

$J_{H,H} = 8.6$  Hz, 1H, Ar-H), 8.05 (d,  $J_{H,H} = 8.5$  Hz, 0.05H, Ar-H), 7.86 (d,  $J_{H,H} = 8.4$  Hz, 0.05H, Ar-H), 7.69\* (d,  $J_{H,H} = 8.0$  Hz, 1H, Ar-H), 7.63\* (t,  $J_{H,H} = 7.9$  Hz, 1H, Ar-H), 7.44\* (t,  $J_{H,H} = 7.5$  Hz, 1H, Ar-H), 2.38 (s, 0.15 H, Ar-CH<sub>3</sub>), 2.15 (s, 0.15H, Ar-CH<sub>3</sub>), 2.05 (s, 0.15H, Ar-CH<sub>3</sub>), 1.97\* (d,  $J_{H,P} = 2.1$  Hz, 3H, Ar-CH<sub>3</sub>), 1.67 (s, 0.45H, <sup>t</sup>Bu), 1.55\* (s, 9H, <sup>t</sup>Bu), 1.48 (s, 0.45H, <sup>t</sup>Bu), 1.15 (s, 0.45H, <sup>t</sup>Bu). <sup>2</sup>H NMR (61 MHz, dichloromethane-*h*<sub>2</sub>) δ 2.73 (br. s, 1H, P<sup>+</sup>-CD<sub>3</sub>). <sup>13</sup>C NMR (101 MHz, dichloromethane-*d*<sub>2</sub>) δ 150.9 (s, C=O<sup>Boc</sup>), 137.0 (d,  $J_{C,P} = 5.6$  Hz, indole-C9 or C8, or C3), 136.4 (d,  $J_{C,P} = 12.2$  Hz, indole-C8 or C9, or C3), 131.0 (d,  $J_{C,P} = 14.4$  Hz, indole-C3 or C8, or C9), 129.6 (s, C<sup>Ar</sup>-H), 124.6 (s, C<sup>Ar</sup>-H), 120.9 (s, C<sup>Ar</sup>-H), 116.5 (s, C<sup>Ar</sup>-H), 116.3 (d,  $J_{C,P} = 128.7$  Hz, indole-C2), 87.8 (s, qC<sup>t-Bu</sup>), 27.9 (s, CH<sub>3</sub><sup>t-Bu</sup>), 24.2 (br. s, P<sup>+</sup>-CD<sub>3</sub>), 10.1 (s, Ar-CH<sub>3</sub>). <sup>31</sup>P NMR (162 MHz, dichloromethane-*d*<sub>2</sub>) δ -2.5 (s, carbon satellites:  $J_{P,C} = 128.9, 79.9$  Hz, 1P), -4.2 (br.s., 0.15P). **ATR-FTIR (neat)**  $\tilde{\nu}$  (cm<sup>-1</sup>): 422 (VW), 461 (VW), 602 (VW), 658 (VW), 701 (W), 722 (W), 741 (W), 760 (M), 822 (W), 846 (W), 886 (W), 1001 (W), 1026 (W), 1043 (VW), 1117 (S), 1151 (M), 1204 (W), 1240 (S), 1314 (S), 1367 (S), 1445 (W), 1478 (W), 1531 (W), 1586 (VW), 1721 (VS), 1737 (M), 2931 (VW), 2966 (W). **ESI-TOF-MS** in CH<sub>3</sub>CN: found 739.4 [*M*]<sup>+</sup> (calcd. 739.4 [*M*]<sup>+</sup>).



**tris-(1H-3-methylindol-2-yl)(<sup>2</sup>H<sub>3</sub>)methylphosphonium chloride (11-*d*<sub>3</sub>).** Salt 11-*d*<sub>3</sub> was synthesized following a synthetic procedure for the analogous proteo-compound published by us elsewhere.<sup>40</sup> Yield: 1.12 g (82.3%).

NMR spectroscopic assignments are based on the assignments for the proteo-analogue. <sup>1</sup>H NMR (400 MHz, DMSO-*d*<sub>6</sub>) δ 12.51 (s, 1H, NH), 7.73 (d,  $J_{H,H} = 8.1$  Hz, 1H, Ar-H), 7.60 (d,  $J_{H,H} = 8.4$  Hz, 1H, Ar-H), 7.40 (t,  $J_{H,H} = 7.6$  Hz, 1H, Ar-H), 7.19 (t,  $J = 7.6$  Hz, 1H, Ar-H), 1.90 (s, 3H, Ar-CH<sub>3</sub>). <sup>2</sup>H NMR (61 MHz, DMSO-*h*<sub>6</sub>) δ 3.23 (s, 1H, P<sup>+</sup>-CD<sub>3</sub>). <sup>13</sup>C NMR (101 MHz, DMSO-*d*<sub>6</sub>) δ 139.8 (d,  $J_{C,P} = 11.4$  Hz, indole-C8), 128.0 (d,  $J_{C,P} = 13.0$  Hz, indole C9 or C3), 126.9 (d,  $J_{C,P} = 15.8$  Hz, indole C3 or C9), 126.1 (s, C<sup>Ar</sup>-H), 120.34 (s, C<sup>Ar</sup>-H), 120.25 (s, C<sup>Ar</sup>-H), 112.7 (s, C<sup>Ar</sup>-H), 108.6 (d,  $J_{C,P} = 120.2$  Hz, indole-C2), 12.1 (br.s., P<sup>+</sup>-CD<sub>3</sub>), 8.2 (s, Ar-CH<sub>3</sub>). <sup>31</sup>P NMR (162 MHz, DMSO-*d*<sub>6</sub>) δ -14.2 (s, carbon satellites:  $J_{P,C} = 120.1, 58.2$  Hz, 1H). **ATR-FTIR (neat)**  $\tilde{\nu}$  (cm<sup>-1</sup>): 425 (S), 453 (W), 515 (W), 557 (W), 607 (W), 703 (S), 741 (VS), 812 (S), 892 (W), 942 (W), 1024 (M), 1042 (M), 1130 (M), 1151 (M), 1203 (S), 1238 (M), 1295 (W), 1331 (S), 1383 (W), 1430 (M), 1513 (S), 1578 (W), 1616 (W), 2118 (W), 2220 (W), 2847 (S), 2914 (S), 2973 (S), 3019 (S), 3058 (S), 3444 (W). **ESI-TOF-MS** in CH<sub>3</sub>CN: found 439.2 [*M*]<sup>+</sup> (calcd. 439.2 [*M*]<sup>+</sup>).



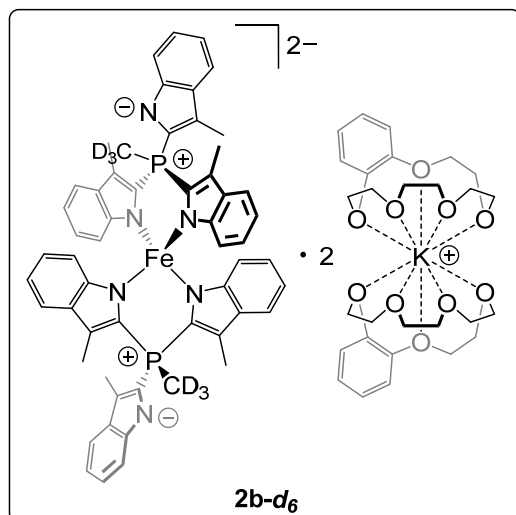
**(TSMP-*d*<sub>3</sub>)K<sub>2</sub> (1-*d*<sub>3</sub>).** Salt 1-*d*<sub>3</sub> was synthesized following a synthetic procedure for the analogous proteo-compound using KH as a base and published by us elsewhere.<sup>40</sup> Deprotonation occurs quantitatively with the yield of 1.45 g. Due to the presence of the K<sup>+</sup> cations, 1-*d*<sub>3</sub> always retains a certain of THF, which, in this particular batch, was identified to be 16.8%, using quantitative <sup>1</sup>H NMR experiments.

NMR spectroscopic assignments are based on the assignments for the proteo-analogue. <sup>1</sup>H NMR (400 MHz, acetonitrile-*d*<sub>3</sub>) δ 7.42 (d,  $J_{H,H} = 8.0$  Hz, 1H, Ar-H), 7.31 (d,  $J_{H,H} = 8.3$  Hz, 1H, Ar-H),

6.85 (t,  $J_{\text{H,H}} = 7.2$  Hz, 1H, Ar-H), 6.75 (t,  $J_{\text{H,H}} = 7.1$  Hz, 1H, Ar-H), 2.08 (d,  $J_{\text{H,P}} = 1.2$  Hz, 3H, Ar-CH<sub>3</sub>).  $^2\text{H NMR}$  (61 MHz, acetonitrile- $h_3$ )  $\delta$  2.57 (s, 1H, P<sup>+</sup>-CD<sub>3</sub>).  $^{13}\text{C NMR}$  (101 MHz, acetonitrile- $d_3$ )  $\delta$  149.6 (d,  $J_{\text{C,P}} = 24.2$  Hz, indole-C8), 132.2 (d,  $J_{\text{C,P}} = 10.9$  Hz, indole-C9 or C3), 128.5 (d,  $J_{\text{C,P}} = 117.6$  Hz, indole-C2), 119.3 (s, C<sup>Ar</sup>-H), 119.0 (d,  $J = 0.9$  Hz, C<sup>Ar</sup>-H), 118.6 (d,  $J = 1.0$  Hz, C<sup>Ar</sup>-H), 117.2 (d,  $J_{\text{C,P}} = 26.4$  Hz, indole-C3 or C9), 115.9 (d,  $J = 1.3$  Hz, C<sup>Ar</sup>-H), 14.0 (m,  $J = 32.0$ , 63.5 Hz, P<sup>+</sup>-CD<sub>3</sub>), 10.3 (s, Ar-CH<sub>3</sub>).  $^{31}\text{P NMR}$  (162 MHz, acetonitrile- $d_3$ )  $\delta$  -8.2 (s).

### 3.8.2.3 Deuterium-labeled complexes

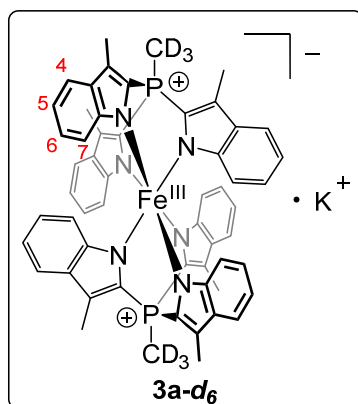
Deuterium-labeled complexes [(TSMF- $d_3$ )<sub>2</sub>Fe<sup>III</sup>]K (**3a-d<sub>6</sub>**), [(TSMF- $d_3$ )<sub>2</sub>Fe<sup>III</sup>]PPh<sub>4</sub> (**3b-d<sub>6</sub>**) and [(TSMF- $d_3$ )<sub>2</sub>Fe<sup>IV</sup>] (**4-d<sub>6</sub>**), were prepared following the procedures for the respective proteo-analogues **3a**, **3b** and **4** (see Section 3.8.2.1). Even though compound **3a-d<sub>6</sub>** was synthesized by *in situ* oxidation of the [(TSMF- $d_3$ )<sub>2</sub>Fe<sup>II</sup>]K<sub>2</sub> (**2a-d<sub>6</sub>**) intermediate, the tetrakis(benzo-15-crown-5)adduct of the latter, [(TSMF- $d_3$ )<sub>2</sub>Fe<sup>II</sup>][(B15C5)<sub>2</sub>K]<sub>2</sub> (**2b-d<sub>6</sub>**), was still isolated for the sake of completeness. It can be compared with the corresponding proteo-analogue published by us elsewhere.<sup>40</sup>



[(TSMF- $d_3$ )<sub>2</sub>Fe<sup>II</sup>][(B15C5)<sub>2</sub>K]<sub>2</sub> (**2b-d<sub>6</sub>**). Salt **2b-d<sub>6</sub>** was synthesized following a synthetic procedure for the analogous proteo-compound published by us elsewhere.<sup>40</sup> Yield: 0.315 g (42.5%).

Our previous studies suggest that the proteo-analogue **2b** exists in solution in more than one form,<sup>40</sup> therefore the assignment of paramagnetic  $^1\text{H NMR}$  signals is expected to be highly non-trivial. Hence, we did not expend effort for establishing the signal identities.

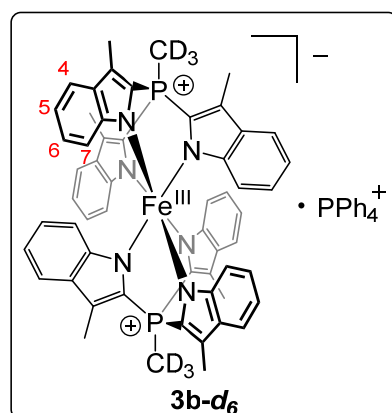
$^1\text{H NMR}$  (400 MHz, Acetonitrile- $d_3$ )  $\delta$  66.3 (br. s.), 21.6 (br. s.), 14.5 (br. s.), 6.88 (br. s., Ar-H of benzo-15-crown-5), 6.72 (br. s., Ar-H of benzo-15-crown-5), 6.1 (br. s.), 4.42 – 2.97 (m, aliphatic C-H of benzo-15-crown-5), -0.6 (br. s.), -0.9 (br. s.), -6.1 (br. s., P<sup>+</sup>-CH<sub>x</sub>D<sub>3-x</sub>, due to  $^1\text{H}$  isotopic impurities in the starting CD<sub>3</sub>I).  $^2\text{H NMR}$  (61 MHz, Acetonitrile- $h_3$ )  $\delta$  -6.0 (br. s., P<sup>+</sup>-CD<sub>3</sub>).  $^{31}\text{P NMR}$  (162 MHz, Acetonitrile- $d_3$ )  $\delta$  104.8 (br. s.). **ATR-FTIR** (neat)  $\tilde{\nu}$  (cm<sup>-1</sup>): 431 (M), 563 (W), 612 (W), 708 (M), 740 (S), 813 (M), 853 (W), 937 (M), 1044 (S), 1076 (M), 1098 (S), 1122 (VS), 1216 (S), 1252 (VS), 1296 (M), 1336 (M), 1362 (M), 1454 (M), 1504 (S), 1597 (W), 2863 (M), 2904 (M), 3041 (W). **ESI-TOF-MS** spectra in CH<sub>3</sub>CN recorded in a negative mode show a product of one-electron oxidation of **2b-d<sub>6</sub>**, which is in line with its high air-sensitivity: 928.3 [ $M$ ]<sup>-</sup> (calcd. 928.3 [ $M$ ]<sup>-</sup>).



**[(TSMP- $d_3$ ) $_2$ Fe $^{III}$ ]**K (3a- $d_6$ ).** Salt **3a- $d_6$**  was synthesized following a synthetic procedure for the analogous proteo-compound **3a** (see Section 3.8.2.1). Yield: 0.215 g (58.3%).**

All measurements described below were performed at 298K. The assignments of  $^1H$  NMR signals are discussed in detail in Appendix B15.  $^1H$  NMR (400 MHz, acetonitrile- $d_3$ )  $\delta$  70.3 (br. s., 3H, Ar- $CH_3$ ), 30.1 (br. s., 1H,  $H^4$ ), 11.8 (br. s., 0.09H,  $P^+-CH_xD_{3-x}$ , due to  $^1H$  isotopic impurities in the starting  $CD_3I$ ), -4.5 (br. s., 1H,  $H^6$ ), -7.1 (br. s., 1H,  $H^5$ ).  $^2H$  NMR (61 MHz, acetonitrile- $h_3$ )  $\delta$  11.6 (br. s., 1H,  $P^+-CD_3$ ).  $^{31}P$  NMR (162 MHz, acetonitrile- $d_3$ )  $\delta$  -237.5 (br.

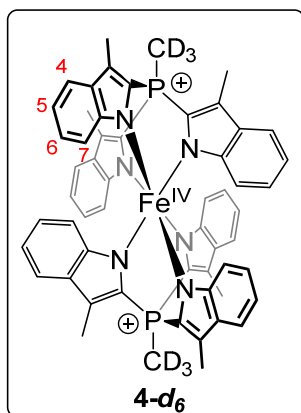
s.). **ESI-TOF-MS** spectra in  $CH_3CN$ : 928.3 [ $M$ ] $^-$  (calcd. 928.3 [ $M$ ] $^-$ ).



**[(TSMP- $d_3$ ) $_2$ Fe $^{III}$ ]**PPh $_4$  (3b- $d_6$ ).** Salt **3b- $d_6$**  was synthesized following a synthetic procedure for the analogous proteo-compound **3b** (see Section 3.8.2.1). Yield: 0.083 g (quantitative yield).**

All measurements described below were performed at 298K. The assignments of the  $^1H$  NMR signals are discussed in detail in Appendix B15. While the  $^1H$  NMR spectra show the increased intensity of the [ $PPh_4$ ] $^+$  signals with respect to what is needed to match the stoichiometry of **3b- $d_6$** , the  $^{31}P$  spectra display the expected 1:2 intensity ratio. A similar situation was observed for the proteo-analogue **3b** (see Section 3.8.2.1), which we connect

with problematic base line correction due to the presence of an intense dichloromethane signal.  $^1H$  NMR (400 MHz, dichloromethane- $d_2$ )  $\delta$  68.6 (br. s., 3H, Ar- $CH_3$ ), 27.7 (br. s., 1H,  $H^4$ ), 8.55 – 6.51 (m, intensity unreliable/see above, [ $PPh_4$ ] $^+$ ), -4.5 (br. s., 1H,  $H^6$ ), -6.8 (br. s., 1H,  $H^5$ ).  $^2H$  NMR (61 MHz, dichloromethane- $h_2$ )  $\delta$  12.2 (br. s., 1H,  $P^+-CH_3$ ).  $^{31}P$  NMR (162 MHz, dichloromethane- $d_2$ )  $\delta$  23.1 (s, 1P, [ $PPh_4$ ] $^+$ ), -216.7 (br. s., 2P,  $P^+-CD_3$ ).



**[(TSMP- $d_3$ ) $_2$ Fe $^{IV}$ ] (4- $d_6$ ).** Complex **4- $d_6$**  was synthesized following a synthetic procedure for the analogous proteo-compound **4** (see Section 3.8.2.1). Yield: 0.040 g (92.4%).

All measurements described below were performed at 298 K. The assignments of  $^1H$  NMR signals are discussed in detail in Appendix B17.  $^{31}P$  NMR signals were not observed in the probed spectral range (-500 to +500 ppm).  $^1H$  NMR (400 MHz, dichloromethane- $d_2$ )  $\delta$  145.9 (br. s., 3H, Ar- $CH_3$ ), -12.8 (s, 1H,  $H^5$ ), -22.2 (s, 1H,  $H^6$ ), -27.5 (br. s., 1H,  $H^7$ ), -32.0 (br. s., 1H,  $H^4$ ).  $^2H$  NMR (61 MHz, dichloromethane- $h_2$ )  $\delta$  6.98 (br. s., 1H,  $P^+-CH_3$ ). **ESI-TOF-MS** spectra in  $CH_3CN$  recorded in a negative mode show a product of one-electron reduction of **4**: 928.3 [ $M$ ] $^-$  (calcd. 928.3 [ $M$ ] $^-$ ).

### 3.8.2.4 Additional experiments

**Attempted synthesis of [(TSMP)<sub>2</sub>Fe<sup>III</sup>]K (3a) using FeCl<sub>3</sub>.** A solution of FeCl<sub>3</sub> (0.0055 g, 0.035 mmol, 1.0 equiv.) in acetonitrile (4.0 ml) was added dropwise over a minute to a solution of TSMPK<sub>2</sub> salt (**1**) (contains 28.6 wt% of THF, 0.050 g, 0.070 mmol, 2.1 equiv.) in acetonitrile (8.0 ml), which resulted in deep-blue coloration of the mixture. The reaction was allowed to stir for 4h, upon which it was filtered, and the solvent was evaporated *in vacuo*. <sup>1</sup>H NMR spectrum in acetonitrile-*d*<sub>3</sub> shows the presence of multiple paramagnetic species, one which is target complex **3a**, although in rather low relative abundance.

### 3.8.3 X-ray crystal structure determinations

CCDC 2245041-2245045 contain the supplementary crystallographic data for this paper. These data can be obtained free of charge from The Cambridge Crystallographic Data Centre *via* [www.ccdc.cam.ac.uk/data\\_request/cif](http://www.ccdc.cam.ac.uk/data_request/cif).

**[(TSMP)<sub>2</sub>Fe<sup>III</sup>]K (3a).** C<sub>60</sub>H<sub>54</sub>FeKN<sub>8</sub>P<sub>2</sub> · 2C<sub>2</sub>H<sub>3</sub>N, Fw = 1126.11, black block, 0.44 × 0.23 × 0.17 mm<sup>3</sup>, triclinic,  $\overline{P1}$  (no. 2), a = 10.9377(4), b = 14.5055(5), c = 18.1385(5) Å, α = 96.885(2), β = 97.281(2), γ = 101.149(1) °, V = 2769.74(15) Å<sup>3</sup>, Z = 2, D<sub>x</sub> = 1.350 g/cm<sup>3</sup>, μ = 0.46 mm<sup>-1</sup>. The diffraction experiment was performed on a Bruker Kappa ApexII diffractometer with sealed tube and Triumph monochromator (λ = 0.71073 Å) at a temperature of 150(2) K up to a resolution of (sin θ/λ)<sub>max</sub> = 0.65 Å<sup>-1</sup>. The crystal appeared to be twinned with a twofold rotation about uvw=[1,0,0] as twin operation. Consequently, two orientation matrices were used for the intensity integration with the Eval15 software.<sup>81</sup> The integration results were written in HKLF5 format.<sup>82</sup> A multi-scan absorption correction and scaling was performed with TWINABS<sup>83,84</sup> (correction range 0.63-0.75). A total of 106370 reflections was measured, 12737 reflections were unique (R<sub>int</sub> = 0.026), 11548 reflections were observed [I > 2σ(I)]. The structure was solved with Patterson superposition methods using SHELXT.<sup>85</sup> Structure refinement was performed with SHELXL-2018<sup>86</sup> on F<sup>2</sup> of all reflections. Non-hydrogen atoms were refined freely with anisotropic displacement parameters. All hydrogen atoms were located in difference Fourier maps and refined with a riding model. 719 Parameters were refined with no restraints. R1/wR2 [I > 2σ(I)]: 0.0322 / 0.0902. R1/wR2 [all refl.]: 0.0360 / 0.0927. S = 1.044. Twin fraction BASF=0.1631(7). Residual electron density between -0.41 and 0.44 e/Å<sup>3</sup>. Geometry calculations and checking for higher symmetry was performed with the PLATON program.<sup>87</sup>

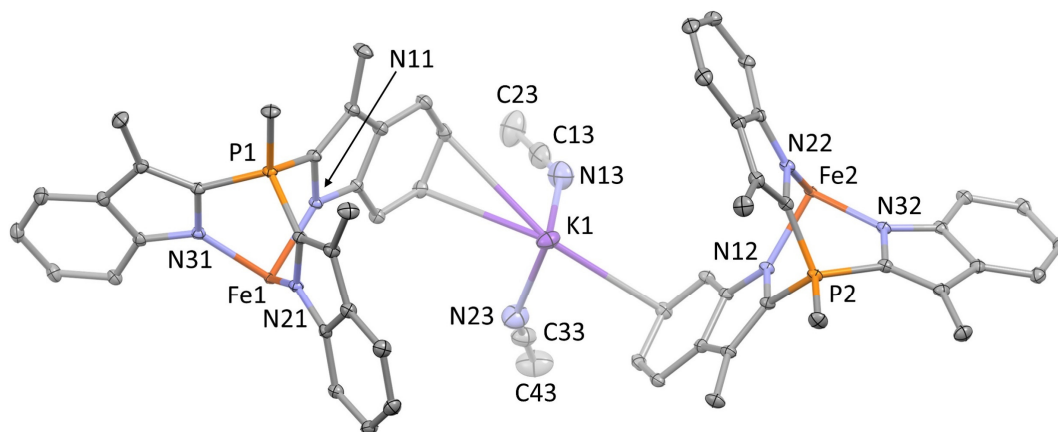


Figure 3.16. Asymmetric unit in the crystal of  $[(\text{TSMF})_2\text{Fe}^{\text{III}}]\text{K}$  (**3a**). Iron atoms are on special positions, therefore only half of the coordination environment is shown. Displacement ellipsoids are drawn at the 30% probability level. Hydrogen atoms, potassium cation and acetonitrile solvent molecules are omitted for clarity. Symmetry code *i*: 1-*x*, 1-*y*, -*z*. Selected bond distances (Å) and angles (°): Fe1-N11 1.9885(11), Fe1-N21 2.0020(12), Fe1-N31 1.9805(12), N11-Fe1-N21 91.11(5), N21-Fe1-N31 90.70(5), N31-Fe1-N11 90.73(5); Fe2-N12 1.9889(12), Fe2-N22 1.9885(12), Fe2-N32 1.9552(12), N12-Fe2-N22 91.56(5), N22-Fe2-N32 90.44(5), N32-Fe2-N12 91.16(5).

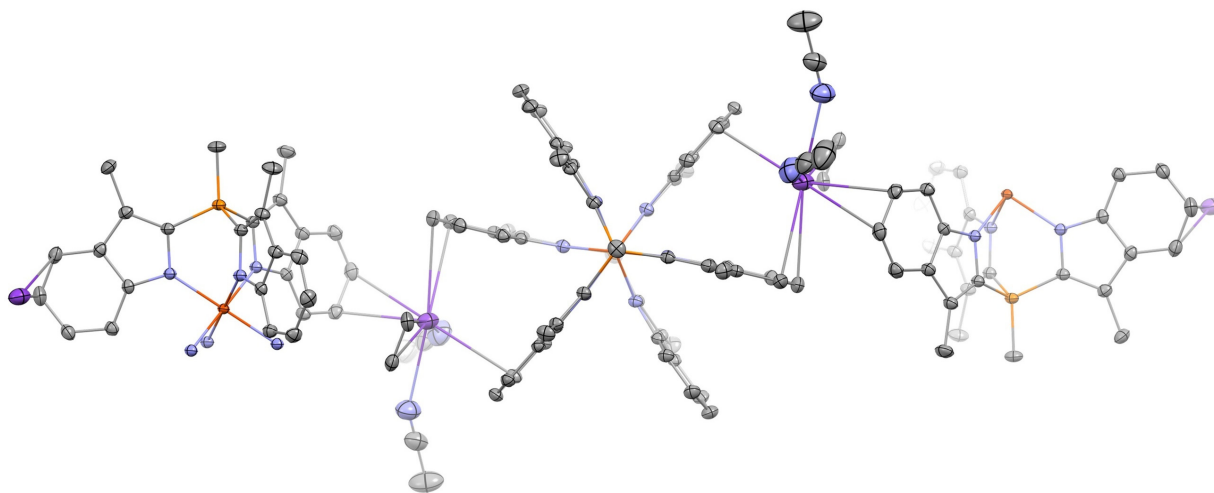


Figure 3.17. Coordination polymer in the [0,1,-1] direction in the crystal structure of  $[(\text{TSMF})_2\text{Fe}^{\text{III}}]\text{K}$  (**3a**). Displacement ellipsoids are drawn at the 30% probability level. Hydrogen atoms and non-coordinated acetonitrile molecules are omitted for clarity. Symmetry codes *i*: 1-*x*, -*y*, 1-*z*; *ii*: 1-*x*, 1-*y*, -*z*.

**[(TSMP)<sub>2</sub>Fe<sup>III</sup>]PPh<sub>4</sub> (3b).** [C<sub>56</sub>H<sub>48</sub>FeN<sub>6</sub>P<sub>2</sub>](C<sub>24</sub>H<sub>20</sub>P) + disordered solvent, Fw = 1262.16,<sup>a</sup> black plate, 0.36 × 0.16 × 0.05 mm<sup>3</sup>, triclinic,  $P\bar{1}$  (no. 2), a = 14.1299(3), b = 15.4113(4), c = 17.9403(3) Å, α = 85.134(1), β = 83.361(1), γ = 85.674(1) °, V = 3857.99(13) Å<sup>3</sup>, Z = 2, D<sub>x</sub> = 1.087 g/cm<sup>3</sup>,<sup>a</sup> μ = 0.30 mm<sup>-1</sup>.<sup>a</sup> The diffraction experiment was performed on a Bruker Kappa ApexII diffractometer with sealed tube and Triumph monochromator (λ = 0.71073 Å) at a temperature of 150(2) K up to a resolution of (sin θ/λ)<sub>max</sub> = 0.65 Å<sup>-1</sup>. The Eval15 software<sup>81</sup> was used for the intensity integration. A multi-scan absorption correction and scaling was performed with SADABS<sup>83,84</sup> (correction range 0.67-0.75). A total of 85393 reflections was measured, 17698 reflections were unique (R<sub>int</sub> = 0.068), 12087 reflections were observed [I > 2σ(I)]. The structure was solved with Patterson superposition methods using SHELXT.<sup>85</sup> Structure refinement was performed with SHELXL-2018<sup>86</sup> on F<sup>2</sup> of all reflections. The crystal structure contains voids (957 Å<sup>3</sup> / unit cell) filled with disordered solvent molecules. Their contribution to the structure factors was secured by back-Fourier transformation using the SQUEEZE algorithm<sup>88</sup> resulting in 285 electrons / unit cell. Non-hydrogen atoms were refined freely with anisotropic displacement parameters. One phenyl ring in the PPh<sub>4</sub> ion was refined with a disorder model. All hydrogen atoms were introduced in calculated positions and refined with a riding model. 877 Parameters were refined with 280 restraints (distances, angles, displacement parameters and ring flatness in PPh<sub>4</sub>). R1/wR2 [I > 2σ(I)]: 0.0483 / 0.1174. R1/wR2 [all refl.]: 0.0787 / 0.1291. S = 1.033. Residual electron density between -0.41 and 0.76 e/Å<sup>3</sup>. Geometry calculations and checking for higher symmetry was performed with the PLATON program.<sup>87</sup>

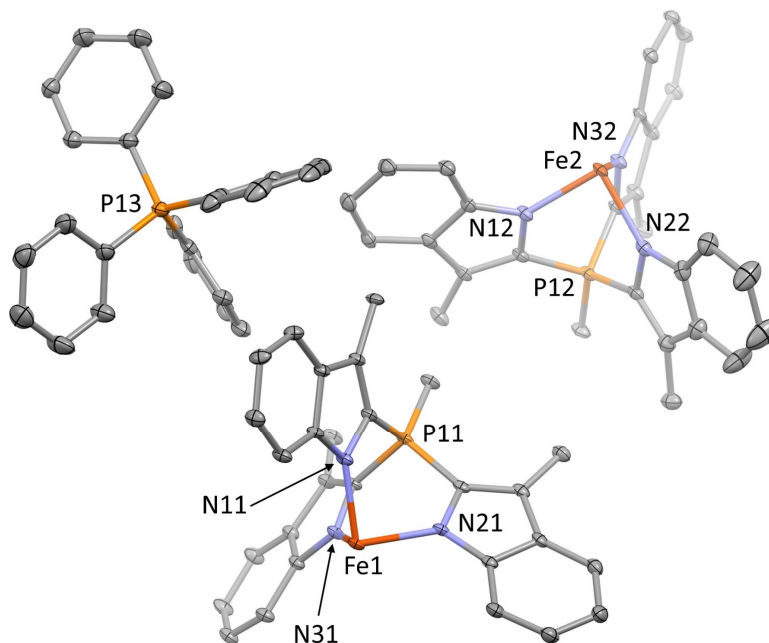


Figure 3.18. Asymmetric unit in the crystal of [(TSMP)<sub>2</sub>Fe<sup>III</sup>]PPh<sub>4</sub> (3b). Iron atoms are on special positions, therefore only half of the coordination environment is shown. Displacement ellipsoids

<sup>a</sup> Derived values do not contain the contribution of the disordered solvent molecules.



are drawn at the 30% probability level. Hydrogen atoms,  $PPh_4$  cation and severely disordered solvent molecules are omitted for clarity. Symmetry code  $i$ :  $-x, 1-y, 1-z$ . Selected bond distances (Å) and angles ( $^\circ$ ): Fe1-N11 1.9717(16), Fe1-N21 2.0025(17), Fe1-N31 1.9802(17), N11-Fe1-N21 90.52(7), N21-Fe1-N31 90.76(7), N31-Fe1-N11 91.24(7); Fe2-N12 2.0369(17), Fe2-N22 2.0313(18), Fe2-N32 2.0343(17), N12-Fe2-N22 89.64(7), N22-Fe2-N32 90.17(7), N32-Fe2-N12 90.06(7).

**[(TSM $P$ ) $_2$ Fe $^{III}$ ][(B15C5) $_2$ K] (3c).**  $[C_{56}H_{48}FeN_6P_2](C_{28}H_{40}KO_{10}) \cdot 1.5(C_5H_5N)$ , Fw = 1617.14, dark-blue needle,  $0.34 \times 0.07 \times 0.05$  mm $^3$ , triclinic,  $\bar{P}1$  (no. 2),  $a = 15.1846(9)$ ,  $b = 17.2956(8)$ ,  $c = 17.6868(7)$  Å,  $\alpha = 111.250(2)$ ,  $\beta = 101.333(2)$ ,  $\gamma = 105.495(2)$   $^\circ$ ,  $V = 3943.1(3)$  Å $^3$ ,  $Z = 2$ ,  $D_x = 1.362$  g/cm $^3$ ,  $\mu = 0.35$  mm $^{-1}$ . The diffraction experiment was performed on a Bruker Kappa ApexII diffractometer with sealed tube and Triumph monochromator ( $\lambda = 0.71073$  Å) at a temperature of 100(2) K up to a resolution of  $(\sin \theta/\lambda)_{max} = 0.61$  Å $^{-1}$ . The Eval15 software<sup>81</sup> was used for the intensity integration. A numerical absorption correction and scaling was performed with SADABS<sup>83,84</sup> (correction range 0.73-1.00). A total of 61310 reflections was measured, 14678 reflections were unique ( $R_{int} = 0.092$ ), 9168 reflections were observed [ $I > 2\sigma(I)$ ]. The structure was solved with Patterson superposition methods using SHELXT.<sup>85</sup> Structure refinement was performed with SHELXL-2018<sup>86</sup> on  $F^2$  of all reflections. Non-hydrogen atoms were refined freely with anisotropic displacement parameters. One pyridine molecule was disordered on an inversion center. All hydrogen atoms were introduced in calculated positions and refined with a riding model. 1056 Parameters were refined with 205 restraints (distances, angles, displacement parameters and ring flatness in the pyridine molecules).  $R1/wR2$  [ $I > 2\sigma(I)$ ]: 0.0516 / 0.1067.  $R1/wR2$  [all refl.]: 0.1058 / 0.1267.  $S = 1.010$ . Residual electron density between  $-0.50$  and  $0.47$  e/Å $^3$ . Geometry calculations and checking for higher symmetry was performed with the PLATON program.<sup>87</sup>

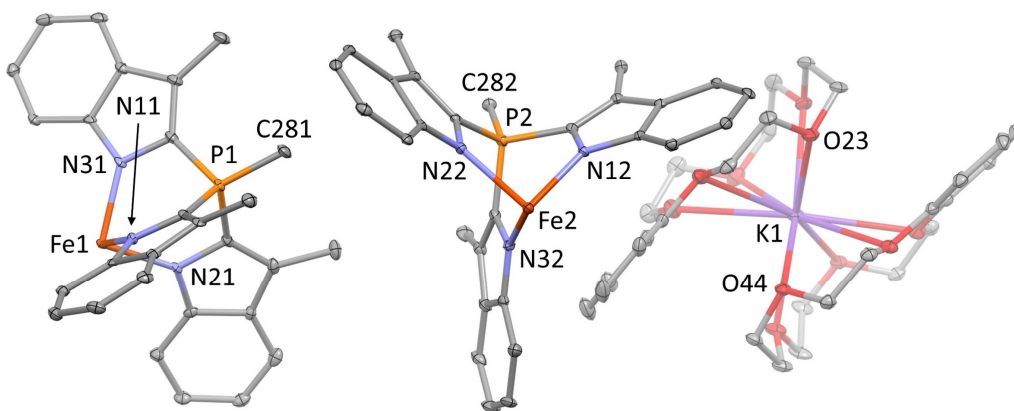


**Figure 3.19.** Asymmetric unit in the crystal of [(TSM $P$ ) $_2$ Fe $^{III}$ ][(B15C5) $_2$ K] (3c). Iron atoms are on special positions, therefore only half of the coordination environment is shown. Displacement ellipsoids are drawn at the 30% probability level. Hydrogen atoms, K[benzo-15-crown-5] cation and pyridine solvent molecules are omitted for clarity. Symmetry code  $i$ :  $-x, 1-y, -z$ . Selected bond distances (Å) and angles ( $^\circ$ ): Fe1-N11 1.970(2), Fe1-N21 1.976(2), Fe1-N31 2.008(2), N11-Fe1-N21

90.67(10), N21-Fe1-N31 91.00(10), N31-Fe1-N11 90.94(10); Fe2-N12 2.136(2), Fe2-N22 2.136(2), Fe2-N32 2.123(3), N12-Fe2-N22 87.56(9), N22-Fe-N32 87.51(9), N32-Fe2-N12 87.69(9).

**[(TSPM)<sub>2</sub>Fe<sup>IV</sup>] (4)**. C<sub>56</sub>H<sub>48</sub>FeN<sub>6</sub>P<sub>2</sub> · 6(C<sub>5</sub>H<sub>5</sub>N), Fw = 1397.39, black plate, 0.23 × 0.20 × 0.05 mm<sup>3</sup>, triclinic, P  $\bar{1}$  (no. 2), a = 11.5781(6), b = 12.1341(10), c = 14.4610(10) Å, α = 106.027(3), β = 94.678(3), γ = 114.093(2) °, V = 1738.3(2) Å<sup>3</sup>, Z = 1, D<sub>x</sub> = 1.335 g/cm<sup>3</sup>, μ = 0.32 mm<sup>-1</sup>. The diffraction experiment was performed on a Bruker Kappa ApexII diffractometer with sealed tube and Triumph monochromator (λ = 0.71073 Å) at a temperature of 150(2) K up to a resolution of (sin θ/λ)<sub>max</sub> = 0.53 Å<sup>-1</sup>. The Eval15 software<sup>81</sup> was used for the intensity integration. A multi-scan absorption correction and scaling was performed with SADABS<sup>83,84</sup> (correction range 0.58-0.74). A total of 22469 reflections was measured, 4263 reflections were unique (R<sub>int</sub> = 0.104), 2766 reflections were observed [I > 2σ(I)]. The structure was solved with Patterson superposition methods using SHELXT.<sup>85</sup> Structure refinement was performed with SHELXL-2018<sup>86</sup> on F<sup>2</sup> of all reflections. Non-hydrogen atoms were refined freely with anisotropic displacement parameters. All hydrogen atoms were introduced in calculated positions and refined with a riding model. 461 Parameters were refined with no restraints. R1/wR2 [I > 2σ(I)]: 0.0745 / 0.2036. R1/wR2 [all refl.]: 0.1229 / 0.2310. S = 1.167. Residual electron density between -0.32 and 0.57 e/Å<sup>3</sup>. Geometry calculations and checking for higher symmetry was performed with the PLATON program.<sup>87</sup>

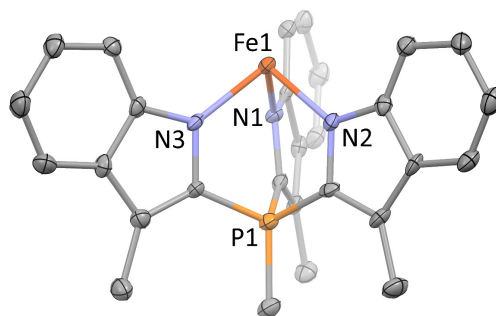


*Figure 3.20.* Asymmetric unit in the crystal of [(TSPM)<sub>2</sub>Fe<sup>IV</sup>] (4). Iron atom is on a special position, therefore only half of the coordination environment is shown. Displacement ellipsoids are drawn at the 30% probability level. Hydrogen atoms and pyridine solvent molecules are omitted for clarity. Symmetry code *i*: 1-x, 1-y, 1-z. Selected bond distances (Å) and angles (°): Fe1-N1 1.966(6), Fe1-N2 1.975(5), Fe1-N3 1.966(6), N1-Fe1-N2 91.6(2), N2-Fe1-N3 91.0(2), N3-Fe1-N1 90.7(2).

**[(TSPM)<sub>2</sub>Ga<sup>III</sup>]K (5a)**. C<sub>58</sub>H<sub>51</sub>GaKN<sub>7</sub>P<sub>2</sub> · C<sub>4</sub>H<sub>10</sub>O · C<sub>2</sub>H<sub>3</sub>N, Fw = 1131.99, colourless plate, 0.45 × 0.25 × 0.11 mm<sup>3</sup>, triclinic, P  $\bar{1}$  (no. 2), a = 11.0948(4), b = 14.7420(5), c = 17.6613(9) Å, α = 98.145(2), β = 99.810(3), γ = 100.918(2) °, V = 2749.36(19) Å<sup>3</sup>, Z = 2, D<sub>x</sub> = 1.367 g/cm<sup>3</sup>, μ = 0.69 mm<sup>-1</sup>. The diffraction experiment was performed on a Bruker Kappa ApexII diffractometer with sealed tube and Triumph monochromator (λ = 0.71073 Å) at a temperature of 150(2) K up to a resolution of (sin θ/λ)<sub>max</sub> = 0.65 Å<sup>-1</sup>. The crystal appeared to be broken in several fragments. The three major fragments were integrated using three orientation matrices with the Eval15 software.<sup>81</sup>

The integration results were written in HKLF5 format.<sup>82</sup> A multi-scan absorption correction and scaling was performed with TWINABS<sup>83,84</sup> (correction range 0.66-0.75). A total of 85413 reflections was measured, 14706 reflections were unique ( $R_{int} = 0.038$ ), 12207 reflections were observed [ $I > 2\sigma(I)$ ]. The structure was solved with Patterson superposition methods using SHELXT.<sup>85</sup> Structure refinement was performed with SHELXL-2018<sup>86</sup> on  $F^2$  of all reflections. Non-hydrogen atoms were refined freely with anisotropic displacement parameters. The diethyl ether solvent molecule was refined with a disorder model. All hydrogen atoms were introduced in calculated positions and refined with a riding model. 722 Parameters were refined with 68 restraints (distances, angles and displacement parameters in the disordered diethyl ether).  $R1/wR2$  [ $I > 2\sigma(I)$ ]: 0.0433 / 0.1191.  $R1/wR2$  [all refl.]: 0.0541 / 0.1275.  $S = 1.039$ . Scale factors of additional fragments, BASF=0.193(4) and 0.074(3). Residual electron density between -1.41 and 1.05  $e/\text{\AA}^3$ . Geometry calculations and checking for higher symmetry was performed with the PLATON program.<sup>87</sup>

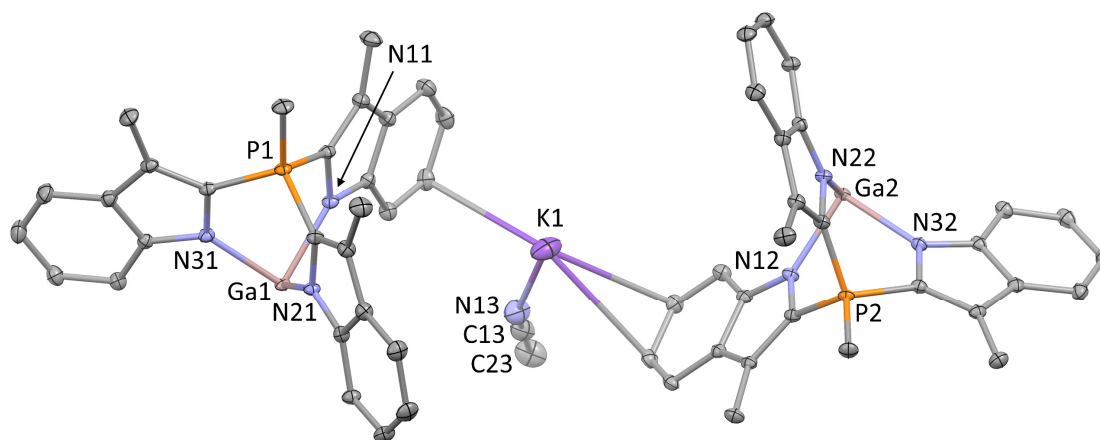


**Figure 3.21.** Asymmetric unit in the crystal of  $[(TSMP)_2Ga^{III}]K$  (**5a**). Gallium atoms are on special positions, therefore only half of the coordination environment is shown. Displacement ellipsoids are drawn at the 30% probability level. Hydrogen atoms, potassium cation and solvent molecules are omitted for clarity. Symmetry code  $i$ : 1-x, 1-y, -z. Selected bond distances ( $\text{\AA}$ ) and angles ( $^\circ$ ): N31-Ga1 2.0470(18), N11-Ga1 2.075(2), N21-Ga1 2.0845(19), N31-Ga1-N11 89.11(7), N31-Ga1-N21 88.93(7), N21-Ga1-N11 89.17(8); Ga2-N22 2.0783(18), Ga2-N32 2.0636(19), Ga2-N12 2.0691(19), N12-Ga2-N22 89.89(7), N12-Ga2-N32 88.78(8), N32-Ga2-N22 88.69(7).

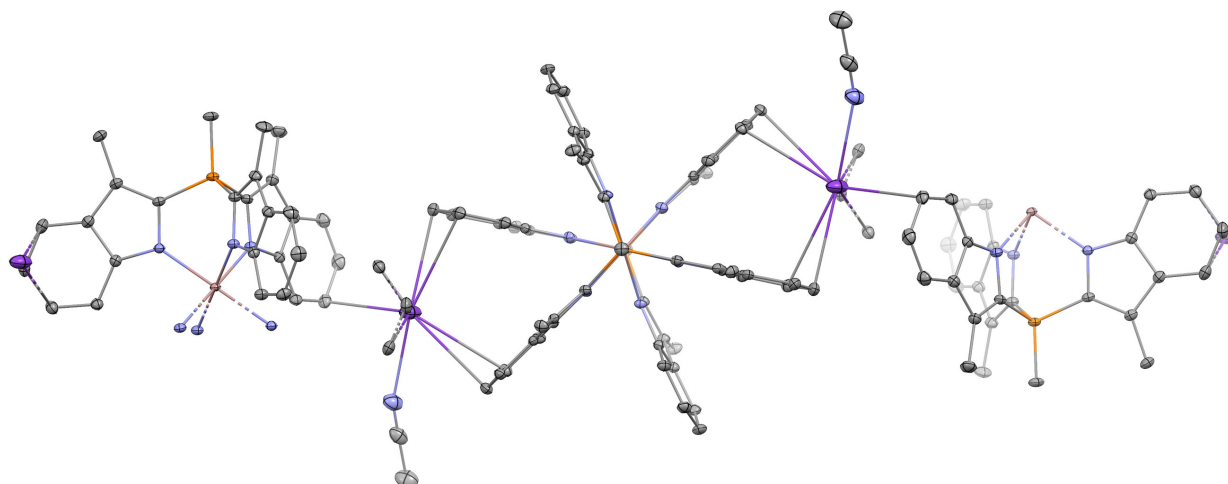


Figure 3.22. Coordination polymer in the [0,1,-1] direction in the crystal structure of  $[(\text{TSM})_2\text{Ga}^{\text{III}}]\text{K}$  (**5a**). Displacement ellipsoids are drawn at the 30% probability level. Hydrogen atoms and non-coordinated acetonitrile and diethyl ether molecules are omitted for clarity. Symmetry codes *i*: 1-*x*, -*y*, 1-*z*; *ii*: 1-*x*, 1-*y*, -*z*.

### 3.8.4 Computational details

All calculations were performed using ORCA 4.2.<sup>89,90</sup> The absence of imaginary frequencies was confirmed for all structures. Ground-state electronic structure calculations and Mössbauer parameter predictions were performed at the B3LYP-D3BJ/def2-TZVP (CP(PPP) for Fe) level of theory using a geometry optimized at the BP86-D3BJ/def2-TZVP level. The BP86 functional generally provides accurate geometries at affordable computational cost, and no relevant discrepancy with the crystallographic geometry was observed. The hybrid B3LYP functional generally reproduces Mössbauer parameters well with appropriate calibration.<sup>65</sup> Hyperfine coupling constants were calculated using B3LYP, TPSSH and PBE0 functionals with D3BJ dispersion correction and def2-TZVPP basis set. The respective geometries were optimized with the same functionals (PBE was used instead of PBE0 to save computational time), same dispersion correction and def2-TZVP basis set. The hyperfine coupling constant calculated using PBE0 showed the best agreement with the experiment and, therefore, were chosen for further discussion. TD-DFT spectra were calculated using B3LYP, TPSSH and PBE functionals along with D3BJ dispersion correction and 6-31G(d,p) basis set due to limitations of the computational infrastructure. TPSSH showed the best agreement with the experiment and, therefore, was chosen for further discussion. TD-DFT spectra and the corresponding Natural Transition Orbitals (NTOs) were calculated for the first 50 excitations.

For XAS spectroscopy, the ligand field multiplet calculations have been performed with the CTM4XAS software.<sup>61</sup> The Fe(III) calculation used a  $3d^5$  ground state with atomic parameters for the electron-electron interactions and the 2p and 3d spin-orbit coupling. The ligand field parameter 10Dq was set equal to 3.0 eV, which makes the high-spin  $S = 5/2$  and low-spin  $S = 1/2$  states almost degenerate. The spectra of the  $S = 5/2$  and  $S = 1/2$  states have been calculated and added as

described in the text. The Fe(IV) spectrum has been calculated using DFT-derived ordering of the 3d orbitals, which relates to a 10Dq value of 4.0 eV and a Ds value of 1.0 eV.

### 3.9 References

- (1) Solomon, E. I.; Brunold, T. C.; Davis, M. I.; Kemsley, J. N.; Lee, S.-K.; Lehnert, N.; Neese, F.; Skulan, A. J.; Yang, Y.-S.; Zhou, J. Geometric and Electronic Structure/Function Correlations in Non-Heme Iron Enzymes. *Chem. Rev.* **2000**, *100* (1), pp 235–350. DOI: 10.1021/cr9900275.
- (2) Costas, M.; Mehn, M. P.; Jensen, M. P.; Que, L. Dioxygen Activation at Mononuclear Nonheme Iron Active Sites: Enzymes, Models, and Intermediates. *Chem. Rev.* **2004**, *104* (2), pp 939–986. DOI: 10.1021/cr020628n.
- (3) Nam, W. High-Valent Iron(IV)–Oxo Complexes of Heme and Non-Heme Ligands in Oxygenation Reactions. *Acc. Chem. Res.* **2007**, *40* (7), pp 522–531. DOI: 10.1021/ar700027f.
- (4) Groves, J. T. High-Valent Iron in Chemical and Biological Oxidations. *J. Inorg. Biochem.* **2006**, *100* (4), pp 434–447. DOI: 10.1016/j.jinorgbio.2006.01.012.
- (5) Que, L.; Tolman, W. B. Biologically Inspired Oxidation Catalysis. *Nature* **2008**, *455* (7211), pp 333–340. DOI: 10.1038/nature07371.
- (6) Berry, J. F.; DeBeer George, S.; Neese, F. Electronic Structure and Spectroscopy of “Superoxidized” Iron Centers in Model Systems: Theoretical and Experimental Trends. *Phys. Chem. Chem. Phys.* **2008**, *10* (30), pp 4361–4374. DOI: 10.1039/b801803k.
- (7) Betley, T. a; Surendranath, Y.; Childress, M. V.; Alliger, G. E.; Fu, R.; Cummins, C. C.; Nocera, D. G. A Ligand Field Chemistry of Oxygen Generation by the Oxygen-Evolving Complex and Synthetic Active Sites. *Philos. Trans. R. Soc. B Biol. Sci.* **2008**, *363* (1494), pp 1293–1303. DOI: 10.1098/rstb.2007.2226.
- (8) Mas-Ballesté, R.; Que, L. Iron-Catalyzed Olefin Epoxidation in the Presence of Acetic Acid: Insights into the Nature of the Metal-Based Oxidant. *J. Am. Chem. Soc.* **2007**, *129* (51), pp 15964–15972. DOI: 10.1021/ja075115i.
- (9) Kaizer, J.; Klinker, E. J.; Oh, N. Y.; Rohde, J.-U.; Song, W. J.; Stubna, A.; Kim, J.; Münck, E.; Nam, W.; Que, L. Nonheme Fe<sup>IV</sup>O Complexes That Can Oxidize the C–H Bonds of Cyclohexane at Room Temperature. *J. Am. Chem. Soc.* **2004**, *126* (2), pp 472–473. DOI: 10.1021/ja037288n.
- (10) Cramer, S. A.; Jenkins, D. M. Synthesis of Aziridines from Alkenes and Aryl Azides with a Reusable Macrocyclic Tetracarbene Iron Catalyst. *J. Am. Chem. Soc.* **2011**, *133* (48), pp 19342–19345. DOI: 10.1021/ja2090965.
- (11) Nieto, I.; Ding, F.; Bontchev, R. P.; Wang, H.; Smith, J. M. Thermodynamics of Hydrogen Atom Transfer to a High-Valent Iron Imido Complex. *J. Am. Chem. Soc.* **2008**, *130* (9), pp 2716–2717. DOI: 10.1021/ja0776834.
- (12) Sabenya, G.; Gamba, I.; Gómez, L.; Clémancey, M.; Frisch, J. R.; Klinker, E. J.; Blondin, G.; Torelli, S.; Que, L.; Martin-Diaconescu, V.; Latour, J.-M.; Lloret-Fillol, J.; Costas, M. Octahedral Iron(IV)–Tosylimido Complexes Exhibiting Single Electron-Oxidation Reactivity. *Chem. Sci.* **2019**, *10* (41), pp 9513–9529. DOI: 10.1039/C9SC02526J.
- (13) Scepaniak, J. J.; Vogel, C. S.; Khusniyarov, M. M.; Heinemann, F. W.; Meyer, K.; Smith, J. M. Synthesis, Structure, and Reactivity of an Iron(V) Nitride. *Science* **2011**, *331* (6020), pp 1049–1052. DOI: 10.1126/science.1198315.
- (14) Vogel, C.; Heinemann, F. W.; Sutter, J.; Anthon, C.; Meyer, K. An Iron Nitride Complex. *Angew. Chemie Int. Ed.* **2008**, *47* (14), pp 2681–2684. DOI: 10.1002/anie.200800600.
- (15) Betley, T. A.; Peters, J. C. A Tetrahedrally Coordinated L<sub>3</sub>Fe–N<sub>x</sub> Platform That Accommodates Terminal Nitride (Fe<sup>IV</sup>:N) and Dinitrogen (Fe<sup>I</sup>–N<sub>2</sub>–Fe<sup>I</sup>) Ligands. *J. Am. Chem. Soc.* **2004**, *126* (20), pp 6252–6254. DOI: 10.1021/ja048713v.
- (16) Scepaniak, J. J.; Fulton, M. D.; Bontchev, R. P.; Duesler, E. N.; Kirk, M. L.; Smith, J. M. Structural and Spectroscopic Characterization of an Electrophilic Iron Nitrido Complex. *J. Am. Chem. Soc.* **2008**, *130* (32), pp 10515–10517. DOI: 10.1021/ja8027372.
- (17) Chanda, A.; Popescu, D.-L.; de Oliveira, F. T.; Bominaar, E. L.; Ryabov, A. D.; Münck, E.; Collins, T. J. High-Valent Iron Complexes with Tetraamido Macrocyclic Ligands: Structures, Mössbauer Spectroscopy, and DFT Calculations. *J. Inorg. Biochem.* **2006**, *100* (4), pp 606–619. DOI: 10.1016/j.jinorgbio.2005.12.016.
- (18) Lewis, R. A.; Wu, G.; Hayton, T. W. Synthesis and Characterization of an Iron(IV) Ketimide

- Complex. *J. Am. Chem. Soc.* **2010**, *132* (37), pp 12814–12816. DOI: 10.1021/ja104934n.
- (19) Rau, J. V; Nunziante Cesaro, S.; Chilingarov, N. S.; Leskiv, M. S.; Balducci, G.; Sidorov, L. N. Mass Spectrometric and FTIR Spectroscopic Identification of FeF<sub>4</sub> Molecules in Gaseous Phase. *Inorg. Chem. Commun.* **2003**, *6* (6), pp 643–645. DOI: 10.1016/S1387-7003(03)00070-4.
- (20) Schlöder, T.; Vent-Schmidt, T.; Riedel, S. A Matrix-Isolation and Quantum-Chemical Investigation of FeF<sub>4</sub>. *Angew. Chemie Int. Ed.* **2012**, *51* (48), pp 12063–12067. DOI: 10.1002/anie.201206464.
- (21) Bower, B. K.; Tennent, H. G. Transition Metal Bicyclo[2.2.1]Hept-1-Yls. *J. Am. Chem. Soc.* **1972**, *94* (7), pp 2512–2514. DOI: 10.1021/ja00762a056.
- (22) Lewis, R. A.; Smiles, D. E.; Darmon, J. M.; Stieber, S. C. E.; Wu, G.; Hayton, T. W. Reactivity and Mössbauer Spectroscopic Characterization of an Fe(IV) Ketimide Complex and Reinvestigation of an Fe(IV) Norbornyl Complex. *Inorg. Chem.* **2013**, *52* (14), pp 8218–8227. DOI: 10.1021/ic401096p.
- (23) Casitas, A.; Rees, J. A.; Goddard, R.; Bill, E.; DeBeer, S.; Fürstner, A. Two Exceptional Homoleptic Iron(IV) Tetraalkyl Complexes. *Angew. Chemie* **2017**, *129* (34), pp 10242–10247. DOI: 10.1002/ange.201612299.
- (24) Malischewski, M.; Adelhardt, M.; Sutter, J.; Meyer, K.; Seppelt, K. Isolation and Structural and Electronic Characterization of Salts of the Decamethylferrocene Dication. *Science* **2016**, *353* (6300), pp 678–682. DOI: 10.1126/science.aaf6362.
- (25) Pasek, E. A.; Straub, D. K. Tris(N,N-Disubstituted Dithiocarbamato)Iron(IV) Tetrafluoroborates. *Inorg. Chem.* **1972**, *11* (2), pp 259–263. DOI: 10.1021/ic50108a012.
- (26) Petrouleas, V.; Petridis, D. Moessbauer Quadrupole Splitting Analysis of Iron(IV) Dithio Chelates. *Inorg. Chem.* **1977**, *16* (6), pp 1306–1309. DOI: 10.1021/ic50172a011.
- (27) Milsman, C.; Sproules, S.; Bill, E.; Weyhermüller, T.; George, S. D.; Wieghardt, K. Stabilization of High-Valent Fe<sup>IV</sup>S<sub>6</sub>-Cores by Dithiocarbamate(1-) and 1,2-Dithiolate(2-) Ligands in Octahedral [Fe<sup>IV</sup>(Et<sub>2</sub>Dtc)<sub>3-n</sub>(Mnt)<sub>n</sub>]<sup>(N-1)-</sup> Complexes (N=0, 1, 2, 3): A Spectroscop. *Chem. Eur. J.* **2010**, *16* (12), pp 3628–3645. DOI: 10.1002/chem.200903381.
- (28) Tomy, S.; Shylin, S. I.; Bykov, D.; Ksenofontov, V.; Gumienna-Kontecka, E.; Bon, V.; Fritsky, I. O. Indefinitely Stable Iron(IV) Cage Complexes Formed in Water by Air Oxidation. *Nat. Commun.* **2017**, *8*, p 14099. DOI: 10.1038/ncomms14099.
- (29) Prakash, O.; Chábera, P.; Rosemann, N. W.; Huang, P.; Häggström, L.; Ericsson, T.; Strand, D.; Persson, P.; Bendix, J.; Lomoth, R.; Wärnmark, K. A Stable Homoleptic Organometallic Iron(IV) Complex. *Chem. – A Eur. J.* **2020**, *26* (56), pp 12728–12732. DOI: 10.1002/chem.202002158.
- (30) Harman, W. H.; Chang, C. J. N<sub>2</sub>O Activation and Oxidation Reactivity from a Non-Heme Iron Pyrrole Platform. *J. Am. Chem. Soc.* **2007**, *129* (49), pp 15128–15129. DOI: 10.1021/ja076842g.
- (31) Poulos, T. L. Heme Enzyme Structure and Function. *Chem. Rev.* **2014**, *114* (7), pp 3919–3962. DOI: 10.1021/cr400415k.
- (32) *Chemistry and Biochemistry of B12*; Banerjee, R., Ed.; Wiley: New York, 1999.
- (33) Lee, C.-H.; S. Lindsey, J. One-Flask Synthesis of Meso-Substituted Dipyrromethanes and Their Application in the Synthesis of Trans-Substituted Porphyrin Building Blocks. *Tetrahedron* **1994**, *50* (39), pp 11427–11440. DOI: 10.1016/S0040-4020(01)89282-6.
- (34) Swartz, D. L.; Odom, A. L. Synthesis, Structure, and Hydroamination Kinetics of (2,2'-Diaryldipyrrolyl) methane- and Bis(2-Arylpyrrolyl)Titanium Complexes. *Organometallics* **2006**, *25* (26), pp 6125–6133. DOI: 10.1021/om0607088.
- (35) King, E. R.; Betley, T. A. Unusual Electronic Structure of First Row Transition Metal Complexes Featuring Redox-Active Dipyrromethane Ligands. *J. Am. Chem. Soc.* **2009**, *131* (40), pp 14374–14380. DOI: 10.1021/ja903997a.
- (36) Novak, A.; Blake, A. J.; Wilson, C.; Love, J. B. Titanium and Zirconium Complexes Supported by Dipyrrolide Ligands. *Chem. Commun.* **2002**, No. 23, pp 2796–2797. DOI: 10.1039/b208751k.
- (37) Love, J. B.; Salyer, P. A.; Bailey, A. S.; Wilson, C.; Blake, A. J.; Davies, E. S.; Evans, D. J. The Dipyrrolide Ligand as a Template for the Spontaneous Formation of a Tetranuclear Iron(II) Complex. *Chem. Commun.* **2003**, *52* (14), pp 1390–1391. DOI: 10.1039/b303485b.
- (38) Sazama, G. T.; Betley, T. A. Ligand-Centered Redox Activity: Redox Properties of 3d

- Transition Metal Ions Ligated by the Weak-Field Tris(Pyrrrolyl)Ethane Trianion. *Inorg. Chem.* **2010**, *49* (5), pp 2512–2524. DOI: 10.1021/ic100028y.
- (39) Chapter 2 of This Thesis.
- (40) Tretiakov, S.; Damen, J. A. M.; Lutz, M.; Moret, M.-E. A Dianionic C<sub>3</sub>-Symmetric Scorpionate: Synthesis and Coordination Chemistry. *Dalt. Trans.* **2020**, *49* (39), pp 13549–13556. DOI: 10.1039/D0DT02601H.
- (41) Tretiakov, S.; Witteman, L.; Lutz, M.; Moret, M. Strain-Modulated Reactivity: An Acidic Silane. *Angew. Chemie Int. Ed.* **2021**, *60* (17), pp 9618–9626. DOI: 10.1002/anie.202015960.
- (42) Koningsbruggen, P. J.; Maeda, Y.; Oshio, H. Iron(III) Spin Crossover Compounds. In *Topics in Current Chemistry: Spin Crossover in Transition Metal Compounds I*; Springer-Verlag: Berlin, Heidelberg, 2004; Vol. 1, pp 259–324. DOI: 10.1007/b95409.
- (43) Harding, D. J.; Harding, P.; Phonsri, W. Spin Crossover in Iron(III) Complexes. *Coord. Chem. Rev.* **2016**, *313* (September 2015), pp 38–61. DOI: 10.1016/j.ccr.2016.01.006.
- (44) Krejčík, M.; Daněk, M.; Hartl, F. Simple Construction of an Infrared Optically Transparent Thin-Layer Electrochemical Cell. *J. Electroanal. Chem. Interfacial Electrochem.* **1991**, *317* (1–2), pp 179–187. DOI: 10.1016/0022-0728(91)85012-E.
- (45) Knof, U.; Weyhermüller, T.; Wolter, T.; Wiegardt, K.; Bill, E.; Butzlaff, C.; Trautwein, A. X. How “Innocent” Are Pentane-2,4-Dionebis(S-Alkylisothiosemicarbazonato) Ligands in Biomimetic Fe<sup>II</sup> and Fe<sup>IV</sup> Complexes? *Angew. Chemie Int. Ed. English* **1993**, *32* (11), pp 1635–1638. DOI: 10.1002/anie.199316351.
- (46) Lacy, D. C.; Gupta, R.; Stone, K. L.; Greaves, J.; Ziller, J. W.; Hendrich, M. P.; Borovik, A. S. Formation, Structure, and EPR Detection of a High Spin Fe<sup>IV</sup>—Oxo Species Derived from Either an Fe<sup>III</sup>—Oxo or Fe<sup>III</sup>—OH Complex. *J. Am. Chem. Soc.* **2010**, *132* (35), pp 12188–12190. DOI: 10.1021/ja1047818.
- (47) Savéant, J.-M. *Elements of Molecular and Biomolecular Electrochemistry: An Electrochemical Approach to Electron Transfer Chemistry*; John Wiley & Sons: Hoboken, NJ, 2006.
- (48) Walker, F. A. Magnetic Spectroscopic (EPR, ESEEM, Mössbauer, MCD and NMR) Studies of Low-Spin Ferriheme Centers and Their Corresponding Heme Proteins. *Coord. Chem. Rev.* **1999**, *185–186*, pp 471–534. DOI: 10.1016/S0010-8545(99)00029-6.
- (49) Sorai, M.; Seki, S. Phonon Coupled Cooperative Low-Spin <sup>1</sup>A<sub>1</sub>High-Spin <sup>5</sup>T<sub>2</sub> Transition in [Fe(Phen)<sub>2</sub>(NCS)<sub>2</sub>] and [Fe(Phen)<sub>2</sub>(NCSe)<sub>2</sub>] Crystals. *J. Phys. Chem. Solids* **1974**, *35* (4), pp 555–570. DOI: 10.1016/S0022-3697(74)80010-7.
- (50) Kahn, O. *Molecular Magnetism*; VCH Publishers, Inc.: New York (US), Weinheim (DE), Cambridge (UK), 1993; pp 26–29.
- (51) Kahn, O. *Molecular Magnetism*; VCH Publishers, Inc.: New York (US), Weinheim (DE), Cambridge (UK), 1993; p 56.
- (52) Kelly, C. T.; Griffin, M.; Esien, K.; Felton, S.; Müller-Bunz, H.; Morgan, G. G. Crystallographic Detection of the Spin State in Fe<sup>III</sup> Complexes. *Cryst. Growth Des.* **2022**, *22* (11), pp 6429–6439. DOI: 10.1021/acs.cgd.2c00468.
- (53) Evans, D. F. 400. The Determination of the Paramagnetic Susceptibility of Substances in Solution by Nuclear Magnetic Resonance. *J. Chem. Soc.* **1959**, pp 2003–2005. DOI: 10.1039/jr9590002003.
- (54) Piguet, C. Paramagnetic Susceptibility by NMR: The “Solvent Correction” Removed for Large Paramagnetic Molecules. *J. Chem. Educ.* **1997**, *74* (7), p 815. DOI: 10.1021/ed074p815.
- (55) Sur, S. K. Measurement of Magnetic Susceptibility and Magnetic Moment of Paramagnetic Molecules in Solution by High-Field Fourier Transform NMR Spectroscopy. *J. Magn. Reson.* **1989**, *82* (1), pp 169–173. DOI: 10.1016/0022-2364(89)90178-9.
- (56) Nikovskiy, I.; Aleshin, D. Y.; Novikov, V. V.; Polezhaev, A. V.; Khakina, E. A.; Melnikova, E. K.; Nelyubina, Y. V. Selective Pathway toward Heteroleptic Spin-Crossover Iron(II) Complexes with Pyridine-Based N-Donor Ligands. *Inorg. Chem.* **2022**, *61* (51), pp 20866–20877. DOI: 10.1021/acs.inorgchem.2c03270.
- (57) Novikov, V. V.; Ananyev, I. V.; Pavlov, A. A.; Fedin, M. V.; Lyssenko, K. A.; Voloshin, Y. Z. Spin-Crossover Anticooperativity Induced by Weak Intermolecular Interactions. *J. Phys. Chem. Lett.* **2014**, *5* (3), pp 496–500. DOI: 10.1021/jz402678q.
- (58) Estrader, M.; Salinas Uber, J.; Barrios, L. A.; Garcia, J.; Lloyd-Williams, P.; Roubeau, O.;



- Teat, S. J.; Aromí, G. A Magneto-optical Molecular Device: Interplay of Spin Crossover, Luminescence, Photomagnetism, and Photochromism. *Angew. Chemie Int. Ed.* **2017**, *56* (49), pp 15622–15627. DOI: 10.1002/anie.201709136.
- (59) Nelyubina, Y.; Polezhaev, A.; Pavlov, A.; Aleshin, D.; Savkina, S.; Efimov, N.; Aliev, T.; Novikov, V. Intramolecular Spin State Locking in Iron(II) 2,6-Di(Pyrazol-3-Yl)Pyridine Complexes by Phenyl Groups: An Experimental Study. *Magnetochemistry* **2018**, *4* (4), p 46. DOI: 10.3390/magnetochemistry4040046.
- (60) Datta, D.; Saitow, M.; Sandhöfer, B.; Neese, F. <sup>57</sup>Fe Mössbauer Parameters from Domain Based Local Pair-Natural Orbital Coupled-Cluster Theory. *J. Chem. Phys.* **2020**, *153* (20), p 204101. DOI: 10.1063/5.0022215.
- (61) Stavitski, E.; de Groot, F. M. F. The CTM4XAS Program for EELS and XAS Spectral Shape Analysis of Transition Metal L Edges. *Micron* **2010**, *41* (7), pp 687–694. DOI: 10.1016/j.micron.2010.06.005.
- (62) de Groot, F.; Kotani, A. *Core Level Spectroscopy of Solids*, 1st Ed.; CRC Press, 2008. DOI: 10.1201/9781420008425.
- (63) Orchard, A. F. *Magnetochemistry (Oxford Chemistry Primers, 75)*; Oxford University Press; Oxford, UK, 2003.
- (64) Schnegg, A. Very-High-Frequency EPR. *eMagRes* **2017**, *6*, pp 115–132. DOI: 10.1002/9780470034590.emrstm1526.
- (65) Römel, M.; Ye, S.; Neese, F. Calibration of Modern Density Functional Theory Methods for the Prediction of <sup>57</sup>Fe Mössbauer Isomer Shifts: Meta-GGA and Double-Hybrid Functionals. *Inorg. Chem.* **2009**, *48* (3), pp 784–785. DOI: 10.1021/ic801535v.
- (66) Dunn, T. M. Spin-Orbit Coupling in the First and Second Transition Series. *Trans. Faraday Soc.* **1961**, *57*, pp 1441–1444. DOI: 10.1039/tf9615701441.
- (67) Martin, R. L. Natural Transition Orbitals. *J. Chem. Phys.* **2003**, *118* (11), pp 4775–4777. DOI: 10.1063/1.1558471.
- (68) Fulmer, G. R.; Miller, A. J. M.; Sherden, N. H.; Gottlieb, H. E.; Nudelman, A.; Stoltz, B. M.; Bercaw, J. E.; Goldberg, K. I. NMR Chemical Shifts of Trace Impurities: Common Laboratory Solvents, Organics, and Gases in Deuterated Solvents Relevant to the Organometallic Chemist. *Organometallics* **2010**, *29* (9), pp 2176–2179. DOI: 10.1021/om100106e.
- (69) MestReNova v.9.0.1-13254. Mestrelab Research S.L. 2014.
- (70) Kupčič, E.; Freeman, R. Fast Multidimensional NMR by Polarization Sharing. *Magn. Reson. Chem.* **2007**, *45* (1), pp 2–4. DOI: 10.1002/mrc.1931.
- (71) VnmrJ 4.2, Revision A. Agilent Technologies: Santa Clara, USA 2014.
- (72) Bain, G. A.; Berry, J. F. Diamagnetic Corrections and Pascal's Constants. *J. Chem. Educ.* **2008**, *85* (4), p 532. DOI: 10.1021/ed085p532.
- (73) Lee, S.-J.; Titus, C. J.; Alonso Mori, R.; Baker, M. L.; Bennett, D. A.; Cho, H.-M.; Doriese, W. B.; Fowler, J. W.; Gaffney, K. J.; Gallo, A.; Gard, J. D.; Hilton, G. C.; Jang, H.; Joe, Y. II; Kenney, C. J.; Knight, J.; Kroll, T.; Lee, J.-S.; Li, D.; Lu, D.; Marks, R.; Miniti, M. P.; Morgan, K. M.; Ogasawara, H.; O'Neil, G. C.; Reintsema, C. D.; Schmidt, D. R.; Sokaras, D.; Ullom, J. N.; Weng, T.-C.; Williams, C.; Young, B. A.; Swetz, D. S.; Irwin, K. D.; Nordlund, D. Soft X-Ray Spectroscopy with Transition-Edge Sensors at Stanford Synchrotron Radiation Lightsource Beamline 10-1. *Rev. Sci. Instrum.* **2019**, *90* (11), p 113101. DOI: 10.1063/1.5119155.
- (74) Nehr Korn, J.; Martins, B. M.; Holldack, K.; Stoll, S.; Dobbek, H.; Bittl, R.; Schnegg, A. Zero-Field Splittings in MetHb and MetMb with Aquo and Fluoro Ligands: A FD-FT THz-EPR Study. *Mol. Phys.* **2013**, *111* (18–19), pp 2696–2707. DOI: 10.1080/00268976.2013.809806.
- (75) Nehr Korn, J.; Holldack, K.; Bittl, R.; Schnegg, A. Recent Progress in Synchrotron-Based Frequency-Domain Fourier-Transform THz-EPR. *J. Magn. Reson.* **2017**, *280*, pp 10–19. DOI: 10.1016/j.jmr.2017.04.001.
- (76) Schnegg, A.; Behrends, J.; Lips, K.; Bittl, R.; Holldack, K. Frequency Domain Fourier Transform THz-EPR on Single Molecule Magnets Using Coherent Synchrotron Radiation. *Phys. Chem. Chem. Phys.* **2009**, *11* (31), pp 6820–6825. DOI: 10.1039/b905745e.
- (77) Nehr Korn, J.; Schnegg, A.; Holldack, K.; Stoll, S. General Magnetic Transition Dipole Moments for Electron Paramagnetic Resonance. *Phys. Rev. Lett.* **2015**, *114* (1), p 010801. DOI: 10.1103/PhysRevLett.114.010801.

- (78) Nehr Korn, J.; Telser, J.; Holldack, K.; Stoll, S.; Schnegg, A. Simulating Frequency-Domain Electron Paramagnetic Resonance: Bridging the Gap between Experiment and Magnetic Parameters for High-Spin Transition-Metal Ion Complexes. *J. Phys. Chem. B* **2015**, *119* (43), pp 13816–13824. DOI: 10.1021/acs.jpcc.5b04156.
- (79) Stoll, S.; Schweiger, A. EasySpin, a Comprehensive Software Package for Spectral Simulation and Analysis in EPR. *J. Magn. Reson.* **2006**, *178* (1), pp 42–55. DOI: 10.1016/j.jmr.2005.08.013.
- (80) Yatsunyk, L. A.; Walker, F. A. Structural, NMR, and EPR Studies of  $S = 1/2$  and  $S = 3/2$  Fe(III) Bis(4-Cyanopyridine) Complexes of Dodecasubstituted Porphyrins. *Inorg. Chem.* **2004**, *43* (2), pp 757–777. DOI: 10.1021/ic035010q.
- (81) Schreurs, A. M. M.; Xian, X.; Kroon-Batenburg, L. M. J. EVAL15: A Diffraction Data Integration Method Based on Ab Initio Predicted Profiles. *J. Appl. Crystallogr.* **2010**, *43* (1), pp 70–82. DOI: 10.1107/S0021889809043234.
- (82) Herbst-Irmer, R.; Sheldrick, G. M. Refinement of Twinned Structures with SHELXL97. *Acta Crystallogr. Sect. B Struct. Sci.* **1998**, *54* (4), pp 443–449. DOI: 10.1107/S0108768197018454.
- (83) Sheldrick, G. M. SADABS. Universität Göttingen, Germany 2014.
- (84) Sheldrick, G. M. TWINABS. Universität Göttingen, Germany 2014.
- (85) Sheldrick, G. M. SHELXT – Integrated Space-Group and Crystal-Structure Determination. *Acta Crystallogr. Sect. A Found. Adv.* **2015**, *71* (1), pp 3–8. DOI: 10.1107/S2053273314026370.
- (86) Sheldrick, G. M. Crystal Structure Refinement with SHELXL. *Acta Crystallogr. Sect. C Struct. Chem.* **2015**, *71* (1), pp 3–8. DOI: 10.1107/S2053229614024218.
- (87) Spek, A. L. Structure Validation in Chemical Crystallography. *Acta Crystallogr. Sect. D Biol. Crystallogr.* **2009**, *65* (2), pp 148–155. DOI: 10.1107/S090744490804362X.
- (88) Spek, A. L. PLATON SQUEEZE: A Tool for the Calculation of the Disordered Solvent Contribution to the Calculated Structure Factors. *Acta Crystallogr. Sect. C Struct. Chem.* **2015**, *71* (1), pp 9–18. DOI: 10.1107/S2053229614024929.
- (89) Neese, F. The ORCA Program System. *WIREs Comput. Mol. Sci.* **2012**, *2* (1), pp 73–78. DOI: 10.1002/wcms.81.
- (90) Neese, F. Software Update: The ORCA Program System, Version 4.0. *WIREs Comput. Mol. Sci.* **2018**, *8* (1). DOI: 10.1002/wcms.1327.



# Chapter 4

---

## Strain-Modulated Reactivity: an Acidic Silane<sup>a</sup>

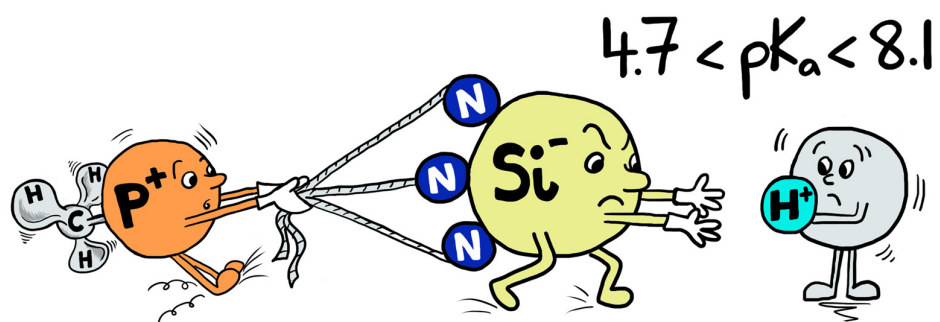
---

### Abstract

Compounds of main-group elements such as silicon are attractive candidates for green and inexpensive catalysts. For them to compete with state-of-the-art transition metal complexes, new reactivity modes must be unlocked and controlled, which can be achieved through strain. Using a tris(2-skatyl)methylphosphonium ([TSM<sub>3</sub>PH<sub>3</sub>]<sup>+</sup>) scaffold, we prepared the strained cationic silane [TSMPSiH]<sup>+</sup>. In stark contrast with the generally hydridic Si–H bond character, it is acidic with an experimental  $pK_a^{\text{DMSO}}$  within 4.7–8.1, lower than in phenol, benzoic acid and the few hydrosilanes with reported  $pK_a$ 's. We show that ring strain significantly contributes to this unusual acidity along with inductive and electrostatic effects. The conjugate base, TSMPSi, activates a THF molecule in the presence of CH-acids to generate a highly fluxional alkoxy silane *via* trace amounts of [TSMPSiH]<sup>+</sup> functioning as a strain-release Lewis acid. This reaction involves a formal oxidation state change from Si(II) to Si(IV), presenting intriguing similarities with transition metal-mediated processes.

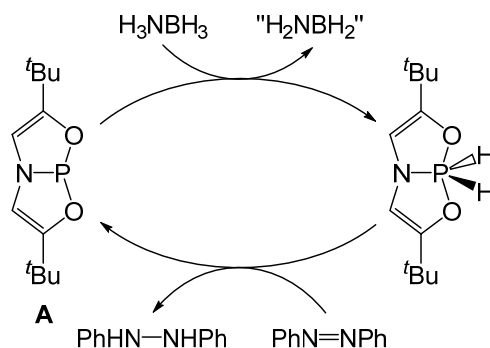
---

<sup>a</sup> This chapter is based on: Tretiakov, S.; Witteman, L.; Lutz, M.; Moret, M. Strain-Modulated Reactivity: An Acidic Silane. *Angew. Chemie Int. Ed.* **2021**, *60* (17), 9618–9626. DOI: 10.1002/anie.202015960.



## 4.1 Introduction

The main-group elements, sometimes also named *s*- and *p*-block elements, are a diverse part of the periodic table. They are the most prevalent components of the Earth's crust and have enormous economic, industrial and environmental significance. Despite all that, their catalytic applications are still scarce compared to those of transition metals,<sup>1–12</sup> although strategies aiming to bridge this gap have recently emerged. In particular, incorporating a main-group element into a strained ring system can unlock unusual reactivity. For example, forcing non-trigonal geometries at a phosphorus(III) center can give it an electrophilic character in addition to the natural nucleophilicity arising from the lone pair.<sup>13</sup> Such *biphilic* compounds have been shown to engage in unusual bond activation pathways such as (reversible) oxidative addition of E–H bonds (E=OR, NR<sub>2</sub>, Ru). A prominent example of this is the catalytic reduction of azobenzene facilitated by a T-shaped P(III) compound **A** (Scheme 4.1).<sup>14</sup>

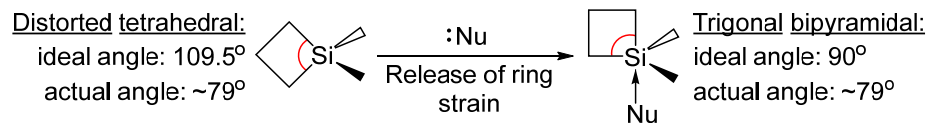


Scheme 4.1. Catalytic reduction of azobenzene.<sup>14</sup>

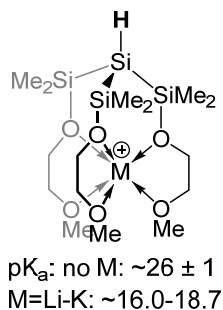
Both Lewis<sup>15</sup> and Brønsted<sup>16,17</sup> acid-base properties can also be manipulated using strain. In particular, Denmark's "strain-release Lewis acidity"<sup>15</sup> is based on the fact that the angle strain is partially relieved upon binding of a nucleophile (Figure 4.1A). It has been most extensively studied for silicon<sup>18–22</sup> resulting in a number of highly-enantioselective synthetic protocols (most often C–C bond forming) that employ strained silanes as directing groups,<sup>23,24</sup> but also extends to other elements such as germanium<sup>15</sup> and aluminium.<sup>25–28</sup>

Because of the generally hydridic character of Si–H bonds, Brønsted SiH-acids are rare in general. Recent examples by Krempner and co-workers<sup>29</sup> and Beckmann and co-workers,<sup>30</sup> shown in Figure 4.1B, mostly rely on electronic effects. In this chapter, we show that ring strain can significantly contribute to the acidic character of a Si–H bond.

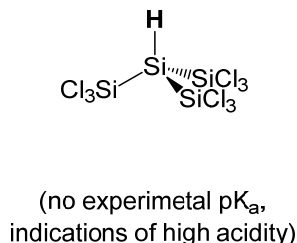
Herein, we report the silanide-silane acid-base pair TSMPSi (**1**)/[TSMPSiH]<sup>+</sup> (**2**), with an unusually low solution p*K*<sub>a</sub><sup>DMSO</sup> (Figure 4.1B). It is experimentally shown to

**(A) The concept of Strain-Release Lewis Acidity:****(B) Brønsted acidity of selected silanes:**

*Krempner and co-workers*  
(electronics):



*Beckmann and co-workers*  
(electronics):



*This work*  
(electronics + strain):

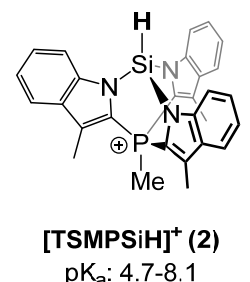


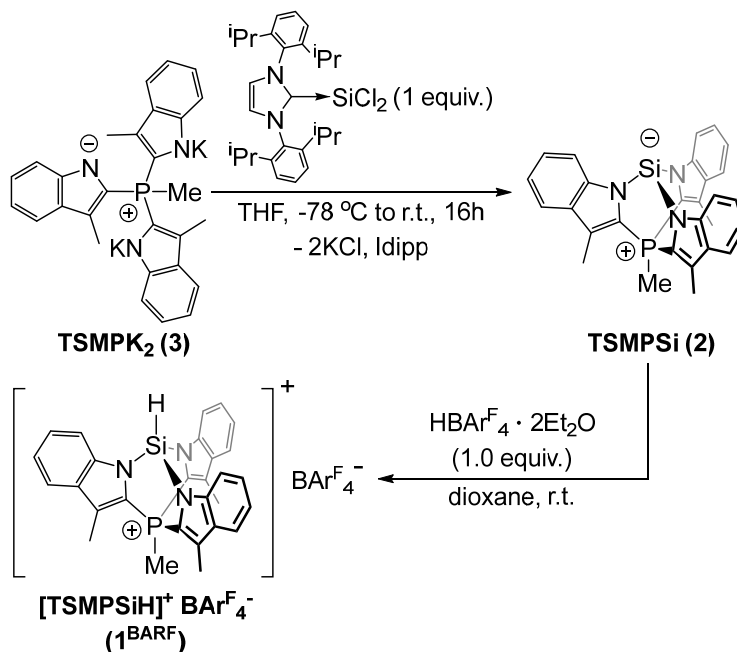
*Figure 4.1.* A) An example of strain-release Lewis acidity for siletanes.<sup>4</sup> B) Selected acidic silanes and the silane discussed in this work (acidic protons are shown in bold). Experimental  $pK_a$  values are given as projected onto the DMSO scale.

lie between 4.7 and 8.1, which is more acidic than phenol, benzoic acid ( $pK_a^{\text{DMSO}}$  of 18.0<sup>31</sup> and 11.1,<sup>32</sup> respectively), and other silanes of which the  $pK_a^{\text{DMSO}}$  was reported. We analyze the physicochemical origins of this unusual acidity in terms of inductive and electrostatic effects and confirm its link to ring strain. In addition, the reactivity of both TSMPSi (**1**) and [TSMPSiH]<sup>+</sup> (**2**) is investigated. The increase in strain that generally accompanies quaternization of the silicon atom in **1**, together with charge separation effects, render it a weaker nucleophile than typical silicon anions. Moreover, we provide evidence that, under the influence of strain, quaternized **1** can transfer a methyl group thus engaging into “strain-release methyl transfer”. Finally, **2** shows strain-release Lewis acidity that manifests itself in the coordination and activation of a THF molecule towards attack by weak nucleophiles, such as highly-delocalized aromatic anions. The product of THF ring-opening exhibits a high degree of fluxionality, which is analyzed using a combination of spectroscopic and computational tools.

## 4.2 Synthesis and characterization of the acid-base pair

Zwitterionic Si(II) silanide TSMPSi (**1**) was isolated from the reaction of the tris-indolide salt TSM $PK_2$  (**3**)<sup>33,34</sup> with Idipp $\rightarrow$ SiCl<sub>2</sub> used as a Si(II) source (*Scheme 4.2*).<sup>35</sup> The corresponding cationic Si(IV) silane, [TSMPSiH]<sup>+</sup>BAR<sub>4</sub><sup>-</sup> (**2**<sup>BARF</sup>), was synthesized by protonation with an equimolar amount of Brookhart’s acid (HBAR<sub>4</sub><sup>F</sup>·2Et<sub>2</sub>O). Attempted protonation with HCl led to an intractable mixture of

insoluble products, highlighting the importance of a non-coordinating anion in this reaction (see *Appendix C1*).



Scheme 4.2. Synthesis of zwitterion **1** and its protonated salt **2<sup>BARF</sup>**.

The  $^1\text{H}$  NMR spectra of TSMPSi (**1**) in THF- $d_8$  and  $[\text{TSMPSiH}]^+\text{BArF}_4^-$  (**2<sup>BARF</sup>**) in DCM- $d_2$  each show a single set of four aromatic signals indicating  $C_3$  symmetry that corresponds to a heterobicyclo[2.2.2]octane topology. The  $^{29}\text{Si}$  NMR spectrum of **1** shows a doublet at  $-48.0$  ppm with  $^3J_{\text{Si,P}}=4.3$  Hz, which is consistent with the DFT-calculated values of  $-56.2$  ppm and  $7.9$  Hz, respectively (see *Appendix C2*). Upon protonation of **1** into **2<sup>BARF</sup>**, the  $^{29}\text{Si}$  NMR signal becomes a doublet of doublets at  $-46.4$  ppm with  $^1J_{\text{Si,H}}=318.4$  Hz and  $^3J_{\text{Si,P}}=8.0$  Hz, consistent with a tetrahedral tertiary silane. The respective DFT-calculated NMR parameters,  $-59.0$  ppm,  $-342.3$  and  $-7.5$  Hz (see *Appendix C2*), are in a good agreement with the experiment. Even though the Si-H signal in  $^1\text{H}$  NMR of **2<sup>BARF</sup>** is obscured by aromatic multiplets, its position at  $7.52$  ppm can be clearly determined from  $^1\text{H}$ - $^{29}\text{Si}$  ASAP-HMQC spectra.

The structures of both **1** and **2<sup>BARF</sup>** were determined by X-ray crystallography (*Figure 4.2*) using crystals grown from benzene/*n*-hexane and DCM/1,4-dioxane, respectively. The asymmetric unit of **1** contains two independent molecules, each featuring a tricoordinate anionic silicon center. A sum of the  $\text{N}^{\wedge}\text{Si}^{\wedge}\text{N}$  angles close to  $270^\circ$ , namely  $277.43(13)/277.51(14)^\circ$ , indicates a high *s*-character of the anionic lone pair.



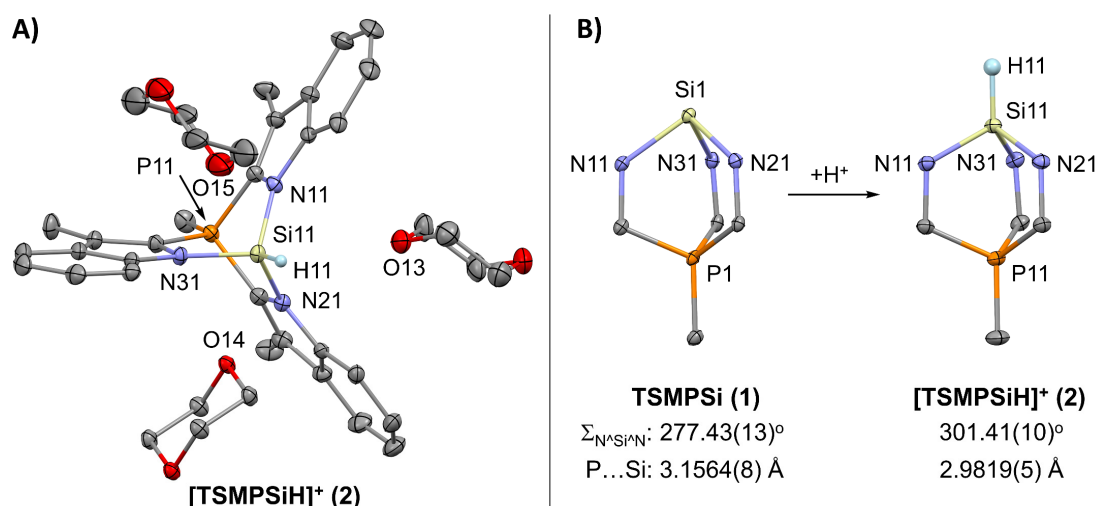


Figure 4.2. A) Molecular structure of a cationic unit of  $2^{\text{BARF}}$  from X-ray crystal structure determination. Displacement ellipsoids are drawn at 30% probability level. The  $\text{BARF}_4^-$  counterion and hydrogen atoms, except for Si–H, are omitted for clarity. B) Structural changes in the bicyclic cage before and after protonation according to X-ray crystallography. Only one independent molecule of TSMPSi (1) is shown. Selected bond distances and angles are given in Section 4.10.3.

The structure of  $2^{\text{BARF}}$  features a tetrahedral Si center; the Si-bound H atom could be located from the difference Fourier maps. Interestingly, every cationic unit of  $2^{\text{BARF}}$  is surrounded by three 1,4-dioxane molecules<sup>a</sup> with Si–O distances within 2.7807(13)–3.2260(16) Å, which is shorter than the sum of van der Waals radii (3.62 Å),<sup>36</sup> suggesting weak Si···O interactions. The latter are best described as interactions between the O-centered lone pairs and the  $\sigma$ -hole opposite the polar Si–N bonds.<sup>37,38</sup> The silane hydrogen atom shows rather short contacts to the dioxane oxygens, but the Si<sup>∧</sup>H<sup>∧</sup>O angles of 82.7(10)–92.0(10)<sup>o</sup> are unfavorable for hydrogen bonding. The above suggests that the silicon center has a Lewis acidic character, while the Si–H bond remains polarized towards the hydrogen and is hence not prone to engage in hydrogen bonding.

It is worth pointing out that protonation causes marked geometrical changes around Si (Figure 4.2B), wherein the Si–N distances shorten from 1.840(2)–1.864(2) Å in **1** to 1.752(1)–1.762(2) Å in  $2^{\text{BARF}}$ . Concomitantly, the sum of N<sup>∧</sup>Si<sup>∧</sup>N angles increases from 277.43(13)/277.51(14)<sup>o</sup> in **1** to 301.41(10)<sup>o</sup> in  $2^{\text{BARF}}$ , while the intracyclic Si<sup>∧</sup>N<sup>∧</sup>C angles decrease from 125.05(13)–126.36(14)<sup>o</sup> in **1** to 119.11(10)–119.32(9)<sup>o</sup> in  $2^{\text{BARF}}$ . No other bond in the molecule changes by >0.02 Å, and no flat angle deforms by >2.9<sup>o</sup>. In other words, structural perturbations due to proton addition are mostly confined to the SiN<sub>3</sub> fragment. The observed changes are consistent with

<sup>a</sup> At least one of the dioxane positions is partly occupied by *n*-hexane molecules (Section 4.10.3), which indicates rather weak Si···O interactions.

an increased *s*-character of the Si–N bonding orbitals as the Si-centered electron pair in **1** acquires higher *p*-character upon protonation, which is in line with Bent's rule.<sup>39</sup>

### 4.3 Experimental solution $pK_a$ determination

Examining the solid-state structure of TSMPSi (**1**) as well as  $\kappa^3$  complexes of Fe(II), Ni(II) and Cu(I) with the TMSP scaffold,<sup>40</sup> it becomes apparent that the latter favors N<sup>^E^N</sup> angles that are close to 90°. Hence, the N<sup>^Si^N</sup> angles of about 100° in [TSMPSiH]<sup>+</sup> (**2**) are expected to generate strain within the cage structure. In addition, the  $^1J_{\text{Si,H}}$  coupling constant in **2**<sup>BARF</sup> (318.4 Hz) is significantly larger than that in the electronically similar yet unstrained tris-*N*-pyrrolylsilane (284.5 Hz).<sup>41</sup> Similar increased  $^1J_{\text{C,H}}$  coupling constants in strained hydrocarbons<sup>17</sup> have been correlated to a high acidity of the corresponding C–H bonds. These considerations, combined with the overall positive charge of [TSMPSiH]<sup>+</sup> (**2**), led us to anticipate its high SiH-acidity.

To test this, we undertook experimental  $pK_a$  measurements. Of the several existing ways to measure  $pK_a$  in non-aqueous media,<sup>42</sup> we chose a bracketing approach: the basic form **1** was dissolved together with acids of known  $pK_a$ , and proton transfer was monitored using NMR. CH-acidic fluorenes **4** and **5** as well as 2,6-lutidinium-BARF<sub>4</sub> salt **6** were used as reference acids (*Figure 4.3*). Fluorenes have previously been used to measure the acidity of silanes,<sup>29,43</sup> and their conjugate bases are strongly delocalized anions which are not expected to coordinate to the protonated silicon center. 2,6-Lutidine is also unlikely to coordinate due to steric bulk. Because of the intrinsically low kinetic acidity of most CH-acids, we chose dioxane-*d*<sub>8</sub> as a solvent, reasoning that a hydrogen bond acceptor could promote fast and efficient proton transfer. It was given preference over the much more common THF-*d*<sub>8</sub> due to its lesser sensitivity to strong acids and lower susceptibility to (catalytic) ring-opening (see *Section 4.6*). To ensure that an acid-base equilibrium is reached, the measurements were repeated starting from **2**<sup>BARF</sup> and the conjugate bases of the reference acids.

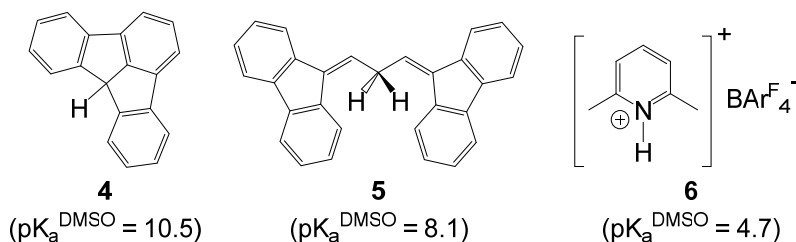
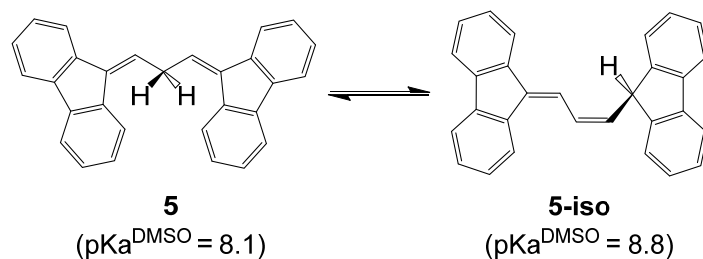


*Figure 4.3.* Acids used in experimental studies.<sup>44,45</sup>

While the acidity of the reference acids that we used is known only in DMSO, cationic silane **2** cannot exist in this solvent and immediately degrades. However, given a linear correlation between acidities in different solvents (i.e. the relative acidity does not change from one solvent to another),<sup>46</sup> one can still perform an acid-base reaction in dioxane-*d*<sub>8</sub> and project the result onto the DMSO acidity scale.<sup>a</sup> Even though the projected  $pK_a$  does not reflect solvent-specific effects (viz. degradation), it allows for comparison with  $pK_a$  of other acids most of which are only known in DMSO.<sup>46,47</sup>

Silanide **1** is not protonated by fluoradene (**4**) which has a  $pK_a^{\text{DMSO}}$  of 10.5. With the stronger CH-acid **5** ( $pK_a^{\text{DMSO}} = 8.1$ ), the protonation is also not observed directly. However, **5** undergoes base-catalysed isomerization in the presence of TSMPSi (**1**) (Scheme 4.3; see Appendix C3), suggesting comparable acidities. Additionally, the solution becomes pale blue, indicating the presence of a small concentration of the delocalized anion obtained by deprotonating **5**. Finally, protonation of **1** with 2,6-lutidinium-BAr<sup>F</sup><sub>4</sub> (**6**) in dioxane-*d*<sub>8</sub> is complete with release of free 2,6-lutidine. Thus, one can conclude that the projected  $pK_a$  of silane **2** in DMSO lies between 4.7 and 8.1.



Scheme 4.3. Tautomerization of fluorene **5**.<sup>44,48</sup>

The high acidity of cationic silane **2** is remarkable in view of the general hydridic character of silicon-bound hydrogen atoms. In fact, it is more acidic than phenol and benzoic acid ( $pK_a^{\text{DMSO}}$  of 18.0<sup>31</sup> and 11.1,<sup>32</sup> respectively). It is also considerably more acidic than the few hydrosilanes whose  $pK_a$  has been measured: triphenylsilane ( $pK_a^{\text{THF}} \approx 35.1$ ),<sup>49</sup> tris(trimethylsilyl)silane ( $pK_a^{\text{ether}} \approx 29.4$ ),<sup>43</sup> as well as the cationic alkali metal-silane complexes shown in Figure 4.1B.<sup>29</sup> In the latter series, the introduction of a cationic center into the molecule decreases the  $pK_a$  in benzene by six to eleven orders of magnitude, suggesting that [TSMPSiH]<sup>+</sup> (**2**) owes

<sup>a</sup> There are indications that there may be separate linear correlations between  $pK_a$ 's in DMSO and THF for cationic and neutral acids. At least, this is the case for metal hydrides.<sup>116</sup> It is unclear, however, how to treat cationic acids whose conjugate bases are zwitterions. In the only paper that deals with experimental  $pK_a$  of zwitterionic silanes,<sup>29</sup> the values are derived under an assumption that there is no difference between cationic and neutral  $pK_a$  correlations. For the sake of comparison, we derived experimental  $pK_a$  of the cationic silane **2** under the same assumption.

at least a part of its acidity to the presence of a positive charge in the molecule. It is additionally worth mentioning that trichlorosilane,<sup>50</sup> tris(pentafluoroethyl)silane,<sup>51</sup> and tris(trichlorosilyl)silane<sup>30</sup> display acidic reactivity in solution, but no experimental  $pK_a$  has been reported to our knowledge.

#### 4.4 Computational analysis of acidity of [TSMPSiH]<sup>+</sup> (**2**)

##### 4.4.1 Factors contributing to the acidity

The high acidity of cationic silane [TSMPSiH]<sup>+</sup> (**2**) can be ascribed to three cumulative effects: the strong electron-withdrawing effect of indolyl nitrogens, ring strain, and the overall positive charge. The respective contributions of these effects can, in principle, be roughly estimated by comparing solution acidity of a series of silanes: SiH<sub>4</sub>, tris-*N*-skatylsilane (**A** in *Figure 4.4*), the neutral isoelectronic Si-tethered analogue of **2** (**B** in *Figure 4.4*; see also *Appendix C4*), and **2** itself. More specifically, the acidity difference between SiH<sub>4</sub> and **A** would reflect the electron withdrawal, the difference between **A** and **B** would be reflective of strain, and the difference between **B** and **2** would give information about the influence of charge.

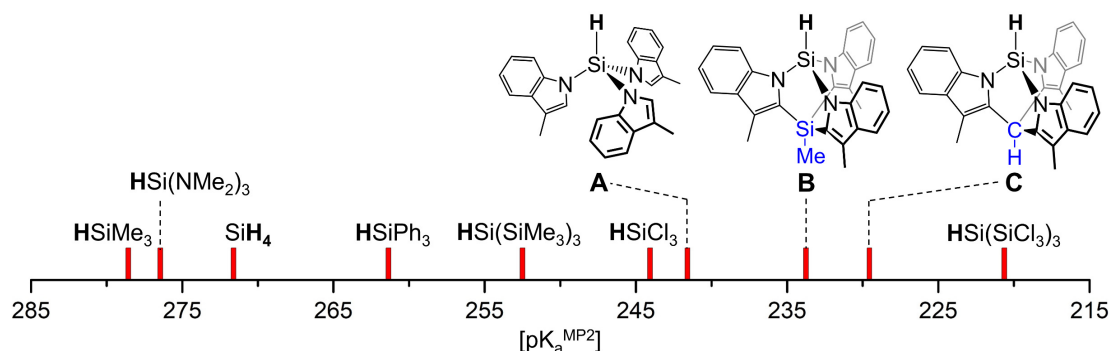


*Figure 4.4.* Comparison of MP2-calculated gas-phase acidities for neutral silanes, including tris(trichlorosilyl)silane, HSi(SiCl<sub>3</sub>)<sub>3</sub>, from Beckmann and co-workers<sup>30</sup> The  $pK_a^{\text{MP2}}$  of cationic silane **2** (177.7) is not shown on the scale along with neutral silanes since it cannot be directly compared (see text).

Unfortunately, the solution acidities of SiH<sub>4</sub>, **A** and **B** are experimentally unknown. Furthermore, the lack of reference experimental data hampers the development of reliable procedures for calculating these. This problem can be partly circumvented by taking a detour *via* gas-phase  $pK_a$  values, which can be calculated with high precision by modern quantum chemical methods.<sup>52</sup> There is an empirical linear dependence between gas-phase and solution  $pK_a$ 's within the same class of

acids,<sup>a,53,54</sup> which is possible due to the fact that the free energy difference between an acid and a base is attenuated by differential solvation effects that are specific for the acid class, electric charge and solvent. Such correlations have been documented for phenols,<sup>55</sup> alcohols,<sup>54,56</sup> amines,<sup>57</sup> thiols,<sup>57</sup> and CH-acids.<sup>58,59</sup>

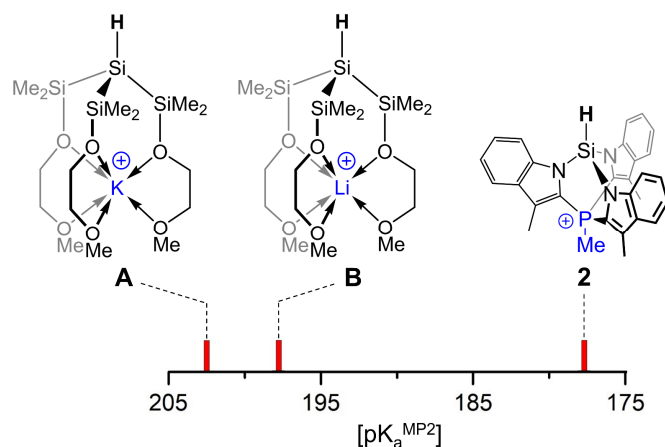


Figure 4.5. Comparison of MP2-calculated gas-phase acidities for cationic silanes.

In this way, the gas-phase  $pK_a$  of 177.7 calculated for **2** can be compared to the gas-phase  $pK_a$  of other cationic silanes described by Krempner and co-workers (**A** and **B** in Figure 4.5),<sup>29</sup> which we calculate as being 202.5 for **A** and 197.8 for **B** (see Appendix C5). Knowing that the  $pK_a^{\text{DMSO}}$  values for the latter two silanes are 22.3 and 19.8, respectively,<sup>29</sup> and assuming a linear correlation, one arrives to a projected  $pK_a^{\text{DMSO}}$  of 7.3 for **2**, which falls within the experimental interval of 4.7-8.1. This gives us confidence in the ability of the computed gas-phase  $pK_a$ 's to accurately reflect trends in solution for silanes as well.

Now, comparing calculated gas-phase  $pK_a^{\text{MP2}}$  of  $\text{SiH}_4$  (271.6) to that of tris-*N*-skatyl silane **A** (241.6) shows that inductive effects reduce the  $pK_a^{\text{MP2}}$  by roughly 30.0 units. Constraining *N*-skatyl moieties into the cage structure **B** ( $pK_a^{\text{MP2}}$ =234.5) decreases the sum of  $\text{N}^{\wedge}\text{Si}^{\wedge}\text{N}$  angles ( $\Sigma_{\text{N}^{\wedge}\text{Si}^{\wedge}\text{N}}$ ) from 324.7° in **A** to 311.6° **B**, while reducing the  $pK_a^{\text{MP2}}$  by an additional 7.1 units, which is about one fourth of the electron withdrawal contribution. This trend is continued by the more constrained C-tethered analogue **C**, which has not been observed experimentally, but its conjugate

<sup>a</sup> Projecting gas-phase acidities onto solution is only valid within one class of acids. Otherwise, differences in solvation effects make such a comparison highly unreliable. To exemplify, toluene and water have very similar gas-phase acidities (381.1 and 372.1 kcal/mol, respectively),<sup>117</sup> whereas in aqueous solution the benzyl anion is a much stronger base than the hydroxyl anion. Additionally, solvation effects strongly depend on molecular charge and only cancel out when two acids of the same charge are compared.

base has been isolated.<sup>a,35</sup> With a  $\Sigma_{\text{N}^{\ominus}\text{Si}^{\ominus}\text{N}}$  of 300.5°, its gas-phase  $\text{p}K_{\text{a}}^{\text{MP2}}$  equals 229.6. The increased acidity of **B** and **C** is also in line with a build-up of strain (9.0 and 16.5 kcal/mol, respectively) with reference to corresponding conjugate bases as analyzed by a series of homodesmotic equations (see *Appendix C6*). In other words, deprotonation is accompanied by strain release, which significantly contributes to the acidity of **B**, **C**, and, by extension, compound **2**.

As for the influence of charge, the calculated gas-phase  $\text{p}K_{\text{a}}^{\text{MP2}}$  of **2** (177.7) is, as expected, much lower than that of **B** (234.5) due to electrostatic effects. Because of a difference in solvation of neutral and charged species,<sup>52</sup> these effects are expected to remain significant but be strongly attenuated in solution relative to electron withdrawal and strain. Therefore, the influence of the positive charge on the solution acidity of **2** is difficult to quantify.

To qualitatively assess the role of the positive charge in the acidity of **2**, we performed Natural Bonding Orbital (NBO) analysis of the deprotonated form **1**. It showed that the anionic lone pair on silicon is hosted in an orbital with predominant *s*-character ( $\text{sp}^{0.41}$  hybridization). The corresponding Natural Localized Molecular Orbital (NLMO) is composed of Si atomic orbitals by 98.1%, with only minor delocalization into  $\sigma^*(\text{C}-\text{N})$  orbitals due to hyperconjugation (*Figure 4.6*).

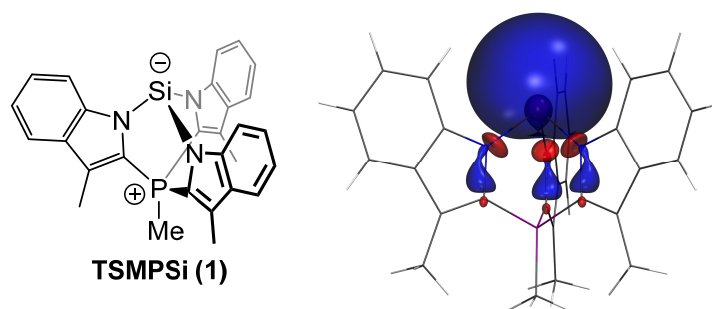


*Figure 4.6.* NLMO plot of anionic lone pair in TSMPSi (**1**) (isocontour=0.02). Calculations were performed in vacuum at the B3LYP-GD3BJ/6-311++G\*\* level of theory.

In other words, the Lewis structure **1** used to denote the zwitterionic silanide is a good description of its electronic structure. Therefore, the high acidity of **2** does not originate from increased delocalization of the negative charge in its conjugate base **1**, and the interaction between the zwitterionic charges is almost entirely electrostatic. It is also fair to say that, despite **2** being a formally cationic acid, the influence of charge on the acidity, while significant, should not be overwhelming and is likely comparable to that of the electron withdrawal. This can be deduced

<sup>a</sup> All attempts to generate the conjugate acid to **C** in *Figure 4.4* following the same procedure as for **2**<sup>BARF</sup> led to intractable mixtures of products accompanied by fluoride abstraction from  $\text{BAr}^{\text{F}_4}$  anion, as evidenced by <sup>1</sup>H and <sup>19</sup>F NMR spectra.

from the fact that, aside from more common cationic acids like oxonium ions or ammonium salts, deprotonation of **2** into **1** does not quench the positive charge in the molecule but rather affects the overall charge balance. Still, despite **1** being formally a neutral species, its zwitterionic character makes it more energetic than a truly neutral molecule, thus reducing the free energy gain upon deprotonation of **2** and, consequently, the acidity.

#### 4.4.2 On the role of strain

More insight into the influence of strain on the acidity of silanes **A-C** (Figure 4.4) and **2** can be obtained by decomposing the deprotonation reaction into two formal stages (Table 4.1).<sup>60</sup> In the first stage, a proton is abstracted from the silane with all other atomic coordinates frozen. The energy of this process ( $\Delta E_1$ ) gauges the penalty of charge separation in the course of heterolytic Si–H bond dissociation followed by electronic relaxation. In the second stage, the deprotonated silane is allowed to relax to the geometry of the corresponding anion, which is described by the respective energy difference ( $\Delta E_2$ ). In essence,  $\Delta E_2$  characterizes how strongly the geometry of the silane resembles that of the corresponding silanide. The larger the discrepancy between geometries, the more energy is gained during relaxation, leading to a more negative total energy balance and therefore higher acidity. It is important to note that upon relaxation of deprotonated **B**, **C** and **2**, the  $N^{\wedge}C^{\wedge}X$  and  $C^{\wedge}X^{\wedge}C$  angles barely change while most of the relaxation occurs within the  $SiN_3$  fragment, which is analogous to the differences between the X-ray crystal structures of **2**<sup>BARF</sup> and **1** (Figure 4.2B).

The  $\Delta E_1$  energies become progressively more negative from **A** to **C** (total difference of  $-20.7$  kcal/mol), which correlates with decreasing  $N^{\wedge}Si^{\wedge}N$  valence angles in the respective silanes. Consequently, acute angles around silicon imposed by the ligand destabilize the silane allowing for easier proton abstraction, and thus higher acidity. Because of the different molecular charge, comparing  $\Delta E_1$  of cationic silane **2** with that of neutral silanes **A-C** would be meaningless.

During the second stage, relaxation,  $\Delta E_2$  energies become progressively less negative from **A** to **C** (total difference of  $+4.0$  kcal/mol), which means that constraint makes the geometry of a silane closer to that of the corresponding anion, hence reducing the acidity. While there is a similarity in valence angles between **2** and its isoelectronic analogue **B**, relaxation for the former is  $3.4$  kcal/mol less negative. We connect this to the fact that the distance between positive phosphonium and negative silanide atoms increases upon relaxation. This should reduce electrostatic stabilization, hence slightly increasing  $\Delta E_2$  and lowering the acidity.

Table 4.1. Deprotonation energy decomposition scheme at the B3LYP-GD3BJ/6-311++G\*\* level of theory.  $\Delta E$  reflects changes in SCF energy.

X	$\Delta E$ , kcal/mol			Change of valence angles upon relaxation			
	$\Delta E_1$	$\Delta E_2$	$\Delta E_1 + \Delta E_2$	$N^{\wedge}Si^{\wedge}N$	$Si^{\wedge}N^{\wedge}C$	$N^{\wedge}C^{\wedge}X$	$C^{\wedge}X^{\wedge}C$
3 x H ( <b>A</b> )	374.1	-27.4	346.7	108.2°→94.4°	126.7°→128.7°	119.7°	-
	↓-10.4	↓+1.4	↓-9.0				
SiMe ( <b>B</b> )	363.7	-26.0	337.7	103.9°→93.6°	118.1°→126.4°	113.5°→112.5°	101.1°→102.0°
	↓-10.3	↓+2.6	↓-7.7				
CH ( <b>C</b> )	353.4	-23.4	330.0	100.2°→89.7°	112.7°→120.8°	115.5°→115.3°	108.6°→108.1°
		↓+0.8					
P <sup>+</sup> Me ( <b>2</b> )	-	-22.6	-	101.8°→91.6°	118.4°→126.6°	112.7°→111.8°	103.7°→104.3°

Even though  $\Delta E_1$  and  $\Delta E_2$  contribute to the gas-phase acidity in an opposite way, changes associated with  $\Delta E_1$  have larger magnitude, which leads to higher acidity with acuter  $N^{\wedge}Si^{\wedge}N$  angles. The progression of  $\Delta E_1$  in Table 4.1 is related to subtle differences in electronic structure as shown by a Natural Bonding Orbital (NBO) analysis of the respective silanes (see Appendix C7). The composition of the Si–H bonding NBO in tris-*N*-skatyl silane (**A**) is  $sp^{2.04}d^{0.02}$ . The *s*-character significantly increases in the cage compounds **B** ( $sp^{2.01}d^{0.02}$ ), **C** ( $sp^{1.90}d^{0.02}$ ), and in the cationic silane **2** ( $sp^{1.82}d^{0.02}$ ). This translates into a subtle shift in bond polarization: the Si–H bond remains overall polarized towards hydrogen, as was inferred from the interaction of **2** with dioxane in the solid state (*vide supra*), but the Si contribution to the Si–H bonding NBO increases from 41.3% in **A** to 41.8% in **B**, 42.5% in **C**, and 43.5% in **2**. This relative shift reduces  $\Delta E_1$  and makes strained silanes more electronically similar to their respective anions with the silicon lone pair in the latter ranging in hybridization from  $sp^{0.47}$  in **B** to  $sp^{0.41}$  in TSMPSi (**1**). Overall, this makes heterolytic Si–H bond dissociation in strained silanes more favorable than in unstrained ones.

In simpler terms, there is a difference between the static properties of a molecule and its reactivity. While the silicon-bound hydrogen has a hydridic character, to estimate the acidity, one has to consider the relative stability of both the acid and the conjugate base, and not only the charge distribution in the acid. As shown above, deprotonation is accompanied by substantial electronic and structural changes that stabilize the anion, resulting in the acidity of the Si–H bond. In general, the lesser are the electronic changes and the more the acid resembles its conjugate base, the higher the acidity. In this respect, the Si–H bond in **2** is polarized towards hydrogen,



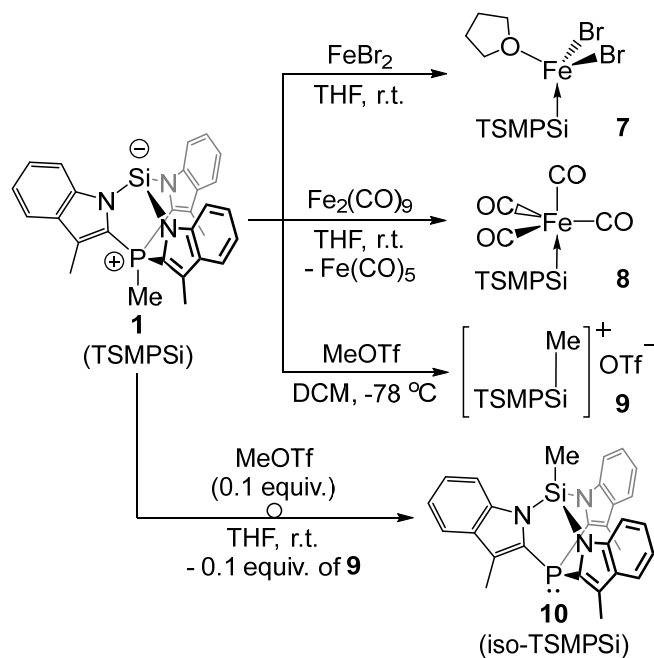
but less so than those of the other discussed silanes. This makes **2** more electronically similar to its deprotonated form **1** than other silanes are to their respective anions, which yields the lower  $pK_a$  of **2**.

#### 4.5 Reactivity of the zwitterionic silanide TSMPSi (**1**)

The high acidity of  $[\text{TSMPSiH}]^+$  (**2**) suggests that the stabilized Si anion in TSMPSi (**1**) should behave as a relatively weak nucleophile, which was assessed by a series of reactions (*Scheme 4.4*). Treatment with  $\text{FeBr}_2$  in THF afforded the insoluble stable complex  $(\text{TSMPSi})\text{FeBr}_2(\text{THF})$  (**7**), which was identified crystallographically. This reaction is likely solubility-driven, since no complexation was observed with  $\text{Fe}(\text{OTf})_2$  and  $\text{Fe}(\text{acac})_2$ , suggesting only a weak interaction with the Fe(II) centers. Reaction of **1** with  $\text{Fe}_2(\text{CO})_9$  afforded  $(\text{TSMPSi})\text{Fe}(\text{CO})_4$  (**8**) as a stable complex, suggesting that the softer (in the HSAB sense)  $\text{Fe}(\text{CO})_4$  fragment is a better match for the soft  $\text{Si}^-$  center in **1**.<sup>a</sup> Finally, reaction of **1** with 1 equiv. of MeOTf resulted in methylation at silicon to form the cationic cage compound  $[\text{TSMPSiMe}]^+\text{OTf}^-$  (**9**). Quaternization of the silicon atom is evidenced by a change of the  $^{29}\text{Si}$  NMR chemical shift from  $-48.0$  ppm in **1** to  $34.4$  and  $-22.5$  ppm in **8** and **9**, respectively. Additionally, the  $^{29}\text{Si}$  NMR signal in **9** shows as a pentet ( $J_{\text{Si,H}} \approx J_{\text{Si,P}} = 8.1$  Hz) consistent with the assigned structure.

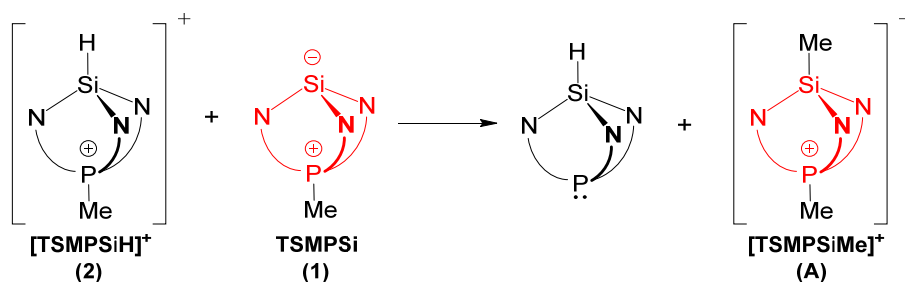
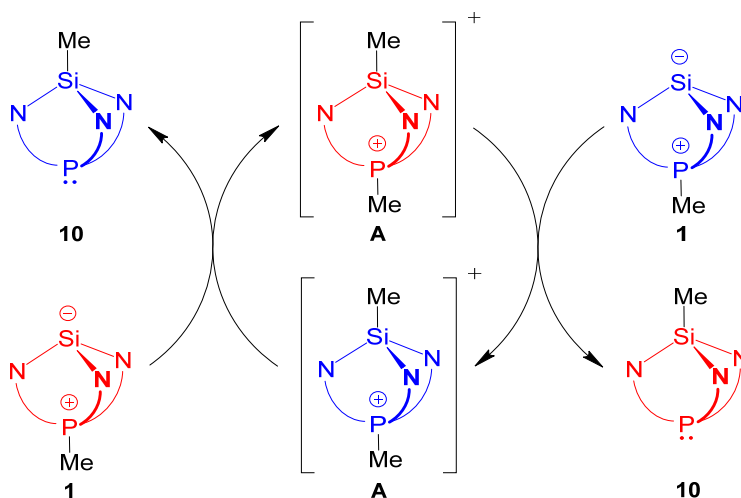
The relatively low donicity of the silicon center in TSMPSi (**1**) is also apparent from analysis of the CO-stretching frequencies of its complexes with metal carbonyls (see *Appendix C9*), which places **1** in the vicinity of silylenes and  $\text{P}(\text{NMe}_2)_3$  rather than other silicon anions. An obvious explanation for this is the presence of a positive charge in the molecule, which electrostatically stabilizes the negative charge on silicon rendering it less available for bonding. The second factor that contributes to weak nucleophilicity is a build-up of strain that occurs upon quaternization. The strain penalty can be separated from electrostatic effects and approximated by analyzing a series of homodesmotic equations involving a Si-tethered analogue of **1** (see *Appendix C6*). There, complexation with an  $\text{FeBr}_2(\text{THF})$  center leads to a  $4.5$  kcal/mol increase in strain, whereas methylation and protonation provide  $8.3$  and  $9.0$  kcal/mol of an increase, respectively, confirming a likely contribution of ring strain to the weakened nucleophilicity of **1**.

<sup>a</sup> Considering the potential of TSMPSi (**1**) as a ligand for transition metal centers, we characterized its steric properties both in terms of Tolman cone angle<sup>118</sup> and percent buried volume ( $\%V_{\text{bur}}$ ).<sup>119</sup> Tolman cone angle for **1** derived from DFT-optimized geometries of  $\text{LNi}(\text{CO})_3$  complexes is  $200.1^\circ$ , which is close to that of tris(*o*-tolyl)phosphine,  $194 \pm 6^\circ$ .<sup>120</sup> The calculations based on  $\%V_{\text{bur}}$  agree with this conclusion (see *Appendix C8* for more detail).



Scheme 4.4. Reactivity of zwitterionic TSMPSi (**1**).

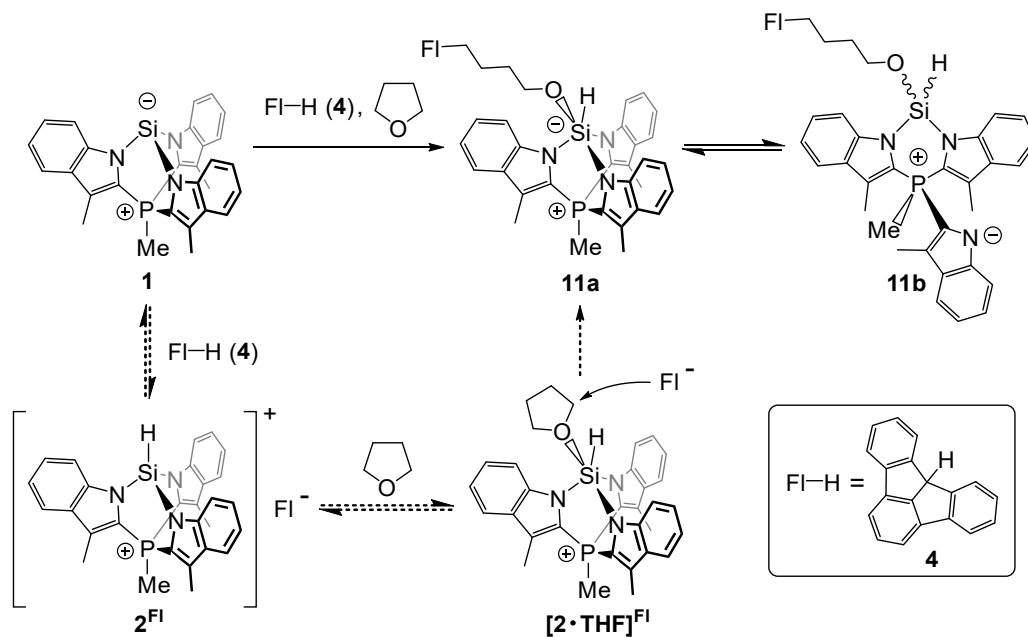
The isolated zwitterion **1** is kinetically stable in solution despite the presence of a nucleophilic Si<sup>-</sup> site and an electrophilic P<sup>+</sup>-Me unit in the same molecule. For reference, the charge-neutral isomer iso-TSMPSi (**10** in Scheme 4.4; >98% by <sup>1</sup>H NMR) could be quantitatively prepared by stirring zwitterion TSMPSi (**1**) with 0.25 equiv. of potassium graphite in benzene. Whereas the reaction mechanism is unclear in this case, this method was used to prepare clean samples of **10** for full characterization. Interestingly, exposing **1** to a catalytic amount (0.1 equiv.) of MeOTf also resulted in nearly complete isomerization of **1** to iso-TSMPSi (**10**). This suggests that the cation [TSMPSiMe]<sup>+</sup> in **9** is subject to nucleophilic attack at the phosphonium methyl group by a molecule of **1**, forming **10** and generating a new molecule of [TSMPSiMe]<sup>+</sup>. The enhanced electrophilicity of the P-bound methyl group in [TSMPSiMe]<sup>+</sup> likely originates from a combination of its overall positive charge and increased ring strain. As a matter of fact, isomerization also occurs in the presence of 0.25 equiv. of HBAR<sup>F</sup><sub>4</sub>·2Et<sub>2</sub>O and CH-acids (*vide infra*) to form **2**<sup>BARF</sup> *in situ*. This leads one to conclude that this process is catalytic in nature and is linked to partial quaternization of anionic silicon in zwitterion **1** (Scheme 4.5). The loss of the P-bound methyl group from either [TSMPSiH]<sup>+</sup> (**2**) or [TSMPSiMe]<sup>+</sup> (**9**) reduces the strain of the cage structure, which, along with charge cancellation, provides an additional driving force for this “strain-release methyl transfer” reaction.

**Initiation:****Catalysis:**

Scheme 4.5. Suggested mechanism for isomerization of TSMPSi (1). The path of an individual molecule,  $1 \rightarrow A \rightarrow 10$ , is coded in colour.

**4.6 Reactivity of the cationic silane [TSMPSiH]<sup>+</sup> (2)**

Interestingly, recording NMR spectra of [TSMPSiH]<sup>+</sup>BARF<sub>4</sub><sup>-</sup> (**2**<sup>BARF</sup>) in THF-*d*<sub>8</sub> instead of DCM-*d*<sub>2</sub> results in dramatic changes in the <sup>29</sup>Si signal. The doublet of doublets shifts to -91.0 ppm (vs. -46.4 ppm in DCM-*d*<sub>2</sub>) with <sup>1</sup>J<sub>Si,H</sub>=368.4 Hz (vs. 318.4 Hz) and <sup>3</sup>J<sub>Si,P</sub>=6.7 Hz (vs. 8.0 Hz). We propose that this is due to coordination of a THF molecule resulting in a pentacoordinate silicon center (**2**·THF in Scheme 4.6). NMR parameters calculated for **2**·THF using DFT reproduce the experiment reasonably well, being -104.9 ppm, -392.7 and -7.3 Hz respectively (see Appendix C2). Importantly, the <sup>31</sup>P NMR signal of **2**<sup>BARF</sup> only shifts from -7.6 ppm in DCM-*d*<sub>2</sub> to -7.0 ppm in THF-*d*<sub>8</sub>, ruling out THF interaction with the phosphonium center. Another point of note is that <sup>1</sup>H and <sup>13</sup>C spectra of **2**<sup>BARF</sup> in THF-*d*<sub>8</sub> remain in line with C<sub>3</sub> symmetry, in contrast with the expected breaking of symmetry upon coordination of THF. This suggests a fluxional process such as Berry-like pseudorotation or reversible dissociation.



Scheme 4.6. THF ring-opening with fluoradene (4). The suggested reaction mechanism is shown with dashed arrows.

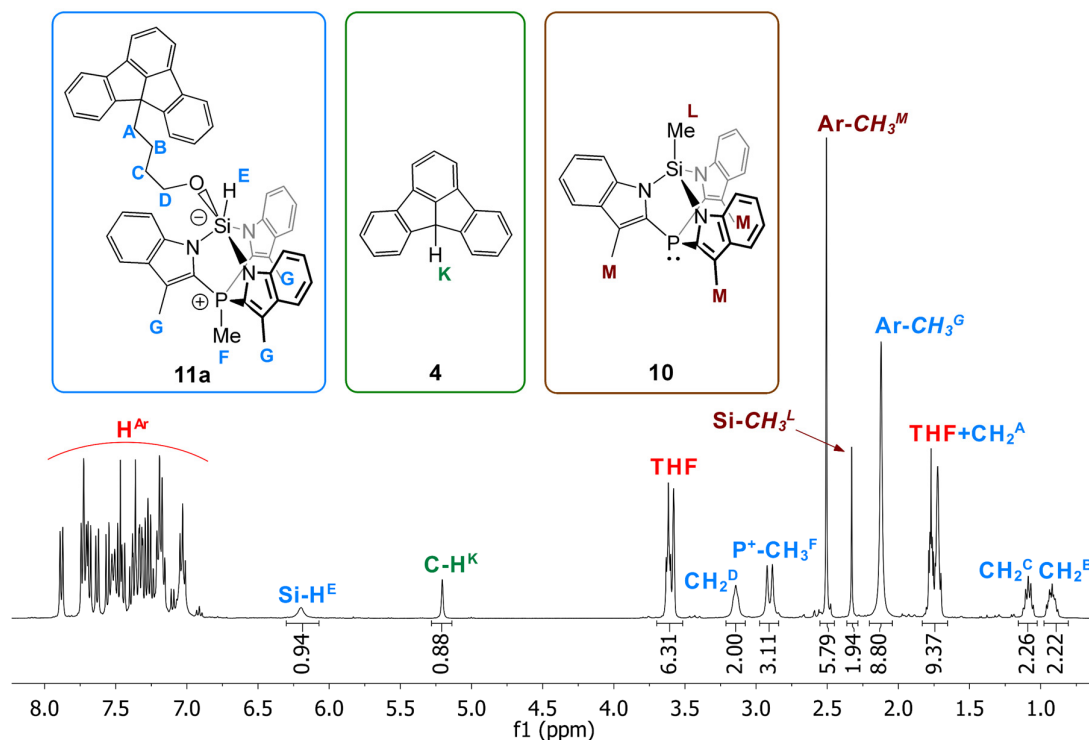


Figure 4.7.  $^1\text{H}$  NMR (400 MHz) spectrum of the reaction between TSMPSi (1), fluoradene (4) and THF- $h_8$ , recorded in THF- $d_8$  at 25 °C. Even though 11a is in thermal equilibrium with the cage-opening product 11b, only the structure of 11a is shown for simplicity.

THF coordination to silicon in  $[\text{TSMPSiH}]^+$  (**2**) is key to the observed reactivity of TSMPSi (**1**) with the CH-acidic fluoradene (**4**,  $\text{p}K_{\text{a}}^{\text{DMSO}}=10.5$ ) in THF- $h_8$  (Scheme 4.6). Next to a moderate amount of the isomerization product iso-TSMPSi (**10**; *vide supra*), the main product was spectroscopically identified as the THF ring-opening product **11a**, which exists in a dynamic equilibrium with the open form **11b**.  $^1\text{H}$  NMR spectra of the mixture (**11a/b**) in THF- $d_8$  at 25 °C (Figure 4.7) display a number of broadened peaks corresponding to protons of the Si–H, methyl phosphonium, and aromatic groups as well as four methylene signals between 0.75 and 3.25 ppm. The latter disappear if the reaction is conducted in THF- $d_8$  instead of THF- $h_8$ , which indicates that they belong to a  $-(\text{CH}_2)_4-$  fragment from a THF ring-opening reaction. Moreover,  $^1\text{H}$  COSY spectrum shows that they form an isolated spin system (Figure 4.8), while the NOE spectra (Figure 4.9) indicate that the termini of the  $-(\text{CH}_2)_4-$  fragment are located in spatial proximity to one aromatic doublet each, with the oxygen-bound terminus also being close to a Si–H proton. Interestingly, a correlation is also observed with an aromatic methyl group,  $\text{CH}_3^{\text{G}}$ , which cannot happen for the closed structure **11a** due to a large distance between the resonating protons. It can only be the case if one of indolyl arms dissociates from silicon and engages into free rotation around C–P bond, giving an open form **11b**. The occurrence of this dynamic process is also consistent with observed line-broadening in the  $^1\text{H}$  NMR spectrum (Figure 4.7). On a related note, despite breaking of equivalence of the aromatic methyl groups, they still show as one signal in the  $^1\text{H}$  spectrum. This apparent contradiction can be resolved if there is an additional dynamic process in **11a** that exchanges these positions (*vide infra*).

The formation of **11a/b** can be explained by the generation of a small amount of the Si(IV) cation  $[\text{TMSPSiH}]^+$  (**2**) as the fluoradenide salt **2<sup>Fl</sup>** in an acid/base equilibrium with Si(II) compound TSMPSi (**1**) and **4**. The cation then acts as a strain-release Lewis acid for THF, generating the complex **2·THF** characterized above (Scheme 4.6), which undergoes ring opening upon nucleophilic attack by the deprotonated fluoradene (**4**). These last steps can also be interpreted as the activation of THF by the transient frustrated Lewis pair **2<sup>Fl</sup>**.<sup>61</sup> Interestingly, products similar to **11a/b** form with other tested fluorenes of  $\text{p}K_{\text{a}}^{\text{DMSO}}$  within 8.1–11.6 (Appendix C10), while less acidic fluorenes exclusively lead to isomerisation into iso-TSMPSi (**10**). This can be understood from the fact that stronger acids will generate higher equilibrium concentration of the fluorene anion, thus opening a kinetic pathway for the THF ring opening. This reaction sequence involves the insertion of both the Si center and a neutral molecule (THF) into a C–H bond coupled with a formal oxidation state change from Si(II) in TSMPSi (**1**) to Si(IV) in  $[\text{TMSPSiH}]^+$  (**2**), which presents intriguing similarities with transition metal-mediated processes. In the overall reaction, the silicon center sequentially acts as a nucleophile (base) and an electrophile (Lewis acid), demonstrating biphilic character that can be traced back to ring strain in  $[\text{TSMPSiH}]^+$  (**2**).

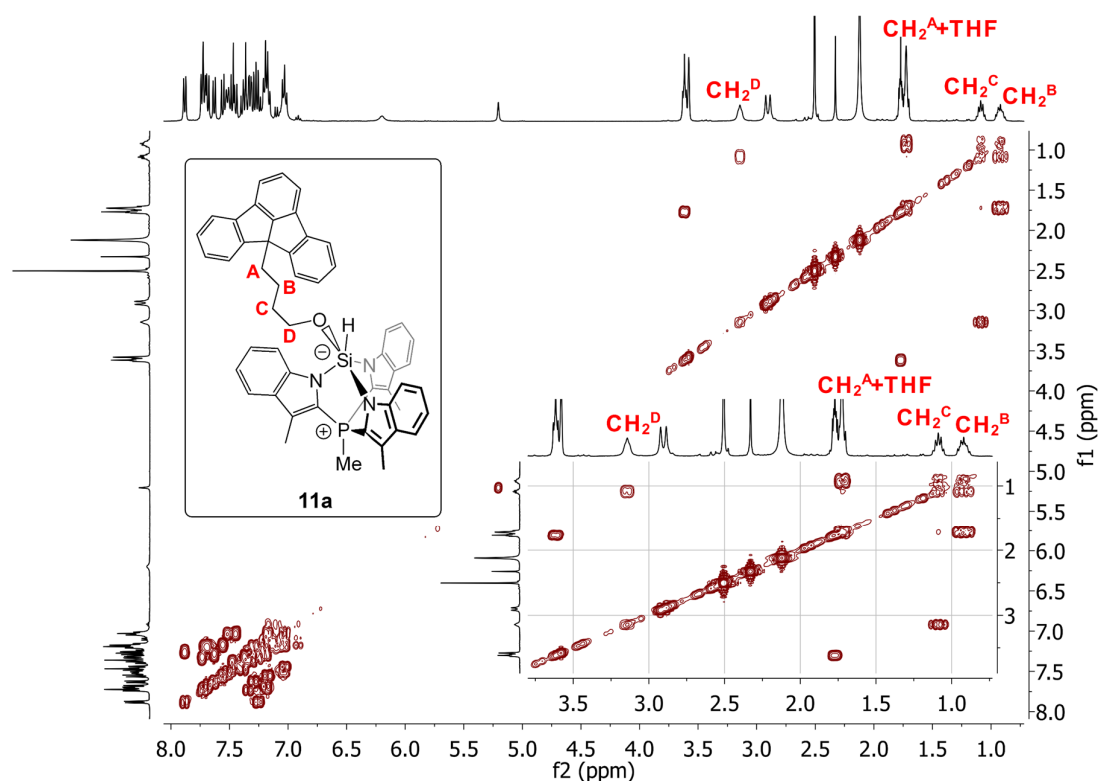


Figure 4.8.  $^1\text{H}$  gCOSY spectrum (400 MHz) of the reaction between TSMPSi (**1**), fluoradene (**4**) and THF- $h_8$ , recorded in THF- $d_8$  at 25 °C. Even though **11a** is in thermal equilibrium with the cage-opening product **11b**, only the structure of **11a** is shown for simplicity.

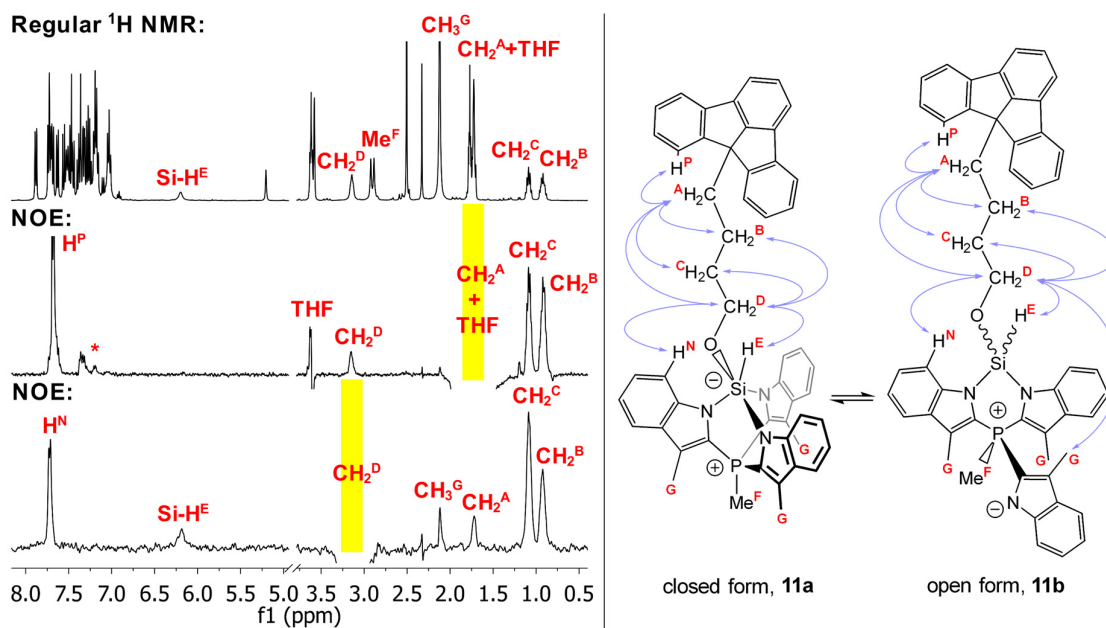


Figure 4.9. Left panel:  $^1\text{H}$  NMR (400 MHz) and 1D NOE spectra of the reaction between TSMPSi (**1**), fluoradene (**4**) and THF- $h_8$ , recorded in THF- $d_8$  at 25 °C. Assignments are shown only for the solvent and THF ring-opening product **11a/b**. Yellow rectangles show saturation windows. Right panel: NOE correlations mapped on the structural formulae of isomeric forms.

## 4.7 Fluxionality of the THF ring-opening product **11a/b**

As discussed in the previous section, the NOE spectra (*Figure 4.9*) show that the closed and open forms **11a** and **11b**, respectively, exist in a dynamic equilibrium. Furthermore, as mentioned above, there appears to be another dynamic process that equalizes the axial and equatorial indolide arms in **11a** so that they are indistinguishable in the  $^1\text{H}$  NMR spectra. This intriguing flexibility of the TSMP scaffold invites further investigation, which we conduct by means of a combination of variable-temperature NMR and computational studies below.

### 4.7.1 Cage opening

The THF ring-opening product **11a/b** displays rich dynamic behavior in solution, which could be further elucidated by using variable-temperature  $^1\text{H}$  and  $^{31}\text{P}$  NMR spectroscopy (*Figure 4.10*). Both nuclei show notable and simultaneous changes with temperature. More specifically, at 60 °C, all peaks assigned to the THF ring-opening product **11a/b** are sharp. As temperature decreases, these peaks move around and broaden, almost coalescing with the baseline between 0 and –20 °C. At lower temperature, they reappear (albeit broadened) at different chemical shifts which barely change between –60 and –89 °C.

This behaviour is diagnostic of a dynamic equilibrium between two chemical entities in solution, which is consistent with the NOE spectra in *Figure 4.9*. The fact that, in  $^{31}\text{P}$  NMR spectra, there is only one quaternary phosphonium peak visible per measurement implies that equilibrium between the two forms **11a/b** is fast, and the observable chemical shift is a population-weighted average of the shifts of two individual forms. In this case, it is possible to regressively find thermodynamic parameters of the interconversion *via* temperature-dependent equilibrium constant using *Eq. 4.1* (see *Appendix C11*).

$$\delta = \frac{\delta_A + \delta_B \exp\left(\frac{\Delta_r S}{R} - \frac{\Delta_r H}{RT}\right)}{1 + \exp\left(\frac{\Delta_r S}{R} - \frac{\Delta_r H}{RT}\right)}, \quad \text{Eq. 4.1}$$

where  $\delta_A$  and  $\delta_B$  are the  $^{31}\text{P}$  shifts of pure **11a** and **11b**, respectively;  $\Delta_r H$  and  $\Delta_r S$  are enthalpy and entropy of the interconversion;  $T$  is temperature,  $R$  is a universal gas constant.

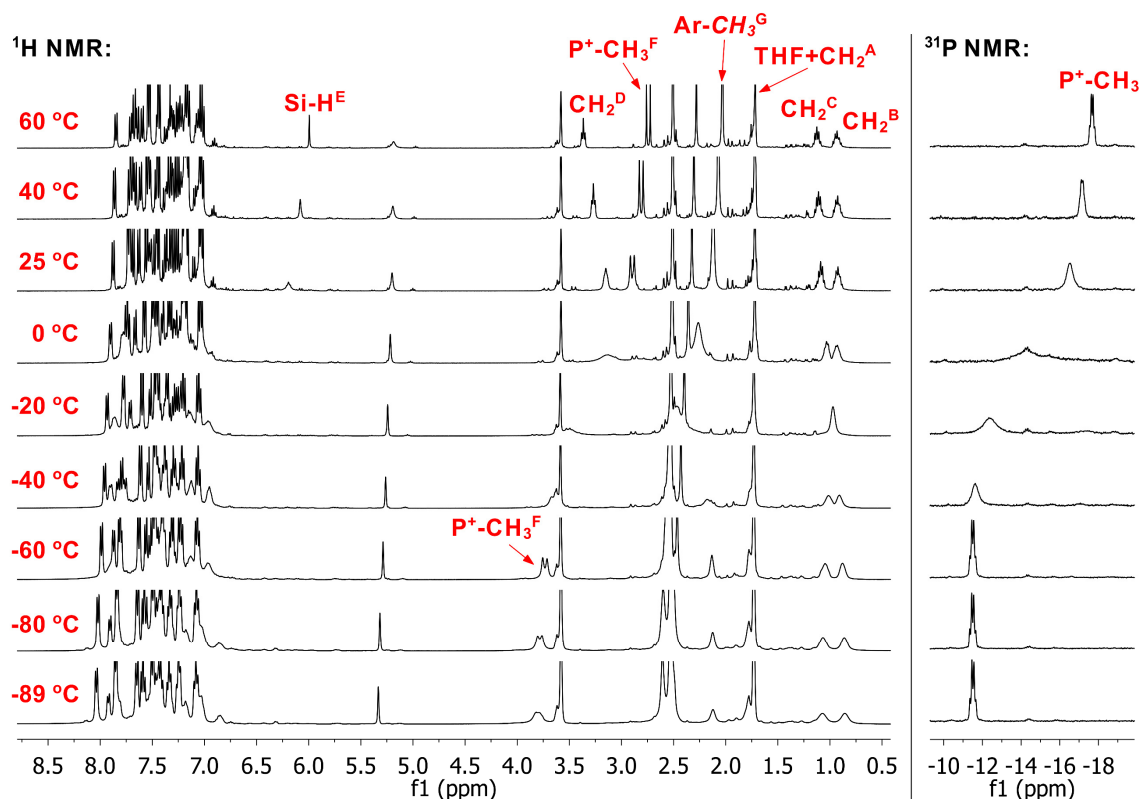


Figure 4.10. Variable-temperature  $^1\text{H}$  (400 MHz) and  $^{31}\text{P}$  (162 MHz) NMR spectra of the reaction between TSMPSi (**1**), fluoradene (**5**) and THF- $h_8$ , measured in THF- $d_8$ . All labeled peaks belong to ring-opening product **11a/b**. In  $^{31}\text{P}$  spectra, the signal of isomer iso-TSMPSi (**10**) at ca.  $-125$  ppm is not shown.

A regressive thermodynamic analysis shows that the transition starts above  $-60$  °C and is 78.5% complete at 25 °C with  $\Delta_r H = 10.4$  kcal/mol and  $\Delta_r S = 37.5$  cal $\cdot$ mol $^{-1}\cdot$ K $^{-1}$  (see Appendix C11). These thermodynamic parameters are consistent with a ring-opening equilibrium between **11a** and **11b** involving breaking of a Si–N bond (Scheme 4.6). Confirming this interpretation, the  $^{29}\text{Si}$  NMR signal of **11a**,  $-120.2$  ppm at  $-89$  °C indicative of a penta- or hexacoordinate silane,<sup>62</sup> shifts to  $-74.9$  ppm at 25 °C (Figure 4.11). Unfortunately, no  $^{29}\text{Si}$  resonance was observed at a higher temperature (60 °C), likely due to reduced signal intensity because of the smaller population difference between nuclear magnetic energy levels. However, with consideration of the 78.5% complete transition at 25 °C, one can arrive to an extrapolated value of  $-62.5$  ppm for pure **11b**, which is typical for tetrahedral silanes.<sup>62</sup>

As for  $^1J_{\text{Si,H}}$  spin-spin coupling constants, both the  $^1\text{H}$  (Figure 4.10) and  $^{29}\text{Si}$  spectra (Figure 4.11) of **11a** at  $-89$  °C show the Si–H peaks that are too broad for the coupling effects to be detected. However, the  $^1J_{\text{Si,H}}$  coupling constant for **11b** was extracted by superimposing  $^1\text{H}\{^{13}\text{C}\}$  and  $^1\text{H}\{^{29}\text{Si}\}$  spectra at 60 °C (Figure 4.12), which gave 310.1 Hz.



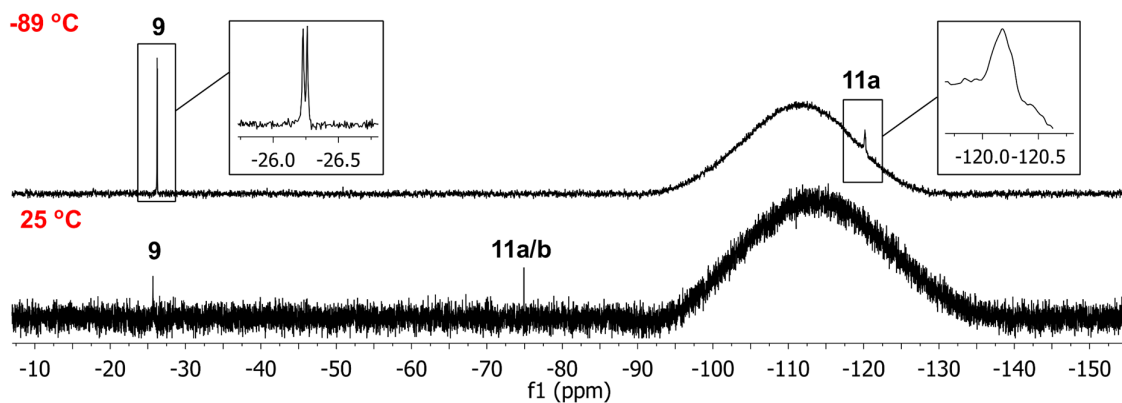


Figure 4.11. Variable-temperature  $^{29}\text{Si}$  NMR (79.5 MHz) spectra of the reaction between TSMPSi (**1**), fluoradene (**4**) and THF- $h_8$ , recorded in THF- $d_8$ .

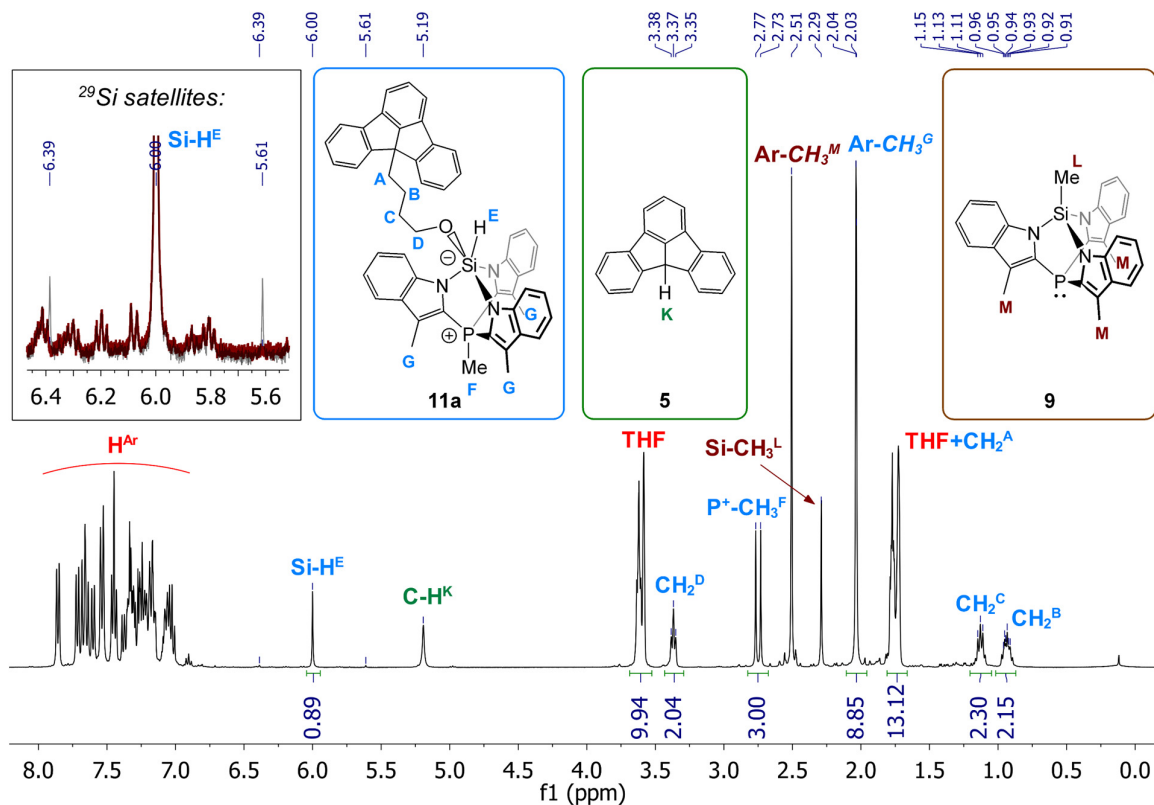
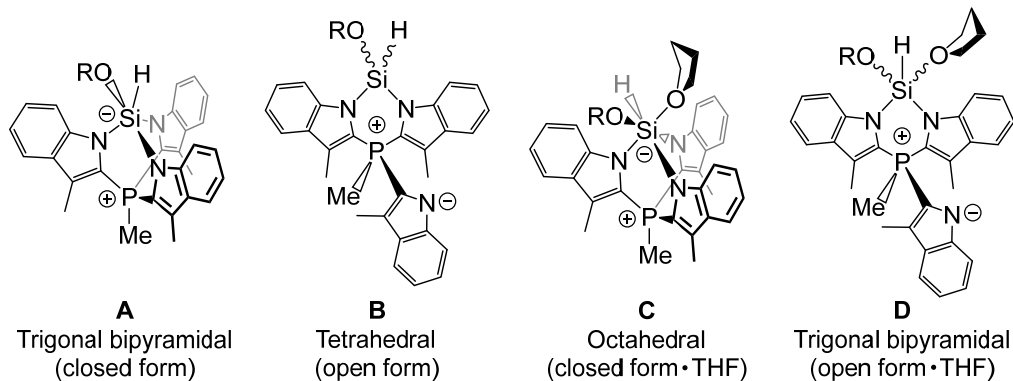
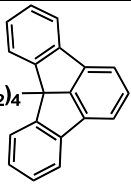


Figure 4.12.  $^1\text{H}\{^{13}\text{C}\}$  NMR (400 MHz) spectrum of the reaction between TSMPSi (**1**), fluoradene (**4**) and THF- $h_8$ , recorded in THF- $d_8$  at 60 °C. An insert in the upper-left corner shows an overlay of  $^1\text{H}\{^{13}\text{C}\}$  (grey) and  $^1\text{H}\{^{29}\text{Si}\}$  (maroon) spectra, thus allowing to identify  $^1J_{\text{Si,H}}$ .

In order to reinforce our assignments of temperature-dependent speciation in solution, we calculated  $^{29}\text{Si}$  NMR chemical shifts and  $^1J_{\text{Si,H}}$  coupling constants for possible geometries on silicon using truncated molecular models (Table 4.2). The fluoradene moiety and four methylenes were reduced to a methyl group as it was not expected to significantly influence the values of interest and greatly reduced com-

**Table 4.2.** Comparison of calculated and experimental assigned chemical shifts ( $\delta$ ) and spin-spin coupling constants ( $J$ ) for different geometries on silicon. Experimental spin-spin coupling constant  $^1J_{\text{Si,H}}$  is given as an absolute value. Geometry optimizations were performed in vacuum at B3LYP-GD3BJ/6-311++G\*\* level of theory, while the NMR parameters were calculated in THF (PCM solvation) using B3LYP-GD3BJ/IGLO-III for C, H, P, Si, O atoms and 6-311++G\*\* for Fe atoms.



Geometry on silicon	NMR parameters	
	R = Me (calculated, truncated model)	 (experimental, assigned)
<b>A:</b> Trigonal bipyramidal (closed form)	$\delta(^{29}\text{Si}) = -124.9$ ppm $^1J_{\text{Si,H}} = -372.0$ Hz	<b>11a:</b> $\delta(^{29}\text{Si}) = -120.2$ ppm <sup>a</sup>
<b>B:</b> Tetrahedral (open form)	(values for <i>E/Z</i> geometry) $\delta(^{29}\text{Si}) = -56.9/-57.5$ ppm $^1J_{\text{Si,H}} = -309.1/-333.2$ Hz	<b>11b:</b> $\delta(^{29}\text{Si}) = -62.5$ ppm <sup>b</sup> $^1J_{\text{Si,H}} = 310.1$ Hz
<b>C:</b> Octahedral (closed form·THF)	$\delta(^{29}\text{Si}) = -171.33$ ppm $^1J_{\text{Si,H}} = -357.8$ Hz	-
<b>D:</b> Trigonal bipyramidal (open form·THF)	(values for <i>E/Z</i> geometry) $\delta(^{29}\text{Si}) = -62.5/-57.8$ ppm $^1J_{\text{Si,H}} = -349.0/-358.7$ Hz	-

putational time. Optimization of pentacoordinate geometries for **11a** always led to a minimum with an alkoxy group in an axial position of a trigonal bipyramid due to the high apicophilicity of oxygen.

As can be seen, the observed  $^{29}\text{Si}$  chemical shift for **11a** corresponds well to the calculated value for the closed trigonal bipyramidal geometry **A**. The situation with **11b** is somewhat more complicated: while the observed  $^1J_{\text{Si,H}}$  coupling constant is consistent with the calculated value for the tetrahedral open form **B**,  $^{29}\text{Si}$  chemical

<sup>a</sup> The signal is too broad for any  $^1J_{\text{Si,H}}$ -coupling to be observed.

<sup>b</sup> Extrapolated (see explanation in the text).

shifts do not allow to formally exclude the trigonal bipyramidal THF-coordinated open form **D**. Yet, the reaction entropy for a hypothetical transition from **A** into **D** would be less than zero due to an overwhelming negative contribution of THF coordination. This contradicts the experimental  $\Delta_r S$  of 37.5 cal/(mol·K) based on variable-temperature  $^{31}\text{P}$  NMR chemical shifts (*vide supra*). Therefore, we assign the species observed in solution to geometries **A** and **B**.

#### 4.7.2 Positional exchange

An NOE correlation between the oxygen-bound methylene and the aromatic methyl groups (*Figure 4.9*) indicates that **11b** at least partially exists as the *Z*-stereoisomer with the free indolide and the alkoxy substituent on the same side of the central six-membered ring (**11b-Z** in *Figure 4.13*). Only in this case can the methylene and the methyl groups approach one another by 3.3 Å sufficient for NOE, as shown by our DFT calculations. Otherwise, for any energetically-affordable rotamer of the *E*-form (**11b-E** in *Figure 4.13*), this distance is larger than 5 Å, which is a general NOE cut-off. This situation may appear surprising at first sight, considering that the ring-opening should proceed from the lowest-energy configuration of **11a**, which, according to DFT, has a trigonal bipyramidal silicon center with an axial alkoxy group. There, dissociation of the most labile apical Si–N bond should lead to the **11b-E** isomer. Consequently, **11b-Z** likely forms *via* another mechanism that involves a certain degree of geometric fluxionality around silicon in **11a**, sampling geometries leading to **11b-Z** upon reversible dissociation. Supporting the presence of an additional dynamic process in the system,  $^1\text{H}$  spectra of **11a/b** (*Figure 4.7*) show only one aromatic methyl signal, whereas both the closed (**11a**) and the open (**11b**) isomers should display two signals in a ratio of 2:1 as a result of breaking of the  $\text{C}_3$  symmetry.

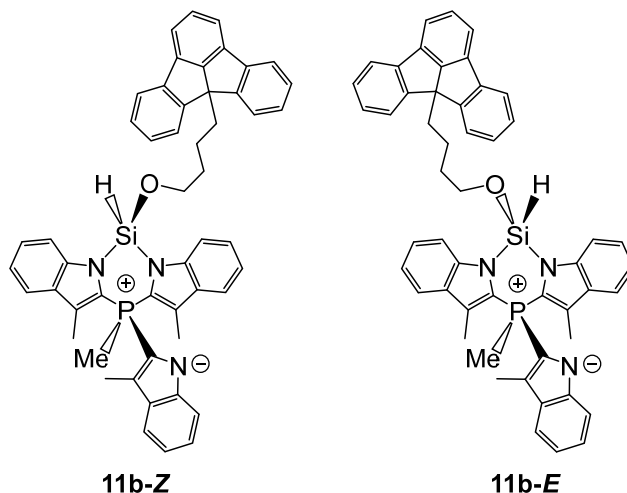
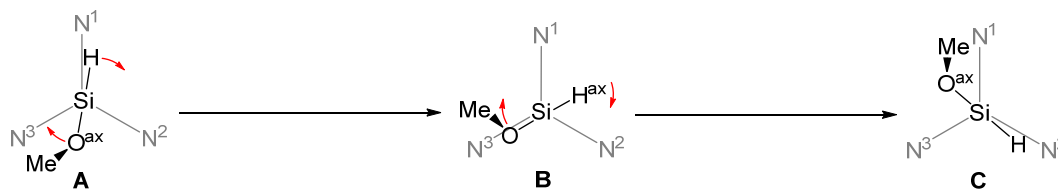


*Figure 4.13.* Discussed open configurations **11b-Z** and **E**.

Represented as a three-fold cyclic permutation:



Represented as two consecutive Berry-like pseudorotations:

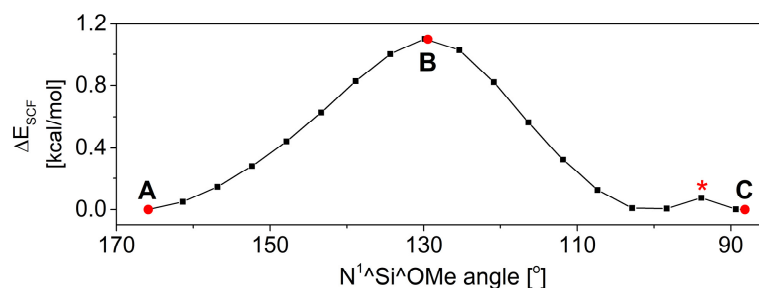
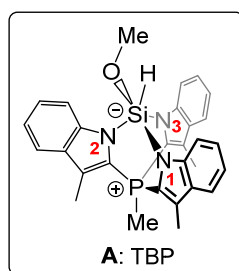
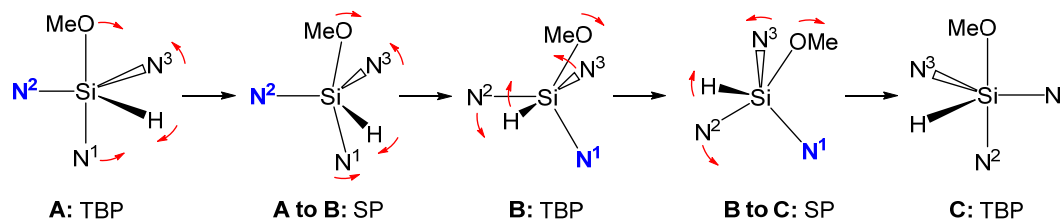


Figure 4.14. Computational analysis of positional exchange in a truncated model of **11a** (**Heq1** in the scheme) in a vacuum at the B3LYP-GD3BJ/6-31+G\* level of theory. *Top panel*: two different representations of the positional exchange; pivots for Berry-type deformations<sup>65</sup> are labelled in blue; TBP = trigonal bipyramid, SP = square pyramid. *Bottom-left panel*: structural formula of the truncated model. *Bottom-right panel*: potential energy as a function of N<sup>1</sup>Si<sup>1</sup>OMe in the course of the stereomutation.

In order to explore the possibility of a positional exchange around the silicon atom, we undertook a relaxed potential energy surface (PES) scan in a truncated model of **11a** (**A** in Figure 4.14;  $\Delta E_{\text{SCF}}$  taken as 0.0 kcal/mol for a reference), which avoids complications associated with local conformational energy minima of the tetramethylene chain. During the scan, the N<sup>1</sup>Si<sup>1</sup>OMe angle was gradually varied from 165.9° to 88.2° with all other coordinates optimized at each point. The resulting cyclic interchange of one axial and two equatorial nitrogen atoms gave the degenerate structure **C**. Due to its complexity, this transformation can be represented in two different ways (Figure 4.14). Most obviously, it can be viewed as a threefold cyclic permutation – one of the five possible general permutation types derived by Muetterties<sup>63,64</sup> based on topological analysis (type 4 stereomutation in his own classification, or M2 stereomutation according to Lammertsma and co-workers<sup>65</sup>). Alternatively, it can be represented as two consecutive Berry-type deformations,<sup>65</sup> each having its own pivot (a substituent that does not move in the course of permutation). In the course of this permutation, the potential energy curve exhibits two maxima. A smaller maximum (92.9°, 0.2 kcal/mol) labelled with an

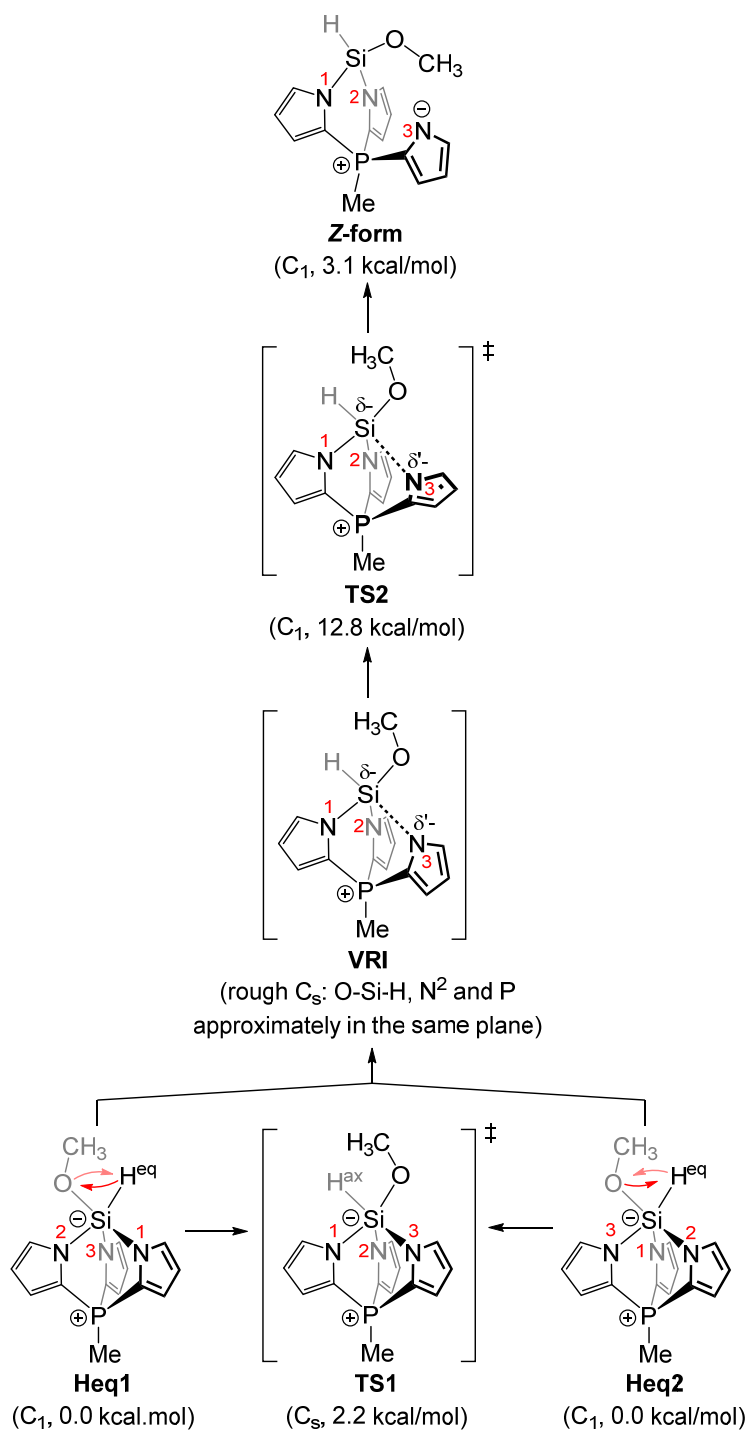
asterisk is likely an artifact of the PES algorithm.<sup>a</sup> Point **B** (130.6°, 1.0 kcal/mol) corresponds to an apicophilic methoxy group in an equatorial position and can be regarded as an approximation of a transition state for the cyclic interchange. Optimization of the said transition state using the Berny algorithm ('opt=ts' option in the Gaussian 16 program<sup>66</sup>) gives  $\Delta E_{\text{SCF}}$  of 1.0 kcal/mol and  $\Delta G^\ddagger$  of 2.2 kcal/mol, which is an extremely low barrier. Overall, this analysis shows that the TSMP ligand scaffold is flexible enough to allow for low-energy positional exchange on silicon. Unfortunately, we were not able to connect the optimized transition state with the degenerate minimal geometries **A** and **C** using the intrinsic reaction coordinate (IRC).<sup>67</sup> This is presumably due to the overall flatness of the potential energy hypersurface and, thus, the IRC algorithm failing to find a gradient.

Still, the above analysis does not ascertain the origins of **11b-Z** as the only geometry that could lead to its formation is **B**, which is also a transition state and therefore is not capable of such dissociation. This situation may indicate the presence of a bifurcation on the potential energy surface,<sup>68,69</sup> which was explored by a two-dimensional potential energy surface scan. In order to save computational time, the system was further truncated by replacing the 3-methylindole rings with pyrroles (*Scheme 4.7*). One-dimensional angular scan (*Figure 4.15, bottom panel*) reveals a similar shape as in *Figure 4.14* before truncation, thereby confirming our assumption that truncation does not dramatically affect the dynamic properties of the system.

The two-dimensional scan (*Figure 4.15, top panel*) was built on top of the one-dimensional one, where, for every angle, the distance between the silicon atom and the N<sup>3</sup> nitrogen atom, dissociation of which leads to the *Z*-isomer, was incrementally increased. The scan reveals several stationary points that correspond to either minimum energy geometries (**Heq1**, **Heq2** and **Z-form**) or transition states (**TS1** and **TS2**). These were optimized separately, and their energies are given in *Scheme 4.7*.

Making use of the principle of microscopic reversibility and changing the perspective, let us now consider the reverse reaction – closure of the **Z-form**. It appears that the corresponding **TS2** is directly followed by **TS1** with no energy minimum in-between. Such a disposition is known<sup>68,69</sup> to give rise to a post-transition-state bifurcation where a reaction path splits into two branches leading to the alternative products, **Heq1** and **Heq2** in this case. The branching occurs at the valley-ridge inflection point (**VRI**) where the PES valley changes into a dynamically-unstable ridge.<sup>70</sup> This reaction type cannot be described as stepwise or concerted and is instead referred to as a two-step-no-intermediate mechanism.<sup>71</sup>

<sup>a</sup> *Note on the relaxed PES scans:* the scanning algorithm in the Gaussian 16 is not a full pointwise optimization of the potential energy surface, but it gives a feeling where maxima may exist. Various discontinuities observed during the relaxed scans are known artifacts and may arise from sudden reorientations of atomic groups in the course of optimization.



Scheme 4.7. Interpretation of the points and paths in relaxed PES scans in Figure 4.15 in terms of molecular geometry at B3LYP-GD3BJ/6-31+G\* level of theory in vacuum. Where applicable, symmetry point group and  $\Delta G$  are indicated in parenthesis.

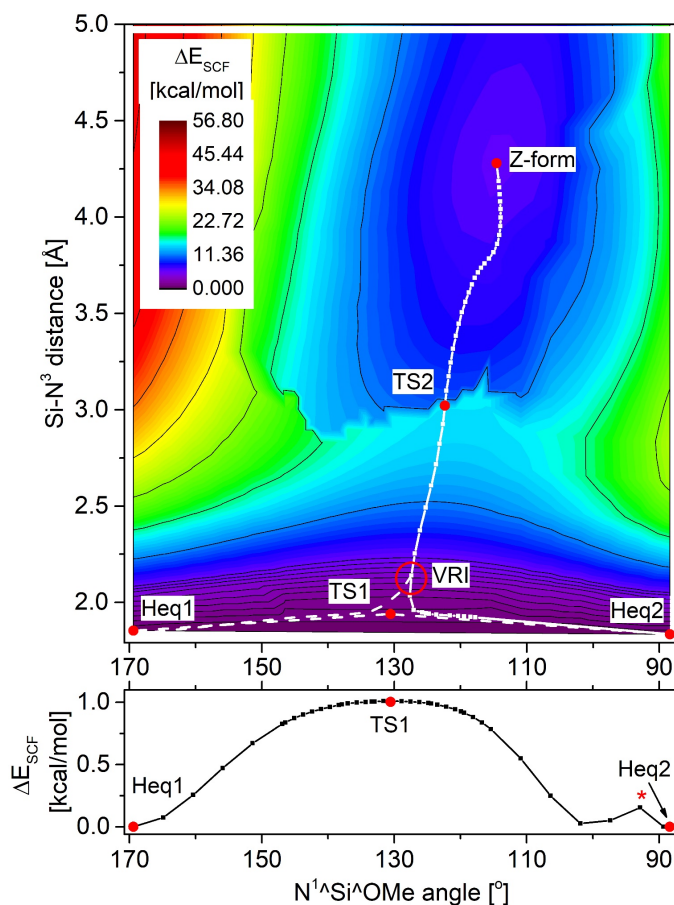


Figure 4.15. Two- (top plot) and one-dimensional (bottom plot) relaxed PES scans at the B3LYP-GD3BJ/6-31+G\* level of theory in vacuum. Stationary points as well as the hypothetical **VRI** region are indicated explicitly. Reaction paths are shown in white. Solid line was used for the paths derived by the IRC with the separate IRC steps marked along. Dashed line was used for the hypothetical paths. In the two-dimensional PES scan, contour lines are shown for every 5.68 kcal/mol increment, except for the lowest ten, which are shown for every 0.568 kcal/mol.

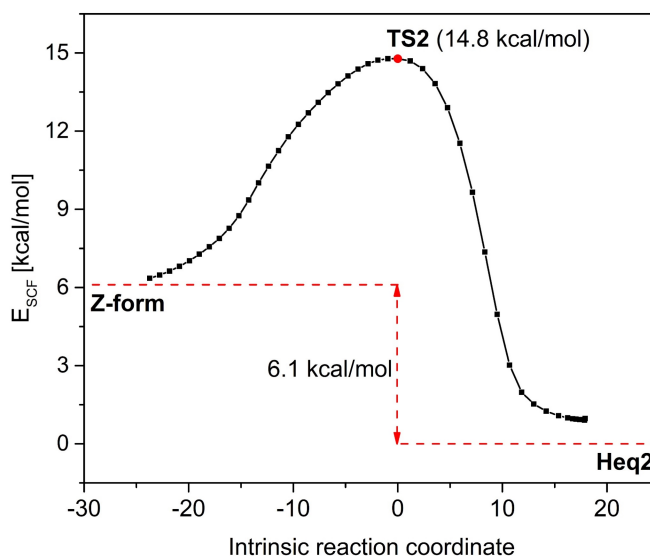


Figure 4.16. IRC path that connects **Z-form** and **Heq2** via **TS2**. Geometry optimization at the end of each branch leads directly to the respective forms. Level of theory: B3LYP-GD3BJ/6-31+G\*.

In order to confirm the connection between the transition states and the corresponding PES minima, as well as to visualize the reaction path, we resorted to IRC (intrinsic reaction coordinate) calculations.<sup>67</sup> We could not connect **Heq1** and **Heq2** via **TS1**. Presumably, due to the flatness of PES between these points, and, therefore, the IRC algorithm failing to find a gradient. While we were able to easily find a path between **TS2** and **Z-form**, an IRC calculation from **TS2** led to **Heq2** only (Figure 4.16). It is not surprising since, mathematically, the IRC path is a unique solution of an autonomous system of differential equations and, therefore, no branching can occur before reaching the next stationary point.<sup>72,73</sup> Oftentimes, in such situations, IRC simply connects **TS1** and **TS2** giving a dynamically unstable reaction path.<sup>69</sup> This is not the case for our system because of another fundamental property of IRC: while on the intrinsic reaction path, a molecular system can never lose symmetry. Whereas **TS2** and **Heq2** are asymmetric ( $C_1$  group), **TS1** possesses a mirror plane ( $C_s$  group), therefore, the path connects the former two. Precisely locating the point where the branching towards **Heq1** occurs, i.e. **VRI**, is a challenging problem:<sup>68,69</sup> the position of a valley-ridge inflection point, in general, depends on the chosen coordinate system.<sup>74</sup> For the purpose of our discussion, the exact location of **VRI** plays a minor role, therefore we did not expend effort for finding it. Instead, we make an educated guess about the region where it should occur based on the shape of the PES. As mentioned above, a **VRI** appears when two transition states follow one another with no energy minima in-between. Along the reaction path from **TS2** to **TS1**, the curvature of the PES changes from negative to positive. Since **TS2** is much more energetic than **TS1** ( $\Delta E_{\text{SCF}}$  of 14.8 vs. 1.0 kcal/mol), the contribution of its curvature along the path is also larger, shifting the inflection



point (**VRI**) closer to **TS1**. Indeed, a visual inspection of the two-dimensional PES scan in *Figure 4.15* reveals a flat region next to **TS1**. This is where the intrinsic reaction path between **TS2** and **Heq2** should split off towards **Heq1**. Hence, we draw an approximate subpath that connects the **VRI** region and **Heq1**.

Now, let us look at interpretation of the points and paths on PES in terms of molecular geometry (*Scheme 4.7*). With decreasing the N<sup>1</sup>Si<sup>1</sup>OMe angle, roughly trigonal bipyramidal **Heq1** ( $\Delta G$  of 0.0 kcal/mol taken as a reference) can undergo a three-fold cyclic permutation. The same in reverse applies for **Heq2**. The transition state for this process is very low-lying (**TS1**;  $\Delta G^\ddagger$  of 2.2 kcal/mol). However, shortly before reaching **TS1**, the system can take another path where the Si-N<sup>3</sup> bond starts dissociating. At the initial stages of this process, the molecular geometry closely resembles that of **TS1**. Whether the reaction path starts at **Heq1** or **Heq2**, it anyway ends up at **VRI**, which is the point of convergence of the two branches. There, the molecular system has a rough mirror symmetry with the O-Si-H, N<sup>3</sup> and P atoms approximately in the same plane. From there, *via* further elongation of the Si-N<sup>3</sup> bond, the system proceeds to the asymmetric **TS2** ( $\Delta G^\ddagger$  of 12.8 kcal/mol) and to the final product, **Z-form** ( $\Delta G$  of 3.1 kcal/mol). For comparison, a transition barrier from **Heq1** to an **E-form** (not shown in *Scheme 4.7*) has  $\Delta G^\ddagger$  of 9.6 kcal/mol,<sup>a</sup> whereas the form itself has  $\Delta G$  of 4.5 kcal/mol. Overall, this implies that both geometric isomers of the open form are thermally accessible at room temperature. Projecting these conclusions onto the experimental system can explain our observations.

To conclude the study of fluxionality in compound **11**, while the NOE spectra (*Figure 4.9*) indicate the presence of **11b-Z**, the comparable free energy of the isomer **11b-E** and low computed barriers for interconversion of the truncated model suggest that both stereoisomers likely coexist with **11a** in a thermal equilibrium. Interestingly, the formation of **11b-Z** from the closed form **11a** proceeds via an unusual “two step no intermediate” mechanism consisting of a Berry-like stereomutation followed by Si-N bond dissociation. These observations demonstrate that, besides its ability to support facile interconversion of Si(II) and Si(IV) species, the strained TSMP platform confers much conformational flexibility to the latter, as it allows virtually all thermodynamically accessible 4-coordinate and 5-coordinate geometries to be sampled at room temperature or below.

---

<sup>a</sup> The corresponding transition state was located using QST3 algorithm in Gaussian 16.<sup>66</sup> Due to the high curvature and overall flatness of the corresponding PES, IRC algorithm fails to connect the transition state with **Heq1** and **E-form**. Still, minor manual displacement of the transition state along the imaginary normal mode followed by the geometry optimization yields both **Heq1** and **E-form**. This indirectly confirms that the transition state in question lies on the minimal energy path between the two geometries.

## 4.8 Conclusions and outlook

The constrained valence angles around the silicon atom at the bridgehead position of the bicyclic cationic silane  $[\text{TSMPSiH}]^+$  (**2**) have a profound effect on its reactivity.

First, at odds with the general hydridic character of silicon-bound hydrogen atoms,  $[\text{TSMPSiH}]^+$  (**2**) exhibits an exceptionally low  $\text{p}K_{\text{a}}^{\text{DMSO}}$  within 4.7-8.1, which makes it more acidic than phenol, benzoic acid ( $\text{p}K_{\text{a}}^{\text{DMSO}}$  of 18.0<sup>31</sup> and 11.1,<sup>32</sup> respectively) and the few silanes of which  $\text{p}K_{\text{a}}^{\text{DMSO}}$  was reported.<sup>43,49</sup> While this high acidity originates in part from the electron-withdrawing effect of the substituents on silicon and overall positive charge of **2**, it is significantly enhanced by the unusually acute  $\text{N}^{\wedge}\text{Si}^{\wedge}\text{N}$  angles imposed by the heterobicyclo[2.2.2]octane scaffold. Namely, DFT calculations suggest that strain increases the *s*-character of the Si–H bonding pair, polarizing the bond towards silicon and facilitating its heterolytic dissociation.

Then, protonation (or methylation) of the anionic Si atom in TSMPSi (**1**) increases the reactivity of the opposing methylphosphonium unit, which can transfer a methyl group with release of strain. This opens up a charge neutralization pathway to form the phosphine/methylsilane isomer iso-TSMPSi (**10**) by intermolecular methyl transfer.

Finally, next to its high Brønsted acidity,  $[\text{TSMPSiH}]^+$  (**2**) also behaves as a strain-release Lewis acid, coordinating a THF molecule so that the silicon atom assumes a trigonal bipyramidal geometry. This is accompanied by activation of  $\alpha$ -carbons of the THF ring, which makes it susceptible to such weak nucleophiles as highly-stabilized aromatic anions. In particular, the conjugate base TSMPSi (**1**) reacts with fluoradene (**4**) in THF to afford the linear product **11a/b**, which forms by nucleophilic ring opening of a THF molecule coordinated to  $[\text{TSMPSiH}]^+$  (**2**). In this process, the Si center sequentially acts as a nucleophile (base) and then as an electrophile (Lewis acid) to facilitate the activation of two relatively unreactive molecules, suggesting the potential of such cage compounds as biphilic main-group centers. This reaction sequence also illustrates the ability of the TSMP scaffold to support both the Si(II) and Si(IV) states along with the processes that interconvert them under mild conditions. Furthermore, the trigonal bipyramidal silicon center in the addition product **11a** undergoes several facile fluxional processes (positional exchange and reversible Si–N bond dissociation), illustrating the flexibility of the TSMPSi (**1**) platform in terms of accessible geometries.

These observations collectively illustrate how a combination of charge, inductive effects and strain can significantly manipulate the properties of a silicon atom leading to unusual reactivity. The various reactive pathways accessible to the strained cage structure  $[\text{TSMPSiH}]^+$  (**2**) suggest that this or a related platform may

serve as an entry point into novel bond activation strategies based on the Si(II)/Si(IV) couple. Such research is presently ongoing in our laboratories.

#### **4.9 Author contributions and acknowledgements**

Serhii Tretiakov and Dr. Marc-Etienne Moret conceived the project. Serhii Tretiakov performed all synthetic work as well as spectral measurements followed by interpretation thereof, except for ESI-TOF-MS spectrometry carried out by Dr. Thomas Ran, for which he is greatly acknowledged. Dr. Martin Lutz conducted single crystal X-ray diffraction experiments along with solving the structures. The major bulk of computational work was performed by Serhii Tretiakov with initial support from Dr. Léon Witteman for NMR chemical shifts and relaxed PES scan calculations. The authors thank E. C. Monkcom for the TOC artwork, and Dr G. van Koten, Dr. R. J. M. Klein Gebbink, Dr. D. L. J. Broere and Dr. Léon Witteman for insightful discussions. Serhii Tretiakov wrote this chapter based on the corresponding publication<sup>34</sup> and with input from Dr. Marc-Etienne Moret. All authors read and approved the final version.

## 4.10 Experimental and computational methods

### 4.10.1 General remarks

All reactions were conducted under a nitrogen atmosphere with strict exclusion of moisture by using standard glovebox or Schlenk techniques.

Acetonitrile, diethyl ether, toluene and *n*-hexane were dried with an MBRAUN MB SPS-79 system. Acetonitrile was additionally dried by passing through a column of activated alumina after being kept over ca. 5 wt.% of 3Å molecular sieves over 48 h. THF and dioxane were distilled from benzophenone/Na. DCM and aniline were distilled from CaH<sub>2</sub>. Benzene was dried over ca. 5 wt.% of 3Å molecular sieves over 48h. Dried solvents were degassed by sparging with dry nitrogen for 30 min and stored over molecular sieves in a glovebox, except for acetonitrile which was stored without the sieves. THF-*d*<sub>8</sub>, pyridine-*d*<sub>5</sub> and dioxane-*d*<sub>8</sub> were purchased from ABCR, other deuterated solvents were acquired from Cambridge Isotope Laboratories, Inc. Deuterated solvents were dried as indicated above for their proteo-analogues, except for dioxane-*d*<sub>8</sub> which was dried by passing through a column of activated alumina. Pyridine-*d*<sub>5</sub> was dried by distillation over CaH<sub>2</sub>. Dried deuterated solvents were degassed by four freeze-pump-thaw cycles and stored in a glovebox over molecular sieves, except for acetonitrile-*d*<sub>3</sub> which was stored without the sieves.

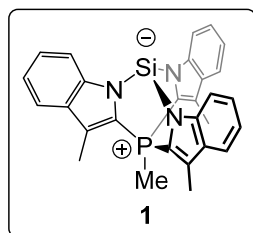
Fe(OTf)<sub>2</sub> was purchased from ABCR and 9-cyano-9*H*-fluorene (**17**) was acquired from Enamine Ltd. All other chemicals were purchased from Sigma-Aldrich. FeBr<sub>2</sub> was acquired in anhydrous form. Potassium hydride was supplied as a 30 wt.% suspension in mineral oil, which was washed away with several portions of *n*-hexane before further use. 2,6-Lutidine was dried by distillation over CaH<sub>2</sub> and degassed by bubbling dry dinitrogen for 30 min, after which it was stored in a glovebox over 4Å molecular sieves. All other commercially obtained chemicals were used as received. The FeCl<sub>2</sub>·1.5THF adduct was prepared by extraction of FeCl<sub>2</sub> with anhydrous THF using a Soxhlet extractor. Potassium graphite (KC<sub>8</sub>) and Idipp·SiCl<sub>2</sub> were synthesized according to literature procedures.<sup>75,76</sup> After purification, according to <sup>1</sup>H NMR, Idipp·SiCl<sub>2</sub> was still contaminated with ~10 wt.% of unidentified Idipp-containing impurities. NaBAR<sup>F</sup><sub>4</sub> was prepared following a reported procedure.<sup>77</sup> Before drying, an additional recrystallization step from fluorobenzene was required in order to achieve higher purity. HBAR<sup>F</sup><sub>4</sub>·2Et<sub>2</sub>O was prepared from NaBAR<sup>F</sup><sub>4</sub> according to the literature procedure.<sup>78</sup> The TSM<sup>F</sup>PK<sub>2</sub> salt (**3**) was synthesized following the published procedure.<sup>40</sup>

Unless otherwise stated, the NMR measurements were performed at 298 K on a Varian VNMR400 or Varian MRF400 spectrometer, chemical shifts are reported relative to TMS with the residual solvent signal as internal standard.<sup>79</sup> All NMR experiments involving air-sensitive compounds were conducted in J. Young NMR tubes under nitrogen atmosphere. Peak multiplicity was quoted as s (singlet), d (doublet), t (triplet) and so on. In cases of unresolved couplings that strongly affected the line shape of individual components of an otherwise well-defined multiplet, the effective multiplicity was quoted as 's', 'd', 't' and so on. ASAPHMQC NMR experiments were conducted using the corresponding pulse sequence<sup>80</sup> as implemented in the VnmrJ 4.2 software.<sup>81</sup> IR spectra were recorded on a Perkin-Elmer Spectrum Two FT-IR spectrometer. The bands were classified by an absorption intensity as: very weak (VW; 0-10% of the most intense absorption in the spectrum), weak (W; 10-30%), medium (M; 30-60%), strong (S; 60-90%), very strong (VS; 90-100%). UV-Vis spectra were measured on a PerkinElmer Lambda 35 spectrometer. ESI-MS measurements were performed on a Waters LCT Premier XE KE317 spectrometer. Elemental analysis was conducted by Medac Ltd.

For the sake of brevity, the NMR, IR and UV-Vis spectra of isolated compounds are not shown in this chapter. These can be found in the respective publication.<sup>34</sup>

## 4.10.2 Synthesis and characterization

### 4.10.2.1 Silicon and germanium<sup>a</sup> compounds

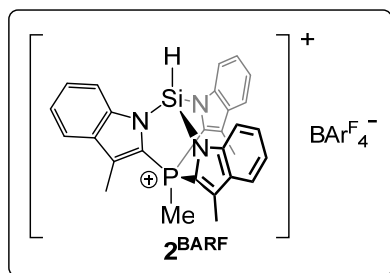


**TSMPSi (1).** A solution of Idipp-SiCl<sub>2</sub> (90 wt.% purity, 3.055 g, 5.630 mmol, 1.050 equiv.) in THF (20.0 ml) was added dropwise to dipotassium salt **3** (contains 21.5 wt.% of THF, 3.494 g, 5.360 mmol, 1.000 equiv.) in THF (140 ml) at -78 °C. The mixture was stirred at low temperature for 4h and then allowed to warm up to room temperature overnight. Next day, the reaction was filtered, and the solid was washed with THF (3 x 10.0 ml). The solvent from combined organic fractions was removed *in vacuo*. The solid was dissolved in a minimal amount of PhMe/CH<sub>3</sub>CN 1:1 (v/v) solvent mixture, carefully topped up with an equal volume of Et<sub>2</sub>O and placed into a freezer overnight at -36 °C. The precipitate was filtered off the next day and, in order to remove the traces of other solvents, was thrice resuspended in THF (10.0 ml) followed by drying *in vacuo*. The procedure yielded fine light-beige powder. The residual THF content of 19.0 wt.% was determined using quantitative <sup>1</sup>H NMR measurements in 4:1 benzene-*d*<sub>6</sub>/acetonitrile-*d*<sub>3</sub> solvent mixture. With the product mass of 2.017 g, this gives 66.0% yield. Crystals suitable for X-ray diffraction analysis were grown by vapor diffusion of *n*-hexane into a solution of **1** in benzene at room temperature.

The <sup>1</sup>H and <sup>13</sup>C NMR spectra of **1** show a single set of signals in aromatic region indicating C<sub>3</sub> symmetry that corresponds to heterobicyclo[2.2.2]octane topology. Moreover, both <sup>1</sup>H and <sup>29</sup>Si spectra show a good agreement with the DFT-calculated NMR parameters (see *Appendix C2*). Some NMR spectra are contaminated with small amounts of isomer **10**, which has better solubility than **1** in most solvents. In case of an overlap with a solvent signal, where possible, integral intensities in <sup>1</sup>H NMR spectra were extracted using MNova<sup>82</sup> peak deconvolution tool. <sup>1</sup>H NMR (400 MHz, Pyridine-*d*<sub>5</sub>) δ 8.54 (d, *J*<sub>H,H</sub> = 8.4 Hz, 1H, Ar-H), 7.61 (d, *J*<sub>H,H</sub> = 8.0 Hz, 1H, Ar-H), 7.41 (t, *J*<sub>H,H</sub> = 7.6 Hz, 1H, Ar-H), 7.20 (t, *J*<sub>H,H</sub> = 7.3 Hz, 1H, Ar-H), 4.07 (d, *J*<sub>H,P</sub> = 16.2 Hz, 1H, P<sup>+</sup>-CH<sub>3</sub>), 2.52 (d, *J*<sub>H,P</sub> = 1.8 Hz, 3H, Ar-CH<sub>3</sub>). <sup>1</sup>H NMR (400 MHz, THF-*d*<sub>8</sub>) δ 8.11 (d, *J*<sub>H,H</sub> = 8.5 Hz, 1H, Ar-H), 7.46 (d, *J*<sub>H,H</sub> = 8.0, 1.0 Hz, 1H, Ar-H), 7.18 (t, *J*<sub>H,H</sub> = 7.6 Hz, 1H, Ar-H), 6.97 (t, *J*<sub>H,H</sub> = 7.4 Hz, 1H, Ar-H), 3.67 – 3.56 (m, obscured by the overlap with the THF-*h*<sub>8</sub> peak, P<sup>+</sup>-CH<sub>3</sub>), 2.59 (d, *J*<sub>H,P</sub> = 1.8 Hz, 3H, Ar-CH<sub>3</sub>). <sup>1</sup>H NMR (400 MHz, Methylene Chloride-*d*<sub>2</sub>) δ 8.14 (d, *J*<sub>H,H</sub> = 8.5 Hz, 1H, Ar-H), 7.52 (d, *J*<sub>H,H</sub> = 8.0 Hz, 1H, Ar-H), 7.27 (t, *J*<sub>H,H</sub> = 7.7 Hz, 1H, Ar-H), 7.06 (t, *J*<sub>H,H</sub> = 7.4 Hz, 1H, Ar-H), 3.28 (d, *J*<sub>H,P</sub> = 15.8 Hz, 1H, P<sup>+</sup>-CH<sub>3</sub>), 2.59 (d, *J*<sub>H,P</sub> = 1.9 Hz, 3H, Ar-CH<sub>3</sub>). <sup>1</sup>H NMR (400 MHz, 1,4-Dioxane-*d*<sub>8</sub>) δ 8.14 (d, *J*<sub>H,H</sub> = 8.5 Hz, 1H, Ar-H), 7.46 (d, *J*<sub>H,H</sub> = 7.9 Hz, 1H, Ar-H), 7.23 (t, *J*<sub>H,H</sub> = 7.7 Hz, 1H, Ar-H), 7.00 (t, *J*<sub>H,H</sub> = 7.5 Hz, 1H, Ar-H), 3.40 (d, *J*<sub>H,P</sub> = 16.3 Hz, 1H, P<sup>+</sup>-CH<sub>3</sub>), 2.58 (d, *J*<sub>H,P</sub> = 1.8 Hz, 3H, Ar-CH<sub>3</sub>). <sup>1</sup>H NMR (400 MHz, Benzene-*d*<sub>6</sub>) δ 8.55 ('d', *J*<sub>H,H</sub> = 8.5 Hz, 1H, Ar-H), 7.48 ('d', *J*<sub>H,H</sub> = 8.0 Hz, 1H, Ar-H), 7.23 ('t', *J*<sub>H,H</sub> = 7.6 Hz, 1H, Ar-H), 7.13 ('t', *J*<sub>H,H</sub> = 7.6 Hz, 1H, Ar-H), 2.08 – 1.98 (m, 4H, P<sup>+</sup>-CH<sub>3</sub>, Ar-CH<sub>3</sub>). <sup>1</sup>H NMR (400 MHz, Acetonitrile-*d*<sub>3</sub>/Benzene-*d*<sub>6</sub> 1:4 (v/v); referenced against the residual benzene peak at 7.16 ppm) δ 8.21 ('d', *J*<sub>H,H</sub> = 8.5 Hz, 1H, Ar-H), 7.43 ('d', *J*<sub>H,H</sub> =

<sup>a</sup> Germanium compounds **12** and **14** are not mentioned in the main text, yet they are still discussed in *Appendix C1*. For the sake of simplicity, their synthesis and characterization are described in the current section.

8.1 Hz, 1H, Ar-H), 7.14 (‘t’,  $J = 7.8$  Hz, overlaps with residual benzene peak, Ar-H), 6.99 (‘t’,  $J_{\text{H,H}} = 7.3$  Hz, 1H, Ar-H), 3.02 (d,  $J_{\text{H,P}} = 16.0$  Hz, 1H,  $\text{P}^+\text{-CH}_3$ ), 2.40 (d,  $J_{\text{H,P}} = 1.9$  Hz, 3H, Ar- $\text{CH}_3$ ).  $^{13}\text{C}$  NMR (101 MHz, Pyridine- $d_5$ )  $\delta$  147.7 (d,  $J_{\text{C,P}} = 10.9$  Hz, indole-C8), 130.9 (d,  $J_{\text{C,P}} = 14.2$  Hz, indole-C9 or C3), 126.2 ( $\text{C}^{\text{Ar-H}}$ ), 123.2 (d,  $J_{\text{C,P}} = 17.5$  Hz, indole-C3 or C9), 121.8 (d,  $J_{\text{C,P}} = 115.7$  Hz, indole-C2), 121.7 (d,  $J_{\text{C,P}} = 1.6$  Hz,  $\text{C}^{\text{Ar-H}}$ ), 121.4 ( $\text{C}^{\text{Ar-H}}$ ), 115.3 (d,  $J_{\text{C,P}} = 2.0$  Hz,  $\text{C}^{\text{Ar-H}}$ ), 11.0 (Ar- $\text{CH}_3$ ), 2.3 (d,  $J_{\text{C,P}} = 56.2$  Hz,  $\text{P}^+\text{-CH}_3$ ).  $^{31}\text{P}$  NMR (162 MHz, Pyridine- $d_5$ )  $\delta$  -7.7 (q,  $J_{\text{P,H}} = 16.1$  Hz, carbon satellites:  $J_{\text{P,C}} = 115.6, 55.9, 17.0, 13.8, 10.5$  Hz).  $^{31}\text{P}$  NMR (162 MHz, THF- $d_8$ )  $\delta$  -7.3 (q,  $J_{\text{P,H}} = 16.2$  Hz, carbon satellites:  $J_{\text{P,C}} = 116.1$  Hz).  $^{31}\text{P}$  NMR (162 MHz, Methylene Chloride- $d_2$ )  $\delta$  -10.2 (q,  $J_{\text{P,H}} = 16.0$  Hz, additional couplings resulting into carbon satellites:  $J_{\text{P,C}} = 117.3$  Hz).  $^{31}\text{P}$  NMR (162 MHz, Dioxane- $h_8$ )  $\delta$  -9.5.  $^{31}\text{P}$  NMR (162 MHz, Benzene- $d_6$ )  $\delta$  -10.9 (q,  $J_{\text{P,H}} = 16.0$  Hz).  $^{31}\text{P}$  NMR (162 MHz, Acetonitrile- $d_3$ /Benzene- $d_6$  1:4 (v/v))  $\delta$  -9.70 (q,  $J_{\text{P,H}} = 16.1$  Hz).  $^{29}\text{Si}$  NMR (79 MHz, Pyridine- $d_5$ )  $\delta$  -47.5 (d,  $J_{\text{Si,P}} = 4.4$  Hz).  $^{29}\text{Si}$  NMR (79 MHz, THF- $d_8$ )  $\delta$  -48.0 (d,  $J_{\text{Si,P}} = 4.3$  Hz). No satisfactory elemental analysis could be obtained due to the high reactivity of **1**.



[TSMPSiH] $^+\text{BARF}_4^-$  (**2** $^{\text{BARF}}$ ). Depending on the solvent, compound **2** $^{\text{BARF}}$  shows two different sets of NMR signals consistent with different coordination environment of the silicon. Namely, in DCM- $d_2$ ,  $^{29}\text{Si}$  shifts are consistent with a tetrahedral silicon atom, whereas in THF- $d_8$   $^{29}\text{Si}$  spectra indicate pentacoordination. Below, we provide two alternative procedures that can be used in order to synthesize **2** $^{\text{BARF}}$ : one which is THF-free (*Procedure A*) and another in

THF as a reaction solvent (*Procedure B*). While the former, according to NMR, yields some amount of unidentified side-products and, thus, only qualifies as “generation”, the latter provides clean **2** $^{\text{BARF}}$  and can be considered preparative.

*Procedure A (THF-free generation)*. All manipulations were performed in a J. Young NMR tube. Silanide **1** (contains 19.0 wt.% of THF, 0.035 g, 0.061 mmol, 1.0 equiv.) was suspended in 2.0 ml of dioxane. The suspension was cooled in a freezer until it solidified. This was followed by drying *in vacuo* to a constant mass, resuspending in dioxane, cooling and another cycle of drying. Solid  $\text{HBARF}_4 \cdot 2\text{Et}_2\text{O}$  (0.062 g, 0.061 mmol, 1.0 equiv.) suspended in 1.0 ml of dioxane was then added. The suspension was quickly stirred, upon which the mixture almost cleared up and then immediately turned into a gelatinous white mass. It was, again, cooled in a freezer and dried *in vacuo* to a constant mass. The white solid was completely redissolved in  $\sim 0.5$  ml of DCM- $d_2$  for the NMR measurements. Crystals suitable for X-ray diffraction analysis were grown by layering a DCM solution of **2** $^{\text{BARF}}$  with dioxane in a J. Young NMR tube and leaving it standing for 3 days.

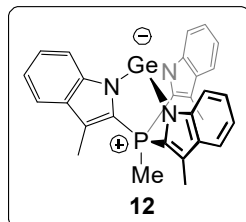
Both  $^1\text{H}$  and  $^{13}\text{C}$  NMR spectra in DCM- $d_2$  are consistent with a heterobicyclo[2.2.2]octane topology of the cationic silane **2**. Even though the signal of the Si–H hydrogen atom is obscured by aromatic multiplets, its position can be clearly determined from  $^1\text{H}$ - $^{29}\text{Si}$  ASAPHMQC spectra. The NMR spectra are sufficiently clean in order to make conclusions about atomic connectivity. Yet, there is a number of unidentified trace impurities. Furthermore, NMR data suggest the presence of a small amount (ca. 15%) of a contaminating  $\text{BARF}_4^-$  salt, possibly  $\text{NaBARF}_4$  or  $\text{HBARF}_4$ . In order to assign  $\text{BARF}_4^-$ -derived signals, we used the spectra of  $\text{NaBARF}_4$  in THF- $d_8$  as a reference (*see Procedure B*). While the chemical shifts slightly differ from those in DCM- $d_2$ , the number of signals and their multiplicity still hold and, therefore, can be used for the assignment. Experimental NMR parameters show a good agreement with the DFT-calculated values (*see*

*Appendix C2*).  $^1\text{H NMR}$  (400 MHz, Methylene Chloride- $d_2$ )  $\delta$  7.78 – 7.70 (m, 11H of which 8H: C(2)<sup>Ar</sup>-H of  $\text{BAr}^{\text{F}_4}$  + 3H: Ar-H of cationic silane), 7.68 (d,  $J_{\text{H,H}} = 8.2$  Hz, 3H of cationic silane), 7.58 – 7.51 (m, 8H of which 1H: Si-H of cationic silane + 4H: C(4)<sup>Ar</sup>-H of  $\text{BAr}^{\text{F}_4}$  + 3H: Ar-H of cationic silane), 7.33 (t,  $J_{\text{H,H}} = 7.5$  Hz, 3H, Ar-H of cationic silane), 3.54 (d,  $J_{\text{H,P}} = 16.0$  Hz, 3H, P<sup>+</sup>-CH<sub>3</sub> of cationic silane), 2.65 (d,  $J_{\text{H,P}} = 2.0$  Hz, 9H, Ar-CH<sub>3</sub> of cationic silane).  $^{13}\text{C NMR}$  (101 MHz, Methylene Chloride- $d_2$ )  $\delta$  162.3 (q,  $J_{\text{C,B}} = 49.8$  Hz, C<sup>Ar-11B</sup> of  $\text{BAr}^{\text{F}_4}$ ), 143.1 (d,  $J_{\text{C,P}} = 8.7$  Hz, indole-C8 of cationic silane), 135.4 (br.s., C(2)<sup>Ar</sup>-H of  $\text{BAr}^{\text{F}_4}$ ), 130.2 (d,  $J_{\text{C,P}} = 14.7$  Hz, indole-C9 or C3 of cationic silane), 129.7 (d,  $J_{\text{C,P}} = 13.8$  Hz, indole-C3 or C9 of cationic silane), 129.4 (qq,  $J_{\text{C,F}} = 31.4$ , 2.9 Hz, C(3)<sup>Ar</sup>-CF<sub>3</sub> of  $\text{BAr}^{\text{F}_4}$ ), 128.8 (C<sup>Ar</sup>-H of cationic silane), 123.7 (C<sup>Ar</sup>-H of cationic silane), 125.2 (q,  $J_{\text{C,F}} = 272.4$  Hz, CF<sub>3</sub> of  $\text{BAr}^{\text{F}_4}$ ), 122.0 (d,  $J_{\text{C,P}} = 1.4$  Hz, C<sup>Ar</sup>-H of cationic silane), 118.1 (hept,  $J_{\text{C,F}} = 4.0$  Hz, C(4)<sup>Ar</sup>-H of  $\text{BAr}^{\text{F}_4}$ ), 117.4 (d,  $J_{\text{C,P}} = 111.3$  Hz, indole-C2 of cationic silane), 113.1 (d,  $J_{\text{C,P}} = 1.7$  Hz, C<sup>Ar</sup>-H of cationic silane), 10.8 (Ar-CH<sub>3</sub> of cationic silane), 2.3 (d,  $J_{\text{C,P}} = 57.8$  Hz, P<sup>+</sup>-CH<sub>3</sub> of cationic silane).  $^{31}\text{P NMR}$  (162 MHz, Methylene Chloride- $d_2$ )  $\delta$  -7.6 (q,  $J_{\text{P,H}} = 16.0$  Hz, carbon satellites:  $J_{\text{P,C}} = 111.0$ , 14.4, 8.4 Hz).  $^{29}\text{Si NMR}$  (79 MHz, Methylene Chloride- $d_2$ )  $\delta$  -46.4 (dd,  $J_{\text{Si,H}} = 318.4$  Hz,  $J_{\text{Si,P}} = 8.0$  Hz).  $^{11}\text{B NMR}$  (128 MHz, Methylene Chloride- $d_2$ )  $\delta$  -6.61,  $^{13}\text{C}$ -satellites at -6.62 (d,  $J_{\text{B,C}} = 49.9$  Hz).  $^{19}\text{F NMR}$  (376 MHz, Methylene Chloride- $d_2$ )  $\delta$  -62.83,  $^{13}\text{C}$ -satellites at -62.84 (d,  $J_{\text{F,C}} = 30.9$  Hz) and -62.96 (d,  $J_{\text{F,C}} = 272.4$  Hz).

*Procedure B (preparative procedure in THF)*. Silanide **1** (contains 19.0 wt.% of THF, 0.067 g, 0.12 mmol, 1.1 equiv.) was dissolved in THF (18.0 ml) and cooled to -78 °C. Under vigorous stirring, a freshly prepared solution of  $\text{HAr}^{\text{F}_4} \cdot 2\text{Et}_2\text{O}$  (0.107 g, 0.106 mmol, 1.00 equiv.) in THF (12.0 ml) was added dropwise. The reaction mixture was stirred for 10 min and then allowed to warm to room temperature. After removal of THF under vacuum, the solid residue was extracted with ether, which was removed *in vacuo* giving 0.150 g of amorphous white powder.

According to NMR data, protonation is quantitative. The solid contains an undetermined amount of solvating THF that precludes an accurate determination of the reaction yield. Additionally, NMR data suggest the presence of a small amount (ca. 10%) of a contaminating  $\text{BAr}^{\text{F}_4}$  salt, possibly  $\text{NaBAr}^{\text{F}_4}$  or  $\text{HAr}^{\text{F}_4}$ . In order to assign  $\text{BAr}^{\text{F}_4}$ -derived signals, we used the spectra of  $\text{NaBAr}^{\text{F}_4}$  for a reference. Compared to the measurements in  $\text{DCM}-d_2$  (see *Procedure A*), the NMR spectra of  $2^{\text{BArF}}$  in  $\text{THF}-d_8$  undergo a dramatic change. While  $^1\text{H}$  and  $^{13}\text{C}$  signals remain in line with  $\text{C}_3$  symmetry,  $^{29}\text{Si}$  spectra indicate a pentacoordinate silicon center with THF molecule as the fifth ligand, which is also in agreement with the DFT-calculated NMR parameters (see *Appendix C2*). The retention of  $\text{C}_3$  symmetry in both  $^1\text{H}$  and  $^{13}\text{C}$  spectra, despite breaking of such symmetry upon coordination of THF, hints at a fluxional process, which may be either positional exchange or reversible dissociation.  $^1\text{H NMR}$  (400 MHz,  $\text{THF}-d_8$ )  $\delta$  7.90 – 7.82 (m, 8H, C(2)<sup>Ar</sup>-H of  $\text{BAr}^{\text{F}_4}$ ), 7.77 (d,  $J_{\text{H,H}} = 8.5$  Hz, 3H, Ar-H of cationic silane), 7.69 (d,  $J_{\text{H,H}} = 8.1$  Hz, 3H, Ar-H of cationic silane), 7.63 (s, 4H, C(4)<sup>Ar</sup>-H of  $\text{BAr}^{\text{F}_4}$ ), 7.51 (s, 1H, Si-H of cationic silane), 7.42 (t,  $J_{\text{H,H}} = 7.7$  Hz, 3H, Ar-H of cationic silane), 7.22 (t,  $J_{\text{H,H}} = 7.5$  Hz, 3H, Ar-H of cationic silane), 3.94 (d,  $J_{\text{H,P}} = 16.6$  Hz, 3H, P<sup>+</sup>-CH<sub>3</sub> of cationic silane), 2.70 (d,  $J_{\text{H,P}} = 2.0$  Hz, 9H, Ar-CH<sub>3</sub> of cationic silane).  $^{13}\text{C NMR}$  (101 MHz,  $\text{THF}-d_8$ )  $\delta$  162.9 (hept,  $J_{\text{C,B}} = 16.8$  Hz, C<sup>Ar-10B</sup> of  $\text{BAr}^{\text{F}_4}$ ), 162.9 (q,  $J_{\text{C,B}} = 49.8$  Hz, C<sup>Ar-11B</sup> of  $\text{BAr}^{\text{F}_4}$ ), 144.0 (d,  $J_{\text{C,P}} = 9.3$  Hz, indole-C8 of cationic silane), 135.7 (br.s., C(2)<sup>Ar</sup>-H of  $\text{BAr}^{\text{F}_4}$ ), 130.22 (d,  $J_{\text{C,P}} = 14.0$  Hz, indole-C9 or C3 of cationic silane), 130.15 (qq,  $J_{\text{C,F}} = 31.6$ , 2.9 Hz, C(3)<sup>Ar</sup>-CF<sub>3</sub> of  $\text{BAr}^{\text{F}_4}$ ), 127.2 (C<sup>Ar</sup>-H of cationic silane), 126.7 (d,  $J_{\text{C,P}} = 15.5$  Hz, indole-C3 or C9 of cationic silane), 125.6 (q,  $J_{\text{C,F}} = 272.3$  Hz, CF<sub>3</sub> of  $\text{BAr}^{\text{F}_4}$ ), 122.4 (C<sup>Ar</sup>-H of cationic silane), 121.7 (d,  $J_{\text{C,P}} = 1.5$  Hz, C<sup>Ar</sup>-H of cationic silane), 120.3 (d,  $J_{\text{C,P}} = 110.5$  Hz, indole-C2 of cationic silane), 118.3 (hept,  $J_{\text{C,F}} = 3.6$  Hz, C(4)<sup>Ar</sup>-H of  $\text{BAr}^{\text{F}_4}$ ), 114.0 (d,  $J_{\text{C,P}} = 1.9$  Hz, C<sup>Ar</sup>-H of cationic silane), 9.6 (Ar-CH<sub>3</sub> of cationic

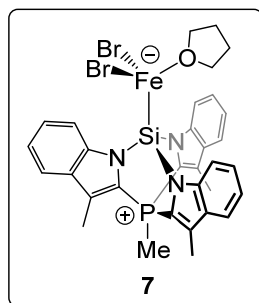
silane), 0.6 (d,  $J_{C,P} = 55.5$  Hz,  $P^+-CH_3$  of cationic silane).  $^{31}P$  NMR (162 MHz, THF- $d_8$ )  $\delta$  -7.0 (q,  $J_{P,H} = 16.7$  Hz, carbon satellites:  $J_{P,C} = 110.3, 14.7, 8.5$  Hz).  $^{29}Si$  NMR (79 MHz, THF- $d_8$ )  $\delta$  -91.0 (dd,  $J_{Si,H} = 368.4$  Hz,  $J_{Si,P} = 6.7$  Hz).  $^{11}B$  NMR (128 MHz, THF- $d_8$ )  $\delta$  -4.61,  $^{13}C$ -satellites at -4.62 (d,  $J_{B,C} = 49.8$  Hz).  $^{19}F$  NMR (376 MHz, THF- $d_8$ )  $\delta$  -61.55,  $^{13}C$ -satellites at -61.56 (d,  $J_{F,C} = 31.2$  Hz) and -61.68 (d,  $J_{F,C} = 272.3$  Hz). No satisfactory elemental analysis could be obtained due to high reactivity of **2**<sup>BARF</sup>.



**TSMPPGe (12).** Dipotassium salt **3** (contains 21.5 wt.% of THF, 0.385 g, 0.590 mmol, 1.00 equiv.) was suspended in THF (6.0 ml) and cooled down to -78 °C. With vigorous stirring, a solution of  $GeCl_2$ -dioxane adduct (0.274 g, 1.18 mmol, 2.00 equiv.) in THF (2.0 ml) was added dropwise over a minute. The reaction was stirred at -78 °C over 4h and then allowed to warm up to room temperature overnight. Next morning, the grey-yellow suspension was filtered to yield a bright-yellow solution.

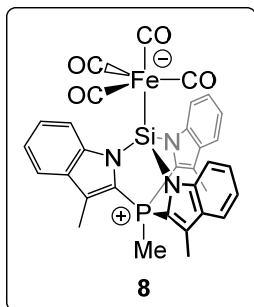
The solvent was removed *in vacuo*, the solid was dissolved in DCM, filtered and the solvent was, again, removed *in vacuo* to yield a fine white powder (0.243 g, 81.4%). Crystals suitable for X-ray diffraction analysis were grown by vapor diffusion of *n*-hexane into a solution of **12** in THF at room temperature.

The  $^1H$  and  $^{13}C$  NMR spectra of **12** show a single set of signals in aromatic region indicating  $C_3$  symmetry that corresponds to heterobicyclo[2.2.2]octane topology.  $^1H$  NMR (400 MHz, Pyridine- $d_5$ )  $\delta$  8.15 (d,  $J_{H,H} = 8.4$  Hz, 1H, Ar-H), 7.65 (d,  $J_{H,H} = 8.0$  Hz, 1H, Ar-H), 7.38 (t,  $J_{H,H} = 7.6$  Hz, 1H, Ar-H), 7.20 (t,  $J_{H,H} = 7.4$  Hz, 1H, Ar-H), 3.94 (d,  $J_{H,P} = 15.8$  Hz, 1H,  $P^+-CH_3$ ), 2.57 (d,  $J_{H,P} = 1.8$  Hz, 3H, Ar- $CH_3$ ).  $^{13}C$  NMR (101 MHz, Pyridine- $d_5$ )  $\delta$  146.7 (d,  $J_{C,P} = 12.0$  Hz, indole-C8), 130.0 (d,  $J_{C,P} = 13.8$  Hz, indole-C9 or C3), 125.0 ( $C^{Ar}$ -H), 121.1 (d,  $J_{C,P} = 18.7$  Hz, indole-C3 or C9), 120.9 (d,  $J_{C,P} = 1.5$  Hz,  $C^{Ar}$ -H), 120.6 (d,  $J_{C,P} = 117.1$  Hz, indole-C2), 120.2 ( $C^{Ar}$ -H), 114.2 (d,  $J_{C,P} = 2.2$  Hz,  $C^{Ar}$ -H), 10.3 (Ar- $CH_3$ ), 2.5 (d,  $J_{C,P} = 56.4$  Hz,  $P^+-CH_3$ ).  $^{31}P$  NMR (162 MHz, Pyridine- $d_5$ )  $\delta$  -8.5 (q,  $J_{P,H} = 15.9$  Hz, carbon satellites:  $J_{P,C} = 116.9, 56.6, 18.5, 12.5$  Hz). **ESI-TOF-MS** in THF with KCl: found 508.1019 [ $M+H$ ]<sup>+</sup>, 582.0355 [ $M+H+KCl$ ]<sup>+</sup> (calcd. 508.1004 [ $M+H$ ]<sup>+</sup>, 582.0325 [ $M+H+KCl$ ]<sup>+</sup>). No satisfactory elemental analysis could be obtained due to high reactivity of **12**.



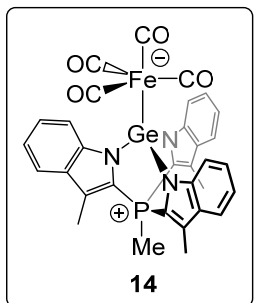
**(TSMPSi)FeBr<sub>2</sub>(THF) (7).** Crystals suitable for X-ray diffraction analysis were grown in a J. Young NMR tube by layering saturated THF solution of silanide **1** over a saturated THF solution of  $FeBr_2$  and  $PPh_3$ . The thin plates that form in the course of slow diffusion are insoluble in all conventional solvents, both polar and non-polar, i.e. *n*-hexane, toluene, diethyl ether, DCM, dioxane, THF and acetonitrile. No satisfactory elemental analysis could be obtained due to high reactivity of **7**.





**(TSMPSi)Fe(CO)<sub>4</sub> (8)**. Solid diiron nonacarbonyl (0.044 g, 0.12 mmol, 1.0 equiv.) and silanide **1** (contains 19.0 wt.% of THF, 0.068 g, 0.12 mmol, 1.0 equiv.) were mixed in a vial equipped with a stirring bar. THF (8.0 ml) was added and the reaction was stirred overnight. As the reaction progressed, the orange color of the mixture shifted into red. Afterwards, the solvent was removed *in vacuo*, the beige powder was washed with DCM (2.0 ml) and THF (1.0 ml). Drying *in vacuo* afforded iron tetracarbonyl silanide complex **8** with 79% yield (0.060 g).

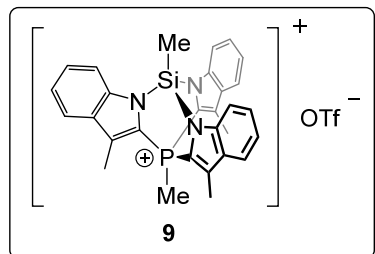
Both <sup>1</sup>H and <sup>13</sup>C NMR spectra of **8** are consistent with C<sub>3</sub> symmetry that corresponds to heterobicyclo[2.2.2]octane topology. Experimental NMR parameters show a moderate agreement with the DFT-calculated values (see *Appendix C2*). The <sup>13</sup>C resonances corresponding to the carbonyls come as two distinct singlets, which indicates slow axial-equatorial exchange at room temperature, analogously to the related phosphine complexes.<sup>83</sup> Solution IR spectrum of **8** in THF shows three strong absorptions at around 2000 cm<sup>-1</sup> consistent with trigonal bipyramidal geometry of the carbonyl complex.<sup>83,84</sup> **<sup>1</sup>H NMR** (400 MHz, Pyridine-*d*<sub>5</sub>) δ 9.37 (d, *J*<sub>H,H</sub> = 9.0 Hz, 1H, Ar-H), 7.65 – 7.52 (m, 2H+solvent peak, Ar-H), 7.29 (t, *J*<sub>H,H</sub> = 7.5 Hz, 1H, Ar-H), 4.21 (d, *J*<sub>H,P</sub> = 16.1 Hz, 1H, P<sup>+</sup>-CH<sub>3</sub>), 2.54 (d, *J*<sub>H,P</sub> = 1.9 Hz, 3H, Ar-CH<sub>3</sub>). **<sup>13</sup>C NMR** (101 MHz, Pyridine-*d*<sub>5</sub>) δ 223.2 (Fe-CO, axial), 212.8 (Fe-CO, equatorial), 145.5 (d, *J*<sub>C,P</sub> = 10.0 Hz, indole-C8), 130.7 (d, *J*<sub>C,P</sub> = 14.2 Hz, indole-C9 or C3), 126.6 (C<sup>Ar</sup>-H), 125.5 (d, *J*<sub>C,P</sub> = 15.9 Hz, indole-C3 or C9), 121.8 (C<sup>Ar</sup>-H), 120.87 (C<sup>Ar</sup>-H), 119.3 (d, *J*<sub>C,P</sub> = 111.3 Hz, indole-C2), 117.0 (C<sup>Ar</sup>-H), 9.7 (d, *J*<sub>C,P</sub> = 7.7 Hz, Ar-CH<sub>3</sub>), 1.6 (d, *J*<sub>C,P</sub> = 56.7 Hz, P<sup>+</sup>-CH<sub>3</sub>). **<sup>31</sup>P NMR** (162 MHz, Pyridine-*d*<sub>5</sub>) δ -9.5 (q, *J*<sub>P,H</sub> = 16.1 Hz, carbon satellites: *J*<sub>P,C</sub> = 111.6, 14.8, 9.9 Hz). **<sup>29</sup>Si NMR** (79 MHz, Pyridine-*d*<sub>5</sub>) δ 34.4 (d, *J* = 4.6 Hz). **IR** (THF solution)  $\tilde{\nu}$  (cm<sup>-1</sup>): 1926, 1961, 2038. **ESI-TOF-MS** in acetonitrile: found 628.0607 [*M-H*]<sup>-</sup> (calcd. 628.0546 [*M-H*]<sup>-</sup>). No satisfactory elemental analysis could be obtained due to the high reactivity of **8**.



**(TSMPGe)Fe(CO)<sub>4</sub> (14)**. Solid diiron nonacarbonyl (0.044 g, 0.12 mmol, 1.0 equiv.) and germanide **12** (0.061 g, 0.12 mmol, 1.0 equiv.) were mixed in a vial equipped with a stirring bar. Dry THF (8.0 ml) was added, and the reaction was stirred overnight. As the reaction progressed, the orange color of the mixture became deeper. Afterwards, the solvent was removed *in vacuo*, and the resulting beige powder was washed with DCM (2.0 ml) and THF (1.0 ml). Drying *in vacuo* afforded iron tetracarbonyl germanide complex **14** with 85% yield (0.069 g).

Both <sup>1</sup>H and <sup>13</sup>C NMR spectra of **14** are consistent with C<sub>3</sub> symmetry that corresponds to heterobicyclo[2.2.2]octane topology. The <sup>13</sup>C resonances corresponding to the carbonyls come as a broad signal, which indicates slow axial-equatorial exchange at room temperature, analogously to the related phosphine complexes.<sup>83</sup> Solution IR spectrum of **14** in THF shows three strong absorptions at around 2000 cm<sup>-1</sup> consistent with trigonal bipyramidal geometry of the carbonyl complex.<sup>83,84</sup> **<sup>1</sup>H NMR** (400 MHz, Pyridine-*d*<sub>5</sub>) δ 9.04 (d, *J*<sub>H,H</sub> = 8.6 Hz, 1H, Ar-H), 7.63 (d, *J*<sub>H,H</sub> = 8.0 Hz, 1H, Ar-H), 7.59 (t, *J*<sub>H,H</sub> = 7.8 Hz, 1H, Ar-H), 7.26 (t, *J*<sub>H,H</sub> = 7.4 Hz, 1H, Ar-H), 4.12 (d, *J*<sub>H,P</sub> = 16.0 Hz, 1H, P<sup>+</sup>-CH<sub>3</sub>), 2.56 (d, *J*<sub>H,P</sub> = 1.9 Hz, 3H, Ar-CH<sub>3</sub>). **<sup>13</sup>C NMR** (101 MHz, Pyridine-*d*<sub>5</sub>) δ 212.6 (br.s, Fe-(CO)<sub>4</sub>), 146.9 (d, *J*<sub>C,P</sub> = 10.5 Hz, indole-C8), 131.1 (d, *J*<sub>C,P</sub> = 14.0 Hz, indole-C9 or C3), 127.2 (C<sup>Ar</sup>-H), 122.1 (C<sup>Ar</sup>-H), 122.0 (C<sup>Ar</sup>-H), 120.0 (d, *J*<sub>C,P</sub> = 112.9 Hz, indole-C2), 116.0 (C<sup>Ar</sup>-H), 10.8 (d, *J*<sub>C,P</sub> = 6.0 Hz, Ar-CH<sub>3</sub>), 3.2 (d, *J*<sub>C,P</sub> = 57.2 Hz, P<sup>+</sup>-CH<sub>3</sub>). One signal is missing: according to <sup>31</sup>P satellites, there should be another doublet

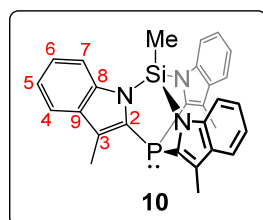
with  $J_{P,C} = 16.3$  Hz. It likely overlaps with a solvent peak.  $^{31}\text{P}$  NMR (162 MHz, Pyridine- $d_5$ )  $\delta$  -9.1 (q,  $J_{P,H} = 16.0$  Hz, carbon satellites:  $J_{P,C} = 113.1, 16.3, 14.1, 10.5$  Hz). IR (THF solution)  $\tilde{\nu}$  ( $\text{cm}^{-1}$ ): 1941, 1970, 2047. ESI-TOF-MS in THF: found 692.0002 [ $M+\text{OH}$ ] $^+$  (calcd. 692.0102 [ $M+\text{OH}$ ] $^+$ ). No satisfactory elemental analysis could be obtained due to the high reactivity of **14**.



**[TSMPSiMe] $^+$ OTf $^-$  (9)**. Silanide **1** (contains 19.0 wt.% of THF, 0.040 g, 0.070 mmol, 1.0 equiv.) was dissolved in DCM (15.0 ml), and the solvent was evaporated *in vacuo*. This operation was repeated two extra times to remove the majority of THF trapped in **1**. The resulting solid was dissolved in DCM (15.0 ml) for the fourth time, and the solution was cooled down to -78 °C. Methyl triflate (8  $\mu\text{l}$ , 0.01 g, 0.07 mmol, 1 equiv.) in DCM (0.2 ml) was added dropwise over 0.5 min with vigorous

stirring. The reaction was allowed to warm up to room temperature, and the solvent was removed *in vacuo* to give white powder (99%, 0.044 g). Without further purification, the solid was analysed by NMR, which showed >95% purity.

The  $^1\text{H}$  and  $^{13}\text{C}$  NMR spectra of **9** show a single set of signals in aromatic region indicating  $C_3$  symmetry that corresponds to heterobicyclo[2.2.2]octane topology. Experimental NMR parameters show a good agreement with the DFT-calculated values (see Appendix C2).  $^1\text{H}$  NMR (400 MHz, Methylene Chloride- $d_2$ )  $\delta$  7.62 – 7.53 (m, 2H, Ar-H), 7.46 (t,  $J_{H,H} = 7.7$  Hz, 1H, Ar-H), 7.25 (t,  $J_{H,H} = 7.5$  Hz, 1H, Ar-H), 3.82 (d,  $J_{H,P} = 15.8$  Hz, 1H,  $\text{P}^+\text{-CH}_3$ ), 2.68 (d,  $J_{H,P} = 2.0$  Hz, 3H, Ar- $\text{CH}_3$ ), 2.47 (s, 1H, Si- $\text{CH}_3$ ).  $^{13}\text{C}$  NMR (101 MHz, Methylene Chloride- $d_2$ )  $\delta$  143.2 (d,  $J = 9.0$  Hz, indole-C8), 130.0 (d,  $J = 14.0$  Hz, indole-C9 or C3), 129.6 (d,  $J = 15.0$  Hz, indole-C3 or C9), 128.1 ( $\text{C}^{\text{Ar}}\text{-H}$ ), 122.9 (d,  $J = 1.3$  Hz,  $\text{C}^{\text{Ar}}\text{-H}$ ), 121.9 (d,  $J = 1.3$  Hz,  $\text{C}^{\text{Ar}}\text{-H}$ ), 118.0 (d,  $J = 110.1$  Hz, indole-C2), 112.9 (d,  $J = 1.7$  Hz,  $\text{C}^{\text{Ar}}\text{-H}$ ), 10.5 (d,  $J = 1.0$  Hz, Ar- $\text{CH}_3$ ), 1.9 (d,  $J = 56.1$  Hz,  $\text{P}^+\text{-CH}_3$ ), -3.5 (Si- $\text{CH}_3$ ).  $^{31}\text{P}$  NMR (162 MHz, Methylene Chloride- $d_2$ )  $\delta$  -8.25 (q,  $J_{P,H} = 16.0$  Hz, carbon satellites:  $J_{P,C} = 110.1, 55.7, 14.3, 8.4$  Hz).  $^{29}\text{Si}$  NMR (79 MHz, Methylene Chloride- $d_2$ )  $\delta$  -22.5 (p,  $J_{\text{Si,H}} = J_{\text{Si,P}} = 8.1$  Hz).  $^{19}\text{F}$  NMR (376 MHz, Methylene Chloride- $d_2$ )  $\delta$  -78.8. No satisfactory elemental analysis could be obtained due to high reactivity of **9**.



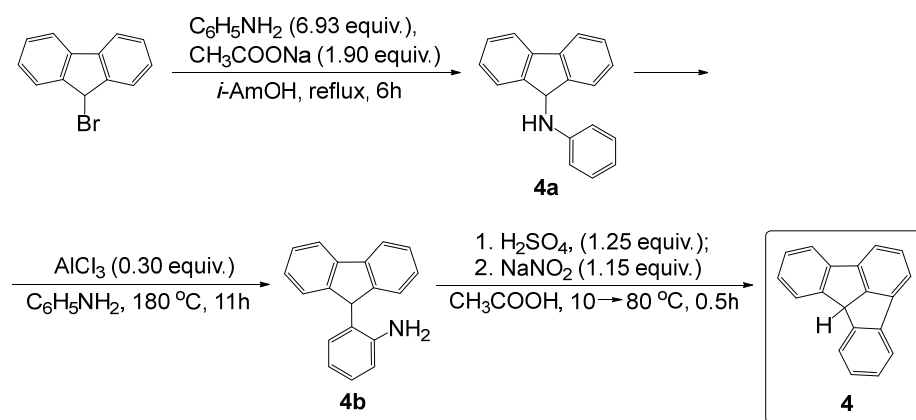
**iso-TSMPSi (10)**. Silanide **1** (contains 19.0 wt.% of THF, 0.020 g, 0.035 mmol, 1.0 equiv.) was dissolved in benzene (16.0 ml), and a suspension of  $\text{KC}_8$  (1.2 mg, 0.0088 mmol, 0.25 equiv.) in benzene (5.0 ml) was added with vigorous stirring at room temperature. After 5 min of stirring, the bronze coloration of  $\text{KC}_8$  disappeared and yellow-grey suspension was stirred for 16h. Afterwards, the reaction was filtered, and the filtrate was freed from solvent *in vacuo* to yield an amorphous yellow solid in a quantitative yield with respect to **1** (99%, 0.016 g). Crystals suitable for X-ray diffraction analysis were grown by vapor diffusion of *n*-hexane into a solution of **10** in pyridine at room temperature.

The  $^1\text{H}$  and  $^{13}\text{C}$  NMR spectra of **10** show a single set of signals in aromatic region indicating  $C_3$  symmetry that corresponds to heterobicyclo[2.2.2]octane topology. Experimental NMR parameters show a good agreement with the DFT-calculated values (see Appendix C2).  $^1\text{H}$  NMR (400 MHz, THF- $d_8$ )  $\delta$  7.56 (d,  $J_{H,H} = 8.3$  Hz, 1H,  $\text{H}^7$ ), 7.45 (d,  $J_{H,H} = 7.8$  Hz, 1H,  $\text{H}^4$ ), 7.18 (ddd,  $J_{H,H} = 8.3, 7.0, 1.3$  Hz, 1H,  $\text{H}^6$ ), 7.03 (t,  $J_{H,H} = 7.4$  Hz, 1H,  $\text{H}^5$ ), 2.51 (d,  $J_{H,P} = 1.1$  Hz, 3H, Ar- $\text{CH}_3$ ), 2.34 (s, 1H, Si- $\text{CH}_3$ ).  $^1\text{H}$  NMR (400 MHz, Benzene- $d_6$ )  $\delta$  7.43 (dd,  $J_{H,H} = 6.7, 1.2$  Hz, 1H, Ar-H), 7.23 – 7.15 (m, overlaps with a solvent peak, Ar-H), 7.14 – 7.10 (m, 1H, Ar-H), 2.46 (d,

$J_{\text{H,P}} = 1.1$  Hz, 3H, Ar-CH<sub>3</sub>), 1.22 (s, 1H, Si-CH<sub>3</sub>). <sup>13</sup>C NMR (101 MHz, THF-*d*<sub>8</sub>) δ 142.6 (indole-C8), 133.6 (d,  $J_{\text{C,P}} = 9.9$  Hz, indole-C3 or C9), 131.5 (d,  $J_{\text{C,P}} = 7.5$  Hz, indole-C9 or C3), 124.6 (indole-C6), 124.2 (d,  $J_{\text{C,P}} = 29.8$  Hz, indole-C2), 121.0 (indole-C5), 120.5 (d,  $J_{\text{C,P}} = 1.9$  Hz, indole-C4), 113.0 (indole-C7), 10.1 (d,  $J_{\text{C,P}} = 10.4$  Hz, Ar-CH<sub>3</sub>), -4.3 (Si-CH<sub>3</sub>). <sup>13</sup>C NMR (101 MHz, Benzene-*d*<sub>6</sub>) δ 142.0 (indole-C8), 133.1 (d,  $J_{\text{C,P}} = 10.2$  Hz, indole-C9 or C3), 131.3 (d,  $J_{\text{C,P}} = 7.3$  Hz, indole-C3 or C9), 124.3 (d,  $J_{\text{C,P}} = 29.9$  Hz, indole-C2), 124.2 (C<sup>Ar</sup>-H), 120.8 (C<sup>Ar</sup>-H), 120.7 (d,  $J_{\text{C,P}} = 1.9$  Hz, C<sup>Ar</sup>-H), 112.4 (C<sup>Ar</sup>-H), 10.2 (d,  $J_{\text{C,P}} = 10.0$  Hz, Ar-CH<sub>3</sub>), -4.8 (Si-CH<sub>3</sub>). <sup>31</sup>P NMR (162 MHz, THF-*d*<sub>8</sub>) δ -124.8. <sup>31</sup>P NMR (162 MHz, Benzene-*d*<sub>6</sub>) δ -124.1. <sup>29</sup>Si NMR (79 MHz, THF-*d*<sub>8</sub>) δ -25.7 (qd,  $J_{\text{Si,H}} = 8.4$  Hz;  $J_{\text{Si,P}} = 2.9$  Hz). <sup>29</sup>Si NMR (79 MHz, Benzene-*d*<sub>6</sub>) δ -26.8 (qd,  $J_{\text{Si,H}} = 8.2$  Hz;  $J_{\text{Si,P}} = 2.7$  Hz). No satisfactory elemental analysis could be obtained due to high reactivity of **10**.

#### 4.10.2.2 Fluorenes<sup>a</sup>

**Fluoradene (4)**. Compound **4** was synthesized following the synthetic route in *Scheme 4.8*. Intermediates **4a** and **4b** as well as the final product **4** were prepared using reported procedures.<sup>85–87</sup>



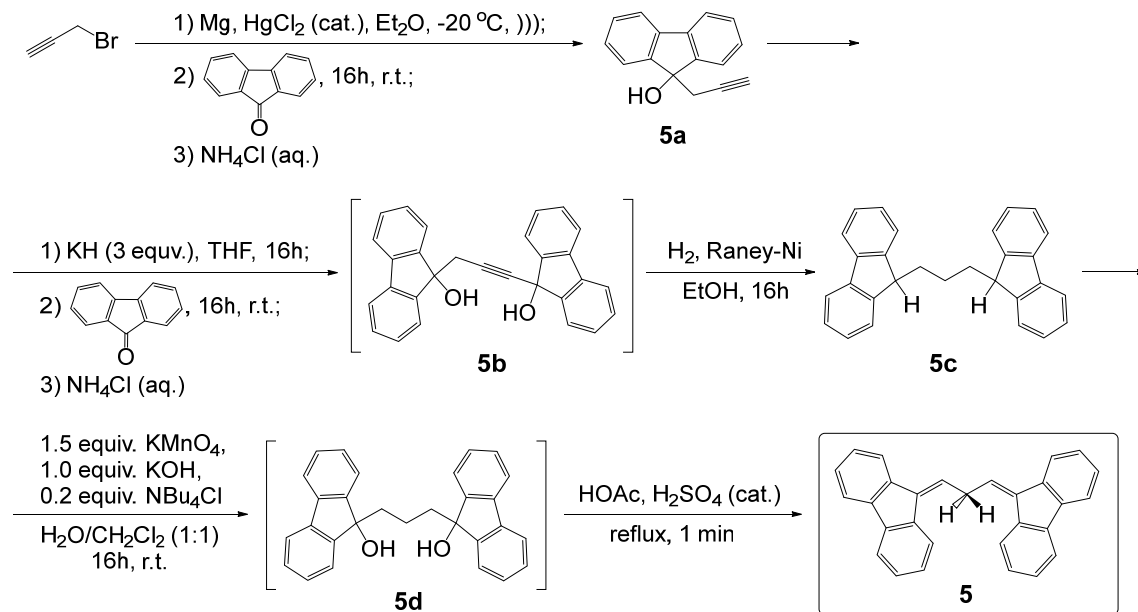
*Scheme 4.8*. Synthesis of fluoradene (**4**).

To the best of our knowledge, there are no published characterization data on **4** beyond elemental analysis and electronic spectra.<sup>87</sup> Below, we provide NMR and ESI-MS data that are fully consistent with the structure of **4**. <sup>1</sup>H NMR (400 MHz, Chloroform-*d*) δ 7.85 (dd,  $J_{\text{H,H}} = 7.4, 0.9$  Hz, 2H, Ar-H), 7.75 (d,  $J_{\text{H,H}} = 7.6$  Hz, 2H, Ar-H), 7.52 – 7.43 (m, 3H, Ar-H), 7.40 (‘t’,  $J_{\text{H,H}} = 7.5$  Hz, 2H, Ar-H), 7.31 (dd,  $J_{\text{H,H}} = 7.5, 1.3$  Hz, 2H, Ar-H), 5.21 (s, 1H, C(sp<sup>3</sup>)-H). <sup>1</sup>H NMR (400 MHz, THF-*d*<sub>8</sub>) δ 7.89 (‘d’,  $J_{\text{H,H}} = 7.5$  Hz, 1H, Ar-H), 7.74 (‘d’,  $J_{\text{H,H}} = 7.6$  Hz, 1H, Ar-H), 7.48 (‘d’,  $J_{\text{H,H}} = 7.4$  Hz, 1H, Ar-H), 7.39 (ddd,  $J_{\text{H,H}} = 8.0, 6.6, 0.9$  Hz, 1H, Ar-H), 7.34 (‘t’,  $J_{\text{H,H}} = 7.6$  Hz, 1H, Ar-H), 7.26 (ddd,  $J_{\text{H,H}} = 7.5, 1.2$  Hz, 1H, Ar-H), 5.21 (s, 1H, C(sp<sup>3</sup>)-H). <sup>1</sup>H 1D zTOCSY spectra show two aromatic spin systems in 8:3 ratio. <sup>13</sup>C NMR (101 MHz, Chloroform-*d*) δ 161.3, 147.4, 144.91, 139.9, 130.2, 127.5, 126.4, 125.5, 122.0, 119.1, 55.3 (C(sp<sup>3</sup>)-H). <sup>13</sup>C NMR (101 MHz, THF-*d*<sub>8</sub>) δ 162.4, 148.5, 145.9, 140.9, 131.0, 128.3, 127.2, 126.4, 122.70, 119.8, 56.3 (C(sp<sup>3</sup>)-H). <sup>13</sup>C and <sup>1</sup>H-<sup>13</sup>C ASAPHMQC spectra show four

<sup>a</sup> Fluorenes **15–18** are not mentioned in the main text, yet they are still discussed in *Appendix C10*. For the sake of simplicity, their synthesis and characterization are described in the current section.

quaternary carbon atoms. **ESI-TOF-MS** in THF with  $\text{NEt}_3$ : found 239.0848 [ $M-H$ ] (calcd. 239.0861 [ $M-H$ ]).

**1,3-di(9H-fluoren-9-ylidene)propane (5)**. Compound **5** was prepared following the synthetic route outlined in *Scheme 4.9*. Only intermediates **5a**, **5c** and well as the final product **5** were isolated and characterized. Intermediates **5b** and **5d** were used without purification.



*Scheme 4.9.* Synthesis of 1,3-di(9H-fluoren-9-ylidene)propane (**5**).

**9-(2-Propynyl)-9H-fluoren-9-ol (5a)**. An oven-dried Schlenk tube was charged with  $\text{HgCl}_2$  (0.014 g, 0.052 mmol,  $2.9 \cdot 10^{-4}$  equiv.), magnesium turnings (3.37 g, 139 mmol, 5.00 equiv.) and dry ether (30.0 ml) under nitrogen. The mixture was sonicated for 5 min., and a solution of propargyl bromide in toluene (80 wt.% solution, 6.0 ml, 55 mmol, 2.0 equiv.) was added in two parts. The first part (0.20 ml) was added in one portion, upon which the reaction started warming up as was indicated by gentle boiling of ether. The rest of the propargyl bromide solution was added dropwise at  $-20$  °C over an hour. After stirring at  $-20$  °C for another hour, a solution of fluorenone (5.00 g, 27.8 mmol, 1.00 equiv.) in THF (40.0 ml) was added dropwise at  $-10$  °C over an hour. The reaction was allowed to warm up to room temperature, stirred for another hour, after which it was quenched with saturated aqueous solution of  $\text{NH}_4\text{Cl}$  (~100 ml) until all magnesium dissolved. The organic layer was separated, and the aqueous layer was extracted with ether (3 x 50.0 ml). The combined organic layers were dried over anhydrous  $\text{Na}_2\text{SO}_4$ . The solvents were removed *in vacuo* to yield a light-yellow oil that, upon trituration with hexane, crystallized into an off-white powder. The yield is 85.1% (5.20 g) with respect to fluorenone, >95% purity according to NMR spectroscopy.

$^1\text{H NMR}$  (400 MHz, Chloroform-*d*)  $\delta$  7.68 (d,  $J_{\text{H,H}} = 7.3$  Hz, 2H, Ar-H), 7.62 (d,  $J_{\text{H,H}} = 7.4$  Hz, 2H, Ar-H), 7.39 (ddd,  $J_{\text{H,H}} = 7.5, 7.5, 1.2$  Hz, 2H, Ar-H), 7.32 (ddd,  $J_{\text{H,H}} = 7.4, 7.4, 1.1$  Hz, 2H, Ar-H), 2.88 (d,  $J_{\text{H,H}} = 2.6$  Hz, 2H,  $\text{CH}_2$ ), 2.53 (s, 1H, OH), 2.05 (t,  $J = 2.6$  Hz, 1H, C(sp)-H).  $^{13}\text{C NMR}$  (101 MHz, Chloroform-*d*)  $\delta$  147.6, 139.4, 129.5, 128.1, 123.8, 120.1, 80.0 (C(sp)), 79.7 (C(sp)), 71.1 (qC(sp<sup>3</sup>)), 30.6 ( $\text{CH}_2$ ). **ESI-TOF-MS** in THF with  $\text{HCOOH}$ : found 203.0801 [ $M\text{-OH}$ ]<sup>+</sup> (calcd. 203.0861 [ $M\text{-OH}$ ]<sup>+</sup>).

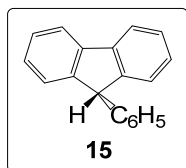
*1,3-di(9H-fluoren-9-yl)propane (5c)*. An oven-dried Schlenk tube under nitrogen was charged with 9-(2-propynyl)-9H-fluoren-9-ol (**5a**, 5.20 g, 23.6 mmol, 1.00 equiv.) in THF (50.0 ml). Slowly and under stirring, solid KH (2.84 g, 70.8 mmol, 3.00 equiv.) was added. The reaction was left to stir overnight to yield a dark-red solution. Solid fluorenone (4.25 g, 23.6 mmol, 1.00 equiv.) was added to the mixture, and stirring continued for another night. The resulting brown reaction mixture was then carefully poured into brine (~50 ml) followed by extraction with toluene (3 x 50 ml). The combined organic layers were dried over anhydrous Na<sub>2</sub>SO<sub>4</sub>, and the solvents were removed *in vacuo* to yield a yellow oil (crude **5b**). Without any further purification, the oil was added to a suspension of Raney nickel (27.7 g) in ethanol (~300 ml) and stirred under H<sub>2</sub> (1 atm.) gas overnight. In the morning, an abundant white flaky precipitate had appeared. The suspension was filtered through a celite pad; the solid residue was extracted with DCM until white flakes had completely dissolved. (*Caution: Raney nickel must be never left dry, otherwise it self-ignites in air!*) After filtration, the solid residue was immediately suspended in water, and Raney nickel was dissolved by careful addition of concentrated sulfuric acid and disposed of. The combined organic filtrate and washings were dried *in vacuo*, which yielded a colourless oil. Upon recrystallization from hexane, white needles were obtained with 71.2% yield (3.13 g) and >95% purity according to NMR spectroscopy.

**<sup>1</sup>H NMR** (400 MHz, Chloroform-*d*) δ 7.80 (d,  $J_{\text{H,H}} = 7.5$  Hz, 4H, Ar-H), 7.47 – 7.37 (m, 8H, Ar-H), 7.32 (td,  $J_{\text{H,H}} = 7.4, 7.4, 1.2$  Hz, 4H, Ar-H), 3.95 (t,  $J_{\text{H,H}} = 6.1$  Hz, 2H, C(sp<sup>3</sup>)-H), 2.09 – 1.90 (m, 4H, 1,3-CH<sub>2</sub>), 1.48 – 1.27 (m, 2H, 2-CH<sub>2</sub>). **<sup>13</sup>C NMR** (101 MHz, Chloroform-*d*) δ 147.6, 141.1, 127.0, 126.9, 124.5, 119.9, 47.3 (C(sp<sup>3</sup>)-H), 33.4 (1,3-CH<sub>2</sub>), 22.9 (2-CH<sub>2</sub>). **ESI-TOF-MS** in THF with AgNO<sub>3</sub>: found 479.0768 [*M*+Ag]<sup>+</sup> (calcd. 479.0929 [*M*+Ag]<sup>+</sup>).

*1,3-di(9H-fluoren-9-ylidene)propane (5)*. Oxidation step was adapted from Gannon and Krause,<sup>88</sup> dehydration was adapted from Kuhn *et al.*<sup>89</sup> To 1,3-di(9H-fluoren-9-yl)propane (**5c**, 0.40 g, 1.1 mmol, 1.0 equiv.) in DCM (5.0 ml) was added a solution of KMnO<sub>4</sub> (0.255 g, 1.61 mmol, 1.50 equiv.), KOH (0.060 g, 1.1 mmol, 1.0 equiv.) and tetrabutylammonium chloride (0.060 g, 0.22 mmol, 0.20 equiv.) in water (5.0 ml). The mixture was stirred for 16h, after which it was acidified with HOAc (0.5 ml), and solid NaHSO<sub>3</sub> was added until the brown coloration disappeared. The organic layer was separated, and the mixture was extracted with DCM (3 x 5.0 ml). The combined organic layers were dried over anhydrous Na<sub>2</sub>SO<sub>4</sub> followed by removal of DCM on a rotary evaporator to yield a yellow oil (crude **5d**). Without any further purification, the oil was dissolved in boiling HOAc (10.0 ml) and 1 drop of concentrated H<sub>2</sub>SO<sub>4</sub> was added. Immediately after, the reaction was cooled down to room temperature and diluted with water, resulting into grey precipitate. The latter was washed with water, dried and recrystallized from toluene/ethanol to furnish fibrous yellowish needles with 69.8% yield (0.275 g) and >95% purity according to NMR spectroscopy.

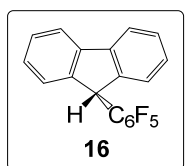
To the best of our knowledge, there are no published characterization data on **5** beyond elemental analysis and electronic spectra.<sup>89</sup> Below, we provide NMR and ESI-MS data that are fully consistent with the structure of **5**, as well as electronic spectra that are identical to the published ones. **<sup>1</sup>H NMR** (400 MHz, Chloroform-*d*) δ 7.91 (d,  $J_{\text{H,H}} = 7.6$  Hz, 2H, Ar-H), 7.80 (d,  $J_{\text{H,H}} = 7.5$  Hz, 2H, Ar-H), 7.73 (d,  $J_{\text{H,H}} = 7.5$  Hz, 2H, Ar-H), 7.69 (d,  $J_{\text{H,H}} = 7.5$  Hz, 2H, Ar-H), 7.45 – 7.26 (m, 8H, Ar-H), 6.94 (t,  $J_{\text{H,H}} = 7.3$  Hz, 2H, =CH), 4.36 (t,  $J_{\text{H,H}} = 7.3$  Hz, 2H, CH<sub>2</sub>). **<sup>1</sup>H NMR** (400 MHz, THF-*d*<sub>8</sub>) δ 8.01 (d,  $J = 7.6$  Hz, 2H, Ar-H), 7.82 (d,  $J = 7.3$  Hz, 2H, Ar-H), 7.75 (d,  $J = 7.7$  Hz, 4H, Ar-H), 7.45 – 7.20 (m, 8H, Ar-H), 7.05 (t,  $J = 7.3$  Hz, 2H, =CH), 4.42 (t,  $J = 7.3$  Hz, 2H, CH<sub>2</sub>). **<sup>1</sup>H NMR** (400 MHz, 1,4-Dioxane-*h*<sub>8</sub>) δ 8.00 (d,  $J_{\text{H,H}} = 7.5$  Hz, 2H, Ar-H), 7.83 (d,  $J_{\text{H,H}} = 7.1$  Hz, 2H, Ar-H), 7.80 – 7.72 (m, 4H, Ar-H), 7.48 – 7.20 (m, 8H, Ar-H),

7.03 (t,  $J_{\text{H,H}} = 7.3$  Hz, 2H, =CH), 4.41 (t,  $J_{\text{H,H}} = 7.3$  Hz, 2H, CH<sub>2</sub>). <sup>1</sup>H 1D zTOCSY spectra in chloroform-*d* show two aromatic and one mixed spin system in a ratio of 4:4:2. <sup>13</sup>C NMR (101 MHz, Chloroform-*d*) δ 141.3, 139.3, 139.0, 137.3, 137.2, 128.4, 128.0, 127.4, 127.2, 126.9 (=CH), 125.3, 120.2, 120.1, 119.7, 29.59 (CH<sub>2</sub>). <sup>13</sup>C NMR (101 MHz, THF-*d*<sub>8</sub>) δ 142.2, 140.3, 139.9, 138.1, 138.0, 129.0, 128.6, 128.0, 128.0, 127.8, 126.1, 120.9, 120.7, 120.3, 30.30 (CH<sub>2</sub>). <sup>13</sup>C and <sup>1</sup>H-<sup>13</sup>C ASAPHMQC spectra in chloroform-*d* shows 5 quaternary carbon signals. **UV-Vis** (diethyl ether): λ<sub>max</sub> (ε)=316 (3.6·10<sup>4</sup>), 303 (2.6·10<sup>4</sup>), 286 (2.8·10<sup>4</sup>), 257 (8.1·10<sup>4</sup>), 248 nm (6.4·10<sup>4</sup> cm<sup>-1</sup>M<sup>-1</sup>). **ESI-TOF-MS** in THF with KCl: found 407.2058 [*M*+K]<sup>+</sup> (calcd. 407.1202 [*M*+K]<sup>+</sup>).



**9-Phenyl-9H-fluorene (15).** Compound **15** was synthesized following a literature procedure.<sup>90</sup> <sup>1</sup>H and <sup>13</sup>C NMR spectra in chloroform-*d* match the reported ones. As a reference for THF ring-opening studies, below we provide the list of <sup>1</sup>H NMR signals of **15** in THF-*d*<sub>8</sub>.

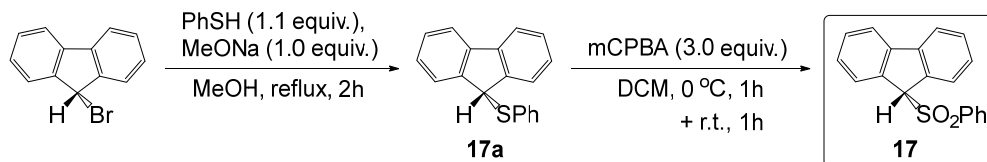
<sup>1</sup>H NMR (400 MHz, THF-*d*<sub>8</sub>) δ 7.82 (d,  $J = 7.6$  Hz, 2H, Ar-H), 7.34 (t,  $J = 7.4$  Hz, 2H, Ar-H), 7.30 – 7.14 (m, 7H, Ar-H), 7.06 (d,  $J = 7.1$  Hz, 2H, Ar-H), 5.08 (s, 1H, C(sp<sup>3</sup>)-H).



**9-Pentafluorophenyl-9H-fluorene (16).** Compound **16** was synthesized following a literature procedure.<sup>91</sup> <sup>1</sup>H and <sup>13</sup>C NMR spectra in chloroform-*d* match the reported ones. As a reference for THF ring-opening studies, below we provide the list of <sup>1</sup>H NMR signals of **16** in THF-*d*<sub>8</sub>.

<sup>1</sup>H NMR (400 MHz, THF-*d*<sub>8</sub>) δ 7.87 (d,  $J = 7.7$  Hz, 2H, Ar-H), 7.41 (t,  $J = 7.5$  Hz, 2H, Ar-H), 7.33 (d,  $J = 7.5$  Hz, 2H, Ar-H), 7.27 (t,  $J = 7.4$  Hz, 2H, Ar-H), 5.53 (s, 1H, C(sp<sup>3</sup>)-H).

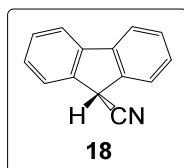
**9-Phenylsulfonyl-9H-fluorene (17).** Compound **17** was synthesized following the synthetic route shown in *Scheme 4.10*. Intermediate **17a** as well as the final product **17** were prepared following reported procedures.<sup>92,93</sup>



*Scheme 4.10.* Synthesis of 9-phenylsulfonyl-9H-fluorene (**17**).

<sup>1</sup>H and <sup>13</sup>C NMR spectra in chloroform-*d* match the reported ones.<sup>93</sup> As a reference for THF ring-opening studies, below we provide the list of <sup>1</sup>H NMR signals of **17** in THF-*d*<sub>8</sub>.

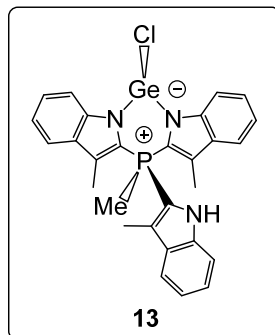
<sup>1</sup>H NMR (400 MHz, THF-*d*<sub>8</sub>) δ 8.01 – 7.91 (m, 2H, Ar-H), 7.55 – 7.47 (m, 2H, Ar-H), 7.40 – 7.32 (m, 4H, Ar-H), 7.32 – 7.25 (m, 1H, Ar-H), 7.11 – 6.99 (m, 4H, Ar-H), 5.63 (s, 1H, C(sp<sup>3</sup>)-H).



**9-Cyano-9H-fluorene (18).** Compound **18** was purchased commercially from Enamine Ltd. As a reference for THF ring-opening studies, below we provide the list of  $^1\text{H}$  NMR signals of **17** in THF- $d_8$ .

$^1\text{H}$  NMR (400 MHz, THF- $d_8$ )  $\delta$  7.86 (d,  $J = 7.5$  Hz, 2H, Ar-H), 7.72 (d,  $J = 7.5$  Hz, 2H, Ar-H), 7.47 (t,  $J = 7.4$  Hz, 2H, Ar-H), 7.40 (t,  $J = 7.4$  Hz, 2H, Ar-H), 5.23 (s, 1H, C(sp $^3$ )-H).

#### 4.10.2.3 Additional experiments



**Reaction of TSMPSi (1) and TSMPPGe (12) with HCl.** Silanide **1** or germanide **12** (0.052 mmol, 1.0 equiv.) was dissolved in THF (10.0 ml), and the solution was cooled down to  $-78$  °C. Ethereal HCl was added dropwise (0.10 N, 0.52 ml, 0.052 mmol, 1.0 equiv.). The reaction was left to warm to room temperature overnight. In the morning, the clear colourless solution was divided in two parts. The first part was placed into a vapor diffusion chamber *vs.* *n*-hexane. For silanide **1**, this yielded a light-beige amorphous powder. For germanide **12**, this yielded colourless blocky crystals identified as **13** by X-ray diffraction. The other part of the reaction mixture was freed of solvent *in vacuo* in order

to be redissolved in THF- $d_8$  for NMR analysis. However, for both **1** and **12**, removal of solvent yielded powders that are completely insoluble in all conventional solvents (benzene, DCM, THF, acetonitrile, pyridine). No satisfactory elemental analysis could be obtained due to the high reactivity of **13**.

**pK $_a$  bracketing experiments in dioxane- $d_8$ .** As discussed in the main text, in order to make sure that protonation experiments reflected a thermodynamic equilibrium, they were performed in two configurations. *Procedure A* employed zwitterion **1** as a base and **4**, **5** or **6** as an acid. *Procedure B* used the cationic silane **2**<sup>BARF</sup> (conjugate acid to **1**) as well as a conjugate base to **4**, **5** or **6**. The zwitterionic silanide **1** used for the experiments contained THF, which stood a risk of undergoing cationic polymerization in the presence of acids, thus, complicating the experiments. In order to exclude THF, **1** (contains 19.0 wt.% of THF, 0.010 g, 0.017 mmol, 1.0 equiv.) was twice dissolved in dioxane- $h_8$  (3.0 ml) followed by evaporation *in vacuo*. This amount of **1** was used for both *Procedures A and B*, and is referred to as “pre-treated zwitterionic silanide **1**” below.

*Procedure A.* All manipulations were performed in a J. Young NMR tube. Fluorene **4** or **5** (0.017 mmol, 1.0 equiv.) was dissolved in ca. 0.3 ml of dioxane- $d_8$ . Alternatively, in order to generate 2,6-lutidinium salt **6** *in situ*, to a suspension of HBARF $_4$ ·2Et $_2$ O (0.018 g, 0.017 mmol, 1.0 equiv.) in ca. 0.3 ml of dioxane- $d_8$  was added 2,6-lutidine (2.0  $\mu$ l, 0.017 mmol, 1.0 equiv.). This was followed by the addition of a solution of pre-treated zwitterionic silanide **1** (1.0 equiv.) in ca. 0.3 ml of dioxane- $d_8$ . The NMR tube was then sealed, shaken for 2 min., and NMR spectra were measured.

*Procedure B.* In order to prepare conjugated bases of fluorenes **4** and **5**, the fluorenes (0.017 mmol, 1.0 equiv.) were mixed with solid KHMDS (0.004 g, 0.02 mmol, 1 equiv.) and dissolved in dioxane- $h_8$  (2.0 ml). The solvent was then evaporated *in vacuo*, and the solid was washed with *n*-hexane (3 x 2.0 ml) followed by additional drying. Cationic silane **2**<sup>BARF</sup> was generated in a J. Young NMR tube by mixing solutions of pre-treated zwitterionic silanide **1** (1.0 equiv.) and

HBAr<sup>F</sup><sub>4</sub>·2Et<sub>2</sub>O (0.018 g, 0.017 mmol, 1.0 equiv.) in dioxane-*d*<sub>8</sub> (ca. 0.3 ml for each). A solution of a previously generated conjugate base to **4** or **5** in dioxane-*d*<sub>8</sub> (ca. 0.6 ml) was then added. Alternatively, a solution of 2,6-lutidine (2.0 μl, 0.017 mmol, 1.0 equiv.) in dioxane-*d*<sub>8</sub> (ca. 0.6 ml) was added. The NMR tube was then sealed, shaken for 2 min., and NMR spectra were measured. The spectra were identical to those obtained in *Procedure A*, provided the related starting materials were used.

**Attempted complexation of TSMPSi (1) with Fe(OTf)<sub>2</sub> and Fe(acac)<sub>2</sub>.** Solid Fe(OTf)<sub>2</sub> or Fe(acac)<sub>2</sub> (0.02 mmol, 1 equiv.) and silanide **1** (0.009 g, 0.02 mmol, 1 equiv.) were mixed in a vial equipped with a stirring bar. Dry THF (10.0 ml) was added, and the clear solution was stirred overnight. The solvent was evaporated *in vacuo* and ~5 mg of the resulting solid was dissolved in THF-*d*<sub>8</sub> to be analysed by NMR spectroscopy. Except for some degree of line-broadening, the spectra were identical to those of free **1**.

**Reactivity of TSMPSi (1) with CH-acids in THF.** Reaction of **1** with fluoradene (**4**) was conducted in both THF-*h*<sub>8</sub> and THF-*d*<sub>8</sub>, whereas the reactions with other CH-acids (**5**, **14-17**) were only undertaken in THF-*d*<sub>8</sub>. Hence, two procedures.

*Procedure A (with fluoradene (4) in THF-h<sub>8</sub>).* THF-*h*<sub>8</sub> (3.0 ml) was added to a mixture of solid silanide **1** (contains 19.0 wt.% of THF, 0.010 g, 0.017 mmol, 1.0 equiv.) and fluoradene (**4**; 0.004 g, 0.02 mmol, 1 equiv.). The mixture was stirred for the next 4h, upon which the solvent was evaporated *in vacuo*. The yellow oily residue was redissolved in THF-*d*<sub>8</sub> (ca. 0.6 ml) and transferred into a J. Young NMR tube. From that point on, if the sample is kept at room temperature, the spectra do not change within at least the next 72h.

*Procedure B (with all CH-acids in THF-d<sub>8</sub>).* THF-*d*<sub>8</sub> (ca. 0.6 ml) was added to a mixture of solid silanide **1** (contains 19.0 wt.% of THF, 0.010 g, 0.017 mmol, 1.0 equiv.) and CH-acid **4**, **5**, **14-17** (1.0 equiv.). The mixture was stirred until dissolution of all solids and transferred into a J. Young NMR tube. Within the next 72h, the reaction was periodically monitored using NMR spectroscopy. The final <sup>1</sup>H and <sup>31</sup>P NMR spectra with CH-acids **4**, **5**, **14-17** are shown in *Figure C10.1* and *Figure C10.2*.

### 4.10.3 X-ray crystal structure determinations

CCDC 2046873-2046878 contain the supplementary crystallographic data for this chapter. These data can be obtained free of charge from The Cambridge Crystallographic Data Centre via [https://www.ccdc.cam.ac.uk/data\\_request/cif](https://www.ccdc.cam.ac.uk/data_request/cif).

**TSMPSi (1).** C<sub>28</sub>H<sub>24</sub>N<sub>3</sub>PSi · 0.75C<sub>6</sub>H<sub>6</sub>, Fw = 520.14, colourless block, 0.34 × 0.25 × 0.17 mm<sup>3</sup>, triclinic, P  $\bar{1}$  (no. 2), a = 13.2558(8), b = 13.7172(7), c = 15.3872(9) Å, α = 83.192(2), β = 72.330(3), γ = 88.256(3)°, V = 2647.0(3) Å<sup>3</sup>, Z = 4, D<sub>x</sub> = 1.305 g/cm<sup>3</sup>, μ = 0.18 mm<sup>-1</sup>. The diffraction experiment was performed on a Bruker Kappa ApexII diffractometer with sealed tube and Triumph monochromator (λ = 0.71073 Å) at a temperature of 100(2) K up to a resolution of (sin θ/λ)<sub>max</sub> = 0.65 Å<sup>-1</sup>. The crystal appeared to be cracked with an angle of 2.42° between the two fragments. Consequently, two orientation matrices were used for the integration with the Eval15 software.<sup>94</sup> A multi-scan absorption correction and scaling was performed with TWINABS<sup>95,96</sup> (correction range 0.60-0.75). A total of 93259 reflections was measured, 12185 reflections were unique (R<sub>int</sub> = 0.053), 8995 reflections were observed [I > 2σ(I)].



The structure was solved with Patterson superposition methods using SHELXT.<sup>97</sup> Structure refinement was performed with SHELXL-2016<sup>98</sup> on  $F^2$  of all reflections based on an HKLF-5 file.<sup>99</sup> Non-hydrogen atoms were refined freely with anisotropic displacement parameters. Hydrogen atoms were introduced in calculated positions and refined with a riding model. 685 Parameters were refined with no restraints.  $R1/wR2$  [ $I > 2\sigma(I)$ ]: 0.0492 / 0.1151.  $R1/wR2$  [all refl.]: 0.0756 / 0.1284.  $S = 1.029$ . Batch scale factor for the two crystal fragments  $BASF = 0.5383(17)$ . Residual electron density between  $-0.36$  and  $0.66 \text{ e}/\text{\AA}^3$ . Geometry calculations and checking for higher symmetry was performed with the PLATON program.<sup>100</sup>

**Discussion:** The derived molecular structure is shown in *Figure 4.17*. The asymmetric unit of TSMPSi (**1**) has two independent molecules, however, despite the approximate molecular  $C_{3v}$  symmetry, they are located on general positions without symmetry. The molecules feature “naked” anionic centers with the sum of the surrounding  $N^{\wedge}Si^{\wedge}N$  angles close to  $270^\circ$ , i.e.  $277.43(13)/277.51(14)^\circ$ . This indicates a high  $s$ -character of the anionic lone pairs. In some of the rings, the P and Si deviate significantly from the aromatic indole plane (*Table 3*).

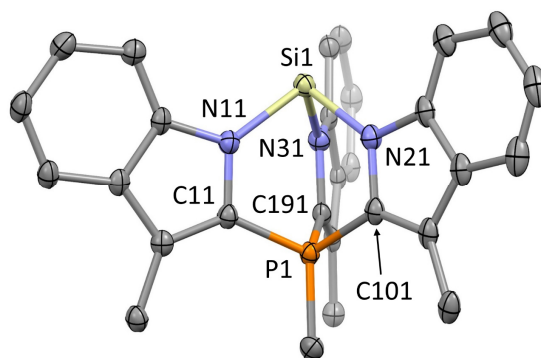


*Figure 4.17.* Molecular structure of zwitterionic TSMPSi (**1**) in the crystal. Displacement ellipsoids are drawn at the 50% probability level. Benzene solvent molecules and hydrogen atoms are omitted for clarity. Selected bond distances ( $\text{\AA}$ ) and angles ( $^\circ$ ): two molecules in the asymmetric unit, molecule 1: Si1-N11 1.8404(18), Si1-N21 1.8581(17), Si1-N31 1.8465(17),  $N11^{\wedge}Si^{\wedge}N21$  92.13(8),  $N21^{\wedge}Si^{\wedge}N31$  93.34(7),  $N31^{\wedge}Si^{\wedge}N11$  91.96(8);  $C11^{\wedge}P1^{\wedge}C101$  104.51(9),  $C11^{\wedge}P1^{\wedge}C191$  105.15(9),  $C101^{\wedge}P1^{\wedge}C191$  101.40(10). molecule 2: N12-Si2 1.8552(18), N22-Si2 1.8441(18), N32-Si2 1.8639(18),  $N12^{\wedge}Si2^{\wedge}N22$  91.87(8),  $N22^{\wedge}Si2^{\wedge}N32$  92.74(8),  $N32^{\wedge}Si2^{\wedge}N12$  92.90(8);  $C12^{\wedge}P2^{\wedge}C102$  104.10(9),  $C12^{\wedge}P2^{\wedge}C192$  104.03(10),  $C102^{\wedge}P2^{\wedge}C192$  103.33(9).

*Table 3.* Crystallographic dihedral angles between least-squares planes in **1** as calculated with the PLATON software.<sup>100</sup>

Plane 1	Plane 2	Angle, $^\circ$
N11,C11,C21,C31,C41,C51,C61,C71,C81	P1,Si1,N11,C11	10.84(8)
N21,C101,C111,C121,C131,C141,C151,C161,C171	P1,Si1,N21,C101	15.40(8)
N31,C191,C201,C211,C221,C231,C241,C251,C261	P1,Si1,N31,C191	5.24(7)
N12,C12,C22,C32,C42,C52,C62,C72,C82	P2,Si2,N12,C12	2.35(7)
N22,C102,C112,C122,C132,C142,C152,C162,C172	P2,Si2,N22,C102	0.59(7)
N32,C192,C202,C212,C222,C232,C242,C252,C262	P2,Si2,N32,C192	3.56(7)

**[TSMPSiH]<sup>+</sup>BARF<sub>4</sub><sup>-</sup> (**2**<sup>BARF</sup>).** [C<sub>28</sub>H<sub>25</sub>N<sub>3</sub>PSi](C<sub>32</sub>H<sub>12</sub>BF<sub>24</sub>) · 2C<sub>4</sub>H<sub>8</sub>O<sub>2</sub> + disordered solvent, Fw = 1502.00<sup>[a]</sup>, colourless block, 0.67 × 0.45 × 0.22 mm<sup>3</sup>, triclinic, P  $\bar{1}$  (no. 2), a = 13.38545(16), b = 15.8323(2), c = 18.8391(2) Å, α = 76.347(1), β = 72.440(1), γ = 70.700(1)°, V = 3551.01(8) Å<sup>3</sup>, Z = 2, D<sub>x</sub> = 1.405 g/cm<sup>3</sup>[a], μ = 0.17 mm<sup>-1</sup>[a]. The diffraction experiment was performed on a Bruker Kappa ApexII diffractometer with sealed tube and Triumph monochromator (λ = 0.71073 Å) at a temperature of 150(2) K up to a resolution of (sin θ/λ)<sub>max</sub> = 0.72 Å<sup>-1</sup>. The crystal appeared to be cracked into two fragments. Consequently, two orientation matrices were used for the integration with the Eval15 software.<sup>94</sup> A multi-scan absorption correction and scaling was performed with TWINABS<sup>95,96</sup> (correction range 0.67-0.75). A total of 187169 reflections was measured, 21735 reflections were unique (R<sub>int</sub> = 0.040), 17594 reflections were observed [I > 2σ(I)]. The structure was solved with Patterson superposition methods using SHELXT.<sup>97</sup> Structure refinement was performed with SHELXL-2018<sup>98</sup> on F<sup>2</sup> of all reflections based on an HKLF-5 file.<sup>99</sup> The crystal structure contains large voids (265 Å<sup>3</sup>/unit cell) filled with severely disordered CH<sub>2</sub>Cl<sub>2</sub> solvent molecules. Their contribution to the structure factors was secured by the SQUEEZE algorithm<sup>101</sup> resulting in 84 electrons / unit cell. Non-hydrogen atoms were refined freely with anisotropic displacement parameters. The Si–H hydrogen atom was located in difference Fourier maps and refined freely with an isotropic displacement parameter. C–H hydrogen atoms were introduced in calculated positions and refined with a riding model. Six of the eight CF<sub>3</sub> groups were refined with a disorder model. Slight disorder in the co-crystallized dioxane molecules was not resolved. Minor presence of *n*-hexane on the dioxane locations cannot be ruled out. 1096 Parameters were refined with 3483 restraints (distances, angles and displacement parameters in the CF<sub>3</sub> groups). R1/wR2 [I > 2σ(I)]: 0.0542 / 0.1531. R1/wR2 [all refl.]: 0.0660 / 0.1620. S = 1.050. Fraction of the second crystal fragment BASF = 0.0780(15). Residual electron density between -0.69 and 2.34 e/Å<sup>3</sup> (positive peak in proximity of dioxane). Geometry calculations and checking for higher symmetry was performed with the PLATON program.<sup>100</sup>

**Discussion:** The derived molecular structure is shown in *Figure 4.18*. The cation of [TSMPSiH]<sup>+</sup>BARF<sub>4</sub><sup>-</sup> (**2**<sup>BARF</sup>) is located on a general position without symmetry. However, there is an approximate, non-crystallographic C<sub>3</sub> symmetry in the cation with an r.m.s. deviation of 0.1231 Å. The silicon-bound hydrogen can be located from the difference Fourier maps. In some of the rings, the P and Si deviate significantly from the aromatic indole plane (*Table 4.4*).

*Table 4.4.* Crystallographic dihedral angles between least-squares planes in **2**<sup>BARF</sup> as calculated with the PLATON software.<sup>100</sup>

Plane 1	Plane 2	Angle, °
N11,C11,C21,C31,C41,C51,C61,C71,C81	P11,Si11,N11,C11	3.35(6)
N21,C101,C111,C121,C131,C141,C151,C161,C171	P11,Si11,N21,C101	3.00(6)
N31,C191,C201,C211,C221,C231,C241,C251,C261	P11,Si11,N31,C191	5.14(7)

Upon protonation of TSMPSi (**1**) into [TSMPSiH]<sup>+</sup> (**2**), the structural changes are mostly confined to the SiN<sub>3</sub> fragment. No other bond in the molecule changes by >0.02 Å, and no flat angle deforms by >2.9°, which is illustrated in *Figure 4.19* and *Table 4.5*.

<sup>a</sup> Derived values do not contain the contribution of the disordered solvent.

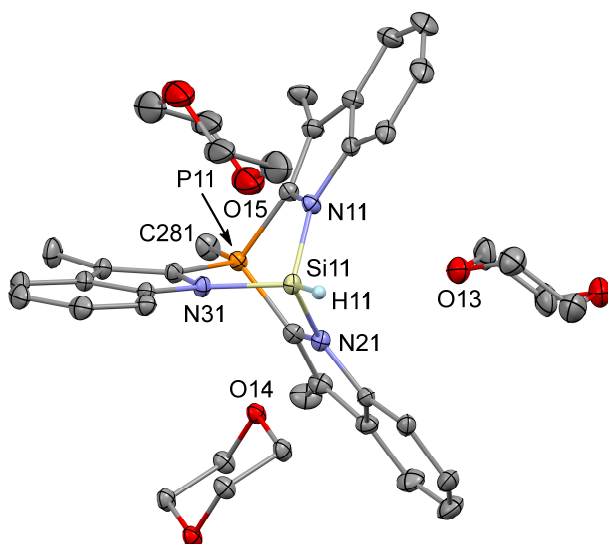


Figure 4.18. Molecular structure of cationic silane **2** in the crystal of [TSMPSiH]<sup>+</sup>BARF<sub>4</sub><sup>-</sup> (**2**<sup>BARF</sup>). Displacement ellipsoids are drawn at the 30% probability level. The BARF<sub>4</sub><sup>-</sup> counterion, severely disordered CH<sub>2</sub>Cl<sub>2</sub>, and hydrogen atoms, except for Si–H, are omitted for clarity. The dioxane molecules involving O14 and O15, respectively, are located on inversion centers. Selected bond distances (Å) and angles (°): Si11–H11 1.319(19), Si11–N11 1.7621(13), Si11–N21 1.7565(12), Si11–N31 1.7525(12), Si11–O13 3.2260(16), Si11–O14 2.7807(13), Si11–O15 3.067(3), H11–O13 2.90(2), H11–O14 2.62(2), H11–O15 2.73(2), N11<sup>^</sup>Si11<sup>^</sup>N21 99.42(6), N11<sup>^</sup>Si11<sup>^</sup>N31 100.33(6), N21<sup>^</sup>Si11<sup>^</sup>N31 101.66(6), N11<sup>^</sup>Si11<sup>^</sup>H11 115.1(8), N21<sup>^</sup>Si11<sup>^</sup>H11 117.1(8), N31<sup>^</sup>Si11<sup>^</sup>H11 119.9(8), C11<sup>^</sup>P11<sup>^</sup>C101 102.58(7), C101<sup>^</sup>P11<sup>^</sup>C191 104.28(7), C11<sup>^</sup>P11<sup>^</sup>C191 102.66(7), Si11<sup>^</sup>H11<sup>^</sup>O13 92.0(10), Si11<sup>^</sup>H11<sup>^</sup>O14 82.7(10), Si11<sup>^</sup>H11<sup>^</sup>O15 91.8(10).

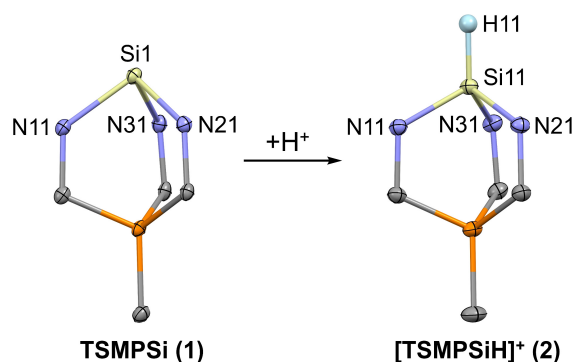


Figure 4.19. Structural changes within the bicyclic cage upon protonation according to the X-ray crystal structure. Only one independent molecular fragment of TSMPSi (**1**) is shown.

Table 4.5. Structural changes within the bicyclic fragment upon protonation according to the X-ray crystal structure. Since a crystal of TSMPSi (1) has two independent molecules in the unit cell, both sets of geometric parameters are given separated by a slash.

Geometric parameter	Value, Å or °	
	TSMPSi (1)	[TSMPSiH] <sup>+</sup> BAR <sub>4</sub> <sup>F<sub>4</sub>-</sup> (2 <sup>BARF</sup> )
Si–N	1.8404(18)-1.8639(18)	1.7525(12)-1.7621(13)
N–C <sup>Ar</sup>	1.400(3)-1.408(2)	1.4174(18)-1.4195(18)
C <sup>Ar</sup> –P	1.768(2)-1.7782(19)	1.7751(15)-1.7753(15)
P <sup>+</sup> –CH <sub>3</sub>	1.780(2)/1.782(2)	1.7756(16)
N <sup>+</sup> Si <sup>+</sup> N	91.87(8)-93.34(7)	99.42(6)-101.66(6)
Σ <sub>N<sup>+</sup>Si<sup>+</sup>N</sub>	277.43(13)/277.51(14)	301.41(10)
Si <sup>+</sup> N <sup>+</sup> C	125.05(13)-126.36(14)	119.11(10)-119.32(9)
N <sup>+</sup> C <sup>+</sup> P	111.00(14)-112.14(14)	113.15(10)-113.40(10)
C <sup>Ar</sup> –P <sup>+</sup> C <sup>Ar</sup>	101.40(10)-105.15(9)	102.58(7)-104.28(7)

**TSMPSi (1).** C<sub>28</sub>H<sub>24</sub>GeN<sub>3</sub>P + disordered solvent, Fw = 506.06<sup>[a]</sup>, colourless block, 0.35 × 0.31 × 0.13 mm<sup>3</sup>, monoclinic, P2<sub>1</sub>/c (no. 14), a = 14.9354(10), b = 8.8055(5), c = 22.7168(15) Å, β = 108.505(4)°, V = 2833.1(3) Å<sup>3</sup>, Z = 4, D<sub>x</sub> = 1.186 g/cm<sup>3</sup>[a], μ = 1.16 mm<sup>-1</sup>[a]. The diffraction experiment was performed on a Bruker Kappa ApexII diffractometer with sealed tube and Triumph monochromator (λ = 0.71073 Å) at a temperature of 150(2) K up to a resolution of (sin θ/λ)<sub>max</sub> = 0.65 Å<sup>-1</sup>. The Eval15 software<sup>94</sup> was used for the intensity integration. For the prediction of the reflection profiles a large isotropic mosaicity of 1.8° was used. Additional weak crystal fragments and diffuse scattering were ignored during the integration. A multi-scan absorption correction and scaling was performed with SADABS<sup>95,96</sup> (correction range 0.58-0.75). A total of 58172 reflections was measured, 6527 reflections were unique (R<sub>int</sub> = 0.045), 5379 reflections were observed [I > 2σ(I)]. The structure was solved with Patterson superposition methods using SHELXT.<sup>97</sup> Structure refinement was performed with SHELXL-2016<sup>98</sup> on F<sup>2</sup> of all reflections. The crystal structure contains large voids (654 Å<sup>3</sup>/unit cell) filled with severely disordered *n*-hexane solvent molecules. Their contribution to the structure factors was secured by the SQUEEZE algorithm<sup>101</sup> resulting in 200 electrons / unit cell. Non-hydrogen atoms were refined freely with anisotropic displacement parameters. Hydrogen atoms were introduced in calculated positions and refined with a riding model. 302 Parameters were refined with no restraints. R1/wR2 [I > 2σ(I)]: 0.0540 / 0.1336. R1/wR2 [all refl.]: 0.0663 / 0.1389. S = 1.190. Residual electron density between -0.41 and 2.90 e/Å<sup>3</sup>. Geometry calculations and checking for higher symmetry was performed with the PLATON program.<sup>100</sup>

**Discussion:** The derived molecular structure is shown in Figure 4.20. Despite the approximate molecular C<sub>3v</sub> symmetry, the molecule is located on a general position without symmetry in the crystal packing. The system features a “naked” anionic center with the sum of the surrounding N<sup>+</sup>Ge<sup>+</sup>N angles close to 270°, i.e. 270.04(19)°. This indicates a high *s*-character of the anionic lone pair. In some of the rings, the P and Si deviate significantly from the aromatic indole plane (Table 4.6).

<sup>a</sup> Derived values do not contain the contribution of the disordered solvent.

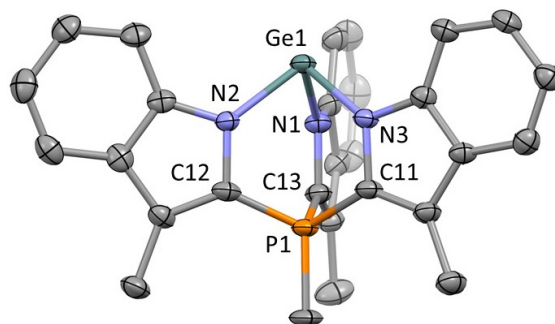


Figure 4.20. Molecular structure of **12** in the crystal. Displacement ellipsoids are drawn at the 50% probability level. Solvent molecules and hydrogen atoms are omitted for clarity. Selected bond distances (Å) and angles (°): Ge1-N1 1.967(3), Ge1-N2 1.976(3), Ge1-N3 1.972(3), N1^Ge1^N2 89.73(11), N2^Ge1^N3 90.25(11), N3^Ge1^N1 90.06(11); C11^P1^C12 106.65(15), C12^P1^C13 103.52(15), C11^P1^C13 103.69(15).

Table 4.6. Crystallographic dihedral angles between least-squares planes in **12** as calculated with the PLATON software.<sup>100</sup>

Plane 1	Plane 2	Angle, °
N1,C11,C21,C31,C41,C51,C61,C71,C81	P1,Ge1,N1,C11	12.51(11)
N2,C12,C22,C32,C42,C52,C62,C72,C82	P1,Ge1,N2,C12	11.29(11)
N3,C13,C23,C33,C43,C53,C63,C73,C83	P1,Ge1,N3,C13	0.71(12)

**(TSMPSi)FeBr<sub>2</sub>(THF) (7)**. C<sub>32</sub>H<sub>32</sub>Br<sub>2</sub>FeN<sub>3</sub>OPSi · 3C<sub>4</sub>H<sub>8</sub>O, Fw = 965.64, yellow block, 0.46 × 0.20 × 0.10 mm<sup>3</sup>, monoclinic, P2<sub>1</sub>/c (no. 14), a = 16.5476(8), b = 12.1769(5), c = 21.8288(9) Å, β = 94.147(2)°, V = 4387.0(3) Å<sup>3</sup>, Z = 4, D<sub>x</sub> = 1.462 g/cm<sup>3</sup>, μ = 2.27 mm<sup>-1</sup>. The diffraction experiment was performed on a Bruker Kappa ApexII diffractometer with sealed tube and Triumph monochromator (λ = 0.71073 Å) at a temperature of 150(2) K up to a resolution of (sin θ/λ)<sub>max</sub> = 0.65 Å<sup>-1</sup>. The Eval15 software<sup>94</sup> was used for the intensity integration. A numerical absorption correction and scaling was performed with SADABS<sup>95,96</sup> (correction range 0.48-0.84). A total of 60843 reflections was measured, 10071 reflections were unique (R<sub>int</sub> = 0.046), 7928 reflections were observed [I > 2σ(I)]. The structure was solved with Patterson superposition methods using SHELXT.<sup>97</sup> Structure refinement was performed with SHELXL-2016<sup>98</sup> on F<sup>2</sup> of all reflections. Non-hydrogen atoms were refined freely with anisotropic displacement parameters. Hydrogen atoms were introduced in calculated positions and refined with a riding model. One non-coordinated THF solvent molecule was refined with a disorder model. 519 Parameters were refined with 245 restraints (distances, angles and displacement parameters in the non-coordinated THF molecules). R1/wR2 [I > 2σ(I)]: 0.0372 / 0.0886. R1/wR2 [all refl.]: 0.0548 / 0.0973. S = 1.015. Residual electron density between -0.60 and 1.00 e/Å<sup>3</sup>. Geometry calculations and checking for higher symmetry was performed with the PLATON program.<sup>100</sup>

**Discussion:** The derived molecular structure is shown in Figure 4.21. The Fe(II) center has a tetrahedral configuration typical for an S = 2 spin state. Fe–Br bond lengths of 2.3857(5) and 2.3976(5) Å are also rather typical for a high-spin iron(II) center.<sup>102–109</sup> The Fe–Si bond distance of 2.4711(7) Å is somewhat longer than that in an analogous complex of FeCl<sub>2</sub>(THF) and C-tethered analogue of **1**, 2.4482(12)/2.4589(12).<sup>35</sup> This indicates a slightly weaker bonding in the case of **7**. As expected, the geometry around silicon is sensitive to coordination. Thus, the sum of crystallographic N^Si^N angles changes from 277.43(13)/277.51(14)° in free TSMPSi (**1**) to

289.42(17)° in complex (TSMPSi)FeBr<sub>2</sub>(THF) (**7**). This change is consistent with Bent's rule.<sup>39</sup> In some of the rings, the P and Si deviate significantly from the aromatic indole plane (*Table 4.7*).

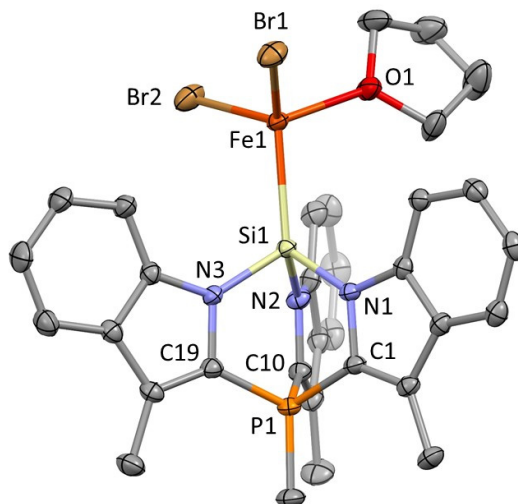


*Figure 4.21.* Molecular structure of (TSMPSi)FeBr<sub>2</sub>(THF) (**7**) in the crystal. Displacement ellipsoids are drawn at the 50% probability level. Hydrogens and non-coordinated THF molecules are omitted for clarity. Selected bond (Å) and angles (°): Si1-N1 1.798(2), Si1-N2 1.812(2), Si1-N3 1.806(2), Fe1-Si1 2.4711(7), Fe1-Br1 2.3976(5), Fe1-Br2 2.3857(5), Fe1-O1 2.0727(19), N1<sup>^</sup>Si1<sup>^</sup>N2 96.55(10), N2<sup>^</sup>Si1<sup>^</sup>N3 96.37(10), N3<sup>^</sup>Si1<sup>^</sup>N1 96.50(10), C1<sup>^</sup>P1<sup>^</sup>C10 102.62(12), C1<sup>^</sup>P1<sup>^</sup>C19 104.07(11), C10<sup>^</sup>P1<sup>^</sup>C19 103.70(12).

*Table 4.7.* Crystallographic dihedral angles between least-squares planes in **7** as calculated with the PLATON software.<sup>100</sup>

Plane 1	Plane 2	Angle, °
N1,C1,C2,C3,C4,C5,C6,C7,C8	P1,Si1,N1,C1	2.93(9)
N2,C10,C11,C12,C13,C14,C15,C16,C17	P1,Si1,N2,C10	2.10(9)
N3,C19,C20,C21,C22,C23,C24,C25,C26	P1,Si1,N3,C19	2.67(9)

**iso-TSMPSi (10).** C<sub>28</sub>H<sub>24</sub>N<sub>3</sub>PSi · C<sub>6</sub>H<sub>6</sub>, Fw = 547.73, colourless block, 0.45 × 0.25 × 0.06 mm<sup>3</sup>, triclinic, P  $\bar{1}$  (no. 2), a = 8.8398(4), b = 12.4251(6), c = 14.7566(7) Å, α = 71.073(3), β = 89.907(2), γ = 71.483(2)°, V = 1444.48(12) Å<sup>3</sup>, Z = 2, D<sub>x</sub> = 1.259 g/cm<sup>3</sup>, μ = 0.17 mm<sup>-1</sup>. The diffraction experiment was performed on a Bruker Kappa ApexII diffractometer with sealed tube and Triumph monochromator (λ = 0.71073 Å) at a temperature of 150(2) K up to a resolution of (sin θ/λ)<sub>max</sub> = 0.65 Å<sup>-1</sup>. The Eval15 software<sup>94</sup> was used for the intensity integration. A multi-scan absorption correction and scaling was performed with SADABS<sup>95,96</sup> (correction range 0.69-0.75). A total of 33226 reflections was measured, 6648 reflections were unique (R<sub>int</sub> = 0.026), 5760 reflections were observed [I > 2σ(I)]. The structure was solved with Patterson superposition methods using SHELXT.<sup>97</sup> Structure refinement was performed with SHELXL-2018<sup>98</sup> on F<sup>2</sup> of all reflections. Non-hydrogen atoms were refined freely with anisotropic displacement parameters. Hydrogen atoms of the Si compound were located in difference Fourier maps. Hydrogen atoms of the hexane were introduced in calculated positions. All hydrogen atoms were refined with a riding model. The *n*-hexane solvent molecule was refined with a disorder model. The solvent disorder could not be fully resolved. 411 Parameters were refined with 144 restraints (distances, angles and displacement parameters in the hexane

molecule). R1/wR2 [ $I > 2\sigma(I)$ ]: 0.0389 / 0.1073. R1/wR2 [all refl.]: 0.0451 / 0.1114. S = 1.062. Residual electron density between -0.37 and 0.44 e/Å<sup>3</sup>. Geometry calculations and checking for higher symmetry was performed with the PLATON program.<sup>100</sup>

**Discussion:** The derived molecular structure is shown in *Figure 4.22*. It features a tetrahedral methylated silicon atom and a tricoordinate phosphorus atom. Due to the absence of the methyl group, the phosphorus atom in iso-TSMPSi (**10**) is more pyramidalized as compared to that in the parent zwitterion TSMPSi (**1**) ( $\Sigma_{C^{\wedge}P^{\wedge}C}$  of 290.67(12)° vs. 311.06(16)/311.46(16)°, respectively). The opposite applies to the silicon atom, which now features wider N<sup>^</sup>Si<sup>^</sup>N angles ( $\Sigma_{N^{\wedge}Si^{\wedge}N}$  of 306.97(10)° vs. 277.43(13)/277.51(14)° in **1**). All these changes comply with Bent's rule.<sup>39</sup> In some of the rings, the P and Si deviate significantly from the aromatic indole plane (*Table 4.8*).

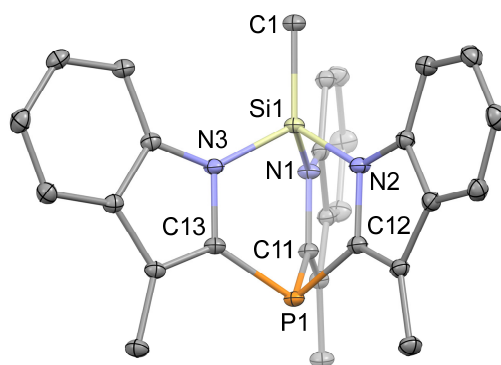


*Figure 4.22.* Molecular structure of iso-TSMPSi (**10**) in the crystal. Displacement ellipsoids are drawn at the 30% probability level. Hydrogens and *n*-hexane solvent molecules are omitted for clarity. Selected bond lengths (Å) and angles (°): Si1-N1 1.7473(13), Si1-N2 1.7379(13), Si1-N3 1.7416(13), C1-Si1 1.8284(14), N1<sup>^</sup>Si1<sup>^</sup>N2 101.67(6), N2<sup>^</sup>Si1<sup>^</sup>N3 101.87(6), N3<sup>^</sup>Si1<sup>^</sup>N1 103.43(6), C11<sup>^</sup>P1<sup>^</sup>C12 97.91(6), C12<sup>^</sup>P1<sup>^</sup>C13 98.57(7), C11<sup>^</sup>P1<sup>^</sup>C13 94.19(7).

*Table 4.8.* Crystallographic dihedral angles between least-squares planes in **10** as calculated with the PLATON software.<sup>100</sup>

Plane 1	Plane 2	Angle, °
N1,C11,C21,C31,C41,C51,C61,C71,C81	P1,Si1,N1,C11	9.28(5)
N2,C12,C22,C32,C42,C52,C62,C72,C82	P1,Si1,N2,C12	0.97(5)
N3,C13,C23,C33,C43,C53,C63,C73,C83	P1,Si1,N3,C13	11.44(6)

**(TSM-P-H)GeCl (13).**<sup>a</sup> C<sub>28</sub>H<sub>25</sub>ClGeN<sub>3</sub>P · C<sub>4</sub>H<sub>8</sub>O, Fw = 614.62, colourless block, 0.39 × 0.23 × 0.07 mm<sup>3</sup>, monoclinic, P2<sub>1</sub>/n (no. 14), a = 9.4061(3), b = 26.6171(13), c = 12.4032(6) Å, β = 111.723(3)°, V = 2884.8(2) Å<sup>3</sup>, Z = 4, D<sub>x</sub> = 1.415 g/cm<sup>3</sup>, μ = 1.24 mm<sup>-1</sup>. The diffraction experiment was performed on a Bruker Kappa ApexII diffractometer with sealed tube and Triumph monochromator (λ = 0.71073 Å) at a temperature of 150(2) K up to a resolution of (sin θ/λ)<sub>max</sub> = 0.65 Å<sup>-1</sup>. The Eval15 software<sup>94</sup> was used for the intensity integration. A multi-scan absorption correction and scaling was performed with SADABS<sup>95,96</sup> (correction range 0.65-0.75). A total of 66423 reflections was measured, 6640 reflections were unique (R<sub>int</sub> = 0.025), 6078 reflections were observed [ $I > 2\sigma(I)$ ]. The structure was solved with Patterson superposition

<sup>a</sup> Compound **13** is not mentioned in the main text, yet it is still discussed in *Appendix C1*. For the sake of simplicity, its X-ray crystal structure determination is described in the current section.

methods using SHELXT.<sup>97</sup> Structure refinement was performed with SHELXL-2016<sup>98</sup> on  $F^2$  of all reflections. Non-hydrogen atoms were refined freely with anisotropic displacement parameters. All hydrogen atoms were located in difference Fourier maps. The N–H hydrogen atoms was refined freely with an isotropic displacement parameter. The C–H hydrogen atoms were refined with a riding model. 360 Parameters were refined with no restraints.  $R1/wR2$  [ $I > 2\sigma(I)$ ]: 0.0294 / 0.0769.  $R1/wR2$  [all refl.]: 0.0331 / 0.0786.  $S = 1.071$ . Residual electron density between  $-0.33$  and  $0.56 \text{ e}/\text{\AA}^3$ . Geometry calculations and checking for higher symmetry was performed with the PLATON program.<sup>100</sup>

**Discussion:** The derived molecular structure is shown in *Figure 4.23*. The proton at N1 (H1N) is clearly visible in the difference Fourier map. It can be refined freely in the least-squares refinement of the structure. Additionally, the short N1...O14 distance indicates the presence of a hydrogen bond.

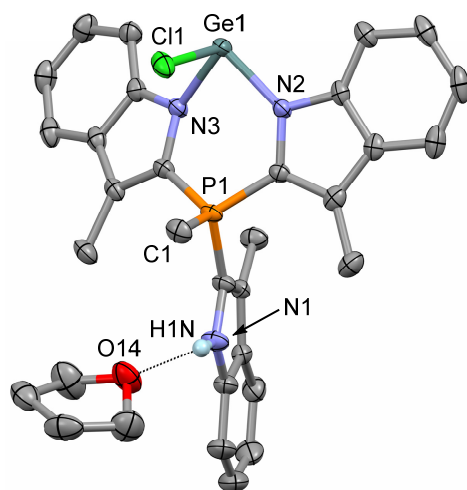


*Figure 4.23.* Molecular structure of (TSMP–H)GeCl (**13**) in the crystal. Displacement ellipsoids are drawn at the 50% probability level. Hydrogens, except for H1N, are omitted for clarity. A THF molecule that forms a hydrogen bond with H1N is shown explicitly. Selected bond distances (Å) and angles (°): Ge1–Cl1 2.3549(5), Ge1–N2 1.9524(15), Ge1–N3 1.9569(14), N1–H1N 0.88(3), H1N...O14 2.14(3), N1...O14 2.913(2), Cl1^Ge1^N2 94.01(4), N2^Ge1^N3 90.96(6), N3^Ge1^Cl1 92.36(4), N1^H1N^O14 146(3).

#### 4.10.4 Computational studies

All calculations were performed using Gaussian 16, Revision A.03.<sup>66</sup> Routine geometry optimizations were carried out in vacuum at the B3LYP-GD3BJ/6-311++G\*\* level of theory. The absence of imaginary frequencies was confirmed for all structures. In case of several possible conformers, the one with the lowest energy was chosen for further calculations. NMR parameters were calculated using GIAO method from stationary geometries at B3LYP-GD3BJ level of theory with IGLO-III basis set for C, H, P, Si, O atoms and 6-311++G\*\* basis set for Fe atoms. Implicit solvation was treated within the Polarizable Continuum Model (PCM).

Gas-phase acidities were derived using both B3LYP-GD3BJ and MP2 with 6-311++G(d,p) basis set. For MP2 calculations, thermal corrections for Gibbs free energy were taken from B3LYP-GD3BJ/6-311++G(d,p) level of theory. It has been shown<sup>52,110</sup> that MP2-derived gas-phase acidities tend to give a better agreement with the experiment than the B3LYP-derived



ones for a wide range of acids; nevertheless, both methods give identical trends. This was also true in our calculations. However, due to the higher precision, we chose MP2-calculated values for a further discussion.

Even though deprotonation decomposition schemes are closely related to the gas-phase acidities, given that B3LYP-GD3BJ and MP2 show identical trends, deprotonation decomposition was treated at B3LYP-GD3BJ/6-311++G\*\* level of theory in order to save computational time.

Carbonyl stretching frequencies in IrCp(CO)L model complexes were calculated as described by Gusev.<sup>111</sup> Namely, geometry optimizations and frequency calculations were performed using MPW1PW91 functional with SDD basis set (associated with ECP) for Ir and 6-311+G(d,p) for all other atoms. Tight geometry optimizations and ultrafine integration grid were employed. The absence of imaginary frequencies was confirmed for all structures.

Relaxed potential energy surface (PES) scans were carried out in vacuum at B3LYP-GD3BJ/6-31+G\* level of theory. Related stationary points were optimized at the same level of theory. The absence of imaginary frequencies was confirmed for all structures, except for transition states: those had one negative vibrational mode, implying a negative force constant.

NBO analysis was done using NBO 6.0 program.<sup>112</sup> NLMOs were visualized using VMD 1.9.3.<sup>113-115</sup>

For the sake of brevity, the geometric coordinates along with corresponding energies are not given in this chapter. These can be found in the respective publication.<sup>34</sup>

## 4.11 References

- (1) Stephan, D. W.; Erker, G. Frustrated Lewis Pairs: Metal-Free Hydrogen Activation and More. *Angew. Chemie Int. Ed.* **2010**, *49* (1), pp 46–76. DOI: 10.1002/anie.200903708.
- (2) Power, P. P. Main-Group Elements as Transition Metals. *Nature* **2010**, *463*, pp 171–177. DOI: 10.1038/nature08634.
- (3) Bayne, J. M.; Stephan, D. W. Phosphorus Lewis Acids: Emerging Reactivity and Applications in Catalysis. *Chem. Soc. Rev.* **2016**, *45* (4), pp 765–774. DOI: 10.1039/C5CS00516G.
- (4) Denmark, S. E.; Sweis, R. F. Design and Implementation of New, Silicon-Based, Cross-Coupling Reactions: Importance of Silicon–Oxygen Bonds. *Acc. Chem. Res.* **2002**, *35* (10), pp 835–846. DOI: 10.1021/ar020001r.
- (5) Frey, G. D.; Lavallo, V.; Donnadiou, B.; Schoeller, W. W.; Bertrand, G. Facile Splitting of Hydrogen and Ammonia by Nucleophilic Activation at a Single Carbon Center. *Science* **2007**, *316* (5823), pp 439–441. DOI: 10.1126/science.1141474.
- (6) Spikes, G. H.; Fettingner, J. C.; Power, P. P. Facile Activation of Dihydrogen by an Unsaturated Heavier Main Group Compound. *J. Am. Chem. Soc.* **2005**, *127* (35), pp 12232–12233. DOI: 10.1021/ja053247a.
- (7) Braunschweig, H.; Dellermann, T.; Dewhurst, R. D.; Ewing, W. C.; Hammond, K.; Jimenez-Halla, J. O. C.; Kramer, T.; Krummenacher, I.; Mies, J.; Phukan, A. K.; Vargas, A. Metal-Free Binding and Coupling of Carbon Monoxide at a Boron–Boron Triple Bond. *Nat. Chem.* **2013**, *5*, pp 1025–1028. DOI: 10.1038/nchem.1778.
- (8) Khan, S.; Sen, S. S.; Roesky, H. W. Activation of Phosphorus by Group 14 Elements in Low Oxidation States. *Chem. Commun.* **2012**, *48* (16), pp 2169–2179. DOI: 10.1039/c2cc17449a.
- (9) Martin, D.; Soleilhavoup, M.; Bertrand, G. Stable Singlet Carbenes as Mimics for Transition Metal Centers. *Chem. Sci.* **2011**, *2* (3), pp 389–399. DOI: 10.1039/C0SC00388C.
- (10) Legare, M.-A.; Courtemanche, M.-A.; Rochette, E.; Fontaine, F.-G. Metal-Free Catalytic C–H Bond Activation and Borylation of Heteroarenes. *Science* **2015**, *349* (6247), pp 513–516. DOI: 10.1126/science.aab3591.
- (11) Braunschweig, H.; Krummenacher, I.; Légaré, M.-A.; Matler, A.; Radacki, K.; Ye, Q. Main-Group Metallomimetics: Transition Metal-like Photolytic CO Substitution at Boron. *J. Am. Chem. Soc.* **2017**, *139* (5), pp 1802–1805. DOI: 10.1021/jacs.6b13047.
- (12) Wilkins, L. C.; Melen, R. L. Enantioselective Main Group Catalysis: Modern Catalysts for Organic Transformations. *Coord. Chem. Rev.* **2016**, *324*, pp 123–139. DOI: 10.1016/j.ccr.2016.07.011.
- (13) Lee, K.; Blake, A. V.; Tanushi, A.; McCarthy, S. M.; Kim, D.; Loria, S. M.; Donahue, C. M.; Spielvogel, K. D.; Keith, J. M.; Daly, S. R.; Radosevich, A. T. Validating the Biphilic Hypothesis of Nontrigonal Phosphorus(III) Compounds. *Angew. Chemie Int. Ed.* **2019**, *58* (21), pp 6993–6998. DOI: 10.1002/anie.201901779.
- (14) Dunn, N. L.; Ha, M.; Radosevich, A. T. Main Group Redox Catalysis: Reversible P<sup>III</sup>/P<sup>V</sup> Redox Cycling at a Phosphorus Platform. *J. Am. Chem. Soc.* **2012**, *134* (28), pp 11330–11333. DOI: 10.1021/ja302963p.
- (15) Denmark, S. E.; Jacobs, R. T.; Dai-Ho, G.; Wilson, S. Synthesis, Structure, and Reactivity of an Organogermanium Lewis Acid. *Organometallics* **1990**, *9* (12), pp 3015–3019. DOI: 10.1021/om00162a006.
- (16) Konishi, S.; Iwai, T.; Sawamura, M. Synthesis, Properties, and Catalytic Application of a Triptycene-Type Borate-Phosphine Ligand. *Organometallics* **2018**, *37* (12), pp 1876–1883. DOI: 10.1021/acs.organomet.8b00113.
- (17) Dicks, A. P. Using Hydrocarbon Acidities To Demonstrate Principles of Organic Structure and Bonding. *J. Chem. Educ.* **2003**, *80* (11), p 1322. DOI: 10.1021/ed080p1322.
- (18) Gericke, R.; Gerlach, D.; Wagler, J. Ring-Strain-Formation Lewis Acidity? A Pentacoordinate Silacyclobutane Comprising Exclusively Equatorial Si–C Bonds. *Organometallics* **2009**, *28* (23), pp 6831–6834. DOI: 10.1021/om900741a.
- (19) Denmark, S. E.; Griedel, B. D.; Coe, D. M.; Schnute, M. E. Chemistry of Enoxysilacyclobutanes: Highly Selective Uncatalyzed Aldol Additions. *J. Am. Chem. Soc.* **1994**, *116* (16), pp 7026–7043. DOI: 10.1021/ja00095a004.
- (20) Laane, J. Synthesis of Silacyclobutane and Some Related Compounds. *J. Am. Chem. Soc.* **1967**, *89* (5), pp 1144–1147. DOI: 10.1021/ja00981a020.
- (21) Kinnaird, J. W. A.; Ng, P. Y.; Kubota, K.; Wang, X.; Leighton, J. L. Strained Silacycles in Organic Synthesis: A New Reagent for the Enantioselective Allylation of Aldehydes. *J. Am. Chem. Soc.* **2002**, *124* (27), pp 7920–7921. DOI: 10.1021/ja0264908.

- (22) Perozzi, E. F.; Michalak, R. S.; Figuly, G. D.; Stevenson, W. H.; Dess, D.; Ross, M. R.; Martin, J. C. Directed Dilithiation of Hexafluorocumyl Alcohol - Formation of a Reagent for the Facile Introduction of a Stabilizing Bidentate Ligand in Compounds of Hypervalent Sulfur (10-S-4), Phosphorus (10-P-5), Silicon (10-Si-5), and Iodine (10-I-3). *J. Org. Chem.* **1981**, *46* (6), pp 1049–1053. DOI: 10.1021/jo00319a001.
- (23) Leighton, J. L. 3.23 Stoichiometric Auxiliary Ligands for Metals and Main Group Elements: Ligands for Silicon. In *Comprehensive Chirality*; Elsevier, 2012; pp 740–750. DOI: 10.1016/B978-0-08-095167-6.00323-2.
- (24) Heckel, T.; Wilhelm, R. Lewis Acids. In *Comprehensive Enantioselective Organocatalysis*; Wiley-VCH Verlag GmbH & Co. KGaA: Weinheim, Germany, 2013; pp 431–462. DOI: 10.1002/9783527658862.ch16.
- (25) Nelson, S. G.; Kim, B.-K.; Peelen, T. J. Lewis Acidity Expressed in Neutral Electron-Rich Aluminum(III) Complexes: An Example of Ligand-Defined Catalysis. *J. Am. Chem. Soc.* **2000**, *122* (38), pp 9318–9319. DOI: 10.1021/ja002415q.
- (26) Nelson, S. G.; Peelen, T. J.; Wan, Z. Catalytic Asymmetric Acyl Halide–Aldehyde Cyclocondensations. A Strategy for Enantioselective Catalyzed Cross Aldol Reactions. *J. Am. Chem. Soc.* **1999**, *121* (41), pp 9742–9743. DOI: 10.1021/ja992369y.
- (27) Nelson, S. G.; Zhu, C.; Shen, X. Catalytic Asymmetric Acyl Halide–Aldehyde Cyclocondensation Reactions of Substituted Ketenes. *J. Am. Chem. Soc.* **2004**, *126* (1), pp 14–15. DOI: 10.1021/ja0391208.
- (28) Wan, Z.; Nelson, S. G. Optically Active Allenes from  $\beta$ -Lactone Templates: Asymmetric Total Synthesis of (–)-Malyngolide. *J. Am. Chem. Soc.* **2000**, *122* (42), pp 10470–10471. DOI: 10.1021/ja002783u.
- (29) Li, H.; Aquino, A. J. A.; Cordes, D. B.; Hase, W. L.; Krempner, C. Electronic Nature of Zwitterionic Alkali Metal Methanides, Silanides and Germanides – a Combined Experimental and Computational Approach. *Chem. Sci.* **2017**, *8* (2), pp 1316–1328. DOI: 10.1039/C6SC02390H.
- (30) Oлару, M.; Hesse, M. F.; Rychagova, E.; Ketkov, S.; Mebs, S.; Beckmann, J. The Weakly Coordinating Tris(Trichlorosilyl)Silyl Anion. *Angew. Chemie Int. Ed.* **2017**, *56* (52), pp 16490–16494. DOI: 10.1002/anie.201710416.
- (31) Bordwell, F. G.; McCallum, R. J.; Olmstead, W. N. Acidities and Hydrogen Bonding of Phenols in Dimethyl Sulfoxide. *J. Org. Chem.* **1984**, *49* (8), pp 1424–1427. DOI: 10.1021/jo00182a020.
- (32) Olmstead, W. N.; Bordwell, F. G. Ion-Pair Association Constants in Dimethyl Sulfoxide. *J. Org. Chem.* **1980**, *45* (16), pp 3299–3305. DOI: 10.1021/jo01304a033.
- (33) Chapter 2 of This Thesis.
- (34) Tretiakov, S.; Witteman, L.; Lutz, M.; Moret, M. Strain-Modulated Reactivity: An Acidic Silane. *Angew. Chemie Int. Ed.* **2021**, *60* (17), pp 9618–9626. DOI: 10.1002/anie.202015960.
- (35) Witteman, L.; Evers, T.; Lutz, M.; Moret, M.-E. A Free Silanide from Nucleophilic Substitution at Silicon(II). *Chem. Eur. J.* **2018**, *24* (47), pp 12236–12240. DOI: 10.1002/chem.201801435.
- (36) Bondi, A. Van Der Waals Volumes and Radii. *J. Phys. Chem.* **1964**, *68* (3), pp 441–451. DOI: 10.1021/j100785a001.
- (37) Bauzá, A.; Mooibroek, T. J.; Frontera, A. Tetrel-Bonding Interaction: Rediscovered Supramolecular Force? *Angew. Chemie Int. Ed.* **2013**, *52* (47), pp 12317–12321. DOI: 10.1002/anie.201306501.
- (38) Steenwinkel, P.; Jastrzebski, J. T. B. H.; Deelman, B.-J.; Grove, D. M.; Kooijman, H.; Veldman, N.; Smeets, W. J. J.; Spek, A. L.; van Koten, G. Hypercoordinate Aryltrialkylsilanes and -Stannanes and Their Use in the Synthesis of Homodinuclear Organometallic Complexes with a 1,4-Phenylene Bridge. *Organometallics* **1997**, *16* (25), pp 5486–5498. DOI: 10.1021/om970492x.
- (39) Weinhold, F.; Landis, C. R. *Valency and Bonding: A Natural Donor-Acceptor Perspective*, 1st ed.; Cambridge University Press: Cambridge, 2005. DOI: 10.1017/CBO9780511614569.
- (40) Tretiakov, S.; Damen, J. A. M.; Lutz, M.; Moret, M.-E. A Dianionic  $C_3$ -Symmetric Scorpionate: Synthesis and Coordination Chemistry. *Dalt. Trans.* **2020**, *49* (39), pp 13549–13556. DOI: 10.1039/D0DT02601H.
- (41) Hübler, K.; Roper, W. R.; Wright, L. J. Tri-*N*-Pyrrolylsilyl Complexes of Ruthenium and Osmium 1. *Organometallics* **1997**, *16* (12), pp 2730–2735. DOI: 10.1021/om970044p.
- (42) Izutsu, K. *Acid-Base Dissociation Constants in Dipolar Aprotic Solvents (IUPAC Chemical Data)*; Blackwell Science; 1st Edition: Oxford, 1990.
- (43) Korogodsky, G.; Bendikov, M.; Bravo-Zhivotovskii, D.; Apeloig, Y. Determination of the Solution Acidity of Tris(trimethylsilyl)silane. *Organometallics* **2002**, *21* (15), pp 3157–3161. DOI: 10.1021/om010821s.
- (44) Ritchie, C. D. Acidity in Nonaqueous Solvents. VII. Proton Transfers in Dipolar Aprotic Solvents. 5. Solvation and Geometric Factors in the Rates of Proton Transfer Reactions. *J. Am. Chem. Soc.* **1969**,

- 91 (24), pp 6749–6753. DOI: 10.1021/ja01052a036.
- (45) *Tables of Rate and Equilibrium Constants of Heterolytic Organic Reactions*; Palm, V., Ed.; VINITI: Moscow-Tartu, 1975.
- (46) Kütt, A.; Selberg, S.; Kaljurand, I.; Tshepelevitsh, S.; Heering, A.; Darnell, A.; Kaupmees, K.; Piirsalu, M.; Leito, I.  $\text{PK}_a$  Values in Organic Chemistry – Making Maximum Use of the Available Data. *Tetrahedron Lett.* **2018**, 59 (42), pp 3738–3748. DOI: 10.1016/j.tetlet.2018.08.054.
- (47) *Bordwell pKa Table*. <http://www.chem.wisc.edu/areas/reich/pkatable/> (accessed 2020-10-10).
- (48) Kuhn, R.; Rewicki, D. Die PK-Werte Doppelbindungsisomerer Kohlenwasserstoffe Mit Gemeinsamem Carbanion. *Tetrahedron Lett.* **1965**, 6 (39), pp 3513–3522. DOI: 10.1016/S0040-4039(01)89335-7.
- (49) Buncel, E.; Venkatachalam, T. K. Carbanion Mechanisms XXI. Solution Acidity of Triphenylsilane. *J. Organomet. Chem.* **2000**, 604 (2), pp 208–210. DOI: 10.1016/S0022-328X(00)00242-4.
- (50) Benkeser, R. A.; Voley, K. M.; Grutzner, J. B.; Smith, W. E. Evidence for the Existence of the Trichlorosilyl Anion. *J. Am. Chem. Soc.* **1970**, 92 (3), pp 697–698. DOI: 10.1021/ja00706a045.
- (51) Schwarze, N.; Steinhauer, S.; Neumann, B.; Stammler, H.-G.; Hoge, B. Nucleophilic Transfer Reactions of the  $[\text{Si}(\text{C}_2\text{F}_5)_3]^-$  Moiety. *Angew. Chemie Int. Ed.* **2016**, 55 (52), pp 16161–16164. DOI: 10.1002/anie.201609575.
- (52) Ding, F.; Smith, J. M.; Wang, H. First-Principles Calculation of  $\text{PK}_a$  Values for Organic Acids in Nonaqueous Solution. *J. Org. Chem.* **2009**, 74 (7), pp 2679–2691. DOI: 10.1021/jo802641r.
- (53) Реутов, О. А.; Курц, А. Л.; Бутин, К. П. *Органическая Химия. Том 1*, 7th ed.; Лаборатория знаний: Москва, 2017.
- (54) Bartmess, J. E.; Scott, J. A.; McIver, R. T. Substituent and Solvation Effects on Gas-Phase Acidities. *J. Am. Chem. Soc.* **1979**, 101 (20), pp 6056–6063. DOI: 10.1021/ja00514a031.
- (55) McIver, R. T.; Silvers, J. H. Gas-Phase Acidity of Monosubstituted Phenols. *J. Am. Chem. Soc.* **1973**, 95 (25), pp 8462–8464. DOI: 10.1021/ja00806a052.
- (56) Boand, G.; Houriet, R.; Gaumann, T. Gas-Phase Acidity of Aliphatic Alcohols. *J. Am. Chem. Soc.* **1983**, 105 (8), pp 2203–2206. DOI: 10.1021/ja00346a600.
- (57) Epshtein, L. M. Hydrogen Bonds and the Reactivity of Organic Compounds in Proton Transfer and Nucleophilic Substitution Reactions. *Russ. Chem. Rev.* **1979**, 48 (9), pp 854–867. DOI: 10.1070/RC1979v048n09ABEH002417.
- (58) Taft, R. W.; Bordwell, F. G. Structural and Solvent Effects Evaluated from Acidities Measured in Dimethyl Sulfoxide and in the Gas Phase. *Acc. Chem. Res.* **1988**, 21 (12), pp 463–469. DOI: 10.1021/ar00156a005.
- (59) Bordwell, F. G.; Bartmess, J. E.; Drucker, G. E.; Margolin, Z.; Matthews, W. S. Acidities of Carbon Acids. V. Correlation of Acidities in Dimethyl Sulfoxide with Gas-Phase Acidities. *J. Am. Chem. Soc.* **1975**, 97 (11), pp 3226–3227. DOI: 10.1021/ja00844a056.
- (60) Bökman, F. On the Relative Acidities of Organic Compounds: Electronic and Geometric Relaxation Energies. *J. Am. Chem. Soc.* **1999**, 121 (48), pp 11217–11222. DOI: 10.1021/ja992759k.
- (61) Birkmann, B.; Voss, T.; Geier, S. J.; Ullrich, M.; Kehr, G.; Erker, G.; Stephan, D. W. Frustrated Lewis Pairs and Ring-Opening of THF, Dioxane, and Thioxane. *Organometallics* **2010**, 29 (21), pp 5310–5319. DOI: 10.1021/om1003896.
- (62) Lindon, J. C.; Tranter, G. E.; Koppenaal, D. *Encyclopedia of Spectroscopy and Spectrometry*; Elsevier Science, 2016.
- (63) Muettterties, E. L. Topological Representation of Stereoisomerism. I. Polytopal Rearrangements. *J. Am. Chem. Soc.* **1969**, 91 (7), pp 1636–1643. DOI: 10.1021/ja01035a009.
- (64) Muettterties, E. L. Topological Representation of Stereoisomerism. II. The Five-Atom Family. *J. Am. Chem. Soc.* **1969**, 91 (15), pp 4115–4122. DOI: 10.1021/ja01043a017.
- (65) Couzijn, E. P. A. A.; Slootweg, J. C.; Ehlers, A. W.; Lammertsma, K. Stereomutation of Pentavalent Compounds: Validating the Berry Pseudorotation, Redressing Ugi's Turnstile Rotation, and Revealing the Two- and Three-Arm Turnstiles. *J. Am. Chem. Soc.* **2010**, 132 (51), pp 18127–18140. DOI: 10.1021/ja105306s.
- (66) Frisch, M. J.; Trucks, G. W.; Schlegel, H. B.; Scuseria, G. E.; Robb, M. A.; Cheeseman, J. R.; Scalmani, G.; Barone, V.; Petersson, G. A.; Nakatsuji, H.; Li, X.; Caricato, M.; Marenich, A. V.; Bloino, J.; Janesko, B. G.; Gomperts, R.; Mennucci, B.; Hratchian, H. P.; Ortiz, J. V.; Izmaylov, A. F.; Sonnenberg, J. L.; Williams-Young, D.; Ding, F.; Lipparini, F.; Egidi, F.; Goings, J.; Peng, B.; Petrone, A.; Henderson, T.; Ranasinghe, D.; Zakrzewski, V. G.; Gao, J.; Rega, N.; Zheng, G.; Liang, W.; Hada, M.; Ehara, M.; Toyota, K.; Fukuda, R.; Hasegawa, J.; Ishida, M.; Nakajima, T.; Honda, Y.; Kitao, O.; Nakai, H.; Vreven, T.; Throssell, K.; Montgomery Jr., J. A.; Peralta, J. E.; Ogliaro, F.; Bearpark, M. J.; Heyd, J. J.; Brothers, E. N.; Kudin, K. N.; Staroverov, V. N.; Keith, T. A.;

- Kobayashi, R.; Normand, J.; Raghavachari, K.; Rendell, A. P.; Burant, J. C.; Iyengar, S. S.; Tomasi, J.; Cossi, M.; Millam, J. M.; Klene, M.; Adamo, C.; Cammi, R.; Ochterski, J. W.; Martin, R. L.; Morokuma, K.; Farkas, O.; Foresman, J. B.; Fox, D. J. Gaussian 16, Revision A.03. Gaussian, Inc.: Wallingford CT 2016.
- (67) Fukui, K. The Path of Chemical Reactions - the IRC Approach. *Acc. Chem. Res.* **1981**, *14* (12), pp 363–368. DOI: 10.1021/ar00072a001.
- (68) Taketsugu, T.; Tajima, N.; Hirao, K. Approaches to Bifurcating Reaction Path. *J. Chem. Phys.* **1996**, *105* (5), pp 1933–1939. DOI: 10.1063/1.472063.
- (69) Ess, D. H.; Wheeler, S. E.; Iafe, R. G.; Xu, L.; Çelebi-Ölçüm, N.; Houk, K. N. Bifurcations on Potential Energy Surfaces of Organic Reactions. *Angew. Chemie Int. Ed.* **2008**, *47* (40), pp 7592–7601. DOI: 10.1002/anie.200800918.
- (70) Valtazanos, P.; Ruedenberg, K. Bifurcations and Transition States. *Theor. Chim. Acta* **1986**, *69*, pp 281–307. DOI: 10.1007/BF00527705.
- (71) Singleton, D. A.; Hang, C.; Szymanski, M. J.; Meyer, M. P.; Leach, A. G.; Kuwata, K. T.; Chen, J. S.; Greer, A.; Foote, C. S.; Houk, K. N. Mechanism of Ene Reactions of Singlet Oxygen. A Two-Step No-Intermediate Mechanism. *J. Am. Chem. Soc.* **2003**, *125* (5), pp 1319–1328. DOI: 10.1021/ja027225p.
- (72) Quapp, W.; Hirsch, M.; Heidrich, D. An Approach to Reaction Path Branching Using Valley-Ridge Inflection Points of Potential-Energy Surfaces. *Theor. Chem. Accounts Theory, Comput. Model. (Theoretica Chim. Acta)* **2004**, *112*, pp 40–51. DOI: 10.1007/s00214-003-0558-8.
- (73) QUAPP, W. REDUCED GRADIENT METHODS AND THEIR RELATION TO REACTION PATHS. *J. Theor. Comput. Chem.* **2003**, *02* (03), pp 385–417. DOI: 10.1142/S0219633603000604.
- (74) Wales, D. J. Potential Energy Surfaces and Coordinate Dependence. *J. Chem. Phys.* **2000**, *113* (9), pp 3926–3927. DOI: 10.1063/1.1288003.
- (75) Fürstner, A. Potassium-Graphite Laminate. In *Encyclopedia of Reagents for Organic Synthesis*; John Wiley & Sons, Ltd: Chichester, UK, 2001. DOI: 10.1002/047084289X.rp217.
- (76) Ghadwal, R. S.; Roesky, H. W.; Merkel, S.; Henn, J.; Stalke, D. Lewis Base Stabilized Dichlorosilylene. *Angew. Chemie Int. Ed.* **2009**, *48* (31), pp 5683–5686. DOI: 10.1002/anie.200901766.
- (77) Yakelis, N. A.; Bergman, R. G. Safe Preparation and Purification of Sodium Tetrakis[(3,5-Trifluoromethyl)Phenyl]Borate (NaBARF<sub>24</sub>): Reliable and Sensitive Analysis of Water in Solutions of Fluorinated Tetraarylborates. *Organometallics* **2005**, *24* (14), pp 3579–3581. DOI: 10.1021/om0501428.
- (78) Brookhart, M.; Grant, B.; Volpe, A. F. [(3,5-(CF<sub>3</sub>)<sub>2</sub>C<sub>6</sub>H<sub>3</sub>)<sub>4</sub>B]<sup>-</sup>[H(OEt)<sub>2</sub>]<sup>+</sup>: A Convenient Reagent for Generation and Stabilization of Cationic, Highly Electrophilic Organometallic Complexes. *Organometallics* **1992**, *11* (11), pp 3920–3922. DOI: 10.1021/om00059a071.
- (79) Fulmer, G. R.; Miller, A. J. M.; Sherden, N. H.; Gottlieb, H. E.; Nudelman, A.; Stoltz, B. M.; Bercaw, J. E.; Goldberg, K. I. NMR Chemical Shifts of Trace Impurities: Common Laboratory Solvents, Organics, and Gases in Deuterated Solvents Relevant to the Organometallic Chemist. *Organometallics* **2010**, *29* (9), pp 2176–2179. DOI: 10.1021/om100106e.
- (80) Kupče, E.; Freeman, R. Fast Multidimensional NMR by Polarization Sharing. *Magn. Reson. Chem.* **2007**, *45* (1), pp 2–4. DOI: 10.1002/mrc.1931.
- (81) VnmrJ 4.2, Revision A. Agilent Technologies: Santa Clara, USA 2014.
- (82) MestReNova v.9.0.1-13254. Mestrelab Research S.L. 2014.
- (83) Barnard, T. S.; Mason, M. R. Hindered Axial–Equatorial Carbonyl Exchange in an Fe(CO)<sub>4</sub>(PR<sub>3</sub>) Complex of a Rigid Bicyclic Phosphine. *Inorg. Chem.* **2001**, *40* (19), pp 5001–5009. DOI: 10.1021/ic001372b.
- (84) Witteman, L.; van Beek, C. B.; van Veenhuizen, O. N.; Lutz, M.; Moret, M.-E. Synthesis and Complexation of a Free Germanide Bearing a Tridentate N-Heterocyclic Substituent. *Organometallics* **2019**, *38* (2), pp 231–239. DOI: 10.1021/acs.organomet.8b00630.
- (85) Hailwood, A. J.; Robinson, R. A Reaction of Fluorene. *J. Chem. Soc.* **1932**, pp 1292–1295. DOI: 10.1039/jr9320001292.
- (86) Sugawara, T.; Nakashima, N.; Yoshihara, K.; Iwamura, H. Low-Temperature and Time-Resolved Absorption Spectral Studies on the Sp- and Ap-2-(9-Fluorenyl)Phenylnitrenes Generated from 1-Azatriptycene and 2-(9-Fluorenyl)Phenyl Azide. *J. Am. Chem. Soc.* **1983**, *105* (4), pp 858–862. DOI: 10.1021/ja00342a036.
- (87) Rapoport, H.; Smolinsky, G. Fluoradene. *J. Am. Chem. Soc.* **1960**, *82* (4), pp 934–941. DOI: 10.1021/ja01489a038.
- (88) Gannon, S. M.; Krause, J. G. Phase-Transfer Permanganate Oxidation of Unfunctionalized Benzylic Positions. *Synthesis (Stuttg.)* **1987**, *1987* (10), pp 915–917. DOI: 10.1055/s-1987-28121.

- (89) Kuhn, R.; Fischer, H.; Neugebauer, F. A.; Fischer, H. Über Hochacide Kohlenwasserstoffe. *Justus Liebigs Ann. Chem.* **1962**, *654* (1), pp 64–81. DOI: 10.1002/jlac.19626540109.
- (90) Vougioukalakis, G. C.; Roubelakis, M. M.; Orfanopoulos, M. Radical Reactivity of Aza[60]Fullerene: Preparation of Monoadducts and Limitations. *J. Org. Chem.* **2010**, *75* (12), pp 4124–4130. DOI: 10.1021/jo100277v.
- (91) Bordwell, F. G.; Branca, J. C.; Bares, J. E.; Filler, R. Enhancement of the Equilibrium Acidities of Carbon Acids by Polyfluoroaryl Substituents. *J. Org. Chem.* **1988**, *53* (4), pp 780–782. DOI: 10.1021/jo00239a016.
- (92) Bavin, P. M. G. ALIPHATIC CHEMISTRY OF FLUORENE:PART IV. PREPARATION AND ALKYLATION OF SOME SULPHIDES AND SULPHONES. *Can. J. Chem.* **1960**, *38* (6), pp 917–922. DOI: 10.1139/v60-129.
- (93) Jakab, G.; Tancon, C.; Zhang, Z.; Lippert, K. M.; Schreiner, P. R. (Thio)Urea Organocatalyst Equilibrium Acidities in DMSO. *Org. Lett.* **2012**, *14* (7), pp 1724–1727. DOI: 10.1021/ol300307c.
- (94) Schreurs, A. M. M.; Xian, X.; Kroon-Batenburg, L. M. J. EVAL15 : A Diffraction Data Integration Method Based on Ab Initio Predicted Profiles. *J. Appl. Crystallogr.* **2010**, *43* (1), pp 70–82. DOI: 10.1107/S0021889809043234.
- (95) Sheldrick, G. M. SADABS. Universität Göttingen, Germany 2014.
- (96) Sheldrick, G. M. TWINABS. Universität Göttingen, Germany 2014.
- (97) Sheldrick, G. M. SHELXT – Integrated Space-Group and Crystal-Structure Determination. *Acta Crystallogr. Sect. A Found. Adv.* **2015**, *71* (1), pp 3–8. DOI: 10.1107/S2053273314026370.
- (98) Sheldrick, G. M. Crystal Structure Refinement with SHELXL. *Acta Crystallogr. Sect. C Struct. Chem.* **2015**, *71* (1), pp 3–8. DOI: 10.1107/S2053229614024218.
- (99) Herbst-Irmer, R.; Sheldrick, G. M. Refinement of Twinned Structures with SHELXL97. *Acta Crystallogr. Sect. B Struct. Sci.* **1998**, *54* (4), pp 443–449. DOI: 10.1107/S0108768197018454.
- (100) Spek, A. L. Structure Validation in Chemical Crystallography. *Acta Crystallogr. Sect. D Biol. Crystallogr.* **2009**, *65* (2), pp 148–155. DOI: 10.1107/S090744490804362X.
- (101) Spek, A. L. PLATON SQUEEZE: A Tool for the Calculation of the Disordered Solvent Contribution to the Calculated Structure Factors. *Acta Crystallogr. Sect. C Struct. Chem.* **2015**, *71* (1), pp 9–18. DOI: 10.1107/S2053229614024929.
- (102) Müller, J.; Heintl, S.; Schwarzmaier, C.; Balázs, G.; Keilwerth, M.; Meyer, K.; Scheer, M. Rearrangement of a P<sub>4</sub> Butterfly Complex-The Formation of a Homoleptic Phosphorus-Iron Sandwich Complex. *Angew. Chemie Int. Ed.* **2017**, *56* (25), pp 7312–7317. DOI: 10.1002/anie.201703175.
- (103) Langer, R.; Bönisch, F.; Maser, L.; Pietzonka, C.; Vondung, L.; Zimmermann, T. P. Substitutional Lability of Diphosphine Ligands in Tetrahedral Iron(II) Chloro Complexes. *Eur. J. Inorg. Chem.* **2015**, *2015* (1), pp 141–148. DOI: 10.1002/ejic.201402859.
- (104) Benito-Garagorri, D.; Kirchner, K.; Mereiter, K. Tetraphenylphosphonium Acetonitriletribromoferrate(II). *Acta Crystallogr. Sect. E Struct. Reports Online* **2006**, *E62*, pp m1136–m1138. DOI: 10.1107/S1600536806014504.
- (105) LePichon, L.; Stephan, D. W.; Gao, X.; Wang, Q. Iron Phosphinimide and Phosphinimine Complexes: Catalyst Precursors for Ethylene Polymerization. *Organometallics* **2002**, *21* (7), pp 1362–1366. DOI: 10.1021/om011041m.
- (106) Chard, E. F.; Thompson, J. R.; Dawe, L. N.; Kozak, C. M. Synthesis and Structure of Iron(III) Complexes of Amine-Bis(Phenolate) Ligands. *Can. J. Chem.* **2014**, *92* (8), pp 758–764. DOI: 10.1139/cjc-2014-0043.
- (107) Holzhaecker, C.; Stöger, B.; Carvalho, M. D.; Ferreira, L. P.; Pittenauer, E.; Allmaier, G.; Veiros, L. F.; Realista, S.; Gil, A.; Calhorda, M. J.; Müller, D.; Kirchner, K. Synthesis and Reactivity of TADDOL-Based Chiral Fe(II) PNP Pincer Complexes-Solution Equilibria between  $\kappa^2P,N$ - and  $\kappa^3P,N,P$ -Bound PNP Pincer Ligands. *Dalt. Trans.* **2015**, *44* (29), pp 13071–13086. DOI: 10.1039/C5DT00832H.
- (108) Kiernicki, J. J.; Norwine, E. E.; Zeller, M.; Szymczak, N. K. Tetrahedral Iron Featuring an Appended Lewis Acid: Distinct Pathways for the Reduction of Hydroxylamine and Hydrazine. *Chem. Commun.* **2019**, *55* (79), pp 11896–11899. DOI: 10.1039/C9CC05720J.
- (109) Govor, E. V.; Sanakis, Y.; Raptis, R. G. Synthesis of Pyrazole (Hemi)Aminals via the Cleavage of Saturated Aliphatic Ether C–O Bonds in the Presence of Ferric Halides. *New J. Chem.* **2017**, *41* (6), pp 2220–2223. DOI: 10.1039/C6NJ03822K.
- (110) Fu, Y.; Liu, L.; Li, R. Q.; Liu, R.; Guo, Q. X. First-Principle Predictions of Absolute PK<sub>a</sub>'s of Organic Acids in Dimethyl Sulfoxide Solution. *J. Am. Chem. Soc.* **2004**, *126* (3), pp 814–822. DOI: 10.1021/ja0378097.

- (111) Gusev, D. G. Donor Properties of a Series of Two-Electron Ligands. *Organometallics* **2009**, *28* (3), pp 763–770. DOI: 10.1021/om800933x.
- (112) Glendening, E. D.; Badenhop, J. K.; Reed, A. E.; Carpenter, J. E.; Bohmann, J. A.; Morales, C. M.; Landis, C. R.; Weinhold, F. NBO 6.0. Theoretical Chemistry Institute, University of Wisconsin: Madison, WI 2013.
- (113) Humphrey, W.; Dalke, A.; Schulten, K. VMD: Visual Molecular Dynamics. *J. Mol. Graph.* **1996**, *14* (1), pp 33–38. DOI: 10.1016/0263-7855(96)00018-5.
- (114) Stone, J. E. An Efficient Library for Parallel Ray Tracing and Animation, University of Missouri-Rolla, 1998.
- (115) Stone, J. E.; Vandivort, K. L.; Schulten, K. GPU-Accelerated Molecular Visualization on Petascale Supercomputing Platforms. In *Proceedings of the 8th International Workshop on Ultrascale Visualization - UltraVis '13*; ACM Press: New York, New York, USA, 2013; pp 1–8. DOI: 10.1145/2535571.2535595.
- (116) Abdur-Rashid, K.; Fong, T. P.; Greaves, B.; Gusev, D. G.; Hinman, J. G.; Landau, S. E.; Lough, A. J.; Morris, R. H. An Acidity Scale for Phosphorus-Containing Compounds Including Metal Hydrides and Dihydrogen Complexes in THF: Toward the Unification of Acidity Scales. *J. Am. Chem. Soc.* **2000**, *122* (38), pp 9155–9171. DOI: 10.1021/ja994428d.
- (117) Linstrom, P. J.; Mallard, W. G., E. *NIST Standard Reference Database 69, October 2018 Release*. NIST Chemistry WebBook. DOI: 10.18434/T4D303.
- (118) Tolman, C. A. Steric Effects of Phosphorus Ligands in Organometallic Chemistry and Homogeneous Catalysis. *Chem. Rev.* **1977**, *77* (3), pp 313–348. DOI: 10.1021/cr60307a002.
- (119) Poater, A.; Ragone, F.; Giudice, S.; Costabile, C.; Dorta, R.; Nolan, S. P.; Cavallo, L. Thermodynamics of *N*-Heterocyclic Carbene Dimerization: The Balance of Sterics and Electronics. *Organometallics* **2008**, *27* (12), pp 2679–2681. DOI: 10.1021/om8001119.
- (120) Tolman, C. A. Phosphorus Ligand Exchange Equilibria on Zerovalent Nickel. Dominant Role for Steric Effects. *J. Am. Chem. Soc.* **1970**, *92* (10), pp 2956–2965. DOI: 10.1021/ja00713a007.

# ***Chapter 5***

---

**Outlook**

---



## 5.1 Concluding remarks and perspective

In the previous chapters, we presented the synthesis and reactivity of the first dianionic  $C_3$ -symmetric scorpionate capable of metal exchange,  $TSMK_2$ , followed by detailed studies of its transition metal and main-group derivatives. This research was performed with the hope to observe charge separation effects that could ultimately be used for fine reactivity and properties control. Whereas the  $TSMK_2$  scaffold does feature rich coordination behavior as well as an ability to stabilize unusual oxidation states ( $Fe^{IV}$  and  $Si^{II}$ ), the charge separation effects are tightly intertwined with electronics and sterics, making it difficult to quantify the contribution of each actor. The situation is aggravated by the absence of a proper theoretical framework that would help to deconvolute these effects. We do, however, make qualitative conclusions based on the comparison with analogous computed and experimental systems that lack strongly separated charges.

In future studies, a deeper understanding of the charge influence may be gained through expanding the scope of the comparison by using analogues of the  $TSMK_2$  salt with a different central atom (*Chart 5.1A*). While the systems with  $E = Al^-$  and  $Si$  are truly isoelectronic to  $TSMK_2$ , the aluminum-containing species may be problematic in terms of kinetic stability, and  $E = B^-$  might be a more functional alternative. Repeating some aspects of the chemistry described in Chapters 2-4 with these analogues is expected to help identify the properties and reactivity differences that emerge primarily due to charge separation. In particular, the solution  $pK_a^{DMSO}$  determination of  $TSMSiSiH$  (*Chart 5.1B*), which is a Si-tethered analogue of  $[TSMPSiH]^+$  described in Chapter 4, would allow to cleanly isolate the contribution of a positive charge into the acidity of  $[TSMPSiH]^+$ . Similarly, spectroscopic analysis of  $[(TSMSi)_2Fe^{IV}]^{2-}$  (*Chart 5.1C*), analogous to  $[(TSMK)_2Fe^{IV}]^0$  from Chapter 3, would allow to detect subtle ligand field differences that may emerge due to electrostatic stabilization of a  $d_{z^2}$  orbital.

Charge separation aside, one may also follow up on other findings presented in this thesis. Chapter 3 showcases a strategy for stabilizing a high-valent late-transition metal center in the  $[(TSMK)_2Fe^{IV}]^0$  complex. One may extend this approach to other first-row metals, such as Co, Ni and Mn. Despite being coordinatively saturated, and likely displaying outer sphere redox chemistry of limited use for catalysis, these compounds may be of fundamental interest for the broader coordination chemistry/inorganic spectroscopy community. More synthetically relevant are heteroleptic complexes with strongly  $\pi$ -donating oxo-, nitride- and imido-ligands, since such compounds have been identified or proposed as key intermediates in a range of important (catalytic) transformations.<sup>1-5</sup> It is briefly discussed in Chapter 2 that chemical oxidation of the

TSMMP-monoligated  $\text{Fe}^{\text{II}}$  and  $\text{Ni}^{\text{II}}$  complexes yields no tractable products. One common strategy is to kinetically stabilize an oxidized metal site by the sterically demanding substituents.<sup>6–13</sup> Therefore, we suggest modifying the TSMMP scaffold on the 7<sup>th</sup> position of the indolide moieties with bulky groups (R in *Chart 5.1D*) in order to shield the high-valent metal center and inhibit possible decomposition pathways.

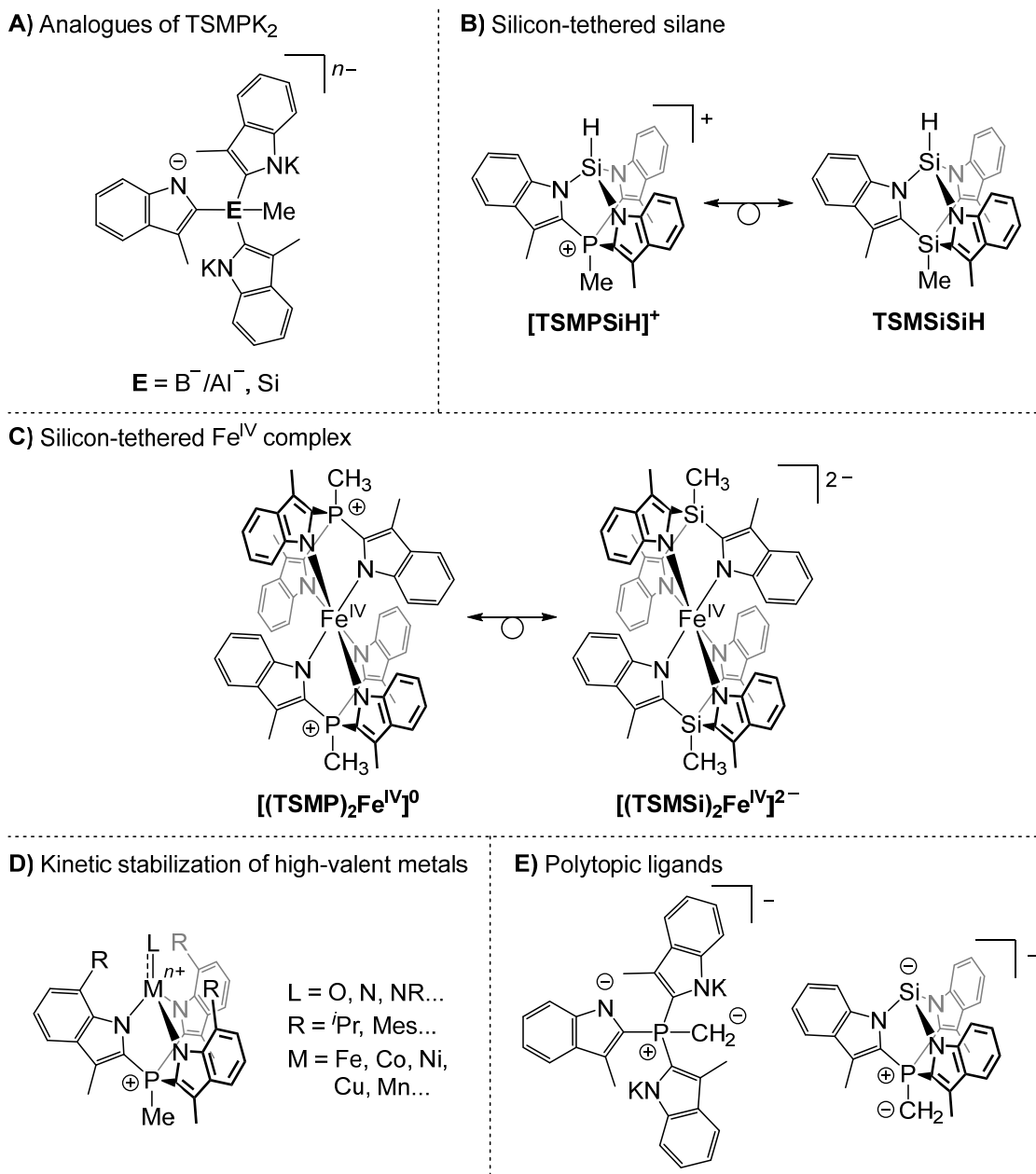


*Chart 5.1.* Suggested miscellaneous research directions.

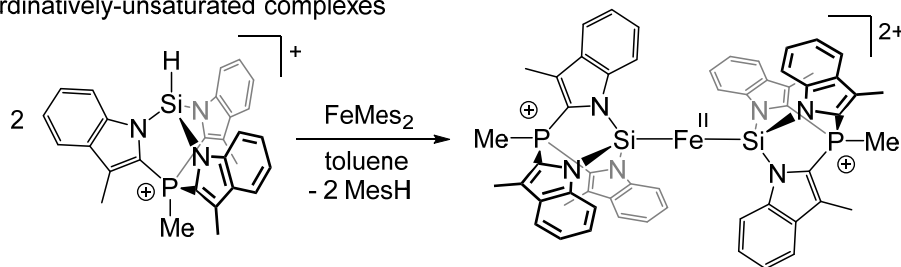
Among the results that were not included in this thesis are deprotonation studies of the phosphonium methyl group in TSMMPK<sub>2</sub> and TSMPSi zwitterions. Treatment of TSMMPK<sub>2</sub> with an equivalent amount of *n*BuLi in THF at  $-78^\circ\text{C}$  yielded ample white

precipitation that, upon reaction with 4.2 equiv. of deuterohydrochloric acid, gave a tetradeuterated  $[\text{TSMPD}_3\text{-}d]^+\text{Cl}^-$ , wherein one of the deuterated positions was on a phosphonium methyl group as evidenced by  $^1\text{H}$ ,  $^2\text{H}$ ,  $^{31}\text{P}$  NMR and mass-spectra. Similarly, treatment of TSMPSi with an equivalent amount of  $n\text{BuLi}$  in THF at  $-78\text{ }^\circ\text{C}$  yielded a  $\text{C}_3$ -symmetric species with a phosphorus-bound methylene group instead of a methyl, as indicated by  $^1\text{H}$  and  $^{31}\text{P}$  NMR. Such polytopic ylidic ligands (*Chart 5.1E*) possess two types of donor sites of different hardness/softness and ligand field strength, which may prove instrumental for the synthesis of bimetallic complexes or spin-crossover/single-chain magnet coordination polymers.<sup>14,15</sup> Another promising potential application lies in the field of low-valent metal-organic frameworks (MOFs), some of which require the presence of harder Lewis donors to form an actual MOF and softer Lewis-basic sites that ligate the low-valent metal centers.<sup>16</sup>

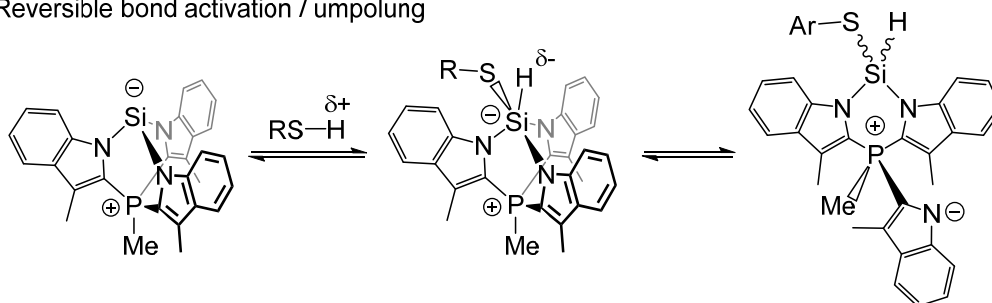
One promising vein of research is the coordination chemistry of TSMPSi from Chapter 4. As such, this zwitterion is a relatively weakly-coordinating ligand, suitable only for soft metal sites akin to  $[\text{Fe}(\text{CO})_4]$ . Repeated attempts to form coordination compounds with  $\text{Fe}(\text{OTf})_2$ ,  $\text{Fe}(\text{acac})_2$ ,  $\text{FeMes}_2$  and  $\text{Fe}(\text{cot})_2$  in THF and/or toluene resulted only in mixtures of the starting materials, as indicated by  $^1\text{H}$  and  $^{31}\text{P}$  NMR. The only exception is complexation with  $\text{FeBr}_2$ , although it is likely driven by insolubility of the resulting  $(\text{TSMPSi})\text{FeBr}_2(\text{THF})$  adduct. We suggest another approach towards a soluble Fe(II) complex that involves protonation of  $\text{FeMes}_2$  with  $[\text{TSMPSiH}]^+\text{BAr}_4^-$  silane synthesized in Chapter 4 (*Chart 5.2A*). Conducted in toluene, this reaction should liberate mesitylene, leaving a naked  $\text{Fe}^{2+}$  ion with no other available lone pair donors but TSMPSi in the vicinity. Depending on stoichiometry, this might result in formation of mono- or bis-ligated complexes. The linear bis-ligated Fe(II) complexes are particularly interesting because the low coordination number restricts the magnitude of the  $d$ -orbital ligand-field splitting, hindering the development of large anisotropies, which may ultimately result in single-molecule magnet behavior.<sup>17-22</sup>

Next, Chapter 4 of this thesis illustrates how a combination of strain and charge separation can modulate redox properties of the main-group elements. The multitude of reaction pathways available for the TSMPSi scaffold, combined with its flexibility, may serve as an entry point into novel bond activation strategies based on the Si(II)/Si(IV) couple. One may envision a process where a silicon of TSMPSi inserts itself into an acidic E–H bond in, for instance, a thiol (*Chart 5.2B*). It is not unreasonable to expect this process to be reversible since a sulphur does not have as high an affinity to silicon as an oxygen. Whereas cleaving the RS–H bond in thiols is not very challenging and can be done by a reasonably strong base, upon addition to TSMPSi the H-atom would lose its acidic character to become a hydride. In other words,

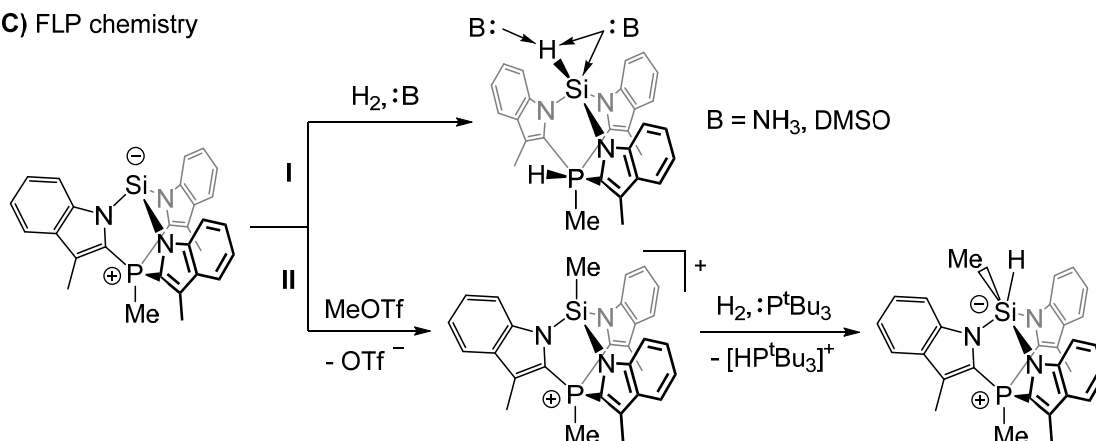
## A) Coordinatively-unsaturated complexes



## B) Reversible bond activation / umpolung



## C) FLP chemistry



## D) Cationic silicon

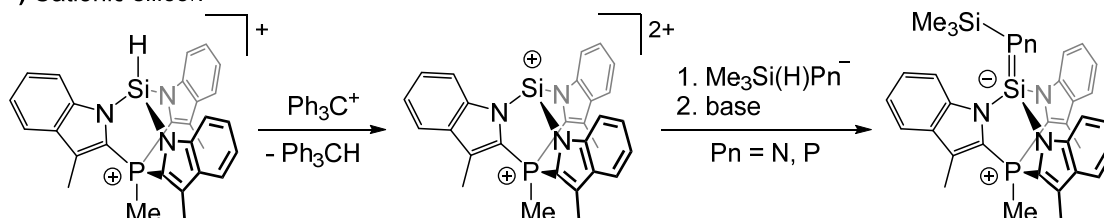


Chart 5.2. Possible research directions with the TSMPSi system.

TSMPSi insertion would lead to umpolung, where the emerging hydride could be used for further transformations.

Expanding on bond activation and considering that TSMPSi has linker-separated Lewis-acidic and basic sites in the same molecule, and as such can be viewed as a frustrated Lewis pair (FLP), it would be interesting to probe dihydrogen activation.

Initial tests, not discussed in this thesis, involved pressurizing TSMPSi dissolved in THF with 2 bars of dihydrogen at room temperature and at 65 °C for 48 h. In both cases,  $^1\text{H}$  and  $^{31}\text{P}$  NMR spectra showed no reaction. Our preliminary DFT calculations suggest that the presence of hard Lewis bases, such as ammonia or DMSO (:B in *Chart 5.2C*, reaction I), may coordinatively stabilize the strained Si–H moiety and allow to split dihydrogen over silicon and phosphorus with a moderately negative free energy balance. Alternatively, one may try to take advantage of the strain-release Lewis acidity of  $[\text{TSMPSiMe}]^+$  discussed in Chapter 4, pairing it with a common bulky Lewis base, such as  $\text{P}^t\text{Bu}_3$  (*Chart 5.2C*, reaction II).

Finally, one might also venture into the chemistry of silicon cations, which have been a point of increased interest over the past years.<sup>23–25</sup> Hydride abstraction from  $[\text{TSMPSiH}]^+$  may lead to a doubly-positive silylium ion (*Chart 5.2D*). It is expected to be pyramidal due to the constraints imposed by the cage structure. This inability to flatten so that an electron hole would occupy an orbital with the lowest *s*-contribution, combined with a double positive charge, is expected to lead to enhanced reactivity, which might be of interest for Lewis acid catalysis and small molecule activation. Furthermore, the silylium ion may serve as a starting point for the synthesis of pnictogen -ene compounds (*Chart 5.2D*). The double bond in those is likely to possess strong ylidic character, having potential applications for small molecule activation.

## 5.2 References

- (1) Mondal, B.; Roy, L.; Neese, F.; Ye, S. High-Valent Iron-Oxo and -Nitrido Complexes: Bonding and Reactivity. *Isr. J. Chem.* **2016**, *56* (9–10), pp 763–772. DOI: 10.1002/ijch.201600028.
- (2) McDonald, A. R.; Que, L. High-Valent Nonheme Iron-Oxo Complexes: Synthesis, Structure, and Spectroscopy. *Coord. Chem. Rev.* **2013**, *257* (2), pp 414–428. DOI: 10.1016/j.ccr.2012.08.002.
- (3) Mehn, M. P.; Peters, J. C. Mid- to High-Valent Imido and Nitrido Complexes of Iron. *J. Inorg. Biochem.* **2006**, *100* (4), pp 634–643. DOI: 10.1016/j.jinorgbio.2006.01.023.
- (4) Larson, V. A.; Battistella, B.; Ray, K.; Lehnert, N.; Nam, W. Iron and Manganese Oxo Complexes, Oxo Wall and Beyond. *Nat. Rev. Chem.* **2020**, *4* (8), pp 404–419. DOI: 10.1038/s41570-020-0197-9.
- (5) Karmalkar, D. G.; Larson, V. A.; Malik, D. D.; Lee, Y.-M.; Seo, M. S.; Kim, J.; Vasiliauskas, D.; Shearer, J.; Lehnert, N.; Nam, W. Preparation and Characterization of a Formally Ni<sup>IV</sup>-Oxo Complex with a Triplet Ground State and Application in Oxidation Reactions. *J. Am. Chem. Soc.* **2022**, *144* (49), pp 22698–22712. DOI: 10.1021/jacs.2c10196.
- (6) Sazama, G. T.; Betley, T. A. Ligand-Centered Redox Activity: Redox Properties of 3d Transition Metal Ions Ligated by the Weak-Field Tris(Pyrrrolyl)Ethane Trianion. *Inorg. Chem.* **2010**, *49* (5), pp 2512–2524. DOI: 10.1021/ic100028y.
- (7) MacBeth, C. E.; Golombek, A. P.; Young, V. G.; Yang, C.; Kuczera, K.; Hendrich, M. P.; Borovik, A. S. O<sub>2</sub> Activation by Nonheme Iron Complexes: A Monomeric Fe(III)-Oxo Complex Derived From O<sub>2</sub>. *Science* **2000**, *289* (5481), pp 938–941. DOI: 10.1126/science.289.5481.938.
- (8) MacBeth, C. E.; Gupta, R.; Mitchell-Koch, K. R.; Young, V. G.; Lushington, G. H.; Thompson, W. H.; Hendrich, M. P.; Borovik, A. S. Utilization of Hydrogen Bonds To Stabilize M–O(H) Units: Synthesis and Properties of Monomeric Iron and Manganese Complexes with Terminal Oxo and Hydroxo Ligands. *J. Am. Chem. Soc.* **2004**, *126* (8), pp 2556–2567. DOI: 10.1021/ja0305151.
- (9) Goetz, M. K.; Hill, E. A.; Filatov, A. S.; Anderson, J. S. Isolation of a Terminal Co(III)-Oxo Complex. *J. Am. Chem. Soc.* **2018**, *140* (41), pp 13176–13180. DOI: 10.1021/jacs.8b07399.
- (10) Mao, W.; Fehn, D.; Heinemann, F. W.; Scheurer, A.; van Gastel, M.; Jannuzzi, S. A. V.; DeBeer, S.; Munz, D.; Meyer, K. Umpolung in a Pair of Cobalt(III) Terminal Imido/Imidyl Complexes. *Angew. Chemie Int. Ed.* **2022**, *61* (36). DOI: 10.1002/anie.202206848.
- (11) Cheng, J.; Liu, J.; Leng, X.; Lohmiller, T.; Schnegg, A.; Bill, E.; Ye, S.; Deng, L. A Two-Coordinate Iron(II) Imido Complex with NHC Ligation: Synthesis, Characterization, and Its Diversified Reactivity of Nitrene Transfer and C–H Bond Activation. *Inorg. Chem.* **2019**, *58* (11), pp 7634–7644. DOI: 10.1021/acs.inorgchem.9b01147.
- (12) Keilwerth, M.; Grunwald, L.; Mao, W.; Heinemann, F. W.; Sutter, J.; Bill, E.; Meyer, K. Ligand Tailoring Toward an Air-Stable Iron(V) Nitrido Complex. *J. Am. Chem. Soc.* **2021**, *143* (3), pp 1458–1465. DOI: 10.1021/jacs.0c11141.
- (13) Zolnhofer, E. M.; Käß, M.; Khusniyarov, M. M.; Heinemann, F. W.; Maron, L.; van Gastel, M.; Bill, E.; Meyer, K. An Intermediate Cobalt(IV) Nitrido Complex and Its N-Migratory Insertion Product. *J. Am. Chem. Soc.* **2014**, *136* (42), pp 15072–15078. DOI: 10.1021/ja508144j.
- (14) Lochenie, C.; Schötz, K.; Panzer, F.; Kurz, H.; Maier, B.; Puchler, F.; Agarwal, S.; Köhler, A.; Weber, B. Spin-Crossover Iron(II) Coordination Polymer with Fluorescent Properties: Correlation between Emission Properties and Spin State. *J. Am. Chem. Soc.* **2018**, *140* (2), pp 700–709. DOI: 10.1021/jacs.7b10571.
- (15) Bogani, L.; Vindigni, A.; Sessoli, R.; Gatteschi, D. Single Chain Magnets: Where to from Here? *J. Mater. Chem.* **2008**, *18* (40), p 4750. DOI: 10.1039/b807824f.
- (16) Sikma, R. E.; Balto, K. P.; Figueroa, J. S.; Cohen, S. M. Metal–Organic Frameworks with Low-Valent Metal Nodes. *Angew. Chemie Int. Ed.* **2022**, *61* (33). DOI: 10.1002/anie.202206353.
- (17) Zadrozny, J. M.; Xiao, D. J.; Atanasov, M.; Long, G. J.; Grandjean, F.; Neese, F.; Long, J. R. Magnetic Blocking in a Linear Iron(I) Complex. *Nat. Chem.* **2013**, *5* (7), pp 577–581. DOI: 10.1038/nchem.1630.
- (18) Reiff, W. M.; LaPointe, A. M.; Witten, E. H. Virtual Free Ion Magnetism and the Absence of Jahn–Teller Distortion in a Linear Two-Coordinate Complex of High-Spin Iron(II). *J. Am. Chem. Soc.* **2004**, *126* (33), pp 10206–10207. DOI: 10.1021/ja030632w.
- (19) Reiff, W. M.; Schulz, C. E.; Whangbo, M.-H.; Seo, J. I.; Lee, Y. S.; Potratz, G. R.; Spicer, C. W.; Girolami, G. S. Consequences of a Linear Two-Coordinate Geometry for the Orbital Magnetism and

- Jahn–Teller Distortion Behavior of the High Spin Iron(II) Complex  $\text{Fe}[\text{N}(\text{t-Bu})_2]_2$ . *J. Am. Chem. Soc.* **2009**, *131* (2), pp 404–405. DOI: 10.1021/ja806660f.
- (20) Merrill, W. A.; Stich, T. A.; Brynda, M.; Yeagle, G. J.; Fettinger, J. C.; De Hont, R.; Reiff, W. M.; Schulz, C. E.; Britt, R. D.; Power, P. P. Direct Spectroscopic Observation of Large Quenching of First-Order Orbital Angular Momentum with Bending in Monomeric, Two-Coordinate Fe(II) Primary Amido Complexes and the Profound Magnetic Effects of the Absence of Jahn– and Renner–Teller Distortions In. *J. Am. Chem. Soc.* **2009**, *131* (35), pp 12693–12702. DOI: 10.1021/ja903439t.
- (21) Zadrozny, J. M.; Atanasov, M.; Bryan, A. M.; Lin, C.-Y.; Rekken, B. D.; Power, P. P.; Neese, F.; Long, J. R. Slow Magnetization Dynamics in a Series of Two-Coordinate Iron(Ii) Complexes. *Chem. Sci.* **2013**, *4* (1), pp 125–138. DOI: 10.1039/C2SC20801F.
- (22) Atanasov, M.; Zadrozny, J. M.; Long, J. R.; Neese, F. A Theoretical Analysis of Chemical Bonding, Vibronic Coupling, and Magnetic Anisotropy in Linear Iron(II) Complexes with Single-Molecule Magnet Behavior. *Chem. Sci.* **2013**, *4* (1), pp 139–156. DOI: 10.1039/C2SC21394J.
- (23) Klare, H. F. T.; Oestreich, M. Silylium Ions in Catalysis. *Dalt. Trans.* **2010**, *39* (39), pp 9176–9184. DOI: 10.1039/c003097j.
- (24) Klare, H. F. T.; Albers, L.; Süsse, L.; Keess, S.; Müller, T.; Oestreich, M. Silylium Ions: From Elusive Reactive Intermediates to Potent Catalysts. *Chem. Rev.* **2021**, *121* (10), pp 5889–5985. DOI: 10.1021/acs.chemrev.0c00855.
- (25) Schulz, A.; Villinger, A. “Tamed” Silylium Ions: Versatile in Catalysis. *Angew. Chemie Int. Ed.* **2012**, *51* (19), pp 4526–4528. DOI: 10.1002/anie.201108320.

## Summary

Faced with new global challenges, mankind experiences an unprecedented pressure for developing more sustainable and waste-effective chemical processes, which requires a high degree of reactivity control. Aside from varying conditions, chemists have come up with a number of clever ways to steer reactivity in a preferred direction. Among these are the use of elements with an incomplete electron shell, such as transition metals or main-group compounds (often in unusual oxidation states), introducing strain or charge separation (CS). The latter approach remains largely underutilised and, therefore, was chosen to be the central point of this thesis.

The current work introduces a ligand with built-in CS that allows to study its effects in the contexts of both transition metal and main-group chemistry. The novel 1,3-zwitterionic scaffold tris-skatylmethylphosphonium (TSM<sup>2-</sup>), isolated as a potassium salt TSM<sub>2</sub>PK<sub>2</sub> (**1** in *Figure 6.1*), is also the first known C<sub>3</sub>-symmetric dianionic homoscorpionate capable of metal exchange.

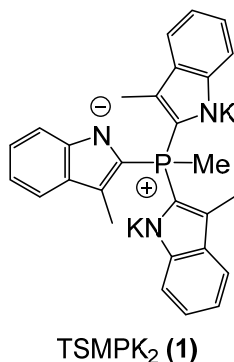


*Figure 6.1.* 1,3-Zwitterionic TSM<sub>2</sub>PK<sub>2</sub> salt (**1**).

**Chapter 1** of this thesis provides a general overview of the mechanisms through which CS may affect reactivity and physical properties. First of all, CS generates static electric fields, which may polarize neighbouring electrons, thereby influencing electronic structure and reactivity in both natural and synthetic systems. We specifically dwell on enzymatic catalysis as it illustrates in full an almost untapped potential of such electrostatic reactivity control. Secondly, CS in zwitterions stores energy, which can be used for chemical transformations or to achieve designer-made HOMO-LUMO gaps. Herein, we categorize zwitterions based on the distance between separated charges: we start with 1,1-zwitterions or elementenes (carbenes, nitrenes, silylenes etc.) that feature a negative electron lone pair and a positive vacant orbital on the same atom, and end with remote zwitterions with two and more neutral atoms between the charges. Finally, we consider catalytically-active coordination compounds, wherein the charge of the



second coordination sphere balances that on a metal, obviating the need for counterions. This greatly simplifies association behavior in solution, allowing for more systematic and straightforward catalyst design. Overall, this chapter provides a guide through the broad and somewhat abstract field of CS-induced reactivity and properties control, while also charting out possible directions in which this approach could develop.

**Chapter 2** describes the synthesis and coordination behavior of the TSM $\text{P}K_2$  salt (**1** in *Figure 6.1*). X-ray diffraction of its single crystals is consistent with the  $^1\text{H}$ ,  $^{13}\text{C}$  and  $^{31}\text{P}$  NMR measurements, and shows an expected K:P ratio of 2:1. The existence of a trianionic monocationic phosphonium salt is, to our knowledge, unprecedented. Despite a possibility of recombination between negatively charged indolides and a positively charged phosphonium atom, compound **1** is stable both in the solid state and solution.

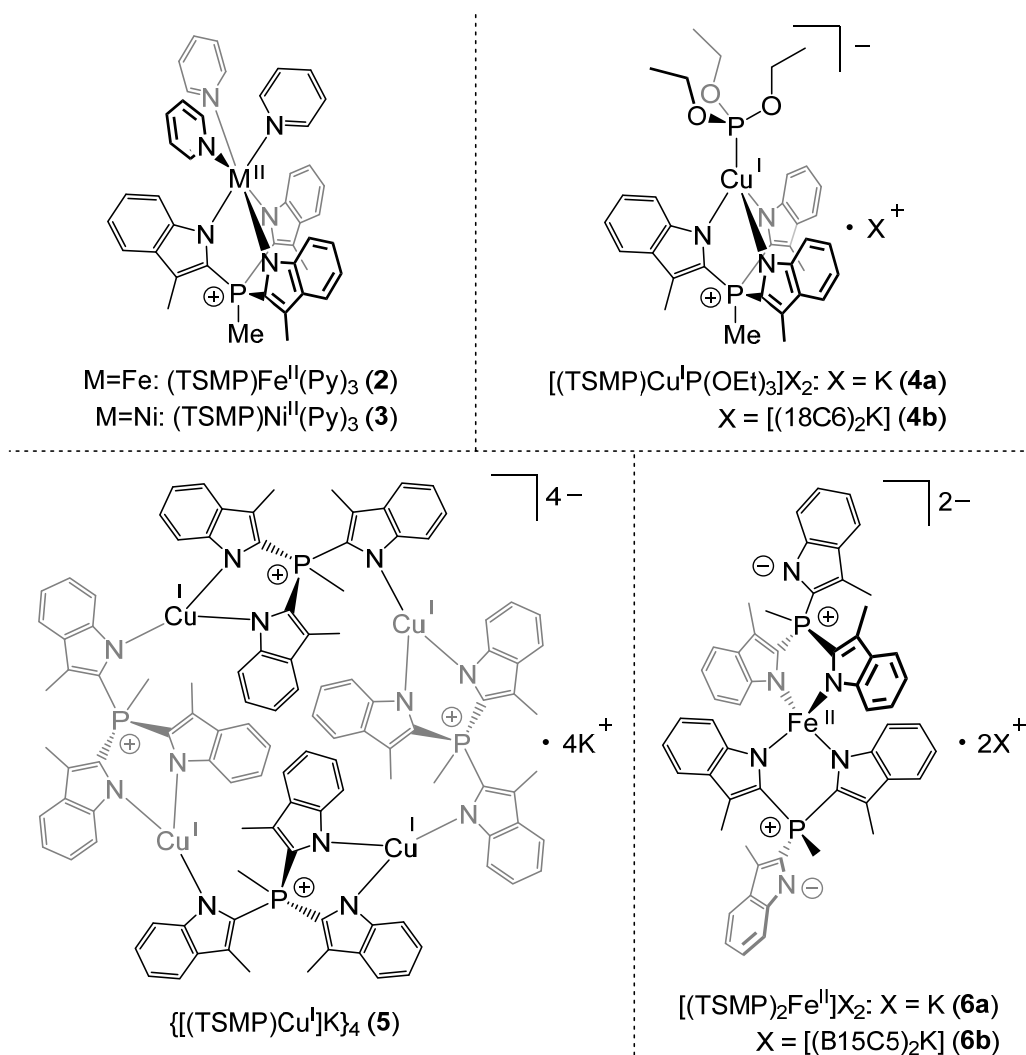


*Figure 6.2.* Various binding modes of the TSM $\text{P}^{2-}$  ligand.

Complexation of **1** with Fe(II), Ni(II) and Cu(I) salts shows diverse coordination behavior depending on the metal, stoichiometry and the presence of co-ligands (*Figure 6.2*). The expected scorpionate  $\kappa^3$  binding mode is observed in octahedral, high-spin complexes (TSMP)M<sup>II</sup>(Py)<sub>3</sub> (**2**: M=Fe,  $S = 2$ ; **3**: M=Ni,  $S = 1$ ) as well as in the tetrahedral [(TSMP)Cu<sup>I</sup>P(OEt)<sub>3</sub>]<sup>-</sup> (**4**). The bridging  $\mu^2:\kappa^2:\kappa^1$  mode is preferred with Cu(I) in the absence of a co-ligand, affording the tetrameric complex {[(TSMP)Cu<sup>I</sup>]K<sup>+</sup>}<sub>4</sub> (**5**). Finally, formal displacement of the pyridine ligands in **2** for a second equivalent of TSMP<sup>2-</sup> gives a high-spin ( $S = 2$ ) pseudotetrahedral 2:1 complex [(TSMP)<sub>2</sub>Fe<sup>II</sup>]<sup>2-</sup> (**6**) with the ligands in  $\kappa^2$  coordination mode. The reduction in coordination number is likely due to electrostatic repulsion of the negatively-charged indolides, as well as their weaker  $\pi$ -accepting character compared to pyridine.

The redox properties of the above metal complexes were probed both electrochemically (cyclic voltammetry, CV) and chemically (oxidation with 1 equiv. of Fc<sup>+</sup>BF<sub>4</sub><sup>-</sup>). Ni(II) complex **3** and Cu(I) complexes **4** and **5** show no electrochemically (quasi-)reversible behaviour. Chemical oxidation leads to insoluble or ill-defined products. The CV of mono-TSMP Fe(II) complex **2** shows several redox events, two of which are a quasi-reversible pair. Nevertheless, chemical oxidation leads, again, to an intractable mixture of products. Similarly, the CV of bis-TSMP Fe(II) complex **6** shows several events with a quasi-reversible pair. Gratifyingly, in this case chemical oxidation affords a well-defined Fe(III) complex that is further discussed in the next chapter.

Overall, the various observed coordination modes of the TSMP<sup>2-</sup> ligand demonstrate its versatility and potential for future applications. In particular, the accessibility of electrically neutral fragments in the +II oxidation state is attractive for solution phase application with first-row transition metals.

**Chapter 3** follows up on the oxidation of [(TSMP)<sub>2</sub>Fe<sup>II</sup>]<sup>2-</sup> (**6**). Reaction of the dipotassium salt [(TSMP)<sub>2</sub>Fe<sup>II</sup>]K<sub>2</sub> (**6a**) with ferrocenium or tritylium tetrafluoroborate in acetonitrile furnishes a deep-blue complex [(TSMP)<sub>2</sub>Fe<sup>III</sup>]<sup>-</sup> (**7**; *Figure 6.3*) as a potassium salt **7a**. To modify the solubility, the potassium ion can be exchanged for a tetraphenylphosphonium (**7b**) or encapsulated with two benzo-15-crown-5 ether molecules (**7c**). Further oxidation of **7b** with molecular iodine in DCM yields a moderately-soluble electroneutral complex [(TSMP)<sub>2</sub>Fe<sup>IV</sup>] (**8**; *Figure 6.3*) as a bottle-green solid. Cyclic voltammetry shows that **6-8** are electrochemically connected and can be reversibly converted into one another.

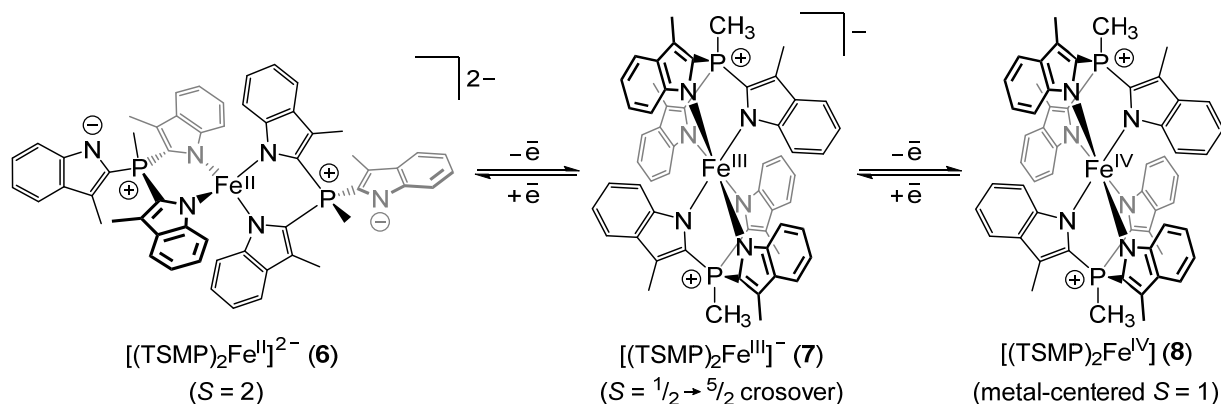


Figure 6.3. Metal complexes discussed in **Chapter 3**. Counterions are not shown for clarity.

The solid-state structures of  $[(\text{TSMP})_2\text{Fe}^{\text{III}}]^{-}$  (**7**) and  $[(\text{TSMP})_2\text{Fe}^{\text{IV}}]$  (**8**) were elucidated by single-crystal X-ray diffraction. Both **7** and **8** feature hexacoordinate iron centers with approximate octahedral symmetry. Remarkably, depending on the counter-ion, **7** can exist either in a low-spin state ( $S = 1/2$ ; **7a** and **7b**) or as a 1:1 mixture of low- and high-spin ( $S = 5/2$ ) components (**7c**), as evidenced by two different sets of Fe–N bond lengths  $\sim 0.1 \text{ \AA}$  apart. Solution  $^1\text{H}$  NMR spectra of both **7** and **8** were fully assigned and are consistent with the respective solid-state structures, wherein each compound features six paramagnetically shifted and broadened signals in accordance with  $D_{3d}$  symmetry.

The simultaneous existence of two spin states in the crystal of **7c** hinted at the possibility of spin crossover. Indeed, SQUID magnetometry of microcrystalline powder of **7a** reveals an  $S = 1/2 \rightarrow 5/2$  transition with  $T_c$  of 450 K and  $n\Delta H$  of 15.4 kJ/mol as fitted by the domain model of Sorai and Seki. The effective solution magnetic moment of **7a** measured by Evans method in  $\text{DCM-}d_2$  at variable temperature can be fitted to give  $\Delta H$  of  $18.1 \pm 1.4$  kJ/mol,  $\Delta S$  of  $73 \pm 6$  J/(mol\*K) and  $T_c$  of  $249 \pm 1$  K. While the  $T_c$  difference of  $\sim 200$  K between the solid state and solution is very high, it is known that in some cases crystal packing may lock molecules in a fixed spin state, slow down the spin transition by anticooperative effects or even prevent it from happening whatsoever. To the best of our knowledge, **7** is the first synthetic complex with an  $\text{Fe}^{\text{III}}\text{N}_6$  core that undergoes thermal spin crossover. This behavior is likely due to  $\text{TSMP}^{2-}$  being a relatively weak-field ligand because of the absence of low-lying  $\pi^*$ -orbitals in the extended aromatic systems.

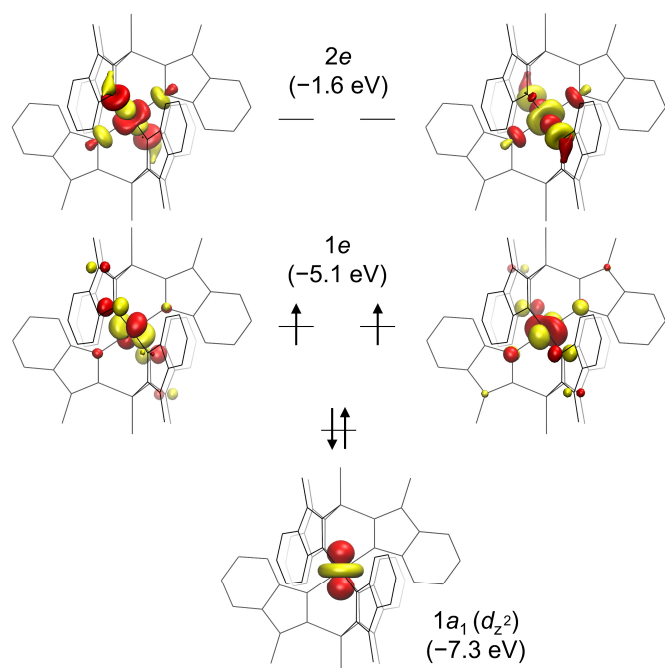


Figure 6.4. DFT-calculated quasi-restricted frontier orbitals of the ground state of **8**. Orbital energies are given in parentheses.

metal-centered character: cyclic voltammetry, Mössbauer and X-ray absorption spectroscopies. Next, we delve into the magnetic properties of the established genuine Fe(IV) center using three other techniques: Superconducting Quantum Interference Device (SQUID) magnetometry, Frequency-Domain Fourier-Transform THz-EPR spectroscopy and paramagnetic  $^1\text{H}$  NMR studies. The former two allow to establish a clear intermediate-spin ( $S = 1$ )  $^3\text{A}_2$  ground state with  $g_{\text{iso}} = 1.98$ , positive axial ZFS parameter ( $D = +19.1 \text{ cm}^{-1}$ ) and very low rhombicity ( $E \leq 0.3 \text{ cm}^{-1}$ ). Variable-temperature  $^1\text{H}$  NMR studies verify that these parameters also hold for **8** in solution.

Quantum chemical calculations support the above spectral assignments and add another level of detail to our characterization of the electronic structure of **8**. More specifically, Mössbauer spectral parameters are well reproduced by the DFT calculations for the  $S = 1$  state, which is also the least energetic one compared to the alternative singlet and quintet states. Due to molecular  $D_{3d}$  symmetry, the  $d$  energy levels have the splitting typical for the trigonally distorted environment (Figure 6.4): a pure doubly occupied  $d_{z^2}$  orbital is isolated from the rest of the  $d$ -manifold. At the same time, the mixing between the remaining  $d$ -orbitals gives rise to the  $\pi$ -antibonding  $1e$  SOMO and  $\sigma$ -antibonding  $2e$  LUMO levels.

Of note, in (Figure 6.4) the  $d_{z^2}$  orbital points at two positively-charged phosphonium atoms. DFT calculations for the isoelectronic Si-tethered analogue of **8** show that its

Oxidized iron compounds beyond Fe(III) are commonly invoked as intermediates in (biological) oxidation reactions. While there are now numerous examples of isolable Fe(IV) model compounds, only a few are devoid of strongly  $\pi$ -donating ligands, and homoleptic examples are exceedingly rare. This prompted us to conduct a detailed study of the electronic structure of  $[(\text{TSMMP})_2\text{Fe}^{\text{IV}}]$  (**8**), pertaining to which two extremes are possible: a genuine Fe(IV) compound or an Fe(III) compound with a radical on the  $\text{TSMMP}^{2-}$  scaffold.

In addition, these two states could mix, forming a multi-reference system. We use three key techniques to show that oxidation bears an exclusive

$d_{z^2}$  orbital is 0.2 eV higher in energy than in **8**, which may be due to the lack of electrostatic stabilization. Finally, CASSCF calculations for **8** yield a fairly isotropic  $g$ -tensor ( $g_{\parallel} = 2.00$ ,  $g_{\perp} = 2.04$ ,  $g_{\text{iso}} = 2.03$ ), a moderate axial ZFS parameter  $D$  of  $15.3 \text{ cm}^{-1}$  and zero rhombicity, in strong agreement with SQUID and THz-EPR measurements. This, essentially, seals the assignment of the ground-state electronic structure of **8**.

At last, we briefly touch upon the excited electronic states of **4** by means optical absorption spectroscopy. Aside from multiple  $\pi \rightarrow \pi^*$  transitions in the UV region, the compound features a moderate absorption within 480-375 nm and another strong one that, rather unusually, peaks in the near-IR region ( $\lambda_{\text{max}} = 1234 \text{ nm}$ ). TD-DFT calculations reproduce these features in good agreement with the experiment. Natural Transition Orbital (NTO) analysis shows that the former feature is mostly a mixture of  $\pi \rightarrow d_{2e}$  LMCT and  $\pi \rightarrow \pi^*$  ICT, while the latter is almost entirely  $\pi \rightarrow d_{1e}$  LMCT.

Overall, this chapter outlines a successful strategy to stabilize an Fe(IV) center, relying on a tripodal ligand combining weakly  $\pi$ -donating indolide moieties with a remote positive charge. The extensive self-consistent spectroscopic and computational data presented therein give detailed insight into the electronic structure of Fe(IV) in a high symmetry environment and will serve as a reference for the identification and characterization of such centers.

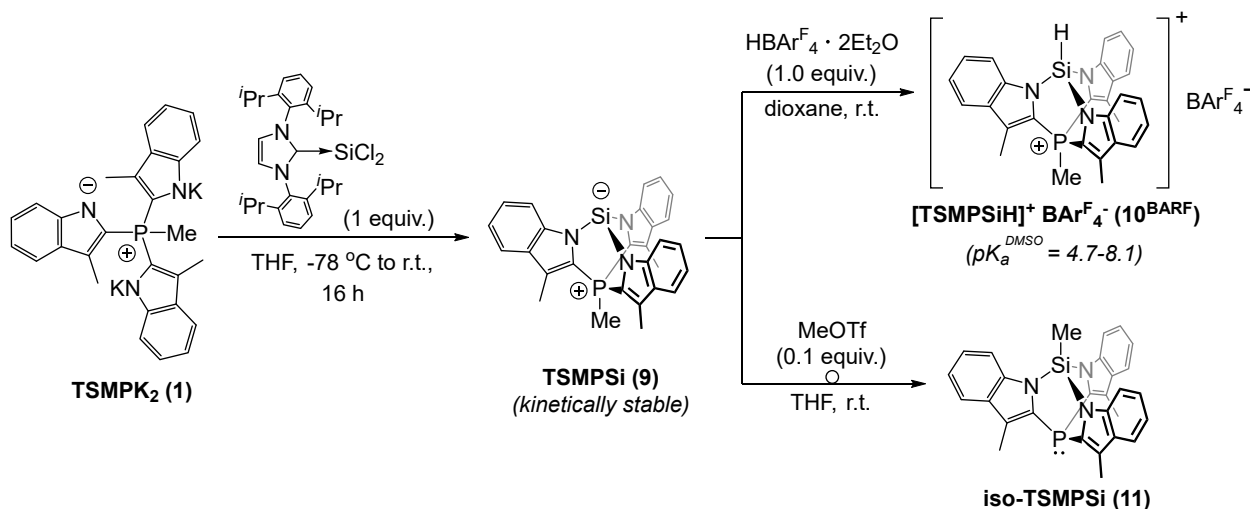


Figure 6.5. Synthesis of silanide **9** and its reactivity.

In **Chapter 4**, we investigate the ability of the  $\text{TSMPSi}^{2-}$  ligand to stabilize a negatively charged silicon atom and influence its reactivity. We exchange the potassium cations of  $\text{TSMPSi}^{2-}$  (**1**) for a silicon from an NHC-stabilized Si(II) precursor (Figure 6.5). This reaction yields a kinetically stable, isolable,  $C_3$ -symmetric, zwitterionic silanide, **TSMPSi** (**9**). The  $\text{N}^{\wedge}\text{Si}^{\wedge}\text{N}$  angles are close to  $90^{\circ}$ , which, according to Bent's rule,

indicates a high *s*-character of the anionic lone pair. This is consistent with NBO analysis, that also shows that the lone pair is localized on the silicon atom by 98.1%.

Intrigued by the possible effect of a positive phosphonium charge on acidity of protonated **9**, we attempted this reaction with 1 equiv. of  $\text{HBAr}^{\text{F}}_4 \cdot 2\text{Et}_2\text{O}$ , which yielded the  $\text{C}_3$ -symmetric cationic silane **10**<sup>BARF</sup> (Figure 6.5). According to single crystal X-ray diffraction, structural perturbations due to proton addition are mostly confined to the  $\text{SiN}_3$  fragment: the Si–N distances shorten, while the  $\text{N}^{\wedge}\text{Si}^{\wedge}\text{N}$  angles widen. This indicates an increase in strain upon protonation. At odds with the general hydridic character of silicon-bound hydrogen atoms,  $[\text{TSMPSiH}]^+$  (**10**) exhibits an exceptionally low  $\text{p}K_{\text{a}}^{\text{DMSO}}$  within 4.7–8.1, which was measured by a bracketing approach, making it more acidic than phenol, benzoic acid ( $\text{p}K_{\text{a}}^{\text{DMSO}}$  of 18.0 and 11.1, respectively) and the few silanes for which a  $\text{p}K_{\text{a}}$  was reported. While this high acidity originates in part from the electron-withdrawing effect of the substituents on silicon and overall positive charge of **10**, it is significantly enhanced by the unusually acute  $\text{N}^{\wedge}\text{Si}^{\wedge}\text{N}$  angles imposed by the TSMP scaffold. DFT calculations suggest that strain enhances the *s*-character of the Si–H bonding pair, polarizing the bond towards silicon and facilitating its heterolytic dissociation. Next to its low basicity, **9** is a relatively weak donor ligand for transition metals. This is apparent from analysis of the CO-stretching frequencies of its complexes with metal carbonyls, which places it in the vicinity of silylenes and  $\text{P}(\text{NMe}_2)_3$  rather than other silicon anions, which we also connect with strain and the influence of a positive charge.

Not only protonation of **9**, but quaternization of its Si atom in general increases the strain. This opens up a charge neutralization pathway, wherein a methyl of the opposing methylphosphonium unit can be transferred to another molecule of **9**, releasing strain and leading to phosphine/methylsilane isomer iso-TSMPSi (**11**) (Figure 6.5).

Next to its high Brønsted acidity,  $[\text{TSMPSiH}]^+$  (**10**) also behaves as a strain-release Lewis acid, coordinating a THF molecule so that the silicon atom assumes a trigonal bipyramidal geometry. This is accompanied by activation of  $\alpha$ -carbons of the THF ring, which makes it susceptible to such weak nucleophiles as highly-stabilized aromatic anions. In particular, the conjugate base TSMPSi (**9**) reacts with fluoradene (**12**) in THF to afford the linear product **13a/b** (Figure 6.6), which forms by nucleophilic ring opening of a THF molecule coordinated to **10**.

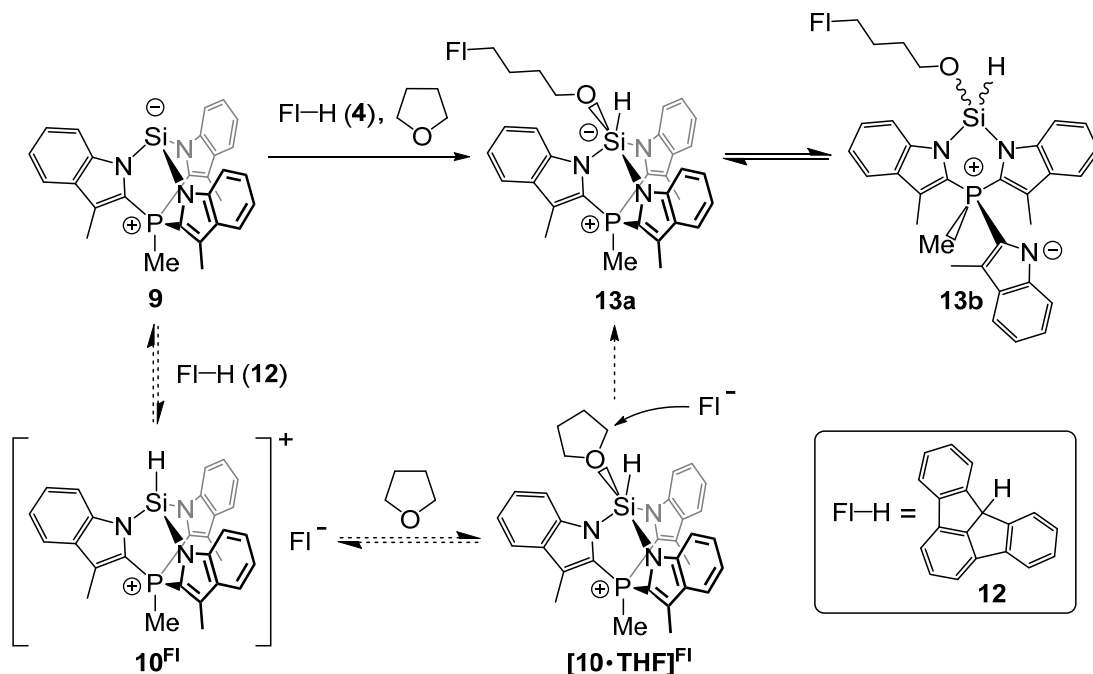


Figure 6.6. THF ring-opening with fluoradene (12). The suggested reaction mechanism is shown with dashed arrows.

In this process, the Si center sequentially acts as a nucleophile (base) and then as an electrophile (Lewis acid) to facilitate the activation of two relatively unreactive molecules, suggesting the potential of such cage compounds as biphilic main-group centers. This reaction sequence also illustrates the ability of the TSMPSi scaffold to support both the Si(II) and Si(IV) states along with the processes that interconvert them under mild conditions. Furthermore, the trigonal bipyramidal silicon center in the addition product **13a** undergoes several facile fluxional processes (positional exchange and reversible Si–N bond dissociation), illustrating the flexibility of the TSMPSi (**9**) platform in terms of accessible geometries.

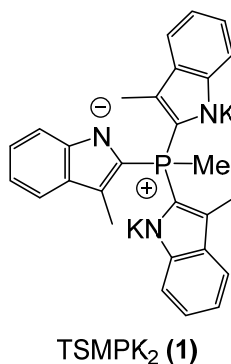
These observations collectively illustrate how a combination of charge, inductive effects and strain can significantly manipulate the properties of a Si–H bond leading to unusual reactivity. The various reactive pathways accessible to the strained cage structure  $[\text{TSMPSiH}]^+$  (**10**) suggest that this or a related platform may serve as an entry point into novel bond activation strategies based on the Si(II)/Si(IV) couple.

**Chapter 5**, the outlook, takes a bird’s-eye view on the work presented in this thesis, while also providing suggestions on the follow-up and possible improvements.

## Samenvatting

Geconfronteerd met nieuwe wereldwijde uitdagingen, ervaart de mensheid een ongekende druk om duurzamere en afval-efficiëntere chemische processen te ontwikkelen, wat een hoge mate van reactiviteitscontrole vereist. Afgezien van wisselende omstandigheden hebben chemici een aantal slimme manieren bedacht om de reactiviteit in een gewenste richting te sturen. Hiertoe behoren het gebruik van elementen met een onvolledig gevulde elektronenschil, zoals overgangsmetalen of hoofdgroepverbindingen (vaak in ongebruikelijke oxidatietoestanden), waarbij spanning of ladingsscheiding (LS) wordt geïntroduceerd. Deze laatste aanpak blijft grotendeels onderbenut en is daarom gekozen als hoofdonderwerp van dit proefschrift.

Het huidige werk introduceert een ligand met ingebouwde LS die het mogelijk maakt om de effecten ervan te bestuderen in de context van zowel overgangsmetaal- als hoofdgroepchemie. Het nieuwe 1,3-zwitterionische synthon tris-skatylmethylfosfonium ( $\text{TSMP}^{2-}$ ), geïsoleerd als het kaliumzout  $\text{TSMPK}_2$  (**1** in *Figuur 7.1*), is ook het eerste bekende  $C_3$ -symmetrische, dianionische homoscorpionaat dat in staat is tot metaaluitwisseling.



*Figuur 7.1.* Het 1,3-zwitterionische  $\text{TSMPK}_2$ -zout (**1**).

**Hoofdstuk 1** van dit proefschrift geeft een algemeen overzicht van de mechanismen waardoor LS reactiviteit en fysische eigenschappen kan beïnvloeden. Allereerst genereert LS statische elektrische velden, die naburige elektronen kunnen polariseren, waardoor de elektronische structuur en reactiviteit in zowel natuurlijke als synthetische systemen wordt beïnvloed. We staan specifiek stil bij enzymatische katalyse, omdat het het bijna onbenutte potentieel van een dergelijke controle van elektrostatische reactiviteit volledig illustreert. Ten tweede slaat LS in zwitterionen energie op, die kan worden gebruikt voor chemische transformaties of om op maat gemaakte HOMO-LUMO-gaten te realiseren. Hierin categoriseren we zwitterionen op basis van de afstand tussen gescheiden ladingen: we beginnen met 1,1-zwitterionen of elementenen (carbenen, nitrenen, silylenen enz.) die een negatief vrij elektronenpaar hebben en een

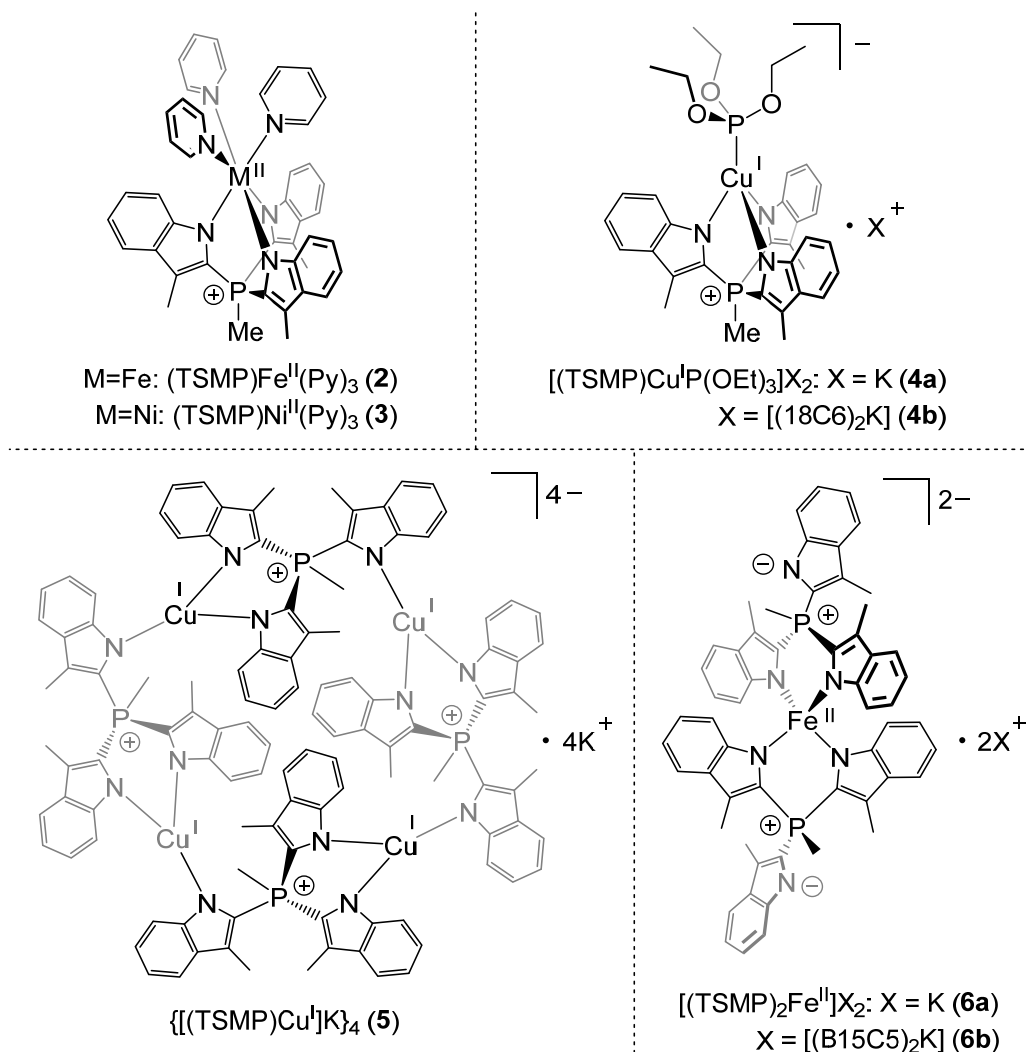


positief lege orbitaal op hetzelfde atoom, en eindigen met zwitterionen met twee en meer neutrale atomen tussen de ladingen. Ten slotte beschouwen we katalytisch actieve coördinatieverbindingen, waarbij de lading van de tweede ligandsfeer de lading van het metaal compenseert, waardoor de behoefte aan tegenionen overbodig wordt. Dit vereenvoudigt het associatiegedrag in oplossing aanzienlijk, waardoor een meer systematisch en voor de hand liggend katalysatorontwerp mogelijk is. In het algemeen biedt dit hoofdstuk een leidraad door het brede en enigszins abstracte veld van LS-geïnduceerde reactiviteit en controle van eigenschappen, terwijl het ook mogelijke richtingen in kaart brengt waarin deze benadering zich zou kunnen ontwikkelen.

**Hoofdstuk 2** beschrijft de synthese en het coördinatiegedrag van TSMPK<sub>2</sub>-zout **1** (zie *Figuur 7.1*). Röntgendiffractie van de éénkristallen komt overeen met de <sup>1</sup>H-, <sup>13</sup>C- en <sup>31</sup>P-NMR-metingen en vertoont de verwachte K:P-verhouding van 2:1. Het bestaan van een trianionisch monokationisch fosfoniumzout is, voorzover ons bekend, ongekend. Ondanks de mogelijkheid van recombinitie tussen negatief geladen indoliden en een positief geladen fosfoniumatoom, is verbinding **1** zowel in vaste toestand als in oplossing stabiel.

Complexatie van **1** met Fe(II), Ni(II) en Cu(I)-zouten vertoont divers coördinatiegedrag, afhankelijk van het metaal, de stoichiometrie en de aanwezigheid van co-liganden (*Figuur 7.2*). De verwachte κ<sup>3</sup>-bindingsmodus van het scorpionaat wordt waargenomen in octaëdrische, hoge-spin complexen (TSMP)M<sup>II</sup>(Py)<sub>3</sub> (**2**: M=Fe, S = 2; **3**: M=Ni, S = 1), evenals in het tetraëdrische complex [(TSMP)Cu<sup>I</sup>P(OEt)<sub>3</sub>]<sup>-</sup> (**4**). De bruggende μ<sup>2</sup>:κ<sup>2</sup>:κ<sup>1</sup>-modus heeft de voorkeur met Cu(I) in afwezigheid van een co-ligand, wat het tetramere complex {[(TSMP)Cu<sup>I</sup>]K}<sub>4</sub> (**5**) oplevert. Ten slotte geeft de formele vervanging van de pyridineliganden in **2** voor een tweede equivalent van TSMP<sup>2-</sup> een hoog-spin (S = 2) pseudotetraëdrisch 2:1-complex [(TSMP)<sub>2</sub>Fe<sup>II</sup>]<sup>2-</sup> (**6**) met de liganden in κ<sup>2</sup>-coördinatiemodus. De afname van het coördinatiegetal is waarschijnlijk te wijten aan elektrostatische afstoting van de negatief geladen indoliden en hun zwakkere π-accepterende karakter in vergelijking met pyridine.

De redox-eigenschappen van de bovenstaande metaalcomplexen werden zowel elektrochemisch (cyclische voltammetrie, CV) als chemisch (oxidatie met 1 equiv. Fc<sup>+</sup>BF<sub>4</sub><sup>-</sup>) onderzocht. Ni(II)-complex **3** en Cu(I)-complexen **4** en **5** vertonen geen elektrochemisch (quasi-)reversibel gedrag. Chemische oxidatie leidt tot onoplosbare of slecht gedefinieerde producten. Het CV van mono-TSMP Fe(II)-complex **2** toont verschillende redoxprocessen, waarvan er twee een quasi-reversibel paar zijn. Opnieuw leidt chemische oxidatie tot een hardnekkige mengelmoes van producten. Evenzo toont het CV van bis-TSMP Fe(II)-complex **6** verschillende redoxprocessen met een quasi-reversibel paar. Gelukkig levert chemische oxidatie in dit geval een goed gedefinieerd Fe(III)-complex op dat in het volgende hoofdstuk verder wordt besproken.

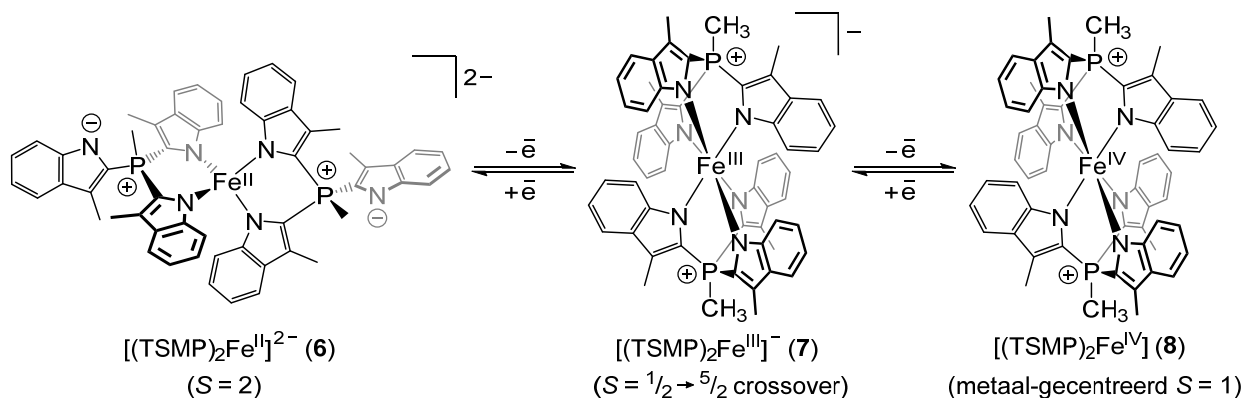


Figuur 7.2. Verschillende bindingswijzen van het TSMP<sup>2-</sup> ligand.

Over het algemeen tonen de verschillende waargenomen coördinatiemodi van het TSMP<sup>2-</sup> ligand diens veelzijdigheid en potentieel voor toekomstige toepassingen aan. Met name de toegankelijkheid van elektrisch neutrale fragmenten in de oxidatietoestand +II is aantrekkelijk voor toepassing in combinatie met eerste-rij-overgangsmetalen in oplossing.

**Hoofdstuk 3** gaat in op de oxidatie van [(TSMP)<sub>2</sub>Fe<sup>II</sup>]<sup>2-</sup> (**6**). Reactie van het dikaliumzout [(TSMP)<sub>2</sub>Fe<sup>II</sup>]K<sub>2</sub> (**6a**) met ferrocenium of trityliumtetrafluoroboraat in acetonitril levert een diepblauw complex [(TSMP)<sub>2</sub>Fe<sup>III</sup>]<sup>-</sup> (**7**; Figuur 7.3) op als kaliumzout **7a**. Om de oplosbaarheid te wijzigen, kan het kaliumion worden uitgewisseld voor een tetrafenylfosfonium-ion (**7b**) of worden ingekapseld met twee benzo-15-kroon-5-ethermoleculen (**7c**). Verdere oxidatie van **7b** met moleculair jodium in dichloormethaan levert het matig oplosbare, elektroneutrale complex [(TSMP)<sub>2</sub>Fe<sup>IV</sup>]

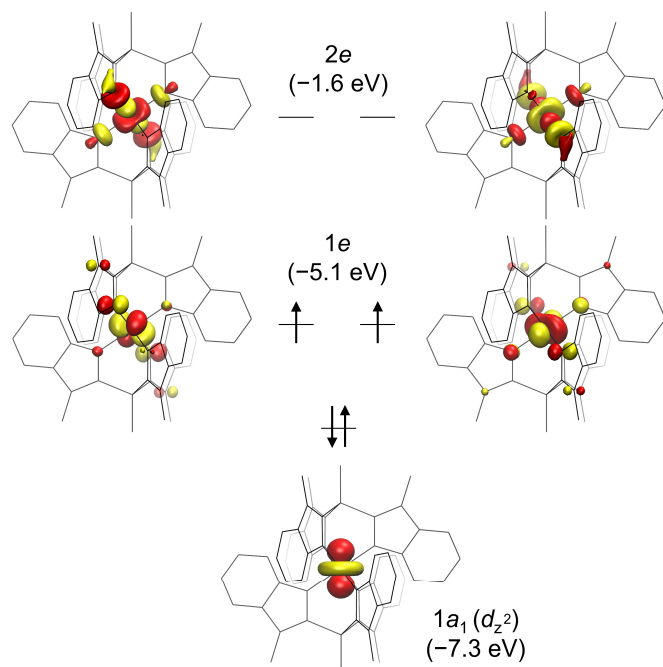
(**8**; *Figuur 7.3*) op als een flesgroene vaste stof. Cyclische voltammetrie laat zien dat **6-8** elektrochemisch verbonden zijn en reversibel in elkaar kunnen worden omgezet.



*Figuur 7.3.* Metaalcomplexen besproken in **Hoofdstuk 3**. Tegenionen zijn voor de duidelijkheid niet weergegeven.

De vaste-stofstructuren van  $[(\text{TSMP})_2\text{Fe}^{\text{III}}]^{-}$  (**7**) en  $[(\text{TSMP})_2\text{Fe}^{\text{IV}}]$  (**8**) werden opgehelderd met behulp van röntgendiffractie aan één-kristallen. Zowel **7** als **8** hebben zes-gecoördineerde ijzercentra met een bijna octaëdrische symmetrie. Opmerkelijk genoeg kan **7**, afhankelijk van het tegenion, bestaan in een toestand met lage spin ( $S = 1/2$ ; **7a** en **7b**) of als een 1:1-mengsel van lage en hoge spin ( $S = 5/2$ ) componenten (**7c**), zoals blijkt uit twee verschillende sets van Fe–N-bindingslengtes  $\sim 0,1 \text{ \AA}$  uit elkaar.  $^1\text{H}$  NMR-spectra van zowel **7** als **8** in oplossing werden volledig toegewezen en zijn consistent met de respectievelijke vastestof structuren, waarbij elke verbinding zes paramagnetisch verschoven en verbrede signalen bevat in overeenstemming met  $D_{3d}$ -symmetrie.

Het gelijktijdige bestaan van twee spintoestanden in het kristal van **7c** wees op de mogelijkheid van spin-overgang. SQUID-magnetometrie van microkristallijn poeder van **7a** onthult inderdaad een  $S = 1/2 \rightarrow 5/2$ -overgang met  $T_c = 450 \text{ K}$  en  $n\Delta H = 15,4 \text{ kJ/mol}$ , zoals gefit door het domeinmodel van Sorai en Seki. Het effectief magnetisch moment van **7a** in oplossing en gemeten met de Evans-methode in  $\text{DCM-}d_2$  bij variabele temperatuur kan worden gefit om  $\Delta H = 18,1 \pm 1,4 \text{ kJ/mol}$ ,  $\Delta S = 73 \pm 6 \text{ J/(mol} \cdot \text{K)}$  en  $T_c = 249 \pm 1 \text{ K}$  te geven. Hoewel het  $T_c$ -verschil van  $\sim 200 \text{ K}$  tussen de vaste toestand en de oplossing erg hoog is, is het bekend dat in sommige gevallen kristalpakking moleculen in een vaste spintoestand kan vergrendelen, de spinovergang kan vertragen door anticoöperatieve effecten of zelfs kan voorkomen dat het überhaupt gebeurt. Voor zover ons bekend is **7** het eerste synthetische complex met een  $\text{Fe}^{\text{III}}\text{N}_6$ -kern die thermische spin crossover gedrag vertoont. Dit gedrag is waarschijnlijk te wijten aan het feit dat  $\text{TSMP}^{2-}$  een relatief zwak-veld ligand is vanwege de afwezigheid van laaggelegen  $\pi^*$ -orbitalen in de indolfragmenten.



*Figuur 7.4.* DFT-berekende quasi-beperkte grensorbitalen van de grondtoestand **8**. Orbitale energieën staan tussen haakjes.

en een multi-referentiesysteem vormen. De drie belangrijkste technieken die we gebruikt hebben om aan te tonen dat oxidatie in **8** exclusief heeft op het metaal zijn cyclische voltammetrie, Mössbauer en röntgenabsorptiespectroscopie. Vervolgens hebben we de magnetische eigenschappen van het Fe(IV)-centrum bestudeerd met behulp van drie andere technieken: Supergeleidende Quantum Interferentie Apparaat (SQUID) magnetometrie, Frequentie-Domein Fourier-Transformatie THz-EPR spectroscopie en paramagnetische  $^1\text{H}$  NMR studies. De eerste twee maakten het mogelijk om een duidelijke intermediaire spin ( $S = 1$ )  $^3\text{A}_2$  grondtoestand met  $g_{iso} = 1.98$ , een positieve axiale nul-veldsplittings parameter ( $D = +19,1 \text{ cm}^{-1}$ ) en een zeer lage rhombiciteit ( $E \leq 0,3 \text{ cm}^{-1}$ ) vast te stellen.  $^1\text{H}$  NMR-metingen bij variabele temperatuur bevestigen dat deze parameters ook gelden voor **8** in oplossing.

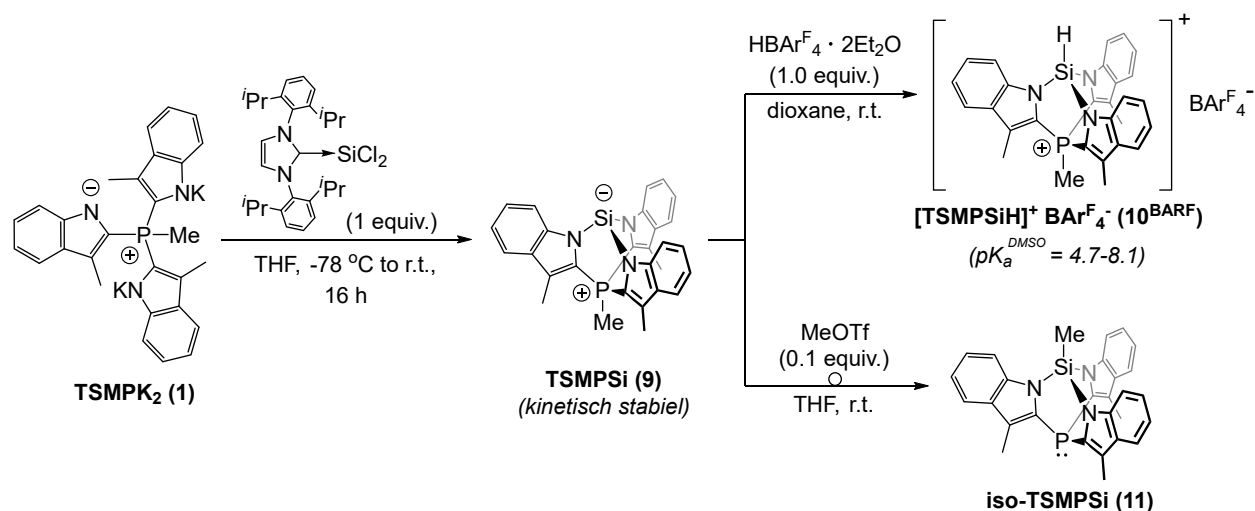
Kwantumchemische berekeningen ondersteunen bovenstaande spectrale toewijzingen en voegen een ander detailniveau toe aan onze karakterisering van de elektronische structuur van **8**. Meer specifiek worden de spectrale Mössbauer parameters goed gereproduceerd door de DFT-berekeningen voor de  $S = 1$ -toestand, die ook de laagste in energie is vergeleken met de alternatieve singlet- en kwintetstaten. Vanwege de moleculaire  $D_{3d}$ -symmetrie splitsen de  $d$ -energieniveaus op een wijze die typerend is voor de verstoorde trigonale omgeving (*Figuur 7.4*): een pure dubbelbezette  $d_{z^2}$  orbitaal is geïsoleerd van de rest van de  $d$ -orbitalen. Tegelijkertijd geeft de vermenging tussen de resterende  $d$ -orbitalen aanleiding tot de  $\pi$ -antibindende  $1e$  SOMO en  $\sigma$ -antibindende  $2e$  LUMO niveaus.

Geoxideerde ijzerverbindingen met een hogere oxidatietoestand dan Fe(III) worden vaak voorgesteld als intermediair in (biologische) oxidatiereacties. Hoewel er nu talloze voorbeelden zijn van isoleerbare Fe(IV)-modelverbindingen, zijn er maar een paar zonder sterk  $\pi$ -donerende liganden, en homoleptische voorbeelden zijn buitengewoon zeldzaam. Dit was voor ons aanleiding om een gedetailleerde studie te doen naar de elektronische structuur van  $[(\text{TSMP})_2\text{Fe}^{\text{IV}}]$  (**8**), waarbij twee uitersten mogelijk zijn: een echte Fe(IV)-verbinding of een Fe(III)-verbinding met een radicaal op het  $\text{TSMP}^{2-}$  raamwerk. Bovendien kunnen deze twee toestanden mengen

*Figuur 7.4* laat tevens zien dat het  $d_{z^2}$  orbitaal naar de tweevoudig positief geladen fosfoniumatomen wijst. DFT-berekeningen aan de iso-elektronische Si-verankerde analoog van **8** laten zien dat diens  $d_{z^2}$  orbitaal 0,2 eV hoger is in energie dan die van **8**, wat mogelijk te wijten is aan het ontbreken van elektrostatische stabilisatie. Ten slotte leveren CASSCF-berekeningen voor **8** een redelijk isotrope  $g$ -tensor op ( $g_{\parallel} = 2,00$ ,  $g_{\perp} = 2,04$ ,  $g_{iso} = 2,03$ ), een gematigde axiale ZFS-parameter  $D$  van  $15,3 \text{ cm}^{-1}$  en nul rhombiciteit, in sterke overeenstemming met de SQUID en THz-EPR-metingen. Dit concludeert in wezen de toewijzing van de elektronische grondtoestandstructuur van **8**.

Ten slotte gaan we kort in op de aangeslagen elektronische toestanden van **4** door middel van optische absorptiespectroscopie. Afgezien van meerdere  $\pi \rightarrow \pi^*$ -overgangen in het UV-gebied, toont **4** een zwakke absorptie in de 480-375 nm regio en een sterke absorptie die, nogal ongebruikelijk, piekt in het nabij-IR-gebied ( $\lambda_{\max} = 1234 \text{ nm}$ ). TD-DFT-berekeningen reproduceren deze kenmerken in goede overeenstemming met het experiment. Analyse van de Natuurlijke Overgangs Orbitalen (NTO) laat zien dat de zwakke absorptie vooral een mengsel is van  $\pi \rightarrow d_{2e}$  LMCT en  $\pi \rightarrow \pi^*$  ICT, terwijl de intense overgang bijna volledig  $\pi \rightarrow d_{1e}$  LMCT is.

Al met al schetst dit hoofdstuk een succesvolle strategie om een Fe(IV)-centrum te stabiliseren, waarbij gebruik gemaakt wordt van een tridentaat ligand dat zwak  $\pi$ -donerende indolidegroepen combineert met een gedistantieerde positieve lading. De uitgebreide en consistente spectroscopische en computationele bevindingen in het hoofdstuk geven een gedetailleerd inzicht in de elektronische structuur van Fe(IV) in een omgeving met hoge symmetrie en kunnen dienen als referentie voor de identificatie en karakterisering van soortgelijke hoog-valente metaalcentra.



*Figuur 7.5.* Synthese van silanide **9** en zijn reactiviteit.

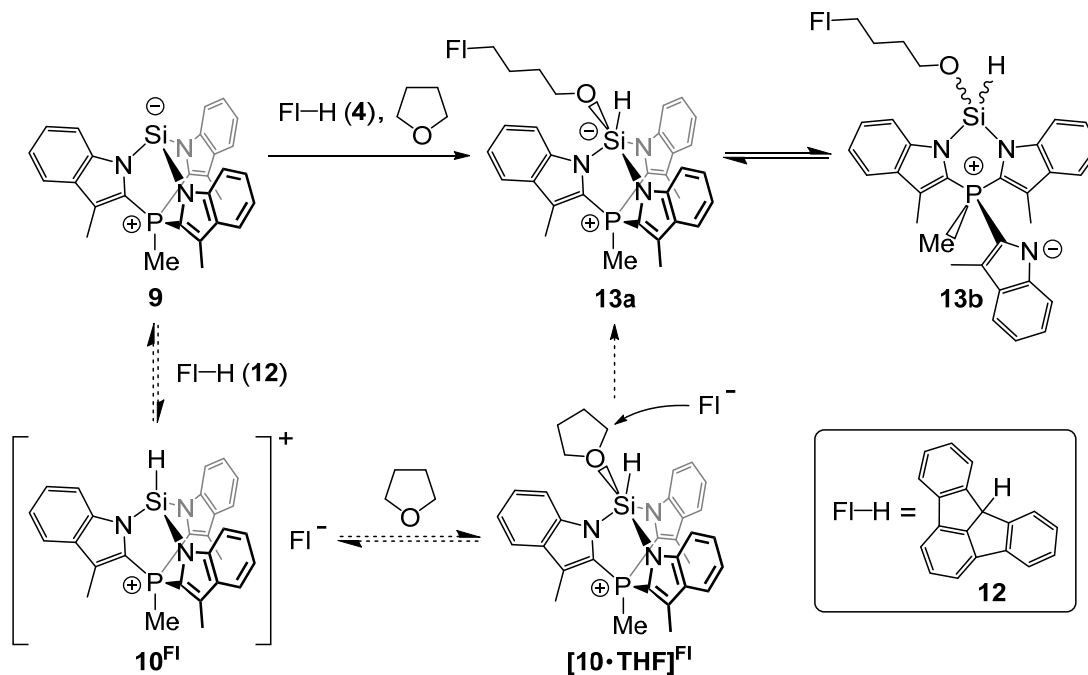
In **Hoofdstuk 4** hebben we het vermogen van de  $\text{TSMP}^{2-}$  ligand om een negatief geladen siliciumatoom te stabiliseren en zijn reactiviteit te beïnvloeden onderzocht. Uitwisseling van de kaliumkationen van  $\text{TSMPK}_2$  (**1**) voor een silicium-atoom van een NHC-gestabiliseerde Si(II)-precursorlevert het kinetisch stabiele en isoleerbare,  $C_3$ -symmetrisch en zwitterionisch silanide  $\text{TSMPSi}$  (**9**) op (*Figuur 7.5*). De  $\text{N}^{\wedge}\text{Si}^{\wedge}\text{N}$ -hoeken in **9** zijn bijna  $90^\circ$ , wat volgens de regel van Bent wijst op een hoog  $s$ -karakter van het anionische elektronenpaar. Dit komt overeen met NBO-analyse, die ook laat zien dat het elektronenpaar voor 98,1% op het siliciumatoom is gelokaliseerd.

Geïnteriseerd door het mogelijke effect van een positieve fosfoniumlading op de zuurtegraad van geprotoneerd **9**, hebben we het  $C_3$ -symmetrische kationische silaan  $\mathbf{10}^{\text{BARF}}$  gesynthetiseerd door de reactie van **9** met 1 equiv.  $\text{HBAr}^{\text{F}_4} \cdot 2\text{Et}_2\text{O}$  (*Figuur 7.5*). De kristalstructuur van **10** laat zien dat structurele verstoringen als gevolg van de protonering op silicium zich vooral beperken tot het  $\text{SiN}_3$ -fragment: de Si–N-afstanden worden korter, terwijl de  $\text{N}^{\wedge}\text{Si}^{\wedge}\text{N}$ -hoeken groter worden. Dit laatste duidt op een toename van de ringspanning bij protonering. In strijd met het algemene hydridische karakter van aan silicium gebonden waterstofatomen, vertoont  $[\text{TSMPSiH}]^+$  (**10**) een uitzonderlijk lage  $\text{p}K_a^{\text{DMSO}}$  tussen 4,7-8,1, die werd gemeten met een bracketingbenadering. Dit maakt **10** zuurder dan fenol, benzoëzuur ( $\text{p}K_a^{\text{DMSO}}$  van respectievelijk 18,0 en 11,1) en de weinige silanen waarvoor een  $\text{p}K_a$  is gerapporteerd. Hoewel deze hoge zuurtegraad gedeeltelijk afkomstig is van het elektronenonttrekkend effect van de substituenten op silicium en de algehele positieve lading van **10**, wordt deze aanzienlijk versterkt door de ongewoon kleine  $\text{N}^{\wedge}\text{Si}^{\wedge}\text{N}$ -hoeken die worden opgelegd door het TSMP-raamwerk. DFT-berekeningen suggereren dat ringspanning het  $s$ -karakter van het Si–H-bindingspaar verhoogt, de binding naar silicium polariseert en de heterolytische dissociatie ervan vergemakkelijkt. Naast zijn lage basiciteit is **9** een relatief zwak donorligand voor overgangsmetalen. Dit blijkt uit de analyse van de CO-strekkfrequenties van diens complexen met metaalcarbonylen, waardoor het in de buurt van silylenen en  $\text{P}(\text{NMe}_2)_3$  komt te liggen in plaats van andere siliciumanionen, hetgeen we ook in verband brengen met de ringspanning en de invloed van een positieve lading.

Niet alleen protonering van **9**, maar quaternisering van het Si-atoom in het algemeen verhoogt de ringspanning. Dit opent een pad voor ladingsneutralisatie, waarbij een methyl van de tegengestelde methylfosfonium-eenheid kan worden verplaatst naar een ander molecuul van **9**, waardoor ringspanning afneemt en wat leidt tot het fosfine/methylsilaan-isomeer iso- $\text{TSMPSi}$  (**11**) (*Figuur 7.5*).

Naast zijn hoge Brønsted-zuurtegraad, gedraagt  $[\text{TSMPSiH}]^+$  (**10**) zich ook als een Lewis-zuur, dat een THF-molecuul coördineert zodat het siliciumatoom een trigonale bipyramidale geometrie aanneemt wat de ringspanning verlaagt. De coordinatie gaat gepaard met activering van  $\alpha$ -koolstoffen van de THF-ring, waardoor deze vatbaar

wordt voor zwakke nucleofielen zoals zeer gestabiliseerde aromatische anionen. In het bijzonder reageert de geconjugeerde base TSMPSi (**9**) met fluoradeen (**12**) in THF om het lineaire product **13a/b** (Figuur 7.6) op te leveren, dat wordt gevormd door nucleofiele ringopening van een THF-molecuul gecoördineerd aan **10**.



Figuur 7.6. THF-ringopening met fluoradeen (**12**). Het voorgestelde reactiemechanisme wordt weergegeven met gestippelde pijlen.

In dit proces fungeert het Si-centrum achtereenvolgens als een nucleofiel (base) en vervolgens als een elektrofiel (Lewis-zuur) om de activering van twee relatief niet-reactieve moleculen te vergemakkelijken, wat het potentieel van dergelijke kooiverbindingen als bifiele hoofdgroepcentra suggereert. Deze reactievolgorde illustreert ook het vermogen van het TSMPSi-platform om zowel de Si(II)- als Si(IV)-toestanden te ondersteunen, samen met de processen die deze onder milde omstandigheden in elkaar omzetten. Bovendien ondergaat het trigonale bipyramidale siliciumcentrum in het additieproduct **13a** gemakkelijk verschillende fluxionele processen (positionele uitwisseling en reversibele Si–N-bindingsdissociatie), wat de flexibiliteit van het TSMPSi (**9**) platform illustreert in termen van toegankelijke geometrieën.

Tezamen illustreren deze waarnemingen hoe een combinatie van lading, inductieve effecten en spanning de eigenschappen van een Si–H-binding aanzienlijk kan manipuleren, wat leidt tot ongebruikelijke reactiviteit. De verschillende reactiepaden die toegankelijk zijn voor de gespannen kooistructuur  $[\text{TSMPSiH}]^+$  (**10**) suggereren dat

deze, of een gerelateerd platform, kan dienen als uitgangspunt voor nieuwe bindingsactiveringsstrategieën op basis van het Si(II)/Si(IV)-koppel.

Tenslotte geeft **Hoofdstuk 5** een overzicht van het werk dat in dit proefschrift wordt gepresenteerd, en biedt het een perspectief op het vervolg van dit werk en mogelijke verdere ontwikkelingen hierop.





## Acknowledgements

Dear reader,

As you are holding this thesis – either to read it in full, or a particular piece, or even this last deeply personal section – you are the first one I would like to express my gratitude to.

This whole work has been a rollercoaster of emotion, challenge and (self-)discovery. Thousands of hours spent in the lab and at my laptop, hundreds of experiments and spectral measurements, dozens of meetings and research stays, and only a fraction of this work made its way into the final thesis. Paradoxically, this book is not where the main product of all this time and effort can be found. Instead, he is writing this section right now, trying to comprehend what happened over these years and how it changed him. Looking back, it has been an intense exercise in perseverance and resistance to repetitive failure with often vague and hard-to-formulate problems that needed to be approached scientifically. Frequently, it was necessary to make conclusions based on very limited data or to independently master entirely new fields that were beyond the scope of my education. Lastly, under the gravity of impossible life circumstances, putting this book together took half as much time as all the experimental work. Yet in retrospect, all these twists and turns were necessary for me to become my present self.

None of this work would have been possible without my supervisor, **Dr. Marc-Etienne Moret**, and his kindness, encouragement and support. Thank you, Marc-Etienne, for sharing your advice, encyclopedic knowledge and a level-headed perspective on things. Thank you for giving me plenty of room to satisfy my curiosity, while also being on board with these endeavors. Finally, thank you for always having time for me and stepping in to help when necessary. You are one of the most intelligent people I know and one of the very few with whom I can have honest, abstract and outright weird discussions (work-related or else) without it feeling weird. It was a privilege being your student!

I would also like to express my gratitude to my promoter, **Prof. Dr. Robertus J. M. Klein Gebbink**. Bert, thank you for the final touch on my chapters: your attention to detail and general suggestions helped me improve my thesis a great deal. I also appreciated your input during group meetings and work discussions, which warranted success in several key parts of my projects. Finally, thank you for realistic career advice and sharing your experience on how to navigate myself through bureaucratic procedures. It was a pleasure working with you!

**Dr. Milka H. M. Westbeek**, I am not even sure where to start expressing my gratitude. I got to know you as an energetic and somewhat quirky group secretary, but you turned out to be so much more than that. You stepped in at a turning point of my PhD, and, surely, I would not have made it this far without you. Your strength, optimism, unconditional acceptance of others and willingness to keep on fighting despite all odds have made you my role model! Sometimes I think that I want to be like you when I finally grow up.

I wish to thank **Dr. Martin Lutz**. Martin, a lot of my work simply would not be if it were not for your X-ray crystallography. Your data was a shining beacon amidst the dark ocean of experimental uncertainty, and every structure from you was a cause for celebration. I can

rightfully call you the overlord of infinite order. Separate thanks for your calm and professional demeanor!

A big thanks goes to **Prof. Dr. Gerard van Koten** for his insightful advice on some of my work, although it is a shame we never had a chance to talk in person. **Dr. Daniël L. J. Broere** is also acknowledged for his constructive feedback and suggestions, especially on the main-group chemistry.

**Dr. Emily Monkcom**, a loyal friend and companion throughout my entire PhD journey. You were the closest person to family one could have at a workplace. Thank you for being there for me, be it lending your credit card (my sugar momma!), helping me move, correcting my English, travelling together to conferences and summer schools or even sitting next to one another in silence after a fourteen-hour long workday. I will fondly remember our dinners, midnight bike rides, trips to tulip fields, meme exchange and extended complaint sessions. Also, thanks for the graphical abstract for the silicon paper and thesis formatting template, which I have shamelessly stolen. Now that you are finally free, I hope that your life will fall into balance once again!

A big appreciation goes to **Dr. Johann T. B. H. Jastrzebski** and **Dr. Thomas N. Ran**. Many thanks for having kept the labs running! Despite most of your work occurring in the background, it was still very much valued. Johann, thank you for all the help with NMR measurements and entertaining stories you have told. As far as I am concerned, you were not a part of the OCC, you were the OCC. Thomas, your help with ESI-MS measurements and VMD was much appreciated, as well as tolerating all my weird orders and requests. I still must ask this one last question: there is nothing wrong but where is the fire extinguisher?

**Dr. Léon Witteman**, thanks for mentoring me in the first months of my time at the OCC as well as sharing your computational chemistry and technical NMR expertise. I am also grateful to you and **Sharon Witteman** for help with housing when I ended up in a difficult situation, it saved me a lot of trouble. The latter also applies to you, **Dr. Jacco Hoekstra**. I had a lot of fun being your *flatmate*. Our meme exchange was at times more productive than my writing process. Sorry for the trash bin and birds are not real! **Dr. Alessio Orsino**, you kept me company during weekends, late evenings and overnight experiments in the lab. I will warmly remember our honest and profound conversations about life and how we ended up where we were.

**Luke Riddell**, thank you for keeping me company during the end of my PhD and post-doc times, for all the memes, pseudo-Lovecraftian humor, countless bike rides and cheese dates! I hope in the end your PhD will go smoother than mine.

**Errikos Kounalis, Maartje Otten, Roel Bienenmann, Cody van Beek, Fanshi Li, Sander de Vos, Martine Tiddens** and **Stas Melnikov**, thank you, guys, for having been good and social colleagues one can rely on. Errikos and Maartje, separate kudos to you for helping with translating my summary into Dutch.

**Daniël de Bruin** and **Yuri Damen**, thank you for being my students. Having you around added color to my time as a PhD and helped me decide on the future course of my work. Daniël, I appreciate the strong bond and exchange of favors that we had when we both were going

through tough times. Yuri, in addition to your intelligence, you were a never-ending source of randomness, which made it very pleasant to have you around!

**Silvia Benschop**, thank you for keeping the group administration in check! I felt I could always rely on you.

Aside from names mentioned in the acknowledgements to each experimental chapter, I would like to thank the following people for their advice and support: **Dr. Andrea Darù** / **Dr. Jeremy Harvey** / **Dr. Tetiana Sergeieva** (computational chemistry), **Dr. Pradip Ghosh** (electrochemistry), **Svetlana Belitser** (fitting and statistical treatment of data), **Charl Riemersma** / **Anne-miek de Vries** / **Olga Novak** / **Dr. Emily Monkcom** / **Roel Bienenmann** / **Martine Tiddens** (graphic design). And, of course, thanks to the rest of the OCC group for the working atmosphere!

Last but not least, I would like to give my sincere thanks to my family for their support and encouragement. Мама, повзрослев, я вижу как ответственно ты подошла к моему воспитанию, насколько хорошее у меня было детство и какой ценой это вам с бабушкой досталось. Спасибо, за всё, что ты для меня делала, что стойчески выслушивала моё нытьё все эти годы, пытаясь меня приободрить. Ты самый близкий мне человек на этой земле и таких, как ты больше не будет. Дедушка, хоть тебя больше нет с нами, спасибо за то, что всегда ставил семью во главе угла и делал для нас всё, что мог. Тебя очень не хватает.



## About the author

Serhii Tretiakov

born June 8, 1990 in Dnipropetrovsk, Ukraine

### Education:

- 06/2016–05/2020      PhD candidate, Marie Curie “NoNoMeCat” ITN  
Supervisor: Dr. Marc-Etienne Moret  
Promotor: Prof. Dr. Robertus J. M. Klein Gebbink  
Utrecht University, Utrecht (the Netherlands)
- 11/2014–03/2015      BASF "Explore Together" Research Intern – Polymer Chemistry  
Supervisor: Dr. Hoang Trang Tran-Thien  
BASF Auxiliary Chemicals Co. Ltd, Shanghai (China)
- 10/2012–08/2014      Joint Chemistry Euromaster® of Science – Spectroscopy and Synthesis  
Master Program: "Advanced Spectroscopy in Chemistry"  
Leipzig University (Germany) and University of Bergen (Norway)  
MSc project: “Towards a Synthesis of the Marine Alkaloid Naamidine B”  
Supervisor: Prof. Dr. Hans-René Bjørsvik
- 09/2007–06/2012      BSc and MSc in Chemistry – General, Organic and Medicinal Chemistry  
Oles Honchar Dnipropetrovsk National University, Dnipro (Ukraine)  
MSc project: “*cis*- and *trans*-Aminoalcohols of Sulfolane Family. Synthesis  
and Heterocyclization”  
Supervisor: Prof. Dr. Sergey Okovitiy

### Work experience:

- 02/2022–02/2023      Research Chemist – Process Chemistry  
Symeres B.V., Groningen (the Netherlands)
- 08/2021–02/2022      Researcher – Computational and Experimental NMR  
Supervisor: Dr. Marc-Etienne Moret  
Utrecht University, Utrecht (the Netherlands)
- 06/2020–12/2020      Postdoctoral Researcher – Analytical Chemistry of Lignin  
Supervisor: Prof. Dr. Pieter Bruijninx  
Utrecht University, Utrecht (the Netherlands)  
(in Collaboration with Avantium N.V.)

## List of publications:

- Scientific publications:*
- **Tretiakov, S.**, Witteman, L., Lutz, M., Moret, M.-E. *Angewandte Chemie*, 2020, 60 (17), 9618-9626.
  - **Tretiakov, S.**, Damen, J. A. M., Lutz, M., Moret, M.-E. (2020). *Dalton Transactions*, 2020, 49, 13549-13556. – chosen as a HOT article by the editorial team
  - Palchykov, V. A., Zarovnaya, I. S., **Tretiakov, S. V.**, Reshetnyak, A. V., Omelchenko, I. V., Shishkin, O. V., & Okovytyy, S. I. *Journal of Molecular Structure*, 2018, 1157, 149–158.
  - Gaponov, A. A., Zlenko, E. T., Shishkina, S. V., Shishkin, O. V., Antypenko, O. M., **Tretiakov, S. V.**, & Palchikov, V. A. *Medicinal Chemistry Research*, 2016, 1–13.
  - Kas'yan, L.I., Prid'ma, S.A., Pal'chikov, V.A., Kas'yan, A.O., Turov, A.V., Tokar', A.V. and **Tret'yakov, S.V.** *Russian Journal of Organic Chemistry*, 2010, 46 (5), 637-643.
  - Kas'yan, L.I., Prid'ma, S.A., Karat, L D., Palchikov, V.A., **Tretiakov, S.V.** *Problems of Chemistry and Chemical Technology*, 2010, 1, 9-16.
- Patents:*
- Zarovna, I.S.; **Tretiakov, S.V.**; Palchykov, V.O. Synthesis of *trans*-4-hydroxytetrahydrothiophene-3-sulfonylchloride-1,1-dioxide. UA Patent 92891 U, March 31, 2014.

## Honors and awards:

- Member of BASF European Talent Pool (2015)
- Erasmus Mundus Scholarship (2012-2014)
- Viktor Pinchuk “Zavtra.UA” Foundation scholarship (awarded twice: in 2011 and 2012)
- 1<sup>st</sup> prize at the Ukrainian competition of student research works in natural sciences and engineering (March 2011)
- Scholarship of the President of Ukraine (first term of academic year 2010/2011)
- M.S. Hrushevskiy scholarship (second term of academic year 2009/2010)
- Prize-winner at the Chemical Olympiad at Dnipropetrovsk National University (2009/2010)
- Dnipropetrovsk National University Academic Council scholarship (second term of academic year 2008/2009)
- Prize-winner of the Youth Academy of Sciences (2006/2007)

---

## **Appendices**

---





# Appendix A

## Supporting Information to Chapter 2

**Appendix A1.**  $^1\text{H}$ - $^{31}\text{P}$  ASAPHMQC spectrum of tris-2-(*N*-Boc-skatyl)methylphosphonium iodide (**5**) in  $\text{DCM-}d_2$  (Figure A1.1). Peaks labelled as **A** and **B** belong to tris-*exo* (**5a**) and bis-*exo*-mono-*endo* (**5b**) rotamers, correspondingly.

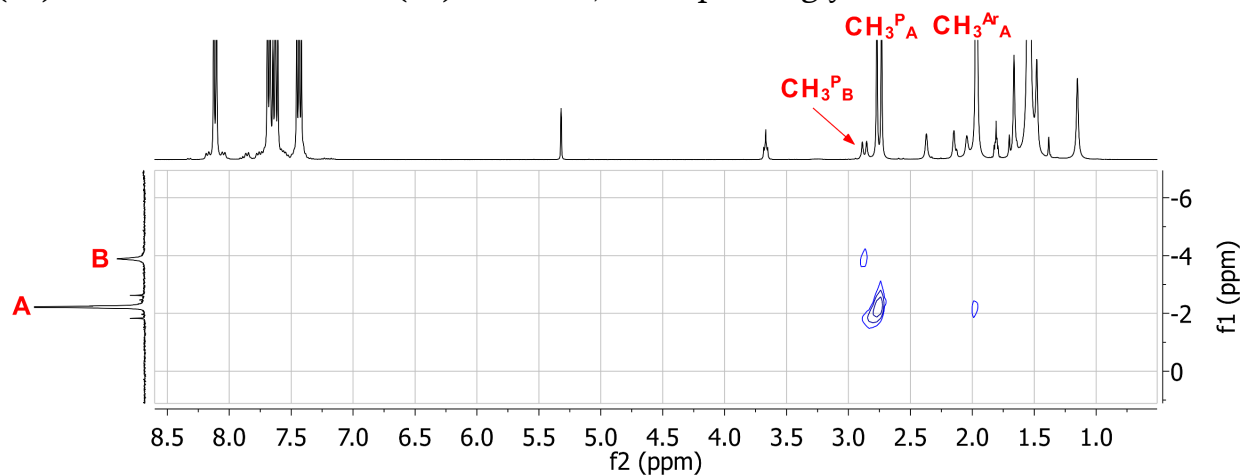


Figure A1.1.  $^1\text{H}$ - $^{31}\text{P}$  ASAPHMQC spectrum of **5** in  $\text{DCM-}d_2$ .

**Appendix A2.**  $^1\text{H}$  NMR spectra (400 MHz) of complex **8** in acetonitrile- $d_3$  (Figure A2.1) before and after addition of 4 equiv. of  $\text{P}(\text{OEt})_3$ . Note that the addition provides a spectrum with higher symmetry.

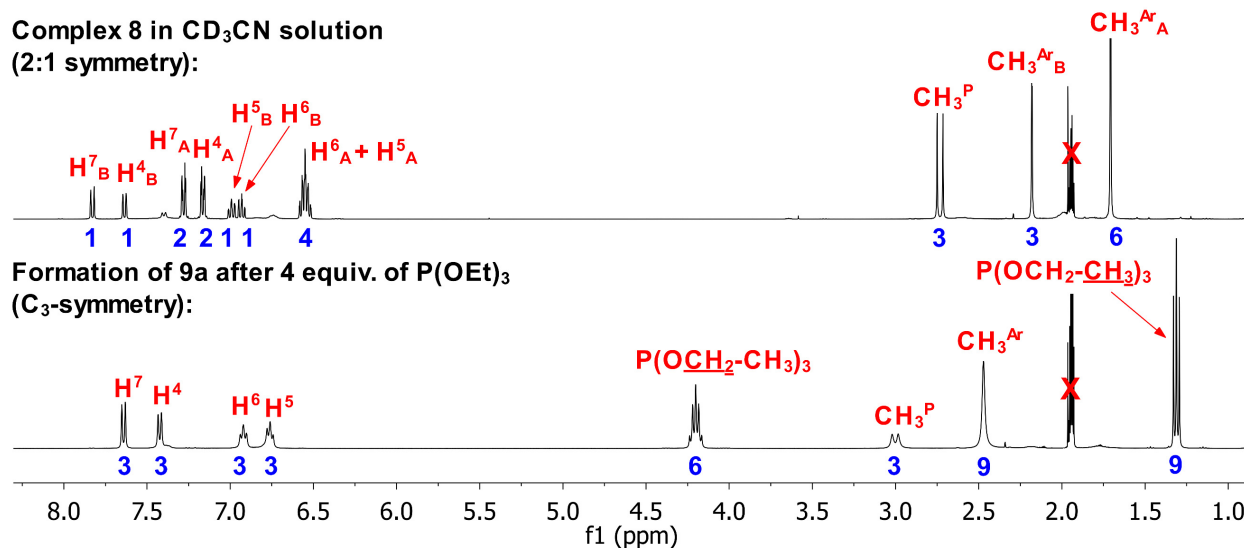


Figure A2.1.  $^1\text{H}$  NMR spectrum of **8** in acetonitrile- $d_3$  at 25 °C before and after addition of  $\text{P}(\text{OEt})_3$ . Integral intensities shown in blue were rounded to the nearest integer.

**Appendix A3.**  $^1\text{H}$  (400 MHz) 1D NOE spectra of  $[(\text{TSMMP})\text{CuP}(\text{OEt})_3]\text{K}$  complex (**9a**) in acetonitrile- $d_3$  (Figure A3.1).

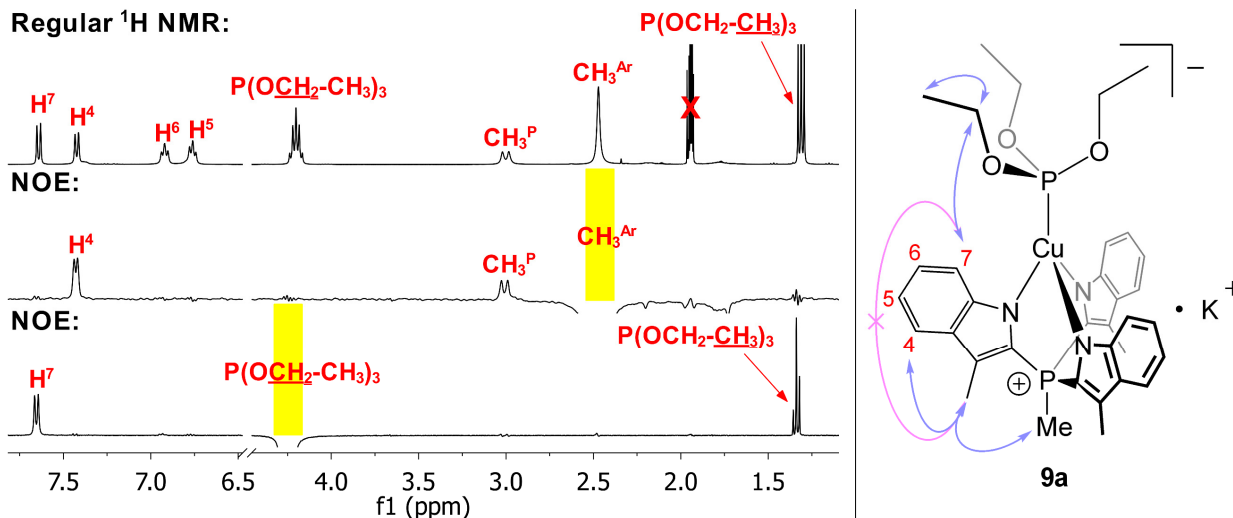


Figure A3.1. Left panel:  $^1\text{H}$  NMR (400 MHz) and 1D NOE spectra of  $[(\text{TSMMP})\text{CuP}(\text{OEt})_3]\text{K}$  complex (**9a**) in acetonitrile- $d_3$  at 25 °C. Yellow rectangles show saturation windows. Right panel: NOE correlations mapped on the structural formula of **9a**. Due to  $C_3$ -symmetry of the molecule, only the unique ones are shown. Lilac arrows indicate detected NOE correlations, a pink arrow shows a correlation that cannot be observed due to large distance between resonating protons. Nevertheless, this correlation is present in the spectra of  $\{[(\text{TSMMP})\text{Cu}]\text{K}\}_4$  (**8**) due to its oligomeric nature.

**Appendix A4.** Cyclic voltammograms (CVs) of compounds **8**, **9b** and **11**. All CVs were measured under nitrogen atmosphere using ca. 8 mM solutions of the respective complexes in 0.1 M  $n\text{Bu}_4\text{NPF}_6$  acetonitrile electrolyte. Scan rate was chosen to be 100 mV/s. Referencing was done with respect to the ferrocenium/ferrocene redox couple. The measurements always started from the open-circuit potential. After a full scan through a redox window on the electrolyte, the scan range was progressively narrowed in order to isolate all features or sets of overlapping features. Furthermore, all scans were performed in two opposite directions. In cases when the same CV profiles were obtained regardless of the scan direction, only one of the two is shown. If, within one scan, CV profiles differ from one cycle to another, all cycles are shown.

All CVs show a number of irreversible redox events (Figures A4.1-3) accompanied by precipitation of dense amorphous films on the working electrode.

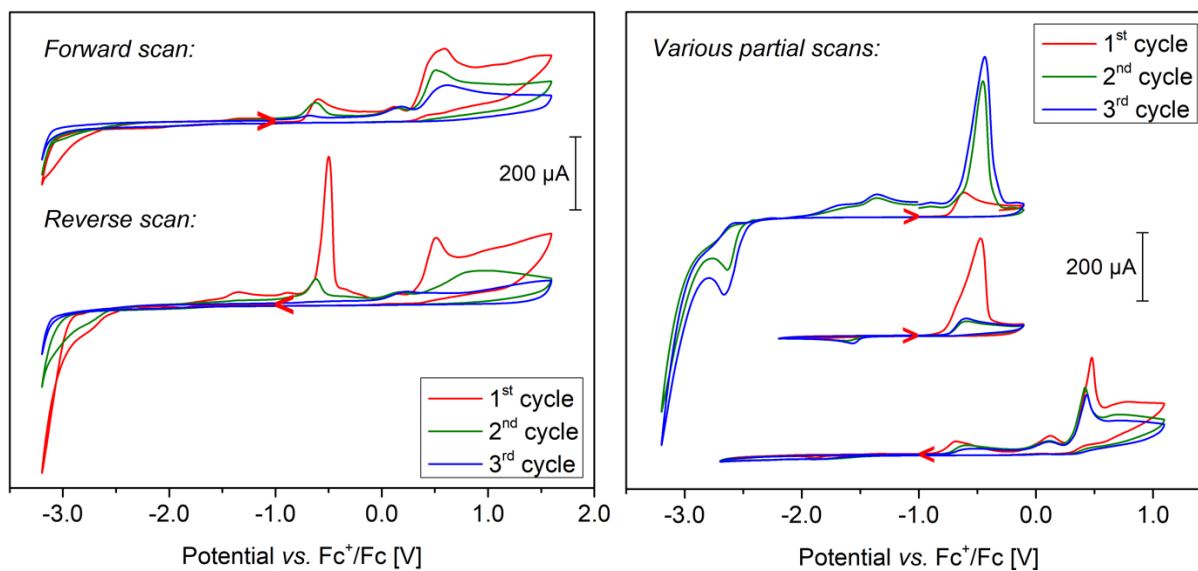


Figure A4.1. CV of compound **8**. The scans start at the open-circuit potential at  $-1.00$  V.

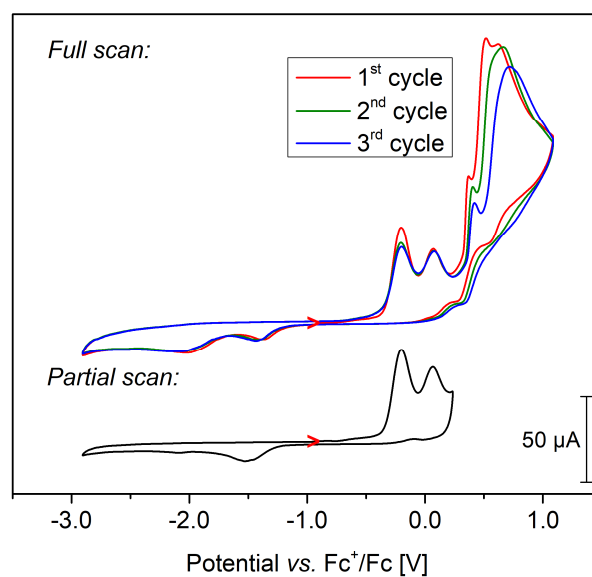


Figure A4.2. CV of compound **9b**. The scans start at the open-circuit potential at  $-900$  mV.

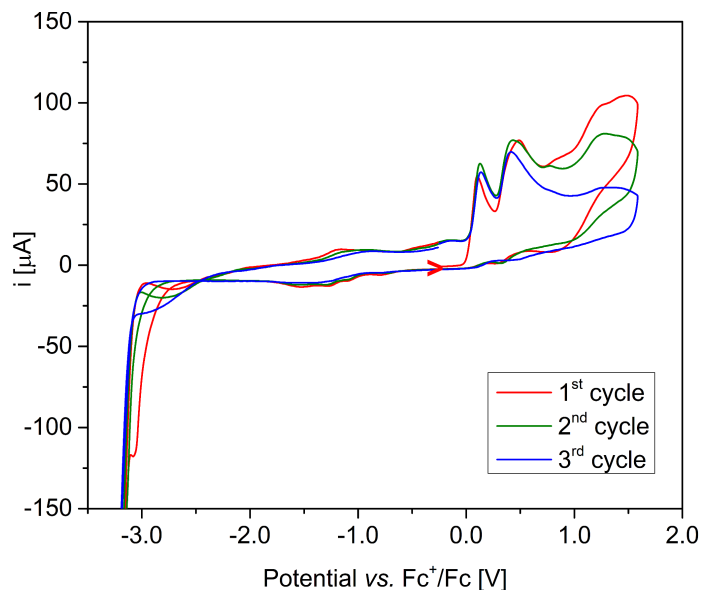


Figure A4.3. CV of compound **11**. Measurements start at the open-circuit potential of  $-250$  mV.

#### Appendix A5. Variable-temperature NMR studies of compound **12b**.

Variable-temperature  $^1\text{H}$  NMR spectra in acetonitrile- $d_3$  are shown in Figure A5.1. They feature a number of paramagnetic peaks four of which (**A-D**) are well-defined throughout most of the covered temperature range. They obey Curie's law (Figure A5.2), which excludes the possibility of spin-crossover. Note that, while paramagnetic signals generally tend to broaden at lower temperature, peaks **A** and **B** show an opposite trend. Such behaviour implies an additional source of line-broadening, which may be complex dynamics behaviour in solution.

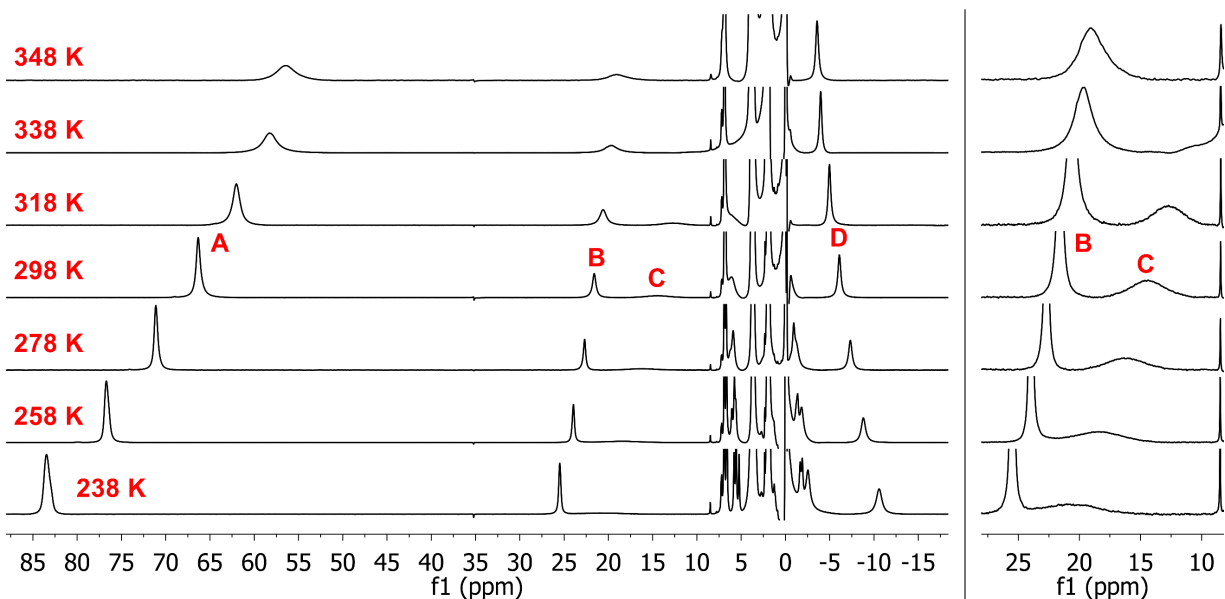
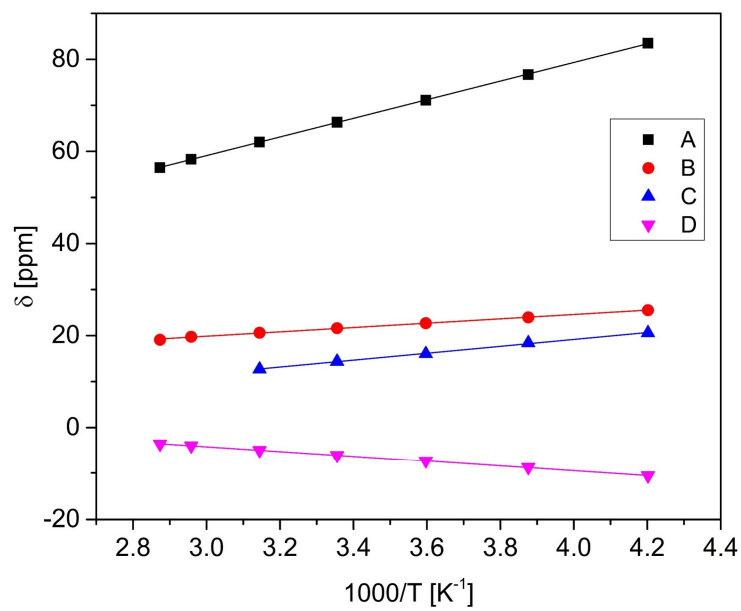


Figure A5.1. Variable-temperature  $^1\text{H}$  NMR (400 MHz) spectra of **12b** in acetonitrile- $d_3$ .



*Figure A5.2.* Linear dependence of chemical shifts vs. inverse temperature demonstrating Curie behavior. Linear fitting parameters for: **A**: Intercept:  $-1.63 \pm 0.21$ , Slope:  $20.23 \pm 0.06$ ; Adj.  $R^2$ : 0.99993; **B**: Intercept:  $5.70 \pm 0.27$ ; Slope:  $4.72 \pm 0.08$ ; Adj.  $R^2$ : 0.99779; **C**: Intercept:  $-10.84 \pm 0.43$ ; Slope:  $7.5 \pm 0.12$ ; Adj.  $R^2$ : 0.99845; **D**: Intercept:  $11.61 \pm 0.08$ ; Slope:  $-5.27 \pm 0.02$ ; Adj.  $R^2$ : 0.99985.

---

# Appendix B

## Supporting Information to Chapter 3

### Appendix B1. Cyclic voltammetry of $[(\text{TSMSP})_2\text{Fe}^{\text{III}}]\text{K}$ (**3a**).

Cyclic voltammograms (CVs) measured for the  $[(\text{TSMSP})_2\text{Fe}^{\text{II}}][(\text{B15C5})_2\text{K}]_2$  (**2b**) and  $[(\text{TSMSP})_2\text{Fe}^{\text{III}}]\text{K}$  (**3a**) salts show common features but also a few differences (*Figure B1.1*). Specifically, events **B** and **C**, which correspond to the  $[(\text{TSMSP})_2\text{Fe}^{\text{III}}]^-$  (**3**) /  $[(\text{TSMSP})_2\text{Fe}^{\text{IV}}]^0$  (**4**) redox couple, are identical for both **2b** and **3a**, and are centered at  $E_{1/2} = -0.41$  V vs.  $\text{Fc}/\text{Fc}^+$ . Similarly to **2b** (see main text), **B** and **C** in **3a** represent a quasi-reversible electron transfer<sup>1</sup> as shown by the linear dependence of peak current ( $i_p$ ) vs. square root of the scan rate ( $v^{1/2}$ ; *Figure B1.2, right panel*) and strong dependence of the peak separation on the scan rate.

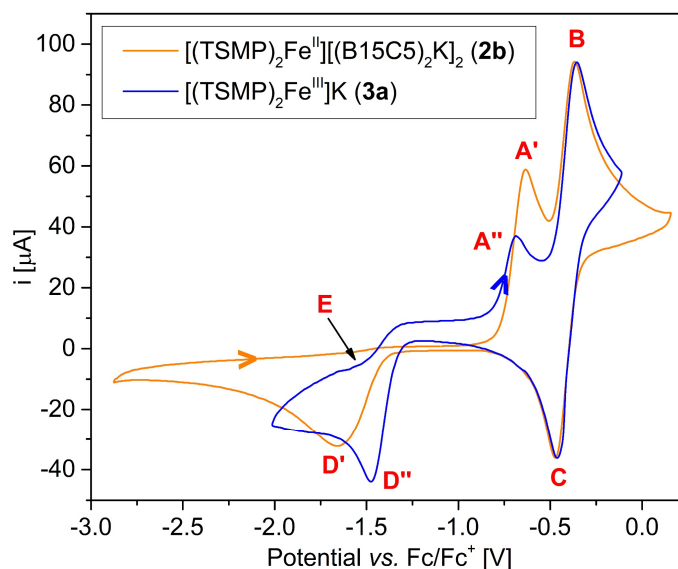


*Figure B1.1.* Overlay of CVs measured for **2b** and **3a**. The measurements were performed in ca. 8 mM solution in 0.1 M  $n\text{Bu}_4\text{NPF}_6$  acetonitrile electrolyte. Potentials are referenced with respect to  $\text{Fc}/\text{Fc}^+$  redox couple. The CV of **2b** can be repeated at least a hundred times at the rates within 25–250 mV/s with no visible changes, which implies chemical reversibility of the redox cycle it represents.

At the same time, the events associated with the  $[(\text{TSMSP})_2\text{Fe}^{\text{II}}]^{2-}$  (**2**) species, coded as **A'/A''** and **D'/D''** in *Figure B1.1*, occur at slightly different potentials for  $[(\text{TSMSP})_2\text{Fe}^{\text{III}}]\text{K}$  (**3a**) and for  $[(\text{TSMSP})_2\text{Fe}^{\text{II}}][(\text{B15C5})_2\text{K}]_2$  (**2b**). Moreover, the CV of **3a** exhibits an additional feature **E**, which can only be related to the oxidation of **2** as



shown by the reductive CV scan of **3a** (Figure B1.2, left panel). Our previous studies and, in particular, variable-temperature  $^1\text{H}$  NMR spectroscopy,<sup>2</sup> indicate that **2** exists in more than one form in solution, which may be due to oligomerization and/or an equilibrium between pseudotetrahedral and octahedral coordination modes. The reorganization energy between these forms and the octahedral solution structure of  $[(\text{TSMP})_2\text{Fe}^{\text{III}}]^-$  (**3**) (see Appendix B15) is expected to be rather large, which is consistent with the electrochemical irreversibility of events **A**, **D** and **E**. We hypothesize that this reorganization energy as well as speciation of **2** in solution are modified by ion pairing, yielding the observed potential shifts and the new feature **E** in Figure B1.1.

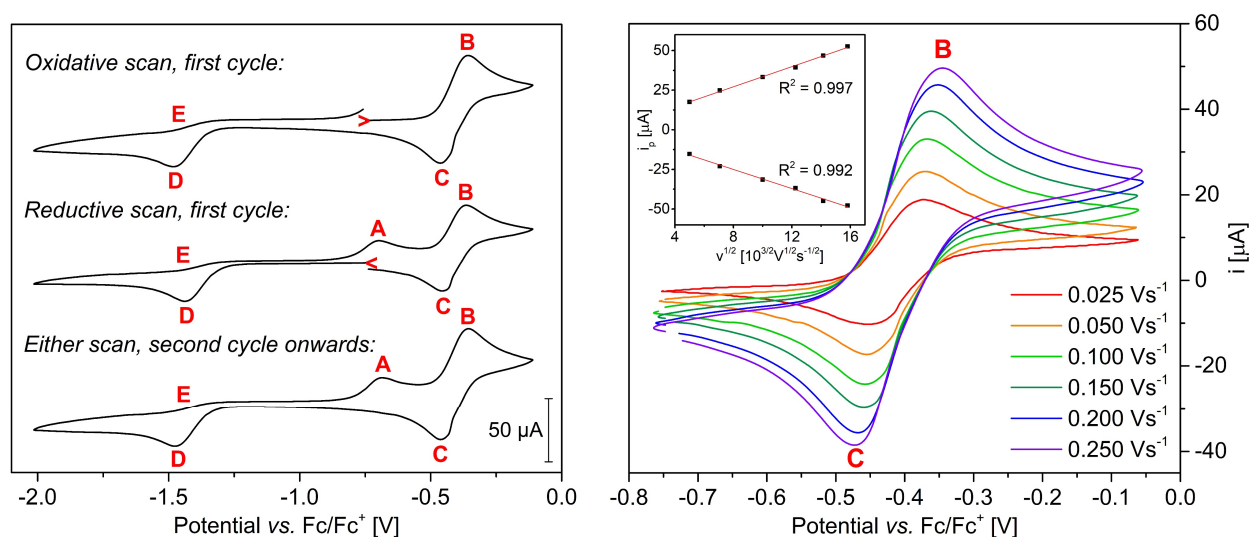


Figure B1.2. Cyclic voltammogram of compound **3a** (ca. 8 mM solution) in 0.1 M  $n\text{Bu}_4\text{NPF}_6$  acetonitrile electrolyte. Potentials are referenced with respect to  $\text{Fc}^+/\text{Fc}$  redox couple. *Left panel*: overview scans at the rate of 100 mV/s; the full scan starts from an open-circuit potential of -0.75 V). *Right panel*: a quasi-reversible redox pair **B-C** centered at  $E_{1/2} = -0.41$  V; an insert shows linear dependence of the peak current vs. square root of the scan rate.

## Appendix B2. Solution spin-crossover fit for $[(\text{TSMP})_2\text{Fe}^{\text{III}}]^-$ (**3**).

Hexacoordinate  $[(\text{TSMP})_2\text{Fe}^{\text{III}}]^-$  (**3**) complex undergoes thermal spin-crossover (SCO) in solution. It is evident from strongly temperature-dependent effective solution magnetic moment ( $\mu_{\text{eff}}$ ) as measured by Evans method.<sup>3-5</sup> The results of such measurements are shown in Figure B2.1 for potassium salt  $[(\text{TSMP})_2\text{Fe}^{\text{III}}]\text{K}$  (**3a**) in acetonitrile- $d_3$  and pyridine- $d_5$ , and for tetraphenylphosphonium salt  $[(\text{TSMP})_2\text{Fe}^{\text{III}}]\text{PPh}_4$  (**3b**) in dichloromethane- $d_2$ . Different NMR solvents were chosen to cover broader tem-

perature range; salt **3b** was used for the experiments in dichloromethane- $d_2$  because otherwise **3a** is virtually insoluble in this solvent.

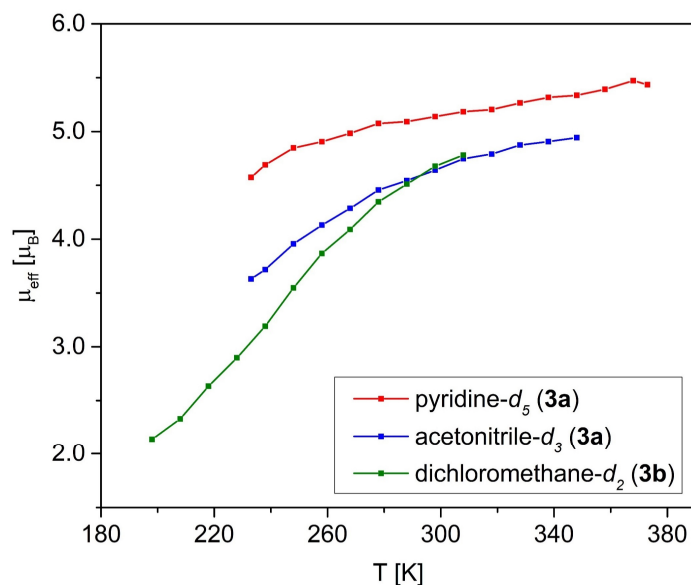
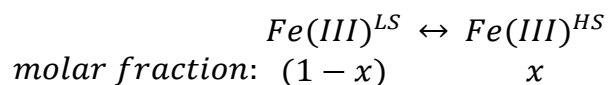


Figure B2.1. SCO curve for the  $[(\text{TSMP})_2\text{Fe}^{\text{III}}]^-$  (**3**) complex as obtained by Evans method in different solvents. Experimental datapoints are connected with straight segments for clarity. Explored temperature ranges are limited by the freezing and boiling points of the respective NMR solvents or precipitation of the compound at low temperature. Every curve is an average of four measurements.

Despite a relatively high error associated with the Evans method (5-10% depending on concentration),<sup>6</sup> the curvature of the plots as well as the absolute  $\mu_{eff}$  values show that spin-crossover of  $[(\text{TSMP})_2\text{Fe}^{\text{III}}]^-$  (**3**) in solution is solvent- and, potentially, counterion-dependent. Thus, the difference between  $\mu_{eff}$  in acetonitrile- $d_3$  and pyridine- $d_5$  is larger at 233 K than at 348 K. SCO of  $[(\text{TSMP})_2\text{Fe}^{\text{III}}]\text{K}$  (**3a**) in acetonitrile- $d_3$  and pyridine- $d_5$  cannot be compared with that of  $[(\text{TSMP})_2\text{Fe}^{\text{III}}]\text{PPh}_4$  (**3b**) in dichloromethane- $d_2$  due to a different cation and possibility of ion-pairing in low-polar dichloromethane. Nevertheless, the crossover curve for **3b** is the most informative since it spans through both low- and high- $\mu_{eff}$  regions. It is possible to fit this transition and extract its thermodynamic parameters using regressive thermodynamic analysis.

The effective magnetic moment  $\mu_{eff}$  of  $[(\text{TSMP})_2\text{Fe}^{\text{III}}]\text{PPh}_4$  (**3b**) can be expressed *via* magnetic moments of pure low- and high-spin states,  $\mu_{LS}$  and  $\mu_{HS}$  respectively, using their molar fractions:



$$\mu_{eff} = \mu_{LS} + (\mu_{HS} - \mu_{LS})x \quad \text{Eq. B2.1}$$

Molar fractions and  $\mu_{eff}$ , in turn, can be expressed *via* the crossover equilibrium constant  $K$ :

$$K = \frac{x}{1-x} \quad \text{Eq. B2.2}$$

$$\mu_{eff} = \mu_{LS} + (\mu_{HS} - \mu_{LS}) \frac{K}{1+K} \quad \text{Eq. B2.3}$$

And equilibrium constant  $K$  can be related to thermodynamics of the SCO as shown below (assuming that  $\Delta H$  and  $\Delta S$  are temperature-independent within the probed range):

$$-RT \ln K = \Delta H - T \Delta S \quad \text{Eq. B2.4}$$

$$K = \exp\left(\frac{\Delta S}{R} - \frac{\Delta H}{RT}\right) \quad \text{Eq. B2.5}$$

Rearranging the above equations gives the following regression model:

$$\mu_{eff} = \mu_{LS} + \frac{\mu_{HS} - \mu_{LS}}{1 + \exp\left(\frac{\Delta H}{RT} - \frac{\Delta S}{R}\right)} \quad \text{Eq. B2.6}$$

Due to having twelve data points, in addition to crossover enthalpy and entropy, one can also fit the limiting magnetic moments  $\mu_{LS}$  and  $\mu_{HS}$ . The fitted curve is shown in a *Figure B2.2*.

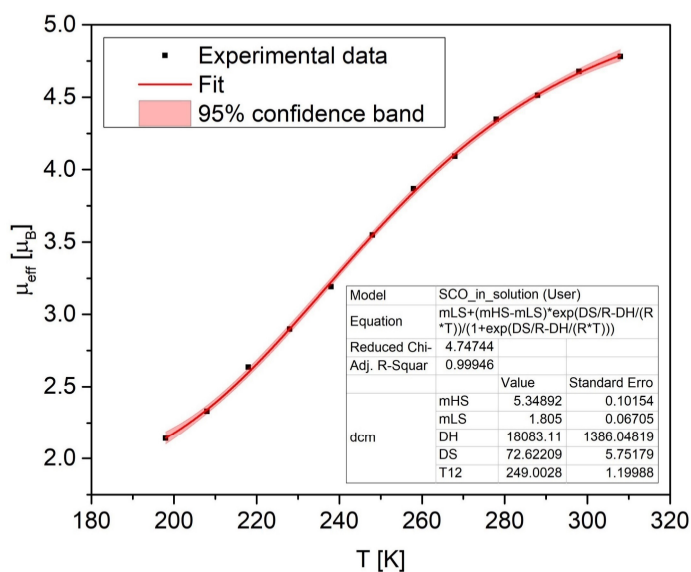


Figure B2.2. Fitted SCO of **3b** in dichloromethane- $d_2$  using regression model in Eq. B2.6.

Derived  $\Delta H$  and  $\Delta S$  are  $18.1 \pm 1.4$  kJ/mol and  $72.6 \pm 5.8$  J/(mol·K), respectively. This gives the critical temperature  $\Delta H/\Delta S = T_c$  of  $249 \pm 1$  K. The limiting magnetic moments  $\mu_{LS}$  and  $\mu_{HS}$  of  $1.81 \pm 0.07$  and  $5.35 \pm 0.10$   $\mu_B$ , respectively, are close to the spin-only expectation values for the low-spin  $S = 1/2$  ( $1.73$   $\mu_B$ ) and high-spin  $S = 5/2$  ( $5.92$   $\mu_B$ ) states.

A similar fit can be performed on the data for  $[(\text{TSMMP})_2\text{Fe}^{\text{III}}]\text{K}$  (**3a**) in acetonitrile- $d_3$ , although with higher uncertainty (Figure B2.3). Thus, while the limiting  $\mu_{HS}$  value is close to the that obtained for  $[(\text{TSMMP})_2\text{Fe}^{\text{III}}]\text{PPh}_4$  (**3b**) in dichloromethane- $d_2$  ( $5.23 \pm 0.08$  vs.  $5.35 \pm 0.10$   $\mu_B$ ), there are rather big errors associated with the lower value  $\mu_{LS}$  ( $2.35 \pm 0.45$  vs.  $1.81 \pm 0.07$   $\mu_B$ ). This is mainly due to the fact that the SCO in acetonitrile- $d_3$  does not cover the low  $\mu_{eff}$  range, which leads to high uncertainty in that part of the curve if predicted from the experimental values. Hence, the  $\Delta H$  of  $14.4 \pm 2.4$  kJ/mol,  $\Delta S$  of  $59.6 \pm 8.0$  J/(mol·K) and  $T_c$  of  $240 \pm 9$  K, which are similar to those fitted for **3b** in dichloromethane- $d_2$  but with a higher standard error.

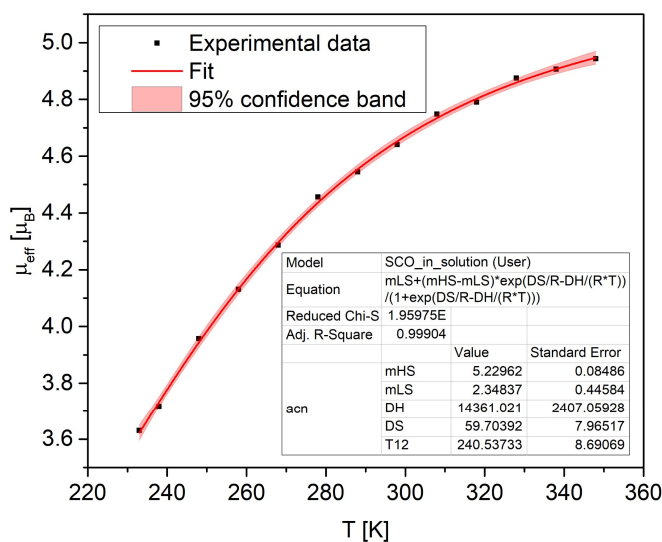
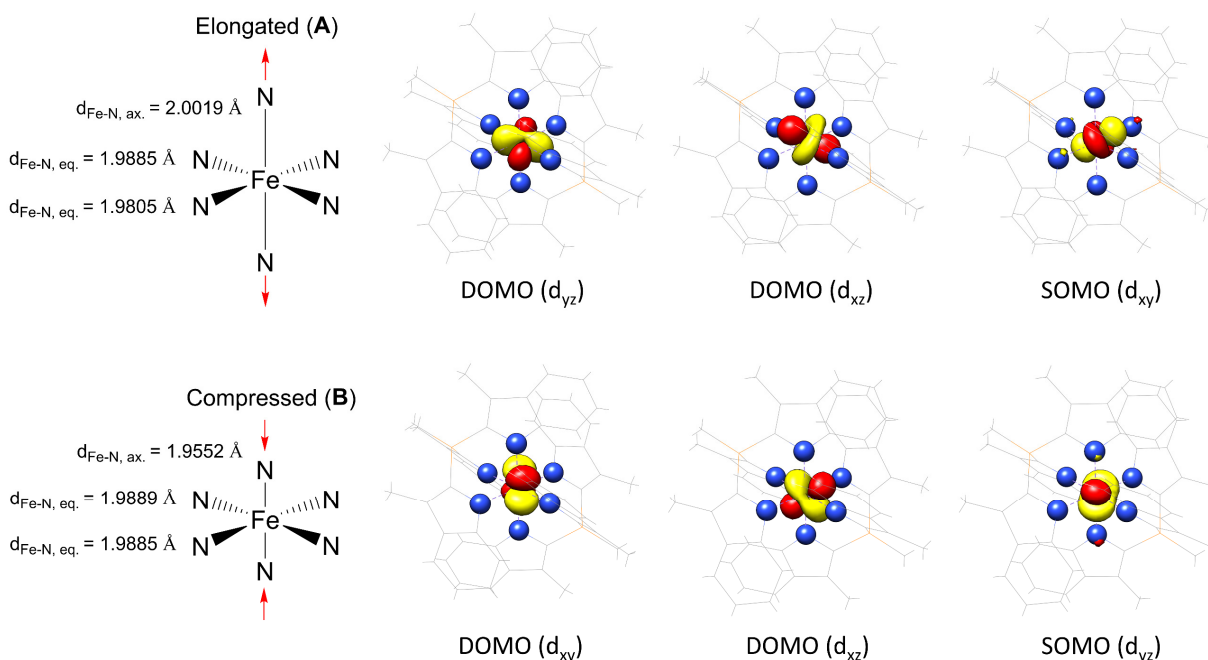


Figure B2.3. Fitted SCO of **3a** in acetonitrile- $d_3$  using regression model in Eq. B2.6.

Attempted fit for the SCO of  $[(\text{TSMMP})_2\text{Fe}^{\text{III}}]\text{K}$  (**3a**) in pyridine- $d_5$  leads to an unusable curve with large uncertainties for the crossover parameters. It is not surprising, considering that the system is very close to the top plateau of the SCO sigmoid with only 3-4 data point in the low-temperature region containing information about the steep part of the curve.

**Appendix B3.** Electronic structure of [(TSMMP)<sub>2</sub>Fe<sup>III</sup>]**K** (**3a**) in the crystal.

The electronic structure of the ferric species within the crystal structure of **3a** was computed. Its unit cell contains two independent molecular anions **A** and **B**: anion **A** has four shorter Fe–N bonds of ca. 1.988 Å and two longer Fe–N ones of ca. 2.002 Å, and anion **B** has four longer Fe–N bonds of ca. 1.988 Å and two shorter Fe–N ones of ca. 1.955 Å. Thus, the coordination geometry of both isomers is best described as an elongated (**A**) and a compressed (**B**) octahedron, respectively. Both isomers are nearly isoenergetic with a marginal energy difference of 0.6 kcal/mol. Despite these similarities, **A** and **B** have distinct electron configurations, namely,  $(d_{xy})^1(d_{xz})^2(d_{yz})^2$  and  $(d_{xy})^2(d_{xz})^2(d_{yz})^1$ , respectively (*Figure B3.1*). As such, the ground state in both **A** and **B** possesses orbital near-degeneracy and hence sizeable unquenched orbital angular momentum, consistent with the measured effective magnetic moment being larger than the spin-only value. The computed Mössbauer parameters (*Table B3.1*) are in reasonable agreement with the experiment. Repeated attempts to measure EPR spectra of **3a** yielded poorly reproducible data with the observed spectral features being highly dependent on minute details of sample preparation. This may be a consequence of the high dependency of the SCO process on microenvironmental factors as well as the presence of different electronic configurations as discussed above.



*Figure B3.1.* Localized filled and half-filled molecular orbitals of anions **A** and **B** calculated on X-ray crystallographic geometries at B3LYP/def2-TZVP level of theory with the CP(PPP) basis set for Fe. The orbitals heavily mix and were named after a dominant contributor.

Table B3.1. Relative SCF energies and  $^{57}\text{Fe}$  Mössbauer spectral parameters calculated at the B3LYP/def2-TZVP level of theory with the CP(PPP) basis set for Fe for the two independent molecules of **3a**, compared to the experimental parameters.

Molecule	$\delta$ , mm/s	$\Delta E_Q$ , mm/s	Relative energy, kcal/mol
A	0.29	2.19	0.6
B	0.26	2.18	0.0
Exp.	0.25	1.63	-

#### Appendix B4. Solid state SQUID magnetometry of $[(\text{TSMMP})_2\text{Fe}^{\text{III}}][(\text{B15C5})_2\text{K}]$ (**3c**).

Interestingly, the bis-benzo-15-crown-5 adduct  $[(\text{TSMMP})_2\text{Fe}^{\text{III}}][(\text{B15C5})_2\text{K}]$  (**3c**) displays an apparent intermediate-spin ( $S=3/2$ ) state at low temperatures ( $\mu_{eff}$  of  $3.61 \mu_B$  compared to the spin-only expectation value of  $3.88 \mu_B$ ) and starts crossing over towards the high-spin ( $S = 5/2$ ) state upon heating to ca. 140 K. As discussed in the main text, this apparent intermediate-spin state is actually an average of the low- and high-spin components co-existing in the crystal, as shown by X-ray crystallographic studies (see Section 3.8.3).

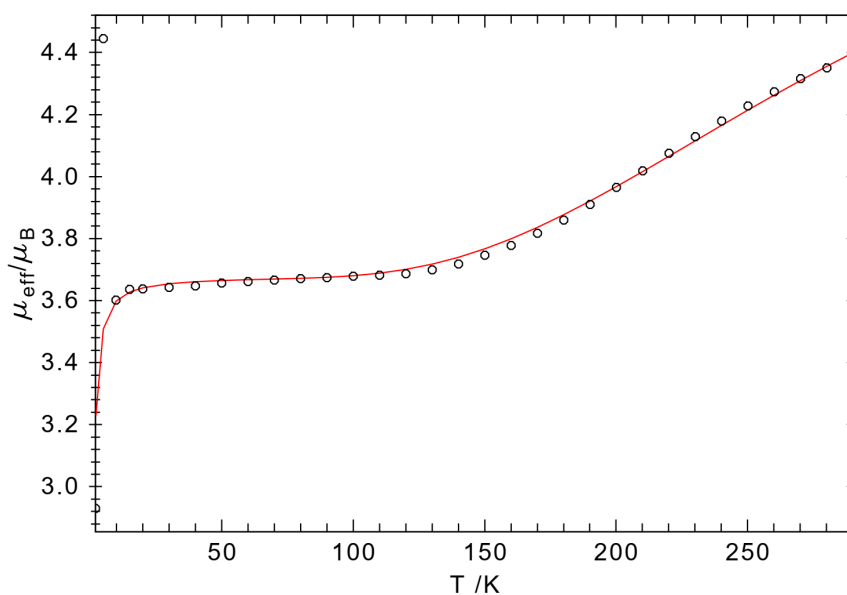


Figure B4.1. VT SQUID  $\mu_{eff}$  measurement of microcrystalline solid sample of **3c**. The simulation with the domain model<sup>7</sup> gave  $T_c = 500$  K and  $n\Delta H = 10.9$  kJ/mol.

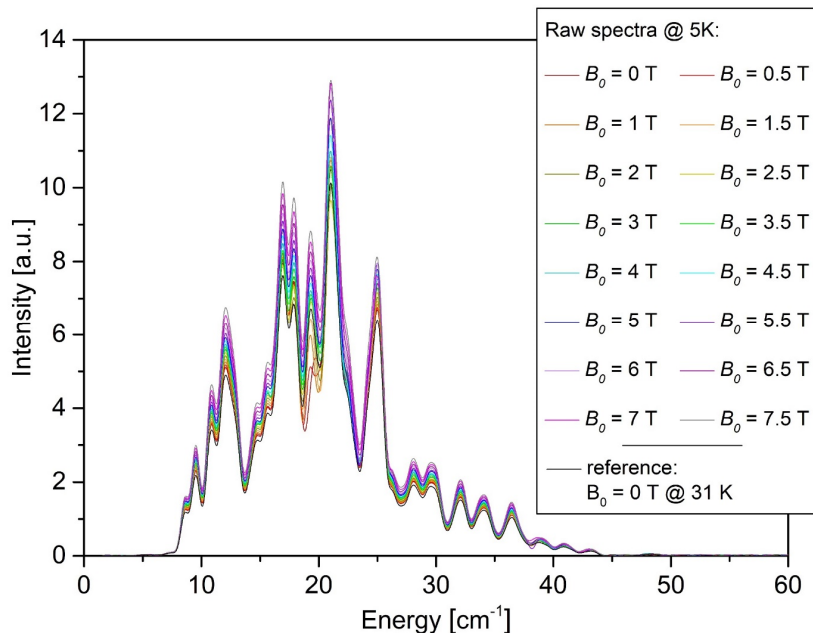
**Appendix B5.** THz-EPR studies: raw experimental spectra.

Figure B5.1. Transmittance THz-EPR spectra of **4**.

**Appendix B6.** THz-EPR studies: general energy diagram.

Assuming that nothing is known about **4** aside from the fact that it is an  $S = 1$  system with a positive  $D$ -value, as shown by SQUID magnetometry (see the main text), its spin Hamiltonian can be written as follows:

$$\hat{H} = D \left( \hat{S}_z^2 - \frac{1}{3} \hat{S}^2 \right) + E (\hat{S}_x^2 - \hat{S}_y^2) + \mu_B \mathbf{B}_0 \mathbf{g} \hat{S}, \quad \text{Eq. B6.1}$$

where the first and second terms describe the axial and rhombic zero-field splitting (ZFS) with  $\hat{S} = (\hat{S}_x, \hat{S}_y, \hat{S}_z)^T$  being the vector spin operator. The third term describes the interaction of the spin with the external magnetic field  $\mathbf{B}_0$ , where  $\mu_B$  is the Bohr magneton and  $\mathbf{g}$  is the  $g$ -tensor.

The corresponding energy eigenvalues can be found by diagonalization of this Hamiltonian. Assuming for a general case the rhombic parameter  $E \neq 0$ , the field-dependent energy diagram depicted in *Figure B6.1* is obtained.

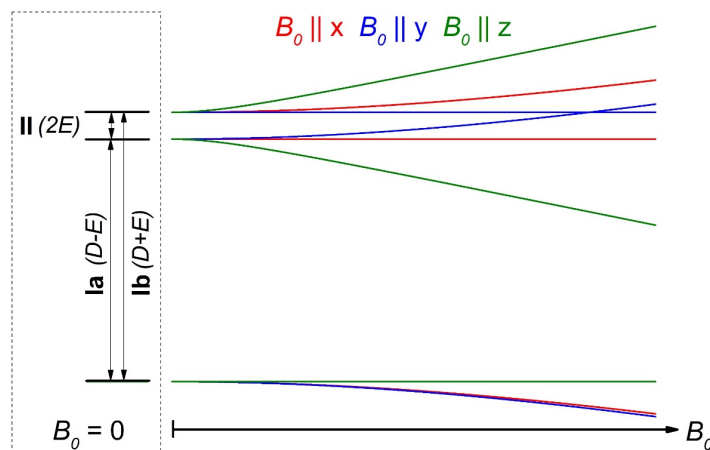


Figure B6.1. Energy splitting in an  $S = 1$  system according to the spin Hamiltonian in Eq. B6.1. The left-hand side shows energy levels in the absence of an external magnetic field ( $B_0 = 0$ ). On the right-hand side are shown the energies for different external field orientations assuming the  $g$ -tensor is isotropic and  $D \gg \mu_B B_0$ .

A positive  $D$ -value leads to a ground state singlet, while non-zero rhombicity ( $E \neq 0$ ) lifts the degeneracy of the excited state, yielding two sublevels with an energy gap of  $2E$  (transition **II**). Respectively, transitions from the ground to the excited state, **Ia** and **Ib**, have energies of  $D - E$  and  $D + E$ . Due to the presence of ZFS, the direction of an external magnetic field ( $B_0$ ) modulates the splitting of the energy levels. More specifically, for a field applied along the major anisotropy axis ( $z$ -axis), the splitting of the excited state changes linearly with the external magnetic field, while the energy of the ground-state remains constant. Contrarily, for directions perpendicular to the  $z$ -axis, the energy of the ground state decreases at higher fields, and as for the excited state, the energy of one sublevel increases, while that of the other remains constant.

### Appendix B7. The negative relative absorbance feature at $\sim 18.4 \text{ cm}^{-1}$ .

Interestingly, the experimental zero-field spectrum has a feature with negative relative absorbance around  $18.4 \text{ cm}^{-1}$ , directly below the ZFS energy, indicative of a higher absorption in the reference transmission spectrum measured at 31 K as opposed to the transmittance measured at 4.8 K (Figure B7.1). A similar situation was observed for another  $S = 1$  molecule.<sup>8</sup> This feature does not react to increasing  $B_0$ , and also manifests as a lowering of the relative absorbance at higher  $B_0$ , which allows to assign it to a high-temperature effect in the zero-field reference spectrum. All potential reasons for this phenomenon are discussed elsewhere<sup>8</sup> and go beyond the used spin Hamiltonian in Eq. B6.1. This explains why this feature is not reflected in our simulations, although the simulations at higher magnetic fields do show some



negative absorbance, albeit centered at  $19.1\text{ cm}^{-1}$ . A closer examination of the zero-field reference transmittance at 31 K and the spectrum at 4.8 K (*Figure B7.1*) shows that the former is more intense at around  $19.1\text{ cm}^{-1}$  (transition I), which is the cause of the positive absorbance in *Figure 10* (see main text). As the 4.8 K signals broaden with increasing  $B_0$ , while the same zero-field 31 K absorbance is used as reference throughout, the central signal intensity becomes lower at 4.8 K than in the reference (*Figure B7.2*), resulting in the calculated negative relative absorbance.

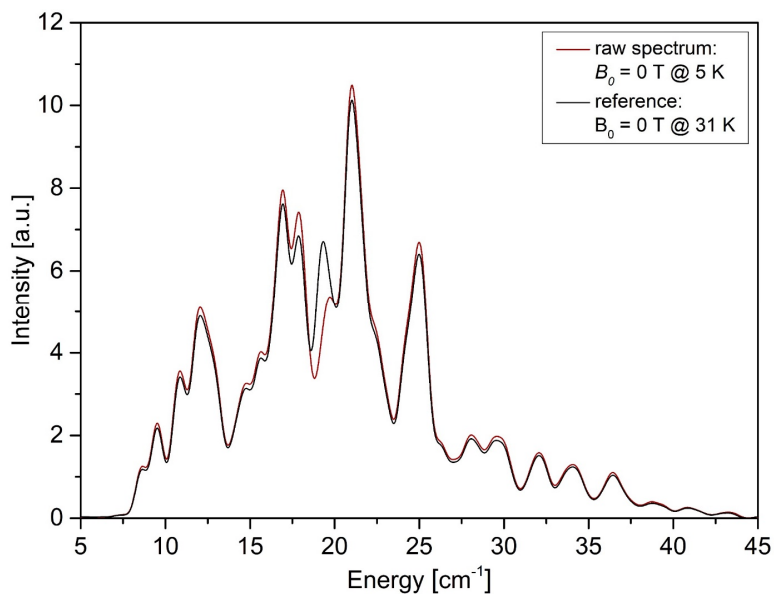


*Figure B7.1.* Comparison of the zero-field transmittance spectrum of **4** at 4.8 K and the reference spectrum at 31 K.

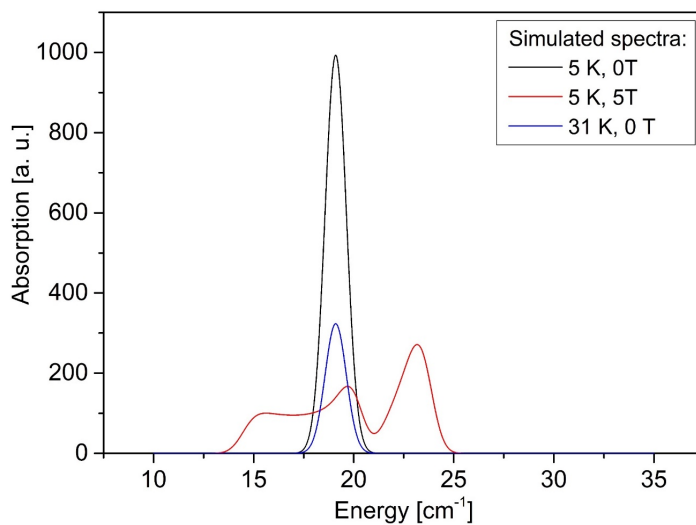


*Figure B7.2.* Simulated absorption spectra for **4** using the spin Hamiltonian in *Eq. B6.1* with  $D = 19.1\text{ cm}^{-1}$ ,  $E = 0\text{ cm}^{-1}$  and an isotropic  $g$ -value of 1.97.

## Appendix B8. THz-EPR studies: alternative interpretations.

It is worth to discuss the alternative interpretations of the experimental data. Firstly, since the THz-EPR experiments are incapable of distinguishing the sign of  $D$ , simulations with a negative value (*Figure B8.1*), while differing slightly, still give acceptable fits. However, a negative  $D$  would contradict the SQUID magnetometry results (see main text), therefore this possibility can be dismissed. Secondly, notwithstanding the estimated  $E$  of  $\leq 0.3 \text{ cm}^{-1}$ , it may be that  $E$  is actually much larger so that some transitions lie outside the experimentally probed spectral range. However, such simulations reveal that one would observe a field dependence that is unlike the experiment (*Figure B8.1*). Hence, this scenario can also be excluded.

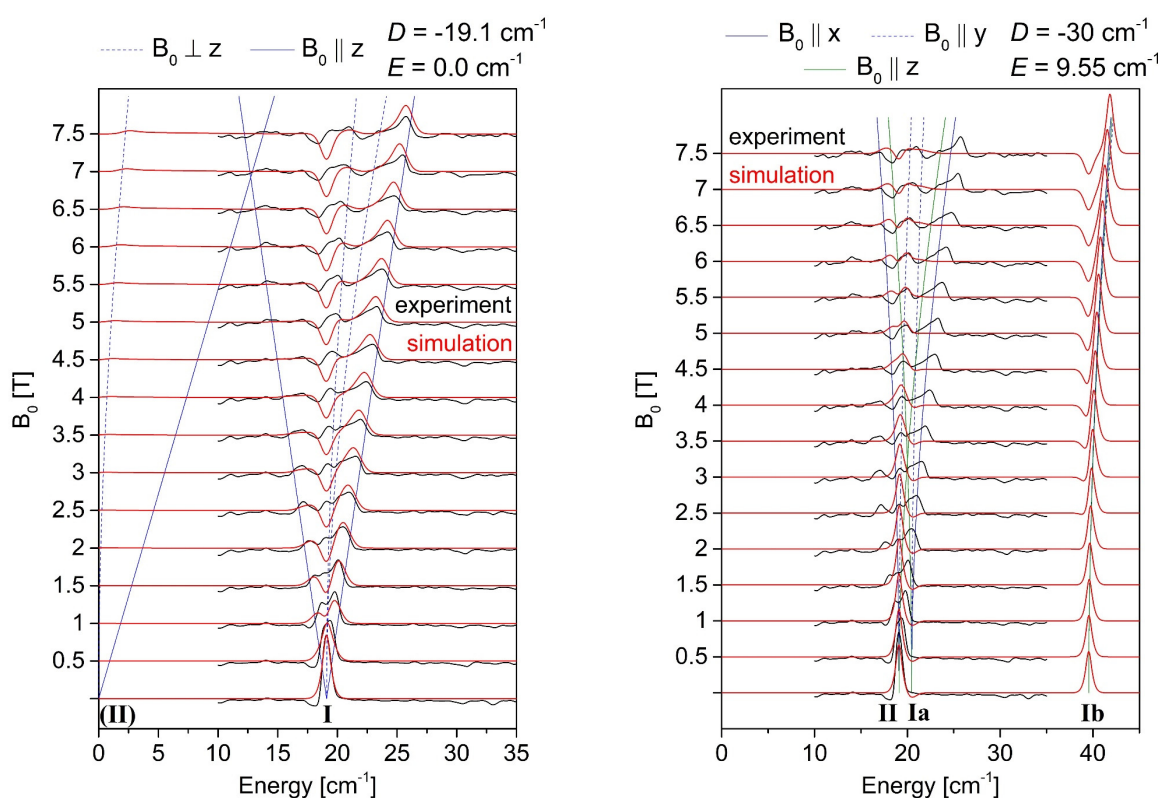


*Figure B8.1.* Dismissed alternative interpretations of THz-EPR spectra of **4**. Relative absorbance spectra (black lines) are offset for the magnetic field  $B_0$  at which they were measured. Simulations for the spin Hamiltonian in Eq. B6.1 are shown in red. The spectra were simulated with an axial  $g$ -value of 1.97 and the ZFS parameters indicated separately at the top right corner of each set of spectra. Calculated transition energies for magnetic fields applied parallel to the  $x$ ,  $y$ , and  $z$ -axes are shown as dashed and solid blue and green lines, respectively.

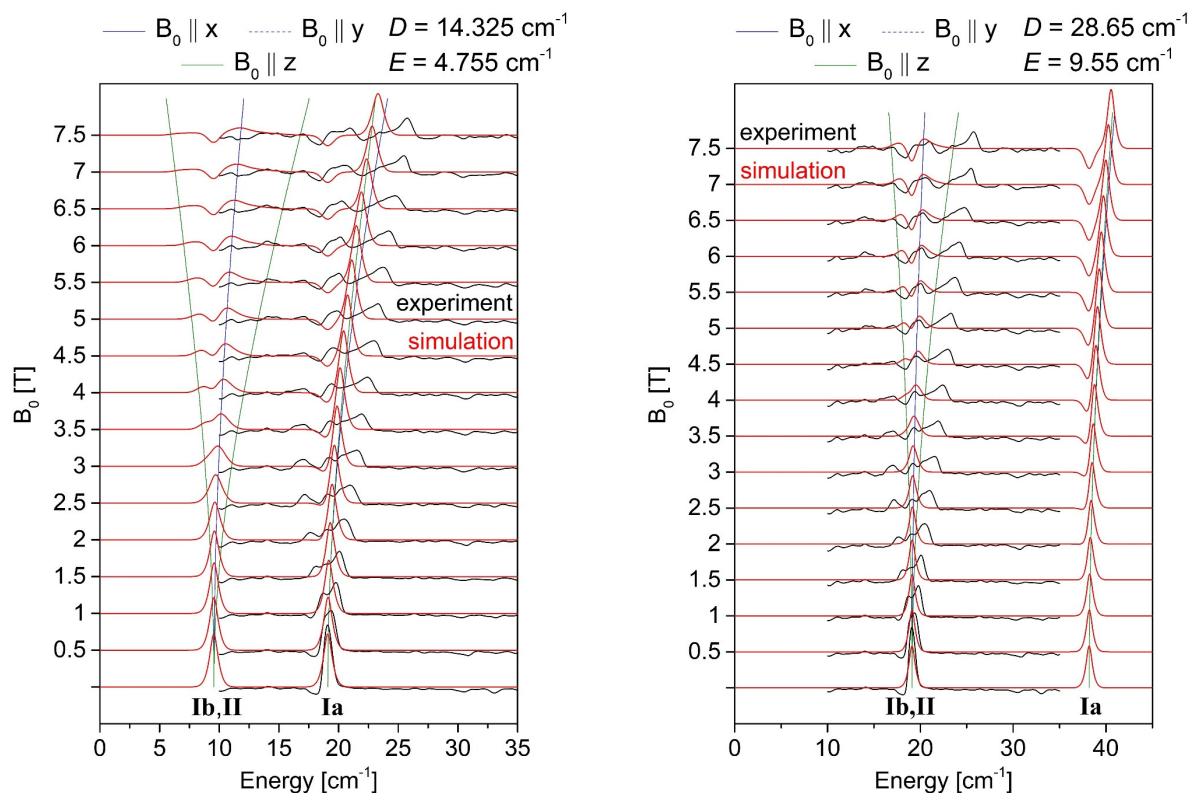
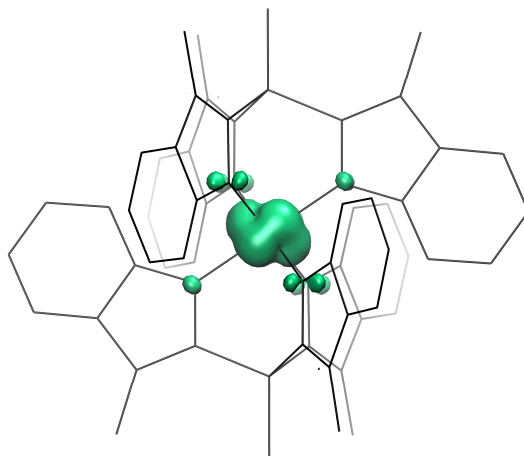


Figure B8.1. (continued). Dismissed alternative interpretations of THz-EPR spectra of **4**. For the shown spectra,  $E = D/3$  leads to invariance with respect to the sign of  $D$ . Furthermore, transitions **Ib** and **II** have the same energy. Their field dependence is, however, not entirely identical, which is not shown in the respective spectra. More specifically, the field dependences of **Ib** and **II** are identical for  $B_0 \parallel x$ . The field dependence of **Ib** for  $B_0 \parallel y$  is identical to the field dependence of **II** for  $B_0 \parallel z$  and vice versa.

While the relative absorbance spectra do not allow to precisely determine the transverse ( $\perp z$ ) components of the  $g$ -tensor, its axial component ( $\parallel z$ ) is clearly constrained as 1.97, since it defines the maximum and minimum transition energies and thus the total width of the signals.

**Appendix B9.** DFT calculations: spin density in [(TSMMP)<sub>2</sub>Fe<sup>IV</sup>]<sup>0</sup> (**4**).

*Figure B9.1.* Spin density distribution in **4** (isocontour=0.01). Calculations were performed at B3LYP-D3BJ/def2-TZVP (CP(PPP) for Fe) level of theory using a geometry optimized at BP86-D3BJ/def2-TZVP level.

**Appendix B10.** <sup>57</sup>Fe Mössbauer spectroscopy: detailed analysis of the quadrupole splitting.

The quadrupole splitting is related to the electric field gradient (EFG) tensor, which is a symmetric 3×3 matrix. This tensor possesses a set of proper axes in which it is diagonal. Additionally, it is traceless, meaning that only two parameters are sufficient to describe it: the axial component  $V_{zz}$  and the asymmetry parameter  $\eta$ , which can be expressed as follows:

$$\eta = \frac{V_{xx} - V_{yy}}{V_{zz}}, \quad \text{Eq. B10.1}$$

where  $|V_{zz}| \geq |V_{xx}| \geq |V_{yy}|$  by convention.

The quadrupole splitting  $\Delta E_Q$  is related to these parameters *via* the following expression:

$$\Delta E_Q = \frac{eQ V_{zz}}{2} \sqrt{1 + \frac{\eta^2}{3}}, \quad \text{Eq. B10.2}$$

where  $eQ$  is the quadrupolar moment of a <sup>57</sup>Fe nucleus.

Due to the high symmetry of the molecule of **4** ( $C_3$ -axis), the asymmetry parameter is very close to zero ( $\eta = 0.05$ ). Hence,  $V_{ZZ}$  is the only parameter determining the quadrupolar splitting.

It is possible to partition  $V_{ZZ}$  into a set of atomic orbital contributions:

$$V_{ZZ} = \sum_{\mu} \sum_{\nu} P_{\mu\nu} \langle \phi_{\mu} | V_{ZZ} | \phi_{\nu} \rangle, \quad \text{Eq. B10.3}$$

where  $P_{\mu\nu} = \sum_i c_{\mu i}^* c_{\nu i}$ , the  $c_{\mu i}$  are the coefficients of the atomic orbital  $|\phi_{\mu}\rangle$  in the molecular orbital  $i$ .

Differentiation of the atomic orbitals on iron and those on the ligand gives:

$$\begin{aligned} V_{ZZ} = & \sum_{\mu}^{Fe} \sum_{\nu}^{Fe} P_{\mu\nu} \langle \phi_{\mu} | V_{ZZ} | \phi_{\nu} \rangle + \sum_{\mu}^{Fe} \sum_{\nu}^L (P_{\mu\nu} \langle \phi_{\nu} | V_{ZZ} | \phi_{\mu} \rangle + P_{\nu\mu} \langle \phi_{\nu} | V_{ZZ} | \phi_{\mu} \rangle) \\ & + \sum_{\mu}^L \sum_{\nu}^L P_{\mu\nu} \langle \phi_{\mu} | V_{ZZ} | \phi_{\nu} \rangle + \sum_{\mu}^L \sum_{\nu}^{L'} P_{\mu\nu} \langle \phi_{\mu} | V_{ZZ} | \phi_{\nu} \rangle. \end{aligned} \quad \text{Eq. B10.4}$$

The first term corresponds to the one-center contribution, the second one corresponds to the two-center bond contribution, the third one corresponds to the two-center point charge contribution, and the fourth term relates to the three-center contribution.

The one-center contribution is normally a dominant term, and can be further expanded into a core orbital and molecular orbital (or valence) contributions:

$$\begin{aligned} \sum_{\mu}^{Fe} \sum_{\nu}^{Fe} P_{\mu\nu} \langle \phi_{\mu} | V_{ZZ} | \phi_{\nu} \rangle = & \\ = & \sum_i^{core} \sum_{\mu}^{Fe} \sum_{\nu}^{Fe} c_{\mu i}^* c_{\nu i} \langle \phi_{\mu} | V_{ZZ} | \phi_{\nu} \rangle + \sum_i^{valence} \sum_{\mu}^{Fe} \sum_{\nu}^{Fe} c_{\mu i}^* c_{\nu i} \langle \phi_{\mu} | V_{ZZ} | \phi_{\nu} \rangle = \\ = & V_{ZZ}^{1c-core} + V_{ZZ}^{1c-valence}. \end{aligned} \quad \text{Eq. B10.5}$$

This gives a total of five terms:

$$V_{ZZ} = V_{ZZ}^{1c-core} + V_{ZZ}^{1c-valence} + V_{ZZ}^{2c-bond} + V_{ZZ}^{2c-PC} + V_{ZZ}^{3c}, \quad \text{Eq. B10.6}$$

where  $V_{ZZ}^{1c-core}$  – a one-center core orbital contribution;  $V_{ZZ}^{1c-valence}$  – a one-center valence contribution;  $V_{ZZ}^{2c-bond}$  – a two-center bond contribution;  $V_{ZZ}^{2c-PC}$  – a two-center point charge contribution;  $V_{ZZ}^{3c}$  – a three-center contribution.

The values of these contributions are given in *Table B10.1*. As emphasized in the main text, the valence contribution ( $V_{ZZ}^{1c-valence}$ ) is dominant over all others. At the same time, the three-center contribution ( $V_{ZZ}^{3c}$ ) is so weak that it can be neglected.

*Table B10.1.* Contributions to the axial component  $V_{ZZ}$  of the EFG tensor (expressed in a.u.<sup>-3</sup>).

$V_{ZZ}^{1c-core}$	$V_{ZZ}^{1c-valence}$	$V_{ZZ}^{2c-bond}$	$V_{ZZ}^{2c-PC}$	<b>Total (<math>V_{ZZ}</math>)</b>
+0.06	-0.92	-0.40	0.04	-1.22

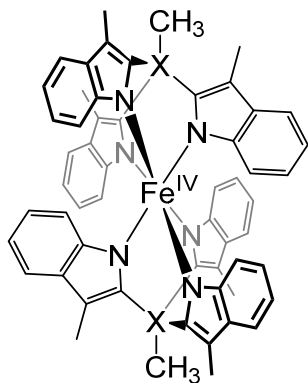
The valence contribution can be further partitioned between non-bonding  $1a_1$ ,  $\pi$ -antibonding  $1e$ ,  $\sigma$ -bonding and  $\pi$ -bonding orbitals (*Table B10.2*). The analysis shows that the  $1a_1$  contribution dominates over that of  $1e$  orbitals. As specified in the main text, this is due to the mixing between the ( $d_{xy}, d_{x^2-y^2}$ ) and ( $d_{xz}, d_{yz}$ ) orbital pairs, which have opposite contributions to the  $1e$ -related part of  $V_{ZZ}^{1c-valence}$ . Furthermore, the  $1e$  orbitals are significantly  $\pi$ -antibonding, which reduces their one-center contribution. However, the corresponding  $\pi$ -bonding orbitals have a significant  $1e$  character. Therefore, they have a non-negligible positive valence contribution, especially considering that these orbitals are doubly-occupied.

*Table B10.2.* Orbital contributions to the valence axial component of  $V_{ZZ}^{1c-valence}$  of the EFG tensor (expressed in a.u.<sup>-3</sup>).

$1a_1$	$1e$	$\sigma$ -bonding	$\pi$ -bonding	<b>Total (<math>V_{ZZ}^{1c-valence}</math>)</b>
-5.00	+2.04	+0.17	+2.05	-0.92

## Appendix B11. Computational geometries of [(TSMP)<sub>2</sub>Fe<sup>IV</sup>] (4) and its Si-tethered analogue.

Table B11.1. Comparison of selected parameters from computationally optimized geometries of [(TSMP)<sub>2</sub>Fe<sup>IV</sup>] (4) and its Si-tethered analogue A. Level of theory: BP86-D3BJ/def2-TZVP.



Geometric parameter	X=P <sup>+</sup> (4)	X=Si (A)
Fe-N	1.95	1.97
N-C <sup>Ar</sup>	1.39	1.40
C <sup>Ar</sup> -X	1.76	1.85
X-Me	1.80	1.89
Fe...X	3.16	3.25
N^Fe^N	91.9	92.7
Fe-N-C <sup>Ar</sup>	124.1	124.8
N-C <sup>Ar</sup> -X	112.5	113.3
C <sup>Ar</sup> X^Me	106.0	114.7

## Appendix B12. CASSCF calculations: ZFS parameters of [(TSMP)<sub>2</sub>Fe<sup>IV</sup>]<sup>0</sup> (4).

The zero-field splitting arises from two physical effects, namely spin-spin coupling and spin-orbit coupling. The axial parameter of the zero-field splitting may be calculated by effective Hamiltonian theory. It is a sum of contributions arising from the ground state (spin-spin coupling) and each excited Born-Oppenheimer states (spin-orbit coupling). Only the states with a spin quantum number  $S$  identical to or different from that of the ground state by  $\pm 1$  have a non-zero contribution to the zero-field splitting.

A state contribution is proportional to  $\frac{\zeta}{\Delta E}$ , where  $\zeta$  is the spin-orbit coupling constant and  $\Delta E$  the excitation energy of the state. The threshold of 24 000 cm<sup>-1</sup> (48  $\zeta$ ) was chosen as the limit above which the states contributions can be neglected. The energies and individual contributions of each state are reported in Table B12.1.

Table B12.1. Individual contributions of the excited states to the axial parameter  $D$  of the zero-field splitting.

Energy [cm <sup>-1</sup> ]	Configuration	Multiplicity	Contribution to $D$ [cm <sup>-1</sup> ]
0	98% (1a <sub>1</sub> ) <sup>2</sup> (1e <sub>x</sub> ) <sup>1</sup> (1e <sub>y</sub> ) <sup>1</sup>	3	0
10 827	97% (1a <sub>1</sub> ) <sup>1</sup> (1e <sub>x</sub> ) <sup>2</sup> (1e <sub>y</sub> ) <sup>1</sup>	3	+2.111
10 864	97% (1a <sub>1</sub> ) <sup>1</sup> (1e <sub>x</sub> ) <sup>1</sup> (1e <sub>y</sub> ) <sup>2</sup>	3	+2.095

Table B12.1 (continued). Individual contributions of the excited states to the axial parameter  $D$  of the zero-field splitting.

Energy [cm <sup>-1</sup> ]	Configuration	Multiplicity	Contribution to $D$ [cm <sup>-1</sup> ]
12 249	68 % (1a <sub>1</sub> ) <sup>2</sup> (1e <sub>x</sub> ) <sup>1</sup> (1e <sub>y</sub> ) <sup>1</sup> 10% (1a <sub>1</sub> ) <sup>2</sup> (1e <sub>x</sub> ) <sup>2</sup> 10% (1a <sub>1</sub> ) <sup>2</sup> (1e <sub>y</sub> ) <sup>2</sup>	1	-0.253
12 257	34% (1a <sub>1</sub> ) <sup>2</sup> (1e <sub>x</sub> ) <sup>2</sup> 34% (1a <sub>1</sub> ) <sup>2</sup> (1e <sub>y</sub> ) <sup>2</sup> 21% (1a <sub>1</sub> ) <sup>2</sup> (1e <sub>x</sub> ) <sup>1</sup> (1e <sub>y</sub> ) <sup>1</sup>	1	-0.253
19 054	(1a <sub>1</sub> ) <sup>1</sup> (1e <sub>x</sub> ) <sup>1</sup> (1e <sub>y</sub> ) <sup>1</sup> (2e <sub>x</sub> ) <sup>1</sup>	5	-0.810
19 083	(1a <sub>1</sub> ) <sup>1</sup> (1e <sub>x</sub> ) <sup>1</sup> (1e <sub>y</sub> ) <sup>1</sup> (2e <sub>y</sub> ) <sup>1</sup>	5	-0.810
20 478	31% (1e <sub>x</sub> ) <sup>2</sup> (1e <sub>y</sub> ) <sup>2</sup> 29% (1a <sub>1</sub> ) <sup>2</sup> (1e <sub>x</sub> ) <sup>2</sup> 29% (1a <sub>1</sub> ) <sup>2</sup> (1e <sub>y</sub> ) <sup>2</sup>	1	+10.267
24 142	89% (1a <sub>1</sub> ) <sup>1</sup> (1e <sub>x</sub> ) <sup>2</sup> (1e <sub>y</sub> ) <sup>1</sup>	1	-0.864
24 170	89% (1a <sub>1</sub> ) <sup>1</sup> (1e <sub>x</sub> ) <sup>1</sup> (1e <sub>y</sub> ) <sup>2</sup>	1	-0.860
37 787	43% (1e <sub>x</sub> ) <sup>2</sup> (1e <sub>y</sub> ) <sup>2</sup> 11% (1a <sub>1</sub> ) <sup>2</sup> (1e <sub>x</sub> ) <sup>1</sup> (2e <sub>y</sub> ) <sup>1</sup> 11% (1a <sub>1</sub> ) <sup>2</sup> (1e <sub>y</sub> ) <sup>1</sup> (2e <sub>x</sub> ) <sup>1</sup> 8% (1e <sub>x</sub> ) <sup>1</sup> (1e <sub>y</sub> ) <sup>2</sup> (2e <sub>y</sub> ) <sup>1</sup> 8% (1e <sub>x</sub> ) <sup>2</sup> (1e <sub>y</sub> ) <sup>1</sup> (2e <sub>x</sub> ) <sup>1</sup> 6% % (1a <sub>1</sub> ) <sup>2</sup> (1e <sub>x</sub> ) <sup>2</sup> 6% % (1a <sub>1</sub> ) <sup>2</sup> (1e <sub>y</sub> ) <sup>2</sup>	1	+3.763
43 878	20% (1a <sub>1</sub> ) <sup>1</sup> (1e <sub>x</sub> ) <sup>1</sup> (1e <sub>y</sub> ) <sup>1</sup> (2e <sub>x</sub> ) <sup>1</sup> 19% (1a <sub>1</sub> ) <sup>2</sup> (1e <sub>y</sub> ) <sup>1</sup> (2e <sub>x</sub> ) <sup>1</sup> 18% (1a <sub>1</sub> ) <sup>2</sup> (1e <sub>x</sub> ) <sup>1</sup> (2e <sub>y</sub> ) <sup>1</sup> 10% (1a <sub>1</sub> ) <sup>1</sup> (1e <sub>x</sub> ) <sup>2</sup> (2e <sub>y</sub> ) <sup>1</sup> 10% (1a <sub>1</sub> ) <sup>1</sup> (1e <sub>y</sub> ) <sup>2</sup> (2e <sub>y</sub> ) <sup>1</sup> 8% (1a <sub>1</sub> ) <sup>1</sup> (1e <sub>x</sub> ) <sup>1</sup> (1e <sub>y</sub> ) <sup>1</sup> (2e <sub>y</sub> ) <sup>1</sup>	1	+0.943
45 689	22% (1a <sub>1</sub> ) <sup>2</sup> (1e <sub>x</sub> ) <sup>1</sup> (2e <sub>x</sub> ) <sup>1</sup> 21% (1a <sub>1</sub> ) <sup>2</sup> (1e <sub>y</sub> ) <sup>1</sup> (2e <sub>y</sub> ) <sup>1</sup> 16% (1a <sub>1</sub> ) <sup>1</sup> (1e <sub>x</sub> ) <sup>1</sup> (1e <sub>y</sub> ) <sup>1</sup> (2e <sub>y</sub> ) <sup>1</sup> 8% (1a <sub>1</sub> ) <sup>1</sup> (1e <sub>x</sub> ) <sup>2</sup> (2e <sub>x</sub> ) <sup>1</sup> 8% (1a <sub>1</sub> ) <sup>1</sup> (1e <sub>y</sub> ) <sup>2</sup> (2e <sub>x</sub> ) <sup>1</sup> 6% (1a <sub>1</sub> ) <sup>1</sup> (1e <sub>x</sub> ) <sup>1</sup> (1e <sub>y</sub> ) <sup>1</sup> (2e <sub>x</sub> ) <sup>1</sup>	1	0

### Appendix B13. Paramagnetic NMR theory: on the origin of paramagnetic shifts.

Despite the plethora of information that can be extracted from the NMR experiments on paramagnetic systems, their potential remains severely underused. There are several literature sources that cover paramagnetic NMR at a rather introductory<sup>9,10</sup> or a



more fundamental level.<sup>11–15</sup> However, for the sake of further discussion, the origin of chemical shifts and linewidths in such systems will be briefly covered below.

Consider a system of coupled nuclear ( $I = 1/2$ ) and electronic ( $S = 1/2$ ) spins in an external magnetic field (*Figure B13.1*). Nuclear Zeeman splitting leads to two states with separation of  $\Delta E_N$ . Every nuclear state undergoes subsequent electron Zeeman splitting of  $\Delta E_e$  yielding four states with different combinations of projected spin angular momenta,  $m_l$  and  $m_s$ , on the external field. These states are further modified by  $\pm A/4$ , where  $A$  is a hyperfine coupling constant between the corresponding nucleus and the unpaired electron, yielding states characterized by energies  $E_1$  through  $E_4$ , between which transitions take place.

Depending on the quantum numbers that change, NMR ( $\Delta m_l = \pm 1$ ) or EPR ( $\Delta m_s = \pm 1$ ) transitions can occur. Yet, regardless of the kind of transition, they contain the same structural and electronic information that can often be extracted.<sup>9</sup>

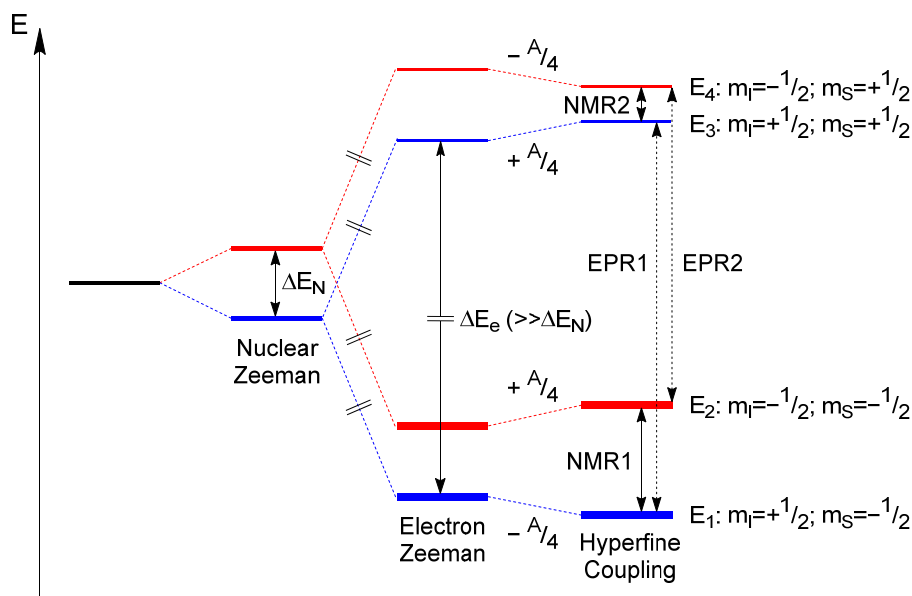


*Figure B13.1.* A system of nuclear and electronic spins that couple with a hyperfine constant  $A$ . The scale in the figure is distorted: electronic Zeeman splitting ( $\Delta E_e$ ) is four orders of magnitude larger than nuclear Zeeman splitting ( $\Delta E_N$ ). Relative line thickness denotes a difference in thermal population.

An astute reader may have noticed that, despite two NMR transitions shown in *Figure B13.1*, one normally observes singlets in paramagnetic NMR spectra. This is due to the fact that nuclei relax on the timescale of seconds whereas the lifetime of electronic states is within  $10^{-5}$  to  $10^{-13}$  s.<sup>10,15</sup> Therefore, a nucleus experiences an average oscillating field of an electron rapidly flipping between  $m_s = -1/2$  and  $+1/2$  states. Normally,

the frequency of this field is many orders of magnitude higher than the nuclear Larmor frequency, which yields a singlet that is an average of the exchanging states. In principle, this should cancel the hyperfine coupling leading to a chemical shift indistinguishable from that in the absence of an unpaired electron (orbital or diamagnetic shift,  $\delta^{dia}$ ). However, due to the high gyromagnetic ratio of the electron, the Zeeman splitting ( $\Delta E_e$ ) is so large that thermal populations of  $m_S = -1/2$  and  $+1/2$  states are not equal, therefore complete cancellation does not occur, giving a singlet shifted away from  $\delta^{dia}$  by a certain value called a hyperfine shift ( $\delta^{HF}$ ). Thus, in effect, a paramagnetic NMR signal is a weighted average of a hyperfine doublet where the weights are thermal populations of the  $m_S = -1/2$  and  $+1/2$  electronic states.

Summing up the above, the observed paramagnetic NMR chemical shift ( $\delta^{obs}$ ) can be broken down in two parts: an orbital or diamagnetic term ( $\delta^{dia}$ ) and a hyperfine term ( $\delta^{HF}$ ). The former is a would-be chemical shift should an unpaired electron not be present. It is defined by the nuclear Zeeman splitting energy ( $\Delta E_N$ ) and, to a first approximation, is temperature-independent due to a small magnitude of  $\Delta E_N$  (radiofrequency range). The hyperfine term,  $\delta^{HF}$ , originates from coupling between electronic and nuclear magnetic moments and is strongly temperature-dependent because of the different thermal populations of the  $m_S$  electronic states.

There are many possible contributors to the  $\delta^{HF}$ ,<sup>12</sup> however Fermi contact ( $\delta^{FC}$ ) and pseudocontact ( $\delta^{PC}$ , also named dipolar) shifts are the most important.

$$\delta^{obs} = \delta^{dia} + \delta^{HF} \cong \delta^{dia} + \delta^{FC} + \delta^{PC}. \quad \text{Eq. B13.1}$$

Fermi contact shift ( $\delta^{FC}$ ) originates from scalar electron-nuclear coupling through chemical bonds. More specifically, metal-centered unpaired electrons result into non-zero spin density on other atoms in the molecule either *via* direct delocalization through  $\sigma$ - and  $\pi$ -bonds or indirectly through spin polarization.<sup>16</sup> Spin density influences NMR chemical shifts if it resides in orbitals of s-character which have non-zero electron density on a nucleus. In a way, this mechanism is analogous to scalar or  $J$ -coupling in solution NMR experiments on diamagnetic systems. Both effects also quickly vanish with the number of bonds separating coupled spins unless  $\pi$ -conjugated systems are involved. Fermi-contact shift can be expressed *via* isotropic hyperfine coupling constant  $A_{iso}$  as shown below:

$$\delta^{FC} = \frac{S(S+1)\mu_B}{3kTg_N\mu_N} g_{iso} \cdot A_{iso}, \quad \text{Eq. B13.2}$$

where  $S$  – electronic spin quantum number of the complex;  $\mu_B$  – Bohr magneton;  $g_N$  – nuclear g-value;  $\mu_N$  – nuclear magneton;  $k$  – Boltzmann constant;  $T$  – temperature;  $g_{iso}$  – isotropic electronic g-value of the system;  $A_{iso}$  – isotropic hyperfine coupling constant.

Pseudocontact shift ( $\delta^{PC}$ ) is a result of non-mediated through-space coupling between nuclear and electronic magnetic moments. It is analogous to dipolar coupling in the solid-state NMR experiments. In general,  $\delta^{PC}$  are more difficult to describe mathematically since, due to spin delocalization, there may be several sources of the magnetic moment. In the simplest case, assuming a metal center to be a point magnetic dipole and the only source of the magnetic moment (the so-called point-dipole approximation),  $\delta^{PC}$  can be expressed as follows:

$$\delta^{PC} = \frac{1}{12\pi r^3} \left[ \Delta\chi_{ax} (3\cos^2\theta - 1) + \frac{3}{2} \Delta\chi_{rh} \sin^2\theta \cos 2\varphi \right], \quad \text{Eq. B13.3}$$

where  $r$ ,  $\theta$  and  $\varphi$  – spherical coordinates of a nucleus within the intrinsic frame of magnetic susceptibility tensor;  $\Delta\chi_{ax}$  and  $\Delta\chi_{rh}$  – temperature-dependent axial anisotropy and rhombicity of the above tensor. The latter two are defined as:

$$\Delta\chi_{ax} = \tilde{\chi}_{zz} - \frac{\tilde{\chi}_{xx} - \tilde{\chi}_{yy}}{2}, \quad \text{Eq. B13.4}$$

$$\Delta\chi_{rh} = \tilde{\chi}_{xx} - \tilde{\chi}_{yy}, \quad \text{Eq. B13.5}$$

where  $\tilde{\chi}_{xx}$ ,  $\tilde{\chi}_{yy}$  and  $\tilde{\chi}_{zz}$  are components of a diagonalized magnetic susceptibility tensor. The origin of magnetic susceptibility tensor is at the position of the paramagnetic center.

For system with more than one unpaired electron,  $\Delta\chi_{ax}$  and  $\Delta\chi_{rh}$  can be further expressed *via* other spectroscopic observables as:<sup>17–19</sup>

$$\Delta\chi_{ax} = -W \cdot \left[ g_{zz}^2 D_z - \frac{g_{xx}^2 D_x + g_{yy}^2 D_y}{2} \right], \quad \text{Eq. B13.6}$$

$$\Delta\chi_{rh} = -W \cdot [g_{xx}^2 D_x - g_{yy}^2 D_y], \quad \text{Eq. B13.7}$$

with

$$W = \frac{\mu_0 \mu_B^2 S(S+1)(2S-1)(2S+3)}{30(k_B T)^2}, \quad \text{Eq. B13.8}$$

where  $g_{xx}$ ,  $g_{yy}$ ,  $g_{zz}$ ,  $D_x$ ,  $D_y$ ,  $D_z$  are diagonal components of g- and ZFS-tensors, respectively;  $\mu_0$  – vacuum permeability;  $\mu_B$  – Bohr magneton;  $S$  – spin quantum number of the system;  $k_B$  – Boltzmann constant;  $T$  – temperature. In turn, the diagonal components of the ZFS-tensor are connected with (measurable) ZFS parameters  $D$  and  $E$  as follows:

$$D = \frac{3}{2}D_z, \quad \text{Eq. B13.9}$$

$$E = \frac{1}{2}(D_x - D_y). \quad \text{Eq. B13.10}$$

This, however, does not mean that systems with a single unpaired electron have no pseudocontact shifts due to having no ZFS. On the contrary, such systems may have sizeable  $\delta^{PC}$  that can be taken into account by departing from the ZFS formalism and directly considering the spin-orbit coupling.

As can be seen from the Eq. B13.3, pseudocontact shifts are strongly orientation-dependent and inversely scale with cubed distance  $r$ . Nevertheless, while contact shifts tend to vanish after several bonds, pseudocontact shifts can persist up to 50 Å. In most cases, the point-dipole approximation gives reasonable results, especially if M···H distances are  $>5\text{Å}$ , but sometimes more sophisticated models must be used.<sup>20,21</sup>

By using observed and diamagnetic chemical shifts ( $\delta^{obs}$  and  $\delta^{dia}$ , respectively) and by knowing the equations for hyperfine shift ( $\delta^{HF}$ ), it is possible to extract structural and electronic information about a paramagnetic species.<sup>10</sup> Several approximations are normally employed. First of all, diamagnetic shifts ( $\delta^{dia}$ ) are taken from an isostructural closed-shell analogue, for instance  $\delta^{dia}$  for an Fe(III) metal complex can be taken from a Ga(III) one or even from a free ligand. As another approximation, very often only either a contact ( $\delta^{FC}$ ) or a pseudocontact ( $\delta^{PC}$ ) term is considered. The former is thought to dominate in organic radicals and covalent d-block compounds<sup>22–25</sup> with the latter being prominent for f-block compounds.<sup>13</sup> A good diagnostic criterion for a strong Fermi-contact contribution is a linear dependence of hyperfine shift on inverse temperature ( $T^{-1}$ ), which follows from Eq. B13.2. In other words, a Fermi contact-dominated hyperfine shift can be regarded as local paramagnetic susceptibility and should follow Curie's law:  $\delta^{HF}T = const$ . Should the pseudocontact shift contribution be significant,  $T^{-1}$  behavior is complemented by the  $T^{-2}$  dependence<sup>9</sup> with the weight of the latter being related to the zero-field splitting (ZFS) or spin-orbit coupling in the system (Eq. B13.3–Eq. B13.8).<sup>26</sup>

Discussed sources of hyperfine shift considered in time can lead to fast nuclear relaxation. Combined with Curie relaxation, which is analogous to chemical shift anisotropy relaxation in solution NMR on diamagnetic systems, they define the linewidth. To generalize, for any kind of nuclear relaxation to happen, a nucleus must experience a magnetic field oscillating at or close to its own Larmor frequency. In solution, it can be provided by electron Zeeman transitions, mutual rotation and tumbling of individual magnetic moments. Therefore, mechanics of nuclear relaxation is nuanced with strong dependence on spin density, temperature, molecular mass, viscosity of the solution and availability of several relaxation channels that may act simultaneously. It is often the case, however, that dipolar relaxation dominates for small molecules. If so, for molecular motion that is much faster than nuclear Larmor frequency (the so-called fast motion limit), longitudinal ( $T_{1M}$ ) and transverse ( $T_{2M}$ ) relaxation constants become equal and can be expressed as:<sup>16</sup>

$$\frac{1}{T_{1M}} = \frac{1}{T_{2M}} = \frac{4}{3} \left( \frac{\mu_0}{4\pi} \right)^2 \frac{\gamma^2 g_e^2 \mu_B^2 S(S+1)}{r^6} \tau_c, \quad \text{Eq. B13.11}$$

where  $\mu_0$  – vacuum magnetic permeability;  $\gamma$  – nuclear gyromagnetic ratio;  $g_e$  – isotropic g-value of the complex;  $\mu_B$  – Bohr magneton;  $S$  – spin number of the complex;  $r$  – distance between nuclear and electronic spins (for point dipole approximation, M···H distance);  $\tau_c$  – correlation time for electron-nucleus interaction.

An important consequence of the Eq. B13.11 is that the signal linewidth, which is inversely proportional to transverse relaxation time constant  $T_{2M}$ , is also inversely proportional to  $r^6$ , which allows to roughly assign paramagnetic NMR signals from their linewidth.<sup>13,14</sup> However, the exact linear dependence may be disturbed by the ligand-centered dipolar relaxation or intramolecular rotations. Another important consequence is that linewidth grows quadratically with the number of unpaired electrons. In other words, out of two spin states with similar geometry, the state with higher multiplicity will give broader signals.

#### Appendix B14. Paramagnetic NMR theory: signal assignment.

In general, the strategies used for assigning NMR signals in diamagnetic molecules are not applicable for paramagnetic species. Mainly, due to a much larger range of chemical shifts and the absence of fine structure due to line broadening. Despite that, a number of additional strategies are available based on the understanding of the origin of paramagnetic chemical shifts (see Appendix B13). The most common of them are as follows:<sup>10</sup>

1. Signal widths. As stated in *Appendix B13*, if dipolar relaxation is predominant, which is usually the case, the peak full width at half maximum should be inversely proportional to the sixth power of the distance between the resonating proton and the paramagnetic center ( $\Delta\nu_{1/2} \sim r^{-6}$ ). However, the exact linear dependence may be disturbed by the ligand-centered dipolar relaxation or intramolecular rotations. Still, as a rule of thumb, the broader of the two signals can be assigned to the proton that is closer to a paramagnetic center.
2. Signal areas. Despite unusual chemical shift range, the peak integral intensities are still proportional to the number of resonating protons. However, the integration may be complicated due to the extreme line broadening and residual “ringing” from the excitation pulse,<sup>13</sup> which may distort the base line.
3. (Isotopic) Substitution. Systematic substitution of certain protons in the molecule (mostly, for methyl groups or deuteria) may allow to assign some signals.
4. Signal shifts. Oftentimes, one can make an educated guess as for the mechanism of spin delocalization, which may allow to deduce the sign of a hyperfine shift.<sup>10,13</sup> High-level spin density calculations can be helpful in such situations.
5. Temperature dependence. As discussed in *Appendix B13*, paramagnetic NMR shifts are extremely temperature-dependent. Given strong domination of the Fermi contact term ( $\delta^C$ ), which is normally the case for covalent d-block compounds, observed shift  $\delta^{obs}$  should obey the following law:  $\delta^{obs} = \delta^{dia} + \delta^C = \delta^{dia} + \frac{C}{T}$ . In other words, the dependence of  $\delta^{obs}$  from  $\frac{1}{T}$  should be linear. In such a case, extrapolation to  $\frac{1}{T} = 0$  or  $T \rightarrow \infty$  will eliminate the contact component and reveal the diamagnetic contribution ( $\delta^{dia}$ ). The latter can, in turn, be compared with the shifts of the diamagnetic analogue of the paramagnetic compound in question.
6. Internuclear couplings. As mentioned above, paramagnetic relaxation is fast, which precludes  $J_{H,H}$  coupling from evolving sufficiently long to be seen, with sporadic exceptions.<sup>27</sup> Contrarily, signal assignment can often be aided using  $J_{C,H}$  couplings discernable from the  $^{13}\text{C}$  NMR spectra.
7. Nuclear Overhauser Effect (NOE), saturation transfer and correlation spectra in general. In some cases, for relatively narrow signals, one can obtain correlation spectra that will aid the assignment. These techniques have been worked out in great detail for bioinorganic molecules.<sup>14,28,29</sup>
8. Redox titration. If a paramagnetic species can be synthesized by oxidation/reduction of the diamagnetic precursor, gradual oxidation/reduction of the said precursor may allow to match paramagnetic signals to the assigned signals in the precursor, provided the redox equilibrium is fast on the NMR measurement timescale.

**Appendix B15.** Paramagnetic NMR:  $^1\text{H}$  signal assignment in  $[(\text{TSMMP})_2\text{Fe}^{\text{III}}]^-$  (**3**).

In the assignment of the paramagnetic NMR signals in the  $[(\text{TSMMP})_2\text{Fe}^{\text{III}}]^-$  complex (**3**), we use the line width argument, signal areas and isotopic substitution (see *Appendix B14*). More specifically, in the  $^1\text{H}$  NMR spectrum of  $[(\text{TSMMP})_2\text{Fe}^{\text{III}}]\text{K}$  salt (**3a**) in acetonitrile- $d_3$  at 298 K (*Figure B15.1*), one can see five out of six expected paramagnetically shifted signals. The missing sixth signal can be found in the spectrum of  $[(\text{TSMMP})_2\text{Fe}^{\text{III}}]\text{PPh}_4$  (**3b**) salt at 173 K in dichloromethane- $d_2$  (*Figure B15.2*), where **3b** is more soluble than **3a**. The signal shows as a broad (FWHM >5 ppm) singlet at -36.0 ppm, and is only visible because the  $[(\text{TSMMP})_2\text{Fe}^{\text{III}}]^-$  (**3**) anion almost completely crosses over into the low-spin state (2.1% of the high-spin contribution as estimated from measurements according to Evans method, see *Appendix B2*). Due to a smaller number of unpaired electrons, this leads to less efficient dipolar relaxation (see *Eq. B13.11*) and, thus, narrower line width. Being the broadest in the entire spectrum, this signal should belong to a proton that is by far the closest to the Fe center, assuming there is no significant spin delocalization to the ligand. Computationally optimized geometry of the low-spin ( $S = 1/2$ ) state at the B3LYP-D3BJ/def2-TZVP level of theory (*Figure B15.3*) shows that  $\text{H}^7$  at 3.27 Å is the likeliest source of the signal with the second closest protons,  $\text{CH}_3^{\text{P}}$ , being 5.43 Å away from the metal.

Next, among five paramagnetically shifted signals in the spectrum of  $[(\text{TSMMP})_2\text{Fe}^{\text{III}}]\text{K}$  (**3a**; *Figure B15.1*), only one at 67.8 ppm has triple integral intensity and can be unambiguously assigned to the aryl-bound methyl groups ( $\text{CH}_3^{\text{Ar}}$ ). Another signal at 12.3 ppm is not present in the  $^1\text{H}$  spectrum of the deuterium-labelled analogue **3a- $d_6$**  but shows in the corresponding  $^2\text{H}$  spectrum, and, thus, belongs to the phosphonium-bound methyl group ( $\text{CH}_3^{\text{P}}$ ). The three remaining signals, one at 27.5 ppm and two between 0 and -10 ppm, belong to one proton each and have distinctly different width. Despite the spectrum reflecting a mid-spin-crossover situation (80.8% according to Evans method, see *Appendix B2*), the relative ordering of the  $\text{Fe}\cdots\text{H}$  distances in the the calculated geometries of both spin states retains (*Figure B15.3*). Therefore, assuming there is no significant spin delocalization to the ligand in either of the spin states and that the rate of spin-crossover is much faster than any of the

Larmor frequencies,<sup>a</sup> we assign the remaining signals inversely to the respective Fe···H distances as H<sup>4</sup>, H<sup>6</sup> and H<sup>5</sup>.

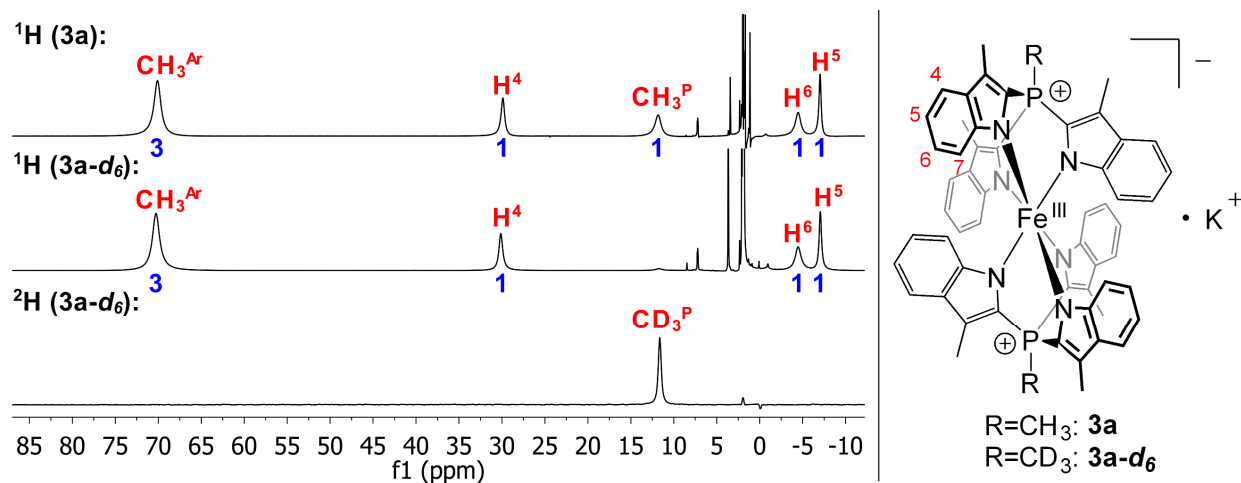


Figure B15.1. Stacked <sup>1</sup>H (400 MHz) and <sup>2</sup>H (61 MHz) NMR spectra of **3a** and its deuterated analogue **3a-d<sub>6</sub>** in acetonitrile at 298 K. Only paramagnetic signals are assigned. The integrals are given in blue and were rounded to the nearest integer.

<sup>a</sup> The assumption that the rate of the SCO is faster than nuclear Larmor frequencies is justified. Unless geometries of the involved spin states differ significantly,<sup>32</sup> SCO occurs at picosecond time scale (THz frequencies). This is six orders of magnitude faster than <sup>1</sup>H Larmor frequencies (MHz range) on modern NMR machines.



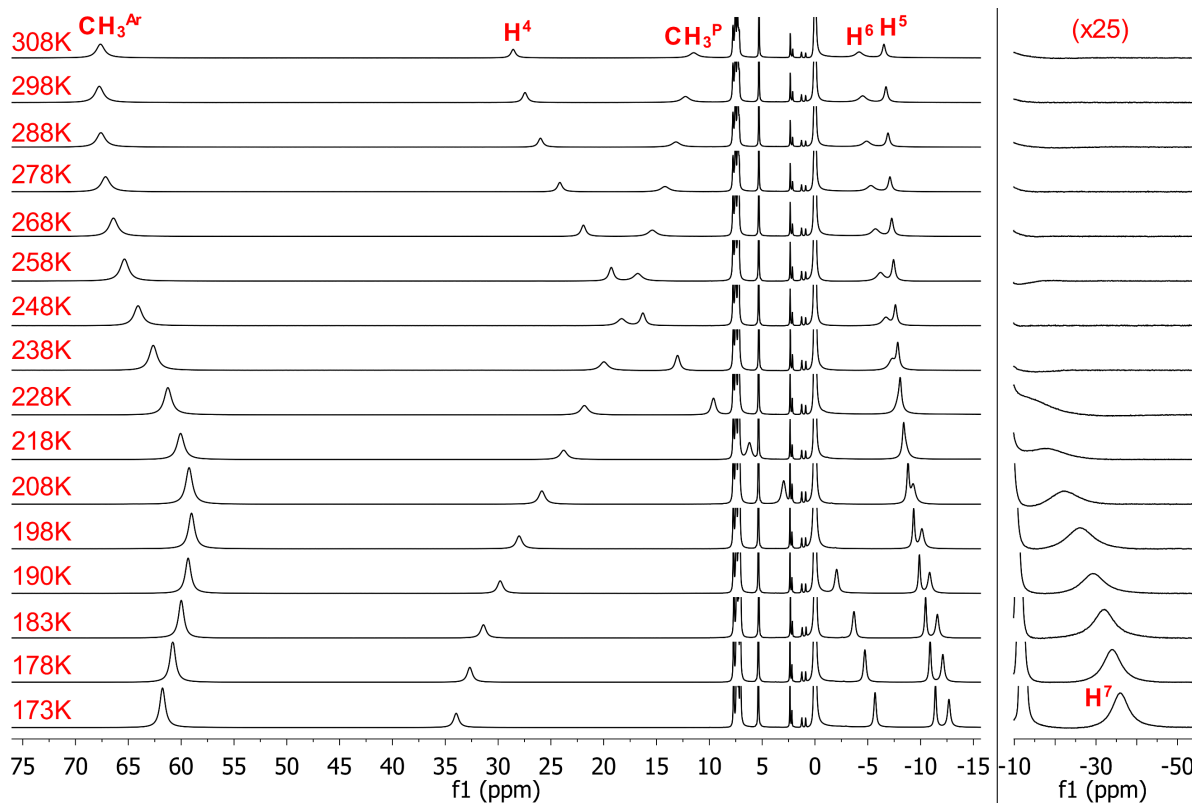


Figure B15.2. Stacked variable-temperature  $^1\text{H}$  (400 MHz) NMR spectra of **3b** in dichloromethane- $d_2$ . Only paramagnetic signals are assigned.

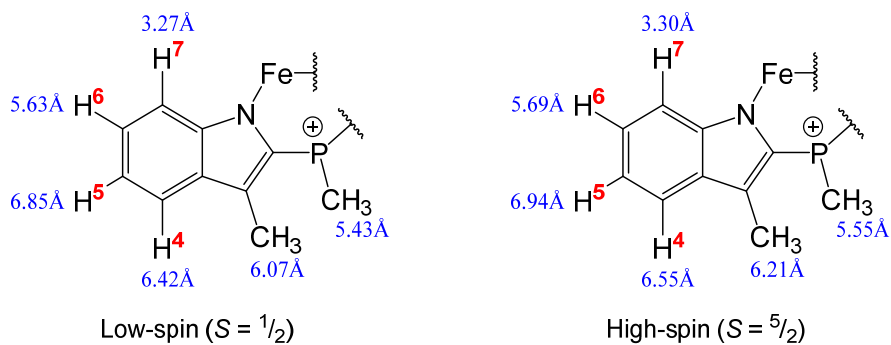


Figure B15.3. Calculated  $\text{Fe}\cdots\text{H}$  distances in low- and high-spin geometries of  $[(\text{TSMPP})_2\text{Fe}^{\text{III}}]^-$  (**3**) optimized at B3LYP-D3BJ/def2-TZVP level of theory in vacuum. The average values for methyl protons were derived by arithmetic averaging.

**Appendix B16.** Paramagnetic NMR: variable-temperature  $^1\text{H}$  spectra of  $[(\text{TSMMP})_2\text{Fe}^{\text{III}}]^-$  (**3**).

Variable-temperature  $^1\text{H}$  NMR chemical shifts of the  $[(\text{TSMMP})_2\text{Fe}^{\text{III}}]^-$  (**3**) complex in different solvents (*Figure B15.2*, *Figure B16.1*, *Figure B16.2*) are consistent with the ongoing SCO. To elaborate, the hyperfine parts ( $\delta^{\text{HF}}$ ) of the observed shifts, obtained by subtraction of the diamagnetic contributions approximated using an isostructural  $[(\text{TSMMP})_2\text{Ga}^{\text{III}}]^-$  (**5a**) analogue (*Table B16.1*, *Table B16.2*, *Table B16.3*), do not obey the Curie's law ( $\delta^{\text{HF}}T \neq \text{const}$ ; *Figure 3.6*, main text). Moreover, temperature behavior of the  $\delta^{\text{HF}}T$  product closely follows the SCO curves obtained by Evans method (*Figure B2.1*), implying that the hyperfine shifts are heavily dominated by the Fermi contact term ( $\delta^{\text{FC}}$ ), as expected for covalent  $d$ -block compounds.<sup>30</sup>

The signals in the discussed  $^1\text{H}$  spectra become sharper in all three solvents at either end of the SCO curve. At high temperatures in acetonitrile- $d_3$  (*Figure B16.1*) and, especially, pyridine- $d_5$  (*Figure B16.2*), the system is close to completely crossing over to the high-spin state (*Figure B2.1*). In these circumstances, despite more efficient dipolar relaxation with a higher number of unpaired electrons (see *Eq. B13.11*), faster temperature-induced electronic relaxation leads to slower nuclear relaxation, causing somewhat sharper signals. Contrarily, at low temperatures in dichloromethane- $d_2$  (*Figure B15.2*), the system is close to completely crossing over to the low-spin state (*Figure B2.1*). Even though low temperatures should prolong electronic relaxation and broaden the signals, dipolar nuclear relaxation, which generally dominates such broadening, is less efficient with fewer unpaired electrons (see *Eq. B13.11*). As a result, the SCO influence prevails, leading to sharper signals at lower temperatures.

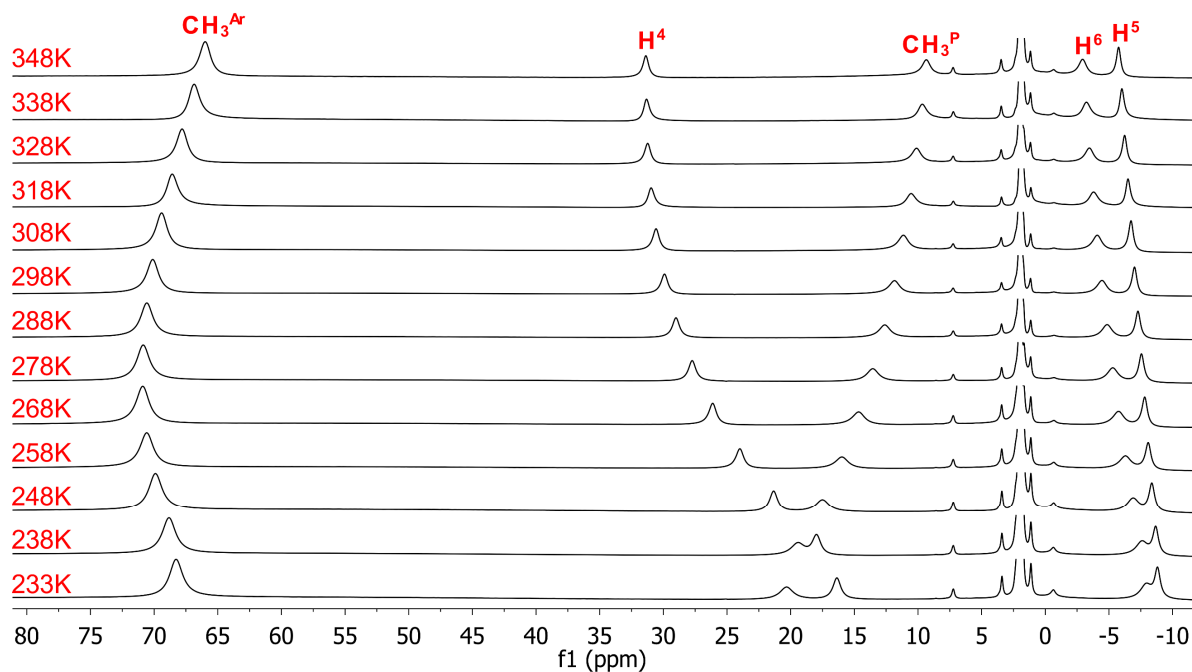


Figure B16.1. Stacked variable-temperature  $^1\text{H}$  (400 MHz) NMR spectra of **3a** in acetonitrile- $d_3$ . Only paramagnetic signals are assigned.

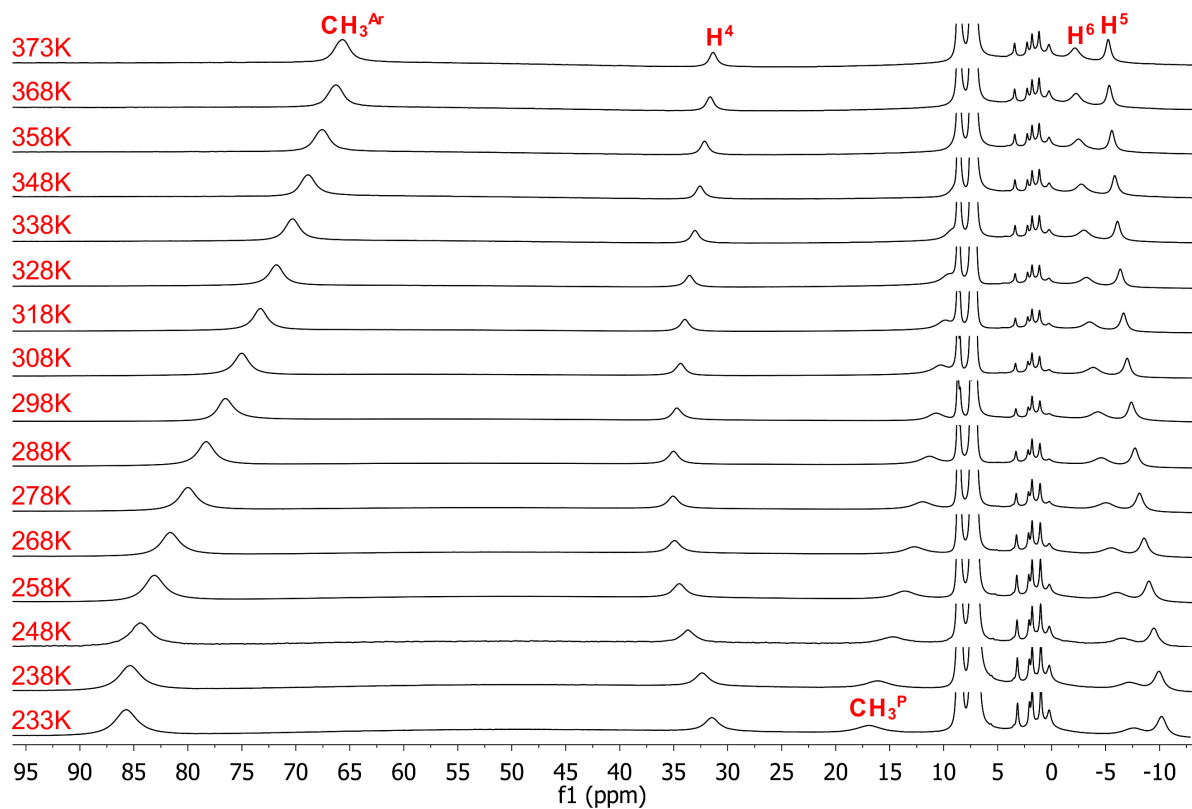


Figure B16.2. Stacked variable-temperature  $^1\text{H}$  (400 MHz) NMR spectra of **3a** in pyridine- $d_5$ . Only paramagnetic signals are assigned.

Table B16.1. Variable-temperature  $^1\text{H}$  NMR (400 MHz) chemical shifts of  $[(\text{TSMP})_2\text{Fe}^{\text{III}}]\text{PPh}_4$  (**3b**) salt in dichloromethane- $d_2$ . Diamagnetic shifts (assumed to be temperature-independent) were measured at 298 K on an isostructural  $[(\text{TSMP})_2\text{Ga}^{\text{III}}]\text{K}$  (**5a**) complex solubilized in the same solvent in the presence of a subequivalent amount of  $\text{PPh}_4\text{I}$  (see Section 3.8.2.1).

T, K	Chemical shift, ppm					
	$\text{CH}_3^{\text{Ar}}$	$\text{H}^4$	$\text{CH}_3^{\text{P}}$	$\text{H}^6$	$\text{H}^5$	$\text{H}^7$
308	67.6	28.6	11.5	-4.2	-6.5	-
298	67.8	27.5	12.3	-4.5	-6.7	-
288	67.6	26.0	13.2	-4.9	-6.9	-
278	67.2	24.2	14.2	-5.3	-7.1	-
268	66.4	21.9	15.4	-5.7	-7.3	-
258	65.4	19.3	16.8	-6.2	-7.4	-
248	64.1	16.3	18.3	-6.7	-7.6	-
238	62.6	13.0	20.0	-7.3	-7.8	-
228	61.3	9.6	21.8	-8.1	-8.1	-
218	60.1	6.2	23.8	-8.4	-8.4	-18.3
208	59.3	3.0	25.9	-9.3	-8.8	-22.3
198	59.0	0.5	28.0	-10.1	-9.4	-26.0
190	59.3	-2.1	29.8	-10.9	-9.9	-29.2
183	60.0	-3.7	31.4	-11.6	-10.5	-32.0
178	60.8	-4.7	32.7	-12.1	-10.9	-34.0
173	61.8	-5.7	34.0	-12.7	-11.4	-36.0
diamagnetic	2.78	7.11	3.47	5.55	6.15	5.21

Table B16.2. Variable-temperature  $^1\text{H}$  NMR (400 MHz) chemical shifts of  $[(\text{TSMP})_2\text{Fe}^{\text{III}}]\text{K}$  (**3a**) salt in acetonitrile- $d_3$ . Diamagnetic shifts (assumed to be temperature-independent) were measured at 298 K on an isostructural  $[(\text{TSMP})_2\text{Ga}^{\text{III}}]\text{K}$  (**5a**) complex in the same solvent.

T, K	Chemical shift, ppm				
	$\text{CH}_3^{\text{Ar}}$	$\text{H}^4$	$\text{CH}_3^{\text{P}}$	$\text{H}^6$	$\text{H}^5$
348	66.0	31.4	9.3	-3.0	-5.8
338	66.9	31.3	9.7	-3.2	-6.0
328	67.8	31.2	10.1	-3.5	-6.3
318	68.6	31.0	10.6	-3.8	-6.5
308	69.4	30.6	11.1	-4.1	-6.8
298	70.1	29.9	11.8	-4.5	-7.0
288	70.6	29.0	12.6	-4.9	-7.3
278	70.8	27.7	13.5	-5.3	-7.6
268	70.9	26.1	14.7	-5.8	-7.8
258	70.6	24.0	16.0	-6.3	-8.1
248	69.9	21.3	17.5	-6.9	-8.4
238	68.8	18.0	19.4	-7.6	-8.7
233	68.3	16.3	20.3	-8.0	-8.8
diamagnetic	2.79	7.12	3.57	5.46	6.15

Table B16.3. Variable-temperature  $^1\text{H}$  NMR (400 MHz) chemical shifts of  $[(\text{TSMP})_2\text{Fe}^{\text{III}}]\text{K}$  (**3a**) salt in pyridine- $d_5$ . Diamagnetic shifts (assumed to be temperature-independent) were measured at 298 K on an isostructural  $[(\text{TSMP})_2\text{Ga}^{\text{III}}]\text{K}$  (**5a**) complex in the same solvent.

T, K	Chemical shift, ppm				
	$\text{CH}_3^{\text{Ar}}$	$\text{H}^4$	$\text{CH}_3^{\text{P}}$	$\text{H}^6$	$\text{H}^5$
373	65.8	31.4	-	-2.1	-5.2
368	66.3	31.7	-	-2.2	-5.3
358	67.6	32.2	-	-2.5	-5.5
348	69.0	32.7	-	-2.7	-5.8
338	70.4	33.1	9.4	-3.0	-6.1
328	71.8	33.6	9.7	-3.2	-6.3
318	73.3	34.0	10.0	-3.5	-6.6
308	75.1	34.4	10.3	-3.9	-7.0
298	76.6	34.8	10.8	-4.2	-7.4
288	78.3	35.1	11.4	-4.6	-7.7
278	80.0	35.1	12.0	-5.0	-8.1
268	81.7	35.0	12.8	-5.5	-8.5
258	83.2	34.5	13.7	-6.0	-9.0
248	84.4	33.7	14.8	-6.6	-9.4
238	85.4	32.4	16.3	-7.2	-9.9
233	85.8	31.5	17.0	-7.7	-10.1
diamagnetic	2.85	7.40	3.74	6.25	6.34

#### Appendix B17. Paramagnetic NMR: $^1\text{H}$ signal assignment in $[(\text{TSMP})_2\text{Fe}^{\text{IV}}]$ (**4**).

The  $^1\text{H}$  NMR spectrum of complex  $[(\text{TSMP})_2\text{Fe}^{\text{IV}}]$  (**4**) in  $\text{DCM-}d_2$  at 298K shows six paramagnetically shifted and broadened signals (*Figure B17.1*), as expected for  $\text{C}_3$ -symmetric heterobicyclo[2.2.2]octane topology of the TSMP scaffold. These signals can be assigned using the set of arguments outlined in *Appendix B14*. To elaborate, out of six signals, only the one at 145.4 ppm has triple integral intensity and, thus, can be unambiguously attributed to the aryl-bound methyl groups ( $\text{CH}_3^{\text{Ar}}$ ). Next, the peak at 7.2 ppm is absent in the  $^1\text{H}$  spectrum of the deuterium-labelled analogue **4- $d_6$**  but shows in the corresponding  $^2\text{H}$  spectrum, which indicates that it belongs to a phosphonium-bound methyl group ( $\text{CH}_3^{\text{P}}$ ). A broad signal at -27.4 ppm clearly corresponds to a proton that is by far the closest to the source of the magnetic moment in the molecule. Considering that the spin density is mainly localized on the Fe atom (see the main text), this means that the signal belongs to the proton with the shortest  $\text{Fe}\cdots\text{H}$  distance, i.e.  $\text{H}^7$  as can be deduced from the molecular geometry optimized at PBE-D3BJ/def2-TZVP level of theory (*Figure B17.2*). The spectral assignment can be completed by inversely matching the full widths at half maximum (FWHM) of the remaining signals to the calculated  $\text{Fe}\cdots\text{H}$  distances for unassigned protons. More specifically, the relatively sharp signals between -10 and -35 ppm have

the FWHM of 156.2, 251.0 and 228.7 Hz from left to right,<sup>a</sup> which allows to assign them as H<sup>5</sup>, H<sup>6</sup> and H<sup>4</sup>.

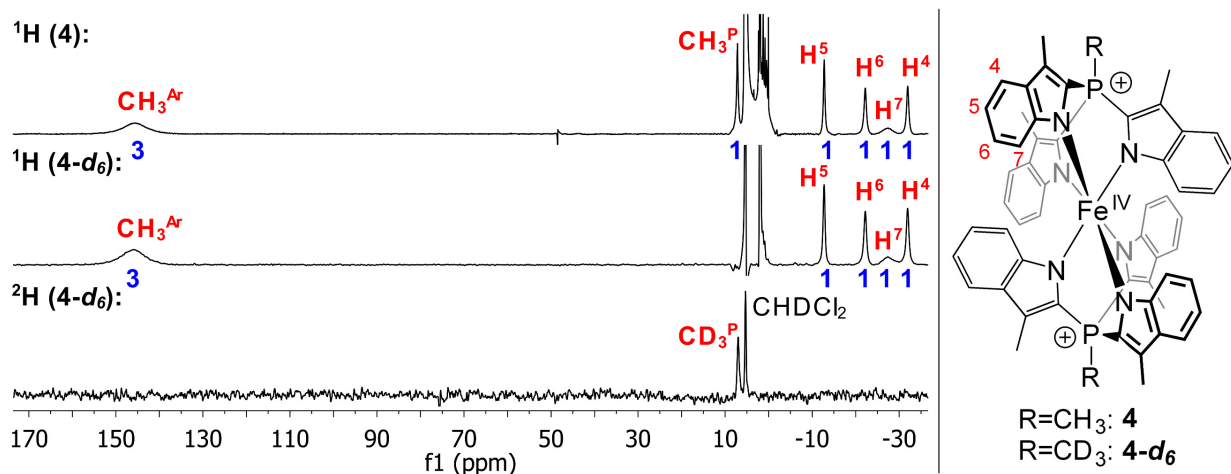


Figure B17.1. Stacked  $^1\text{H}$  (400 MHz) and  $^2\text{H}$  (61 MHz) NMR spectra of **4** and its deuterated analogue **4-d<sub>6</sub>** in dichloromethane at 298 K. Only paramagnetic signals are assigned. The integrals are given in blue and were rounded to the nearest integer.

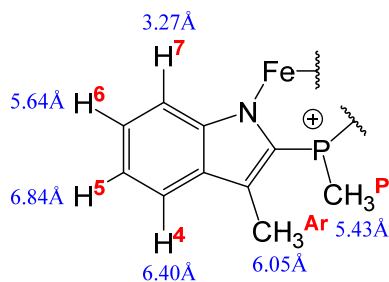


Figure B17.2. Calculated  $\text{Fe}\cdots\text{H}$  distances in  $[(\text{TSMPP})_2\text{Fe}^{\text{IV}}]$  (**4**) optimized at PBE-D3BJ/def2-TZVP level of theory in vacuum. The average values for methyl protons were derived by arithmetic averaging.

<sup>a</sup> Signal linewidths were extracted using MNova peak deconvolution tool.<sup>33</sup>

**Appendix B18.** Paramagnetic NMR: variable-temperature  $^1\text{H}$  spectra of  $[(\text{TSMMP})_2\text{Fe}^{\text{IV}}]$  (**4**).

Variable-temperature  $^1\text{H}$  NMR chemical spectra of **4** are shown in *Figure B18.1*. The spread of chemical shifts becomes monotonously narrower at increased temperatures, which is typical for paramagnetic compounds. The temperature-dependent signal linewidths also evolve in the way one would expect for a paramagnetic system: lower temperatures result in broader signals due to slower electronic relaxation causing faster nuclear relaxation and vice versa. The hyperfine shifts ( $\delta^{\text{HF}}$ ), obtained by subtraction of the diamagnetic contributions approximated using an isostructural  $[(\text{TSMMP})_2\text{Ga}^{\text{III}}]^-$  (**5**) analogue (*Table B18.1*), follow Curie's law. This is evident from the  $\delta^{\text{HF}}T$  product being nearly temperature-independent for most signals (*Figure B18.2*), ruling out the possibility of SCO. The small residual slope for some signals can be attributed to incomplete subtraction of diamagnetic components since the  $[(\text{TSMMP})_2\text{Ga}^{\text{III}}]^-$  (**5**) model only approximates  $\delta^{\text{dia}}$ , or to a very small pseudocontact contribution. The only exception is the  $\text{CH}_3^{\text{Ar}}$  signal, whose slope is relatively noticeable, likely due to incomplete rotational averaging of the chemical shifts of separate protons. Yet, overall, since the hyperfine shifts do not show a  $1/T^2$  dependence, the pseudocontact contribution can be considered very low (see *Appendix B13*), being consistent with nearly isotropic  $g$ -tensor, moderate zero-field splitting of  $+19.1\text{ cm}^{-1}$  and very low rhombicity as derived from SQUID magnetometry and THz-EPR studies as well as computational studies (see main text).

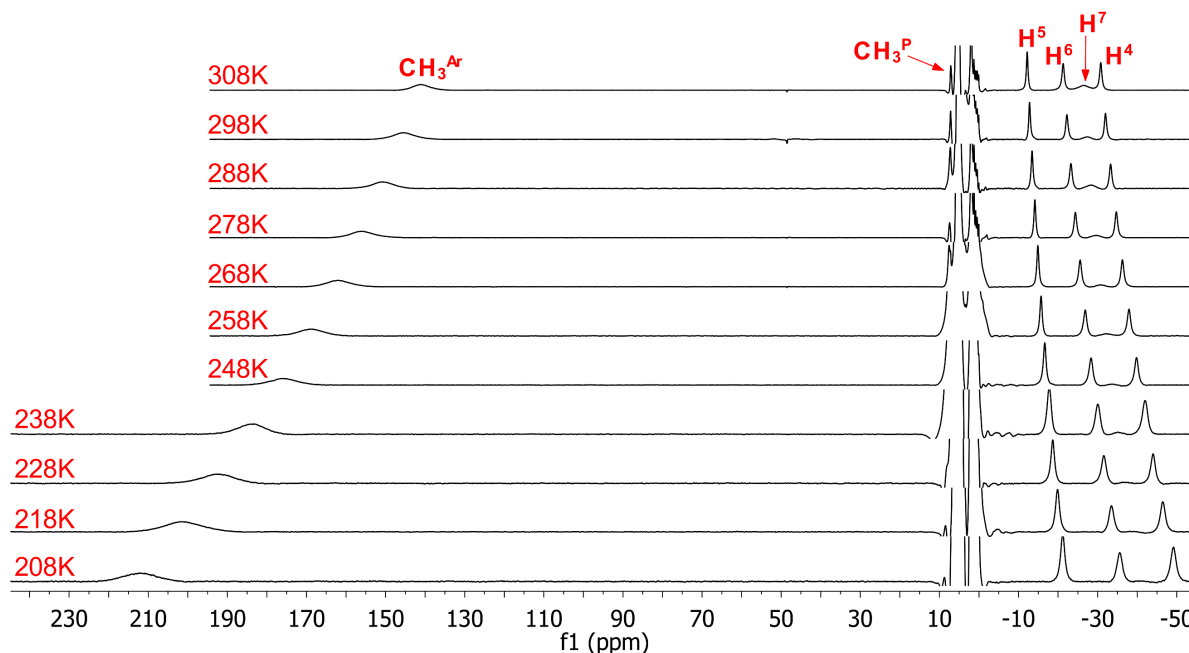


Figure B18.1. Stacked variable-temperature  $^1\text{H}$  (400 MHz) NMR spectra of **4** in dichloromethane- $d_2$ . Only paramagnetic signals are assigned.

Table B18.1. Variable-temperature  $^1\text{H}$  NMR (400 MHz) chemical shifts of  $[(\text{TSMMP})_2\text{Fe}^{\text{IV}}]$  (**4**) in dichloromethane- $d_2$ . Some chemical shifts could not be reliably extracted due to extreme line broadening at low temperatures or the presence of an intense solvent signal in the vicinity. Diamagnetic shifts (assumed to be temperature-independent) were measured at 298 K on an isostructural  $[(\text{TSMMP})_2\text{Ga}^{\text{III}}]\text{K}$  (**5a**) complex solubilized in dichloromethane- $d_2$  in the presence of a subequivalent amount of  $\text{PPh}_4\text{I}$  (Section 3.8.2.1).

T, K	Chemical shift, ppm					
	$\text{CH}_3^{\text{Ar}}$	$\text{CH}_3^{\text{P}}$	$\text{H}^5$	$\text{H}^6$	$\text{H}^7$	$\text{H}^4$
308	141.0	7.1	-12.2	-21.3	-26.4	-30.8
298	145.4	7.2	-12.8	-22.2	-27.4	-32.0
288	151.0	7.2	-13.4	-23.3	-28.4	-33.3
278	156.2	7.4	-14.1	-24.4	-29.6	-34.7
268	162.0	7.6	-14.9	-25.6	-30.8	-36.3
258	168.9	7.7	-15.7	-26.9	-32.2	-37.9
248	176.1	7.8	-16.6	-28.3	-33.6	-39.8
238	184.2	-	-17.7	-30.0	-35.1	-42.0
228	192.5	8.1	-18.7	-31.5	-	-44.0
218	201.4	-	-19.9	-33.5	-	-46.5
208	211.7	-	-21.2	-35.6	-	-49.2
diamagnetic	2.78	3.47	6.15	5.55	5.21	7.11



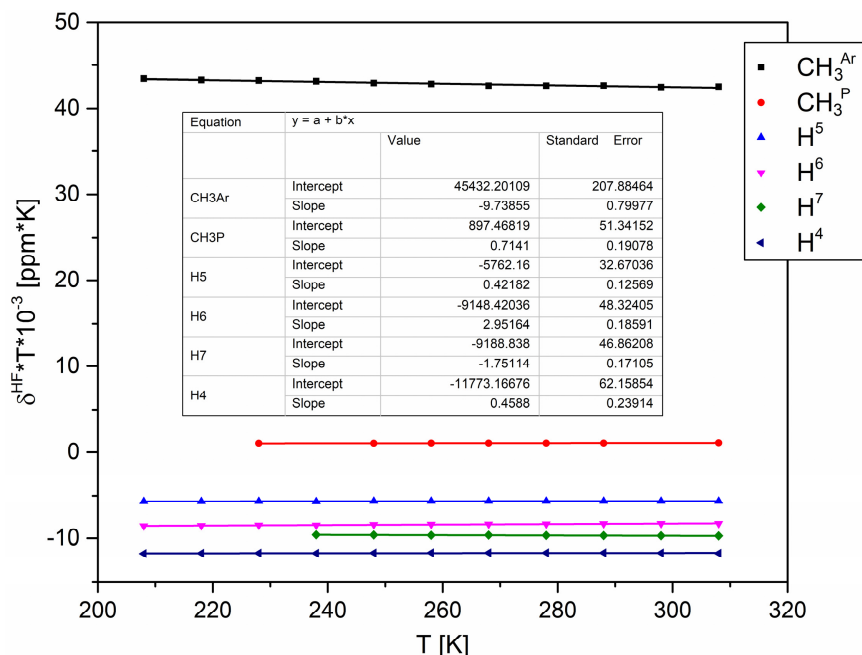


Figure B18.2. Variable-temperature  $^1\text{H}$  NMR (400 MHz)  $\delta^{HF}T$  products of complex  $[(\text{TSMP})_2\text{Fe}^{\text{IV}}]$  (**4**) in dichloromethane- $d_2$  and its linear fits. Dots show experimental values, straight lines show the fits.

### Appendix B19. Paramagnetic NMR: partitioning of $^1\text{H}$ hyperfine shifts in $[(\text{TSMP})_2\text{Fe}^{\text{IV}}]$ (**4**).

An additional confirmation as for the low magnitude of the pseudocontact shifts can be obtained by fitting observed chemical shifts ( $\delta^{obs}$ ) of **4** within the framework of the point dipole approximation (see *Appendix B13*) combined with DFT calculations. The equation for  $\delta^{obs}$  can be written as follows:

$$\delta^{obs} = \delta^{dia} + \delta^{HF} = \delta^{dia} + \delta^{FC} + \delta^{PC}, \quad \text{Eq. B19.1}$$

$$\delta^{obs} = \delta^{dia} + \frac{S(S+1)\mu_B}{3kTg_N\mu_N}g_{iso} \cdot A_{iso} + \frac{1}{12\pi r^3} \left[ \Delta\chi_{ax}(3\cos^2\theta - 1) + \frac{3}{2}\Delta\chi_{rh}\sin^2\theta\cos 2\varphi \right], \quad \text{Eq. B19.2}$$

where,  $\delta^{dia}$  – diamagnetic shift;  $\delta^{HF}$  – hyperfine shift;  $\delta^{FC}$  – Fermi contact shift;  $\delta^{PC}$  – pseudo-contact shift;  $S$  – electronic spin quantum number of the complex;  $\mu_B$  – Bohr magneton;  $g_N$  – nuclear  $g$ -value;  $\mu_N$  – nuclear magneton;  $k$  – Boltzmann constant;  $T$  – temperature;  $g_{iso}$  – isotropic electronic  $g$ -value of the system;  $A_{iso}$  – isotropic hyperfine coupling constant;  $r$ ,  $\theta$  and  $\varphi$  – spherical coordinates of a nucleus within the in-

trinsic frame of magnetic susceptibility tensor;  $\Delta\chi_{ax}$  and  $\Delta\chi_{rh}$  – axial anisotropy and rhombicity of the above tensor.

Since according to SQUID magnetometry and THz-EPR studies (see main text), the zero-field splitting parameter  $E$  is close to zero, magnetic susceptibility rhombicity  $\Delta\chi_{rh}$  also becomes vanishingly small (see Eq. B13.7 and Eq. B13.10), allowing to simplify Eq. B19.2 as follows:

$$\delta^{obs} = \delta^{dia} + \frac{S(S+1)\mu_B}{3kTg_N\mu_N}g_{iso} \cdot A_{iso} + \frac{1}{12\pi r^3}\Delta\chi_{ax}(3\cos^2\theta - 1). \quad \text{Eq. B19.3}$$

Out of all terms and coefficients in the equation,  $\delta^{dia}$  and  $S$  are known experimentally (the former are approximated using an isostructural [(TSMF)<sub>2</sub>Ga<sup>III</sup>]<sup>−</sup> (5) analogue, the latter equals one according to SQUID magnetometry);  $\mu_B$ ,  $k$ ,  $g_N$  and  $\mu_N$  are constants;  $r$  and  $\theta$  are geometric parameters that can be extracted from a DFT-optimized structure;  $A_{iso}$  and  $g_{iso}$  can also be either calculated from DFT or measured experimentally. This leaves only one parameter to be fitted,  $\Delta\chi_{ax}$ , which defines the strength of the pseudocontact contribution.

Following the symmetry of the spin Hamiltonian for [(TSMF)<sub>2</sub>Fe<sup>IV</sup>] (4), the principal axis of the magnetic susceptibility tensor has to coincide with the molecular axis of symmetry of the highest order, which is a C<sub>3</sub>-axis passing through the P–Fe–P atoms. Graphically it can be represented as shown in Figure B19.1, which features a plane with two out of six symmetry-equivalent indolide rings within the D<sub>3d</sub> point group. The principal axis ( $z$ ) points from the iron atom towards one of the phosphorus atoms. The polar angle  $\theta$  is measured with respect to this axis and the origin of coordinates, which is a metal center. The grey plot in polar coordinates in the background corresponds to the  $3\cos^2\theta - 1$  function modulating the magnitude of the pseudocontact shift as can be seen from the Eq. B19.3. This function changes its sign at the magic angle (ca. 54.7°) with respect to the principal axis, thus also flipping the sign of the pseudocontact shift.

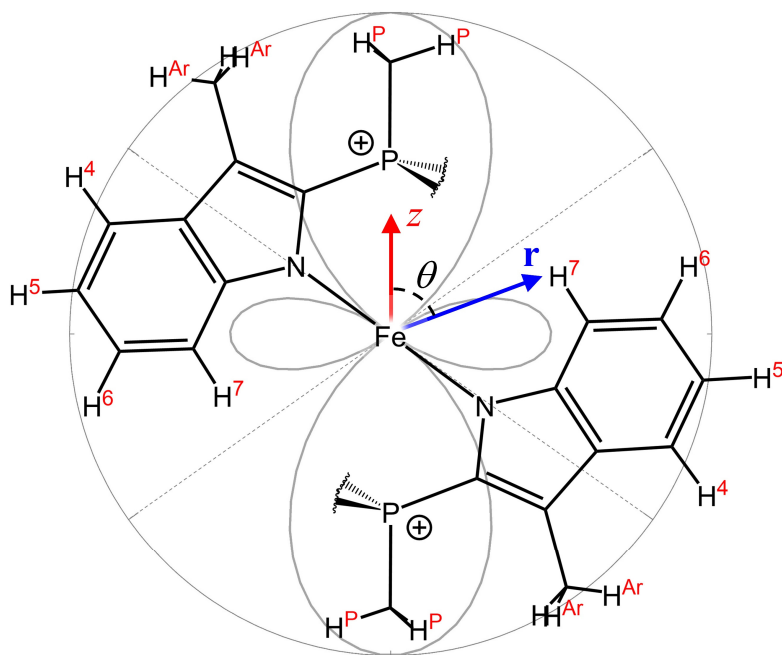


Figure B19.1. Graphical representation of the molecular geometry of **4** optimized at PBE-D3BJ/def2-TZVPP level of theory; angles and relative interatomic distances match the calculated values. Only two out of six symmetry-equivalent ( $D_{3d}$  point group) indolide rings are shown. The hydrogens of the  $\text{CH}_3^{\text{Ar}}$  and  $\text{CH}_3^{\text{P}}$  methyl groups are slightly out of plane but are still shown for clarity. The principal axis of the magnetic susceptibility tensor is given in red. The polar plot in the background corresponds to the  $3\cos^2\theta - 1$  function.

Table B19.1. Results of geometry optimization of **4** at PBE-D3BJ/def2-TZVPP level of theory followed by properties calculation at the PBE0-D3BJ/def2-TZVPP level. No symmetry constraints were imposed on a molecule, which results in small numerical differences between symmetry-equivalent positions. Numbers following underscores indicate separate aromatic rings. The average values (av) were obtained by arithmetic averaging.

Proton	$r$ , Å	$r_{av}$ , Å	$\cos\theta$	$ \cos\theta _{av}$	$A_{iso}$ , MHz	$\delta^{FC}T$ , ppm·K	$\delta^{FC}T_{av}$ , ppm·K
H <sup>4</sup> _1	6.40	6.40	0.42	0.42	-0.733	-15179.11	-15182.22
H <sup>4</sup> _2	6.40		0.42		-0.732	-15170.82	
H <sup>4</sup> _3	6.40		0.42		-0.734	-15197.76	
H <sup>4</sup> _4	6.40		-0.42		-0.734	-15197.76	
H <sup>4</sup> _5	6.40		-0.42		-0.732	-15168.75	
H <sup>4</sup> _6	6.40		-0.42		-0.733	-15179.11	
H <sup>5</sup> _1	6.84	6.84	0.06	0.06	-0.280	-5809.75	-5780.74
H <sup>5</sup> _2	6.84		0.06		-0.278	-5762.10	
H <sup>5</sup> _3	6.84		0.06		-0.279	-5770.38	
H <sup>5</sup> _4	6.84		-0.06		-0.279	-5770.38	
H <sup>5</sup> _5	6.84		-0.06		-0.278	-5760.02	
H <sup>5</sup> _6	6.84		-0.06		-0.281	-5811.82	

Table B19.1 (continued). Results of geometry optimization of **4** at PBE-D3BJ/def2-TZVPP level of theory followed by properties calculation at the PBE0-D3BJ/def2-TZVPP level. No symmetry constraints were imposed on a molecule, which results in small numerical differences between symmetry-equivalent positions. Numbers following underscores indicate separate aromatic rings. The average values (av) were obtained by arithmetic averaging.

Proton	$r$ , Å	$r_{av}$ , Å	$\cos\theta$	$ \cos\theta _{av}$	$A_{iso}$ , MHz	$\delta^{FC}T$ , ppm·K	$\delta^{FC}T_{av}$ , ppm·K	
H <sup>6</sup> _1	5.64	5.64	-0.29	0.29	-0.330	-6827.08	-6841.93	
H <sup>6</sup> _2	5.64		-0.29		-0.330	-6833.29		
H <sup>6</sup> _3	5.64		-0.29		-0.331	-6866.45		
H <sup>6</sup> _4	5.64		0.29		-0.331	-6866.45		
H <sup>6</sup> _5	5.64		0.29		-0.330	-6833.29		
H <sup>6</sup> _6	5.64		0.29		-0.329	-6825.01		
H <sup>7</sup> _1	3.27	3.27	-0.45	0.45	-0.556	-11509.69	-11461.69	
H <sup>7</sup> _2	3.27		-0.45		-0.551	-11422.67		
H <sup>7</sup> _3	3.27		-0.45		-0.553	-11453.74		
H <sup>7</sup> _4	3.27		0.45		-0.553	-11453.74		
H <sup>7</sup> _5	3.27		0.45		-0.551	-11420.59		
H <sup>7</sup> _6	3.27		0.45		-0.556	-11509.69		
CH <sub>3</sub> <sup>Ar</sup> _a_1	5.85	6.05	0.87	0.81	2.332	48317.89	43056.87	
CH <sub>3</sub> <sup>Ar</sup> _b_1	6.34		0.72		0.155	3211.52		43082.07
CH <sub>3</sub> <sup>Ar</sup> _c_1	5.96		0.83		3.751	77716.81		
CH <sub>3</sub> <sup>Ar</sup> _a_2	6.33		0.72		0.212	4396.68		
CH <sub>3</sub> <sup>Ar</sup> _b_2	5.97		0.83		3.833	79413.73		43169.79
CH <sub>3</sub> <sup>Ar</sup> _c_2	5.84		0.87		2.206	45698.95		
CH <sub>3</sub> <sup>Ar</sup> _a_3	5.96		0.83		3.754	77776.89		
CH <sub>3</sub> <sup>Ar</sup> _b_3	5.85		0.87		2.296	47567.85		42920.46
CH <sub>3</sub> <sup>Ar</sup> _c_3	6.34		0.72		0.165	3416.65		
CH <sub>3</sub> <sup>Ar</sup> _a_4	5.96		-0.83		3.751	77723.02		
CH <sub>3</sub> <sup>Ar</sup> _b_4	6.34		-0.72		0.155	3219.81		43082.77
CH <sub>3</sub> <sup>Ar</sup> _c_4	5.85		-0.87		2.331	48305.46		
CH <sub>3</sub> <sup>Ar</sup> _a_5	6.34		-0.72		0.165	3422.86		
CH <sub>3</sub> <sup>Ar</sup> _b_5	5.85		-0.87		2.295	47553.34		42917.70
CH <sub>3</sub> <sup>Ar</sup> _c_5	5.96		-0.83		3.754	77776.89		
CH <sub>3</sub> <sup>Ar</sup> _a_6	5.84		-0.87		2.205	45682.37		
CH <sub>3</sub> <sup>Ar</sup> _b_6	5.97		-0.83		3.833	79415.81		43168.41
CH <sub>3</sub> <sup>Ar</sup> _c_6	6.33		-0.72		0.213	4407.04		
CH <sub>3</sub> <sup>P</sup> _a	5.43	5.43	0.99	0.99	0.075	1549.82	1553.27	
CH <sub>3</sub> <sup>P</sup> _b	5.43		0.99		0.075	1543.60		
CH <sub>3</sub> <sup>P</sup> _c	5.43		0.99		0.076	1568.47		
CH <sub>3</sub> <sup>P</sup> _a'	5.43		-0.99		0.074	1541.53		
CH <sub>3</sub> <sup>P</sup> _b'	5.43		-0.99		0.075	1547.75		
CH <sub>3</sub> <sup>P</sup> _c'	5.43		-0.99		0.076	1568.47		

With these considerations in mind, we used the DFT-optimized structure of **4** to calculate the geometric parameters needed for fitting as well as Fermi contact shifts ( $\delta^{FC}$ ) in the form of temperature-independent Curie constants ( $\delta^{FC}T$ ) (Table B19.1). The latter were derived using the experimental  $g$ -value of 1.97 obtained from THz-EPR studies (see main text), although the calculated  $g$ -value of 2.03 would give only marginally

different results (see *Eq. B13.2*). The fits performed using the model described by *Eq. B19.3* reveal that  $\Delta\chi_{\text{ax}}$  is  $2.5 \cdot 10^{-32} \text{ m}^3$ , which is very low. As a matter of fact, it is lower than the expected error of the DFT calculations, which precludes us from more detailed analysis using *Eq. B13.3-Eq. B13.8*. A separate fit performed for the protons of the  $\text{CH}_3^{\text{P}}$  group, for which the pseudocontact shift should be the largest in the entire molecule (the lowest  $r_{\text{av}}$  and  $|\cos\theta|_{\text{av}}$  in *Table B19.1*), gives an even lower  $\Delta\chi_{\text{ax}}$  of  $5.3 \cdot 10^{-33} \text{ m}^3$ , which is comparable to  $3.2 \cdot 10^{-33} \text{ m}^3$  calculated by substituting the values derived from THz-EPR into *Eq. B13.6*.

In any case, since the fitted  $\Delta\chi_{\text{ax}}$  is very small, the calculated observed shifts show a very good agreement with the experiment even without taking  $\delta^{PC}$  into account (*Figure B19.2*), which also reinforces the paramagnetic signal assignments we made above (*Appendix B17*).

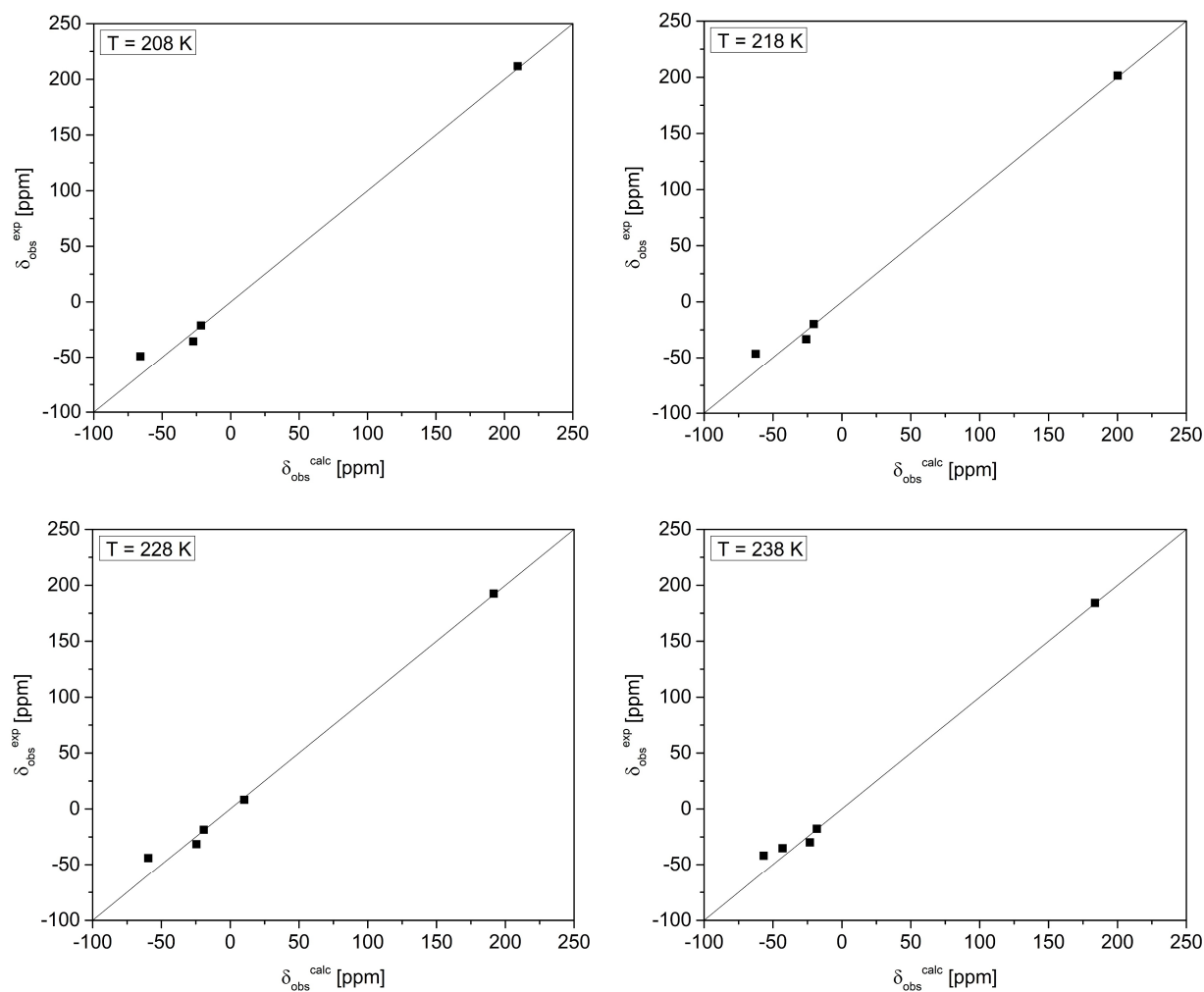


Figure B19.2. Correlation plots of experimental vs. calculated observed chemical shifts for complex 4.

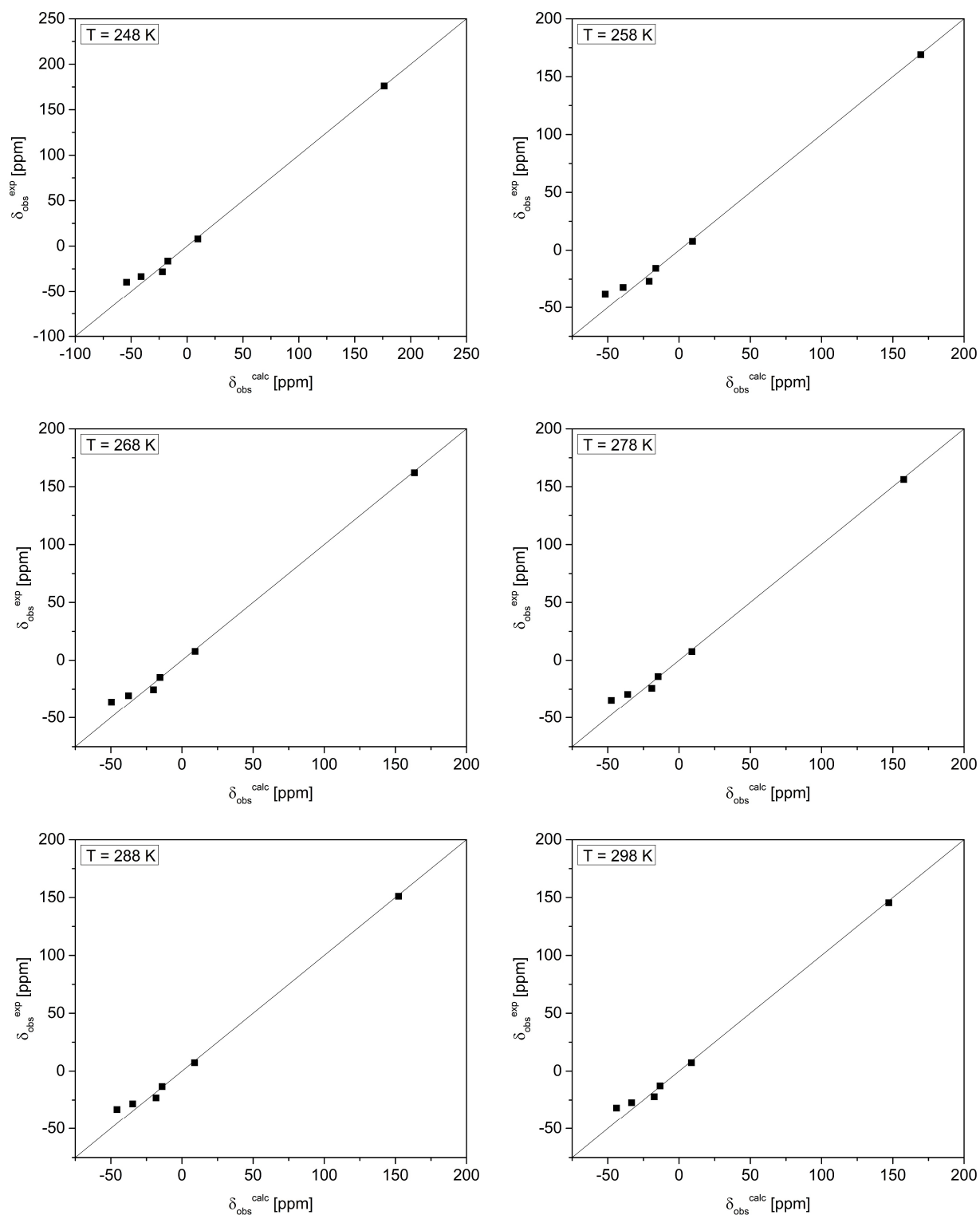


Figure B19.2 (continued). Correlation plots of experimental vs. calculated observed chemical shifts for complex 4.

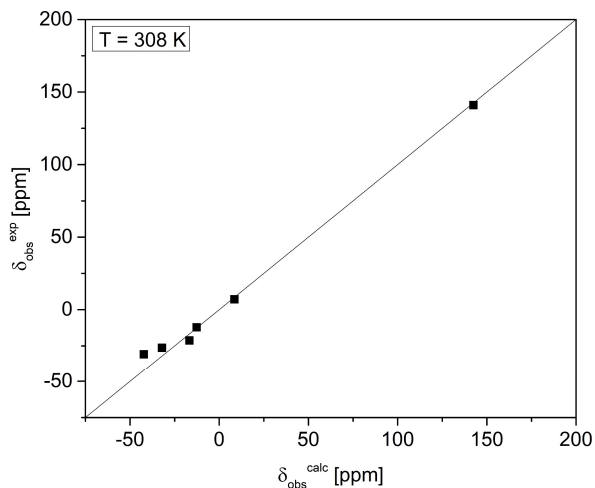


Figure B19.2 (continued). Correlation plots of experimental vs. calculated observed chemical shifts for complex 4.

#### Appendix B20. Variable-temperature UV-Vis spectra of $[(\text{TSMP})_2\text{Fe}^{\text{III}}]\text{PPh}_4$ (**3b**).

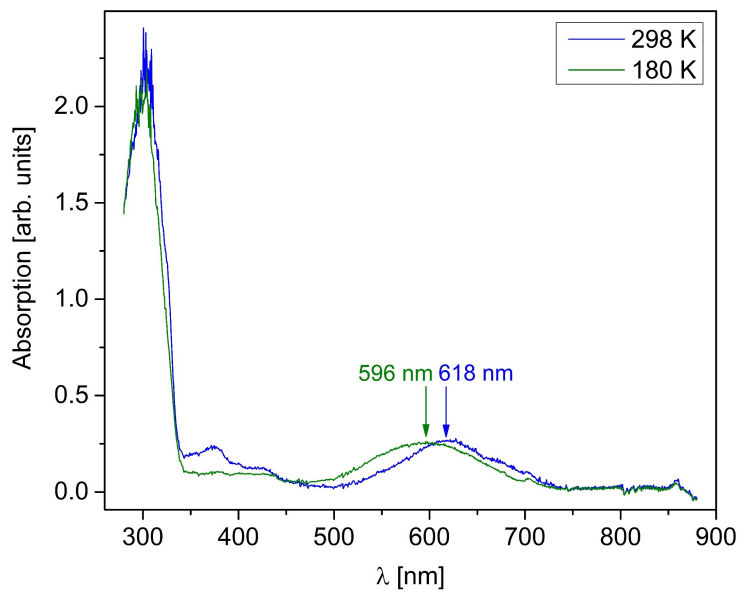


Figure B20.1. Change in UV-Vis spectrum of  $[(\text{TSMP})_2\text{Fe}^{\text{III}}]\text{PPh}_4$  (**3b**) in dichloromethane solution upon cooling. Visual color change is shown in Figure B20.2.

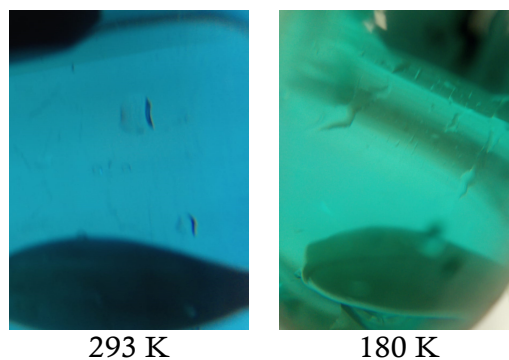


Figure B20.2. Color change of  $[(\text{TSMP})_2\text{Fe}^{\text{III}}]\text{PPh}_4$  (**3b**) in dichloromethane solution upon cooling.

### Appendix B21. TD-DFT-calculated UV-Vis spectra of $[(\text{TSMP})_2\text{Fe}^{\text{IV}}]$ (**4**).

Initial time-dependent density functional theory (TDDFT) calculations for **4** were performed in vacuum at three different levels of theory: TPSSh-D3BJ, B3LYP-D3BJ and PBE0-D3BJ with def2-TZVP basis set for Fe and def2-SVP set for all other atoms, employing optimized geometries from TPSSh-D3BJ/6-31G(d,p), B3LYP-D3BJ/6-31G(d,p) and PBE-D3BJ/6-31G(d,p) levels, respectively. Overall, all three functionals give the spectra that qualitatively reproduce the experiment (Figure B21.1), considering that only the first 50 excitations were calculated. Nevertheless, the best agreement with the experiment is achieved when using TPSSh-D3BJ functional.

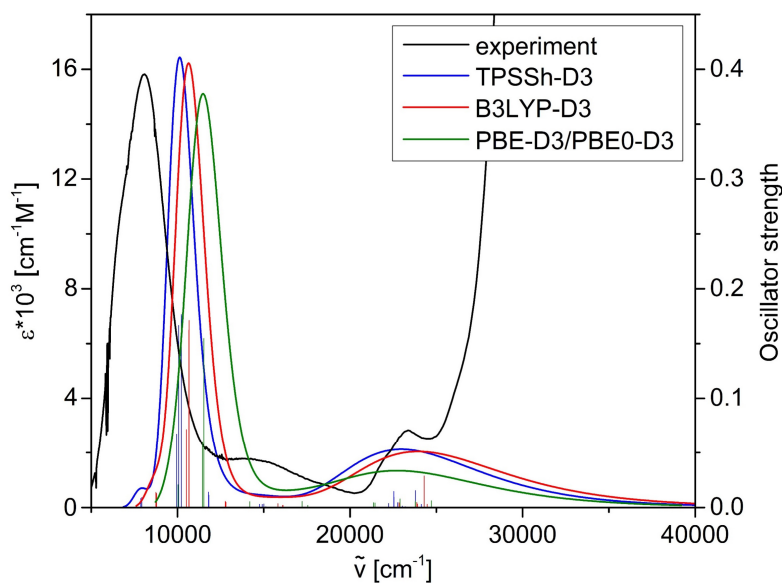


Figure B21.1. Experimental UV-Vis-NIR spectrum of **4** in dichloromethane solution and TDDFT transitions calculated using different functionals. In order to generate realistic spectra, Gaussian broadening with FWHM parameter of 170 nm was applied.



We further explored how calculated TDDFT transitions react to implicit solvation (PCM model) using the media with varied dielectric permeability ( $\epsilon$ ) from vacuum ( $\epsilon = \epsilon_0$ ) to water ( $\epsilon = 80.4$ ) (Figure B21.2). Both the energies of the maxima and transition intensities are weakly sensitive to the medium.

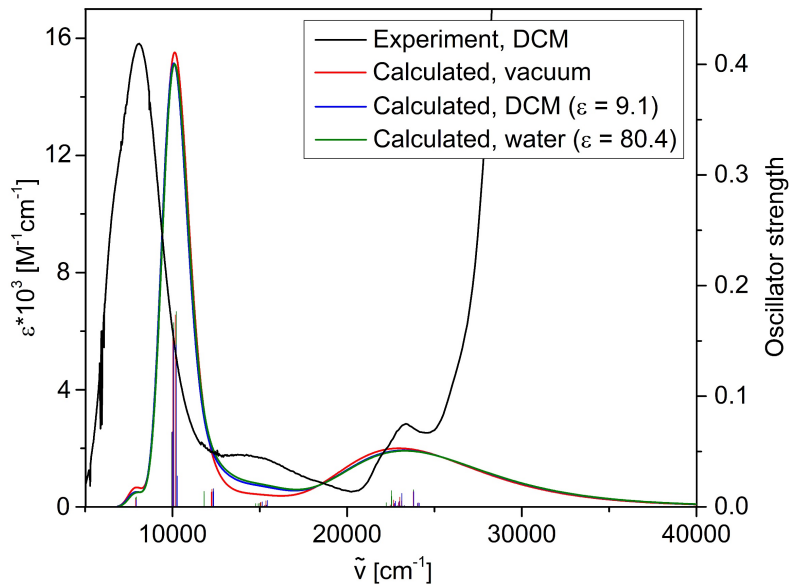


Figure B21.2. Experimental UV-Vis-NIR spectrum of **4** in dichloromethane solution and TDDFT transitions calculated in different media at TPSSh-D3BJ/def2-SVP (with def2-TZVP for Fe) level of theory. In order to generate realistic spectra, Gaussian broadening with FWHM parameter of 170 nm was applied.

Finally, we analyzed the structure of the calculated TDDFT transitions in more detail using Natural Transition Orbital (NTO) analysis.<sup>31</sup> This method performs separate unitary transformations of the occupied and virtual transition molecular orbitals so that only one or very few NTO donor-hole pairs are left with the predominant contribution to the transition. The most intense TDDFT transitions are labeled in Figure B21.3.<sup>a</sup> These transitions can be roughly grouped in two categories: numbers 3 to 22 mostly correspond to  $\pi \rightarrow d_{1e}$  ligand-to-metal charge transfer (LMCT), while numbers 40, 44 and 48 are a mixture of  $\pi \rightarrow d_{2e}$  LMCT and  $\pi \rightarrow \pi^*$  intra-ligand transi-

<sup>a</sup> For the sake of brevity, we did not provide the expansion of the transitions into the respective NTO donor-hole pairs in this appendix. Instead, it can be found in the respective publication: Tretyakov, S.; Lutz, M.; Titus, C. J.; de Groot, F.; Nehr Korn, J.; Lohmiller, T.; Holldack, K.; Schnegg, A.; Tarrago, M. F. X.; Zhang P.; Ye, S.; Aleshin, D.; Pavlov, A.; Novikov, V.; Moret, M.-E. Homoleptic Fe(III) and Fe(IV) Complexes of a Dianionic C<sub>3</sub>-Symmetric Scorpionate. *To be accepted after minor revisions to Inorg. Chem.*, 2023.

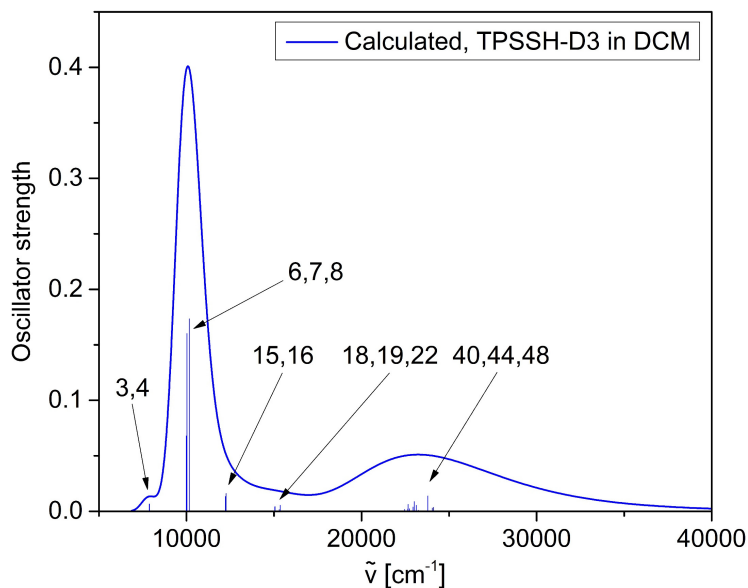


Figure B21.3. UV-Vis-NIR transitions in **4** calculated using TDDFT at TPSSH-D3BJ/def2-SVP (with def2-TZVP for Fe) level of theory in DCM. The most intense transitions are labeled in numbers and are further expanded upon in Table B21.1. In order to generate realistic spectrum, Gaussian broadening with FWHM parameter of 170 nm was applied.

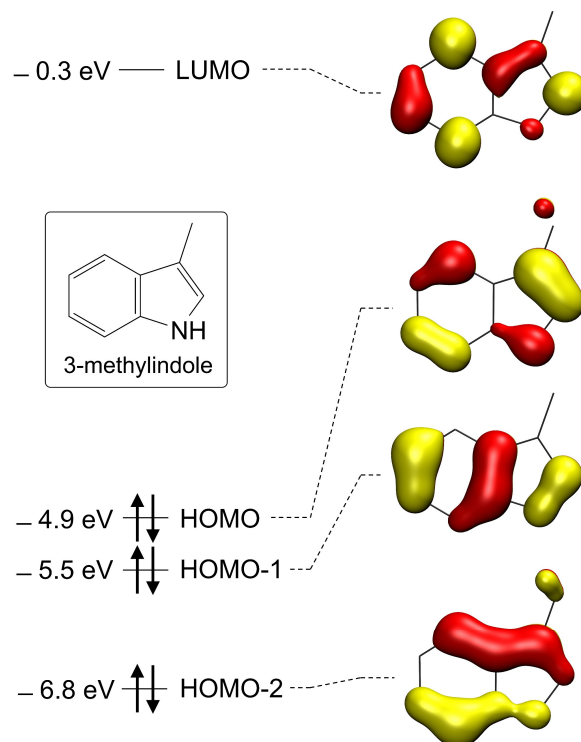


Figure B21.4. Molecular orbitals of 3-methylindole calculated at TPSSH-D3BJ/def2-SVP level of theory in vacuum. All orbitals have  $\pi$ -character, hence only a half of antisymmetric orbital lobes can be seen.

tions (ICT). It is worth noting that ligand-based donor  $\pi$ - and acceptor  $\pi^*$ -orbitals are always pure combinations of 3-methylindole HOMO, HOMO-1 and LUMO-like orbitals (*Figure B21.4*) of separate indolide arms of the TSMP ligand.

## B22 References

- (1) Savéant, J.-M. *Elements of Molecular and Biomolecular Electrochemistry: An Electrochemical Approach to Electron Transfer Chemistry*; John Wiley & Sons: Hoboken, NJ, 2006.
- (2) Tretiakov, S.; Damen, J. A. M.; Lutz, M.; Moret, M.-E. A Dianionic  $C_3$ -Symmetric Scorpionate: Synthesis and Coordination Chemistry. *Dalt. Trans.* **2020**, 49 (39), pp 13549–13556. DOI: 10.1039/D0DT02601H.
- (3) Evans, D. F. 400. The Determination of the Paramagnetic Susceptibility of Substances in Solution by Nuclear Magnetic Resonance. *J. Chem. Soc.* **1959**, pp 2003–2005. DOI: 10.1039/jr9590002003.
- (4) Piguet, C. Paramagnetic Susceptibility by NMR: The “Solvent Correction” Removed for Large Paramagnetic Molecules. *J. Chem. Educ.* **1997**, 74 (7), p 815. DOI: 10.1021/ed074p815.
- (5) Sur, S. K. Measurement of Magnetic Susceptibility and Magnetic Moment of Paramagnetic Molecules in Solution by High-Field Fourier Transform NMR Spectroscopy. *J. Magn. Reson.* **1989**, 82 (1), pp 169–173. DOI: 10.1016/0022-2364(89)90178-9.
- (6) Yatsunyk, L. A.; Walker, F. A. Structural, NMR, and EPR Studies of  $S = 1/2$  and  $S = 3/2$  Fe(III) Bis(4-Cyanopyridine) Complexes of Dodecasubstituted Porphyrins. *Inorg. Chem.* **2004**, 43 (2), pp 757–777. DOI: 10.1021/ic035010q.
- (7) Sorai, M.; Seki, S. Phonon Coupled Cooperative Low-Spin  $^1A_1$ High-Spin  $^5T_2$  Transition in  $[\text{Fe}(\text{Phen})_2(\text{NCS})_2]$  and  $[\text{Fe}(\text{Phen})_2(\text{NCSe})_2]$  Crystals. *J. Phys. Chem. Solids* **1974**, 35 (4), pp 555–570. DOI: 10.1016/S0022-3697(74)80010-7.
- (8) Nehr Korn, J.; Veber, S. L.; Zhukas, L. A.; Novikov, V. V.; Nelyubina, Y. V.; Voloshin, Y. Z.; Holldack, K.; Stoll, S.; Schnegg, A. Determination of Large Zero-Field Splitting in High-Spin Co(I) Clathrochelates. *Inorg. Chem.* **2018**, 57 (24), pp 15330–15340. DOI: 10.1021/acs.inorgchem.8b02670.
- (9) Köhler, F. H. Paramagnetic Complexes in Solution: The NMR Approach. In *Encyclopedia of Magnetic Resonance*; John Wiley & Sons, Ltd: Chichester, UK, 2011. DOI: 10.1002/9780470034590.emrstm1229.
- (10) Köhler, F. H. Probing Spin Densities by Use of NMR Spectroscopy. In *Magnetism: Molecules to Materials*; Wiley-VCH Verlag GmbH & Co. KGaA: Weinheim, Germany, 2003; Vol. 1–5, pp 379–430. DOI: 10.1002/9783527620548.ch12.
- (11) Bertini, I.; Luchinat, C.; Parigi, G. Magnetic Susceptibility in Paramagnetic NMR. *Prog. Nucl. Magn. Reson. Spectrosc.* **2002**, 40 (3), pp 249–273. DOI: 10.1016/S0079-6565(02)00002-X.
- (12) Pell, A. J.; Pintacuda, G.; Grey, C. P. Paramagnetic NMR in Solution and the Solid State. *Prog. Nucl. Magn. Reson. Spectrosc.* **2019**, 111, pp 1–271. DOI: 10.1016/j.pnmrs.2018.05.001.
- (13) Drago, R. S. *Physical Methods for Chemists*, 2nd ed.; Saunders College Publishing: Philadelphia, 1992.
- (14) Bertini, I.; Luchinat, C.; Giacomo, P. *Solution NMR of Paramagnetic Molecules, Volume 2 of Current Methods in Inorganic Chemistry*, 1st ed.; Elsevier Science: Amsterdam, 2001.
- (15) Bertini, I.; Luchinat, C. *NMR of Paramagnetic Molecules in Biological Systems*; Benjamin/Cummings Pub. Co.: Menlo Park, California, 1986.
- (16) Bren, K. L. NMR Analysis of Spin Densities. In *Spin States in Biochemistry and Inorganic Chemistry*; John Wiley & Sons, Ltd: Oxford, UK, 2015; pp 409–434. DOI: 10.1002/9781118898277.ch16.
- (17) Bleaney, B. Nuclear Magnetic Resonance Shifts in Solution Due to Lanthanide Ions. *J. Magn. Reson.* **1972**, 8 (1), pp 91–100. DOI: 10.1016/0022-2364(72)90027-3.
- (18) Bertini, I.; Luchinat, C. NMR of Paramagnetic Substances. *Coord Chem Rev.* **1996**, 150, pp 29–75.

- (19) La Mar, G. N. *NMR of Paramagnetic Molecules - Principles and Applications*; La Mar, G. N., Dew. Horrocks, W., Holm, R. H., Eds.; Academic Press, INC., New York and London, 1973.
- (20) McGarvey, B. R. Theory of the NMR Paramagnetic Shift of Pseudotetrahedral Complexes of Nickel(II) and Cobalt(II). *Inorg. Chem.* **1995**, *34* (24), pp 6000–6007. DOI: 10.1021/ic00128a010.
- (21) Damjanović, M.; Samuel, P. P.; Roesky, H. W.; Enders, M. NMR Analysis of an Fe(I)-Carbene Complex with Strong Magnetic Anisotropy. *Dalt. Trans.* **2017**, *46* (16), pp 5159–5169. DOI: 10.1039/C7DT00408G.
- (22) Mao, J.; Zhang, Y.; Oldfield, E. Nuclear Magnetic Resonance Shifts in Paramagnetic Metalloporphyrins and Metalloproteins. *J. Am. Chem. Soc.* **2002**, *124* (46), pp 13911–13920. DOI: 10.1021/ja020297w.
- (23) Knorr, R.; Hauer, H.; Weiss, A.; Polzer, H.; Ruf, F.; Löw, P.; Dvortsák, P.; Böhrer, P. Unpaired Spin Densities from NMR Shifts and Magnetic Anisotropies of Pseudotetrahedral Cobalt(II) and Nickel(II) Vinamidine Bis(Chelates). *Inorg. Chem.* **2007**, *46* (20), pp 8379–8390. DOI: 10.1021/ic700656r.
- (24) Fernández, P.; Pritzkow, H.; Carbó, J. J.; Hofmann, P.; Enders, M. <sup>1</sup>H NMR Investigation of Paramagnetic Chromium(III) Olefin Polymerization Catalysts: Experimental Results, Shift Assignment and Prediction by Quantum Chemical Calculations. *Organometallics* **2007**, *26* (18), pp 4402–4412. DOI: 10.1021/om070173y.
- (25) Roquette, P.; Maronna, A.; Reinmuth, M.; Kaifer, E.; Enders, M.; Himmel, H.-J. Combining NMR of Dynamic and Paramagnetic Molecules: Fluxional High-Spin Nickel(II) Complexes Bearing Bisguanidine Ligands. *Inorg. Chem.* **2011**, *50* (5), pp 1942–1955. DOI: 10.1021/ic102420x.
- (26) Weber, B.; Walker, F. A. Solution NMR Studies of Iron(II) Spin-Crossover Complexes. *Inorg. Chem.* **2007**, *46* (16), pp 6794–6803. DOI: 10.1021/ic062349e.
- (27) Breikss, A. I.; Nicholson, T.; Jones, A. G.; Davison, A. Synthesis and Characterization of Technetium(III) and Technetium(II) Complexes with Mixed Phosphine, Chloride, and Nitrogen-Donor Ligands. X-Ray Crystal Structure of (2,2'-Bipyridine)Trichloro(Triphenylphosphine)Technetium. *Inorg. Chem.* **1990**, *29* (4), pp 640–645. DOI: 10.1021/ic00329a017.
- (28) *NMR of Paramagnetic Molecules*; Berliner, L. J., Reuben, J., Eds.; Biological Magnetic Resonance; Springer US: Boston, MA, 1993; Vol. 12. DOI: 10.1007/978-1-4615-2886-9.
- (29) Bertini, I.; Turano, P.; Vila, A. J. Nuclear Magnetic Resonance of Paramagnetic Metalloproteins. *Chem. Rev.* **1993**, *93* (8), pp 2833–2932. DOI: 10.1021/cr00024a009.
- (30) DE, S.; Tewary, S.; Garnier, D.; Li, Y.; Gontard, G.; Lisnard, L.; Flambard, A.; Breher, F.; Boillot, M.-L.; Rajaraman, G.; Lescouezec, R. Solution and Solid-State Study of the Spin-Crossover [Fe<sup>II</sup>(R-Bik)<sub>3</sub>](BF<sub>4</sub>)<sub>2</sub> Complexes (R = Me, Et, Vinyl). *Eur. J. Inorg. Chem.* **2017**. DOI: 10.1002/ejic.201701013.
- (31) Martin, R. L. Natural Transition Orbitals. *J. Chem. Phys.* **2003**, *118* (11), pp 4775–4777. DOI: 10.1063/1.1558471.
- (32) Petzold, H.; Djomgoue, P.; Hörner, G.; Lochenie, C.; Weber, B.; Rüffer, T. Bis-Meridional Fe<sup>2+</sup> Spin-crossover Complexes of Phenyl and Pyridyl Substituted 2-(Pyridin-2-Yl)-1,10-Phenanthrolines. *Dalt. Trans.* **2018**, *47* (2), pp 491–506. DOI: 10.1039/C7DT02320K.
- (33) MestReNova v.9.0.1-13254. Mestrelab Research S.L. 2014.

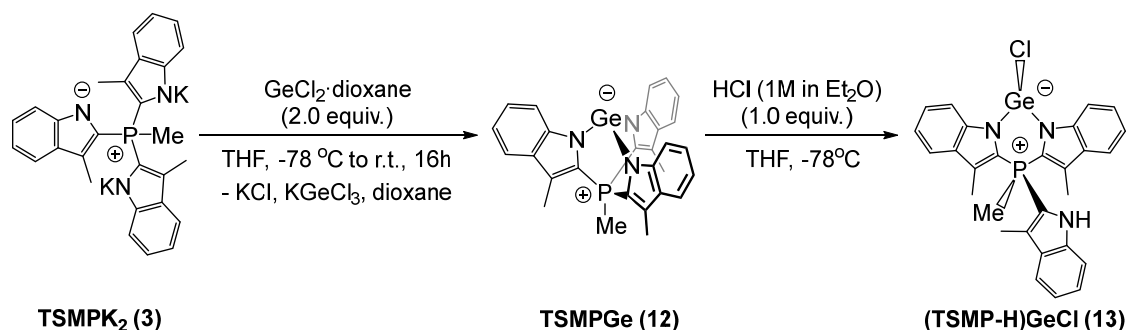


# Appendix C

## Supporting Information to Chapter 4

**Appendix C1.** The importance of a non-coordinating anion for  $2^{\text{BARF}}$  supported by reactions of the germanium analogue **12**.

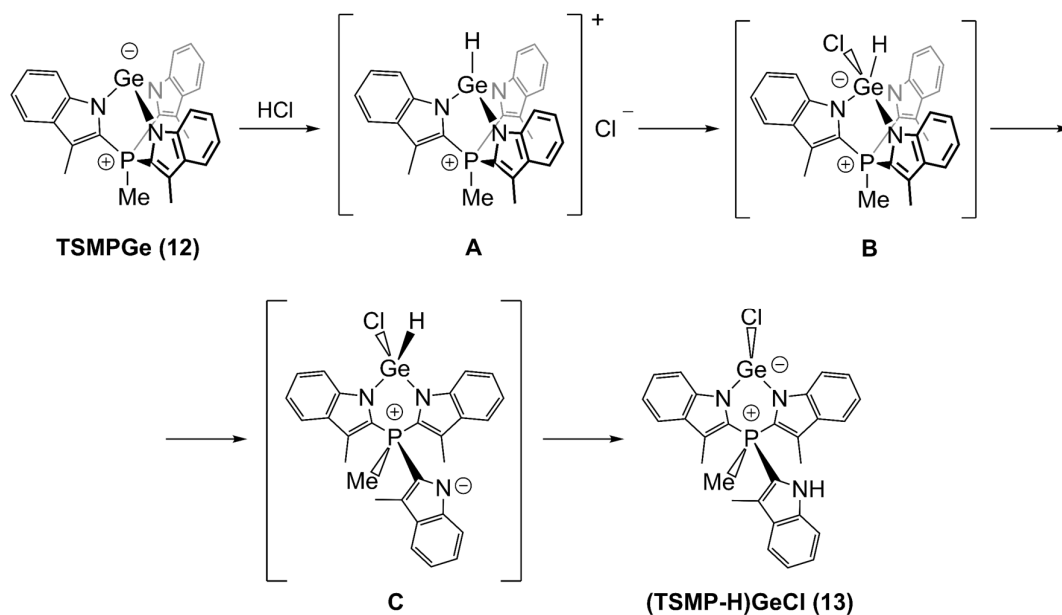
Initial protonation attempts of TSMPSi (**1**) were performed by reacting with an equimolar amount of ethereal hydrogen chloride in THF, although this gave intractable mixtures of products. In view of generally similar reactivity trends between silicon and germanium compounds, and also higher stability of the latter, we then attempted the protonation of a zwitterionic germanium analogue TSMPCGe (**12**; *Scheme C1.1*). This was anticipated to help us identify the intermediates responsible for degradation in case of TSMPSi (**1**). Germanide TSMPCGe (**12**) was prepared using TSMPC<sub>2</sub> (**3**) and following a procedure for the synthesis of an analogous C-tethered compound.<sup>1</sup>



*Scheme C1.1.* Synthesis and attempted protonation of the zwitterionic germanide TSMPCGe (**12**).

Interestingly, the reaction yielded a zwitterionic germanide (TSMP-H)GeCl (**13**), which can be formally considered a product of hydrogen chloride addition to a Ge-N bond in **12**. The structure of insoluble **13** was elucidated by X-ray crystallography (see *Section 4.10.3*) and has a chloride and a methyl group in a *syn* configuration with respect to a six-membered germanocyclic ring.

Taking into account the stereochemistry of **13**, we speculate that its origin goes back to the cationic germane (**A** in *Scheme C1.2*) that is analogous to the desired silane,  $[\text{TSMPSiH}]^+$  (**2**). Namely, **A** can be attacked by its chloride counterion to generate a trigonal bipyramidal intermediate **B**, where the apicophilic chloride occupies an axial position, thus labilizing the bond between germanium the opposing indolide. The breaking of the said bond leads to germane **C** that can be viewed as a tautomer of the final (TSMP-H)GeCl (**13**).

Scheme C1.2. Proposed mechanism of formation of **13**.

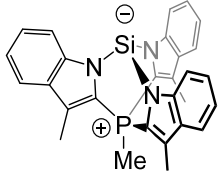
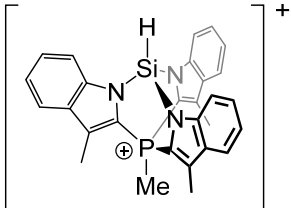
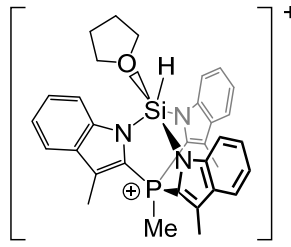
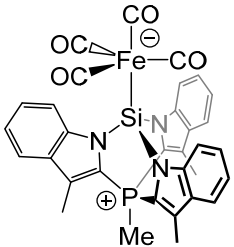
Regarding the origin of the strain-release Lewis acidity of **A**, our reasoning is as follows. By examining the solid-state structures of TSMPSi (**1**) (see Section 4.10.3) as well as  $\kappa^3$  complexes of Fe(II), Ni(II), Cu(I) with the TMS-P scaffold,<sup>2</sup> it becomes apparent that the latter prefers  $\text{N}^{\wedge}\text{E}^{\wedge}\text{N}$  angles that are close to  $90^\circ$ . Coincidentally, this is the angles between bidirectional  $p_x$ ,  $p_y$  and  $p_z$  atomic orbitals. Hence, the higher  $p$ -character of E–N bonds, the lesser the strain. In this respect, germanide **12** is a rather unstrained system since, according to computational NBO analysis, its E–N bonding orbitals have 93.8% of  $p$ -character on average, and its crystallographic  $\text{N}^{\wedge}\text{Ge}^{\wedge}\text{N}$  angles are around  $90^\circ$  (see Section 4.10.3). Protonation of its anionic lone pair, yielding **A**, should steeply increase its  $p$ -character, in accordance with Bent's rule.<sup>3</sup> Consequently, this should lead to a larger  $s$ -character the Ge–N bonding orbitals, thus requiring more obtuse  $\text{N}^{\wedge}\text{Ge}^{\wedge}\text{N}$  angles. Such a change should be in conflict with the preference of the TSM-P scaffold, thus generating strain within the cage structure. This strain could be relieved by coordination of a chloride anion (intermediate **B**). In other words, germane **A** should exhibit strain-release Lewis acidity. It is reasonable to assume that protonation of silanide TSMPSi (**1**) with HCl proceeds in a similar fashion, yet, due to generally higher reactivity of Si compounds, degradation occurs at some stage after coordination of a chloride anion.

If the above reasoning is correct, protonated TSMPSi (**1**) may be possible to obtain using acids with non-coordinating anions. Indeed, reacting **1** with an equimolar amount of Brookhart's acid ( $\text{HBAr}^{\text{F}_4} \cdot 2\text{Et}_2\text{O}$ ) resulted in successful protonation and formation of the desired cationic silane  $[\text{TSMPSiH}]^+ \text{BAr}^{\text{F}_4}^-$  (**2<sup>BARF</sup>**).

## Appendix C2. Calculated NMR parameters for isolated compounds.

Experimental and calculated  $^{29}\text{Si}$  and  $^{31}\text{P}$  NMR parameters of selected silicon compounds are shown in Table C2.1. Experimental spin-spin coupling constants  $J$  are given as absolute values. Regardless of the starting geometry, optimization of THF-coordinated silane **2**·THF always yielded a trigonal bipyramidal silicon center with an axial oxygen atom, which is consistent with high apicophilicity of the latter.

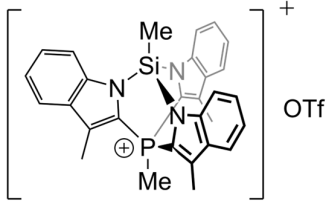
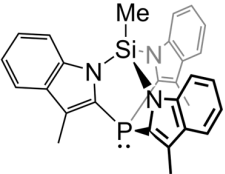
Table C2.1. Calculated  $^{29}\text{Si}$  and  $^{31}\text{P}$  NMR parameters of selected silicon compounds. Experimental spin-spin coupling constants  $J$  are given as absolute values.

Compound	NMR parameters			
	$\delta$ , ppm		$J$ , Hz	
	Experimental	Calculated	Experimental	Calculated
 <p><b>TSMPSi (1)</b></p>	<u>THF-<math>d_5</math></u> : $\delta(^{31}\text{P}) = -7.6$ $\delta(^{29}\text{Si}) = -48.0$ <u>Pyridine-<math>d_5</math></u> : $\delta(^{31}\text{P}) = -7.7$ $\delta(^{29}\text{Si}) = -47.5$	<u>THF-<math>d_5</math></u> : $\delta(^{31}\text{P}) = -14.8$ $\delta(^{29}\text{Si}) = -56.2$ <u>Pyridine-<math>d_5</math></u> : $\delta(^{31}\text{P}) = -14.7$ $\delta(^{29}\text{Si}) = -54.2$	<u>THF-<math>d_5</math></u> : $J_{\text{Si,P}} = 4.3$ <u>Pyridine-<math>d_5</math></u> : $J_{\text{Si,P}} = 4.4$	<u>THF-<math>d_5</math></u> : $J_{\text{Si,P}} = 7.9$ <u>Pyridine-<math>d_5</math></u> : $J_{\text{Si,P}} = 7.8$
 <p><b>[TSMPSiH]<sup>+</sup> (2)</b></p>	<u>2<sup>BARF</sup> in DCM-<math>d_2</math></u> : $\delta(^{31}\text{P}) = -7.6$ $\delta(^{29}\text{Si}) = -46.4$	<u>DCM-<math>d_2</math></u> : $\delta(^{31}\text{P}) = -10.8$ $\delta(^{29}\text{Si}) = -59.0$	<u>2<sup>BARF</sup> in DCM-<math>d_2</math></u> : $J_{\text{Si,P}} = 8.0$ $J_{\text{Si,H}} = 318.4$	<u>DCM-<math>d_2</math></u> : $J_{\text{Si,P}} = -7.5$ $J_{\text{Si,H}} = -342.3$
 <p><b>[TSMPSiH]<sup>+</sup>·THF (2·THF)</b></p>	<u>2<sup>BARF</sup> in THF-<math>d_5</math></u> : $\delta(^{31}\text{P}) = -7.0$ $\delta(^{29}\text{Si}) = -91.0$	<u>THF-<math>d_5</math></u> : $\delta(^{31}\text{P}) = -13.3$ $\delta(^{29}\text{Si}) = -104.9$	<u>2<sup>BARF</sup> in THF-<math>d_5</math></u> : $J_{\text{Si,P}} = 6.7$ $J_{\text{Si,H}} = 368.4$	<u>THF-<math>d_5</math></u> : $J_{\text{Si,P}} = -7.3$ $J_{\text{Si,H}} = -392.7$
 <p><b>(TSMPSi)Fe(CO)<sub>4</sub> (8)</b></p>	<u>Pyridine-<math>d_5</math></u> : $\delta(^{31}\text{P}) = -9.5$ $\delta(^{29}\text{Si}) = 34.4^a$	<u>Pyridine-<math>d_5</math></u> : $\delta(^{31}\text{P}) = -15.7$ $\delta(^{29}\text{Si}) = 53.2^a$	<u>Pyridine-<math>d_5</math></u> : $J_{\text{Si,P}} = 4.6$	<u>Pyridine-<math>d_5</math></u> : $J_{\text{Si,P}} = -3.7$

<sup>a</sup> The discrepancy between calculated and experimental  $^{29}\text{Si}$  shifts is likely due to improper treatment of relativistic effects.<sup>59</sup>

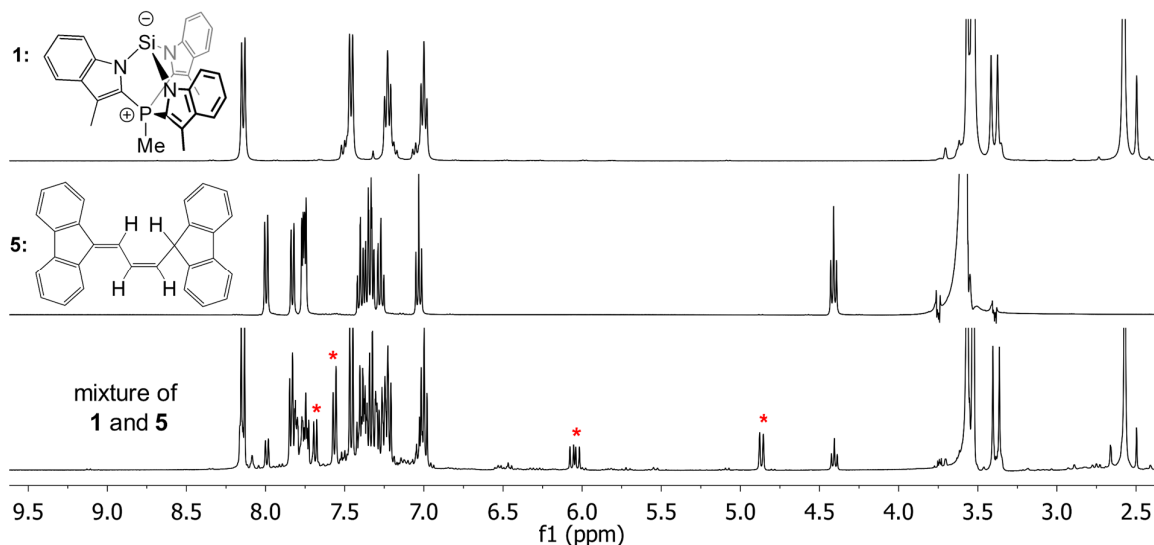


Table C2.1 (continued). Calculated  $^{29}\text{Si}$  and  $^{31}\text{P}$  NMR parameters of selected silicon compounds. Experimental spin-spin coupling constants  $J$  are given as absolute values.

Compound	NMR parameters			
	$\delta$ , ppm		$J$ , Hz	
	Experimental	Calculated	Experimental	Calculated
 <p><b>[TSMPSiMe]<sup>+</sup>OTf<sup>-</sup> (9)</b></p>	<p><u>DCM-<math>d_2</math></u>:  <math>\delta(^{31}\text{P}) = -8.3</math>  <math>\delta(^{29}\text{Si}) = -22.5</math></p>	<p><u>DCM-<math>d_2</math></u>:  <math>\delta(^{31}\text{P}) = -11.8</math>  <math>\delta(^{29}\text{Si}) = -29.1</math></p>	<p><u>DCM-<math>d_2</math></u>:  <math>J_{\text{Si,P}} = 7.9</math>  <math>J_{\text{Si,H}} = 7.9</math></p>	<p><u>DCM-<math>d_2</math></u>:  <math>J_{\text{Si,P}} = -7.6</math>  <math>J_{\text{Si,H}} = 7.5</math></p>
 <p><b>iso-TSMPSi (10)</b></p>	<p><u>THF-<math>d_8</math></u>:  <math>\delta(^{31}\text{P}) = -124.8</math>  <math>\delta(^{29}\text{Si}) = -25.7</math></p>	<p><u>THF-<math>d_8</math></u>:  <math>\delta(^{31}\text{P}) = -126.6</math>  <math>\delta(^{29}\text{Si}) = -33.7</math></p>	<p><u>THF-<math>d_8</math></u>:  <math>J_{\text{Si,P}} = 2.9</math>  <math>J_{\text{Si,H}} = 8.4</math></p>	<p><u>THF-<math>d_8</math></u>:  <math>J_{\text{Si,P}} = -1.8</math>  <math>J_{\text{Si,H}} = 7.4</math></p>

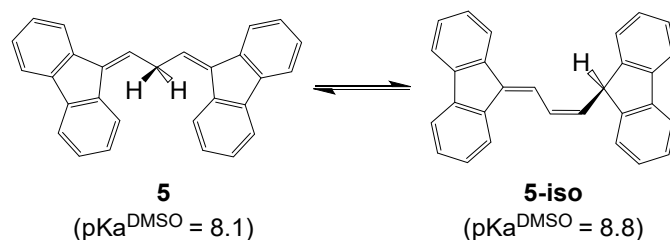
### Appendix C3. Base-catalysed isomerization of fluorene 5.

$^1\text{H}$  NMR shows no direct protonation of zwitterionic TSMPSi (**1**) by CH-acid **5** ( $\text{p}K_{\text{a}}^{\text{DMSO}} = 8.1^4$ ), however the spectrum displays a number of new peaks that do not correspond to any of the starting materials (labelled with asterisks in *Figure C3.1*).



*Figure C3.1.*  $^1\text{H}$  NMR (400 MHz) spectra of silanide **1**, fluorene **5** as well their mixture in dioxane- $d_8$ . Spectrum of **5** was recorded dioxane- $h_8$  with WET solvent suppression. In the bottom panel, asterisks indicate some of the new peaks.

It is known from the literature<sup>4,5</sup> that **5** can convert into the tautomeric form **5-iso** with a close  $pK_a^{\text{DMSO}}$  (Scheme C3.1). Unfortunately, the authors did not publish NMR spectra of the tautomer that we could use for a reference.



Scheme C3.1. Tautomerization of fluorene **5**.<sup>4,5</sup>

However, 1D zTOCSY experiments performed with selective excitation of a new doublet at 4.87 ppm (**A** in Figure C3.2) show four signals with chemical shifts and multiplicities consistent with the non-aromatic spin system of **5-iso**. According to NMR, pure **5** does not tautomerize in dioxane for at least a month. This implies that, even though proton transfer does not occur to a measurable extent, zwitterion **1** may act as a catalytic base that provides a pathway for tautomerization of **5**. A steady concentration of deprotonated **5** in solution is indirectly confirmed by a pale-blue coloration of the mixture of **1** and **5** in dioxane- $d_8$ , which is characteristic of the presence of deprotonated **5**. Consequently, the  $pK_a$  of protonated zwitterion **1** is not much lower than that of fluorene **5**.

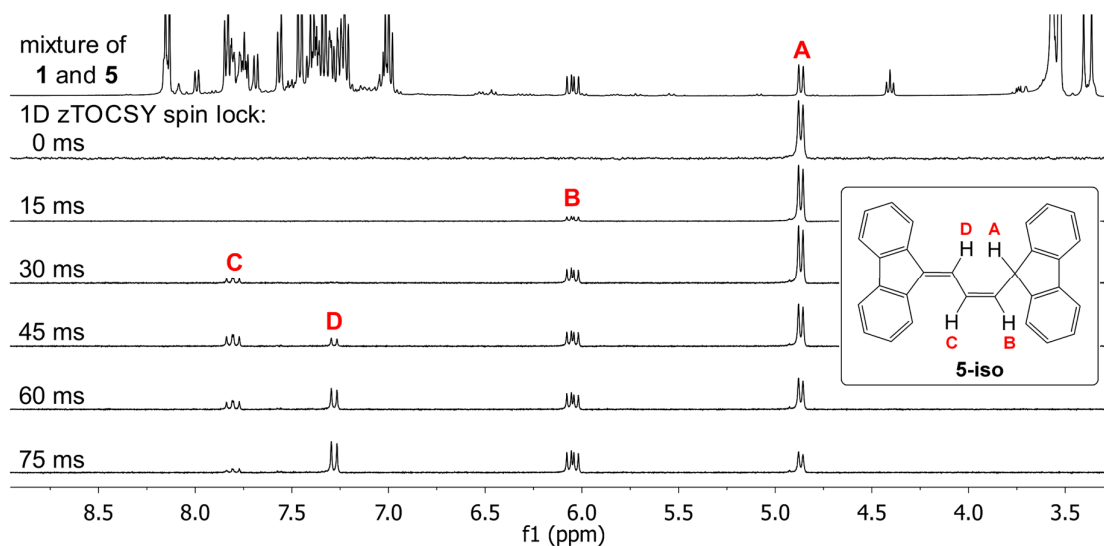
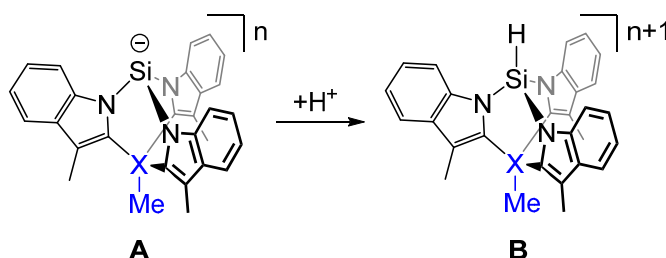


Figure C3.2.  $^1\text{H}$  1D zTOCSY NMR (400 MHz) of a mixture of silanide **1** and fluorene **5** in dioxane- $d_8$ . Top panel is a regular  $^1\text{H}$  NMR spectrum for a reference. Signal **A** is selectively excited.

**Appendix C4.** Comparison of geometries of P<sup>+</sup>- and Si-tethered analogues.

Calculated selected geometric parameters of the zwitterion TSMPSi (**1**), corresponding cationic silane [TSMPSiH]<sup>+</sup> (**2**) and their isoelectronic Si-tethered analogues are shown in *Table C4.1*. Geometries were optimized in vacuum at B3LYP-GD3BJ/6-311++G(d,p) level of theory. Whereas most of the bond lengths and angles match closely, the positive phosphonium atom is slightly smaller than the isoelectronic silicon (longer Si–C<sup>Ar</sup> bonds compared to P<sup>+</sup>–C<sup>Ar</sup>), which should lead to a small difference in strain.

*Table C4.1.* Comparison of the calculated geometries.



Structure	Average distances, Å					Average angles, degrees			
	N–Si	C <sup>Ar</sup> –N	X–C <sup>Ar</sup>	X–CH <sub>3</sub>	Si–H	N <sup>+</sup> Si <sup>–</sup> N	Si <sup>–</sup> N <sup>+</sup> C	N <sup>+</sup> C <sup>–</sup> X	C <sup>Ar</sup> –X <sup>+</sup> C <sup>Ar</sup>
A, X=P <sup>+</sup> ( <b>1</b> )	1.89	1.40	1.78	1.80	-	91.6	126.6	111.8	104.3
A, X=Si	1.88	1.41	1.87	1.87	-	93.6	126.4	112.5	102.0
B, X=P <sup>+</sup> ( <b>2</b> )	1.76	1.42	1.79	1.80	1.46	101.8	118.4	112.7	103.7
B, X=Si	1.75	1.43	1.88	1.86	1.46	103.9	118.1	113.5	101.1

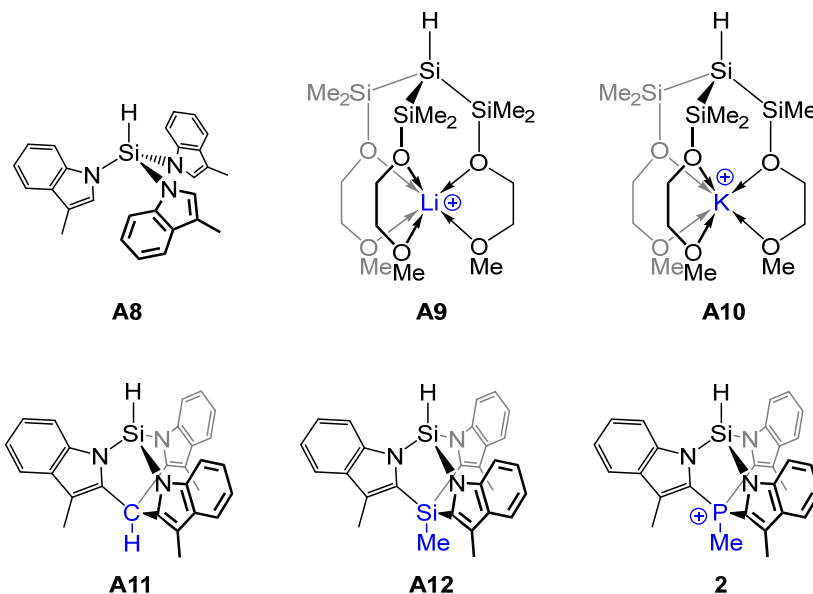
The table above shows that in terms of bond lengths and angles, both before and after quaternization, the analogy between TSMPSi (**1**) and its Si-tethered analogue is maintained.

**Appendix C5.** Gas-phase acidities.

Gas-phase acidities ( $\Delta G$ ) were calculated in vacuum using both B3LYP-GD3BJ and MP2 with the 6-311++G(d,p) basis set. For MP2, thermal corrections for Gibbs free energy were taken from B3LYP-GD3BJ/6-311++G(d,p) calculations in vacuum. It has been shown<sup>6,7</sup> that MP2-derived gas-phase acidities tend to give a better agreement with the experiment than B3LYP for a wide range of acids; nevertheless, both methods show identical trends. This was also true in our calculations. Due to higher precision, we chose MP2-calculated values for further discussion. Gas-phase  $pK_a$ 's at 298 K were calculated as  $0.733\Delta G$ . Calculated and available experimental gas-phase acidities are shown in *Table C5.1*.

Table C5.1. Calculated and experimentally available free energies and  $pK_a$  for spontaneous dissociation of the first silicon-bound proton in the gas phase.

SiH<sub>4</sub>   HSiCl<sub>3</sub>   HSi(SiCl<sub>3</sub>)<sub>3</sub>   HSi(SiMe<sub>3</sub>)<sub>3</sub>   HSi(NMe<sub>2</sub>)<sub>3</sub>   HSiPh<sub>3</sub>   HSiMe<sub>3</sub>  
**A1**   **A2**   **A3**   **A4**   **A5**   **A6**   **A7**



Acid	AH → H <sup>+</sup> + B				
	ΔG, kcal/mol			pK <sub>a</sub>	
	ΔG <sup>DFT</sup>	ΔG <sup>MP2</sup>	ΔG <sup>exp</sup>	pK <sub>a</sub> <sup>DFT</sup>	pK <sub>a</sub> <sup>MP2</sup>
A1	363.9	370.4	365.7 ± 2.0 <sup>8</sup>	266.9	271.6
A2	319.9	332.8	<353.3 ± 2.5 <sup>8</sup>	234.6	244.1
A3	294.9	300.8	-	216.3	220.6
A4	347.8	344.3	346 ± 3 <sup>8</sup>	255.0	252.5
A5	375.4	377.0	-	275.3	276.4
A6	357.8	356.4	-	262.4	261.4
A7	377.8	379.9	-	277.1	278.6
A8	333.7	329.4	-	244.7	241.6
A9	272.8	269.7	-	200.1	197.8
A10	278.2	276.2	-	204.0	202.5
A11	316.9	313.0	-	232.4	229.6
A12	324.5	319.8	-	238.0	234.5
<b>2</b>	248.9	242.4	-	182.5	177.7

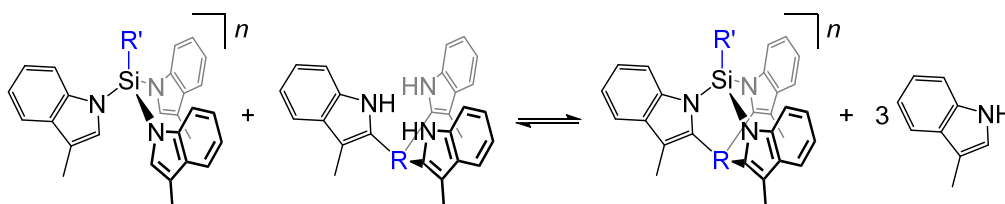
### Appendix C6. On the ring strain in bicyclic systems.

Quaternization of a silicon atom in the discussed bicyclic silanes results in a build-up of ring strain. The latter originates from rehybridization of the silicon as its lone pair gets bound by the acceptor. In accordance with Bent's rule,<sup>3</sup> this binding increases *p*-character of the lone pair, which in turn leads to a larger *s*-character of the Si–N bonding orbitals giving more obtuse N<sup>∧</sup>Si<sup>∧</sup>N angles. These angles might

differ from what is preferred by the rest of the cage structure, resulting in strain. In order to get a quantitative estimate of this effect, and how it differs depending on the size of a bridgehead atom, we resorted to DFT calculations.

The homodesmotic reaction scheme in *Table C6.1* enables to evaluate the strain depending on the nature of a bridgehead atom R and the fourth substituent on silicon R'. It should be noted that this scheme cannot be applied to the silanide TSMPSi (**1**) due to its zwitterionic nature, because otherwise it would lead to a different number of charged species on both sides of the equation. Instead of **1**, we used its isoelectronic Si-tethered analogue. The latter roughly retains the bond lengths and angles compared to the original phosphonium compound, and therefore the steric effects. Nevertheless, its use conserves the number of charges, thus allowing to evaluate the emergent strain without ion destabilization effects in vacuum. Finally, as a measure of strain we chose the reaction enthalpy ( $\Delta H$ ) since it has been used for this purpose historically.<sup>9</sup>

Table C6.1. Strain in the Si- and C-tethered tricyclic silanes as well as in their quaternized forms. Level of theory: B3LYP-GD3BJ/6-311++G\*\* in vacuum.<sup>a</sup> Notations: n=0,-1; LP=lone pair.



R'	R=SiMe		R=CH	
	$\Sigma_{N^{\wedge}Si^{\wedge}N}$ , °	$\Delta H$ , kcal/mol	$\Sigma_{N^{\wedge}Si^{\wedge}N}$ , °	$\Delta H$ , kcal/mol
LP	280.9	22.4	268.9	14.5
	↓ +12.2	↓ +4.5	↓ +12.1	↓ +4.2
FeBr <sub>2</sub> (THF)	293.1	26.9	281.0	18.7
	↓ +16.7	↓ +3.8	↓ +17.3	↓ +9.8
Me	309.8	30.7	298.3	28.5
	↓ -6.4	↓ +0.7	↓ +2.2	↓ +2.5
H	303.4	31.4	300.5	31.0

Following the above analysis, complexation of the Si-tethered silane (R=SiMe) with an FeBr<sub>2</sub>(THF) center leads to 4.5 kcal/mol of an increase in strain, whereas methylation and protonation give 8.3 and 9.0 kcal/mol, respectively, confirming a likely contribution of ring strain to the weakened nucleophilicity of TSMPSi (1). Derivatives of the C-tethered silane (R=CH) are at least as much or more strained than the corresponding Si-tethered analogues due to a smaller size of a bridging C-atom.

<sup>a</sup> In a previous paper from our group,<sup>10</sup> TPSS/TZVP level of theory was used in order to estimate the strain of cage structures. Herein, we reconsider this choice in favor of B3LYP-GD3BJ/6-311++G(d,p). Primarily, because it involves an empirical dispersion correction (GD3BJ) that favors the side of a homodesmotic equation with the least number of particles. Furthermore, geometries optimized at B3LYP-GD3BJ/6-311++G(d,p) level of theory show a good agreement with the data obtained from the X-ray crystal structure (Table C6.2).

Table C6.2. Selected crystal structure (cryst.) and computationally-optimized (theor.) bond distances and angles for silanide 1. For the crystal structure, both independent molecules are considered (see Section 4.10.3).

	Distances, Å				Angles, °			
	Si-N	N-C <sup>Ar</sup>	C <sup>Ar</sup> -P	P <sup>+</sup> -CH <sub>3</sub>	N <sup>-</sup> Si <sup>-</sup> N	Si <sup>-</sup> N <sup>-</sup> C	N <sup>-</sup> C <sup>+</sup> P	C <sup>Ar</sup> ~P <sup>+</sup> C <sup>Ar</sup>
cryst.	1.8404(18)- 1.8639(18)	1.400(3)- 1.408(2)	1.768(2)- 1.7782(19)	1.780(2), 1.782(2)	91.87(8)- 93.34(7)	125.05(13)- 126.36(14)	111.00(14)- 112.14(14)	101.40(10)- 105.15(9)
theor.	1.890	1.401	1.780	1.803	91.60	126.6	111.8	104.3

Despite the protonated Si-tethered cage being more strained than the methylated one, its sum of N<sup>^</sup>Si<sup>^</sup>N angles ( $\Sigma_{\text{N}^{\wedge}\text{Si}^{\wedge}\text{N}}$ ) is smaller than in the methylated structure. This suggests that the precise relationship between  $\Sigma_{\text{N}^{\wedge}\text{Si}^{\wedge}\text{N}}$  and ring strain depends on the fourth substituent on the silicon atom.

#### Appendix C7. Natural Bonding Orbital (NBO) analysis of the deprotonation.

In order to establish the electronic reasons why imposing acute N<sup>^</sup>Si<sup>^</sup>N angles increases acidity, we resorted to Natural Bonding Orbital (NBO) analysis. It was performed according to the deprotonation decomposition scheme used in *Table 4.1* (see main text) for the same structures. The results are shown in *Table C7.1*. The latter contains the orbital composition of the Si-based hybrid in the Si–H NBO which transforms into a lone pair NBO upon deprotonation (B/LP on Si). Additionally, the table shows compositions of hybrids on silicon and nitrogen in Si–N NBO as well as Natural Hybrid Orbital (NHO) bending angles for the respective hybrids.

The analysis shows that the *s*-orbital fraction in the Si-based hybrid of Si–H NBO increases from **A** to **C** as the sum of N<sup>^</sup>Si<sup>^</sup>N angles ( $\Sigma_{\text{N}^{\wedge}\text{Si}^{\wedge}\text{N}}$ ) decreases. Thus, hybridization in tris-*N*-skatyl silane (**A**;  $\Sigma_{\text{N}^{\wedge}\text{Si}^{\wedge}\text{N}}=324.7^\circ$ ) is  $\text{sp}^{2.04}\text{d}^{0.02}$ , whereas in increasingly more constrained Si- and C-tethered analogues **B** ( $\Sigma_{\text{N}^{\wedge}\text{Si}^{\wedge}\text{N}}=311.6^\circ$ ) and **C** ( $\Sigma_{\text{N}^{\wedge}\text{Si}^{\wedge}\text{N}}=300.5^\circ$ ) it is  $\text{sp}^{2.01}\text{d}^{0.02}$  and  $\text{sp}^{1.90}\text{d}^{0.02}$ , respectively. This makes strained silanes more prone to heterolytic dissociation since Si–H bond polarization shifts towards silicon (better illustrated in *Table C7.2*).

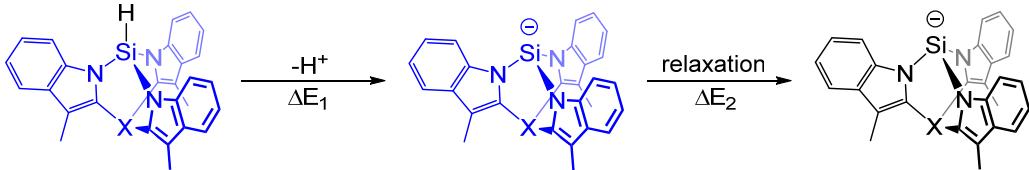
The increasing strain from **A** to **C** is also reflected in the Si–N NHO bending angles in *Table C7.1*. While the bending is rather low in **A** ( $2.5^\circ/<1.0^\circ$ ), it significantly increases in **B** ( $5.7^\circ/4.4^\circ$ ) and **C** ( $12.2^\circ/7.9^\circ$ ), which is in line with the trend we found using homodesmotic schemes to analyse the strain in **B** and **C** (see *Appendix C6*). The bending in **2** ( $6.9^\circ/4.1^\circ$ ) is rather similar to that in **B**, which justifies our choice of **B** as a neutral analogue of **2** (see *Appendix C4*).

Upon proton abstraction with nuclear coordinates frozen, hybridization in all three silanes changes dramatically towards a greater *s*-contribution in accordance with Bent's rule.<sup>3</sup> Final geometry relaxation of all deprotonated silanes maximizes contribution of the 3*s*-orbital to the lone pair on silicon as well as minimises strain (see corresponding NHO bending angles).

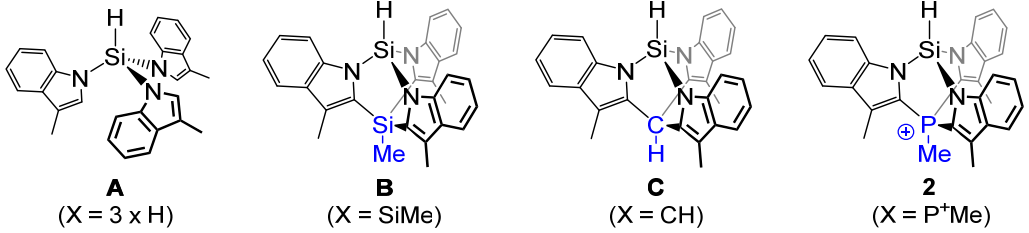
As for [TSMPSiH]<sup>+</sup> (**2**;  $\Sigma_{\text{N}^{\wedge}\text{Si}^{\wedge}\text{N}}=305.5^\circ$ ), while it is rather geometrically similar to **B** (see *Appendix C4*), the 3*s*-contribution to the Si–H bonding pair ( $\text{sp}^{1.82}\text{d}^{0.02}$ ) is larger than for any other discussed silane, which we associate with the presence of a positive charge in the molecule. Other than that, upon deprotonation, its orbital

compositions and NHO bending angles evolve in the same way as outlined above for A-C.

*Table C7.1.* NBO analysis according to deprotonation energy decomposition scheme in *Table 4.1* (see main text). Deprotonated states are shown in square brackets. Calculations were performed in vacuum at B3LYP-GD3BJ/6-311++G\*\* level of theory.



(atomic coordinates frozen)



Structure	NBO composition			NHO bending angles	
	B/LP on Si	Si in Si-N	N in Si-N	Si → N	N → Si
<b>A</b>	$sp^{2.04}d^{0.02}$	$sp^{3.40}d^{0.06}$	$sp^{1.93}$	$2.5^\circ$	$<1.0^\circ$
<b>[A-H<sup>+</sup>]<sup>-</sup> (frozen)</b>	$sp^{1.01}$	$sp^{4.86}d^{0.08}$	$sp^{1.76}$	$13.9^\circ$	$3.3^\circ$
<b>[A-H<sup>+</sup>]<sup>-</sup> (relaxed)</b>	$sp^{0.46}$	$sp^{8.33}d^{0.13}$	$sp^{2.05}$	$1.4^\circ$	$5.9^\circ$
<b>B</b>	$sp^{2.01}d^{0.02}$	$sp^{3.42}d^{0.06}$	$sp^{2.04}$	$5.7^\circ$	$4.4^\circ$
<b>[B-H<sup>+</sup>]<sup>-</sup> (frozen)</b>	$sp^{1.03}$	$sp^{4.82}d^{0.08}$	$sp^{1.80}$	$7.3^\circ$	$3.0^\circ$
<b>[B-H<sup>+</sup>]<sup>-</sup> (relaxed)</b>	$sp^{0.47}$	$sp^{8.18}d^{0.12}$	$sp^{2.11}$	$2.9^\circ$	$\leq 1.0^\circ$
<b>C</b>	$sp^{1.90}d^{0.02}$	$sp^{3.50}d^{0.06}$	$sp^{2.04}$	$12.2^\circ$	$7.9^\circ$
<b>[C-H<sup>+</sup>]<sup>-</sup> (frozen)</b>	$sp^{0.83}$	$sp^{5.51}d^{0.09}$	$sp^{1.78}$	$\leq 1.0^\circ$	$6.1^\circ$
<b>[C-H<sup>+</sup>]<sup>-</sup> (relaxed)</b>	$sp^{0.43}$	$sp^{8.71}d^{0.12}$	$sp^{2.16}$	$7.7^\circ$	$2.9^\circ$
<b>2</b>	$sp^{1.82}d^{0.02}$	$sp^{3.57}d^{0.06}$	$sp^{1.98}$	$6.9^\circ$	$4.1^\circ$
<b>[2-H<sup>+</sup>]<sup>0</sup> (frozen)</b>	$sp^{0.88}$	$sp^{5.31}d^{0.09}$	$sp^{1.76}$	$5.2^\circ$	$2.3^\circ$
<b>[2-H<sup>+</sup>]<sup>0</sup> (relaxed)</b>	$sp^{0.41}$	$sp^{9.11}d^{0.14}$	$sp^{2.07}$	$4.0^\circ$	$1.2^\circ$

*Table C7.2.* NBO analysis for a Si-H bond in silanes in *Table C7.1*. Calculations were performed in vacuum at B3LYP-GD3BJ/6-311++G\*\* level of theory.

Silane	Si-H NBO			Atomic contributions to Si-H NLMO	
	Hybridization on Si	Atomic contributions		%Si	%H
		%Si	%H		
<b>A</b>	$sp^{2.04}d^{0.02}$	41.34	58.66	41.35	57.83
<b>B</b>	$sp^{2.01}d^{0.02}$	41.80	58.20	41.72	57.56
<b>C</b>	$sp^{1.90}d^{0.02}$	42.49	57.51	42.58	56.93
<b>2</b>	$sp^{1.82}d^{0.02}$	43.50	56.50	43.45	55.98



**Appendix C8.** Calculation of steric parameters.

For the reference, Tolman cone angles were calculated (*Chart C8.1*) for the C-tethered germanium and silicon anions **A** and **B**, previously published in our group<sup>1,10</sup> as well as for the P<sup>+</sup>-tethered germanide **12** discussed in *Appendix C1*. This was done as originally described by Tolman<sup>11</sup> but using DFT-optimized geometries of LNi(CO)<sub>3</sub> complexes at B3LYP-GD3BJ/6-311++G(d,p) level of theory. The absence of imaginary frequencies was confirmed for all structures. Van der Waals radii of hydrogen atoms were taken as 1.20 Å.

LNi(CO)<sub>4</sub><sup>n</sup> complexes:

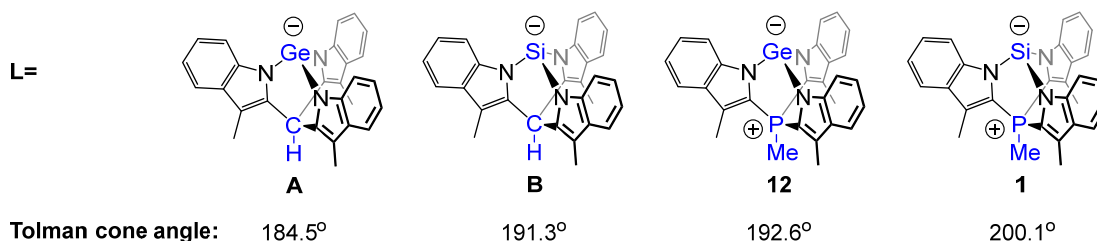


*Chart C8.1.* Calculated Tolman cone angles;  $n=0, -1$ .

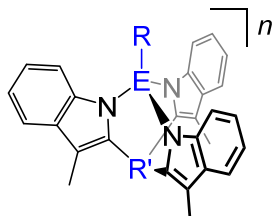
The cone angle for **12**, 192.6°, is most similar to that of tris(*o*-tolyl)phosphine, 194±6°. <sup>12</sup> Due to more obtuse N<sup>∧</sup>Si<sup>∧</sup>N angles, **1** has a larger cone angle of 200.1°. Analogous C-tethered germanide<sup>1</sup> and silanide<sup>10</sup> (**A** and **B** in *Chart C8.1*) have smaller Tolman cone angles of 184.5° and 191.3°, respectively, owing to a smaller size of a carbon bridgehead atom compared to a phosphonium.

Percent buried volumes (%V<sub>bur</sub>)<sup>13</sup> were also calculated from computational geometries at the same level of theory as above using SambVca v.2.1 program.<sup>14</sup> The following parameters were used for SambVca calculations: (1) sphere radius of 3.50 Å; (2) metal-ligand distance of 2.28 Å; (3) hydrogen atoms were omitted; (4) scaled Bond radii were used as recommended by Cavallo and co-workers.<sup>15</sup> For the compounds, the solid-state structure of which is known, percent buried volumes derived from computational geometries show a very good agreement with those calculated using molecular structures from X-ray diffraction (*Table C8.1*). This validates the use of computational geometries for estimating %V<sub>bur</sub> of the real molecules.

In order to investigate whether %V<sub>bur</sub> of zwitterions **12** and **1** as well as that of their C-tethered analogues depends on the sum of angles around the central atom (Σ<sub>N<sup>∧</sup>E<sup>∧</sup>N</sub>), %V<sub>bur</sub> was calculated for uncoordinated tetrel anions as well as for the corresponding quaternized LFeBr<sub>2</sub>(THF), LAuCl and LMe derivatives (*Table C8.1*). For all tetrel anions, the increase of Σ<sub>N<sup>∧</sup>E<sup>∧</sup>N</sub> by ca. 30° amounts into only ca. 2% increase of %V<sub>bur</sub>, which can be considered insignificant.

In order to get an estimate of how  $\%V_{\text{bur}}$  of the cage tetrels compares to that of common phosphines, we used LAuCl model complexes (*Table C8.1*) as suggested by Cavallo and co-workers.<sup>16</sup> In this respect, germanide **12** ( $R'=P^+Me$ ,  $E=Ge$ ,  $\%V_{\text{bur}}=37.2\%$ ) is most similar to tris(pentafluorophenyl)phosphine ( $\%V_{\text{bur}}=37.3\%$ ),<sup>16</sup> whereas silanide **1** ( $R'=P^+Me$ ,  $E=Si$ ,  $\%V_{\text{bur}}=39.0\%$ ) is closest to tris(*o*-tolyl)phosphine ( $\%V_{\text{bur}}=41.4\%$ ).<sup>16</sup> A slight disagreement between Tolman cone angles and  $\%V_{\text{bur}}$  can be assigned to conformational effects. Analogous C-tethered tetrel anions ( $R'=CH$ )<sup>1,10</sup> have smaller  $\%V_{\text{bur}}$  owing to a smaller size of a carbon bridgehead atom compared to a phosphonium.

*Table C8.1.* Buried volumes ( $\%V_{\text{bur}}$ ) of cage tetrel anions. The values given in italics were calculated based on the data from X-ray diffraction, otherwise molecular geometries optimized at B3LYP-GD3BJ/6-311++G\*\* level of theory were used. Notations:  $n=+1, 0, -1$ ; LP=lone pair.



R	R'=CH				R'=P <sup>+</sup> Me			
	E=Si		E=Ge		E=Si		E=Ge	
	$\Sigma_{N^{\wedge}E^{\wedge}N, ^{\circ}}$	$\%V_{\text{bur}}$	$\Sigma_{N^{\wedge}E^{\wedge}N, ^{\circ}}$	$\%V_{\text{bur}}$	$\Sigma_{N^{\wedge}E^{\wedge}N, ^{\circ}}$	$\%V_{\text{bur}}$	$\Sigma_{N^{\wedge}E^{\wedge}N, ^{\circ}}$	$\%V_{\text{bur}}$
LP	268.94	34.8	261.02	32.9	274.80	37.7	266.80	35.7
	<i>272.58(8)</i>	<i>35.3</i>	<i>263.6(4)</i>	<i>33.4</i>	<i>277.43(13)/277.51(14)</i>	<i>38.6</i>	<i>270.04(19)</i>	<i>36.5</i>
FeBr <sub>2</sub> (THF)	280.99	35.6	271.22	34.1	286.06	38.4	276.46	36.5
					<i>289.42(17)</i>	<i>38.6</i>		
AuCl	284.73	36.0	275.67	34.3	290.20	39.0	281.42	37.2
Me	298.31	36.7	289.27	35.0	303.31	39.8	295.04	38.0

### Appendix C9. On donicity of TSMPSi (1).

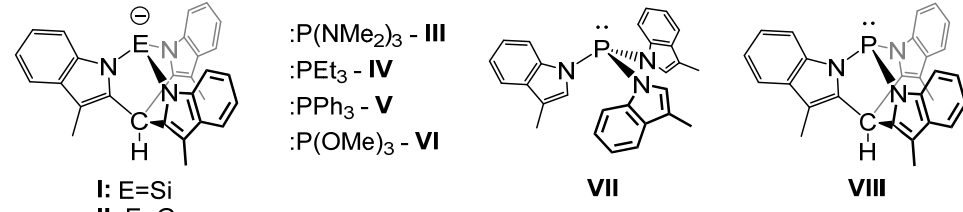
The assessment of the donicity is often done experimentally by comparing  $\tilde{\nu}(\text{CO})$  of the infrared band corresponding to the carbonyl A1 stretching mode in  $\text{LNi}(\text{CO})_3$  complexes, as originally suggested by Tolman.<sup>11</sup> He also pointed out that meaningful data could be obtained with other carbonyls, and  $\text{LNi}(\text{CO})_3$  complexes were chosen primarily due to the ease of preparation. Indeed, reasonable results have been obtained using carbonyl complexes of manganese,<sup>17</sup> chromium,<sup>18–21</sup> vanadium,<sup>22</sup> molybdenum,<sup>22–26</sup> tungsten,<sup>18,22,26–29</sup> iron,<sup>30–35</sup> rhodium<sup>36–42</sup> and iridium.<sup>39,40,43</sup> For our purpose, we chose iron carbonyls with a general formula of  $\text{LFe}(\text{CO})_4$ . This was done following the work of Barnard and Mason<sup>30</sup> who used this approach to characterize structurally-related phosphines.

The respective  $\text{LFe}(\text{CO})_4$  complexes,  $(\text{TSMPSi})\text{Fe}(\text{CO})_4$  (**8**) and the germanium analogue  $(\text{TSMPPe})\text{Fe}(\text{CO})_4$  (**14**) used for the comparison, were prepared by reaction of the corresponding zwitterions, TSMPSi (**1**) and TSMPPe (**12**; see *Appendix C1*), with  $\text{Fe}_2(\text{CO})_9$  in THF. Solution IR spectra of both **8** and **14** in THF show three strong absorptions at around  $2000\text{ cm}^{-1}$  consistent with trigonal bipyramidal geometry of the carbonyl complexes.<sup>1,30</sup> The experimental carbonyl stretching mode frequencies in compounds **8**, **14** as well as some other reported  $\text{LFe}(\text{CO})_4$  complexes are given in a *Table C9.1*. The sequence of fully symmetrical (A1) carbonyl stretching mode frequencies,  $\tilde{\nu}(\text{CO})_1$ , is plotted in *Chart C9.1*.

As expected, the silanides and germanides are more donating than neutral phosphines. Also, germanides tend to be less electron-rich than corresponding silanides due to the slightly higher electronegativity of germanium. It is interesting, however, that steric constraint leads to less donation as exemplified by phosphines **C** and **D**. In their original paper,<sup>30</sup> Barnard and Mason propose that this stems from increased *s*-character of the lone pair in **D** due to smaller  $\text{N}^{\wedge}\text{P}^{\wedge}\text{N}$  angles. Since *s*-orbitals are closer to the nucleus than the *p*-orbitals, the higher *s*-contribution results into less donation. This explanation is in line with the modern understanding of a connection between acid-base properties and strain.<sup>44,45</sup> In this vein, TSMPSi (**1**) and TSMPPe (**12**) should be more donating than their C-tethered counterparts **A** and **B**. Thus, the sum of  $\text{N}^{\wedge}\text{Si}^{\wedge}\text{N}$  angles in the crystal structure of **1** is  $277.43(13)/277.51(14)^\circ$  (see *Section 4.10.3*) which is larger than  $272.58(8)^\circ$ <sup>10</sup> in **A**; the same applies for the  $\text{N}^{\wedge}\text{Ge}^{\wedge}\text{N}$  sum in **12** of  $270.04(19)^\circ$  (see *Section 4.10.3*) vs. that in **B** of  $263.6(4)^\circ$ .<sup>1</sup> However, judging from the carbonyl stretching frequencies, the opposite is true. Our interpretation is that a positive charge in formally neutral **1** and **12** makes them less donating than anionic **A** and **B**.

This analysis, however, comes with two caveats. Firstly, the span of the comparison is limited to the ligands the IR data for the corresponding complexes of which are available, which is very few. Secondly, according to a number of authors,<sup>46,47</sup> not all carbonyl complexes are equally suitable for making conclusions about the donor strength. It has been shown that carbonyl stretching modes in nickel, iron and molybdenum carbonyls are contaminated by mode-mode coupling. The same applies for the derivatives.<sup>46</sup> In very simple terms, coupling arises when not all vibrational energy is concentrated within one bond but is rather delocalized among several bonds of similar energies/force constants and reduced masses. For  $\text{LNi}(\text{CO})_3$  complexes, the contribution associated with mode-mode coupling can reach as much as  $100\text{ cm}^{-1}$  for  $\text{L}=\text{F}^-$ .<sup>46</sup> The stretching modes can also be sensitive to sterics and trans effects, which leads to additional contributions to  $\tilde{\nu}(\text{CO})$  not associated with electronic properties of the ligand. These problems can be overcome by calculating a local Tolman's electronic parameter (LTEP) based on the inherent bond strength defined by the magnitude of the local bond force constant.<sup>46</sup> An alter-

*Table C9.1.* Solution carbonyl stretching frequencies in  $LFe(CO)_4$  complexes according to infrared spectroscopy. Complexes **III-VIII** were measured in hexane, while the rest were measured in THF due to low solubility in hexane. For the sake of comparison, the solvent effects were assumed to be negligible. References in the table show the literature source where a complex was first characterized.



L	$\tilde{\nu}(CO), \text{cm}^{-1}$			L	$\tilde{\nu}(CO), \text{cm}^{-1}$		
	$\tilde{\nu}(CO)_1$	$\tilde{\nu}(CO)_2$	$\tilde{\nu}(CO)_3$		$\tilde{\nu}(CO)_1$	$\tilde{\nu}(CO)_2$	$\tilde{\nu}(CO)_3$
<b>I</b> <sup>10</sup>	2029	N/A	1920	<b>IV</b> <sup>48</sup>	2051	1976	1938
<b>II</b> <sup>1</sup>	2037	1954	1933	<b>V</b> <sup>49</sup>	2052	1979	1947
<b>TSMPSi (1)</b>	2039	1960	1926	<b>VI</b> <sup>50</sup>	2065	1992	1966
<b>TSMPCGe (12)</b>	2047	1970	1941	<b>VII</b> <sup>30</sup>	2065	1997	1966
<b>III</b> <sup>51</sup>	2048	1973	1936	<b>VIII</b> <sup>30</sup>	2076	2006	1977

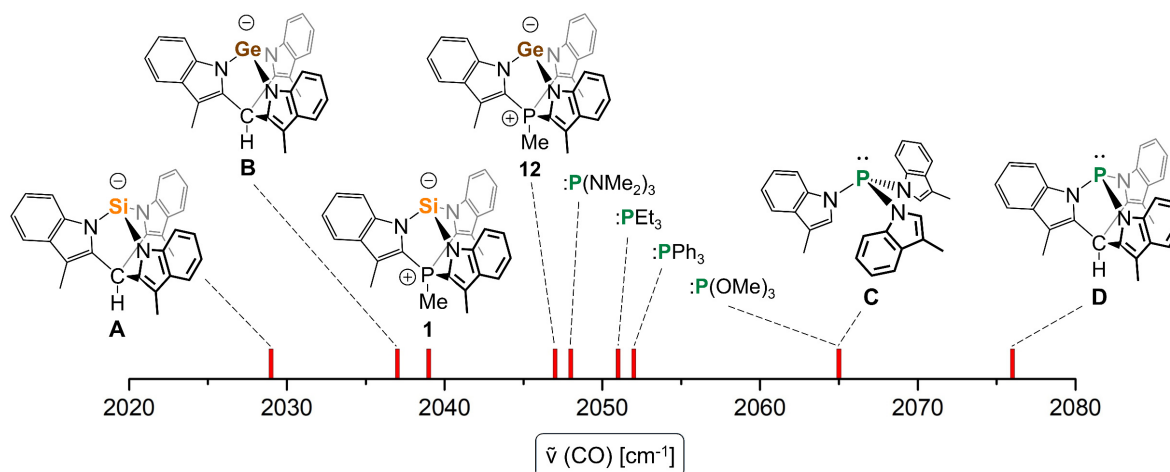
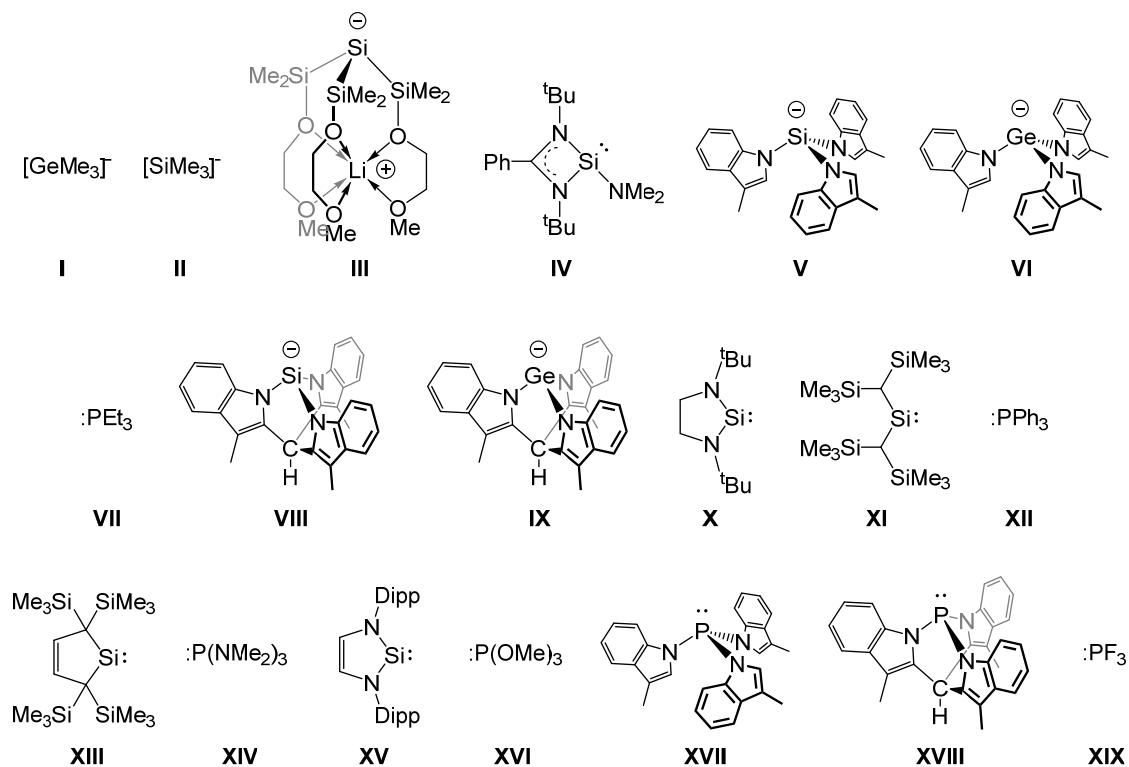


*Chart C9.1.* Experimental  $\tilde{\nu}(CO)$  of carbonyl A1 stretching modes in  $LFe(CO)_4$  complexes for different ligand L.

native computational solution was suggested by Gusev.<sup>47</sup> His argument stems from the fact that there should be a linear correlation between  $\tilde{\nu}(CO)$  and C–O bonding distance for a complex that is used to gauge electronic properties of a ligand. In  $LNi(CO)_3$ , a good correlation is found for phosphines and some carbenes but not *O*- and *N*-donor ligands. Gusev then suggests a model complex,  $IrCp(CO)L$ , in which a linear correlation is observed for a range of ligand families. In essence, this solves the problem of mode-mode coupling, sterics and *trans*-effects in a very general way, since a linear correlation is only observed if these are minimized.

*Table C9.2.* Calculated carbonyl stretching frequencies in IrCp(CO)L model complexes for different L. MPW1PW91 functional with SDD basis set (associated with ECP) for Ir and 6-311+G(d,p) for all other atoms was employed, along with tight geometry optimizations and ultrafine integration grid. References in the table show the literature source where a ligand was first discussed.



L	$\tilde{\nu}(\text{CO}),$ $\text{cm}^{-1}$	$d(\text{CO}),$ $\text{\AA}$	L	$\tilde{\nu}(\text{CO}),$ $\text{cm}^{-1}$	$d(\text{CO}),$ $\text{\AA}$	L	$\tilde{\nu}(\text{CO}),$ $\text{cm}^{-1}$	$d(\text{CO}),$ $\text{\AA}$
<b>I</b>	1955.52	1.17509	<b>VIII</b> <sup>10</sup>	2037.65	1.15981	<b>1</b>	2053.29	1.15690
<b>II</b>	1956.26	1.17521	<b>IX</b> <sup>1</sup>	2038.47	1.15933	<b>12</b>	2055.97	1.15614
<b>III</b> <sup>52</sup>	1988.81	1.16801	<b>X</b> <sup>53</sup>	2044.39	1.15835	<b>XV</b> <sup>54</sup>	2068.56	1.15334
<b>IV</b> <sup>55</sup>	2002.02	1.16554	<b>XI</b>	2045.98	1.15710	<b>XVI</b>	2078.12	1.15255
<b>V</b>	2020.98	1.16267	<b>XII</b>	2048.73	1.15728	<b>XVII</b> <sup>30</sup>	2086.11	1.15057
<b>VI</b>	2024.77	1.16163	<b>XIII</b>	2050.72	1.15618	<b>XVIII</b> <sup>30</sup>	2100.43	1.14838
<b>VII</b>	2035.29	1.15984	<b>XIV</b>	2050.74	1.15740	<b>XIX</b>	2114.81	1.14648

Calculated  $\tilde{\nu}(\text{CO})$  for the model IrCp(CO)L complexes of TSMPSi (**1**), TSMPSiGe (**12**) and other ligands with a range of donor strengths, along with corresponding C–O bonding distances,  $d(\text{CO})$ , are given in *Table C9.2* and plotted in *Chart C9.2*. There is a linear correlation between  $\tilde{\nu}(\text{CO})$  and  $d(\text{CO})$  for all featured ligands (see *Figure C9.1*). In general, the order of donor strength is the same as derived from the experimental data for the LFe(CO)<sub>4</sub> complexes, which reinforces prior conclusions. Additional data points with silanide **A** and germanide **C** confirm that steric constraints lead to the reduction of donor strength for silicon and germanium compounds just like for phosphines. Furthermore, introduction of a positive charge

makes TSMPSi (**1**) more alike to silylenes rather than silicon anions in terms of donor strength. Out of all considered simple phosphines, **1** is most similar to  $\text{P}(\text{NMe}_2)_3$ .

We choose to limit our discussion of the donicity of TSMPSi (**1**) to the  $\text{IrCp}(\text{CO})\text{L}$  model since the latter provides comparison to a larger number of ligands and is expected to be more precise because of minimized mode-mode coupling, sterics and trans effect contributions. Yet, as noted by Gusev,<sup>47</sup> quantifying ligand donor properties is only useful as long as it helps to rationalize and predict the reactivity patterns in coordination chemistry and catalysis. He also argues that ligand properties are not always adequately represented as a single parameter for different ligand types, with which we agree.

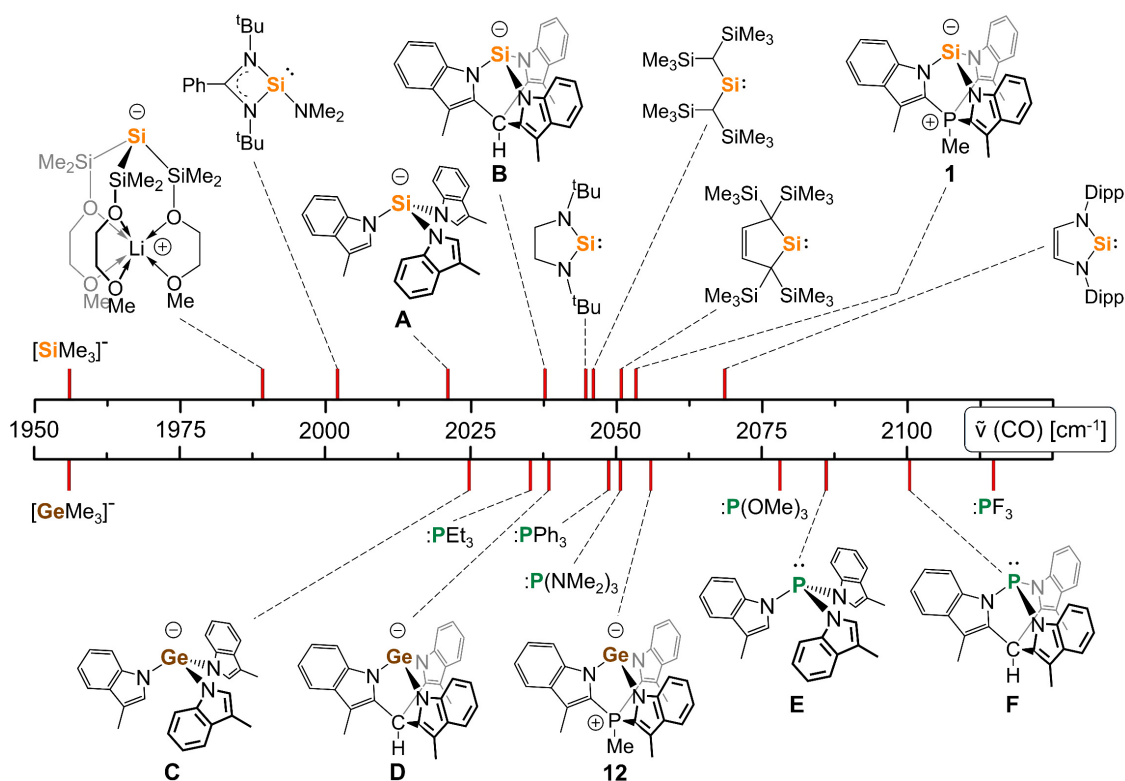


Chart C9.2. Calculated  $\tilde{\nu}(\text{CO})$  of the carbonyl stretching mode in  $\text{IrCp}(\text{CO})\text{L}$  complexes for different ligand L.

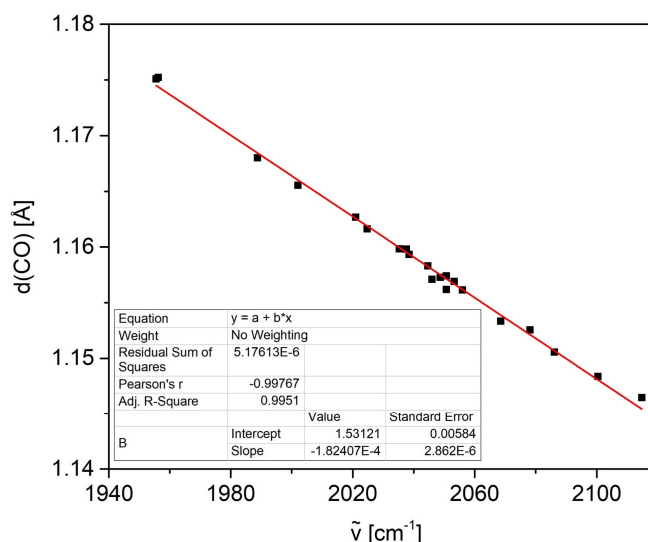


Figure C9.1. Linear correlation between calculated C–O bonding distances and stretching frequencies for IrCp(CO)L model complexes.

## Appendix C10. Reactions with different fluorenes.

We have tested a reaction of TSMPSi (**1**) in THF-*d*<sub>8</sub> with a number of fluorenes with  $pK_a^{\text{DMSO}}$  between 8.1 and 17.9 (Chart C10.1).

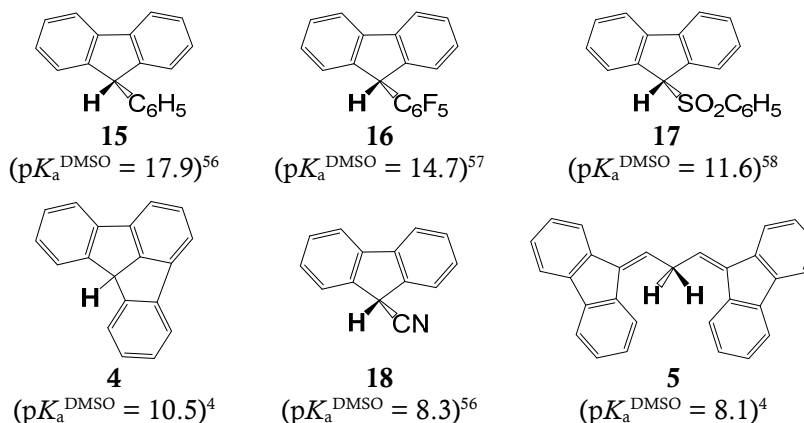


Chart C10.1. CH-acids used in the study. Acidic protons are shown in bold.

As shown by <sup>1</sup>H and <sup>31</sup>P NMR spectra (Figure C10.1 and Figure C10.2) and regardless of  $pK_a^{\text{DMSO}}$ , all fluorenes lead to isomerization of **1** into iso-TSMPSi (**10**) (pathway **A** in Scheme C10.1). This is consistent with a catalytic nature of this transformation, which is discussed in the main text in more detail (Scheme 4.5). Additionally, THF ring-opening (pathway **B** in Scheme C10.1) occurs for fluorenes with  $pK_a^{\text{DMSO}}$  in the range of 8.1–11.6, i.e. **4**, **5**, **17** and **18** (Figure C10.1 and Figure C10.2).

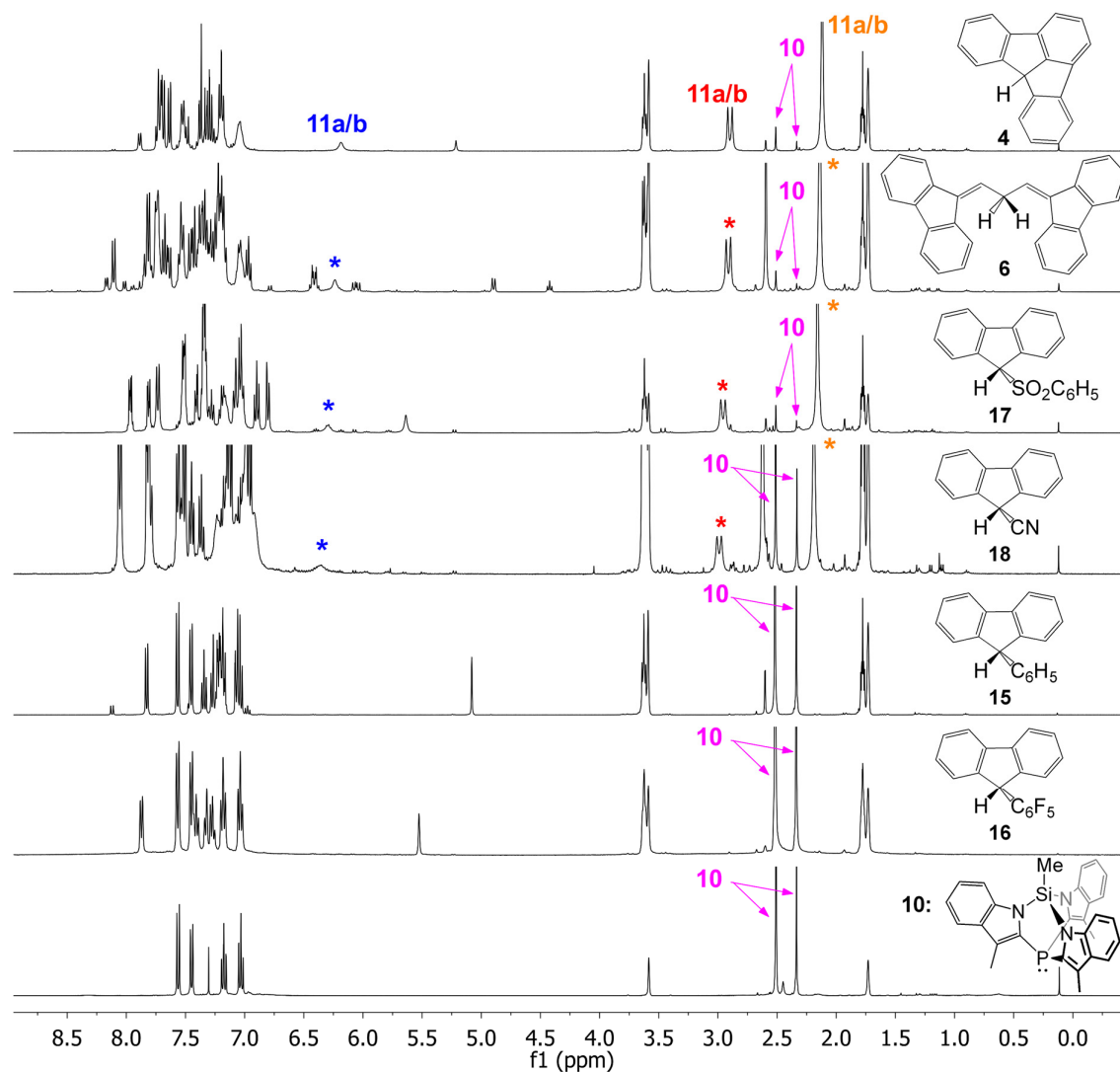


Figure C10.1. <sup>1</sup>H NMR (400 MHz) spectra of a reaction of TSMPSi (**1**) in THF-*d*<sub>8</sub> with a number of fluorenes at 25 °C. Used fluorenes are shown on the right, a spectrum of **10** is given for a reference. Coloured asterisks indicate peaks analogous to those of the THF ring-opening product **11a/b**.



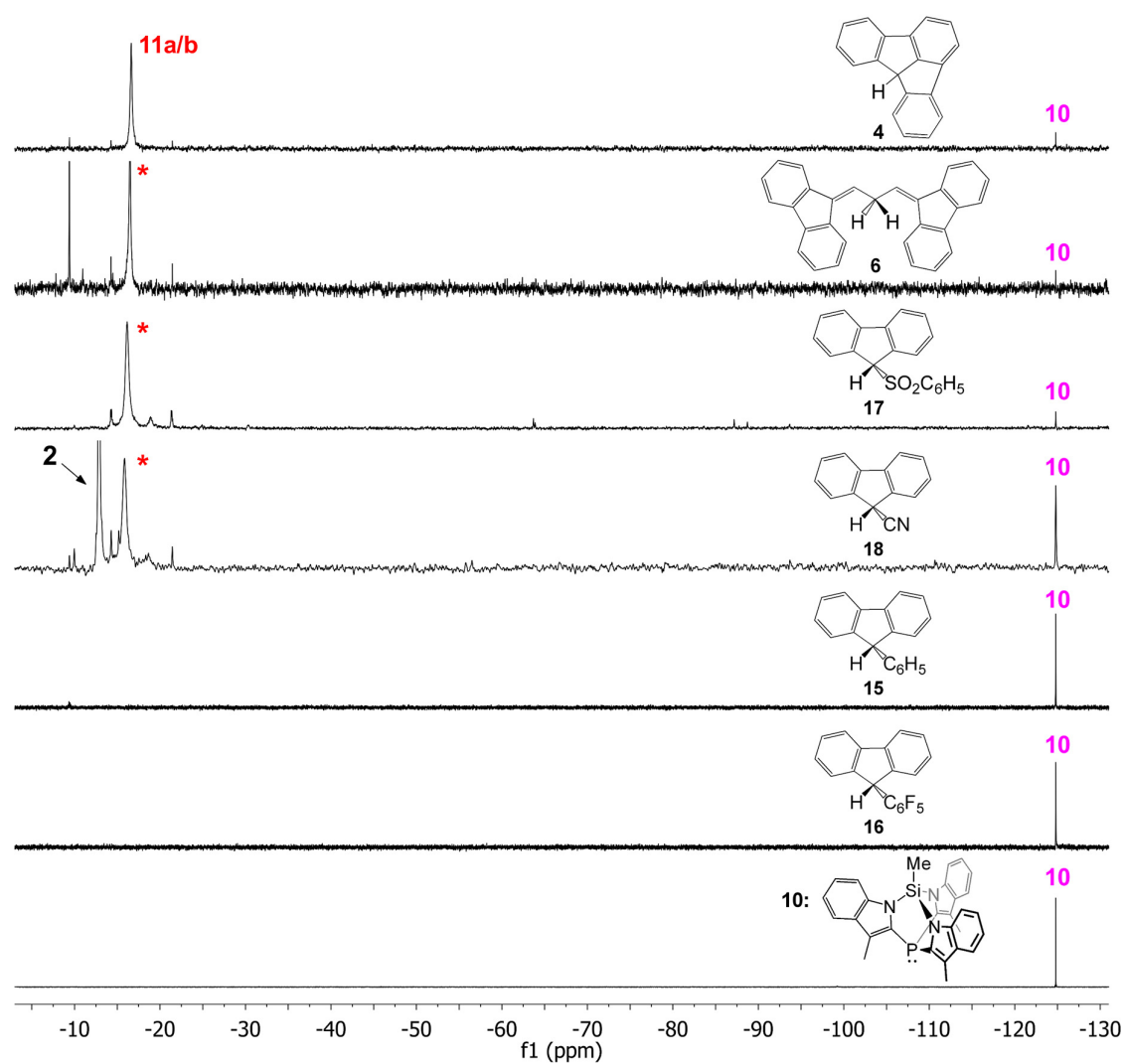
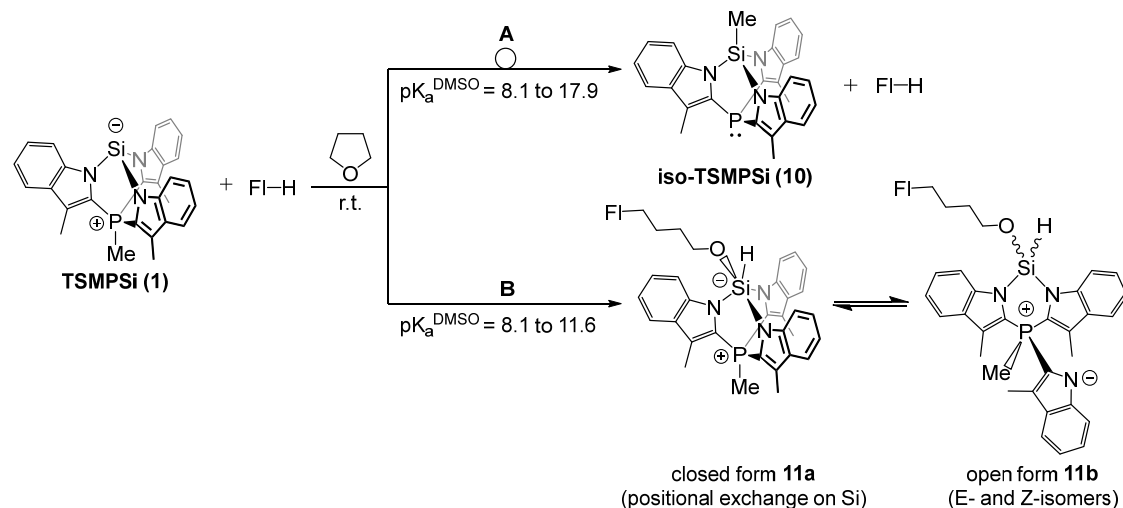


Figure C10.2.  $^{31}\text{P}$  NMR (162 MHz) spectra of a reaction of TSMPSi (**1**) in  $\text{THF-}d_8$  with a number of fluorenes at 25 °C. Used fluorenes are shown on the right, a spectrum of **10** is given for a reference. Coloured asterisks indicate peaks analogous to those of the THF ring-opening product **11a/b**.

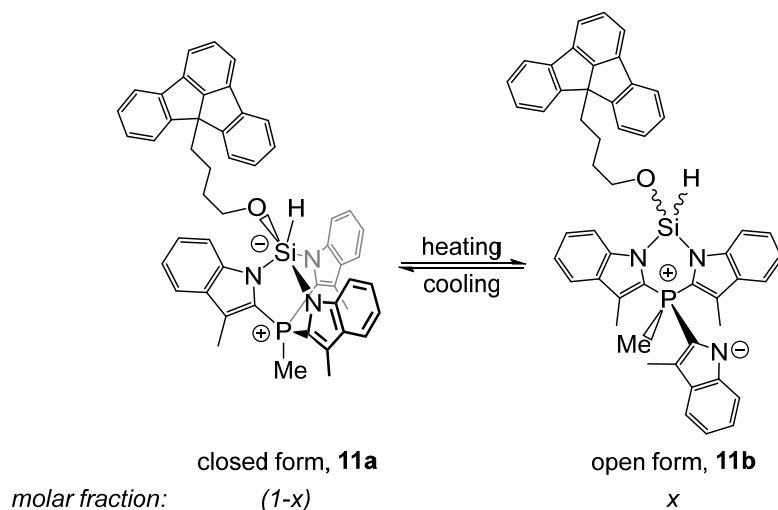
This fact suggests that the THF ring-opening is dependent on the equilibrium concentration of fluorenyl anions in solution, which supports the mechanism proposed in *Scheme 4.6* in the main text.



*Scheme C10.1.* Full reaction manifold of TSMPSi (1) with tested fluorenes.

**Appendix C11.** Variable temperature  $^1\text{H}$  and  $^{31}\text{P}$  NMR of the THF ring-opening reaction.

An equilibrium between the low- (11a) and the high-temperature (11b) forms can be written down as follows:



$$K = \frac{x}{1-x}$$

In this case, the observable chemical shift  $\delta$  can be represented as a weighted average of individual shifts  $\delta_A$  and  $\delta_B$  (assuming the shifts are temperature-independent):

$$\delta = (1-x)\delta_A + x\delta_B.$$

The equilibrium constant  $K$  can be expressed *via*  $\delta$  as:

$$\delta = (1 - x)(\delta_A + K\delta_B)$$

$$\delta = \frac{\delta_A + K\delta_B}{1 + K}.$$

Assuming that  $\Delta_rH$  and  $\Delta_rS$  are temperature-independent,  $K$  can also be written as:

$$-RT\ln K = \Delta_rH - T\Delta_rS$$

$$K = \exp\left(\frac{T\Delta_rS - \Delta_rH}{RT}\right),$$

where  $T$  is temperature,  $R$  is a gas constant,  $\Delta_rH$  and  $\Delta_rS$  are enthalpy and entropy of the interconversion. Thus, one can get a final expression for observed chemical shift:

$$\delta = \frac{\delta_A + \delta_B \exp\left(\frac{\Delta_rS}{R} - \frac{\Delta_rH}{RT}\right)}{1 + \exp\left(\frac{\Delta_rS}{R} - \frac{\Delta_rH}{RT}\right)} \quad \text{Eq. C11.1}$$

However, in order to use the regression model in *Eq. C11.1*, one may need to know the individual chemical shifts of the low- and high-temperature forms,  $\delta_A$  and  $\delta_B$  respectively. Whereas for the low-temperature form it is obvious since  $^{31}\text{P}$  shift stops evolving below  $-60\text{ }^\circ\text{C}$ , it is not clear whether the transition into an open form is complete at  $60\text{ }^\circ\text{C}$ .  $^{31}\text{P}$  NMR measurement at a higher temperature would not be possible since it would boil the solvent (THF- $d_8$ ). Since there are nine data points, in addition to  $\Delta_rH$  and  $\Delta_rS$  of the interconversion, one can also fit chemical shift of the open form  $\delta_B$  (*Figure C11.1*).

As can be seen, the derived model adequately describes evolution of  $^{31}\text{P}$  chemical shift with temperature. Regression analysis shows that the transition is almost complete (96%) at  $60\text{ }^\circ\text{C}$  (333 K). The limiting  $^{31}\text{P}$  shift  $\delta_B$  is  $-17.9\text{ ppm}$ . Positive enthalpy of  $10.4\text{ kcal/mol}$  indicates that transition into an open form is endothermic, which is consistent with breaking of a Si–N bond. Positive entropy of  $37.5\text{ cal/(mol}\cdot\text{K)}$  is also in line with such a process since cage-opening creates additional degrees of freedom.

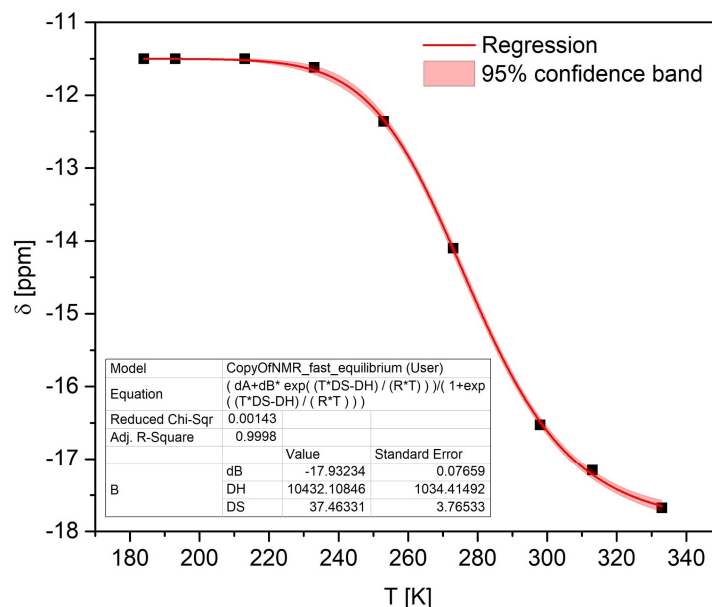


Figure C11.1. Regression analysis of variable-temperature  $^{31}\text{P}$  chemical shifts.

## C12 References

- Wittman, L.; van Beek, C. B.; van Veenhuizen, O. N.; Lutz, M.; Moret, M.-E. Synthesis and Complexation of a Free Germanide Bearing a Tridentate *N*-Heterocyclic Substituent. *Organometallics* **2019**, *38* (2), pp 231–239. DOI: 10.1021/acs.organomet.8b00630.
- Tretiakov, S.; Damen, J. A. M.; Lutz, M.; Moret, M.-E. A Dianionic  $\text{C}_3$ -Symmetric Scorpionate: Synthesis and Coordination Chemistry. *Dalt. Trans.* **2020**, *49* (39), pp 13549–13556. DOI: 10.1039/D0DT02601H.
- Weinhold, F.; Landis, C. R. *Valency and Bonding: A Natural Donor-Acceptor Perspective*, 1st ed.; Cambridge University Press: Cambridge, 2005. DOI: 10.1017/CBO9780511614569.
- Ritchie, C. D. Acidity in Nonaqueous Solvents. VII. Proton Transfers in Dipolar Aprotic Solvents. 5. Solvation and Geometric Factors in the Rates of Proton Transfer Reactions. *J. Am. Chem. Soc.* **1969**, *91* (24), pp 6749–6753. DOI: 10.1021/ja01052a036.
- Kuhn, R.; Rewicki, D. Die PK-Werte Doppelbindungsisomerer Kohlenwasserstoffe Mit Gemeinsamem Carbanion. *Tetrahedron Lett.* **1965**, *6* (39), pp 3513–3522. DOI: 10.1016/S0040-4039(01)89335-7.
- Ding, F.; Smith, J. M.; Wang, H. First-Principles Calculation of  $\text{PK}_a$  Values for Organic Acids in Nonaqueous Solution. *J. Org. Chem.* **2009**, *74* (7), pp 2679–2691. DOI: 10.1021/jo802641r.
- Fu, Y.; Liu, L.; Li, R. Q.; Liu, R.; Guo, Q. X. First-Principle Predictions of Absolute  $\text{PK}_a$ 's of Organic Acids in Dimethyl Sulfoxide Solution. *J. Am. Chem. Soc.* **2004**, *126* (3), pp 814–822. DOI: 10.1021/ja0378097.
- Linstrom, P. J.; Mallard, W. G., E. *NIST Standard Reference Database 69, October 2018 Release*. NIST Chemistry WebBook. DOI: 10.18434/T4D303.
- Anslyn, E. V.; Dougherty, D. A. *Modern Physical Organic Chemistry*; University Science Books: Sausalito, United States, 2011.
- Wittman, L.; Evers, T.; Lutz, M.; Moret, M.-E. A Free Silanide from Nucleophilic Substitution at Silicon(II). *Chem. Eur. J.* **2018**, *24* (47), pp 12236–12240. DOI: 10.1002/chem.201801435.
- Tolman, C. A. Steric Effects of Phosphorus Ligands in Organometallic Chemistry and Homogeneous Catalysis. *Chem. Rev.* **1977**, *77* (3), pp 313–348. DOI: 10.1021/cr60307a002.
- Tolman, C. A. Phosphorus Ligand Exchange Equilibria on Zerovalent Nickel. Dominant Role for Steric Effects. *J. Am. Chem. Soc.* **1970**, *92* (10), pp 2956–2965. DOI: 10.1021/ja00713a007.
- Poater, A.; Ragone, F.; Giudice, S.; Costabile, C.; Dorta, R.; Nolan, S. P.; Cavallo, L. Thermodynamics of *N*-Heterocyclic Carbene Dimerization: The Balance of Sterics and Electronics. *Organometallics* **2008**, *27* (12), pp 2679–2681. DOI: 10.1021/om8001119.

- (14) Falivene, L.; Cao, Z.; Petta, A.; Serra, L.; Poater, A.; Oliva, R.; Scarano, V.; Cavallo, L. Towards the Online Computer-Aided Design of Catalytic Pockets. *Nat. Chem.* **2019**, *11* (10), pp 872–879. DOI: 10.1038/s41557-019-0319-5.
- (15) Poater, A.; Cosenza, B.; Correa, A.; Giudice, S.; Ragone, F.; Scarano, V.; Cavallo, L. SambVca: A Web Application for the Calculation of the Buried Volume of *N*-Heterocyclic Carbene Ligands. *Eur. J. Inorg. Chem.* **2009**, *2009* (13), pp 1759–1766. DOI: 10.1002/ejic.200801160.
- (16) Clavier, H.; Nolan, S. P. Percent Buried Volume for Phosphine and *N*-Heterocyclic Carbene Ligands: Steric Properties in Organometallic Chemistry. *Chem. Commun.* **2010**, *46* (6), p 841. DOI: 10.1039/b922984a.
- (17) Strohmeier, W.; Guttenberger, J. F. S-Haltige Verbindungen Als Liganden in Photochemisch Hergestellten Derivaten Des Cyclopentadienylmangantricarbonyls. *Chem. Ber.* **1964**, *97* (7), pp 1871–1876. DOI: 10.1002/cber.19640970714.
- (18) Horrocks, W. D.; Taylor, R. C. Infrared Spectroscopic Study of Derivatives of Cobalt Tricarbonyl Nitrosyl. *Inorg. Chem.* **1963**, *2* (4), pp 723–727. DOI: 10.1021/ic50008a013.
- (19) Magee, T. A.; Matthews, C. N.; Wang, T. S.; Wotiz, J. H. Organic Derivatives of Chromium, Molybdenum and Tungsten Carbonyls. *J. Am. Chem. Soc.* **1961**, *83* (15), pp 3200–3203. DOI: 10.1021/ja01476a008.
- (20) Bond, A. M.; Carr, S. W.; Colton, R. Study of Substituent Effects, Isomerization and Cross Redox Reactions Associated with Electrochemical Oxidation of Mo(CO)<sub>3</sub>P<sub>3</sub> Systems. *Organometallics* **1984**, *3* (4), pp 541–548. DOI: 10.1021/om00082a005.
- (21) Grim, S. O.; Wheatland, D. A.; McFarlane, W. Phosphorus-31 Nuclear Magnetic Resonance Study of Tertiary Phosphine Derivatives of Group VI Metal Carbonyls. *J. Am. Chem. Soc.* **1967**, *89* (22), pp 5573–5577. DOI: 10.1021/ja00998a012.
- (22) Strohmeier, W.; Müller, F. J. Notizen:  $\pi$ -Acceptorstärke von Phosphinen Als Liganden in Cyclopentadienylmangantricarbonyl Und Nickelcarbonyl. *Zeitschrift für Naturforsch. B* **1967**, *22* (4), pp 451–452. DOI: 10.1515/znb-1967-0416.
- (23) Cotton, F. A. Vibrational Spectra and Bonding in Metal Carbonyls. III. Force Constants and Assignments of CO Stretching Modes in Various Molecules; Evaluation of CO Bond Orders. *Inorg. Chem.* **1964**, *3* (5), pp 702–711. DOI: 10.1021/ic50015a024.
- (24) Alyea, E. C.; Ferguson, G.; Somogyvari, A. Crystal and Molecular Structures of Mo(CO)<sub>5</sub>P(*p*-Tol)<sub>3</sub> and Mo<sub>2</sub>(CO)<sub>8</sub>P(*p*-Tol)<sub>3</sub> and Spectral Properties of Related  $\sigma$ - and  $\pi$ -Bonded Phosphine Complexes. *Organometallics* **1983**, *2* (5), pp 668–674. DOI: 10.1021/om00077a016.
- (25) Dalton, J.; Paul, I.; Smith, J. G.; Stone, F. G. A. Spectroscopic Studies on Organometallic Compounds. Part XI. Infrared Spectra of Pentacarbonyl Complexes of Metals of the Chromium and Manganese Sub-Groups in the Carbonyl Stretching Region. *J. Chem. Soc. A Inorganic, Phys. Theor.* **1968**, p 1195. DOI: 10.1039/j19680001195.
- (26) Brown, R. A.; Dobson, G. R. Octahedral Metal Carbonyls. XXI. Carbonyl and Metal-Carbon Stretching Spectra of Monosubstituted Group VIB Metal Carbonyls. *Inorganica Chim. Acta* **1972**, *6*, pp 65–71. DOI: 10.1016/S0020-1693(00)91760-2.
- (27) Woodard, S. S.; Angelici, R. J.; Dombek, B. D. Carbon-13 Nuclear Magnetic Resonance, Infrared, and Equilibrium Studies of Cis- and Trans-W(CO)<sub>4</sub>(CS)L Complexes. *Inorg. Chem.* **1978**, *17* (6), pp 1634–1639. DOI: 10.1021/ic50184a049.
- (28) Angelici, R. J.; Sister Mary Diana Malone. Infrared Studies of Amine, Pyridine, and Phosphine Derivatives of Tungsten Hexacarbonyl. *Inorg. Chem.* **1967**, *6* (9), pp 1731–1736. DOI: 10.1021/ic50055a026.
- (29) Bancroft, G. M.; Dignard-Bailey, L.; Puddephatt, R. J. Spectroscopic Study of the Effect of Methyl and Phenyl Substituents on the Basicity of Phosphine Ligands in Tungsten Carbonyl Derivatives. *Inorg. Chem.* **1986**, *25* (20), pp 3675–3680. DOI: 10.1021/ic00240a031.
- (30) Barnard, T. S.; Mason, M. R. Hindered Axial–Equatorial Carbonyl Exchange in an Fe(CO)<sub>4</sub>(PR<sub>3</sub>) Complex of a Rigid Bicyclic Phosphine. *Inorg. Chem.* **2001**, *40* (19), pp 5001–5009. DOI: 10.1021/ic001372b.
- (31) Darensbourg, D. J.; Nelson, H. H.; Hyde, C. L. Detailed Analysis of the Carbonyl Stretching Vibrations in Axial and Equatorial Substituted Iron Carbonyl Compounds. Absolute Infrared Intensities and Force Constants of the Carbonyl Ligands. *Inorg. Chem.* **1974**, *13* (9), pp 2135–2145. DOI: 10.1021/ic50139a017.
- (32) Cunningham, D.; Goldschmidt, Z.; Gottlieb, H. E.; Hezroni-Langerman, D. Influence of Phosphine Conformation on the Structure and Stereodynamics of Tetracarbonyl(Tri-*o*-Tolylphosphine)Iron and Pentacarbonyl(Tri-*o*-Tolylphosphine)Chromium. *Inorg. Chem.* **1991**, *30* (25), pp 4683–4685. DOI: 10.1021/ic00025a001.

- (33) Inoue, H.; Nakagome, T.; Kuroiwa, T.; Shirai, T.; Fluck, E. Infrared,  $^{57}\text{Fe}$  Mössbauer, and  $^{31}\text{P}$  NMR Spectroscopic Characterization of  $\text{Fe}(\text{CO})_4\text{L}$  (L = Phosphine and Phosphite). *Zeitschrift für Naturforsch. B* **1987**, *42* (5), pp 573–578. DOI: 10.1515/znb-1987-0510.
- (34) Smith, R. T.; Baird, M. C. Metal Carbonyl Derivatives of a Water Soluble Phosphine. *Inorganica Chim. Acta* **1982**, *62*, pp 135–139. DOI: 10.1016/S0020-1693(00)88492-3.
- (35) Howell, J. A. ; Lovatt, J. D.; McArdle, P.; Cunningham, D.; Maimone, E.; Gottlieb, H. E.; Goldschmidt, Z. The Effect of Fluorine, Trifluoromethyl and Related Substitution on the Donor Properties of Triarylphosphines towards  $[\text{Fe}(\text{CO})_4]$ . *Inorg. Chem. Commun.* **1998**, *1* (3), pp 118–120. DOI: 10.1016/S1387-7003(98)00021-5.
- (36) Otto, S.; Roodt, A. Quantifying the Electronic Cis Effect of Phosphine, Arsine and Stibine Ligands by Use of Rhodium(I) Vaska-Type Complexes. *Inorganica Chim. Acta* **2004**, *357* (1), pp 1–10. DOI: 10.1016/S0020-1693(03)00436-5.
- (37) Serron, S.; Huang, J.; Nolan, S. P. Solution Thermochemical Study of Tertiary Phosphine Ligand Substitution Reactions in the  $\text{Rh}(\text{Acac})(\text{CO})(\text{PR}_3)$  System. *Organometallics* **1998**, *17* (4), pp 534–539. DOI: 10.1021/om970766g.
- (38) Roodt, A.; Otto, S.; Steyl, G. Structure and Solution Behaviour of Rhodium(I) Vaska-Type Complexes for Correlation of Steric and Electronic Properties of Tertiary Phosphine Ligands. *Coord. Chem. Rev.* **2003**, *245* (1–2), pp 121–137. DOI: 10.1016/S0010-8545(03)00069-9.
- (39) Fürstner, A.; Alcarazo, M.; Krause, H.; Lehmann, C. W. Effective Modulation of the Donor Properties of *N*-Heterocyclic Carbene Ligands by “Through-Space” Communication within a Planar Chiral Scaffold. *J. Am. Chem. Soc.* **2007**, *129* (42), pp 12676–12677. DOI: 10.1021/ja076028t.
- (40) Canac, Y.; Lepetit, C.; Abdalilah, M.; Duhayon, C.; Chauvin, R. Diaminocarbene and Phosponium Ylide Ligands: A Systematic Comparison of Their Donor Character. *J. Am. Chem. Soc.* **2008**, *130* (26), pp 8406–8413. DOI: 10.1021/ja801159v.
- (41) Nonnenmacher, M.; Buck, D. M.; Kunz, D. Experimental and Theoretical Investigations on the High-Electron Donor Character of Pyrido-Annulated *N*-Heterocyclic Carbenes. *Beilstein J. Org. Chem.* **2016**, *12*, pp 1884–1896. DOI: 10.3762/bjoc.12.178.
- (42) Huynh, H. V. Electronic Properties of *N*-Heterocyclic Carbenes and Their Experimental Determination. *Chem. Rev.* **2018**, *118* (19), pp 9457–9492. DOI: 10.1021/acs.chemrev.8b00067.
- (43) Kelly III, R. A.; Clavier, H.; Giudice, S.; Scott, N. M.; Stevens, E. D.; Bordner, J.; Samardjiev, I.; Hoff, C. D.; Cavallo, L.; Nolan, S. P. Determination of *N*-Heterocyclic Carbene (NHC) Steric and Electronic Parameters Using the  $[(\text{NHC})\text{Ir}(\text{CO})_2\text{Cl}]$  System. *Organometallics* **2008**, *27* (2), pp 202–210. DOI: 10.1021/om701001g.
- (44) Dicks, A. P. Using Hydrocarbon Acidities To Demonstrate Principles of Organic Structure and Bonding. *J. Chem. Educ.* **2003**, *80* (11), p 1322. DOI: 10.1021/ed080p1322.
- (45) Konishi, S.; Iwai, T.; Sawamura, M. Synthesis, Properties, and Catalytic Application of a Triptycene-Type Borate-Phosphine Ligand. *Organometallics* **2018**, *37* (12), pp 1876–1883. DOI: 10.1021/acs.organomet.8b00113.
- (46) Cremer, D.; Kalescky, R.; Kraka, E. New Approach to Tolman’s Electronic Parameter Based on Local Vibrational Modes. *Inorg. Chem.* **2014**, *53* (1), pp 478–495. DOI: 10.1021/ic4024663.
- (47) Gusev, D. G. Donor Properties of a Series of Two-Electron Ligands. *Organometallics* **2009**, *28* (3), pp 763–770. DOI: 10.1021/om800933x.
- (48) Van Rentergem, M.; Van Der Kelen, G. P.; Claeys, E. C. Study of the Co-Stretching Frequencies and Intensities in Metal-Carbonyl Compounds. Part I. The Compounds  $\text{LFe}(\text{CO})_4$  with L an Organophosphorous Ligand. *J. Mol. Struct.* **1982**, *80*, pp 317–324. DOI: 10.1016/0022-2860(82)87249-9.
- (49) Martin, L. R.; Einstein, F. W. B.; Pomeroy, R. K. Axial-Equatorial Isomerism in the Pentacoordinate Complexes  $\text{M}(\text{CO})_4(\text{EPh}_3)$  (M = Fe, Ru, Os; E = P, As, Sb). *Inorg. Chem.* **1983**, *22* (14), pp 1959–1961. DOI: 10.1021/ic00156a001.
- (50) Udovich, C. A.; Clark, R. J.; Haas, H. Stereochemical Nonrigidity in Iron Carbonyl Fluorophosphine Compounds. *Inorg. Chem.* **1969**, *8* (5), pp 1066–1072. DOI: 10.1021/ic50075a009.
- (51) Kroshefsky, R. D.; Verkade, J. G.; Pipal, J. R. COORDINATION PROPERTIES OF CONSTRAINED AMINOPHOSPHINES. *Phosphorous Sulfur Relat. Elem.* **1979**, *6* (3), pp 377–389. DOI: 10.1080/03086647908069897.
- (52) Li, H.; Aquino, A. J. A.; Cordes, D. B.; Hase, W. L.; Krempner, C. Electronic Nature of Zwitterionic Alkali Metal Methanides, Silanides and Germanides – a Combined Experimental and Computational Approach. *Chem. Sci.* **2017**, *8* (2), pp 1316–1328. DOI: 10.1039/C6SC02390H.
- (53) Denk, M.; Green, J. C.; Metzler, N.; Wagner, M. Electronic Structure of a Stable Silylene: Photoelectron Spectra and Theoretical Calculations of  $\text{Si}(\text{NRCHCHNR})$ ,  $\text{Si}(\text{NRCH}_2\text{CH}_2\text{NR})$  and

- SiH<sub>2</sub>(NRCHCHNR). *J. Chem. Soc. Dalton Trans.* **1994**, No. 16, pp 2405–2410. DOI: 10.1039/dt9940002405.
- (54) Kong, L.; Zhang, J.; Song, H.; Cui, C. *N*-Aryl Substituted Heterocyclic Silylenes. *Dalt. Trans.* **2009**, No. 28, pp 5444–5446. DOI: 10.1039/b905905a.
- (55) So, C.-W.; Roesky, H. W.; Gurubasavaraj, P. M.; Oswald, R. B.; Gamer, M. T.; Jones, P. G.; Blaurock, S. Synthesis and Structures of Heteroleptic Silylenes. *J. Am. Chem. Soc.* **2007**, *129* (39), pp 12049–12054. DOI: 10.1021/ja074019e.
- (56) Matthews, W. S.; Bares, J. E.; Bartmess, J. E.; Bordwell, F. G.; Cornforth, F. J.; Drucker, G. E.; Margolin, Z.; McCallum, R. J.; McCollum, G. J.; Vanier, N. R. Equilibrium Acidities of Carbon Acids. VI. Establishment of an Absolute Scale of Acidities in Dimethyl Sulfoxide Solution. *J. Am. Chem. Soc.* **1975**, *97* (24), pp 7006–7014. DOI: 10.1021/ja00857a010.
- (57) Bordwell, F. G.; Branca, J. C.; Bares, J. E.; Filler, R. Enhancement of the Equilibrium Acidities of Carbon Acids by Polyfluoroaryl Substituents. *J. Org. Chem.* **1988**, *53* (4), pp 780–782. DOI: 10.1021/jo00239a016.
- (58) Bordwell, F. G.; Branca, J. C.; Hughes, D. L.; Olmstead, W. N. Equilibria Involving Organic Anions in Dimethyl Sulfoxide and *N*-Methylpyrrolidin-2-One: Acidities, Ion Pairing, and Hydrogen Bonding. *J. Org. Chem.* **1980**, *45* (16), pp 3305–3313. DOI: 10.1021/jo01304a034.
- (59) Truflandier, L. A.; Brendler, E.; Wagler, J.; Autschbach, J. <sup>29</sup>Si DFT/NMR Observation of Spin-Orbit Effect in Metallasilatrane Sheds Some Light on the Strength of the Metal→Silicon Interaction. *Angew. Chemie Int. Ed.* **2011**, *50* (1), pp 255–259. DOI: 10.1002/anie.201005431.

*The voices of the suns of midnight call us...  
Our eyes are lost in telescopes' wells.  
The stars' and planets' diamonds constell  
In nebulae's and clusters' whirls and corals.*

*From Alpha Canis to the Capricornus  
To Seven Sisters to the Argo's Sail  
They cross the heavens telling their tale,  
The seekers, perseverers and owners.*

*Oh dust of planets! Swarm of holy bees!  
I measured, weighed and totaled all of these,  
I gave them names, and balances, and contours...*

*But knowledge made not stellar fear fade.  
Our memories of darkest ages stayed,  
Evaded holy bath in Lethe's cold course!*

Alex Romanovsky, translator  
"Corona Astralis", Sonnet IV  
By Maximilian Voloshin, 1909



